DEVELOPMENT OF A COUPLED FLUID/STRUCTURE AEROELASTIC SOLVER WITH APPLICATIONS TO VORTEX BREAKDOWN INDUCED TWIN TAIL BUFFETING

by

Steven J. Massey
B.S. May 1990, Virginia Polytechnic Institute & State University, Blacksburg, VA
M.S. May 1994, Old Dominion University, Norfolk, VA

A Dissertation Submitted to the Faculty of
Old Dominion University in Partial Fulfillment of the
Requirement for the Degree of

DOCTOR OF PHILOSOPHY

AEROSPACE ENGINEERING

OLD DOMINION UNIVERSITY
December 1997

Approved by:

Osama A. Kandil (Director)

Norman F. Knight, Jr.

Colin P. Britcher

Robert Bennett (LaRC)

Woodrow Whitlow, Jr. (LaRC)

DEVELOPMENT OF A COUPLED FLUID/STRUCTURE AEROELASTIC SOLVER WITH APPLICATIONS TO VORTEX BREAKDOWN INDUCED TWIN TAIL BUFFETING

©1997 Old Dominion University. All rights reserved.

ABSTRACT

DEVELOPMENT OF A COUPLED FLUID/STRUCTURE AEROELASTIC SOLVER WITH APPLICATIONS TO VORTEX BREAKDOWN INDUCED TWIN TAIL BUFFETING

Steven J. Massey
Old Dominion University
Director: Dr. Osama A. Kandil

Simulation of tail buffet is studied for several delta wing-vertical tail configurations. Flow conditions are chosen such that the wing primary-vortex cores experience vortex breakdown and the resulting turbulent wake flow impinges on the vertical tail. The dimensions and material properties of the vertical tails are chosen such that the deflections are large enough to insure interaction with the flow, and the natural frequencies are high enough to facilitate a practical computational solution. This multi-disciplinary problem is solved sequentially for the fluid flow, the elastic deformations and the grid displacements. The flow is simulated by time accurately solving the laminar, unsteady, compressible, Navier-Stokes equations using an implicit, upwind, flux-difference splitting, finite volume scheme. The elastic vibrations of the tail are modeled by coupled bending and torsion beam equations. These equations are solved accurately in time using the Galerkin method and a five-stage, Runge-Kutta-Verner scheme. The grid for the fluid dynamics calculations is continuously deformed using interpolation functions to smoothly disperse the displacements throughout the computational domain. Tail buffet problems are solved for single tail cases, twin F/A-18 tail cases and twin highly swept generic tail cases. The use of an apex flap for buffet control is also computationally studied. The results demonstrate the effects of inertial structural coupling, Reynolds number, aft

fuselage geometry and spanwise tail location on the tail buffet loads and response. Favorable comparisons with experimental data indicate that the present aeroelastic method is well suited to providing qualitative insight into the tail buffet problem, as well as, quantitative data for refined long duration simulations.

ACKNOWLEDGEMENTS

I would like to express my sincerest appreciation to my dissertation advisor, Prof. Osama A. Kandil, who has provided invaluable guidance and support since the beginning of my master's research in 1992. His high standards of mathematical rigor have made an indelible impression on me and will surely be a great asset in an era of increasing reliance by many on numerical black boxes. As I now enter industry, I look forward to continuing our profitable collaboration on new research projects.

Appreciation is also extended to the members of my dissertation committee, Prof. Norman F. Knight, Prof. Colin P. Britcher of ODU and Dr. Robert M. Bennett and Dr. Woodrow Whitlow, Jr. of NASA Langley Research Center, for reviewing this dissertation and their many insightful comments. Their impressive careers in structural dynamics, unsteady aerodynamics and aeroelasticity, to name a few, add a great deal of credibility to this study.

Special thanks to Dr. Thomas Noll, head of the Aeroelasticity Branch at NASA LaRC, and Dr. Robert Bennett, grant monitor, for their financial support under Grant No. NAG-1-648. Computational resources were provided by NASA Langley Research Center and the Numerical Aerodynamic Simulation (NAS) Program of NASA Ames Research Center, without which this research would not have been possible.

Finally, I would like to express my love, gratitude and appreciation to my wife, Lisa, for her unending love and extreme patience. I am indebted to my parents and extended family in every way and it is now my sincere goal, and will be my distinct pleasure, to begin a lifelong repayment to each of them for the life they have given me.

NOMENCLATURE

English Symbols

A	attachment line
$A(f)$	amplitude of function f
a	local speed of sound
$\vec{a}_t$	absolute acceleration of the tail
b	beam width
d	beam thickness
$\mathcal{C}$	saddle point
C	Sutherland constant
c	wing root chord
$\overline{\overline{c}}$	mean wing aerodynamic chord
c_p	constant pressure specific heat
c_v	constant volume specific heat
E	modulus of elasticity
$\vec{E}_m$	inviscid flux vector
$(\vec{E}_m)_v$	viscous flux vector
e_t	total energy per unit mass
$\mathcal{F}$	spiral saddle point (focus in 2-D)
G	modulus of rigidity
I	area moment of inertia
$I_{zz_{CM}}$	mass moment of inertia about the tail span axis
I_θ	mass moment of inertia about the elastic axis

J	polar moment of inertia, coordinate transformation Jacobian
K	turbulent-kinetic-energy, structural stiffness matrix
k	thermal conductivity coefficient
L	vertical tail length
ℓ	characteristic length
M	integrated moment per unit length on tail, structural mass matrix
M_{RB}	root bending moment
M_{RT}	root twisting moment
m	mass per unit length
N	integrated force per unit length on tail
$n_d i$	i^{th} dominant frequency
p	static pressure
p_0	total pressure
Q	generalized aerodynamic force vector for structural calculations
$q(t)$	generalized structural coordinate
q	heat flux per unit area, dynamic pressure
$\vec{Q}$	vector of conserved flow variables in generalized coordinates
$\vec{q}$	vector of conserved flow variables in Cartesian coordinates
$R^{\pm}$	1-D Riemann invariants
S	separation line
S_t	tail plan area
s_1	wing semispan
T	temperature; kinetic energy
t	time

U	characteristic velocity component
U_m	contravariant velocity component
$\vec{V}$	velocity vector
V	elastic potential energy
W	total work done on tail by aerodynamic loading
w	bending deflection of tail
$u, v, w; u_i$	Cartesian velocity components
x_θ	distance between the elastic and inertial axes
x_s	x coordinate along Λ_s cutting plane
$x, y, z; x_i$	Cartesian coordinates

Greek Symbols

α	angle-of-attack
β	angle-of-yaw, apex flap deflection angle
δ	virtual displacement operator
δ_{ij}	Kronecker delta tensor
ϵ	turbulent dissipation
γ	ratio of specific heats, c_p/c_v
θ	angle of twisting displacement
Λ_s	leading-edge sweep angle
λ	second coefficient of viscosity
μ	molecular viscosity
Ω	characteristic angular velocity magnitude
ϕ	free vibration modes for bending and torsion
ρ	density

τ_{ij}	viscous shear stress tensor
ω	natural frequency
ξ^i	computational coordinates

Dimensionless Groups

C_M	moment per unit length, $\frac{M}{q_\infty S_t}$
C_N	force per unit length, $\frac{N}{q_\infty \bar{\bar{c}}}$
C_p	coefficient of pressure, $\frac{p}{q_\infty}$
C_{RBM}	coefficient of root bending moment, $\frac{M_{RB}}{q_\infty S_t \bar{\bar{c}}}$
C_{RTM}	coefficient of root twisting moment, $\frac{M_{RT}}{q_\infty S_t \bar{\bar{c}}}$
M	Mach number, $\frac{U}{a}$
n	reduced frequency, $\frac{f\bar{\bar{c}}}{U_\infty}$
Pr	Prandtl number, $\frac{\mu c_p}{k}$
Re	root chord Reynolds number, $\frac{\rho U c}{\mu}$
Ro	Rossby number, $\frac{U}{\ell\Omega}$
τ	nondimensional time, $\frac{tU_\infty}{\bar{\bar{c}}}$

Subscripts

∞	far field
$\forall$	volume

Superscripts

$\sim$	dimensional quantities
$\rightarrow$	vector in Cartesian coordinates
$^-$	vector in computational coordinates

CONTENTS

LIST OF FIGURES **xiii**

LIST OF TABLES **xxix**

1 INTRODUCTION **1**
1.1 Motivation . . . 1
1.2 The Present Research . . . 3

2 LITERATURE REVIEW **8**
2.1 Introduction . . . 8
2.2 Vortex Breakdown . . . 8
2.2.1 Historical Perspective . . . 8
2.2.1.1 The Discovery of Vortex Lift . . . 8
2.2.1.2 Early Observations of Vortex Breakdown . . . 9
2.2.2 Physical Characteristics and Topology of Vortex Breakdown . . . 13
2.2.3 Numerical Simulations of Vortex Breakdown . . . 24
2.3 Vortex Breakdown Induced Tail Buffeting . . . 26
2.3.1 Historical Perspective . . . 26
2.3.2 Physical Characteristics of Tail Buffeting . . . 27
2.3.3 Numerical Simulation of Tail Buffeting . . . 30
2.4 Vortex Control Techniques . . . 33

3 FLUID DYNAMICS FORMULATION **36**
3.1 Introduction . . . 36
3.2 Three-Dimensional Navier-Stokes Equations . . . 36
3.3 Computational Fluid Dynamics Formulation . . . 40
3.3.1 Introduction . . . 40
3.3.2 Nondimensionalization . . . 40
3.3.3 Implicit Upwind Conservative Schemes . . . 42
3.3.4 Cell-Centered Finite Volume Formulation . . . 43
3.3.5 Euler Implicit Time Integration . . . 44
3.3.6 Approximate Factorization . . . 45
3.3.7 Roe Flux Difference Splitting . . . 46
3.3.8 Discretization of Viscous Fluxes . . . 50
3.4 Initial and Boundary Conditions . . . 50
3.4.1 Initial Conditions . . . 50
3.4.2 Surface Boundary Conditions . . . 51
3.4.3 Far-Field Boundary Conditions . . . 51
3.4.4 Block Interface Boundary Conditions . . . 52
3.5 Structured CFD Grid Construction Methodology . . . 53
3.5.1 Introduction . . . 53
3.5.2 Single Block Grid . . . 54
3.5.3 Multiblock Grids . . . 57

3.5.4 Grid Motion Algorithm 60

4 STRUCTURAL DYNAMICS FORMULATION 61
4.1 Introduction 61
4.2 Derivation of the Structural Dynamics Equations 61
4.3 Boundary and Initial Conditions 68
4.4 Computational Structural Dynamics Formulation 68
4.5 Multidisciplinary Solution Methodology 72

5 SINGLE SQUARE VERTICAL TAIL BUFFETING 74
5.1 Introduction 74
5.2 Computational Model 75
5.2.1 Model Geometry and Computational Domain 75
5.2.2 Freestream Flow Conditions 76
5.2.3 Tail Material Properties 76
5.3 Low Reynolds Number Cases: $Re = 10^4$ 86
5.3.1 Initial Condition Flow Field 86
5.3.2 Uncoupled Bending and Torsion Response 107
5.3.3 Coupled Bending and Torsion Response 124
5.4 High Reynolds Number Cases: $Re = 10^6$ 137
5.4.1 Initial Condition Flow Field 137
5.4.2 Rigid Tail Load History 149
5.4.3 Uncoupled Bending and Torsion Response 160
5.4.4 Coupled Bending and Torsion Response 173
5.5 Summary 184

6 EFFECT OF AFT FUSELAGE ON TWIN F/A-18 VERTICAL TAIL BUFFETING 187
6.1 Introduction 187
6.2 Wide Fuselage Model 189
6.2.1 Model Geometry and Computational Domain 189
6.2.2 Freestream Flow Conditions 192
6.2.3 Tail Material Properties 192
6.2.4 Initial Conditions, $Re = 10^6$, $M = 0.4$, $\alpha = 30^o$ 193
6.2.5 Load Histories for Rigid Tails 201
6.2.6 Uncoupled Bending and Torsion Response 207
6.3 Narrow Fuselage Model 215
6.3.1 Model Geometry and Computational Domain 215
6.3.2 Freestream Flow Conditions and Tail Material Properties 217
6.3.3 Initial Conditions, $Re = 10^6$, $M = 0.4$, $\alpha = 30^o$ 217
6.3.4 Load Histories for Rigid Tails 223
6.3.5 Uncoupled Bending and Torsion Response 228
6.3.5.1 Comparison with Experimental Data 236
6.4 Open Fuselage Model 239
6.4.1 Model Geometry and Computational Domain 239
6.4.2 Freestream Flow Conditions and Tail Material Properties 241
6.4.3 Initial Conditions, $Re = 0.75 \times 10^6$, $M = 0.3$, $\alpha = 30^o$ 241

6.4.4 Uncoupled Bending and Torsion Response 247
6.4.5 Summary 256

7 EFFECT OF SPANWISE TAIL LOCATION ON TWIN WASHBURN VERTICAL TAIL BUFFETING 258
7.1 Introduction 258
7.2 Model Geometry and Computational Domain 258
7.3 Freestream Flow Conditions 262
7.4 Tail Material Properties 262
7.5 Inboard Twin Tail Model 263
7.5.1 Initial Conditions, $Re = 1.25 \times 10^6$, $M = 0.3$, $\alpha = 35^o$ 263
7.5.2 Uncoupled Bending and Torsion Response 270
7.6 Midspan Twin Tail Case 277
7.6.1 Initial Conditions, $Re = 1.25 \times 10^6$, $M = 0.3$, $\alpha = 35^o$ 277
7.6.2 Uncoupled Bending and Torsion Response 284
7.7 Outboard Twin Tail Model 291
7.7.1 Initial Conditions, $Re = 1.25 \times 10^6$, $M = 0.3$, $\alpha = 35^o$ 291
7.7.2 Uncoupled Bending and Torsion Response 297
7.8 Experimental Validation 304
7.9 Summary 306

8 CONTROL OF TWIN TAIL BUFFETING 308
8.1 Introduction 308
8.2 Initial Conditions 309
8.3 Uncoupled Bending and Torsion Response 317
8.4 Summary 321

9 CONCLUSIONS 322
9.1 Overview 322
9.2 Recommendations for Future Research 327

REFERENCES 328

VITA 334

LIST OF FIGURES

1.1 F-18 HARV smoke and tuft flow visualization for a) $\alpha = 20^o$ b) 25^o and c) 30^o. $M = 0.24$, $Re = 11 \times 10^6$. *NASA Dryden* EC89-0096-206, EC89-0096-226 and EC89-0096-240 6
1.2 Flight data reconstruction of *post-stall reversal* also known as a Herbst turn or J-turn. *NASA Dryden* [1] 7
1.3 Flight data reconstruction of an *offensive spiral* also known as a helicopter gun attack. *NASA Dryden* [1] 7

2.1 Effect of Reynolds number on vortex breakdown on a 63^o delta wing. Retouched and shown in negative. *top*: $\alpha = 20^o$, $Re_c = 5000$; *bottom*: $\alpha = 20^o$, $Re_c = 10,000$. Note; the photo of the bottom wing was warped and has been retouched. Werlé [2]. 11
2.2 Sketch of spiral type vortex breakdown [3]. 12
2.3 Vortex breakdown on a 65^o delta wing in water, $Re = 10^4$ [3]. 14
2.4 Axisymmetric vortex breakdown in a swirling flow through a pipe at moderate (*top*) and slightly higher (*bottom*) inlet swirl ratios. Sarpkaya [4]. 15
2.5 Classification of 2-D (*left*) and 3-D (*right*) critical points by local velocity, Globus et al. [5]. 17
2.6 Sketch of shear layers resulting from boundary layer separations for a sharp edged delta wing at a moderate angle-of-attack with no breakdown. Délery [6]. 18
2.7 Topological sketch of a typical delta wing crossflow plane. Délery [6]. . . 18
2.8 Hydrogen bubble flow visualization of a crossflow plane above a sharp 76^o delta wing in water, $Re = 20,000$, $\alpha = 20^o$. Werlé [7]. 19
2.9 Topological sketch of the left aft wing surface showing skin friction lines, and separation and attachment lines. Délery [6]. 19
2.10 Streamlines plotted on an axial plane showing a typical vortex breakdown topology from computed results for a 76^o delta wing at $\alpha = 35^o$, $Re = 1.25 \times 10^6$, $M = 0.3$. See Chapter 7. 22
2.11 In plane velocity vectors with marked and labeled critical points, $\alpha = 35^o$, $Re = 1.25 \times 10^6$, $M = 0.3$. See Chapter 7. 23
2.12 Contours of the velocity component normal to the axial cutting plane. Dashed lines indicate velocities pointing out of the page. Critical point locations obtained from streamlines are also plotted. $\alpha = 35^o$, $Re = 1.25 \times 10^6$, $M = 0.3$. See Chapter 7. 23
2.13 Contours of total pressure, and labeled critical point locations showing the vortex core expansion following breakdown. $\alpha = 35^o$, $Re = 1.25 \times 10^6$, $M = 0.3$. See Chapter 7. 23
2.14 LEX fence shown a) installed and with b) front and c) top-view flow field topology sketches. Lee and Valerio [8] 35

3.1 Typical crossflow plane at showing the elliptic cone surrounding the trailing edge of the delta wing. 55
3.2 Body grid surfaces for the single square tail configuration. 56
3.3 Symmetry plane and half grid showing streamwise clustering in the single tail configuration. 56
3.4 Five (left) and six (right) block grid structure, showing all block boundaries. 57
3.5 Example of highly stretched grid blocks for a five block configuration. . . 58
3.6 Example cosine-based grid weighting functions. 59

4.1 Delta wing, single vertical tail configuration, showing typical elastic and inertial axes locations. 62
4.2 Sketch of orientations for bending (*left*), torsion (*right*), and combined bending and torsion (*center*). 63

5.1 Fine grid: $83 \times 124 \times 84$ cells. Full and half views showing stream-wise clustering. 78
5.2 Fine grid: $83 \times 124 \times 84$ cells. Full and close-up views showing the crossflow *i-plane* at the wing trailing edge. 79
5.3 Fine grid: $83 \times 124 \times 84$ cells. Full symmetry *j-plane*. 80
5.4 Fine grid: View of symmetry *j-plane* from wing apex to trailing edge of tail. 81
5.5 Fine grid: $83 \times 124 \times 84$ cells. Upper wing surface; 30×64 cells. Tail surface 15×40 cells. 81
5.6 Coarse grid: $83 \times 64 \times 42$ cells. Full and half views showing stream-wise clustering. 82
5.7 Coarse grid: $83 \times 64 \times 42$ cells. Full and close-up views showing the crossflow *i-plane* at the wing trailing edge. 83
5.8 Coarse grid: $83 \times 64 \times 42$ cells. Full symmetry *j-plane*. 84
5.9 Coarse grid: View of symmetry *j-plane* from wing apex to trailing edge of tail. 85
5.10 Coarse grid: $83 \times 64 \times 42$ cells. Upper wing surface; 30×32 cells. Tail surface 15×20 cells. 85
5.11 Three-dimensional and top views of surface pressure and vortex core streamlines. Initial Condition Flow Field: $Re = 10^4$, $M = 0.4$, $\alpha = 38^o$. . 93
5.12 a) Three-dimensional view of total pressure colored vortex core streamlines. b) Three-dimensional view of $j = 13$ plane colored with total pressure slicing through vortex core streamlines. Initial Condition Flow Field: $Re = 10^4$, $M = 0.4$, $\alpha = 38^o$. 94
5.13 a) Side view at incidence showing surface pressure and vortex core streamlines. b) close-up side view, $x = [0, 0.4]$, showing total pressure colored vortex core streamlines. Initial Condition Flow Field: $Re = 10^4$, $M = 0.4$, $\alpha = 38^o$. 95
5.14 Side and three-dimensional views of in-plane streamlines plotted on an opaque vertical plane ($\Lambda_p = 82^o$) slicing through three-dimensional vortex core streamlines. Initial Condition Flow Field: $Re = 10^4$, $M = 0.4$, $\alpha = 38^o$. 96

5.15 Close-up views of in-plane streamlines plotted on opaque and transparent vertical planes ($\Lambda_p = 82^o$) slicing through the three-dimensional vortex core streamlines. Initial Condition Flow Field: $Re = 10^4$, $M = 0.4$, $\alpha = 38^o$. 97
5.16 a) Streamlines, b) velocity vectors, c) normal Mach contours and d) total pressure contours plotted on a vertical plane which bisects the vortex core. Initial Condition Flow Field: $Re = 10^4$, $M = 0.4$, $\alpha = 38^o$. 98
5.17 Contours of total pressure coefficient plotted on a vertical plane which bisects the vortex core. Initial Condition Flow Field: $Re = 10^4$, $M = 0.4$, $\alpha = 38^o$. 99
5.18 Computational surface oil flow plotted using the Line Integral Convolution algorithm of Cabral and Leedom [9]. Initial Condition Flow Field: $Re = 10^4$, $M = 0.4$, $\alpha = 38^o$. 99
5.19 Comparison of computational wing surface oil flow with streamlines restricted to the $k = 2$ plane. Initial Condition Flow Field: $Re = 10^4$, $M = 0.4$, $\alpha = 38^o$. 100
5.20 Comparison of computational tail surface oil flows with streamlines restricted to the $j = 2$ plane for the right side and $j = jdim - 1$ for the left side. Initial Condition Flow Field: $Re = 10^4$, $M = 0.4$, $\alpha = 38^o$. . . . 101
5.21 Mach number on the $k = 2$ plane above wing, surface pressure and pressure coefficient on wing surface. Initial Condition Flow Field: $Re = 10^4$, $M = 0.4$, $\alpha = 38^o$. 102
5.22 Coefficient of pressure on right and left sides of tail, and differential pressure coefficient. Initial Condition Flow Field: $Re = 10^4$, $M = 0.4$, $\alpha = 38^o$. 103
5.23 Total pressure coefficient and streamlines plotted on vertical crossflow planes above wing. Initial Condition Flow Field: $Re = 10^4$, $M = 0.4$, $\alpha = 38^o$. 104
5.24 Total pressure coefficient and streamlines plotted on vertical crossflow planes near the tail. Initial Condition Flow Field: $Re = 10^4$, $M = 0.4$, $\alpha = 38^o$. 105
5.25 Coefficient of pressure on upper and lower wing surfaces at chord stations corresponding to plotted crossflow planes. Initial Condition Flow Field: $Re = 10^4$, $M = 0.4$, $\alpha = 38^o$. 106
5.26 Coefficient of pressure on upper and lower wing surfaces at chord stations corresponding to plotted crossflow planes. Uncoupled Bending and Torsion Case: $\tau = 5.28$, $Re = 10^4$, $M = 0.4$, $\alpha = 38^o$. 113
5.27 Three-dimensional and top views of surface pressure and vortex core streamlines at $\tau = \frac{tU_\infty}{\bar{\bar{c}}} = 5.28$ and $\Delta\tau = 0.00066$. Purple crosses denote critical points associated with either attracting or repelling spiral saddle points. Uncoupled Bending and Torsion Case: $Re = 10^4$, $M = 0.4$, $\alpha = 38^o$. 114
5.28 Side view at angle-of-attack showing surface pressure, vortex core streamlines, and spiral saddle points at $\tau = 5.28$. Uncoupled Bending and Torsion Case: $Re = 10^4$, $M = 0.4$, $\alpha = 38^o$. 115

5.29 Computational surface oil flow at $\tau = 5.28$. Uncoupled Bending and Torsion Case: $Re = 10^4$, $M = 0.4$, $\alpha = 38^o$. 115
5.30 Near surface streamlines. Uncoupled Bending and Torsion Case: $\tau = 5.28$, $Re = 10^4$, $M = 0.4$, $\alpha = 38^o$. 116
5.31 Coefficient of pressure on right and left sides of tail, and differential pressure coefficient. Uncoupled Bending and Torsion Case: $\tau = 5.28$, $Re = 10^4$, $M = 0.4$, $\alpha = 38^o$. 117
5.32 Total pressure coefficient and streamlines plotted on vertical crossflow planes above wing. Uncoupled Bending and Torsion Case: $\tau = 5.28$, $Re = 10^4$, $M = 0.4$, $\alpha = 38^o$. 118
5.33 Total pressure coefficient and streamlines plotted on vertical crossflow planes near the tail. Uncoupled Bending and Torsion Case: $\tau = 5.28$, $Re = 10^4$, $M = 0.4$, $\alpha = 38^o$. 119
5.34 Bending deflection and force distributions along the tail span plotted at integer nondimensional time levels. Uncoupled Bending and Torsion Case: $Re = 10^4$, $M = 0.4$, $\alpha = 38^o$. 120
5.35 Torsion deflection and moment distributions along the tail span plotted at integer nondimensional time levels. Uncoupled Bending and Torsion Case: $Re = 10^4$, $M = 0.4$, $\alpha = 38^o$. 120
5.36 Mean and RMS load distributions along the tail span. Uncoupled Bending and Torsion Case: $Re = 10^4$, $M = 0.4$, $\alpha = 38^o$. 121
5.37 History of root bending moment coefficient and root twisting moment coefficient. Uncoupled Bending and Torsion Case: $Re = 10^4$, $M = 0.4$, $\alpha = 38^o$. 122
5.38 Power spectral density of root bending moment coefficient and root twisting moment coefficient versus reduced frequency. Uncoupled Bending and Torsion Case: $Re = 10^4$, $M = 0.4$, $\alpha = 38^o$. 122
5.39 History of tip bending and torsion deflections and accelerations. Uncoupled Bending and Torsion Case: $Re = 10^4$, $M = 0.4$, $\alpha = 38^o$. 123
5.40 Power spectral density of tip bending and torsion accelerations versus reduced frequency. Uncoupled Bending and Torsion Case: $Re = 10^4$, $M = 0.4$, $\alpha = 38^o$. 123
5.41 Coefficient of pressure on upper and lower wing surfaces at chord stations corresponding to plotted crossflow planes. Coupled Bending and Torsion Case: $\tau = 5.28$, $Re = 10^4$, $M = 0.4$, $\alpha = 38^o$. 126
5.42 Three-dimensional and top views of surface pressure and vortex core streamlines at $\tau = \frac{tU_\infty}{\overline{\overline{c}}} = 5.28$ and $\Delta\tau = 0.00066$. Purple crosses denote critical points associated with either attracting or repelling spiral saddle points. Coupled Bending and Torsion Case: $Re = 10^4$, $M = 0.4$, $\alpha = 38^o$. 127
5.43 Side view at angle-of-attack showing surface pressure, vortex core streamlines, and spiral saddle points at $\tau = 5.28$. Coupled Bending and Torsion Case: $Re = 10^4$, $M = 0.4$, $\alpha = 38^o$. 128
5.44 Computational surface oil flow at $\tau = 5.28$. Coupled Bending and Torsion Case: $Re = 10^4$, $M = 0.4$, $\alpha = 38^o$. 128
5.45 Near surface streamlines. Coupled Bending and Torsion Case: $\tau = 5.28$, $Re = 10^4$, $M = 0.4$, $\alpha = 38^o$. 129

5.46 Coefficient of pressure on right and left sides of tail, and differential pressure coefficient. Coupled Bending and Torsion Case: $\tau = 5.28$, $Re = 10^4$, $M = 0.4$, $\alpha = 38^o$. 130
5.47 Total pressure coefficient and streamlines plotted on vertical crossflow planes above wing. Coupled Bending and Torsion Case: $\tau = 5.28$, $Re = 10^4$, $M = 0.4$, $\alpha = 38^o$. 131
5.48 Total pressure coefficient and streamlines plotted on vertical crossflow planes near the tail. Coupled Bending and Torsion Case: $\tau = 5.28$, $Re = 10^4$, $M = 0.4$, $\alpha = 38^o$. 132
5.49 Bending deflection and force distributions along the tail span plotted at integer nondimensional time levels. Coupled Bending and Torsion Case: $Re = 10^4$, $M = 0.4$, $\alpha = 38^o$. 133
5.50 Torsion deflection and moment distributions along the tail span plotted at integer nondimensional time levels. Coupled Bending and Torsion Case: $Re = 10^4$, $M = 0.4$, $\alpha = 38^o$. 133
5.51 Mean and RMS load distributions along the tail span. Coupled Bending and Torsion Case: $Re = 10^4$, $M = 0.4$, $\alpha = 38^o$. 134
5.52 History of root bending moment coefficient and root twisting moment coefficient. Coupled Bending and Torsion Case: $Re = 10^4$, $M = 0.4$, $\alpha = 38^o$. 135
5.53 Power spectral density of root bending moment coefficient and root twisting moment coefficient versus reduced frequency. Coupled Bending and Torsion Case: $Re = 10^4$, $M = 0.4$, $\alpha = 38^o$. 135
5.54 History of tip bending and torsion deflections and accelerations. Coupled Bending and Torsion Case: $Re = 10^4$, $M = 0.4$, $\alpha = 38^o$. 136
5.55 Power spectral density of tip bending and torsion accelerations versus reduced frequency. Coupled Bending and Torsion Case: $Re = 10^4$, $M = 0.4$, $\alpha = 38^o$. 136
5.56 Three-dimensional and top views of surface pressure and vortex core streamlines. Purple crosses denote critical points associated with either attracting or repelling spiral saddle points. Initial Condition Flow Field: $Re = 10^6$, $M = 0.4$, $\alpha = 38^o$. 140
5.57 Side view at angle-of-attack showing surface pressure, vortex core streamlines, and spiral saddle points. Initial Condition Flow Field: $Re = 10^6$, $M = 0.4$, $\alpha = 38^o$. 141
5.58 Computational surface oil flow. Initial Condition Flow Field: $Re = 10^6$, $M = 0.4$, $\alpha = 38^o$. 141
5.59 Near surface streamlines. Initial Condition Flow Field: $Re = 10^6$, $M = 0.4$, $\alpha = 38^o$. 142
5.60 Coefficient of pressure on right and left sides of tail, and differential pressure coefficient. Initial Condition Flow Field: $Re = 10^6$, $M = 0.4$, $\alpha = 38^o$. 143
5.61 Total pressure coefficient, streamlines, and velocity vectors plotted on vertical crossflow planes above wing at chord stations $x = 0.3, 0.5$. Initial Condition Flow Field: $Re = 10^6$, $M = 0.4$, $\alpha = 38^o$. 144

5.62 Total pressure coefficient, streamlines, and velocity vectors plotted on vertical crossflow planes above wing at chord stations $x = 0.7, 0.9$. Initial Condition Flow Field: $Re = 10^6$, $M = 0.4$, $\alpha = 38^o$. 145
5.63 Total pressure coefficient, streamlines, and velocity vectors plotted on vertical crossflow planes near the tail at $x = 1.1, 1.3$. Initial Condition Flow Field: $Re = 10^6$, $M = 0.4$, $\alpha = 38^o$. 146
5.64 Total pressure coefficient, streamlines, and velocity vectors plotted on a vertical crossflow plane at the tail trailing edge, $x = 1.5$. Initial Condition Flow Field: $Re = 10^6$, $M = 0.4$, $\alpha = 38^o$. 147
5.65 Coefficient of pressure on upper and lower wing surfaces at chord stations corresponding to plotted crossflow planes. Initial Condition Flow Field: $Re = 10^6$, $M = 0.4$, $\alpha = 38^o$. 148
5.66 Coefficient of pressure on upper and lower wing surfaces at chord stations corresponding to plotted crossflow planes. Rigid Tail Case: $Re = 10^6$, $M = 0.4$, $\alpha = 38^o$. 150
5.67 a) Three-dimensional, b) top and c) side views of surface pressure and vortex core streamlines at $\tau = \frac{tU_\infty}{\bar{c}} = 13.2$ and $\Delta\tau = 0.00132$. Purple crosses denote critical points associated with either attracting or repelling spiral saddle points. Rigid Tail Case: $Re = 10^6$, $M = 0.4$, $\alpha = 38^o$. . . . 151
5.68 Near surface streamlines at $\tau = 13.2$. Rigid Tail Case: $Re = 10^6$, $M = 0.4$, $\alpha = 38^o$. 152
5.69 Coefficient of pressure on right and left sides of tail, and differential pressure coefficient. Rigid Tail Case: $\tau = 13.2$, $Re = 10^6$, $M = 0.4$, $\alpha = 38^o$. 153
5.70 Total pressure coefficient and velocity vectors plotted on vertical crossflow planes above wing. Rigid Tail Case: $\tau = 13.2$, $Re = 10^4$, $M = 0.4$, $\alpha = 38^o$. 154
5.71 Total pressure coefficient and velocity vectors plotted on vertical crossflow planes near the tail. Rigid Tail Case: $\tau = 13.2$, $Re = 10^4$, $M = 0.4$, $\alpha = 38^o$. 155
5.72 Hypothetical Bending deflection and force distributions along the tail span plotted at integer nondimensional time levels. Rigid Tail Case: $Re = 10^6$, $M = 0.4$, $\alpha = 38^o$. 156
5.73 Hypothetical torsion deflection and moment distributions along the tail span plotted at integer nondimensional time levels. Rigid Tail Case: $Re = 10^6$, $M = 0.4$, $\alpha = 38^o$. 156
5.74 Mean and RMS load distributions along the tail span. Rigid Tail Case: $Re = 10^6$, $M = 0.4$, $\alpha = 38^o$. 157
5.75 History of root bending moment coefficient and root twisting moment coefficient. Rigid Tail Case: $Re = 10^6$, $M = 0.4$, $\alpha = 38^o$. 158
5.76 Power spectral density of root bending moment coefficient and root twisting moment coefficient versus reduced frequency. Rigid Tail Case: $Re = 10^6$, $M = 0.4$, $\alpha = 38^o$. 158
5.77 History of hypothetical tip bending and torsion deflections and accelerations. Rigid Tail Case: $Re = 10^6$, $M = 0.4$, $\alpha = 38^o$. 159

5.78 Power spectral density of hypothetical tip bending and torsion accelerations versus reduced frequency. Rigid Tail Case: $Re = 10^6$, $M = 0.4$, $\alpha = 38^o$. 159
5.79 Coefficient of pressure on upper and lower wing surfaces at chord stations corresponding to plotted crossflow planes. Uncoupled Bending and Torsion Case: $\tau = 13.2$, $Re = 10^6$, $M = 0.4$, $\alpha = 38^o$. 163
5.80 a) Three-dimensional, b) top and c) side views of surface pressure and vortex core streamlines at $\tau = \frac{tU_\infty}{\bar{c}} = 13.2$ and $\Delta\tau = 0.00132$. Purple crosses denote critical points associated with either attracting or repelling spiral saddle points. Uncoupled Bending and Torsion Case: $Re = 10^6$, $M = 0.4$, $\alpha = 38^o$. 164
5.81 Near surface streamlines at $\tau = 13.2$. Uncoupled Bending and Torsion Case: $Re = 10^6$, $M = 0.4$, $\alpha = 38^o$. 165
5.82 Coefficient of pressure on right and left sides of tail, and differential pressure coefficient. Uncoupled Bending and Torsion Case: $\tau = 13.2$, $Re = 10^6$, $M = 0.4$, $\alpha = 38^o$. 166
5.83 Total pressure coefficient and velocity vectors plotted on vertical crossflow planes above wing. Uncoupled Bending and Torsion Case: $\tau = 13.2$, $Re = 10^6$, $M = 0.4$, $\alpha = 38^o$. 167
5.84 Total pressure coefficient and velocity vectors plotted on vertical crossflow planes near the tail. Uncoupled Bending and Torsion Case: $\tau = 13.2$, $Re = 10^6$, $M = 0.4$, $\alpha = 38^o$. 168
5.85 Bending deflection and force distributions along the tail span plotted at integer nondimensional time levels. Uncoupled Bending and Torsion Case: $Re = 10^6$, $M = 0.4$, $\alpha = 38^o$. 169
5.86 Torsion deflection and moment distributions along the tail span plotted at integer nondimensional time levels. Uncoupled Bending and Torsion Case: $Re = 10^6$, $M = 0.4$, $\alpha = 38^o$. 169
5.87 Mean and RMS load distributions along the tail span. Uncoupled Bending and Torsion Case: $Re = 10^6$, $M = 0.4$, $\alpha = 38^o$. 170
5.88 History of root bending moment coefficient and root twisting moment coefficient. Uncoupled Bending and Torsion Case: $Re = 10^6$, $M = 0.4$, $\alpha = 38^o$. 171
5.89 Power spectral density of root bending moment coefficient and root twisting moment coefficient versus reduced frequency. Uncoupled Bending and Torsion Case: $Re = 10^6$, $M = 0.4$, $\alpha = 38^o$. 171
5.90 History of tip bending and torsion deflections and accelerations. Uncoupled Bending and Torsion Case: $Re = 10^6$, $M = 0.4$, $\alpha = 38^o$. 172
5.91 Power spectral density of tip bending and torsion accelerations versus reduced frequency. Uncoupled Bending and Torsion Case: $Re = 10^6$, $M = 0.4$, $\alpha = 38^o$. 172
5.92 Coefficient of pressure on upper and lower wing surfaces at chord stations corresponding to plotted crossflow planes. Coupled Bending and Torsion Case: $\tau = 13.2$, $Re = 10^6$, $M = 0.4$, $\alpha = 38^o$. 174

5.93 a) Three-dimensional, b) top and c) side views of surface pressure and vortex core streamlines at $\tau = \frac{tU_\infty}{\bar{c}} = 13.2$ and $\Delta\tau = 0.00132$. Purple crosses denote critical points associated with either attracting or repelling spiral saddle points. Coupled Bending and Torsion Case: $Re = 10^6$, $M = 0.4$, $\alpha = 38^o$. 175
5.94 Near surface streamlines at $\tau = 13.2$. Coupled Bending and Torsion Case: $Re = 10^6$, $M = 0.4$, $\alpha = 38^o$. 176
5.95 Coefficient of pressure on right and left sides of tail, and differential pressure coefficient. Coupled Bending and Torsion Case: $\tau = 13.2$, $Re = 10^6$, $M = 0.4$, $\alpha = 38^o$. 177
5.96 Total pressure coefficient and velocity vectors plotted on vertical cross-flow planes above wing. Coupled Bending and Torsion Case: $\tau = 13.2$, $Re = 10^6$, $M = 0.4$, $\alpha = 38^o$. 178
5.97 Total pressure coefficient and velocity vectors plotted on vertical cross-flow planes near the tail. Coupled Bending and Torsion Case: $\tau = 13.2$, $Re = 10^6$, $M = 0.4$, $\alpha = 38^o$. 179
5.98 Bending deflection and force distributions along the tail span plotted at integer nondimensional time levels. Coupled Bending and Torsion Case: $Re = 10^6$, $M = 0.4$, $\alpha = 38^o$. 180
5.99 Torsion deflection and moment distributions along the tail span plotted at integer nondimensional time levels. Coupled Bending and Torsion Case: $Re = 10^6$, $M = 0.4$, $\alpha = 38^o$. 180
5.100 Mean and RMS load distributions along the tail span. Coupled Bending and Torsion Case: $Re = 10^6$, $M = 0.4$, $\alpha = 38^o$. 181
5.101 History of root bending moment coefficient and root twisting moment coefficient. Coupled Bending and Torsion Case: $Re = 10^6$, $M = 0.4$, $\alpha = 38^o$. 182
5.102 Power spectral density of root bending moment coefficient and root twisting moment coefficient versus reduced frequency. Coupled Bending and Torsion Case: $Re = 10^6$, $M = 0.4$, $\alpha = 38^o$. 182
5.103 History of tip bending and torsion deflections and accelerations. Coupled Bending and Torsion Case: $Re = 10^6$, $M = 0.4$, $\alpha = 38^o$. 183
5.104 Power spectral density of tip bending and torsion accelerations versus reduced frequency. Coupled Bending and Torsion Case: $Re = 10^6$, $M = 0.4$, $\alpha = 38^o$. 183

6.1 a) Wide, b) narrow and c) open fuselage configurations for the delta wing twin F/A-18 vertical tail model. 188
6.2 Sketch of McDonnell Douglas F/A-18C. *Public domain clip art.* 190
6.3 View of F/A-18 tail with retracted wing tips shown. *Photo by author.* . . 190
6.4 a) Block boundaries. b) Cutaway view showing individual blocks. c) Close up view of surface grids. Wide Fuselage Case. 191
6.5 a) Three-dimensional, b) top and c) side views of surface pressure and vortex core streamlines. Initial Condition Flow Field: $Re = 10^6$, $M = 0.4$, $\alpha = 30^o$. 195

6.6 Rear view at angle-of-attack showing total pressure contours on a vertical plane bisecting the left vortex core ($\Lambda = 80.4^o$). The right vortex core streamlines are colored yellow and blue as an indicator of swirl ratio. Initial Condition Flow Field: $Re = 10^6$, $M = 0.4$, $\alpha = 30^o$. 196
6.7 Computational surface oil flows. Initial Condition Flow Field: $Re = 10^6$, $M = 0.4$, $\alpha = 30^o$. 196
6.8 Near surface streamlines for the a) inner and b) outer right tail surfaces and the upper wing surface. Initial Condition Flow Field: $Re = 10^6$, $M = 0.4$, $\alpha = 30^o$. 197
6.9 Sketch of a primary - secondary vortex system with a corresponding plot of spanwise surface pressure. Hummel [10] 198
6.10 Coefficient of pressure on upper and lower wing surfaces at chord stations corresponding to plotted crossflow planes. Initial Condition Flow Field: $Re = 10^6$, $M = 0.4$, $\alpha = 30^o$. 198
6.11 Total pressure coefficient and uniformly plotted velocity vectors on vertical crossflow planes above wing. Initial Condition Flow Field: $Re = 10^6$, $M = 0.4$, $\alpha = 30^o$. 199
6.12 Total pressure coefficient and uniformly plotted velocity vectors on vertical crossflow planes near the tails. Initial Condition Flow Field: $Re = 10^6$, $M = 0.4$, $\alpha = 30^o$. 200
6.13 Bending force and twisting moment distributions along the tail span plotted at integer nondimensional time levels for a) right and b) left tails. Wide Rigid Case: $Re = 10^6$, $M = 0.4$, $\alpha = 30^o$. 204
6.14 Mean and RMS load distributions along the right and left tail spans. Wide Rigid Case: $Re = 10^6$, $M = 0.4$, $\alpha = 30^o$. 204
6.15 Mean and RMS differential coefficient of pressure contours on a) right and b) left tails. Wide Rigid Case: $Re = 10^6$, $M = 0.4$, $\alpha = 30^o$. 205
6.16 Differential pressure ($\frac{\Delta p}{q_\infty}$) histories and buffet excitation spectra ($\sqrt{nF(n)}$) at the 45% chord and 60% span location for a) right and b) left tails. Wide Rigid Case: $Re = 10^6$, $M = 0.4$, $\alpha = 30^o$. 205
6.17 History of root bending moment coefficient and root twisting moment coefficient for a) right and b) left tails. Wide Rigid Case: $Re = 10^6$, $M = 0.4$, $\alpha = 30^o$. 206
6.18 Power spectral density of root bending moment coefficient and root twisting moment coefficient versus reduced frequency for a) right and b) left tails. Wide Rigid Case: $Re = 10^6$, $M = 0.4$, $\alpha = 30^o$. 206
6.19 Bending force and twisting moment distributions along the tail span plotted at integer nondimensional time levels for a) right and b) left tails. Wide Flexible Case: $Re = 10^6$, $M = 0.4$, $\alpha = 30^o$. 210
6.20 Mean and RMS load distributions along the right and left tail spans. Wide Flexible Case: $Re = 10^6$, $M = 0.4$, $\alpha = 30^o$. 210
6.21 Mean and RMS differential coefficient of pressure contours on a) right and b) left tails. Wide Flexible Case: $Re = 10^6$, $M = 0.4$, $\alpha = 30^o$. . . . 211
6.22 Differential pressure ($\frac{\Delta p}{q_\infty}$) histories at the 45% chord and 60% span location for a) right and b) left tails. Wide Flexible Case: $Re = 10^6$, $M = 0.4$, $\alpha = 30^o$. 211

6.23 History of root bending moment coefficient and root twisting moment coefficient for a) right and b) left tails. Wide Flexible Case: $Re = 10^6$, $M = 0.4$, $\alpha = 30^o$. 212
6.24 Power spectral density of root bending moment coefficient and root twisting moment coefficient versus reduced frequency for a) right and b) left tails. Wide Flexible Case: $Re = 10^6$, $M = 0.4$, $\alpha = 30^o$. 212
6.25 Right Tail: Bending and torsion deflection distributions along the tail span plotted at integer nondimensional time levels. Wide Flexible Case: $Re = 10^6$, $M = 0.4$, $\alpha = 30^o$. 213
6.26 Right Tail: Time and frequency domain data for tip bending and torsion deflections and accelerations. Wide Flexible Case: $Re = 10^6$, $M = 0.4$, $\alpha = 30^o$. 213
6.27 Left Tail: Bending and torsion deflection distributions along the tail span plotted at integer nondimensional time levels. Wide Flexible Case: $Re = 10^6$, $M = 0.4$, $\alpha = 30^o$. 214
6.28 Left Tail: Time and frequency domain data for tip bending and torsion deflections and accelerations. Wide Flexible Case: $Re = 10^6$, $M = 0.4$, $\alpha = 30^o$. 214
6.29 Diagram of Hummel [11] type delta wing. 215
6.30 a) Block boundaries. b) Cutaway view showing individual blocks. c) Close up view of surface grids. Narrow Fuselage Case. 216
6.31 a) Three-dimensional, b) top and c) side views of surface pressure and vortex core streamlines. Initial Condition Flow Field: $Re = 10^6$, $M = 0.4$, $\alpha = 30^o$. 219
6.32 Near surface streamlines for the a) inner and b) outer right tail surfaces and the upper wing surface. Initial Condition Flow Field: $Re = 10^6$, $M = 0.4$, $\alpha = 30^o$. 220
6.33 Coefficient of pressure on upper and lower wing surfaces at chord stations corresponding to plotted crossflow planes. Initial Condition Flow Field: $Re = 10^6$, $M = 0.4$, $\alpha = 30^o$. 220
6.34 Total pressure coefficient and uniformly plotted velocity vectors on vertical crossflow planes above wing. Initial Condition Flow Field: $Re = 10^6$, $M = 0.4$, $\alpha = 30^o$. 221
6.35 Total pressure coefficient and uniformly plotted velocity vectors on vertical crossflow planes near the tails. Initial Condition Flow Field: $Re = 10^6$, $M = 0.4$, $\alpha = 30^o$. 222
6.36 Bending force and twisting moment distributions along the tail span plotted at integer nondimensional time levels for a) right and b) left tails. Narrow Rigid Case: $Re = 10^6$, $M = 0.4$, $\alpha = 30^o$. 225
6.37 Mean and RMS load distributions along the right and left tail spans. Narrow Rigid Case: $Re = 10^6$, $M = 0.4$, $\alpha = 30^o$. 225
6.38 Mean and RMS differential coefficient of pressure contours on a) right and b) left tails. Narrow Rigid Case: $Re = 10^6$, $M = 0.4$, $\alpha = 30^o$. . . . 226
6.39 Differential pressure ($\frac{\Delta p}{q_\infty}$) histories at the 45% chord and 60% span location for a) right and b) left tails. Narrow Rigid Case: $Re = 10^6$, $M = 0.4$, $\alpha = 30^o$. 226

6.40 History of root bending moment coefficient and root twisting moment coefficient for a) right and b) left tails. Narrow Rigid Case: $Re = 10^6$, $M = 0.4$, $\alpha = 30^o$. 227
6.41 Power spectral density of root bending moment coefficient and root twisting moment coefficient versus reduced frequency for a) right and b) left tails. Narrow Rigid Case: $Re = 10^6$, $M = 0.4$, $\alpha = 30^o$. 227
6.42 Bending force and twisting moment distributions along the tail span plotted at integer nondimensional time levels for a) right and b) left tails. Narrow Flexible Case: $Re = 10^6$, $M = 0.4$, $\alpha = 30^o$. 230
6.43 Mean and RMS load distributions along the right and left tail spans. Narrow Flexible Case: $Re = 10^6$, $M = 0.4$, $\alpha = 30^o$. 231
6.44 Mean and RMS differential coefficient of pressure contours on a) right and b) left tails. Narrow Flexible Case: $Re = 10^6$, $M = 0.4$, $\alpha = 30^o$. . . 232
6.45 Differential pressure ($\frac{\Delta p}{q_\infty}$) histories at the 45% chord and 60% span location for a) right and b) left tails. Narrow Flexible Case: $Re = 10^6$, $M = 0.4$, $\alpha = 30^o$. 232
6.46 History of root bending moment coefficient and root twisting moment coefficient for a) right and b) left tails. Narrow Flexible Case: $Re = 10^6$, $M = 0.4$, $\alpha = 30^o$. 233
6.47 Power spectral density of root bending moment coefficient and root twisting moment coefficient versus reduced frequency for a) right and b) left tails. Narrow Flexible Case: $Re = 10^6$, $M = 0.4$, $\alpha = 30^o$. 233
6.48 Right Tail: Bending and torsion deflection distributions along the tail span plotted at integer nondimensional time levels. Narrow Flexible Case: $Re = 10^6$, $M = 0.4$, $\alpha = 30^o$. 234
6.49 Right Tail: Time and frequency domain data for tip bending and torsion deflections and accelerations. Narrow Flexible Case: $Re = 10^6$, $M = 0.4$, $\alpha = 30^o$. 234
6.50 Left Tail: Bending and torsion deflection distributions along the tail span plotted at integer nondimensional time levels. Narrow Flexible Case: $Re = 10^6$, $M = 0.4$, $\alpha = 30^o$. 235
6.51 Left Tail: Time and frequency domain data for tip bending and torsion deflections and accelerations. Narrow Flexible Case: $Re = 10^6$, $M = 0.4$, $\alpha = 30^o$. 235
6.52 a) Block boundaries. b) Cutaway view showing individual blocks. c) Close up view of surface grids. Open Fuselage Case. 240
6.53 a) Three-dimensional, b) top and c) side views of surface pressure and vortex core streamlines. Initial Condition Flow Field: $Re = 0.75 \times 10^6$, $M = 0.3$, $\alpha = 30^o$. 243
6.54 Near surface streamlines for the a) inner and b) outer right tail surfaces and the upper wing surface. Initial Condition Flow Field: $Re = 0.75 \times 10^6$, $M = 0.3$, $\alpha = 30^o$. 244
6.55 Coefficient of pressure on upper and lower wing surfaces at chord stations corresponding to plotted crossflow planes. Initial Condition Flow Field: $Re = 0.75 \times 10^6$, $M = 0.3$, $\alpha = 30^o$. 244

6.56 Total pressure coefficient and uniformly plotted velocity vectors on vertical crossflow planes above wing. Initial Condition Flow Field: $Re = 0.75 \times 10^6$, $M = 0.3$, $\alpha = 30^o$. 245
6.57 Total pressure coefficient and uniformly plotted velocity vectors on vertical crossflow planes near the tails. Initial Condition Flow Field: $Re = 0.75 \times 10^6$, $M = 0.3$, $\alpha = 30^o$. 246
6.58 Bending force and twisting moment distributions along the tail span plotted at integer nondimensional time levels for a) right and b) left tails. Open Flexible Case: $Re = 0.75 \times 10^6$, $M = 0.3$, $\alpha = 30^o$. 251
6.59 Mean and RMS load distributions along the right and left tail spans. Open Flexible Case: $Re = 0.75 \times 10^6$, $M = 0.3$, $\alpha = 30^o$. 251
6.60 Mean and RMS differential coefficient of pressure contours on a) right and b) left tails. Open Flexible Case: $Re = 0.75 \times 10^6$, $M = 0.3$, $\alpha = 30^o$. 252
6.61 Differential pressure ($\frac{\Delta p}{q_\infty}$) histories at the 45% chord and 60% span location for a) right and b) left tails. Open Flexible Case: $Re = 0.75 \times 10^6$, $M = 0.3$, $\alpha = 30^o$. 252
6.62 History of root bending moment coefficient and root twisting moment coefficient for a) right and b) left tails. Open Flexible Case: $Re = 0.75 \times 10^6$, $M = 0.3$, $\alpha = 30^o$. 253
6.63 Power spectral density of root bending moment coefficient and root twisting moment coefficient versus reduced frequency for a) right and b) left tails. Open Flexible Case: $Re = 0.75 \times 10^6$, $M = 0.3$, $\alpha = 30^o$. 253
6.64 Right Tail: Bending and torsion deflection distributions along the tail span plotted at integer nondimensional time levels. Open Flexible Case: $Re = 0.75 \times 10^6$, $M = 0.3$, $\alpha = 30^o$. 254
6.65 Right Tail: Time and frequency domain data for tip bending and torsion deflections and accelerations. Open Flexible Case: $Re = 0.75 \times 10^6$, $M = 0.3$, $\alpha = 30^o$. 254
6.66 Left Tail: Bending and torsion deflection distributions along the tail span plotted at integer nondimensional time levels. Open Flexible Case: $Re = 0.75 \times 10^6$, $M = 0.3$, $\alpha = 30^o$. 255
6.67 Left Tail: Time and frequency domain data for tip bending and torsion deflections and accelerations. Open Flexible Case: $Re = 0.75 \times 10^6$, $M = 0.3$, $\alpha = 30^o$. 255

7.1 a) Inboard, b) midspan and c) outboard tail configurations. 259
7.2 Location of Washburn pressure transducers. 260
7.3 Block boundaries for Washburn-type cases. 260
7.4 Surface grids for a) Inboard, b) midspan and c) outboard tail configurations. 261
7.5 Three-dimensional and top views of surface pressure and vortex core streamlines. Inboard Initial Condition: $Re = 1.25 \times 10^6$, $M = 0.3$, $\alpha = 35^o$. 265
7.6 Three-dimensional and top views of surface pressure, vortex core streamlines and solid total pressure isosurfaces, $\left(\frac{p_0}{\rho_\infty a_\infty^2} = 0.68\right)$ Inboard Initial Condition: $Re = 1.25 \times 10^6$, $M = 0.3$, $\alpha = 35^o$. 266

7.7 Near surface streamlines for the a) inner and b) outer right tail surfaces and the upper wing surface. Inboard Initial Condition: $Re = 1.25 \times 10^6$, $M = 0.3$, $\alpha = 35^o$. 267
7.8 Coefficient of pressure on upper and lower wing surfaces at chord stations corresponding to plotted crossflow planes. Inboard Initial Condition: $Re = 1.25 \times 10^6$, $M = 0.3$, $\alpha = 35^o$. 267
7.9 Nondimensional total pressure contours and in-plane streamlines plotted on vertical crossflow planes, $x = 1.0, 1.1, 1.2$. Inboard Initial Condition: $Re = 1.25 \times 10^6$, $M = 0.3$, $\alpha = 35^o$. 268
7.10 Nondimensional total pressure contours and in-plane streamlines plotted on vertical crossflow planes, $x = 1.3, 1.4, 1.5$. Inboard Initial Condition: $Re = 1.25 \times 10^6$, $M = 0.3$, $\alpha = 35^o$. 269
7.11 Bending force and twisting moment distributions along the tail span plotted at integer nondimensional time levels for a) right and b) left tails. Inboard Case: $Re = 1.25 \times 10^6$, $M = 0.3$, $\alpha = 35^o$. 271
7.12 Mean and RMS load distributions along the right and left tail spans. Inboard Case: $Re = 1.25 \times 10^6$, $M = 0.3$, $\alpha = 35^o$. 272
7.13 Mean and RMS differential coefficient of pressure contours on a) right and b) left tails. Inboard Case: $Re = 1.25 \times 10^6$, $M = 0.3$, $\alpha = 35^o$. . . . 273
7.14 Differential pressure ($\frac{\Delta p}{q_\infty}$) histories at the 50% chord and 90% span location for a) right and b) left tails. Inboard Case: $Re = 1.25 \times 10^6$, $M = 0.3$, $\alpha = 35^o$. 273
7.15 History of root bending moment coefficient and root twisting moment coefficient for a) right and b) left tails. Inboard Case: $Re = 1.25 \times 10^6$, $M = 0.3$, $\alpha = 35^o$. 274
7.16 Power spectral density of root bending moment coefficient and root twisting moment coefficient versus reduced frequency for a) right and b) left tails. Inboard Case: $Re = 1.25 \times 10^6$, $M = 0.3$, $\alpha = 35^o$. 274
7.17 Right Tail: Bending and torsion deflection distributions along the tail span plotted at integer nondimensional time levels. Inboard Case: $Re = 1.25 \times 10^6$, $M = 0.3$, $\alpha = 35^o$. 275
7.18 Right Tail: Time and frequency domain data for tip bending and torsion deflections and accelerations. Inboard Case: $Re = 1.25 \times 10^6$, $M = 0.3$, $\alpha = 35^o$. 275
7.19 Left Tail: Bending and torsion deflection distributions along the tail span plotted at integer nondimensional time levels. Inboard Case: $Re = 1.25 \times 10^6$, $M = 0.3$, $\alpha = 35^o$. 276
7.20 Left Tail: Time and frequency domain data for tip bending and torsion deflections and accelerations. Inboard Case: $Re = 1.25 \times 10^6$, $M = 0.3$, $\alpha = 35^o$. 276
7.21 Three-dimensional and top views of surface pressure and vortex core streamlines. Midspan Initial Condition: $Re = 1.25 \times 10^6$, $M = 0.3$, $\alpha = 35^o$. 279
7.22 Three-dimensional and top views of surface pressure, vortex core streamlines and solid total pressure isosurfaces. Midspan Initial Condition: $Re = 1.25 \times 10^6$, $M = 0.3$, $\alpha = 35^o$. 280

7.23 Near surface streamlines for the a) inner and b) outer right tail surfaces and the upper wing surface. Midspan Initial Condition: $Re = 1.25 \times 10^6$, $M = 0.3$, $\alpha = 35^o$. 281
7.24 Coefficient of pressure on upper and lower wing surfaces at chord stations corresponding to plotted crossflow planes. Midspan Initial Condition: $Re = 1.25 \times 10^6$, $M = 0.3$, $\alpha = 35^o$. 281
7.25 Nondimensional total pressure contours and in-plane streamlines plotted on vertical crossflow planes, $x = 1.0, 1.1, 1.2$. Midspan Initial Condition: $Re = 1.25 \times 10^6$, $M = 0.3$, $\alpha = 35^o$. 282
7.26 Nondimensional total pressure contours and in-plane streamlines plotted on vertical crossflow planes, $x = 1.3, 1.4, 1.5$. Midspan Initial Condition: $Re = 1.25 \times 10^6$, $M = 0.3$, $\alpha = 35^o$. 283
7.27 Bending force and twisting moment distributions along the tail span plotted at integer nondimensional time levels for a) right and b) left tails. Midspan Case: $Re = 1.25 \times 10^6$, $M = 0.3$, $\alpha = 35^o$. 286
7.28 Mean and RMS load distributions along the right and left tail spans. Midspan Case: $Re = 1.25 \times 10^6$, $M = 0.3$, $\alpha = 35^o$. 286
7.29 Mean and RMS differential coefficient of pressure contours on a) right and b) left tails. Midspan Case: $Re = 1.25 \times 10^6$, $M = 0.3$, $\alpha = 35^o$. . . 287
7.30 Differential pressure ($\frac{\Delta p}{q_\infty}$) histories at the 50% chord and 90% span location for a) right and b) left tails. Midspan Case: $Re = 1.25 \times 10^6$, $M = 0.3$, $\alpha = 35^o$. 287
7.31 History of root bending moment coefficient and root twisting moment coefficient for a) right and b) left tails. Midspan Case: $Re = 1.25 \times 10^6$, $M = 0.3$, $\alpha = 35^o$. 288
7.32 Power spectral density of root bending moment coefficient and root twisting moment coefficient versus reduced frequency for a) right and b) left tails. Midspan Case: $Re = 1.25 \times 10^6$, $M = 0.3$, $\alpha = 35^o$. 288
7.33 Right Tail: Bending and torsion deflection distributions along the tail span plotted at integer nondimensional time levels. Midspan Case: $Re = 1.25 \times 10^6$, $M = 0.3$, $\alpha = 35^o$. 289
7.34 Right Tail: Time and frequency domain data for tip bending and torsion deflections and accelerations. Midspan Case: $Re = 1.25 \times 10^6$, $M = 0.3$, $\alpha = 35^o$. 289
7.35 Left Tail: Bending and torsion deflection distributions along the tail span plotted at integer nondimensional time levels. Midspan Case: $Re = 1.25 \times 10^6$, $M = 0.3$, $\alpha = 35^o$. 290
7.36 Left Tail: Time and frequency domain data for tip bending and torsion deflections and accelerations. Midspan Case: $Re = 1.25 \times 10^6$, $M = 0.3$, $\alpha = 35^o$. 290
7.37 Three-dimensional and top views of surface pressure and vortex core streamlines. Outboard Initial Condition: $Re = 1.25 \times 10^6$, $M = 0.3$, $\alpha = 35^o$. 292
7.38 Three-dimensional and top views of surface pressure, vortex core streamlines and solid total pressure isosurfaces. Outboard Initial Condition: $Re = 1.25 \times 10^6$, $M = 0.3$, $\alpha = 35^o$. 293

7.39 Near surface streamlines for the a) inner and b) outer right tail surfaces and the upper wing surface. Outboard Initial Condition: $Re = 1.25 \times 10^6$, $M = 0.3$, $\alpha = 35^o$. 294
7.40 Coefficient of pressure on upper and lower wing surfaces at chord stations corresponding to plotted crossflow planes. Outboard Initial Condition: $Re = 1.25 \times 10^6$, $M = 0.3$, $\alpha = 35^o$. 294
7.41 Nondimensional total pressure contours and in-plane streamlines plotted on vertical crossflow planes, $x = 1.0, 1.1, 1.2$. Outboard Initial Condition: $Re = 1.25 \times 10^6$, $M = 0.3$, $\alpha = 35^o$. 295
7.42 Nondimensional total pressure contours and in-plane streamlines plotted on vertical crossflow planes, $x = 1.3, 1.4, 1.5$. Outboard Initial Condition: $Re = 1.25 \times 10^6$, $M = 0.3$, $\alpha = 35^o$. 296
7.43 Bending force and twisting moment distributions along the tail span plotted at integer nondimensional time levels for a) right and b) left tails. Outboard Case: $Re = 1.25 \times 10^6$, $M = 0.3$, $\alpha = 35^o$. 298
7.44 Mean and RMS load distributions along the right and left tail spans. Outboard Case: $Re = 1.25 \times 10^6$, $M = 0.3$, $\alpha = 35^o$. 299
7.45 Mean and RMS differential coefficient of pressure contours on a) right and b) left tails. Outboard Case: $Re = 1.25 \times 10^6$, $M = 0.3$, $\alpha = 35^o$. . . 300
7.46 Differential pressure ($\frac{\Delta p}{q_\infty}$) histories at the 50% chord and 90% span location for a) right and b) left tails. Outboard Case: $Re = 1.25 \times 10^6$, $M = 0.3$, $\alpha = 35^o$. 300
7.47 History of root bending moment coefficient and root twisting moment coefficient for a) right and b) left tails. Outboard Case: $Re = 1.25 \times 10^6$, $M = 0.3$, $\alpha = 35^o$. 301
7.48 Power spectral density of root bending moment coefficient and root twisting moment coefficient versus reduced frequency for a) right and b) left tails. Outboard Case: $Re = 1.25 \times 10^6$, $M = 0.3$, $\alpha = 35^o$. 301
7.49 Right Tail: Bending and torsion deflection distributions along the tail span plotted at integer nondimensional time levels. Outboard Case: $Re = 1.25 \times 10^6$, $M = 0.3$, $\alpha = 35^o$. 302
7.50 Right Tail: Time and frequency domain data for tip bending and torsion deflections and accelerations. Outboard Case: $Re = 1.25 \times 10^6$, $M = 0.3$, $\alpha = 35^o$. 302
7.51 Left Tail: Bending and torsion deflection distributions along the tail span plotted at integer nondimensional time levels. Outboard Case: $Re = 1.25 \times 10^6$, $M = 0.3$, $\alpha = 35^o$. 303
7.52 Left Tail: Time and frequency domain data for tip bending and torsion deflections and accelerations. Outboard Case: $Re = 1.25 \times 10^6$, $M = 0.3$, $\alpha = 35^o$. 303

8.1 a) Three-dimensional, b) top and c) side views of surface pressure and vortex core streamlines. Initial Condition: $\beta_{\text{Flap}} = 15^o$, $Re = 1.25 \times 10^6$, $M = 0.3$, $\alpha = 35^o$. 311

8.2 a) Three-dimensional, b) top and c) side views of surface pressure and vortex core streamlines and solid total pressure isosurfaces, $\left(\frac{p_0}{\rho_\infty a_\infty^2} = 0.68\right)$ Initial Condition: $\beta_{\text{Flap}} = 15^o$, $Re = 1.25 \times 10^6$, $M = 0.3$, $\alpha = 35^o$. 312
8.3 Near surface streamlines for the a) inner and b) outer right tail surfaces and the upper wing surface. Initial Condition: $\beta_{\text{Flap}} = 15^o$, $Re = 1.25 \times 10^6$, $M = 0.3$, $\alpha = 35^o$. 313
8.4 Effect of apex flap deflection on wing surface coefficient of pressure at several chord stations. Initial Condition: $\beta_{\text{Flap}} = 15^o$, $Re = 1.25 \times 10^6$, $M = 0.3$, $\alpha = 35^o$. 314
8.5 Nondimensional total pressure contours and in-plane streamlines plotted on vertical crossflow planes, $x = 1.0, 1.1, 1.2$. Initial Condition: $\beta_{Flap} = 15^o$, $Re = 1.25 \times 10^6$, $M = 0.3$, $\alpha = 35^o$. 315
8.6 Nondimensional total pressure contours and in-plane streamlines plotted on vertical crossflow planes, $x = 1.3, 1.4, 1.5$. Initial Condition: $\beta_{Flap} = 15^o$, $Re = 1.25 \times 10^6$, $M = 0.3$, $\alpha = 35^o$. 316
8.7 Effect of apex flap on mean and RMS load distributions along the right tail span. $\beta_{Flap} = 15^o$, $Re = 1.25 \times 10^6$, $M = 0.3$, $\alpha = 35^o$. 318
8.8 Right tail mean and RMS differential coefficient of pressure contours. $\beta_{Flap} = 15^o$, $Re = 1.25 \times 10^6$, $M = 0.3$, $\alpha = 35^o$. 318
8.9 Effect of apex flap on differential pressure $(\frac{\Delta p}{q_\infty})$ histories at the 50% chord and 90% span location for the right tail. $\beta_{Flap} = 15^o$, $Re = 1.25 \times 10^6$, $M = 0.3$, $\alpha = 35^o$. 319
8.10 Effect of apex flap on a) history and b) power spectral density of root bending moment coefficient and root twisting moment coefficient versus reduced frequency for the right tail. $\beta_{Flap} = 15^o$, $Re = 1.25 \times 10^6$, $M = 0.3$, $\alpha = 35^o$. 319
8.11 Effect of apex flap on time and frequency domain data for right tail tip bending and torsion deflections and accelerations. $\beta_{Flap} = 15^o$, $Re = 1.25 \times 10^6$, $M = 0.3$, $\alpha = 35^o$. 320

LIST OF TABLES

5.1 Summary of single square vertical tail buffeting cases. 74
5.2 First six bending and torsion natural frequencies of a cantilevered beam, where the dimensional frequency, f in Hz is nondimensionalized as $\frac{f\bar{\bar{c}}}{U_\infty}$. 77
5.3 Summary of root bending and twisting moment statistics, maximum amplitudes and dominant frequencies. Uncoupled Bending and Torsion Case: $Re = 10^4$, $M = 0.4$, $\alpha = 38^o$. 112
5.4 Summary of tip displacement and acceleration statistics, maximum amplitudes and dominant frequencies. Uncoupled Bending and Torsion Case: $Re = 10^4$, $M = 0.4$, $\alpha = 38^o$. 112
5.5 Summary of root bending and twisting moment statistics, maximum amplitudes and dominant frequencies. Coupled Bending and Torsion Case: $Re = 10^4$, $M = 0.4$, $\alpha = 38^o$. 126
5.6 Summary of tip displacement and acceleration statistics, maximum amplitudes and dominant frequencies. Coupled Bending and Torsion Case: $Re = 10^4$, $M = 0.4$, $\alpha = 38^o$. 126
5.7 Summary of root bending and twisting moment statistics, maximum amplitudes and dominant frequencies. Rigid Tail Case: $Re = 10^6$, $M = 0.4$, $\alpha = 38^o$. 150
5.8 Summary of hypothetical tip displacement and acceleration statistics, maximum amplitudes and dominant frequencies. Rigid Tail Case: $Re = 10^6$, $M = 0.4$, $\alpha = 38^o$. 150
5.9 Summary of root bending and twisting moment statistics, maximum amplitudes and dominant frequencies. Uncoupled Bending and Torsion Case: $Re = 10^6$, $M = 0.4$, $\alpha = 38^o$. 162
5.10 Effect of fluid/structure interaction on root loading. 162
5.11 Summary of tip displacement and acceleration statistics, maximum amplitudes and dominant frequencies. Uncoupled Bending and Torsion Case: $Re = 10^6$, $M = 0.4$, $\alpha = 38^o$. 162
5.12 Effect of increased Reynolds number on root loading. 162
5.13 Effect of increased Reynolds number tip response. 163
5.14 Effect of inertial coupling on root moment loads at $Re = 10^6$, $M = 0.4$, $\alpha = 38^o$. 174
5.15 Effect of inertial coupling on tip response at $Re = 10^6$, $M = 0.4$, $\alpha = 38^o$. 174
5.16 Single square vertical tail buffeting cases. 186
5.17 Summary of root bending and twisting moment statistics, maximum amplitudes and dominant frequencies for all single tail cases. 186
5.18 Summary of tip displacement and acceleration statistics, maximum amplitudes and dominant frequencies all single tail cases. 186

6.1 Summary of twin F/A-18 vertical tail buffeting cases. 188
6.2 Summary of nondimensional pressure ($\frac{p}{q_\infty}$) data at 45% chord and 60% span. Wide Rigid Case: $Re = 10^6$, $M = 0.4$, $\alpha = 30^o$. 203

6.3 Summary of root bending and twisting moment statistics, peak power and dominant frequency. Wide Rigid Case: $Re = 10^6$, $M = 0.4$, $\alpha = 30^o$. 203
6.4 Comparison of averaged nondimensional pressure ($\frac{p}{q_\infty}$) data at 45% chord and 60% span for rigid and flexible tail, wide fuselage cases: $Re = 10^6$, $M = 0.4$, $\alpha = 30^o$. 209
6.5 Comparison of averaged root bending and twisting moment statistics, peak power and dominant frequency for rigid and flexible stiff tail, wide fuselage cases: $Re = 10^6$, $M = 0.4$, $\alpha = 30^o$. 209
6.6 Comparison of averaged nondimensional pressure ($\frac{p}{q_\infty}$) data at 45% chord and 60% span on rigid tails for the wide and narrow fuselage cases: $Re = 10^6$, $M = 0.4$, $\alpha = 30^o$. 224
6.7 Comparison of averaged root bending and twisting moment statistics, peak power and dominant frequency for rigid and stiff tail, wide fuselage cases: $Re = 10^6$, $M = 0.4$, $\alpha = 30^o$. 224
6.8 Comparison of averaged nondimensional pressure ($\frac{p}{q_\infty}$) data at 45% chord and 60% span on flexible stiff tails for the wide and narrow fuselage cases: $Re = 10^6$, $M = 0.4$, $\alpha = 30^o$. 229
6.9 Comparison of averaged root bending and twisting moment statistics, peak power and dominant frequency for wide and narrow fuselage, flexible tail cases: $Re = 10^6$, $M = 0.4$, $\alpha = 30^o$. 229
6.10 Effect of fuselage width reduction on buffeting response. $Re = 10^6$, $M = 0.4$, $\alpha = 30^o$. 230
6.11 Comparison with experimental data for averaged nondimensional pressure ($\frac{p}{q_\infty}$), pressure coefficient (C_p), buffet excitation ($\sqrt{nF(n)}$) dominant frequency (n_d), and buffet excitation peak power at 45% chord and 60% span on the flexible stiff tail for the narrow fuselage case. The length scale is nondimensionalized by $\overline{\overline{c}}_t$. 238
6.12 Experimental data comparison of averaged unsteady root bending moment, peak power and dominant frequency for the flexible stiff tail on the narrow fuselage. The length scale is nondimensionalized by $\overline{\overline{c}}_t$. 238
6.13 Comparison of averaged nondimensional pressure ($\frac{p}{q_\infty}$) data at 45% chord and 60% span on flexible stiff tails for the F/A-18 tail cases. Note, for the wide and narrow cases $M = 0.4$, and for the open case $M = 0.3$. . . . 248
6.14 Comparison of averaged root bending and twisting moment statistics, peak power and dominant frequency for flexible F/A-18 tail cases. 250
6.15 Comparison of stiff(wide, narrow) and soft (open) tail responses. 250

7.1 Summary of twin Washburn-type vertical tail buffeting cases, and experimental range in which nondimensional buffeting data were constant. . . 262
7.2 Comparison of right tail RMS nondimensional pressures ($\frac{p}{q_\infty}$) with experimental data of Washburn et al. [12]. Inboard Case: $\alpha = 35^o$, $M = 0.3$, $Re = 1.25 \times 10^6$. 304
7.3 Comparison of right tail RMS nondimensional pressures ($\frac{p}{q_\infty}$) with experimental data of Washburn et al. [12]. Outboard Case: $\alpha = 35^o$, $M = 0.3$, $Re = 1.25 \times 10^6$. 305

7.4 Comparison of right tail dominant frequencies for buffet excitation, $\sqrt{nF(n)}$, with experimental data of Washburn et al. [12] using length scale of $\overline{\overline{c}}$. Case: $\alpha = 35^o$, $M = 0.3$, $Re = 1.25 \times 10^6$. 305
7.5 Comparison of right tail root bending moment coefficient statistics with experimental data of Washburn et al. [12] using length scale of $\overline{\overline{c}}$. Case: $\alpha = 35^o$, $M = 0.3$, $Re = 1.25 \times 10^6$. 305
7.6 Comparison of right tail nondimensional pressure ($\frac{p}{q_\infty}$) data at 50% chord and 90% span at each tail location. Case: $\alpha = 35^o$, $M = 0.3$, $Re = 1.25 \times 10^6$. 307
7.7 Comparison of averaged root bending and twisting moment statistics, peak power and dominant frequency for each tail location. Case: $\alpha = 35^o$, $M = 0.3$, $Re = 1.25 \times 10^6$. 307
7.8 Comparison of buffet responses for each tail location. Case: $\alpha = 35^o$, $M = 0.3$, $Re = 1.25 \times 10^6$. 307

CHAPTER 1

INTRODUCTION

1.1 Motivation

Current and future requirements for highly maneuverable fighter aircraft have necessitated research into the tail buffeting problem. With the advent of aircraft equipped with thrust vectoring and advanced flight control systems, post-stall departure can now be effectively controlled, making aggressive maneuvering at elevated angle-of-attack a reality. These aircraft maneuver at very high angle-of-attack (HAOA) and under high loading conditions. The tail buffeting problem affects all fighter aircraft to a degree, but is particularly severe for the F/A-18. The production F/A-18 achieves its high maneuverability through the use of wing leading edge extensions (LEX), a delta wing and strategically placed vertical tails. The LEX produces lift at HAOA by generating a pair of vortices that trail over the wing surface. The vortices also entrain air over the vertical tails, maintaining control surface effectiveness at HAOA. This combination of LEX and vertical tail location produces excellent HAOA performance. However, at HAOA, the vortices emanating from the highly swept leading edge extensions breakdown, or burst, before reaching the vertical tails, bathing them in a highly unsteady, swirling flow. This flow produces severe buffeting of the vertical tails and has led to their premature fatigue failure. Figure 1.1 shows smoke and tuft flow visualizations [13], of the F/A-18 High Alpha Research Vehicle, (HARV), at $\alpha = 20^o$, 25^o and 30^o. The forward vortex burst location of the $\alpha = 30^o$ condition produces the largest buffet loads.

The format of this dissertation is based on the *American Institute of Aeronautics and Astronautics Journal* and was typeset in LaTeX 2_ε by the author.

Figures 1.2 and 1.3 depict reconstructions from actual flight data of a post stall reversal, also known as a *Herbst Turn* or *J-Turn*, followed by an offensive spiral or *helicopter gun attack.* In each figure the black and white vehicle is the HARV, while the red vehicle is a NASA chase F/A-18. A prototype thrust vectoring system recently tested on the F/A-18 HARV enabled the aircraft to maneuver at up to 65^o angle-of-attack, and steady-state trim to 70^o angle-of-attack. In Figure 1.2, the velocity vector of the HARV clearly shows the rapid onset of angle-of-attack, with a maximum of 60^o, just before the velocity vector roll and target acquisition, shown by the projected square. The overall maneuver takes about 17 seconds. In Figure 1.3 the HARV has acquired the target at the end of the high alpha reversal, Figure 1.2, and continued to track the target for about 10 seconds in the 50^o–60^o angle-of-attack range. Next generation aircraft such as the F-22 and Joint Strike Fighter will be required to fly these types of maneuvers routinely, thus it is imperative that aircraft designers have the ability to model the flow physics of high alpha, buffet flow with high fidelity at minimal cost.

In general, buffeting refers to the forced vibration of a body under the aerodynamic action of a wake. The principal difference between the phenomena of buffeting and flutter is that flutter is a self-excited vibration while buffeting is a forced vibration. Thus, flutter is a stability problem and buffeting is a structural response problem. The goal of tail buffeting research is to insure that the aerodynamic wake frequencies are far removed from the resonance frequencies of the tail while maintaining the favorable aerodynamics from which the aircraft's agility is derived. This may be accomplished by passive or active control of the wake flow via a wide variety of control solutions, such as suction/blowing and/or control surface deflections. Traditional analysis methods assume that the aerodynamic forces are known when evaluating the buffeting response.

This method allows the structural properties of the vertical tails to be strengthened sufficiently for maximum loading, but still does not alleviate the fatigue problem. The assumption of aerodynamic forces also precludes the approach of modifying the flow to alleviate tail buffeting, since the aerodynamics have been assumed away. For this reason, flow control of the tail buffeting problem has only been attempted experimentally.

Since accurate theoretical models currently do not exist and full aircraft computational simulations are prohibitively expensive, there is a need for a simple model that captures the essence of the tail buffeting phenomenon. The purpose of this study is to create a practical tool for conducting fundamental HAOA tail buffeting research while retaining as much of the physics as possible.

1.2 The Present Research

The goal of this study is to develop an efficient computational simulation of vortex breakdown induced vertical tail buffeting. The basic model under consideration consist of a sharp-edged delta wing placed at a moderately high angle-of-attack in order to produce a strong vortex breakdown flow. Vertical tail(s) of varying geometry are suspended directly behind the trailing edge of the delta wing and modeled as cantilevered beams in bending and torsion. This multi-disciplinary problem is solved sequentially for the fluid flow, the elastic tail deformations and the grid displacements. The fluid flow is simulated by time accurately solving the laminar, unsteady, compressible, Navier-Stokes equations using an implicit, upwind, flux-difference splitting finite volume scheme. The elastic vibrations of the tails are modeled by uncoupled bending and torsion beam equations. These equations are solved accurately in time using the Galerkin method and a five-stage Runge-Kutta-Verner scheme. The grid for the fluid dynamics calculations

is continuously deformed using interpolation functions to disperse the displacements smoothly throughout the computational domain.

In Chapter 2, a survey of the literature on vortex breakdown flows and the resulting tail buffet problem is presented. A historical perspective of vortical flow is given emphasizing early physical observations. The experimental literature is then reviewed focusing on the key physical issues. Next, numerical simulations of vortex breakdown and buffet are surveyed. The review concludes with an introduction to vortex breakdown control techniques.

In Chapter 3, the analytical and numerical basis of the fluid dynamics formulation is presented. The laminar, unsteady, compressible, Navier-Stokes equations are written in the strong conservation form in time-dependent, body-conformed coordinates. *Strong* refers to the pure divergence form of the differential equation and *conservation* refers to the numerical property of the resulting finite difference equation which preserves the conservation of the flow variables at the discrete level. The computational scheme is then formulated, as an implicit, upwind, Roe flux-difference splitting, finite volume scheme. Initial and boundary conditions are discussed. Issues regarding single and multiblock CFD gridding are then presented.

In Chapter 4, the structural tail buffet problem is formulated in detail both analytically and numerically, including boundary conditions. The governing equations for coupled bending and torsional vibrations of a beam are derived from Hamilton's energy principle. The numerical scheme for solving the coupled bending and torsion beam equations using the Galerkin method with six bending modes and six torsion modes is outlined. The chapter then is concluded with a discussion of the general solution method to solve the coupled sets of fluid, structure and grid equations.

Chapters 5 through 8 contain numerical results for the single and twin tail investigations conducted in this study. In Chapter 5, the fundamental issues of inertial coupling, Reynolds number dependence and aeroelastic effects are addressed with regard to single vertical tail buffet.

Chapter 6 addresses the determination of the effect of aft fuselage geometry on twin F/A-18 vertical tail buffet. Three fuselage configurations are considered; wide, narrow and open. Secondarily, the effect of the tail response on the loads will be accessed for the wide and narrow configurations by comparing the rigid tail loads with the dynamically interacting cases. Finally, the effect of decreased tail stiffness will be considered for the open fuselage case.

The focus of Chapter 7 is the determination of the effect of spanwise tail location on the tail buffet loading and response. Three spanwise tail positions are considered; corresponding to 33%, 56% and 78% of the wing semispan. Quantitative comparisons are made with the experimental data of Washburn et al. [12] for the same configuration.

In Chapter 8, the issue of control is addressed. Results are presented for an apex flap deflection scheme which delays the onset of vortex breakdown. The configuration used is the inboard Washburn tail case of the previous chapter, which had the highest level of buffeting for all of the cases studied. The flap is deflected by a single optimum angle which was experimentally [14] found to produce the greatest delay in the onset of breakdown. Chapter 9 concludes the present study with general remarks and recommendations for future investigations.

a) $\alpha = 20^o$

b) $\alpha = 25^o$

c) $\alpha = 30^o$

Figure 1.1: F-18 HARV smoke and tuft flow visualization for a) $\alpha = 20^o$ b) 25^o and c) 30^o. $M = 0.24$, $Re = 11 \times 10^6$. *NASA Dryden* EC89-0096-206, EC89-0096-226 and EC89-0096-240

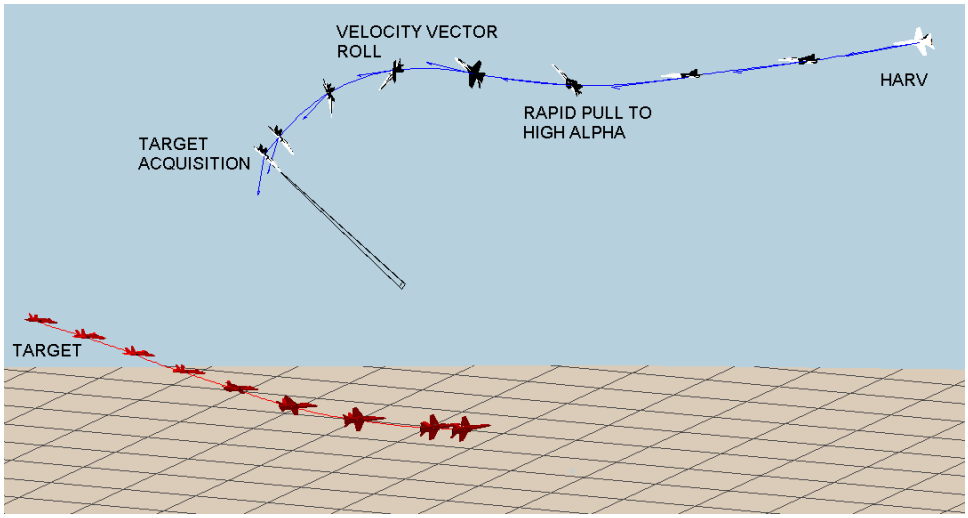

Figure 1.2: Flight data reconstruction of *post-stall reversal* also known as a Herbst turn or J-turn. *NASA Dryden* [1]

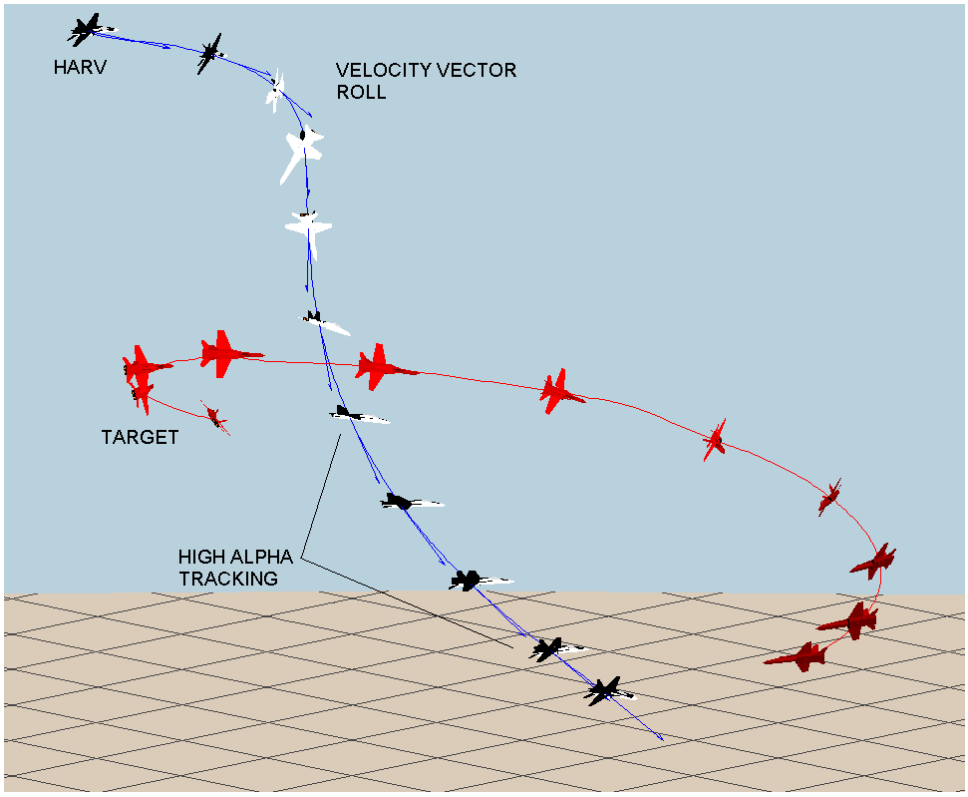

Figure 1.3: Flight data reconstruction of an *offensive spiral* also known as a helicopter gun attack. *NASA Dryden* [1]

CHAPTER 2

LITERATURE REVIEW

2.1 Introduction

One advantage of numerical modeling over wind tunnel experimentation is the ability to easily and economically incorporate a wide variety model geometries and control solutions, such as suction or blowing and/or control surface deflections. The purpose of this study is to develop a simple numerical simulation of vortex breakdown induced tail buffeting to serve as a test bed for investigations into controllability and as a model for the examination of the fundamental physics. Thus, the focus of this review is on the physical nature of these phenomena and methods to numerically simulate them.

2.2 Vortex Breakdown

The literature on vortical flow and vortex breakdown in particular is substantial. These areas have been the subject of intense research for over four decades. Many excellent comprehensive reviews exist. Of particular interest in this study are those of Newsome and Kandil [15], Escudier [16] and Rockwell [17].

2.2.1 Historical Perspective

2.2.1.1 The Discovery of Vortex Lift

Beginning with the first controlled flights of powered aircraft, there has been a quest for ever-increasing speed and maneuverability. As Polhamus [18] recounts in his survey article, the quest for speed is what led to the introduction of highly swept wings

and the discovery of vortex lift. In 1940, Ludwieg [19] experimentally demonstrated that Busemann's [20] 1935 supersonic swept wing theory also applied to subsonic compressibility effects. Thus, German researchers immediately began to design highly swept wings for their Messerschmitt Me 262 jet. The Me 262 first flew in 1942 with a sweep of 18^o. Advanced versions of the Me 262 incorporated wing sweep angles as high as 50^o. Also under consideration were highly swept delta wings, but the end of the war halted German research.

In 1946, researchers at the Langley Memorial Aeronautical Laboratory began studying the captured German DM-1 highly swept delta wing test glider. In an attempt to boost its low speed lift performance, Wilson and Lovell [21] sharpened the leading edge of the DM-1. This caused the flow to separate from the leading edge thereby producing a strong vortex which yielded a large lift increment. Their research provided the first insight into the effects of leading edge radius and Reynolds number on vortex lift.

2.2.1.2 Early Observations of Vortex Breakdown

The phenomenon of vortex breakdown was first documented by Peckham and Atkinson [22] in their 1957 study of vortex lift on "Gothic" wings; which are similar to delta wings, but have curved leading edges in the plan view. They noticed that as the angle of incidence increased beyond 25^o, the length of the vortex core, made visible by natural condensation, decreased from a length of three root-chords downstream of the trailing edge to only 1/4 root-chord at 30^o incidence. They noted that the condensation trail began to "bell-out" before disappearing and attributed this to the core becoming more diffuse.

In 1958, Elle [23], working independently of Peckham and Atkinson [22], noticed the same phenomenon on a delta wing and termed it "vortex breakdown." Elle [23]

suggested that breakdown was caused by the vorticity field away from the core impeding downstream transport of fluid in the core.

In 1960, Werlé [2], using water tunnel visualization, also observed the dependence of breakdown location on the incidence of a delta wing. He suggested that the mechanism for vortex breakdown was the sudden transition of the vortex flow from laminar to turbulent. Werlé also showed the initial dependence of breakdown location on Reynolds number for very low Reynolds numbers. In Figure 2.1, the breakdown position at $Re = 5,000$ is further aft than the case of $Re = 10,000$, which is nearly in its limiting position.

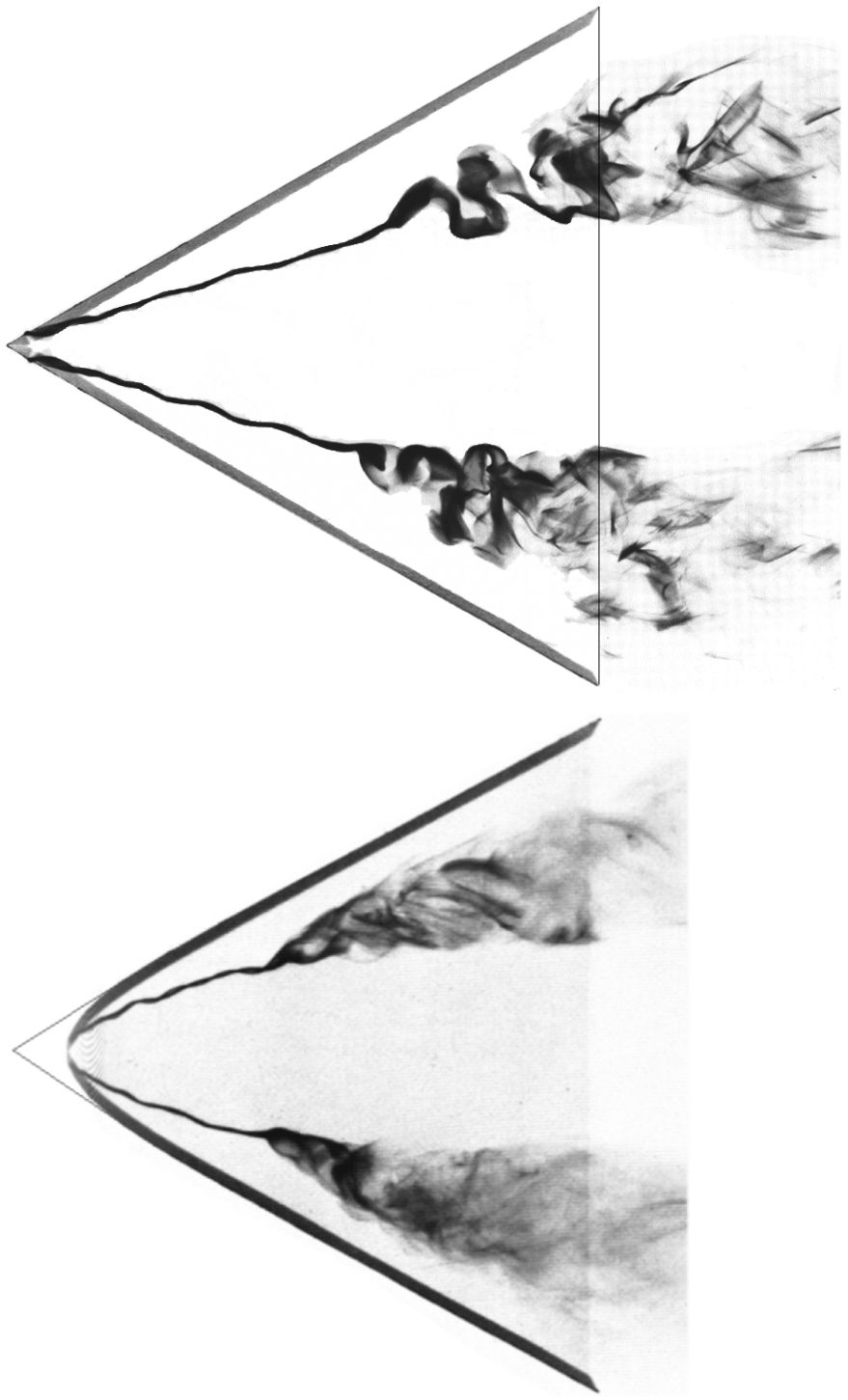

Figure 2.1: Effect of Reynolds number on vortex breakdown on a 63^o delta wing. Retouched and shown in negative. *top*: $\alpha = 20^o$, $Re_c = 5000$; *bottom*: $\alpha = 20^o$, $Re_c = 10,000$. Note; the photo of the bottom wing was warped and has been retouched. Werlé [2].

In near-sonic studies also published in 1960, Elle [24] contended that, because of the relative invariance of breakdown location with respect to Reynolds numbers between 10^4 and 5×10^6, it was improbable that transition was the prime mechanism of breakdown. He conceded, however, that "the phenomenon is apparently due to some sort of instability." Also based on the observed Reynolds number invariance, was his assertion that the weak shock at the breakdown location was a result of the breakdown, not the cause.

In 1961, Lambourne and Bryer [3] published the first comprehensive experimental investigation of vortex breakdown on a delta wing. They identified the two major modes of breakdown: the axisymmetric bubble type and the asymmetric spiral type, shown in Figure 2.2. They suggested that the primary cause of breakdown was

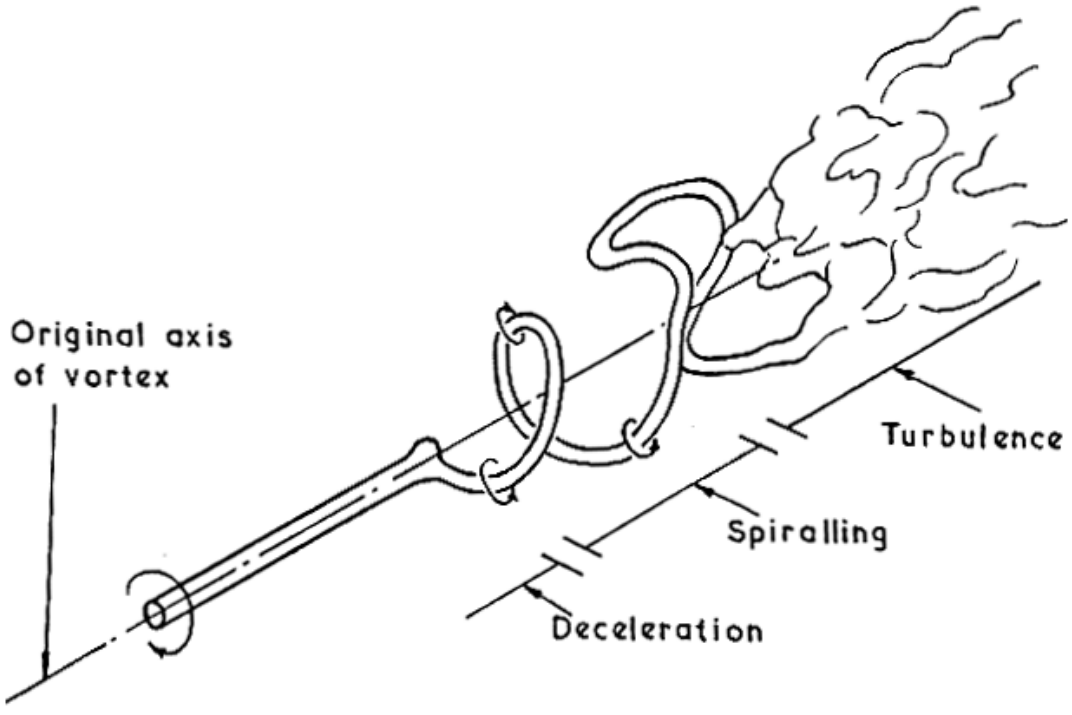

Figure 2.2: Sketch of spiral type vortex breakdown [3].

an increase in pressure along the vortex axis. They also studied the effects of incidence, sweepback, Reynolds number, and upstream and downstream flow perturbations.

In 1960, Squire [25] performed the first analytical study of vortex breakdown. He suggested that breakdown was a result of disturbances propagating upstream along standing waves in the vortex core. His analysis was restricted to cylindrical vortices and symmetrical disturbances.

In 1962, Harvey [26] contended that the simplified flow conditions of the classical cylindrical vortex tube better isolated the mechanisms of breakdown and were more applicable to axisymmetric based theories [25, 27, 28]. This marked an experimental shift away from delta wings, and towards the study of the axisymmetric bubble-type breakdown flows in cylindrical tubes.

A remarkable feature of these early studies, as observed by Escudier [16] and others, is that the key ideas of axial stagnation, sudden transition, instability and wave motion are all present in these early works, but there is still, to this day no generally accepted theoretical description of vortex breakdown. In the author's opinion, this is because the dominant cause of vortex breakdown depends on the flow regime. In the case of a delta wing at high incidence, the dominate cause is the adverse pressure gradient stemming from the wake which then causes the axial stagnation associated with the breakdown.

2.2.2 Physical Characteristics and Topology of Vortex Breakdown

In Lambourne and Bryer's [3] classic photograph, see Figure 2.3, the two dominant modes of vortex breakdown can be seen clearly. The lower vortex shows the nearly axisymmetric swollen core in which the dye has diffused into a recirculating *bubble* region. The upper vortex shows an asymmetric *spiral* filament in which the dye remains

concentrated until the onset of large scale turbulence. Both forms exhibit axial stagnation as well as a region of reversed axial flow. The spiral form can be further classified into three successive stages; a sudden deceleration of the fluid moving along the vortex core, an abrupt kink where the core is deflected spirally for a few revolutions, and finally a transition to large scale turbulence, see Figure 2.2.

The precise relationship of the spiral and bubble forms is still a matter of controversy. Leibovich [29] and Sarpkaya [4, 30, 31] contend that the two forms are fundamentally different phenomenon. Escudier [16] suggests that the axisymmetric or bubble form is fundamental, and that the asymmetric spiral form is a consequence of the instability of the bubble. Figure 2.4 shows bubble type breakdowns of varying symmetry

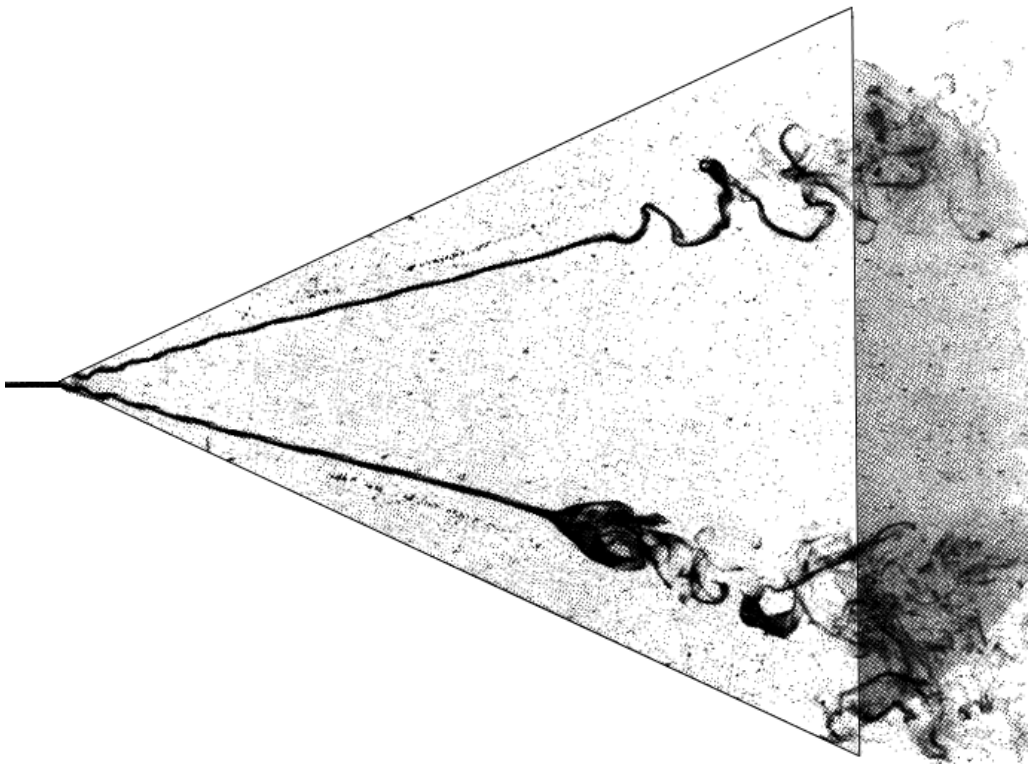

Figure 2.3: Vortex breakdown on a 65^o delta wing in water, $Re = 10^4$ [3].

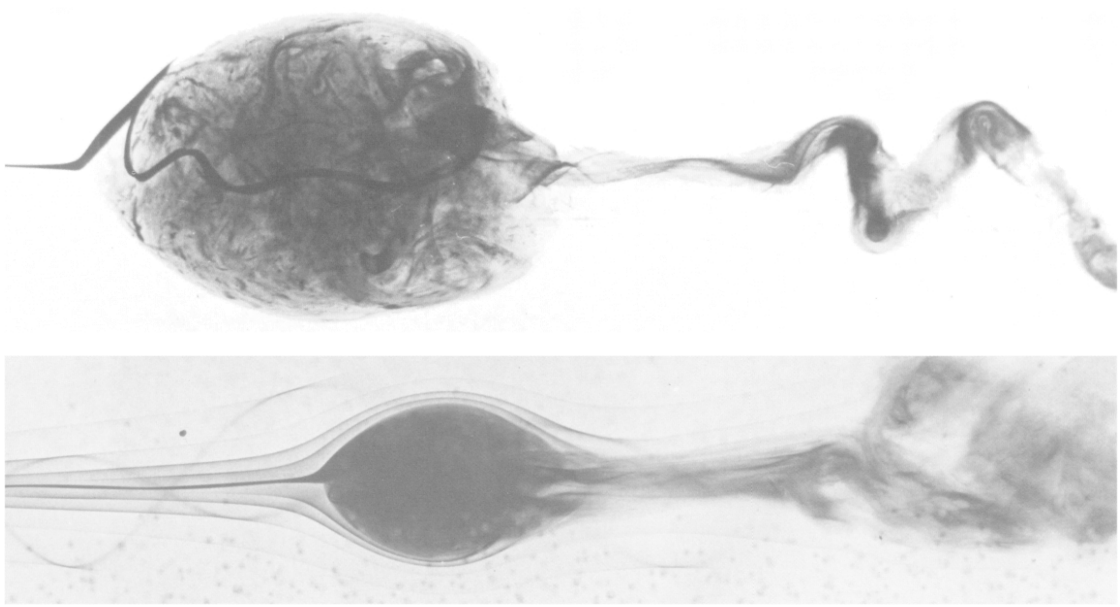

Figure 2.4: Axisymmetric vortex breakdown in a swirling flow through a pipe at moderate (*top*) and slightly higher (*bottom*) inlet swirl ratios. Sarpkaya [4].

for increasing inlet swirl ratio. In delta wing experiments [3], it has been noted that the axisymmetric bubble breakdown occurs only occasionally and is short lived. This would favor the latter description. Regardless of their fundamental relationship, the two forms are very different in structure.

A large portion of the literature stems from experimental investigations of confined vortices generated in tubes, where swirl is introduced by upstream guidevanes. Of particular note are the reports by Harvey [26], Sarpkaya [31], Kirkpatrick [32] and Faler and Leibovich [33]. In general, the vortex in a tube is highly axisymmetrical, radially confined and subject to only small axial variations unless the tube is flared. The vortex generated by a delta wing is formed from the roll-up of the vortex sheet which is continuously shed from the leading edge, so that a significant variation in the axial direction is an inherent feature of the vortex structure. This lack of axial symmetry triggers the

unstable axisymmetric bubble to degenerate to the asymmetric spiral form, commonly found on delta wings. Escudier [34, 35] used a device in which the vortex was generated by a jet tangent to the wall of a cylindrical cavity with a side slot entry which then was exhausted to a cylindrical tube. Although, this process is more closely related to the leading-edge vortex, neither reproduces the type of free vortex flow found on a delta wing.

Thus, for a clear understanding of the fundamental physics of the flow currently under study, a detailed description of the vortical flow over delta wing is in order. Délery [6] gives an excellent physical description of the flow field around a delta wing at incidence based on topological fluid mechanics. Mathematical vector field topology provides a concise grammar in which separated flows can be described rationally. The essential components of vector field topology are the points, curves and surfaces that, taken together, characterize all integral manifolds in $\vec{V}$. Integral manifolds include particle traces, streamlines and stream surfaces. Points in the velocity field where $\vec{V} = 0$ are known as singular or critical points. These points coincide with flow separation and attachment lines, and the stagnation points associated with vortex breakdown. Critical points are characterized by their surrounding local velocity field or more precisely by the eigenvectors and eigenvalues of the Jacobian of velocity at the critical point, see Globus et al. [5] for details. Figure 2.5 shows the three basic types of critical points; nodes, saddles and foci (2-D only). Nodes and foci can be further classified as attracting or repelling based on the local velocity direction. Since the 1970's, a significant amount of mathematical rigor has been incorporated into the theory of topological fluid mechanics, see Tobak and Peake [36] and Levit [37]. Much of the past mathematical effort was expended to develop rigorous topological theorems to *predict* flow features based

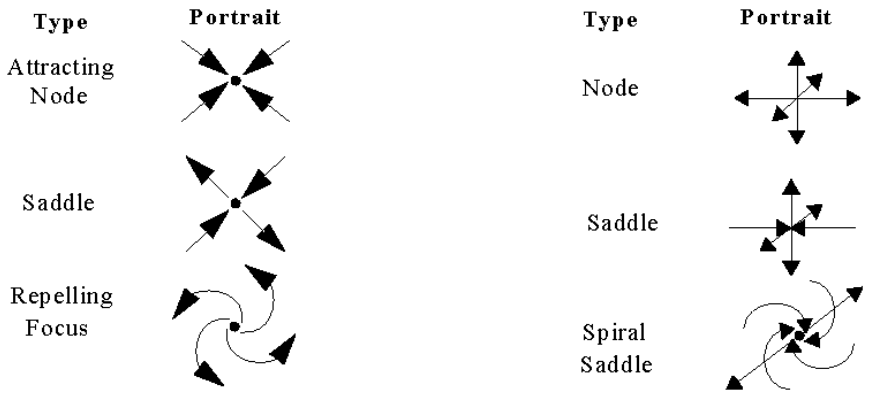

Figure 2.5: Classification of 2-D (*left*) and 3-D (*right*) critical points by local velocity, Globus et al. [5].

on limited observations. An example is the application of the well defined 2-D topology theory applied to the closed surfaces of 3-D bodies to infer off-body flow features. With the advent of CFD and the advancement of modern experimental techniques, such as Laser-Doppler velocimetry, the use of topology has shifted from of method of prediction to means of interpretation. This approach will be used throughout this study.

The flow field about a sharp delta wing at a moderate angle-of-attack is shown in Figure 2.6. Shown in the figure are the shear layers resulting from the primary, secondary and tertiary boundary layer separations along with streamlines and skin friction lines. Figure 2.7 depicts the crossflow topology corresponding to the left side of the delta wing shown in Figure 2.6, where saddle points are marked with $\mathcal{C}$ and foci (in the 2-D sense, or attracting spiral saddles in 3-D) are marked with $\mathcal{F}$. An experimental crossflow visualization by Werlé [7] is shown in Figure 2.8. Streamlines that converge to separation lines are denoted by $\mathcal{S}$, Figure 2.9. Half saddle points $\mathcal{C}_1,\ \mathcal{C}_2,\ \mathcal{C}_3$ correspond to the separation lines, $\mathsf{S}_1,\ \mathsf{S}_2,\ \mathsf{S}_3$ in Figure 2.9 and the half saddle points denoted by $\mathcal{C}_4,\ \mathcal{C}_5,\ \mathcal{C}_6$ correspond to attachment lines, $\mathsf{A}_1,\ \mathsf{A}_2,\ \mathsf{A}_3$.

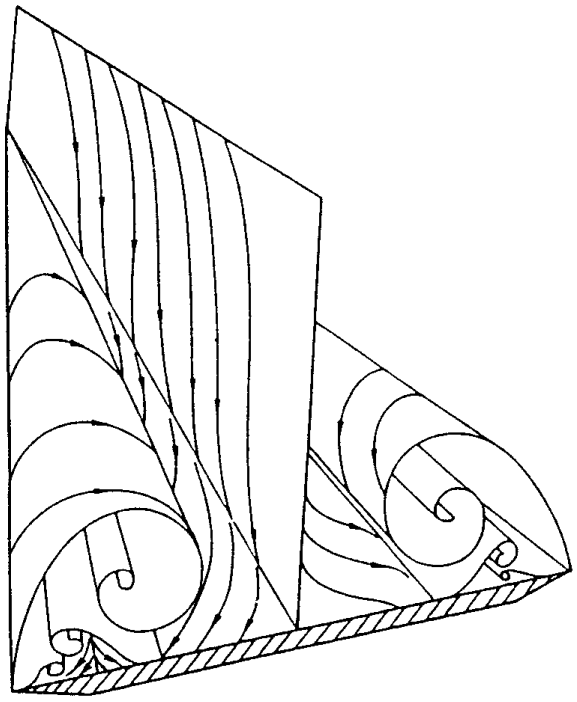

Figure 2.6: Sketch of shear layers resulting from boundary layer separations for a sharp edged delta wing at a moderate angle-of-attack with no breakdown. Délery [6].

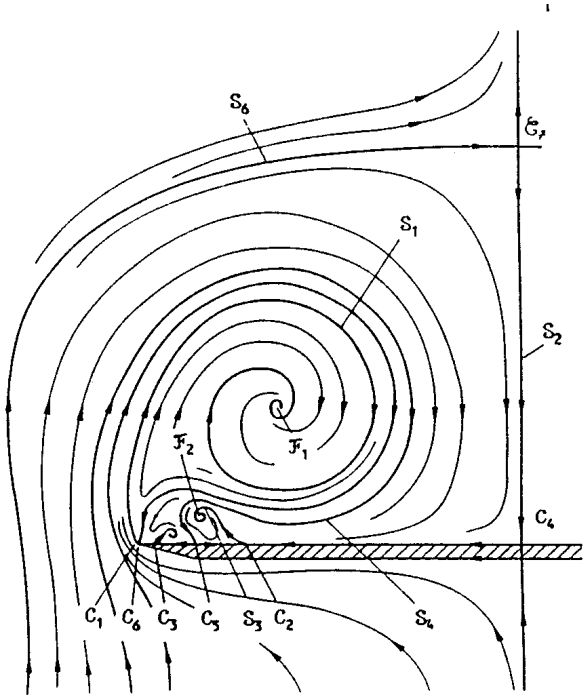

Figure 2.7: Topological sketch of a typical delta wing crossflow plane. Délery [6].

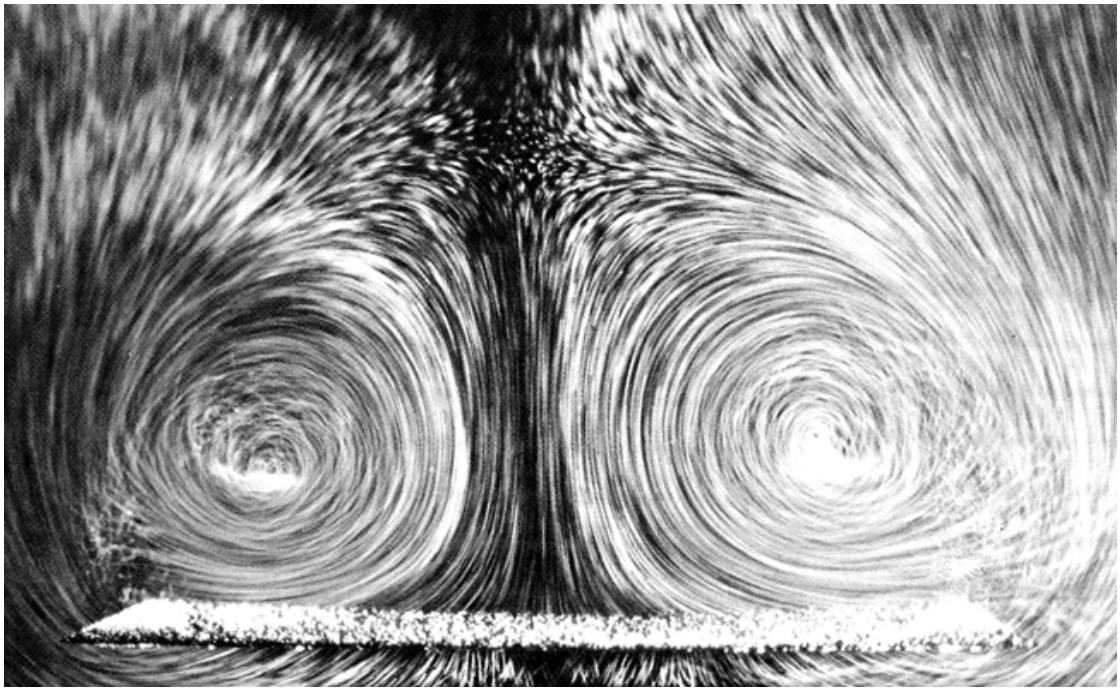

Figure 2.8: Hydrogen bubble flow visualization of a crossflow plane above a sharp 76^o delta wing in water, $Re = 20,000$, $\alpha = 20^o$. Werlé [7].

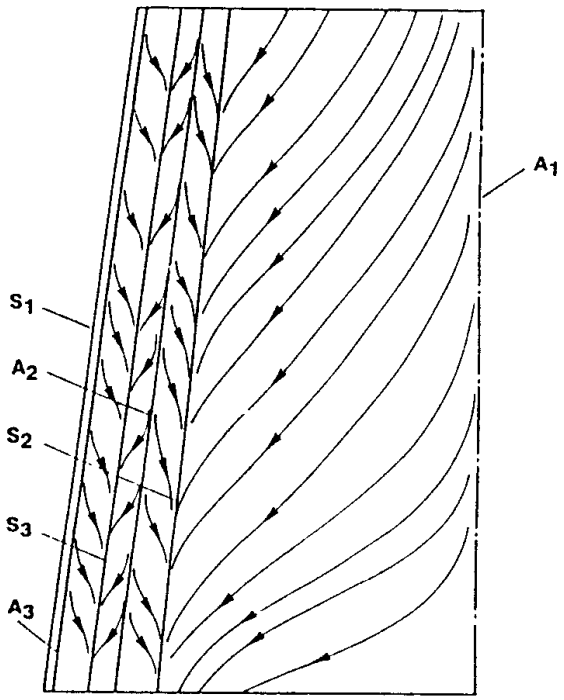

Figure 2.9: Topological sketch of the left aft wing surface showing skin friction lines, and separation and attachment lines. Délery [6].

With the general flow field topology established, attention is now focused specifically on the vortex breakdown. This is accomplished by extracting a vertical slice down the length of the vortex core for a typical numerical solution presented in the current study. In Figures 2.10-2.13, the topology of the vortex breakdown is shown together with plots of velocity and total pressure to reveal their relationships. The vertical axial plane under consideration passes through the tip of the delta wing and the trailing edge spanwise location of $y = 0.17c$. In order to preserve the true geometry of the flow, the arc length coordinate, x_s is used rather than x. Figure 2.10 depicts the in plane streamlines, where the saddle points and foci are denoted by $\mathcal{C}$ and $\mathcal{F}$, respectively. From the arrows on the streamline plots it is evident that both foci are of the attracting type. Areas of flow stagnation and reversal can clearly been seen in Figure 2.11, which shows regularly spaced velocity vectors with marked and labeled critical points. Since the true flow is three dimensional, the normal component of velocity also needs to be considered. In Figure 2.12, contours of the normal velocity component are plotted along with the in plane topology. An important feature of this plot is the boundary contour between negative and positive velocities. If 2-D critical points lie on this contour of zero normal velocity then they are true 3-D critical points, otherwise they are only critical points in a 2-D sense. Thus, from Figure 2.12 $\mathcal{C}_1$ and $\mathcal{F}_1$ are confirmed to be a 3-D saddle and an attracting spiral saddle respectively. Points $\mathcal{C}_2$ and $\mathcal{F}_2$ clearly possess a normal velocity component and hence are not 3-D critical points. The existence of exclusively 2-D critical points, such as $\mathcal{C}_2$ and $\mathcal{F}_2$, are a result of the unsteadiness of the breakdown flow and hence represent the convection of 3-D critical point structures downstream. Another useful quantity in the detection vortex breakdown is total pressure. In Figure 2.13, contours of total pressure are plotted along with the topology obtained from

the streamlines. High gradients in total pressure, seen by clustered contour lines, reveal the boundaries of the vortex core. Another key feature shown in the plot is that the start of the core expansion precedes the first stagnation point in the flow, $\mathcal{C}_1$.

In summary, the key features of the delta wing vortex breakdown flow were accurately described early on by Lambourne and Bryer [3], and they are as follows:

1. Vortex breakdown involves a sudden deceleration of the axial flow accompanied by expansion of the vortex around the stagnant core. A short distance downstream a transition to large-scale turbulence occurs.

2. An essential feature for breakdown to occur is relatively low total pressure in the core of the laminar (pre-breakdown) vortex.

3. A prerequisite for the core flow of a laminar vortex to stagnate is a positive static pressure gradient along the vortex axis.

4. The breakdown position is sensitive to the pressure gradient along the vortex axis, a reduction in the pressure gradient serving to delay breakdown.

5. The required positive pressure gradient could be attributed to viscous actions within the vortex core, or to deceleration of the flow external to the core. A small change in the external flow would suffice, because an external pressure gradient becomes magnified towards the axis of the vortex.

6. Depending on the ratio of the rotational to axial velocity components, spontaneous expansion of a vortex occurs and in turn produces the pressure rise necessary for core stagnation.

7. Breakdowns situated above a delta wing may be attributed to the pressure recovery associated with the existence of the trailing edge.

8. When the breakdown occurs upstream of the trailing edge, its position depends on a combination of incidence and leading-edge sweepback and is largely independent of Reynolds number.

9. The presence of breakdown above the wing surface causes a local loss in suction and modification of the position of surface flow separation. Hummel and Srinivasan [11] showed the resulting abrupt loss of lift can create a substantial nose up pitching moment.

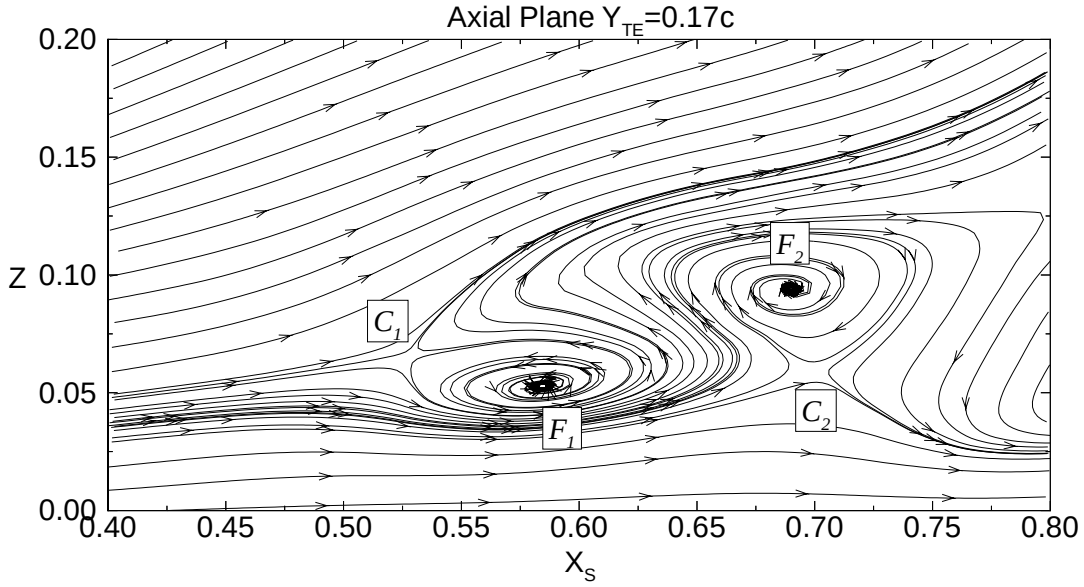

Figure 2.10: Streamlines plotted on an axial plane showing a typical vortex breakdown topology from computed results for a 76^o delta wing at $\alpha = 35^o$, $Re = 1.25 \times 10^6$, $M = 0.3$. See Chapter 7.

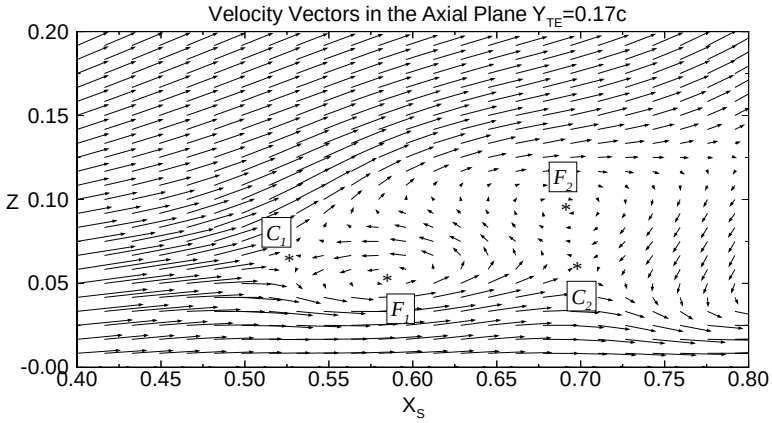

Figure 2.11: In plane velocity vectors with marked and labeled critical points, $\alpha = 35^o$, $Re = 1.25 \times 10^6$, $M = 0.3$. See Chapter 7.

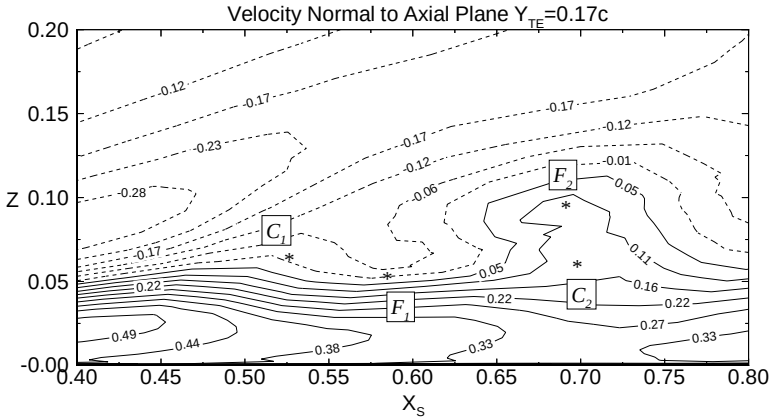

Figure 2.12: Contours of the velocity component normal to the axial cutting plane. Dashed lines indicate velocities pointing out of the page. Critical point locations obtained from streamlines are also plotted. $\alpha = 35^o$, $Re = 1.25 \times 10^6$, $M = 0.3$. See Chapter 7.

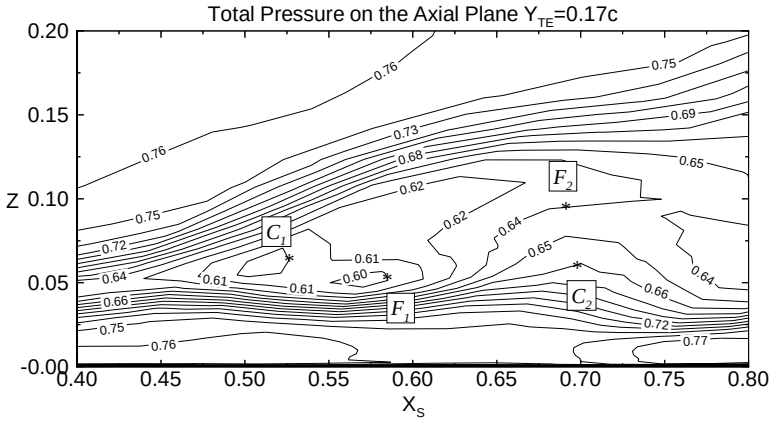

Figure 2.13: Contours of total pressure, and labeled critical point locations showing the vortex core expansion following breakdown. $\alpha = 35^o$, $Re = 1.25 \times 10^6$, $M = 0.3$. See Chapter 7.

2.2.3 Numerical Simulations of Vortex Breakdown

Early computations of vortex breakdown, by Gartshore [38] and others, only considered isolated, axisymmetric, steady vortices. Vortex breakdown was identified as occurring at the location where the calculation procedure could no longer continue due to the excessively high axial gradients, which arise as the stagnation point is approached. In 1987 Spall [39] solved for an isolated vortex at very low Reynolds numbers, using the 3-D incompressible Navier-Stokes equations written in a velocity-vorticity formulation. Using this formulation, the Rossby number, $Ro = \frac{u}{\ell\Omega}$ which represents the ratio of inertial forces to Coriolis forces, was found to be a critical parameter in the prediction of breakdown, where u, ℓ and Ω represent characteristic speed, length and rate of rotation, respectively. The present study is not focused on the onset of breakdown, but rather, the unsteady flow within and especially downstream of breakdown. Thus, attention is focused on methods capable of accurately resolving the entire unsteady flow field.

The first time-accurate, full Navier-Stokes solutions of supersonic vortex breakdown were produced by O. Kandil, H. Kandil and Liu [40]. They considered a supersonic, quasi-axisymmetric vortex flow in a configured circular duct. In general, quasi-axisymmetric solutions are obtained by forcing the components of the flow field vector to be equal on two axial planes, that are in close proximity of each other. In their study, a shock wave was generated near the duct inlet and an unsteady vortex breakdown was predicted behind the shock. The flow was found to be characterized by the evolution, convection and shedding of vortex breakdown bubbles. In papers by O. Kandil, H. Kandil and Liu [40–43], extensive parametric studies were conducted to determine the effects of grid resolution, Reynolds number, inflow/outflow boundary conditions, and inlet swirl ratio. External and three-dimensional flow configurations also were addressed

in the more recent papers. A detailed discussion of these results also can be found in the dissertation by H. Kandil [44].

Advances in algorithms and computational resources have made it possible to retain all of the key physical aspects of the vortex breakdown flow, namely, unsteadiness, viscosity and three-dimensionality. A delta wing with sharp leading edges presents a simple configuration for study. Taylor et al. [45] solved the unsteady, thin-layer Navier-Stokes equations for stable vortex flow over a 76^o delta wing at 20^o incidence. Comparison with experimental data revealed that the computational method under predicts vorticity and total pressure loss in the vortex core. Gordnier and Visbal [46], solved the unsteady, 3-D, full Navier-Stokes equations, for vortex breakdown flow over a 76^o delta wing at 20.5^o incidence. Their results showed that the shear layer emanating from the leading edge is subject to an instability similar to that occurring in a two-dimensional shear layer. Webster and Shang [47] investigated vortex breakdown over a 70^o delta wing at 33^o incidence, also using the full set of governing equations. They noted that the time averaged flow field resembled a bubble type breakdown, while the instantaneous flow field appeared to be the spiral type. In 1993, O. Kandil, H. Kandil and Liu [48], presented the first solutions to the full Navier-Stokes equations for transonic vortex breakdown on a 65^o delta wing.

Vortex breakdown has also been simulated on simplified F/A-18 configurations as a precursor to the study of tail buffeting. In 1990, Rizk, Schiff and Gee [49] modeled the F/A-18 at Mach number and angle-of-attack of 0.24 and 30.3^o, respectively. Results obtained from the solution of the steady, Reynolds averaged Navier-Stokes equations on a Chimera-type grid consisting of 1.7 million grid points, were found to be in qualitative agreement with flight test data.

The effect of turbulence modeling on subsonic delta wing vortex breakdown was assessed by Ekaterinaris and Schiff [50]. They found that the main effect was to increase the amount of vorticity in the vortex feeding sheets, thus increasing the strength of the primary and secondary vortices. This in turn affected the location and size of the breakdown. In a very recent computational study by Rizzetta [51], the effect of a two equation $(K-\epsilon)$ turbulence model on delta wing vortex breakdown was assessed. It was found that the $(K-\epsilon)$ model produced excessive turbulent dissipation, which resulted in enlarged weak vortices with no breakdown. The focus of the present study is on tail buffeting, therefore to avoid issues of turbulence modeling, only the laminar Navier-Stokes equations are considered.

2.3 Vortex Breakdown Induced Tail Buffeting

In general buffeting refers to the forced vibration of a body under the aerodynamic action of a wake. The principal difference between the phenomena of buffeting and flutter is that flutter is a self-excited vibration while buffeting is a forced vibration. Thus, flutter is a stability problem and buffeting is a structural response problem. In this study, the tail buffeting phenomenon is particularly violent and long lasting as it is a result of prolonged high speed, high angle-of-attack maneuvers.

2.3.1 Historical Perspective

The study of the buffeting phenomenon began in earnest with the investigation into the fatal crash of the Junkers low-wing monoplane at Meopham, England in 1930. [52] Eye witnesses reported seeing the plane enter a cloud, suddenly hearing a loud noise and then seeing the pieces of the plane fall to the ground. British investigators concluded that the most likely cause of the accident was buffeting of the tail, brought on by strong

rising air currents. The updrafts effectively increased the angle of incidence, resulting in flow separation over the wing. The tail, situated in the wing's highly turbulent wake flow, was then subjected to severe vibrations, which resulted in its catastrophic failure.

The primary cause of tail buffeting in these early low-wing monoplanes was flow separation at the wing-fuselage junction. In 1934, White and Hood [53] found that adding large wing fillets and an engine cowling greatly reduced buffeting and improved the aircraft's lift-to-drag ratio.

In 1939, Abdrashitov [54] asserted that existing solutions to the tail buffeting problem were based only on qualitative estimates of the phenomenon, and that the quantitative analytical problem had not even been approximately solved. Abdrashitov's analysis considered only the dynamics of the tail, in which the loads were assumed to be harmonic. The tail was modeled as a beam in bending and torsion and solved via Galerkin's method. Remarkably, this parallels the approach used in the present study. Since the forces are obtained directly from the CFD solution, there is no need for all of the additional complexities involved in predicting the buffet loads. In a sense, the theory has come full circle.

2.3.2 Physical Characteristics of Tail Buffeting

Modern fighter aircraft, such as the F/A-18, maneuver at very high angles-of-attack under high loading conditions. The F/A-18 achieves its high maneuverability through the use of wing Leading Edge eXtensions (LEX), a delta wing, and strategically placed vertical tails. The LEX produce lift at high angles-of-attack by generating a pair of vortices that trail over the wing surface. The vortices also entrain air over the vertical tails, maintaining control surface effectiveness at high angle-of-attack. This combination of LEX and vertical tail location produces excellent high angle-of-attack performance.

However, at high speed, high angle-of-attack conditions the vortices emanating from the highly swept leading edge extensions breakdown or burst before reaching the vertical tails, bathing them in a highly turbulent, swirling flow. This flow produces severe buffeting of the vertical tails which leads to premature fatigue failure.

In the past decade, this phenomenon has been the subject of substantial experimental inquiry. In 1983, Triplett [55] conducted wind tunnel studies of a 13% scale F-15 model. He concluded that the predominant vibration mode was first torsion and occurred at 22^o angle-of-attack. He also concluded that tail flexibility has a significant effect on the impinging buffet loads.

In 1989, Fisher, Del Frate and Richwine [56] conducted flight test on the NASA F/A-18 High Alpha Research Vehicle (HARV). Flow visualizations revealed extensive regions of separated, reversed, and vortical flow on the wing at angles-of-attack above 20^o.

Erickson et al. [57] investigated F/A-18 vortex flows at subsonic through transonic speeds using a 6% scale model. They concluded that the LEX vortices are highly compressible, even at very low subsonic Mach numbers. However, compressibility effects are not manifested on the forebody until transonic speeds, where shock-induced boundary layer separation promotes larger and stronger vortices.

Lee and Brown [58] also used the 6% scale F/A-18 model in their wind tunnel studies of tail buffet. Unsteady pressure measurements on the vertical tail were conducted and the vortex flow structure behind the tail was studied. It was observed that the LEX fence has only a small effect on the steady balance measurements such as lift and pitching moment.

Cole, Moss and Doggett [59] conducted wing tunnel test on a 1/6th scale rigid F/A-18 model fitted with flexible vertical tails of two levels of stiffness. They concluded that the buffeting response occurred in the first bending mode, and increased non-linearly with dynamic pressure and peaked at $M = 0.3$. They also classified the buffeting response as "heavy" to "severe."

In a recent NASA technical memorandum [60], Moses and Pendleton compared tail pressure measurements between full-scale and 1/6-scale models. Results were presented in terms of non-dimensional buffet excitation parameter and power spectral densities of root bending moment for an angle-of-attack range of 7^o to 40^o and Mach and Reynolds numbers up to 0.15 and 12.3×10^6, respectively. The LEX fence was confirmed to be effective at reducing buffet loads for $\alpha < 32^o$. It was found that the data trends for the two different size models scaled well using a simple scaling equation.

An experimental investigation of vortex breakdown induced tail buffeting, particularly relevant to this study, is that of Washburn, Jenkins and Ferman [12]. They conducted an extensive investigation into vortex-tail interaction using a 76^o delta wing with twin vertical tails. The vertical tails were placed at nine locations aft of the delta wing. The results showed that the aerodynamic loads were more sensitive to the chordwise tail location than the spanwise location. The buffeting response was seen to decrease as the tails were moved towards the vortex core. It was also shown that the core trajectories upstream of the tail were not influenced by the tail location, but the breakdown location was. Additionally, the investigation showed that the presence of a flexible tail can affect the unsteady pressures on a rigid tail located on the opposite side of the model. This case is the subject of the one of the numerical simulations of this study and is discussed further in Chapter 7.

2.3.3 Numerical Simulation of Tail Buffeting

For design and analysis purposes, a model of the tail buffeting phenomenon is desired. Currently, accurate theoretical models do not exist and accurate full aircraft computational simulations are prohibitively expensive. Thus, there is a need for a simple model that captures the essence of the tail buffeting phenomenon.

In 1990, Edwards [61] assessed the computational cost of direct numerical simulation of tail buffeting. He concluded that computer speed would have to increase by a factor of a thousand before full aircraft computations would become practical, thus reducing a 1000-hour computation to only 1 hour. His time estimates were based on $40\mu\,seconds$ per grid cell per time step for thin-layer Navier Stokes solutions. The current run time for the full Navier-Stokes equations on a single processor of a Cray C90 is $7.8\mu\,seconds$ per grid cell per time step, a factor of only five times faster. Because of this high computational cost, very few numerical studies have been conducted to date [51, 62–75] and of those, the *only* ones to include aeroelastic effects are those by the author's research group [67–75], led by O.A. Kandil.

In 1992, Rizk et al. [62, 63] investigated the unsteady loads on vertical tails by solving the Reynolds-averaged Navier-Stokes equations time accurately for a F/A-18 at $\alpha = 30^o$. The flow field and response were qualitatively similar to some experimentally observed phenomena. To model the symmetric half of the aircraft, a Chimera-type grid consisting of 0.9 million cells was used. Note that, in studies conducted by Kandil, Massey and Kandil [70], the same number of grid points were used to resolve the flow about a simple delta wing. In a later study by the same group [64], a refined grid consisting of 1.7 million cells produced significantly better results for aerodynamic loads. Another issue with the Rizk et al. [62, 63] studies is "weak coupling" between the aero-

dynamics and the structures. The flow only saw a fixed, rigid tail. Thus, all of the inertial effects on the local flow field from the very high accelerations of the tail were neglected. Moreover, their model neglected the aerodynamic damping originating from the interaction between the deflected tail and the flow. These effects have been shown, experimentally [12,55] and computationally [67], to significantly affect the unsteady pressure loading on the tails. Although, this latter concern can be easily alleviated by the implementation of moving grids, the high computational cost of accurately solving for a full aircraft configuration remains.

In the studies by Kandil et al. [67–75], geometrically simple models of two basic types are considered such that the computational resources are only concentrated on the pertinent flow physics. The first model type consists of a configured duct in which the inlet swirling flow is forced to breakdown either through a shock wave (for transonic and supersonic inlet flows) or through a gradual adverse pressure gradient that is generated by the duct wall (for subsonic inlet swirling flows). A vertical cantilevered tail is placed downstream of the breakdown flow. Using this configuration, Kandil and Flanagan [68] and Flanagan [69] solved the unsteady, compressible, full Navier-Stokes equations, assuming quasi-axial symmetry. The tail was modeled as a beam in bending and was coupled with the aerodynamics so as to allow full communication with the flow. Work is currently under way to solve the three-dimensional duct problem with an improved vertical tail model.

The second model type consists of a delta wing at a high angle-of-attack with either, a single vertical tail [67, 70–73] or twin-tails [74, 75] placed at the trailing edge of the wing. In the present study, only the second model type is considered and emphasis is place in the twin-tail configurations.

In 1993, Kandil, Kandil and Massey [67] solved the three-dimensional, unsteady, compressible, full Navier-Stokes equations time accurately on the single tail/delta wing configuration. The tail was modeled as a cantilevered beam in bending only and was fully coupled with the aerodynamics. Variations in tail size, location, and structural properties were investigated. The solutions showed that the tail location, shape, flexibility and motion affect the upstream flow field.

The structural equations were then reformulated by the author to include inertially coupled bending and torsion vibration modes, Kandil, Massey and Kandil [70]. In this study a single flat square tail was considered. The flow field was once again obtained by solving the unsteady, compressible, full Navier-Stokes equations, using an upwind, flux-vector splitting finite-volume scheme. The results show substantial effects of torsional deflections of the tail for the coupled bending-torsion response case in comparison with the bending response case. The results also show that the deflections and loads of the coupled bending-torsion response case are substantially lower than those of the uncoupled bending-torsion response case. These results were the subject of the author's master's thesis [71]. Results for this configuration were then obtained for longer time periods and higher Reynolds numbers using the flux difference splitting scheme of Roe, which introduces less numerical dissipation than flux vector splitting, Kandil, Massey and Sheta [72]. These results are discussed in detail in Chapter 5.

As a transition to a more realistic tail model, Kandil, Sheta and Massey [73] considered a single tail shaped after Washburn et al. [12] mounted at the trailing edge of a cropped delta wing in transonic flow. The wing and flow selection follows that of Kandil et al. [76]. Solutions were obtained at $\alpha = 20^o$ and 28^o. The buffet loads increased with angle-of-attack and did not reach periodicity as in the previous subsonic cases [70].

In 1996, twin vertical tail buffeting was successfully simulated. Kandil, Sheta and Massey [75] considered twin vertical F/A-18 tails mounted behind the same 76^o delta wing used previously. Two spanwise tail positions were studied, one corresponding to the separation distance of the tails being equal to the relative placement of the tails on the actual aircraft and another position inboard, corresponding to the location chosen in the Washburn et al. [12] study. The first spanwise location case, is considered in detail in Chapter 6 as part of a study on the effects of the placement of aft solid surfaces as the root of the tails. The second span location is considered in Chapter 7 as part of a study on the effect of spanwise tail placement using the configuration of Washburn et al. [12]. Early results of the latter study by Kandil, Massey and Sheta [75] agreed well with the experimental data of Washburn et al. [12].

The Washburn experimental study was first published with a companion numerical study by Krist et al. [65]. Unfortunately the choice of a low angle-of-attack and Mach number produced *no vortex breakdown whatsoever*, and therefore no buffet loads. Very recently a numerical simulation of the same configuration was also conducted by Findlay [66]. Although, the flow parameters were sufficient to produce the buffeting breakdown flow, no attempt was made to predict or include aeroelastic effects into Findlay's simulation.

2.4 Vortex Control Techniques

The ultimate purpose of studying the vortex breakdown buffeting problem is to devise a way of alleviating or removing violent buffet loads from the vertical tails without sacrificing high angle-of-attack maneuverability. Although a great deal of studies have been published on the subject of vortical flow control, the majority are concerned with

the control of forebody asymmetry. Vortex asymmetry plays an important role in the ability of an aircraft or missile [77] to maintain yaw control at high angles-of-attack, but has nothing to do with vortex breakdown induced buffeting. The primary methods employed in forebody control are; movable full and miniature nose strakes, jet and slot blowing, and tip suction. A thorough review of the applications of these methods to F/A-18, F-16, X-29A and other aircraft is given by Malcolm [78].

At the next level of specialization is the control of vortex breakdown itself. Studies of vortex breakdown control proceeded closely after the first observations of vortex breakdown. In 1962, Lambourne and Bryer [3] evaluated the effects of upstream flow perturbations, slender bodies placed within the vortex cores, free stream acceleration/deceleration, core suction, trailing edge flaps, and wing camber. Because the majority of the early studies only considered *isolated* vortices in tubes or above clean delta wings, the effect of the vertical tails on the breakdown, and hence the ability to control breakdown can not be determined from these studies alone.

Thus, at the final level of inquiry the question to be answered is, "Does a given vortex control technique reduce the level of vertical tail buffet?" There are essentially two methods of attacking this problem in the flow regime: removing the vortex breakdown while preserving the vortex itself; or diffusing the vortex at some location upstream of the tails so as to optimize the balance between the benefit of vortex lift and the adverse effects of the post breakdown buffeting flow. Perhaps because of the difficulty of preventing breakdown in the presence of vertical tails, the method of choice for the F/A-18 has been diffusion.

Through trial and error the F/A-18 was retro-fitted with a short fence normal to the surface of the LEX, see Figure 2.14, in order to diffuse the vortex strength while

having a minimal effect on aircraft aerodynamics, Lee and Valerio [8]. In flight tests by Lee et al. [79] without the LEX fence, peak accelerations of $450g$ close to the tip of the vertical tail were measured. With the addition of LEX fences, the peak accelerations were reduced to $200g$. While this solution provides significant buffet relief, diffusion does impose an aerodynamic penalty and is less effective at high angles-of-attack [80–82].

Recalling the fact that buffeting is a structural problem at its core, another avenue of attack is the control of the tail itself. This can be accomplished in several ways; engineering a structure or material that is less susceptible to fatigue, using composites to create a strain hardening tail, or active structural control using piezoelectric panels for active stiffening. Although, the first two methods are simpler in the long run, initial test of active buffet damping through the use of piezoelectrics have produced favorable results, e.g., Hauch et al. [83]. In the final analysis, a combination of aerodynamic and structural controls may provide the greatest benefit to high angle-of-attack aviation. In this study only flow control is considered. However, since the structural response was included in the present analysis, the problem of active structural control could be solved by modifying the existing structural subroutines.

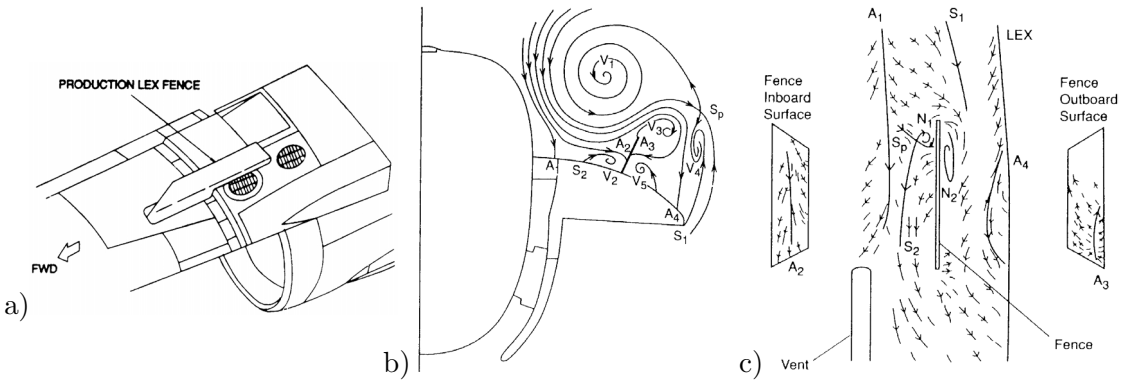

Figure 2.14: LEX fence shown a) installed and with b) front and c) top-view flow field topology sketches. Lee and Valerio [8]

CHAPTER 3

FLUID DYNAMICS FORMULATION

3.1 Introduction

In this study, two sets of governing equations, along with certain initial and boundary conditions, are used to formulate the problem of vortex breakdown induced tail buffeting. The first set is the laminar, unsteady, compressible, full Navier-Stokes equations. The second set consists of the elastic beam equations for coupled bending and torsion vibrations.

For complex flow fields with strong viscous-inviscid interactions, reduced forms of the equations of fluid motion do not provide an adequate model of the flow physics. In the present study, strong viscous-inviscid interactions in the form of large-scale three-dimensional boundary-layer separation require that the full Navier-Stokes equations be considered.

3.2 Three-Dimensional Navier-Stokes Equations

The conservative form of the dimensionless, unsteady, compressible, full Navier-Stokes equations in terms of continuity, momentum and energy are expressed as:

1. Continuity:

$$\frac{\partial \rho}{\partial t} + \frac{\partial}{\partial x_i}(\rho u_i) = 0 \tag{3.1}$$

where according to the Einstein indicial notation, all indices range from 1-3 and repeated indices denote summation.

2. i^{th}-component of the Navier-Stokes Equations:

$$\frac{\partial}{\partial t}(\rho u_i) + \frac{\partial}{\partial x_j}(\rho u_i u_j + \delta_{ij} p) = \frac{\partial \tau_{ij}}{\partial x_j} \tag{3.2}$$

For a Newtonian fluid with Stoke's hypothesis imposed ($\lambda = -\frac{2}{3}\mu$), the shear stress components are given by,

$$\tau_{ij} = \frac{\mu M_\infty}{Re_\infty}\left[\frac{\partial u_i}{\partial x_j} + \frac{\partial u_j}{\partial x_i} - \frac{2}{3}\delta_{ij}\frac{\partial u_k}{\partial x_k}\right] \tag{3.3}$$

3. Energy:

$$\frac{\partial}{\partial t}(\rho e_t) + \frac{\partial}{\partial x_j}\left[\rho u_j\left(e_t + \frac{p}{\rho}\right)\right] = \frac{\partial}{\partial x_j}\left(u_k \tau_{jk} - q_j\right) \tag{3.4}$$

Assuming Fourier conductivity, the heat flux components are given by

$$q_j = -\frac{\mu M_\infty}{Re_\infty Pr(\gamma - 1)}\frac{\partial T}{\partial x_j} \tag{3.5}$$

The Prandtl number is defined as $Pr = \frac{\mu c_p}{k}$ and is assumed to be a constant value of 0.72 for all computations. Pressure is related to the total energy per unit mass, and density for a thermally perfect gas by the equation

$$p = (\gamma - 1)\rho\left[e_t - \frac{1}{2}u_i u_i\right] \tag{3.6}$$

The flow is also assumed to be calorically perfect with the ratio of specific heats (γ) equal to 1.4. The molecular viscosity is calculated from Sutherland's law

$$\frac{\mu}{\mu_\infty} = \left(\frac{T}{T_\infty}\right)^{3/2}\left(\frac{T_\infty + C}{T + C}\right),\ C = 110.4^o K \tag{3.7}$$

The governing equations, Eqs. (3.1-3.4) may be written in nondimensional flux vector form as,

$$\frac{\partial \vec{q}}{\partial t} + \frac{\partial}{\partial x_j}\left[\vec{E}_j - (\vec{E}_v)_j\right] = 0 \tag{3.8}$$

where the flow vector ($\vec{q}$), and the j^{th} inviscid flux ($\vec{E}_j$) and viscous flux vectors ($(\vec{E}_v)_j$) are given by:

$$\vec{q} = \begin{Bmatrix} \rho \\ \rho u_1 \\ \rho u_2 \\ \rho u_3 \\ \rho e_t \end{Bmatrix} \qquad \vec{E}_j = \begin{Bmatrix} \rho u_j \\ \rho u_1 u_j + \delta_{1j} p \\ \rho u_2 u_j + \delta_{2j} p \\ \rho u_3 u_j + \delta_{3j} p \\ \rho u_j \left(e_t + \frac{p}{\rho} \right) \end{Bmatrix} \qquad (\vec{E}_v)_j = \begin{Bmatrix} 0 \\ \tau_{1j} \\ \tau_{2j} \\ \tau_{3j} \\ u_k \tau_{kj} - q_j \end{Bmatrix} \tag{3.9}$$

Because of their favorable conservation properties in supersonic flow, the preceding equations were written on the strong conservation form. Another concern is the implementation of the boundary conditions. In order to assign the boundary conditions on the body surfaces and to handle deforming clustered grids, the governing fluid dynamics equations must be transformed into time-dependent, body-conformed coordinates, ξ^1, ξ^2 and ξ^3; where

$$\xi^m = \xi^m(x_1, x_2, x_3, t) \tag{3.10}$$

Equation (3.8) becomes

$$\frac{\partial \bar{Q}}{\partial t} + \frac{\partial}{\partial \xi^m} \left[\bar{E}_m - (\bar{E}_v)_m \right] = 0 \tag{3.11}$$

where

$$\bar{Q} = \frac{\vec{q}}{J} = \frac{1}{J} \begin{Bmatrix} \rho \\ \rho u_1 \\ \rho u_2 \\ \rho u_3 \\ \rho e_t \end{Bmatrix} \tag{3.12}$$

and $\frac{1}{J} \equiv J^{-1}$ is the Jacobian of the transformation from physical Cartesian space to computational curvilinear coordinates, given by

$$J^{-1} = \frac{\partial(x_1, x_2, x_3)}{\partial(\xi^1, \xi^2, \xi^3)} = \begin{vmatrix} x_{1_{\xi^1}} & x_{1_{\xi^2}} & x_{1_{\xi^3}} \\ x_{2_{\xi^1}} & x_{2_{\xi^2}} & x_{2_{\xi^3}} \\ x_{3_{\xi^1}} & x_{3_{\xi^2}} & x_{3_{\xi^3}} \end{vmatrix} \tag{3.13}$$

This Jacobian is identical to the Jacobian obtained for a time-independent coordinate transformation. This is due to the fact that, the transformed time, τ, is identical to the

physical time variable, t, which is considered absolute. The transformed inviscid flux vector is given by

$$\bar{E}_m = \frac{1}{J}\left\{\frac{\partial \xi^m}{\partial t}\vec{q} + \frac{\partial \xi^m}{\partial x_k}\vec{E}_k\right\} = \frac{1}{J}\begin{Bmatrix} \rho U_m \\ \rho u_1 U_m + \dfrac{\partial \xi^m}{\partial x_1}p \\ \rho u_2 U_m + \dfrac{\partial \xi^m}{\partial x_2}p \\ \rho u_3 U_m + \dfrac{\partial \xi^m}{\partial x_3}p \\ U_m(\rho e_t + p) - \dfrac{\partial \xi^m}{\partial t}p \end{Bmatrix} \tag{3.14}$$

where U_m is the contravariant velocity component in the ξ^m direction given by

$$U_m = \frac{\partial \xi^m}{\partial t} + \frac{\partial \xi^m}{\partial x_k}u_k \tag{3.15}$$

The viscous and heat fluxes are given by

$$(\bar{E}_v)_m = \frac{1}{J}\left\{\frac{\partial \xi^m}{\partial x_k}(\vec{E}_v)_k\right\} = \frac{1}{J}\begin{Bmatrix} 0 \\ \dfrac{\partial \xi^m}{\partial x_k}\tau_{1k} \\ \dfrac{\partial \xi^m}{\partial x_k}\tau_{2k} \\ \dfrac{\partial \xi^m}{\partial x_k}\tau_{3k} \\ \dfrac{\partial \xi^m}{\partial x_k}(u_i\tau_{ik} - q_k) \end{Bmatrix} \tag{3.16}$$

The shear stress and heat conduction components in Eq.(3.16) are given by

$$\tau_{ik} = \frac{\mu M_\infty}{Re_\infty}\left(\frac{\partial \xi^m}{\partial x_k}\frac{\partial u_i}{\partial \xi^m} + \frac{\partial \xi^m}{\partial x_i}\frac{\partial u_k}{\partial \xi^m} - \frac{2}{3}\delta_{ik}\frac{\partial \xi^m}{\partial x_j}\frac{\partial u_j}{\partial \xi^m}\right) \tag{3.17}$$

and

$$q_k = -\frac{\mu M_\infty}{Re_\infty Pr(\gamma - 1)}\frac{\partial \xi^m}{\partial x_k}\frac{\partial a^2}{\partial \xi^m} \tag{3.18}$$

where a is the dimensionless local speed of sound and $a^2 = T$. Expanding the i^{th} momentum element of Eq. (3.16) gives

$$\frac{\partial \xi^m}{\partial x_k}\tau_{ik} = \frac{\mu M_\infty}{Re_\infty}\left[\left(\frac{\partial \xi^m}{\partial x_k}\frac{\partial \xi^n}{\partial x_i} - \frac{2}{3}\frac{\partial \xi^m}{\partial x_i}\frac{\partial \xi^n}{\partial x_k}\right)\frac{\partial u_k}{\partial \xi^n} + \frac{\partial \xi^m}{\partial x_k}\frac{\partial \xi^n}{\partial x_k}\frac{\partial u_i}{\partial \xi^m}\right] \tag{3.19}$$

Expanding the energy element of Eq. (3.16) gives

$$\frac{\partial \xi^m}{\partial x_k}(u_i \tau_{ik} - q_k) = \frac{\mu M_\infty}{Re_\infty}\left[\left(\frac{\partial \xi^m}{\partial x_k}\frac{\partial \xi^n}{\partial x_i} - \frac{2}{3}\frac{\partial \xi^m}{\partial x_i}\frac{\partial \xi^n}{\partial x_k}\right) u_i \frac{\partial u_k}{\partial \xi^n} + \frac{\partial \xi^m}{\partial x_k}\frac{\partial \xi^n}{\partial x_k} u_i \frac{\partial u_i}{\partial \xi^n} + \frac{1}{(\gamma-1)Pr}\frac{\partial \xi^m}{\partial x_k}\frac{\partial (a^2)}{\partial \xi^n}\right] \tag{3.20}$$

3.3 Computational Fluid Dynamics Formulation

3.3.1 Introduction

Throughout this study, an implicit, upwind, finite volume scheme, with Roe [84] flux-difference splitting, is used to integrate the laminar Navier-Stokes equations. The scheme is implemented in a modified version of the CFL3D [85] code, which was upgraded by Kandil et al. [40–43, 76] to solve the fully viscous Navier-Stokes equations. The following sections contain a brief discussion of the components of this scheme. A general survey of methods used to solve the compressible Navier-Stokes equations can be found in the review article of Walters and Thomas [86].

3.3.2 Nondimensionalization

The advantage of nondimensionalizing the governing equations is that the characteristic parameters of the flow such as Mach number, Reynolds number, Prandtl number, etc., become isolated and can be varied independently. This also facilitates comparison with data from other sources. Numerically, nondimensionalization prevents the order of magnitude of individual terms from changing arbitrarily due to the selection of units. Many nondimensionalization schemes are possible. The reference parameters for the dimensionless form of the fluid dynamics equations in the code are $\tilde{c}, \tilde{a}_\infty, \frac{\tilde{c}}{\tilde{a}_\infty}, \tilde{\rho}_\infty$ and $\tilde{\mu}_\infty$ for the length, velocity, time, density and dynamic viscosity, respectively. Performing

the nondimensionalizations yields:

$$t = \frac{\tilde{t}\tilde{a}_\infty}{\tilde{c}} \tag{3.21}$$

$$x_i = \frac{\tilde{x}_i}{\tilde{c}} \tag{3.22}$$

$$\rho = \frac{\tilde{\rho}}{\tilde{\rho}_\infty} \tag{3.23}$$

$$u_i = \frac{\tilde{u}_i}{\tilde{a}_\infty} \tag{3.24}$$

$$p = \frac{\tilde{p}}{\tilde{\rho}_\infty \tilde{a}_\infty^2} \tag{3.25}$$

$$e = \frac{\tilde{e}}{\tilde{\rho}_\infty \tilde{a}_\infty^2} \tag{3.26}$$

$$a = \frac{\tilde{a}}{\tilde{a}_\infty} \tag{3.27}$$

$$T = \frac{\tilde{T}}{\tilde{T}_\infty} = \frac{\gamma p}{\rho} = a^2 \tag{3.28}$$

where ˜ represents dimensional quantities. The freestream parameters are given by;

$$\rho_\infty = 1 \tag{3.29}$$

$$u_{1_\infty} = M_\infty \cos\alpha \cos\beta \tag{3.30}$$

$$u_{2_\infty} = -M_\infty \sin\beta \tag{3.31}$$

$$u_{3_\infty} = M_\infty \sin\alpha \cos\beta \tag{3.32}$$

$$e_{t_\infty} = \frac{1}{\gamma(\gamma-1)} + \frac{M_\infty^2}{2} \tag{3.33}$$

$$p_\infty = \frac{1}{\gamma} \tag{3.34}$$

$$a_\infty = 1 \tag{3.35}$$

$$T_\infty = 1 \tag{3.36}$$

$$V_\infty = \sqrt{u_{1_\infty}^2 + u_{2_\infty}^2 + u_{3_\infty}^2} \tag{3.37}$$

$$M_\infty = \frac{\tilde{V}_\infty}{\tilde{a}_\infty} \tag{3.38}$$

$$Re_\infty = \frac{\tilde{\rho}_\infty \tilde{V}_\infty \tilde{c}}{\tilde{\mu}_\infty} \tag{3.39}$$

where α and β are the angle-of-attack and yaw, respectively.

3.3.3 Implicit Upwind Conservative Schemes

The governing equations may be integrated in time, explicitly or implicitly. Explicit schemes are simpler and more computationally economical per time step. However, numerical stability requirements impose a heavy time step penalty, which substantially increases the total computational cost of the scheme. Implicit methods, while more costly per time step, have a more relaxed stability criterion, which allows larger time steps. Thus, taken on the whole, implicit schemes are more economical and are therefore utilized in the present study. In the future as computers become more parallel, explicit schemes may be more economical.

Upwind methods seek to recognize the direction of propagation of information within a mesh, in accordance with the theory of characteristics, and to take advantage of this knowledge by type-dependent differencing components of the information traveling in opposite directions separately. Upwind methods may be incorporated into either conservative or nonconservative forms of the governing equations. The advantage of the conservative formulation is that shock waves and contact discontinuities evolve as part of the solution. In addition, as grid resolution increases, the location and strength of these discontinuities are accurately resolved. Thus, this approach is applicable to a wide class of problems. The disadvantage is that the nonconservative formulation is more computationally economical, however, it must be supplemented by shock fitting schemes which are not applicable to complex flows. Thus, the upwind, conservative formulation is the most appropriate scheme for general-purpose codes, such as the one used in this study.

3.3.4 Cell-Centered Finite Volume Formulation

Recalling from Eq. (3.11), the conservative flux vector form of the dimensionless, unsteady, compressible, full Navier-Stokes equations in terms of time-dependent, body-conforming coordinates is

$$\frac{\partial \bar{Q}}{\partial t} + \frac{\partial}{\partial \xi^m}\left[\bar{E}_m - (\bar{E}_v)_m\right] = 0 \tag{3.40}$$

Rewriting as an integral statement of conservation gives

$$\int_\forall \frac{\partial \bar{Q}}{\partial t} d\forall + \int_\forall \frac{\partial}{\partial \xi^m}\left[\bar{E}_m - (\bar{E}_v)_m\right] d\forall = 0 \tag{3.41}$$

Application of the divergence theorem to the second term to convert the volume integral to a surface integral yields

$$\int_\forall \frac{\partial}{\partial \xi^m}\left[\bar{E}_m - (\bar{E}_v)_m\right] d\forall = \oint_S \left[\bar{E}_m - (\bar{E}_v)_m\right] \hat{n}_m dS \tag{3.42}$$

where, S is the surface bounding the volume, $\forall$, and $\hat{n}$ is the unit outward normal to S. For a particular cell, the surface integral may be expressed as the sum of the contributions from the six faces of the hexagonal cell.

$$\begin{aligned}
&\oint_S \left[\bar{E}_m - (\bar{E}_v)_m\right] \hat{n}_m dS \\
&\quad \approx \left[\bar{E}_m - (\bar{E}_v)_m\right] \hat{n}_m |\Delta S|\Big|_{i+\frac{1}{2},j,k} + \left[\bar{E}_m - (\bar{E}_v)_m\right] \hat{n}_m |\Delta S|\Big|_{i-\frac{1}{2},j,k} \\
&\quad + \left[\bar{E}_m - (\bar{E}_v)_m\right] \hat{n}_m |\Delta S|\Big|_{i,j+\frac{1}{2},k} + \left[\bar{E}_m - (\bar{E}_v)_m\right] \hat{n}_m |\Delta S|\Big|_{i,j-\frac{1}{2},k} \\
&\quad + \left[\bar{E}_m - (\bar{E}_v)_m\right] \hat{n}_m |\Delta S|\Big|_{i,j,k+\frac{1}{2}} + \left[\bar{E}_m - (\bar{E}_v)_m\right] \hat{n}_m |\Delta S|\Big|_{i,j,k-\frac{1}{2}} \qquad (3.43) \\
&\quad = \left\{\left(\left[\bar{E} - \bar{E}_v\right] \cdot \frac{\nabla \xi^1}{\|\nabla \xi^1\|}\right) \frac{\|\nabla \xi^1\|}{J}\right\}_{i+\frac{1}{2},j,k} - \left\{\left(\left[\bar{E} - \bar{E}_v\right] \cdot \frac{\nabla \xi^1}{\|\nabla \xi^1\|}\right) \frac{\|\nabla \xi^1\|}{J}\right\}_{i-\frac{1}{2},j,k} \\
&\quad + \left\{\left(\left[\bar{E} - \bar{E}_v\right] \cdot \frac{\nabla \xi^2}{\|\nabla \xi^2\|}\right) \frac{\|\nabla \xi^2\|}{J}\right\}_{i,j+\frac{1}{2},k} - \left\{\left(\left[\bar{E} - \bar{E}_v\right] \cdot \frac{\nabla \xi^2}{\|\nabla \xi^2\|}\right) \frac{\|\nabla \xi^2\|}{J}\right\}_{i,j-\frac{1}{2},k} \\
&\quad + \left\{\left(\left[\bar{E} - \bar{E}_v\right] \cdot \frac{\nabla \xi^3}{\|\nabla \xi^3\|}\right) \frac{\|\nabla \xi^3\|}{J}\right\}_{i,j,k+\frac{1}{2}} - \left\{\left(\left[\bar{E} - \bar{E}_v\right] \cdot \frac{\nabla \xi^3}{\|\nabla \xi^3\|}\right) \frac{\|\nabla \xi^3\|}{J}\right\}_{i,j,k-\frac{1}{2}} \qquad (3.44)
\end{aligned}$$

$$= \left[\bar{E}_1 - (\bar{E}_v)_1\right]_{i+\frac{1}{2},j,k} - \left[\bar{E}_1 - (\bar{E}_v)_1\right]_{i-\frac{1}{2},j,k}$$
$$+ \left[\bar{E}_2 - (\bar{E}_v)_2\right]_{i,j+\frac{1}{2},k} - \left[\bar{E}_2 - (\bar{E}_v)_2\right]_{i,j-\frac{1}{2},k}$$
$$+ \left[\bar{E}_3 - (\bar{E}_v)_3\right]_{i,j,k+\frac{1}{2}} - \left[\bar{E}_3 - (\bar{E}_v)_3\right]_{i,j,k-\frac{1}{2}} \tag{3.45}$$

where

$$\frac{\nabla\xi^1}{\|\nabla\xi^1\|} \Rightarrow \frac{\dfrac{\partial\xi^1}{\partial x^r}}{\sqrt{\dfrac{\partial\xi^1}{\partial x^s}\dfrac{\partial\xi^1}{\partial x^s}}} \tag{3.46}$$

which are the direction cosines of the cell face normal to the ξ^1 direction, and

$$\frac{\|\nabla\xi^1\|}{J} \Rightarrow \frac{\sqrt{\dfrac{\partial\xi^1}{\partial x^s}\dfrac{\partial\xi^1}{\partial x^s}}}{J} \equiv \text{directed area of the cell face} \tag{3.47}$$

Substituting Eq. (3.45) into Eq. (3.41) and recognizing that $\frac{1}{J}$ corresponds to the discrete evaluation of the volume bounded by surfaces of constant ξ^1, ξ^2 and ξ^3, gives the final form of the semidiscete finite volume representation of the governing equations.

$$\begin{aligned}\left[\frac{1}{J}\frac{\partial\vec{q}}{\partial t}\right]_{i,j,k} &+ \left[\bar{E}_1 - (\bar{E}_v)_1\right]_{i+\frac{1}{2},j,k} - \left[\bar{E}_1 - (\bar{E}_v)_1\right]_{i-\frac{1}{2},j,k} \\ &+ \left[\bar{E}_2 - (\bar{E}_v)_2\right]_{i,j+\frac{1}{2},k} - \left[\bar{E}_2 - (\bar{E}_v)_2\right]_{i,j-\frac{1}{2},k} \\ &+ \left[\bar{E}_3 - (\bar{E}_v)_3\right]_{i,j,k+\frac{1}{2}} - \left[\bar{E}_3 - (\bar{E}_v)_3\right]_{i,j,k-\frac{1}{2}} = 0\end{aligned} \tag{3.48}$$

3.3.5 Euler Implicit Time Integration

The semidiscrete finite volume representations of the governing equations, Eq. (3.48) are integrated in time using Euler implicit time differencing. Expanding the vector of conserved variables, $\vec{q}$, using a Taylor series gives

$$\vec{q}^{n+1} = \vec{q}^n + \Delta t \left(\frac{\partial\vec{q}}{\partial t}\right)^n + \mathcal{O}(\Delta t)^2 \tag{3.49}$$

The governing equations, Eq. (3.11), at the $n+1$ time level, are given by

$$\frac{1}{J}\left(\frac{\partial \vec{q}}{\partial t}\right)^{n+1} + \left(\frac{\partial}{\partial \xi^m}\left[\bar{E}_m - (\bar{E}_v)_m\right]\right)^{n+1} = 0 \tag{3.50}$$

Substituting the Taylor series expansion, Eq. (3.49), into this equation gives

$$\frac{1}{J}\frac{\Delta \vec{q}}{\Delta t} + \left(\frac{\partial}{\partial \xi^m}\left[\bar{E}_m - (\bar{E}_v)_m\right]\right)^{n+1} = \mathcal{O}(\Delta t) \tag{3.51}$$

where

$$\Delta \vec{q} = \vec{q}^{\,n+1} - \vec{q}^{\,n} \tag{3.52}$$

In terms of a steady state residual, R, Eq. (3.51) may be rewritten as

$$\frac{1}{J}\frac{\Delta \vec{q}}{\Delta t} - \Delta R = R(\vec{q}^{\,n}) \tag{3.53}$$

This set of coupled nonlinear algebraic equations are linearized using Taylor series expansions as follows,

$$\left[\frac{I}{J\Delta t} - \frac{\partial R}{\partial \vec{q}}\right]\Delta \vec{q} = R(\vec{q}^{\,n}) \tag{3.54}$$

In terms of the inviscid and viscous fluxes, we have

$$\left[\frac{I}{J\Delta t} + \delta_{\xi^m}\left(\frac{\partial}{\partial \vec{q}}\left[\bar{E}_m - (\bar{E}_v)_m\right]\right)^n\right]\Delta \vec{q} = -\delta_{\xi^m}\left(\bar{E}_m - (\bar{E}_v)_m\right)^n \tag{3.55}$$

where the spatial derivatives have been replaced by the general difference operators, δ_{ξ^m}.

3.3.6 Approximate Factorization

Because of the high computational cost of solving Eq. (3.55) directly, an approximation within the limits of the accuracy of the original discretization is sought. The basic idea of approximate factorization is to factor the left side of Eq. (3.55) into a sequence of simpler operations. Following Beam and Warming [87], the left side of

Eq. (3.55) can be approximately factored as

$$\left[\frac{I}{J\Delta t}+\delta_{\xi^1}\left(\frac{\partial}{\partial\vec{q}}\left[\bar{E}_1-(\bar{E}_v)_1\right]\right)\right]\left[\frac{I}{J\Delta t}+\delta_{\xi^2}\left(\frac{\partial}{\partial\vec{q}}\left[\bar{E}_2-(\bar{E}_v)_2\right]\right)\right]$$
$$\left[\frac{I}{J\Delta t}+\delta_{\xi^3}\left(\frac{\partial}{\partial\vec{q}}\left[\bar{E}_3-(\bar{E}_v)_3\right]\right)\right]\left[\frac{I}{(J\Delta t)^2}\right]^{-1}\Delta\vec{q}=-\delta_{\xi^m}\left(\bar{E}_m-(\bar{E}_v)_m\right)^n \quad (3.56)$$

In this form, the solution can be obtained by solving the following three one-dimensional problems

$$\left[\frac{I}{J\Delta t}+\delta_{\xi^1}\left(\frac{\partial}{\partial\vec{q}}\left[\bar{E}_1-(\bar{E}_v)_1\right]\right)\right]\Delta\vec{q}^{\,*} = -\delta_{\xi^m}\left(\bar{E}_m-(\bar{E}_v)_m\right)^n \quad (3.57)$$

$$\left[\frac{I}{J\Delta t}+\delta_{\xi^2}\left(\frac{\partial}{\partial\vec{q}}\left[\bar{E}_2-(\bar{E}_v)_2\right]\right)\right]\Delta\vec{q}^{\,**} = \Delta\vec{q}^{\,*} \quad (3.58)$$

$$\left[\frac{I}{J\Delta t}+\delta_{\xi^3}\left(\frac{\partial}{\partial\vec{q}}\left[\bar{E}_3-(\bar{E}_v)_3\right]\right)\right]\Delta\vec{q} = \frac{\Delta\vec{q}^{\,**}}{(J\Delta t)^2} \quad (3.59)$$

where $\vec{q}^{\,*}$ and $\vec{q}^{\,**}$ denote intermediate values. The solution of each of these equations is obtained by solving a block tri-diagonal or penta-diagonal set of equations, depending on the spatial accuracy used.

3.3.7 Roe Flux Difference Splitting

The discretization of the inviscid fluxes is achieved using the technique of flux difference splitting. This approach involves the introduction of locally exact solutions of the one-dimensional Euler equations directly into the discretization process. This method was first devised by Godunov [88] in 1959. The local flow is solved at time $n+1$ via an initial-value problem between the piecewise constant flow states in adjacent cells, $\vec{q}_L, \vec{q}_R$ at time n. This flow problem is the well-known Riemann or shock-tube problem, named after the German mathematician G.F. Riemann who first attempted its solution in 1858. The solution generally contains a shock wave, a contact discontinuity and an expansion fan separating regions of uniform flow conditions.

In the numerical application of Godunov methods, the Riemann problem is solved over successive pairs of cells defining the left and right states over all cells in a given direction. The piecewise constant solution is then obtained by averaging the solutions over each cell. As a result of this averaging process, the exact solution of the Riemann is significantly degraded. This fact coupled with the computational expense of solving the nonlinear algebraic equation associated with the Riemann problem, necessitates an approximate solution to the Riemann problem. Several approximate solvers have been developed and are surveyed in Hirsch [89]. The most successful approximate Riemann solver is the Roe [84] scheme, which is used throughout this study.

The Roe scheme is based on the characteristic decomposition of the flux differences such that the scheme remains conservative. Roe's approach achieves this by extending the linear wave decomposition to non-linear equations. The following development follows that of Kandil [44] and Roe [84].

Consider the one-dimensional initial-value problem for a hyperbolic system of conservation laws,

$$\frac{\partial \bar{Q}}{\partial t} + \frac{\partial \bar{E}_1}{\partial \xi^1} = 0 \tag{3.60}$$

subject to the Riemann problem initial conditions

$$\bar{Q}(\xi^1, 0) \equiv \bar{Q}_L, \;\; (\xi^1 < 0); \quad \bar{Q}(\xi^1, 0) \equiv \bar{Q}_R, \;\; (\xi^1 > 0) \tag{3.61}$$

where $\bar{E}_1$ is a linear function of $\bar{Q}$. Using the chain rule, Eq. (3.60) can be rewritten as

$$\frac{\partial \bar{Q}}{\partial t} + A\frac{\partial \bar{Q}}{\partial \xi^1} = 0 \tag{3.62}$$

where $A = \frac{\partial \bar{E}_1}{\partial \bar{Q}}$. The solution to the Riemann problem in terms of the flux difference is given by

$$\bar{E}_{1_R} - \bar{E}_{1_L} = \sum_{j=1}^{3} \lambda_j \alpha_j \mathbf{e}_j \tag{3.63}$$

where λ_j and $\mathbf{e}_j$ are the eigenvalues and eigenvectors of the Jacobian matrix A, respectively, and α_j represents the strength of the wave. Averaging contributions from the left and right directions gives,

$$\bar{E}_{1_{i+\frac{1}{2}}}(\bar{Q}_R, \bar{Q}_L) = \frac{1}{2}\left[(\bar{E}_{1_L} + \bar{E}_{1_R}) - \sum_{j=1}^{3} |\lambda_j| \alpha_j \mathbf{e}_j\right] \tag{3.64}$$

Now, consider the one-dimensional Euler equation for which $\bar{E}_1$ is a non-linear function of $\bar{Q}$. Roe's scheme extends the linear wave decomposition, which provides an exact solution to Riemann's problem, to non-linear equations. Roe [84] suggested the following solution to the linearized problem,

$$\frac{\partial \bar{Q}}{\partial t} + \hat{A}\frac{\partial \bar{Q}}{\partial \xi^1} = 0 \tag{3.65}$$

where $\hat{A}$ is the Roe-averaged matrix constructed under the following conditions:

1. $\hat{A}$ constitutes a linear mapping from the vector space $\bar{Q}$ to the vector space $\bar{E}_1$.
2. As $\bar{Q}_L \to \bar{Q}_R \to \bar{Q}$, $\hat{A}(\bar{Q}_L, \bar{Q}_R) \to \hat{A}(\bar{Q})$, where $\hat{A} = \frac{\partial \bar{E}_1}{\partial \bar{Q}}$.
3. For any $\bar{Q}_L, \bar{Q}_R$, $\hat{A}(\bar{Q}_L, \bar{Q}_R) \times (\bar{Q}_L - \bar{Q}_R) = \bar{E}_{1_L} - \bar{E}_{1_R}$.
4. The eigenvectors of $\hat{A}$ are linearly independent.

From the third property, the flux difference between the left and right states and the interface fluxes can be written as

$$\bar{E}_{1_L} - \bar{E}_{1_R} = \hat{A}(\bar{Q}_L - \bar{Q}_R) \tag{3.66}$$

The interface flux is then

$$\bar{E}_{1_{i+\frac{1}{2}}}(\bar{Q}_L, \bar{Q}_R) = \frac{1}{2}\left[(\bar{E}_{1_L} + \bar{E}_{1_R}) - |\hat{A}|(\bar{Q}_L - \bar{Q}_R)\right]_{i+\frac{1}{2}} \tag{3.67}$$

For three-dimensional flows, Eq. (3.67) becomes

$$\bar{E}_{m_{i+\frac{1}{2}}}(\bar{Q}_L, \bar{Q}_R) = \frac{1}{2}\left[(\bar{E}_{m_L} + \bar{E}_{m_R}) - |\hat{A}|(\bar{Q}_L - \bar{Q}_R)\right]_{i+\frac{1}{2}}; \; m = 1-3 \tag{3.68}$$

where for the i^{th} direction, j, k and n are kept constant. The last term in this equation is the dissipation contribution to the interface flux and is given by Vatsa [90] as follows

$$|\hat{A}|(\bar{Q}_L - \bar{Q}_R) = \left\{ \begin{array}{c} \alpha_4 \\ \hat{u}_1\alpha_4 + \dfrac{\partial \xi^m}{\partial x_1}\alpha_5 + \alpha_6 \\ \hat{u}_2\alpha_4 + \dfrac{\partial \xi^m}{\partial x_2}\alpha_5 + \alpha_7 \\ \hat{u}_3\alpha_4 + \dfrac{\partial \xi^m}{\partial x_3}\alpha_5 + \alpha_8 \\ \hat{H}\alpha_4 + \hat{\bar{u}}_m\alpha_5 + \hat{u}_1\alpha_6 + \hat{u}_2\alpha_7 + \hat{u}_3\alpha_8 - \left(\dfrac{\hat{a}^2}{\gamma - 1}\right)\alpha_1 \end{array} \right\} \tag{3.69}$$

where

$$\alpha_1 = \left|\frac{\nabla \xi^m}{J}\right| |\hat{\bar{u}}_m| \left(\Delta\rho - \frac{\Delta p}{\hat{a}^2}\right) \tag{3.70}$$

$$\alpha_2 = \frac{1}{2\hat{a}^2}\left|\frac{\nabla \xi^m}{J}\right| |\hat{\bar{u}}_m + \hat{c}| \left(\Delta p + \hat{\rho}\hat{a}\Delta\hat{u}_m\right) \tag{3.71}$$

$$\alpha_3 = \frac{1}{2\hat{a}^2}\left|\frac{\nabla \xi^m}{J}\right| |\hat{\bar{u}}_m - \hat{c}| \left(\Delta p - \hat{\rho}\hat{a}\Delta\hat{u}_m\right) \tag{3.72}$$

$$\alpha_4 = \alpha_1 + \alpha_2 + \alpha_3 \tag{3.73}$$

$$\alpha_5 = \hat{a}(\alpha_2 - \alpha_3) \tag{3.74}$$

$$\alpha_{j+5} = \left|\frac{\nabla \xi^m}{J}\right| |\hat{\bar{u}}_m| \left(\hat{\rho}\Delta u_j - \frac{\partial \xi^m}{\partial x_1}\hat{\rho}\Delta\hat{u}_m\right); \; j = 1-3 \tag{3.75}$$

The Roe-averaged variables are defined as follows

$$\hat{\rho} = \sqrt{\rho_L \rho_R} \tag{3.76}$$

$$\hat{u}_j = \frac{u_{j_L} + u_{j_R}\sqrt{\rho_L\rho_R}}{1 + \sqrt{\rho_L\rho_R}} \tag{3.77}$$

$$\hat{H} = \frac{H_L + H_R\sqrt{\rho_L\rho_R}}{1 + \sqrt{\rho_L\rho_R}} \tag{3.78}$$

$$\hat{a}^2 = (\gamma - 1)\left[\hat{H} - \frac{\hat{u}_1^2 + \hat{u}_2^2 + \hat{u}_3^2}{2}\right] \tag{3.79}$$

3.3.8 Discretization of Viscous Fluxes

In keeping with the flow physics, the viscous fluxes are centrally differenced in space. The cross-derivative terms are approximated second-order accurately as follows,

$$\begin{aligned}\frac{\partial u_1}{\partial \xi^1 \partial \xi^2} &\equiv \delta\delta_{\xi^1\xi^2}(u_1)_{i,j,k} \\ &= \alpha^+ \left(\delta_{\xi^1\xi^2}(u_1)_{i+\frac{1}{2},j+\frac{1}{2},k} + \delta_{\xi^1\xi^2}(u_1)_{i-\frac{1}{2},j-\frac{1}{2},k}\right) \\ &- \alpha^- \left(\delta_{\xi^1\xi^2}(u_1)_{i-\frac{1}{2},j+\frac{1}{2},k} + \delta_{\xi^1\xi^2}(u_1)_{i+\frac{1}{2},j-\frac{1}{2},k}\right) \end{aligned} \tag{3.80}$$

where

$$\delta_{\xi^1\xi^2}(u_1)_{i+\frac{1}{2},j+\frac{1}{2},k} = (u_1)_{i+1,j+1,k} - (u_1)_{i,j+1,k} + (u_1)_{i,j,k} - (u_1)_{i-1,j,k} \tag{3.81}$$

and

$$\alpha^+ + \alpha^- = \frac{1}{2} \tag{3.82}$$

If a symmetric difference is chosen, then $\alpha^+ = \alpha^- = \frac{1}{4}$ which gives

$$\delta_{\xi^1\xi^2}(u_1)_{i,j,k} = \frac{1}{4}\left[(u_1)_{i+1,j+1,k} - (u_1)_{i+1,j-1,k}\right] - \frac{1}{4}\left[(u_1)_{i-1,j+1,k} - (u_1)_{i-1,j-1,k}\right] \tag{3.83}$$

3.4 Initial and Boundary Conditions

3.4.1 Initial Conditions

The fluid flow initial conditions correspond to an undisturbed freestream flow throughout the computational domain. This is equivalent to impulsively placing the wing-tail configuration into the freestream. For the aeroelastic initial conditions, the tails are initially undeformed and motionless. For buffeting cases, the initial fluid state is obtained by pseudo-time-stepping based on the CFL number until the vortex breakdown flow has fully developed.

3.4.2 Surface Boundary Conditions

On the body surfaces, the fluid may neither slip nor penetrate; that is, the relative velocity must equal zero. Additionally, the normal pressure gradient, $\frac{\partial \rho}{\partial \hat{n}}$, is zero on the stationary wing surface. On the moving tails, $\frac{\partial p}{\partial \hat{n}} = -\rho \vec{a}_t \cdot \hat{n}$, where $\vec{a}_t$ is the absolute acceleration of a point on a tail due to bending (w) and torsional (θ) motions. This is given by

$$\vec{a}_t = -r\left[\frac{\partial^2 \theta}{\partial t^2}\sin\theta + \left(\frac{\partial \theta}{\partial t}\right)^2 \cos\theta\right]\hat{i} + \left\{\frac{\partial^2 w}{\partial t^2} + r\left[\frac{\partial^2 \theta}{\partial t^2}\cos\theta - \left(\frac{\partial \theta}{\partial t}\right)^2 \sin\theta\right]\right\}\hat{j} \quad (3.84)$$

where r is the point distance from the elastic axis. All surfaces are also considered adiabatic.

3.4.3 Far-Field Boundary Conditions

For all cases under consideration in this study, the far-field boundary conditions are specified approximately one chord upstream, three chords downstream and three chords in the direction normal to the wing. In order to minimize reflectivity, the inflow/outflow boundary conditions are based on the theory of characteristics. Details of this and other boundary conditions are given in the CFL3D user manual [85]. For a surface of constant ξ^1, the Cartesian velocities in the direction of the outward normal to the grid surface, are determined by

$$u_{1_{face}} = u_{1_{ref}} + \frac{\frac{\partial \xi^1}{\partial x_1}}{|\nabla \xi^1|}(\bar{u}_{face} - \bar{u}_{ref}) \quad (3.85)$$

$$u_{2_{face}} = u_{2_{ref}} + \frac{\frac{\partial \xi^1}{\partial x_2}}{|\nabla \xi^1|}(\bar{u}_{face} - \bar{u}_{ref}) \quad (3.86)$$

$$u_{3_{face}} = u_{3_{ref}} + \frac{\frac{\partial \xi^1}{\partial x_3}}{|\nabla \xi^1|}(\bar{u}_{face} - \bar{u}_{ref}) \quad (3.87)$$

where for inflow *ref* refers to freestream conditions and for the outflow *ref* refers to the values from the cell inside the domain adjacent to the boundary. The velocity normal to

the far-field boundary is obtained from the two locally 1-D Riemann invariants, $R^{\pm}$ as follows

$$\bar{u}_{face} = \frac{1}{2}(R^{+} + R^{-}) \tag{3.88}$$

where

$$R^{\pm} \equiv \frac{\frac{\partial \xi^1}{\partial x_1}}{|\nabla \xi^1|} u_1 + \frac{\frac{\partial \xi^1}{\partial x_2}}{|\nabla \xi^1|} u_2 + \frac{\frac{\partial \xi^1}{\partial x_3}}{|\nabla \xi^1|} u_3 \pm \frac{2a}{\gamma - 1} \tag{3.89}$$

The density and pressure on the boundary are given by

$$\rho_{face} = \left(\frac{a^2_{face}}{\gamma s_{face}} \right)^{\frac{1}{\gamma - 1}} \tag{3.90}$$

$$p_{face} = \frac{\rho_{face} a^2_{face}}{\gamma} \tag{3.91}$$

where the speed of sound is calculated by

$$a_{face} = \frac{\gamma - 1}{4}(R^{+} - R^{-}) \tag{3.92}$$

and the entropy is determined from outside the domain for inflow and inside the domain for outflow as follows,

$$s = \frac{p}{\rho^{\gamma}} \tag{3.93}$$

3.4.4 Block Interface Boundary Conditions

In single block and multiblock grid configurations, internal boundary conditions need to be set anywhere grid boundaries collapse on themselves or touch each other. Examples of the first case are in the region before the wing where the grid lines that cover the wing collapse to a single line. An example of the second case is the symmetry plane and wake plane.

For multiblock grid configurations, boundary conditions must also be set at all block interfaces. There are several methods for doing multiblock computations such as the use of overlapping grids, or grids that share a boundary but do not match cells. In

the present study, all grids share a boundary, and cells match on a one-to-one basis. In this case the boundary data is simply obtained from the neighboring cell in the adjacent block. The advantage of this method is that it eliminates the need for interpolation between blocks and insures conservation across block boundaries. The disadvantage of this method is that it is less flexible when trying to refine only local regions of the grid.

3.5 Structured CFD Grid Construction Methodology

3.5.1 Introduction

A modified Joukowski transformation with exponential stretching is used to create all of the grids used in this study. The transformation is applied in the crossflow (η, ζ) plane for each streamwise x location. The parameters for the Joukowski transformation are given by

$$c = \frac{1+\sqrt{1-e^2}}{2}\tan\delta \qquad s = \frac{e}{2}\tan\delta \tag{3.94}$$

where e is the eccentricity of the elliptical cone and δ is the cone half-angle. For a flat delta wing $e = 1$ and $\delta = \frac{\pi}{2} - \Lambda_s$, where Λ_s is the leading-edge sweep angle. The transformed crossflow coordinate points are defined in terms of the complex variable z as

$$\eta = x\Re(z) \tag{3.95}$$

$$\zeta = x\Im(z) \tag{3.96}$$

where z is given by

$$z = z_b + (z_s - z_b)\bar{r} + \frac{s^2}{z_b + \bar{r}(z_s - z_b)} \tag{3.97}$$

where the body points and shock points are defined as follows

$$z_b = c(\sin\theta + \imath\cos\theta) \tag{3.98}$$

$$z_s = \frac{1}{2}\left\{\frac{r_o}{x}(\sin\theta + \imath\cos\theta) \pm \sqrt{\left[\frac{r_o}{x}(\sin\theta + \imath\cos\theta)\right]^2 - 4s^2}\right\} \tag{3.99}$$

r_o is the radius of the outer boundary and $\bar{r}$ is a stretching function based on an arbitrary parameter β and the k^{th} radial grid point.

$$\bar{r} = -\frac{1}{\beta}\ln\left\{1 - (1 - e^{-\beta})\left[\frac{k-1}{k_d - 1}\right]\right\} \tag{3.100}$$

In these equations, θ is the angle of each radial grid line in the crossflow plane. The sign of the root in Eq. (3.99) is determined from the quadrant of the shock point, positive if $\frac{r_o}{x}\sin\theta > 0$ and negative if $\frac{r_o}{x}\sin\theta = 0$ and $\frac{r_o}{x}\cos\theta > 0$. This algorithm is coded in a delta wing grid (DGRIDGEN) generation program which was distributed with early versions of CFL3D [85]. To generate the grids used in this study, DGRIDGEN was modified extensively by the author. A close-up view of a typical crossflow plane is shown in Figure 3.1.

3.5.2 Single Block Grid

To generate the grid used for the single square tail configuration, seen in Figure 3.2, the only modifications made to the default grid was clustering in the streamwise direction at the leading and trailing edges of the square tail. This clustering can be seen in the symmetry plane and half grid plots, see Figure 3.3.

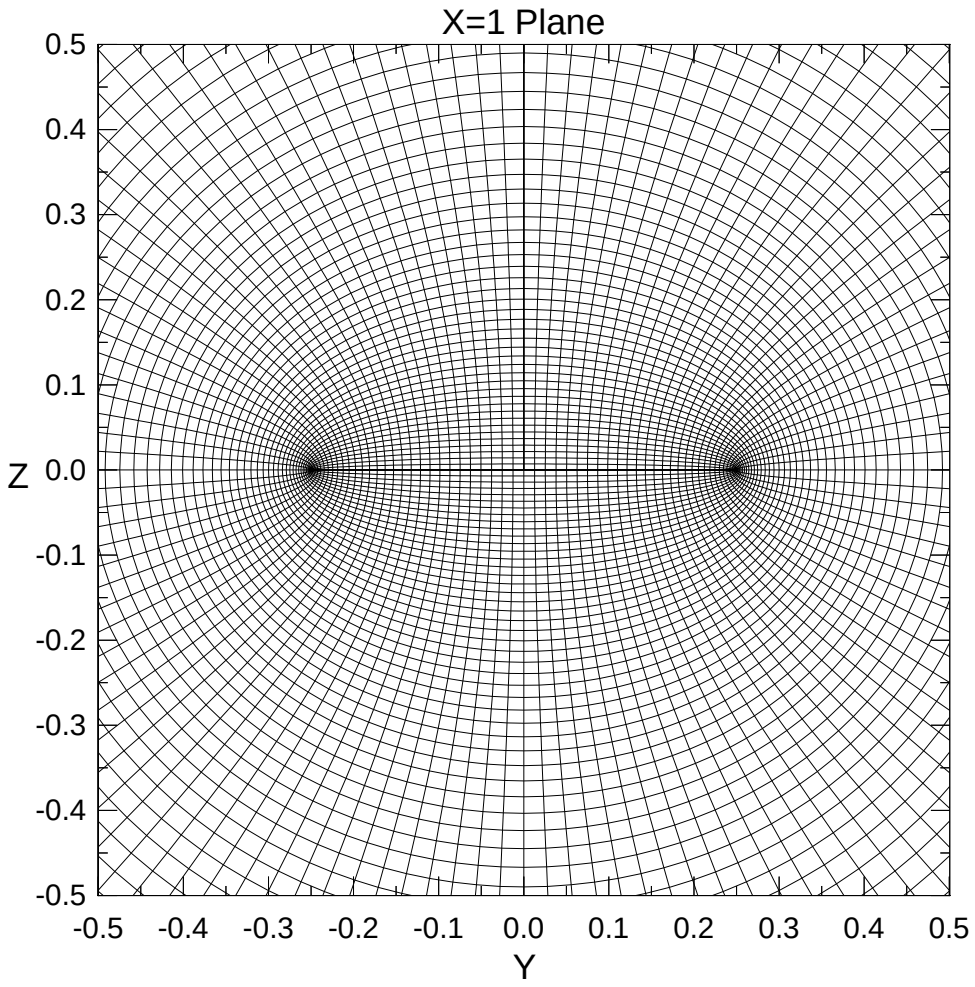

Figure 3.1: Typical crossflow plane at showing the elliptic cone surrounding the trailing edge of the delta wing.

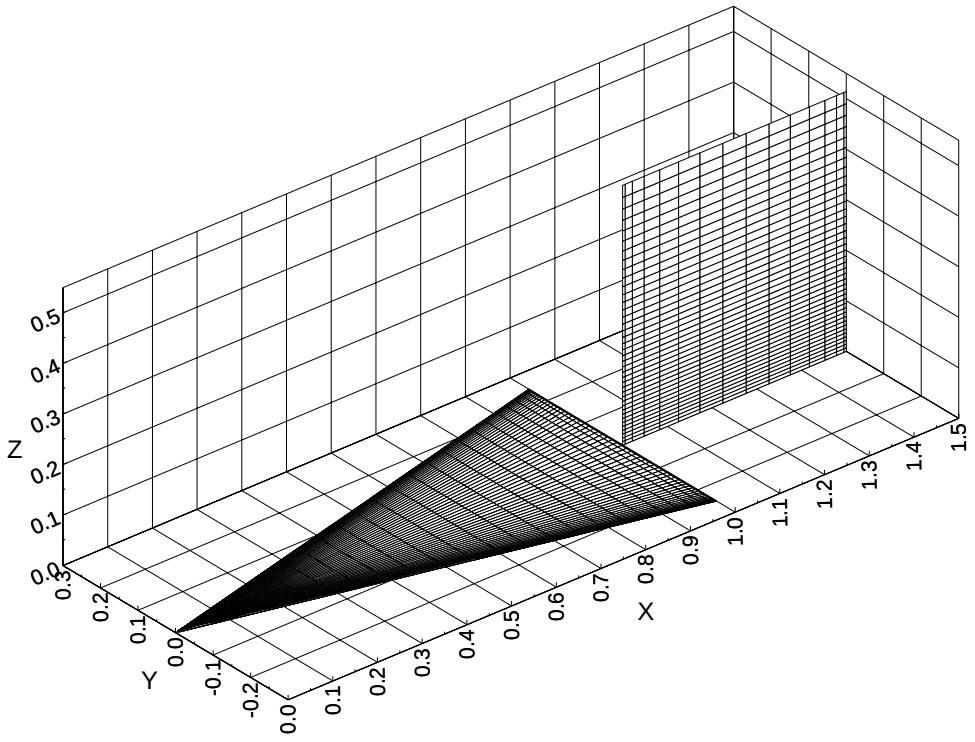

Figure 3.2: Body grid surfaces for the single square tail configuration.

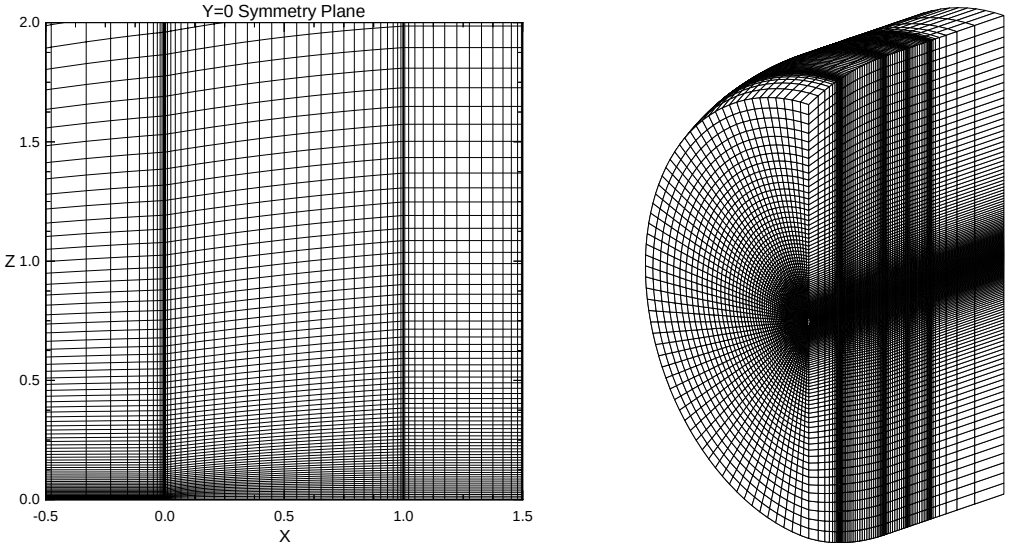

Figure 3.3: Symmetry plane and half grid showing streamwise clustering in the single tail configuration.

3.5.3 Multiblock Grids

The introduction of twin tail models necessitated the use of multiblock grids. The blocking method used throughout this study consists of blocks with C^0 continuity; that is, blocks whose boundaries match each other and with boundary cells that match one-to-one. Based on the type of surface boundary conditions required, either five and six block configurations were used, see Figure 3.4. When the tails are placed on solid surfaces behind the wing, a five block grid is sufficient. Note that with special treatment of the tail surface boundary condition the five block case can be reduced to only four blocks. The six block grid was required to implement the wake boundary conditions around the tails when they were considered to be suspended in the freestream with no supporting solid surfaces. In order to accommodate the twin tail configurations, significant modifications were made to the original DGRIDGEN program. A great deal of ad hoc algebraic grid manipulation was done to conform the original highly orthogonal

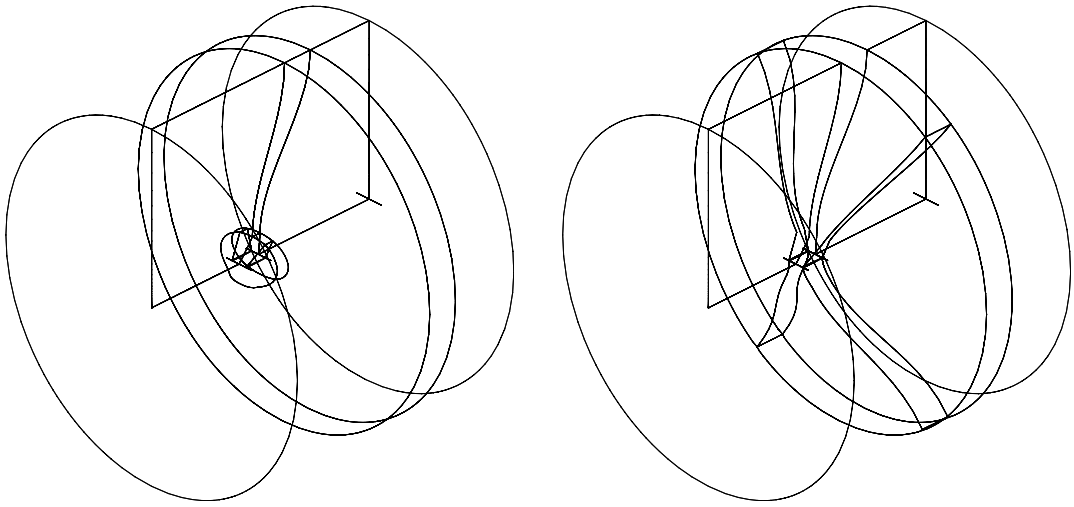

Figure 3.4: Five (left) and six (right) block grid structure, showing all block boundaries.

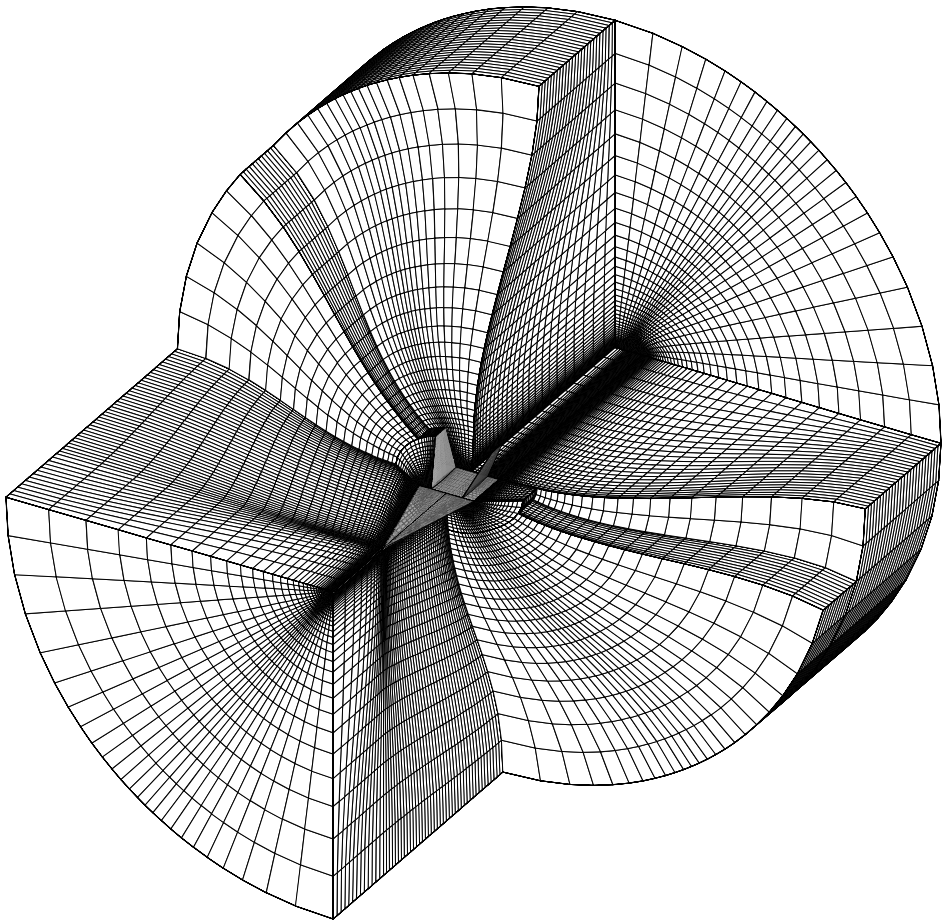

Figure 3.5: Example of highly stretched grid blocks for a five block configuration.

grid, see Figure 3.3 to the new twin tail surfaces, see Figure 3.5. The basic method used to create the new body conforming grids was to define the new boundary surfaces and then stretch the baseline grid smoothly using cosine weighting functions. Consider the distribution of a grid displacement Δx resulting from the difference between the new and old grid boundaries.

$$\xi_{new} = \xi_{old} + f\Delta\xi \tag{3.101}$$

where f is the weighting function. Figure 3.6 depicts two different cosine-based weighting functions of varying smoothness. They are defined by using different portions of a cosine curve as follows,

$$f_1 = \cos\left[\left(\frac{i-i_0}{i_1-i_0}\right)\frac{\pi}{2}\right] \tag{3.102}$$

$$f_2 = \frac{1}{2}\left\{1+\cos\left[\left(\frac{i-i_0}{i_1-i_0}\right)\pi\right]\right\} \tag{3.103}$$

When either of Eqs. (3.102,3.103) are substituted into Eq. (3.101), the new grid is fully deflected at x_0 corresponding to the source of $\Delta\xi$ such at the new tail, and not deflected at all at ξ_1, which corresponds to an undeformed far-field boundary. Note that in Eqs. (3.102,3.103) the weighting functions could alternatively be based on the actual coordinate, ξ rather than its index.

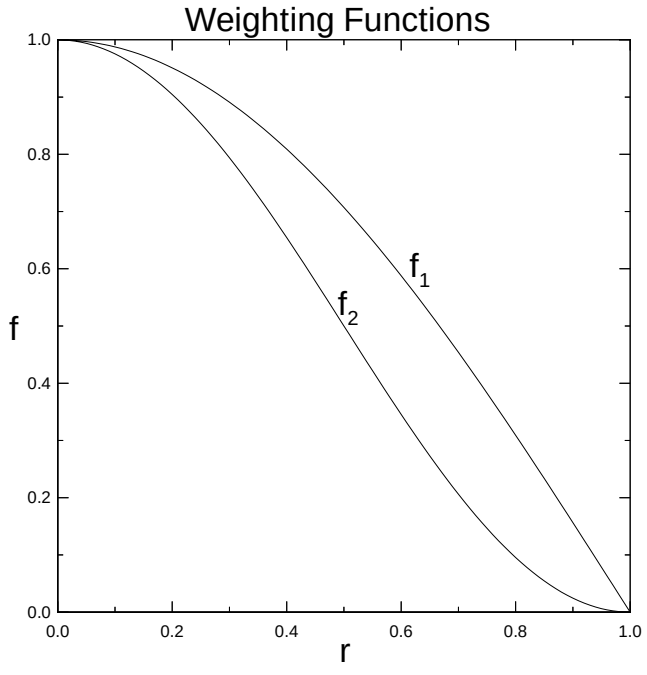

Figure 3.6: Example cosine-based grid weighting functions.

3.5.4 Grid Motion Algorithm

The new grid resulting from the deformations of the twin tails is created in precisely the same way the original grid was stretched to conform to the undeflected twin tail geometry. Because the grid displacements are relatively small, advanced methods of grid deformation such as the Navier-displacement equations are not implemented in this study. Instead, simple interpolation functions, Eq. (3.101) are used to deform the grid smoothly to match the deformations of the tail. These interpolation functions efficiently deform the grid without losing the important contributions of the grid speed and acceleration. From the structural solution at the $n+1$ time step, the grid at $n+1$ is deformed throughout the computational domain using cosine interpolation functions. These functions have the effect of exponentially smoothing the grid displacements away from tail. To handle the independent displacements of the tails, the grid is deflected in two steps corresponding to each tail. Since this occurs before the fluid update, the fluid sees only one grid deflection.

CHAPTER 4

STRUCTURAL DYNAMICS FORMULATION

4.1 Introduction

In this study, each tail is modeled as a cantilevered beam. The tail is allowed to bend and twist about its elastic axis which does not necessarily coincide with its inertial axis. For this case the bending and torsional motions will be elastically coupled in addition to the natural coupling produced by the fluid flow. All structural properties are free to vary in the vertical $z-$direction. All displacements are assumed small, and the cross-section of the beam is assumed to be rigid. The governing equations are formulated using a variational energy approach.

4.2 Derivation of the Structural Dynamics Equations

Neglecting the motion in the $z-$direction the velocity of the center of mass in the $x-$ and $y-$directions is

$$v_x(z,t) = -x_\theta(z)\frac{\partial\theta(z,t)}{\partial t}\sin\theta(z,t) \tag{4.1}$$

$$v_y(z,t) = \frac{\partial w(z,t)}{\partial t} + x_\theta(z)\frac{\partial\theta(z,t)}{\partial t}\cos\theta(z,t) \tag{4.2}$$

where $x_\theta(z)$ is the distance in the positive $x-$direction from the elastic axis to the inertial axis of the tail, see Figure 4.1, and w and θ are the bending and twisting displacements, respectively, as indicated in Figure 4.2. The kinetic energy of the system with the center of mass (CM) moving at $\vec{v}$ and rotating about z at $\frac{\partial\theta(z,t)}{\partial t}$ (ccw positive) is

$$T = \int_0^L \frac{1}{2}\Big[m(z)\vec{v}^2(z,t) + I_{zz_{CM}}(z)\Big(\frac{\partial\theta(z,t)}{\partial t}\Big)^2\Big]dz \tag{4.3}$$

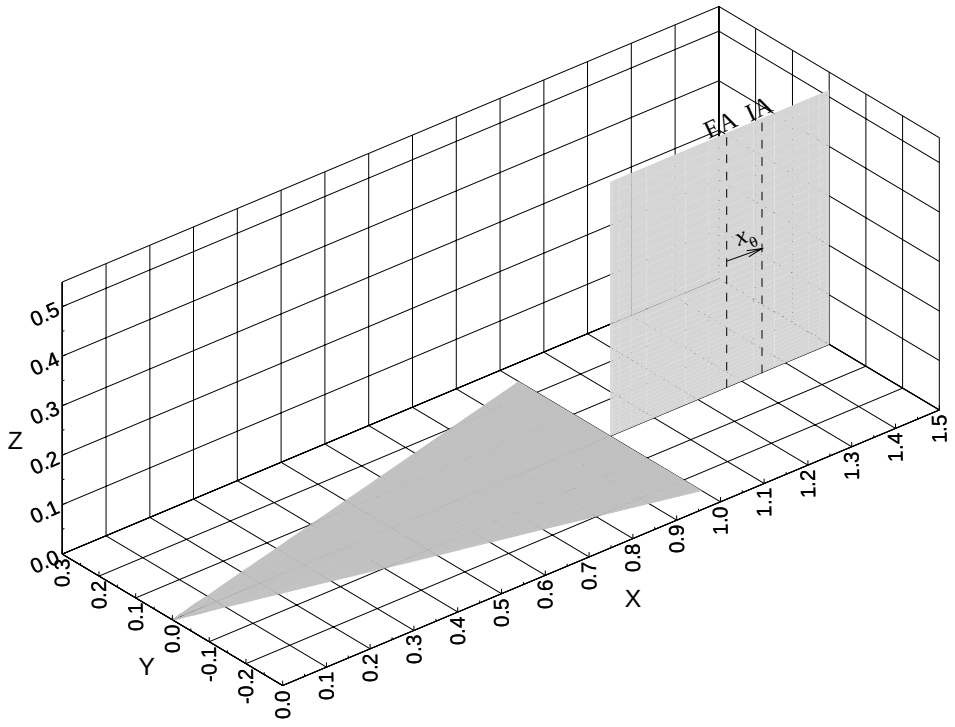

Figure 4.1: Delta wing, single vertical tail configuration, showing typical elastic and inertial axes locations.

$$T = \int_0^L \frac{1}{2}\Big\{m\Big[\Big(x_\theta \frac{\partial \theta}{\partial t}\sin\theta\Big)^2 + \Big(\frac{\partial w}{\partial t} + x_\theta \frac{\partial \theta}{\partial t}\cos\theta\Big)^2\Big] + I_{zz_{CM}}\Big(\frac{\partial \theta}{\partial t}\Big)^2\Big\}dz \tag{4.4}$$

where L is the length of the tail, $m(z)$ is the lumped mass per unit length, $I_{zz_{CM}}$ is the mass moment of inertia about the $z-$axis of the tail; and EI and GJ are the bending stiffness and torsional rigidity, respectively. The elastic potential energy is given by

$$V = \int_0^L \frac{1}{2}\Big[EI(z)\Big(\frac{\partial^2 w}{\partial z^2}\Big)^2 + GJ(z)\Big(\frac{\partial \theta}{\partial z}\Big)^2\Big]dz \tag{4.5}$$

The work done on the system by the force (N) and moment (M) assuming small displacements is

$$W_N(z) = N(z,t)w(z,t) \tag{4.6}$$

$$W_M(z) = \int M(z,t)d\theta = M(z,t)\theta(z,t) \tag{4.7}$$

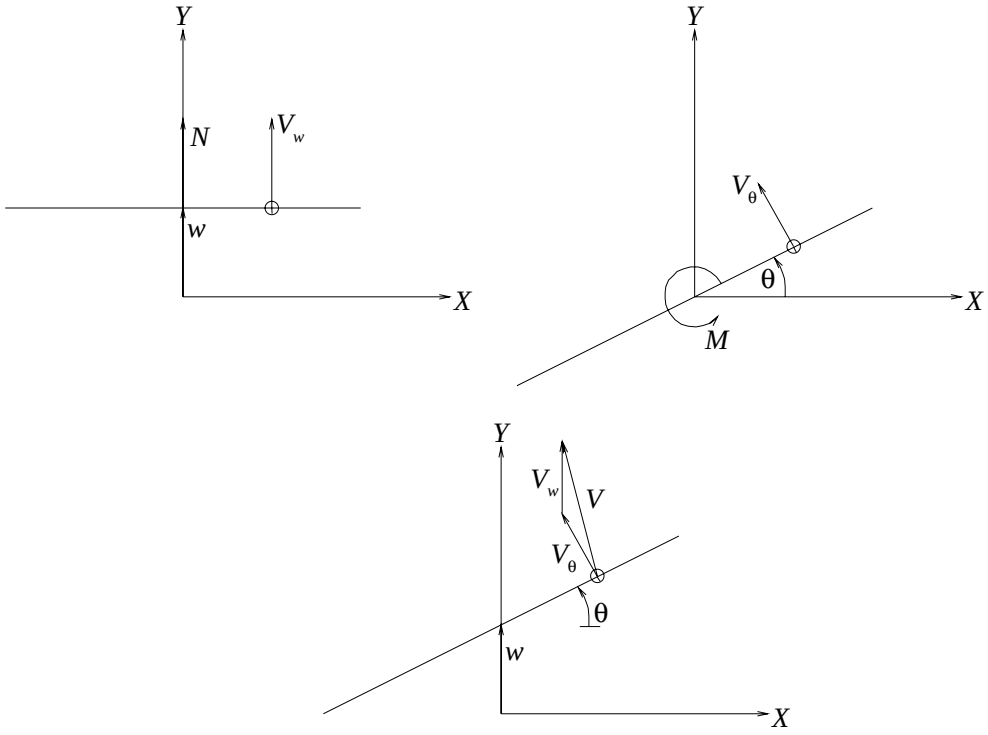

Figure 4.2: Sketch of orientations for bending (*left*), torsion (*right*), and combined bending and torsion (*center*).

thus, the total work done on the system by aerodynamic loading is

$$W = \int_0^L \Big[N(z,t)w(z,t) + M(z,t)\theta(z,t) \Big] dz \tag{4.8}$$

From Hamilton's principle we have,

$$\int_0^\tau (\delta T - \delta V + \delta W) dt = 0 \tag{4.9}$$

Substituting the expressions for kinetic energy, potential energy and total work done gives,

$$\delta\int_0^\tau (T-V+W)dt = \delta\int_0^\tau \Bigg\{\frac{1}{2}\int_0^L \Big\{m\Big[\Big(x_\theta\frac{\partial\theta}{\partial t}\sin\theta\Big)^2+\Big(\frac{\partial w}{\partial t}+x_\theta\frac{\partial\theta}{\partial t}\cos\theta\Big)^2\Big]+I_{zz_{CM}}\Big(\frac{\partial\theta}{\partial t}\Big)^2\Big\}dz - \frac{1}{2}\int_0^L\Big[EI\Big(\frac{\partial^2 w}{\partial z^2}\Big)^2+GJ\Big(\frac{\partial\theta}{\partial z}\Big)^2\Big]dz+\int_0^L(Nw+M\theta)dz\Bigg\}dt=0 \tag{4.10}$$

Distributing δ yields

$$\delta\int_0^\tau (T-V+W)dt = \int_0^\tau\Bigg\{\int_0^L\Big\{m\Big[(x_\theta\frac{\partial\theta}{\partial t}\sin\theta)\delta(x_\theta\frac{\partial\theta}{\partial t}\sin\theta)+(\frac{\partial w}{\partial t}+x_\theta\frac{\partial\theta}{\partial t}\cos\theta)\delta(\frac{\partial w}{\partial t}+x_\theta\frac{\partial\theta}{\partial t}\cos\theta)\Big] +I_{zz_{CM}}\frac{\partial\theta}{\partial t}\delta(\frac{\partial\theta}{\partial t})\Big\}dz-\int_0^L\Big[EI(\frac{\partial^2 w}{\partial z^2})\delta(\frac{\partial^2 w}{\partial z^2})+GJ(\frac{\partial\theta}{\partial z})\delta(\frac{\partial\theta}{\partial z})\Big]dz +\int_0^L(N\delta w+M\delta\theta)dz\Bigg\}dt=0 \tag{4.11}$$

Expanding factored terms yields

$$\begin{aligned}\delta\int_0^\tau (T-V+W)dt = \int_0^\tau\int_0^L\Bigg\{&\underbrace{mx_\theta^2\sin^2\theta\frac{\partial\theta}{\partial t}\delta\Big(\frac{\partial\theta}{\partial t}\Big)}_{1}+mx_\theta^2\Big(\frac{\partial\theta}{\partial t}\Big)^2\sin\theta\cos\theta\,\delta\theta+\underbrace{m\frac{\partial w}{\partial t}\delta\Big(\frac{\partial w}{\partial t}\Big)}_{2}\\ &+\underbrace{m\frac{\partial w}{\partial t}x_\theta\cos\theta\,\delta\Big(\frac{\partial\theta}{\partial t}\Big)}_{3}-m\frac{\partial w}{\partial t}x_\theta\frac{\partial\theta}{\partial t}\sin\theta\,\delta\theta+\underbrace{mx_\theta\frac{\partial\theta}{\partial t}\cos\theta\,\delta\Big(\frac{\partial w}{\partial t}\Big)}_{4}\\ &+\underbrace{mx_\theta^2\frac{\partial\theta}{\partial t}\cos^2\theta\,\delta\Big(\frac{\partial\theta}{\partial t}\Big)}_{5}-mx_\theta^2\Big(\frac{\partial\theta}{\partial t}\Big)^2\cos\theta\sin\theta\,\delta\theta+\underbrace{I_{zz_{CM}}\frac{\partial\theta}{\partial t}\delta\Big(\frac{\partial\theta}{\partial t}\Big)}_{6}\\ &-\underbrace{EI\frac{\partial^2 w}{\partial z^2}\delta\Big(\frac{\partial^2 w}{\partial z^2}\Big)}_{7}-\underbrace{GJ\frac{\partial\theta}{\partial z}\delta\Big(\frac{\partial\theta}{\partial z}\Big)}_{8}+M\delta\theta+N\delta w\Bigg\}dzdt=0\end{aligned} \tag{4.12}$$

Assuming;

$$\delta\Big(\frac{\partial\psi}{\partial t}\Big)=\frac{\partial}{\partial t}(\delta\psi) \tag{4.13}$$

$$\delta\Big(\frac{\partial\psi}{\partial z}\Big)=\frac{\partial}{\partial z}(\delta\psi) \tag{4.14}$$

$$\iint \psi dt\, dz = \iint \psi dz\, dt \tag{4.15}$$

where $\psi \equiv \psi(z,t)$, we can then express the terms containing variations of derivatives, in terms of virtual displacements, δw and $\delta\theta$. This is done using integration by parts and enforcing the temporal invariance definition of virtual displacements. Thus, the labeled terms in Eq. (4.12) are factored as follows:

Term 1:

$$\begin{aligned}
\int_0^\tau mx_\theta^2 \sin^2\theta\, \frac{\partial\theta}{\partial t}\delta\Big(\frac{\partial\theta}{\partial t}\Big)dt &= \int_0^\tau \underbrace{mx_\theta^2 \sin^2\theta\, \frac{\partial\theta}{\partial t}}_{u}\underbrace{\frac{\partial(\delta\theta)}{\partial t}dt}_{dv} \\
&= uv\Big|_0^\tau - \int_0^\tau v\, du \\
&= \underbrace{mx_\theta^2 \sin^2\theta\, \frac{\partial\theta}{\partial t}\delta\theta\Big|_0^\tau}_{=0} - \int_0^\tau \delta\theta \frac{\partial}{\partial t}\Big(mx_\theta^2 \sin^2\theta\, \frac{\partial\theta}{\partial t}\Big)dt \\
&= -\int_0^\tau \delta\theta\, mx_\theta^2\Big[2\sin\theta\cos\theta\,\Big(\frac{\partial\theta}{\partial t}\Big)^2 + \sin^2\theta\, \frac{\partial^2\theta}{\partial t^2}\Big]dt
\end{aligned} \tag{4.16}$$

Term 2:

$$\begin{aligned}
\int_0^\tau m\frac{\partial w}{\partial t}\delta\Big(\frac{\partial w}{\partial t}\Big)dt &= \int_0^\tau m\frac{\partial w}{\partial t}\frac{\partial(\delta w)}{\partial t}dt \\
&= \underbrace{m\frac{\partial w}{\partial t}\delta w\Big|_0^\tau}_{=0} - \int_0^\tau m\,\delta w\frac{\partial^2 w}{\partial t^2}dt
\end{aligned} \tag{4.17}$$

Term 3:

$$\begin{aligned}
\int_0^\tau m\frac{\partial w}{\partial t}x_\theta\cos\theta\,\delta\Big(\frac{\partial\theta}{\partial t}\Big)dt &= \int_0^\tau m\frac{\partial w}{\partial t}x_\theta\cos\theta\,\frac{\partial(\delta\theta)}{\partial t}dt \\
&= \underbrace{m\frac{\partial w}{\partial t}x_\theta\cos\theta\,\delta\theta\Big|_0^\tau}_{=0} - \int_0^\tau \delta\theta\frac{\partial}{\partial t}\Big(m\frac{\partial w}{\partial t}x_\theta\cos\theta\Big)dt \\
&= -\int_0^\tau m\,\delta\theta\, x_\theta\Big(\frac{\partial^2 w}{\partial t^2}\cos\theta - \frac{\partial w}{\partial t}\sin\theta\frac{\partial\theta}{\partial t}\Big)dt
\end{aligned} \tag{4.18}$$

Term 4:

$$\begin{aligned}\int_0^\tau mx_\theta \frac{\partial\theta}{\partial t}\cos\theta\,\delta\Big(\frac{\partial w}{\partial t}\Big)dt &= \int_0^\tau mx_\theta \frac{\partial\theta}{\partial t}\cos\theta\,\frac{\partial(\delta w)}{\partial t}dt \\ &= \underbrace{mx_\theta \frac{\partial\theta}{\partial t}\cos\theta\,\delta w\Big|_0^\tau}_{=0} - \int_0^\tau \delta w\frac{\partial}{\partial t}\Big(mx_\theta\frac{\partial\theta}{\partial t}\cos\theta\Big)dt \\ &= -\int_0^\tau \delta w\, mx_\theta\Big[\frac{\partial^2\theta}{\partial t^2}\cos\theta - \sin\theta\,\Big(\frac{\partial\theta}{\partial t}\Big)^2\Big]dt \qquad (4.19)\end{aligned}$$

Term 5:

$$\begin{aligned}\int_0^\tau mx_\theta^2\cos^2\theta\,\frac{\partial\theta}{\partial t}\delta\Big(\frac{\partial\theta}{\partial t}\Big)dt &= \int_0^\tau mx_\theta^2\cos^2\theta\,\frac{\partial\theta}{\partial t}\frac{\partial(\delta\theta)}{\partial t}dt \\ &= \underbrace{mx_\theta^2\cos^2\theta\,\frac{\partial\theta}{\partial t}\delta\theta\Big|_0^\tau}_{=0} - \int_0^\tau \delta\theta\frac{\partial}{\partial t}\Big(mx_\theta^2\cos^2\theta\,\frac{\partial\theta}{\partial t}\Big)dt \\ &= -\int_0^\tau \delta\theta\, mx_\theta^2\Big[-2\cos\theta\sin\theta\,\Big(\frac{\partial\theta}{\partial t}\Big)^2 + \cos^2\theta\,\frac{\partial^2\theta}{\partial t^2}\Big]dt \qquad (4.20)\end{aligned}$$

Term 6:

$$\begin{aligned}\int_0^\tau I_{zz_{CM}}\frac{\partial\theta}{\partial t}\delta\Big(\frac{\partial\theta}{\partial t}\Big)dt &= \int_0^\tau I_{zz_{CM}}\frac{\partial\theta}{\partial t}\frac{\partial(\delta\theta)}{\partial t}dt \\ &= \underbrace{I_{zz_{CM}}\frac{\partial\theta}{\partial t}\delta\theta\Big|_0^\tau}_{=0} - \int_0^\tau \delta\theta\, I_{zz_{CM}}\frac{\partial^2\theta}{\partial t^2}dt \qquad (4.21)\end{aligned}$$

Term 7:

$$\begin{aligned}\int_0^L EI\frac{\partial^2 w}{\partial z^2}\delta\Big(\frac{\partial^2 w}{\partial z^2}\Big)dz &= \int_0^L EI\frac{\partial^2 w}{\partial z^2}\frac{\partial^2(\delta w)}{\partial z^2}dz \\ &= \underbrace{EI\frac{\partial^2 w}{\partial z^2}\frac{\partial(\delta w)}{\partial z}\Big|_0^L}_{=0,\text{ Boundary Conditions}} - \int_0^L \frac{\partial(\delta w)}{\partial z}\frac{\partial}{\partial z}\Big(EI\frac{\partial^2 w}{\partial z^2}\Big)dz \\ &= \underbrace{-\frac{\partial}{\partial z}\Big(EI\frac{\partial^2 w}{\partial z^2}\Big)\delta w\Big|_0^L}_{=0,\text{ Boundary Conditions}} + \int_0^L \delta w\frac{\partial^2}{\partial z^2}\Big(EI\frac{\partial^2 w}{\partial z^2}\Big)dz \qquad (4.22)\end{aligned}$$

Term 8:

$$\begin{aligned}\int_0^L GJ\frac{\partial\theta}{\partial z}\delta\Big(\frac{\partial\theta}{\partial z}\Big)dz &= \int_0^L GJ\frac{\partial\theta}{\partial z}\frac{\partial(\delta\theta)}{\partial z}dz \\ &= \underbrace{GJ\frac{\partial\theta}{\partial z}\delta\theta\Big|_0^L}_{=0,\text{ Boundary Conditions}} - \int_0^L \delta\theta\frac{\partial}{\partial z}\Big(GJ\frac{\partial\theta}{\partial z}\Big)dz \qquad (4.23)\end{aligned}$$

Substitution of the factored terms, Eqs. (4.16-4.23) back into Eq. (4.12) and distribution of virtual displacements yields

$$\begin{aligned}
&\delta\int_0^\tau (T-V+W)dt = \\
&\quad\int_0^\tau\int_0^L \Bigg\{ -2\delta\theta\, m x_\theta^2 \sin\theta\cos\theta\left(\frac{\partial\theta}{\partial t}\right)^2 - \delta\theta\, m x_\theta^2\sin^2\theta\,\frac{\partial^2\theta}{\partial t^2} + m x_\theta^2\sin\theta\cos\theta\left(\frac{\partial\theta}{\partial t}\right)^2\delta\theta \\
&\quad -m\frac{\partial^2 w}{\partial t^2}\delta w - m x_\theta\,\delta\theta\,\cos\theta\,\frac{\partial^2 w}{\partial t^2} + m x_\theta\delta\theta\frac{\partial w}{\partial t}\sin\theta\,\frac{\partial\theta}{\partial t} - m\frac{\partial w}{\partial t}x_\theta\,\frac{\partial\theta}{\partial t}\sin\theta\,\delta\theta \\
&\quad -m x_\theta\frac{\partial^2\theta}{\partial t^2}\cos\theta\,\delta w + m x_\theta\Big(\frac{\partial\theta}{\partial t}\Big)^2\sin\theta\,\delta w + 2m x_\theta^2\delta\theta\,\cos\theta\sin\theta\left(\frac{\partial\theta}{\partial t}\right)^2 \\
&\quad -\delta\theta\, m x_\theta^2\cos^2\theta\,\frac{\partial^2\theta}{\partial t^2} - m x_\theta^2\Big(\frac{\partial\theta}{\partial t}\Big)^2\cos\theta\sin\theta\,\delta\theta - \delta\theta\, I_{zz_{CM}}\frac{\partial^2\theta}{\partial t^2} \\
&\quad -\delta w\frac{\partial^2}{\partial z^2}\Big(EI\frac{\partial^2 w}{\partial z^2}\Big) + \delta\theta\frac{\partial}{\partial z}\Big(GJ\frac{\partial\theta}{\partial z}\Big) + M\delta\theta + N\delta w\Bigg\}dz\,dt = 0
\end{aligned} \tag{4.24}$$

Collecting terms of Eq. (4.24) on the virtual displacements, yields

$$\begin{aligned}
&\delta\int_0^\tau (T-V+W)dt = \\
&\quad\int_0^\tau\int_0^L \Bigg\{\delta w\Big[-m\frac{\partial^2 w}{\partial t^2} - m x_\theta\cos\theta\,\frac{\partial^2\theta}{\partial t^2} + m x_\theta\sin\theta\left(\frac{\partial\theta}{\partial t}\right)^2 - \frac{\partial^2}{\partial z^2}\Big(EI\frac{\partial^2 w}{\partial z^2}\Big) + N\Big] \\
&\quad +\delta\theta\Big[-m x_\theta^2\frac{\partial^2\theta}{\partial t^2}\underbrace{(\sin^2\theta+\cos^2\theta)}_{=1} - m x_\theta\cos\theta\,\cos\theta\frac{\partial^2 w}{\partial t^2} - I_{zz_{CM}}\frac{\partial^2\theta}{\partial t^2} + \frac{\partial}{\partial z}\Big(GJ\frac{\partial\theta}{\partial z}\Big) \\
&\quad +M\Big]\Bigg\}dz\,dt = 0
\end{aligned} \tag{4.25}$$

The virtual displacements δw and $\delta\theta$ are arbitrary and independent, so they can be set to zero at $z=0$ and $z=L$, and taken as arbitrary for $z\in(0,L)$. Therefore, the terms multiplying the virtual displacements in the integrand must each be zero, which gives

$$\frac{\partial^2}{\partial z^2}\Big(EI\frac{\partial^2 w}{\partial z^2}\Big) + m\frac{\partial^2 w}{\partial t^2} + m x_\theta\cos\theta\,\frac{\partial^2\theta}{\partial t^2} - m x_\theta\sin\theta\left(\frac{\partial\theta}{\partial t}\right)^2 = N \tag{4.26}$$

$$\frac{\partial}{\partial z}\Big(GJ\frac{\partial\theta}{\partial z}\Big) - m x_\theta\cos\theta\,\frac{\partial^2 w}{\partial t^2} - \underbrace{(I_{zz_{CM}} + m x_\theta^2)}_{I_\theta}\frac{\partial^2\theta}{\partial t^2} = -M \tag{4.27}$$

Enforcing the assumption of small displacements gives the final form of the governing equations for coupled bending and torsional vibrations of a beam,

$$\frac{\partial^2}{\partial z^2}\Big[EI(z)\frac{\partial^2 w(z,t)}{\partial z^2}\Big] + m(z)\frac{\partial^2 w(z,t)}{\partial t^2} + m(z)x_\theta(z)\frac{\partial^2 \theta(z,t)}{\partial t^2} = N(z,t) \tag{4.28}$$

$$\frac{\partial}{\partial z}\Big[GJ(z)\frac{\partial \theta(z,t)}{\partial z}\Big] - m(z)x_\theta(z)\frac{\partial^2 w(z,t)}{\partial t^2} - I_\theta(z)\frac{\partial^2 \theta(z,t)}{\partial t^2} = -M(z,t) \tag{4.29}$$

4.3 Boundary and Initial Conditions

The boundary conditions for each tail, which is clamped at the root and free at the tip, are as follows,

$$w(0,t) = \frac{\partial w(0,t)}{\partial z} = \frac{\partial^2 w(L,t)}{\partial z^2} = \frac{\partial}{\partial z}\Big[EI(L)\frac{\partial^2 w(L,t)}{\partial z^2}\Big] = 0 \tag{4.30}$$

$$\theta(0,t) = \frac{\partial \theta(L,t)}{\partial z} = 0 \tag{4.31}$$

The initial conditions consistent with an initially undeformed stationary tail are

$$w(z,0) = \frac{\partial w(z,0)}{\partial t} = 0 \tag{4.32}$$

$$\theta(z,0) = \frac{\partial \theta(z,0)}{\partial t} = 0 \tag{4.33}$$

4.4 Computational Structural Dynamics Formulation

In this study, the structural dynamics equations (4.28-4.29) are solved approximately using the Galerkin method with six bending modes and six torsion modes. This method expands the dependent variables in terms of natural free vibration modes of the system. The resulting error is minimized by weighting these modes such that the error integrated over the domain is zero.

The dependent variables are given by

$$w(z,t) = \sum_{i=1}^{I} q_i(t)\phi_i(z) \qquad \theta(z,t) = \sum_{j=I+1}^{J} q_j(t)\phi_j(z) \tag{4.34}$$

where

$q_i(t) \equiv$ generalized coordinate for bending

$q_j(t) \equiv$ generalized coordinate for torsion

$\phi_i(z) \equiv$ comparison function satisfying the free vibration modes of a beam in bending

$\phi_j(z) \equiv$ comparison function satisfying the free vibration modes of a beam in torsion

$I \equiv$ number of bending modes selected $= 6$

$J \equiv I +$ number of torsion modes selected $= 6 + 6 = 12$

The comparison functions may be any arbitrary functions which satisfy the geometric and natural boundary conditions of each tail. Hence, the free vibration modes for a cantilevered beam may be used for this purpose. The modes are easily derived by solving the uncoupled free bending and torsion equations individually by the method of separation of variables. The i^{th} free vibration bending mode is given by

$$\phi_i(z) = (\sin\beta_i L - \sinh\beta_i L)(\sin\beta_i z - \sinh\beta_i z) + (\cos\beta_i L + \cosh\beta_i L)(\cos\beta_i z - \cosh\beta_i z) \tag{4.35}$$

where $\beta_i L$ is the i^{th} solution to the transcendental equation

$$\cos\beta_i L \ \cosh\beta_i L = -1 \qquad i = 1, 2, \ldots, \infty \tag{4.36}$$

and the i^{th} bending natural frequency is given by

$$\omega_i = \beta_i^2 \sqrt{\frac{EI}{m}} = (\beta_i L)^2 \sqrt{\frac{EI}{mL^4}} \tag{4.37}$$

The j^{th} free torsional vibration mode is given by

$$\phi_j = \sin\left[\frac{(2j-1)\pi z}{2L}\right] \qquad j = 1, 2, \ldots, \infty \tag{4.38}$$

and the j^{th} torsional natural frequency is given by

$$\omega_j = \frac{(2j-1)\pi}{2L}\sqrt{\frac{GJ}{I_\theta}} \tag{4.39}$$

Since Eqs. (4.34) are approximate solutions to Eqs. (4.28-4.29), the resulting errors are given by

$$\epsilon_w(z,t) = \frac{\partial^2}{\partial z^2}\Big[EI\frac{\partial^2 w}{\partial z^2}\Big] + m\frac{\partial^2 w}{\partial t^2} + m\,x_\theta\frac{\partial^2 \theta}{\partial t^2} - N \tag{4.40}$$

$$\epsilon_\theta(z,t) = \frac{\partial}{\partial z}\Big[GJ\frac{\partial \theta}{\partial z}\Big] - m\,x_\theta\frac{\partial^2 w}{\partial t^2} - I_\theta\frac{\partial^2 \theta}{\partial t^2} + M \tag{4.41}$$

The Galerkin method requires that,

$$\int_0^L \epsilon_w(z,t)\phi_r(z)dz = 0,\ r = 1,2,\ldots,I \tag{4.42}$$

$$\int_0^L \epsilon_\theta(z,t)\phi_s(z)dz = 0,\ s = I+1, I+2,\ldots,J \tag{4.43}$$

Substituting the series representations, Eqs. (4.34) into Eqs. (4.42-4.43) gives

$$\int_0^L \left\{ \sum_{i=1}^{I} q_i \frac{d^2}{dz^2}\Big[EI\frac{d^2\phi_i}{dz^2}\Big] + \sum_{i=1}^{I} m\phi_i\frac{d^2 q_i}{dt^2} + \sum_{j=I+1}^{J} m\,x_\theta\phi_j\frac{d^2 q_j}{dt^2} - N \right\}\phi_r dz = 0 \qquad r = 1,2,\ldots,I \tag{4.44}$$

$$\int_0^L \left\{ \sum_{j=I+1}^{J} q_j \frac{d}{dz}\Big[GJ\frac{d\phi_j}{dz}\Big] - \sum_{i=1}^{I} m\,x_\theta\phi_i\frac{d^2 q_i}{dt^2} - \sum_{j=I+1}^{J} I_\theta\phi_j\frac{d^2 q_j}{dt^2} + M \right\}\phi_s dz = 0 \qquad s = I+1, I+2,\ldots,J \tag{4.45}$$

and the boundary conditions, Eqs. (4.30-4.31) become

$$\phi_i(0) = \frac{d\phi_i(0)}{dz} = \frac{d^2\phi_i(L)}{dz^2} = \frac{d}{dz}\Big[EI(L)\frac{d^2\phi_i(L)}{dz^2}\Big] = 0 \qquad i = 1,2,\ldots,I \tag{4.46}$$

$$\phi_j(0) = \frac{d\phi_j(L)}{dz} = 0 \qquad j = I+1, I+2,\ldots,J \tag{4.47}$$

Integration by parts and enforcement of the boundary conditions yields

$$\begin{aligned}\int_0^L \phi_r \frac{d^2}{dz^2}\Big[EI\frac{d^2\phi_i}{dz^2}\Big]dz &= \underbrace{\phi_r \frac{d}{dz}\Big[EI\frac{d^2\phi_i}{dz^2}\Big]\Big|_0^L}_{=0,\ \text{B.C. Eq. (4.46)}} - \int_0^L \frac{d\phi_r}{dz}\frac{d}{dz}\Big[EI\frac{d^2\phi_i}{dz^2}\Big]dz \\ &= \underbrace{-\frac{d\phi_r}{dz}EI\frac{d^2\phi_i}{dz^2}\Big|_0^L}_{=0,\ \text{B.C. Eq. (4.46)}} + \int_0^L EI\frac{d^2\phi_r}{dz^2}\frac{d^2\phi_i}{dz^2}dz \end{aligned} \tag{4.48}$$

$$\int_0^L \phi_s \frac{d}{dz}\Big[GJ\frac{d\phi_j}{dz}\Big]dz = \underbrace{\phi_s \frac{d}{dz}\Big[GJ\frac{d\phi_j}{dz}\Big]\Big|_0^L}_{=0,\ \text{B.C. Eq. (4.47)}} - \int_0^L GJ\frac{d\phi_s}{dz}\frac{d\phi_j}{dz}dz \tag{4.49}$$

In matrix form Eqs. (4.44-4.45) become

$$\begin{aligned}&\Big[\int_0^L EI\frac{d^2\phi_r}{dz^2}\frac{d^2\phi_i}{dz^2}dz\Big]_{r\times i}\Big\{q_i\Big\}_{i\times 1} + \Big[\int_0^L m\phi_r\phi_i dz\Big]_{r\times i}\Big\{\frac{d^2q_i}{dt^2}\Big\}_{i\times 1} \\ &+ \Big[\int_0^L mx_\theta\phi_r\phi_j dz\Big]_{r\times j}\Big\{\frac{d^2q_j}{dt^2}\Big\}_{j\times 1} - \Big\{\int_0^L N\phi_r dz\Big\}_{r\times 1} = \Big\{0\Big\}\end{aligned} \tag{4.50}$$

$$\begin{aligned}&\Big[\int_0^L GJ\frac{d\phi_s}{dz}\frac{d\phi_j}{dz}dz\Big]_{s\times j}\Big\{q_j\Big\}_{j\times 1} + \Big[\int_0^L mx_\theta\phi_s\phi_i dz\Big]_{s\times i}\Big\{\frac{d^2q_i}{dt^2}\Big\}_{i\times 1} \\ &+ \Big[\int_0^L I_\theta\phi_s\phi_j dz\Big]_{s\times j}\Big\{\frac{d^2q_j}{dt^2}\Big\}_{j\times 1} - \Big\{\int_0^L M\phi_s dz\Big\}_{s\times 1} = \Big\{0\Big\}\end{aligned} \tag{4.51}$$

Equations (4.50-4.50) can be further simplified by writing them in partitioned matrix form,

$$\begin{bmatrix} M_{11} & M_{12} \\ M_{21} & M_{22} \end{bmatrix}\begin{Bmatrix} \frac{d^2q_i}{dt^2} \\ \frac{d^2q_j}{dt^2} \end{Bmatrix} + \begin{bmatrix} K_{11} & 0 \\ 0 & K_{22} \end{bmatrix}\begin{Bmatrix} q_i \\ q_j \end{Bmatrix} = \begin{Bmatrix} Q_1 \\ Q_2 \end{Bmatrix} \tag{4.52}$$

where the elements of the mass matrix are given by

$$\begin{aligned} M_{11} &= \int_0^L m\phi_r\phi_i dz \quad & M_{12} &= \int_0^L mx_\theta\phi_r\phi_j dz \\ M_{21} &= \int_0^L mx_\theta\phi_s\phi_i dz \quad & M_{22} &= \int_0^L I_\theta\phi_s\phi_j dz \end{aligned} \tag{4.53}$$

the stiffness elements are given by

$$K_{11} = \int_0^L EI\frac{d^2\phi_r}{dz^2}\frac{d^2\phi_i}{dz^2}dz \quad K_{22} = \int_0^L GJ\frac{d\phi_s}{dz}\frac{d\phi_j}{dz}dz \tag{4.54}$$

and the generalized force elements are given by

$$Q_1 = \int_0^L N\phi_r dz \quad Q_2 = \int_0^L M\phi_s dz \tag{4.55}$$

The original governing equations have now been transformed from a set of two coupled partial differential equations into a set of twelve coupled second-order ordinary differential equations. In compact matrix notation, these equations are written as

$$[M]\{\ddot{q}\} + [K]\{q\} = \{Q\} \tag{4.56}$$

By introduction of a new variable η, the equations may be further reduced to a set of $2J$ coupled first-order ordinary differential equations. Letting

$$\{\eta\} = [I]\{\dot{q}\} \tag{4.57}$$

gives

$$[M]\{\dot{\eta}\} + [K]\{q\} = \{Q\} \tag{4.58}$$

Writing the new system in a state-space like form gives

$$\begin{Bmatrix} \dot{\eta} \\ \dot{q} \end{Bmatrix} = \begin{bmatrix} 0 & -[M]^{-1}[K] \\ [I] & 0 \end{bmatrix} \begin{Bmatrix} \eta \\ q \end{Bmatrix} + \begin{Bmatrix} [M]^{-1}\{Q\} \\ 0 \end{Bmatrix} \tag{4.59}$$

This final form of the governing equations is solved using a five-stage Runge-Kutta-Verner scheme.

4.5 Multidisciplinary Solution Methodology

At this point the solution algorithms for the fluid flow, elastic tail deformations and the grid displacements are well in hand. Now, attention is focused on the method in which these independent disciplines are brought together. The first step is to solve for the flow field under conditions favorable to vortex breakdown. During this step, the

flow field solution and the pressure difference across each tail are obtained. The pressure difference is used to compute the normal force and twisting moment per unit length along each tail. With aerodynamic forces known, the deflections, $w_{i,j,k}$ and $\theta_{i,j,k}$, can be obtained. Next, the grid is smoothly interpolated to conform to the new position and velocity of each tail. In this step, the metric coefficients of the coordinate Jacobian matrix are updated as well as the grid speed, $\frac{\partial \xi^m}{\partial t}$. The cycle is now repeated for the next global time step with the current tail positions and velocities as initial conditions. It should be noted that the time step for the fluid dynamics calculations is generally much smaller than the structural dynamics time step. Hence, $w_{i,j,k}$ and $\theta_{i,j,k}$ need not be calculated for every global time step. However, for the sake of simplicity and because of the relatively low cost of structural calculations, the structures time step is kept in line with the fluid dynamics time step.

CHAPTER 5

SINGLE SQUARE VERTICAL TAIL BUFFETING

5.1 Introduction

In this chapter, the fundamental issues of inertial coupling, Reynolds number dependence and aeroelastic effects are addressed with regard to single square vertical tail buffet. The case definitions are summarized in Table 5.1. Because of the detailed analysis required to address these fundamental issues properly, detailed plots are presented for each case along with the initial condition flow fields. In later chapters, the analysis will be more tightly focused on the buffeting response. The chapter is divided into sections corresponding to each case plus the initial conditions. As each case is presented, it is discussed individually and then compared to the relevant case preceding it. Finally, the results of each case are tabulated in the concluding section for reference.

Case	Elastic Model	Re	α	x_θ
1	Uncoupled Bending and Torsion	10^4	38^o	0.00
2	Coupled Bending and Torsion	10^4	38^o	0.05
3	Rigid Tail	10^6	38^o	0.00
4	Uncoupled Bending and Torsion	10^6	38^o	0.00
5	Coupled Bending and Torsion	10^6	38^o	0.05

Table 5.1: Summary of single square vertical tail buffeting cases.

5.2 Computational Model

5.2.1 Model Geometry and Computational Domain

The model consists of a sharp-edged, flat delta wing of aspect ratio 1 (leading edge sweep of $\Lambda = 76^o$) and a single flat square vertical tail, which is placed in the plane of geometric symmetry. The vertical tail is located directly behind the trailing edge of the wing, with the root edge along the wing symmetry axis.

An O-H type grid of $83 \times 124 \times 84$ cells in the axial, wrap-around and normal directions, respectively, is used to solve for the initial condition flow field for the low Reynolds number case, see Figures 5.1-5.5. Note that all grid dimensions given throughout this study are nondimensionalized by the wing root chord. The grid was generated algebraically by the method described in Section 3.5. Although this grid contains 864,528 cells, it is very wasteful in the far-field radially and lacks any *j-plane* clustering along the vortex cores. Furthermore, this grid is not explicitly designed for capturing vortex breakdown, in that the stream-wise *i-plane* grid density is much coarser than the normal or wrap around distributions. For a vortex flow at low to moderate angles-of-attack, the flow is nearly conical and thus, a coarse stream-wise distribution is justified. However, with the occurrence of breakdown, the stream-wise direction becomes very significant. Essentially, the fine grid represents a fine weekly viscous conical flow grid.

To reduce the spatial accuracy of the wrap around (j) and normal (k) directions to a level closer to that of the axial (i) direction, every other *j-plane* and *k-plane* was removed. This reduced the total number of cells to 223,104 cells, a reduction of 74%. The coarsened grid is shown in Figures 5.6-5.10. Comparison of flow plots for the initial flow state generated from the fine grid with the solution obtained from the coarse grid indicates that the coarse grid produces flow solutions of similar quality to the fine grid.

5.2.2 Freestream Flow Conditions

For each of the single tail cases under consideration, the configuration angle-of-attack is 38^o and the freestream Mach number is 0.4. Solutions are obtained at low and moderate Reynolds numbers of 10^4 and 10^6. The angle-of-attack of 38^o is chosen to complement an earlier study [71] and represents a relatively high value for subsonic tail buffet. The nominal angle-of-attack range for subsonic tail buffet is from 20^o to 40^o with the peak loads occurring near 30^o. Below the lower limit vortex breakdown does not occur and as angle-of-attack increases the burst vortex core becomes more diffuse and passes higher above the tail. The Mach number is chosen to coincide with the severe tail buffet conditions which occur during subsonic high-alpha maneuvers. The low Reynolds number is chosen to facilitate numerical computations since fewer grid cells are required to capture boundary layer effects. The moderate Reynolds number of 10^6 is chosen to bring the simulation closer to flight Reynolds numbers of order 10^7. However, since the single tail grid is not refined to compensate for the increased Reynolds number, the main effect is on the buffeting response.

5.2.3 Tail Material Properties

One of the major goals of this study is to capture the full dynamic interaction between the tail and the flow. For this reason care is taken to optimize the geometric and material properties of the tail to produce a relatively large-amplitude, high-frequency response. A large amplitude relative to the grid spacing normal to the tail is desired so that the movement of the grid will not be lost in the spatial discretization error inherent in the flow solution. The need for a high-frequency response is necessitated by the high computational cost of solving the flow for long periods of time. These conflicting goals are attained by choosing a small tail thickness to boost the amplitude, and a low material

density to increase the frequency. For all of the single tail cases, the tail is modeled as a rectangular beam with thickness $d = 0.005$, width $b = 0.5$ and height $L = 0.5$ normalized by the wing root chord. The dimensionless moduli of elasticity and rigidity, E and G, of the tail material are 1.8×10^5 and 0.692×10^5, respectively. The mass per unit length, m, is 0.0653 and the mass-moment of inertia per unit length about the elastic axis, I_θ, for $x_\theta = 0$ is 0.00136. For the inertially coupled bending and torsion cases, the distance between the inertial and elastic axes, x_θ is 0.05 which gives $I_\theta = 0.00153$. The chosen material properties correspond to a very thin, stiff and light-weight beam. In the following chapters of this study, the twin tails are modeled more realistically. The natural frequencies for the first six bending and torsion modes are listed in Table 5.2.

	ω_1	ω_2	ω_3	ω_4	ω_5	ω_6
Bending	0.16	1.02	2.86	5.60	9.26	13.84
Torsion	0.29	0.88	1.46	2.06	2.63	3.21

Table 5.2: First six bending and torsion natural frequencies of a cantilevered beam, where the dimensional frequency, f in Hz is nondimensionalized as $\frac{f\bar{\bar{c}}}{U_\infty}$.

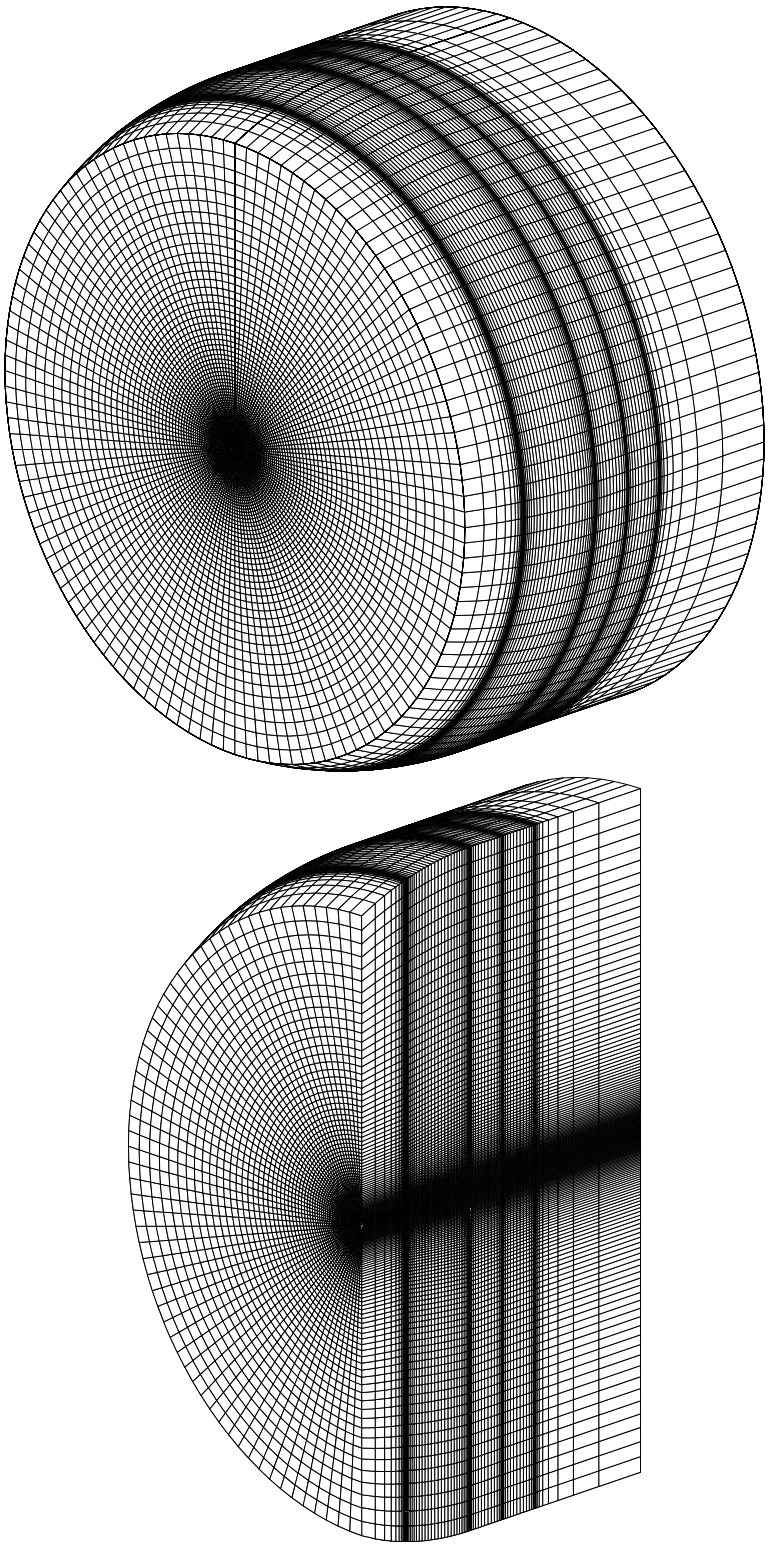

Figure 5.1: Fine grid: $83 \times 124 \times 84$ cells. Full and half views showing stream-wise clustering.

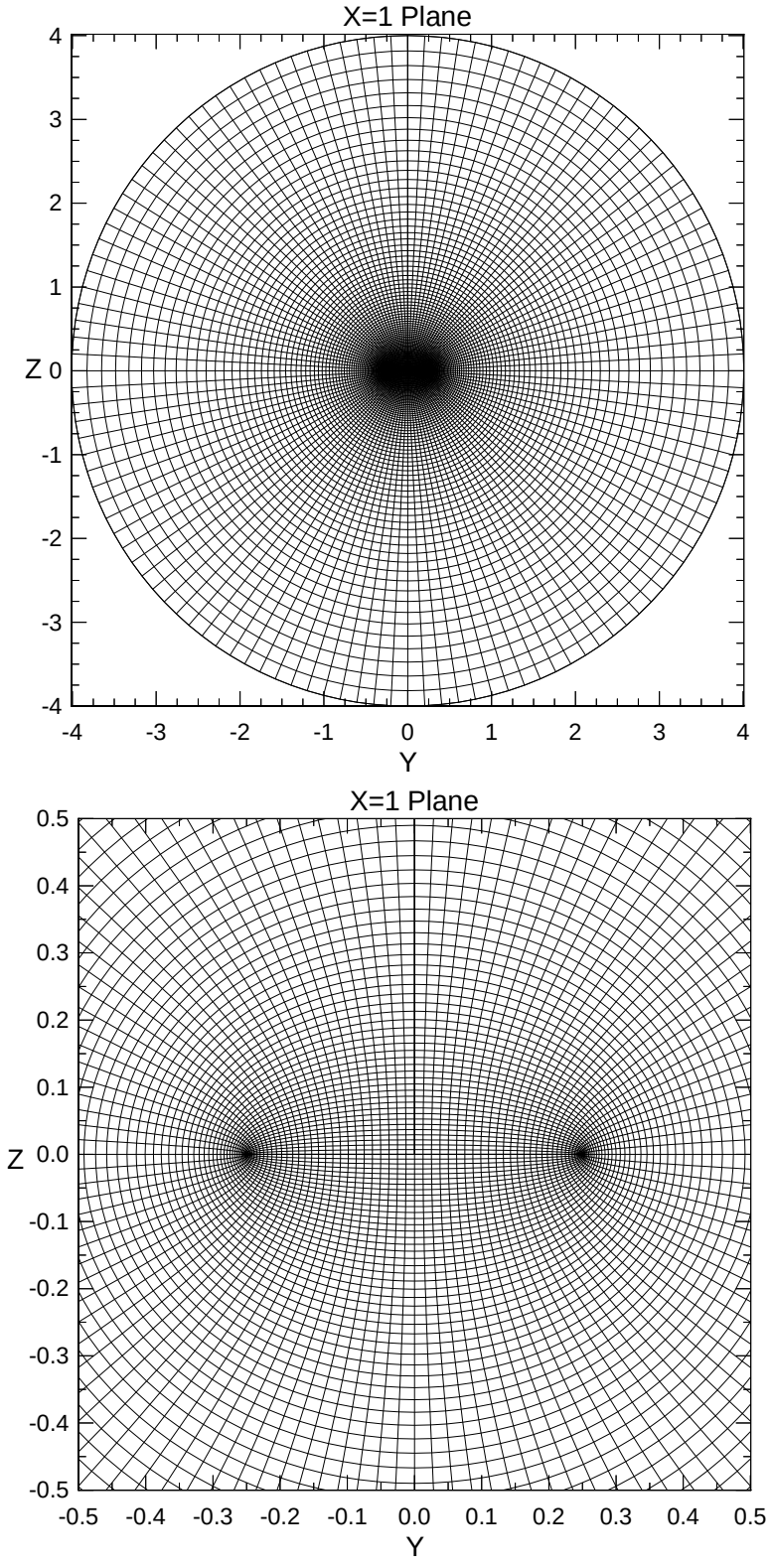

Figure 5.2: Fine grid: $83 \times 124 \times 84$ cells. Full and close-up views showing the crossflow *i-plane* at the wing trailing edge.

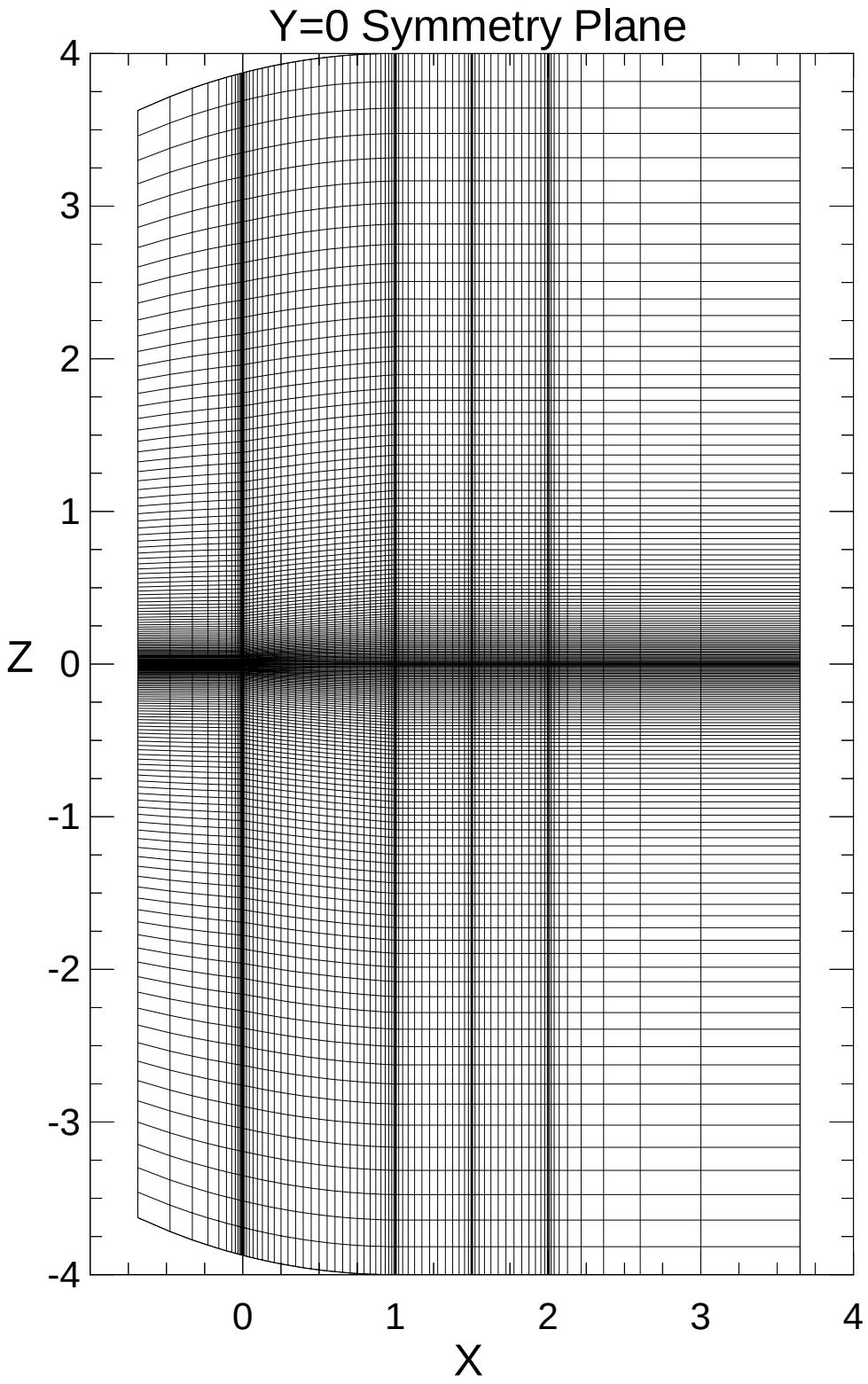

Figure 5.3: Fine grid: $83 \times 124 \times 84$ cells. Full symmetry *j-plane*.

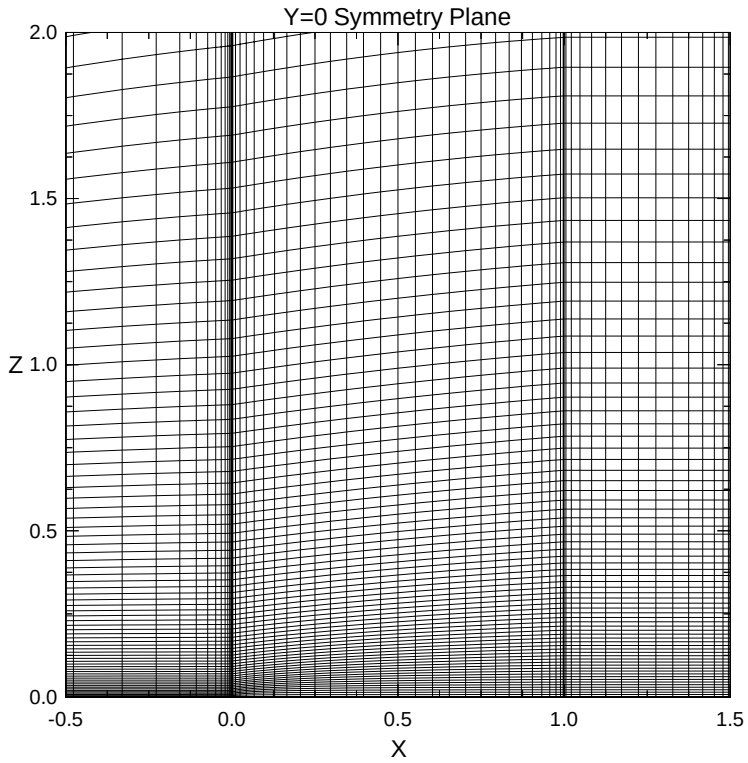

Figure 5.4: Fine grid: View of symmetry *j-plane* from wing apex to trailing edge of tail.

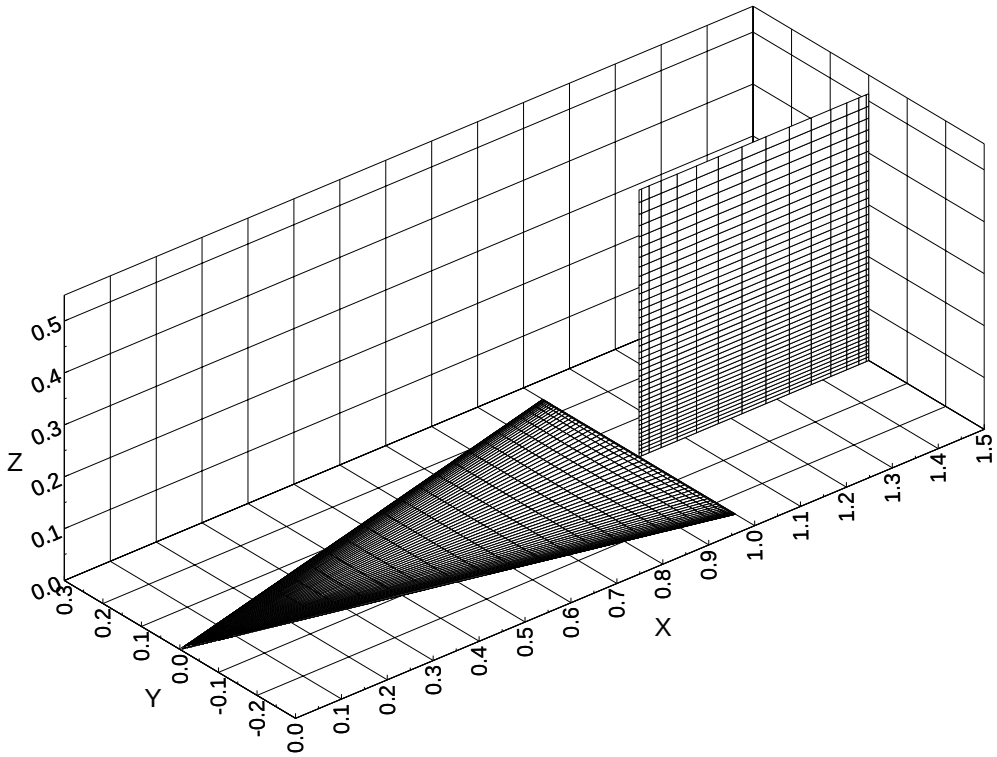

Figure 5.5: Fine grid: $83 \times 124 \times 84$ cells. Upper wing surface; 30×64 cells. Tail surface 15×40 cells.

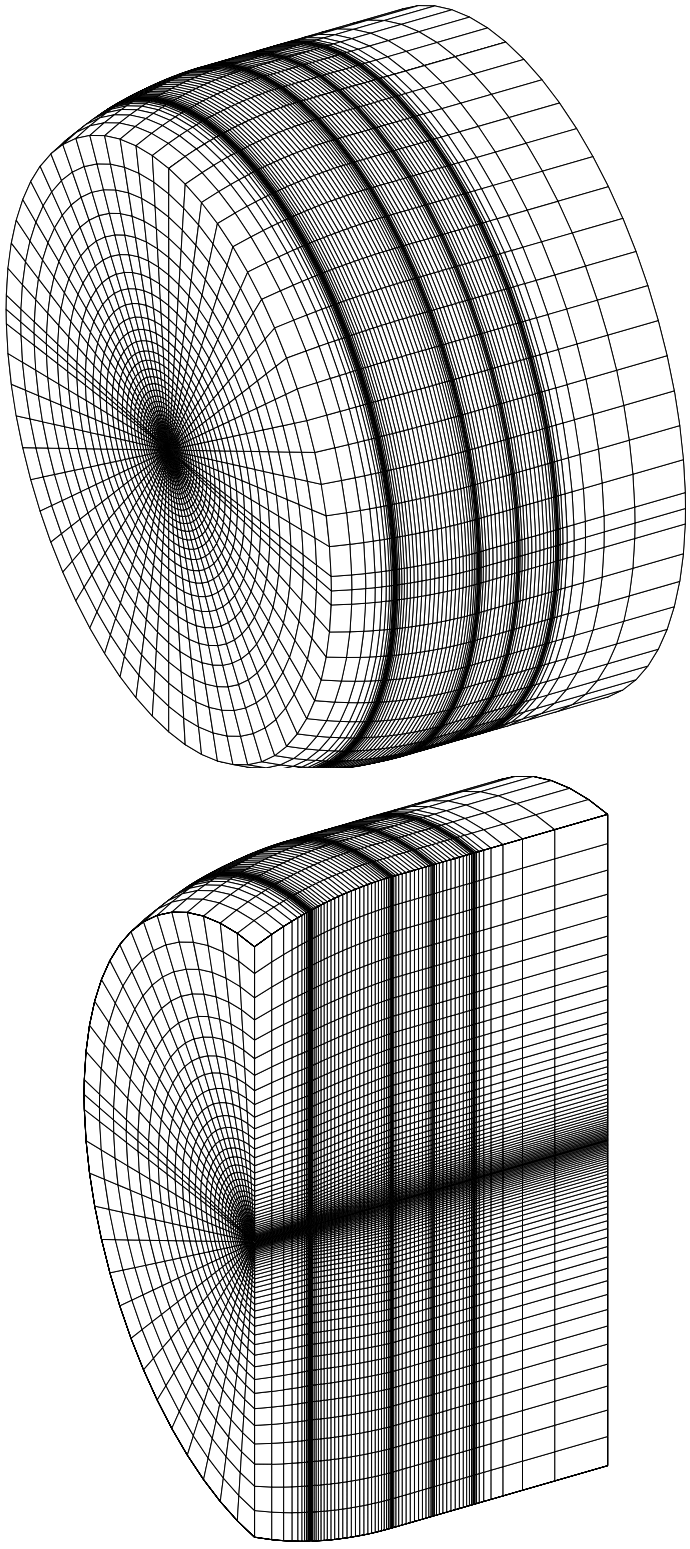

Figure 5.6: Coarse grid: $83 \times 64 \times 42$ cells. Full and half views showing stream-wise clustering.

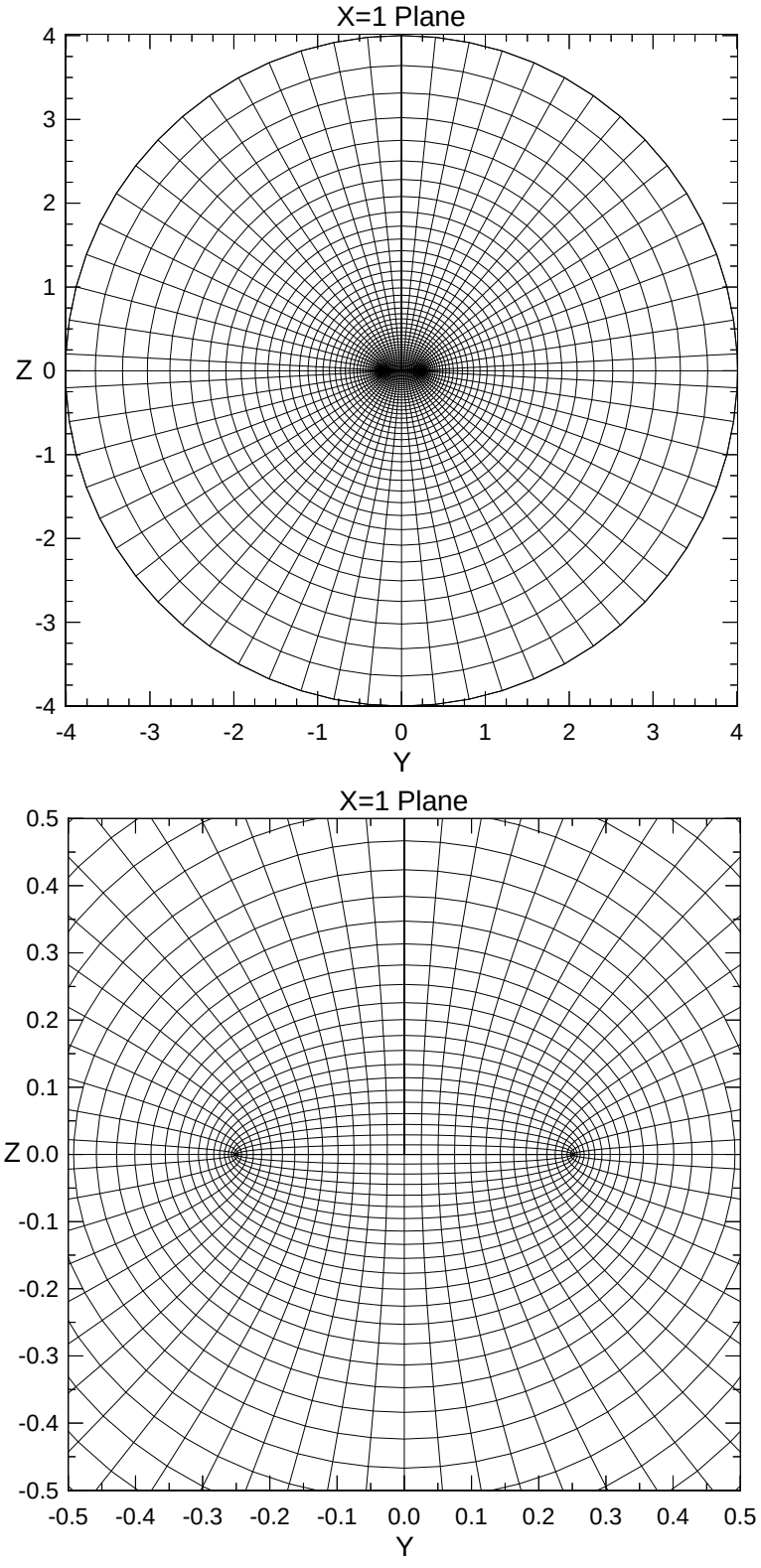

Figure 5.7: Coarse grid: $83 \times 64 \times 42$ cells. Full and close-up views showing the crossflow *i-plane* at the wing trailing edge.

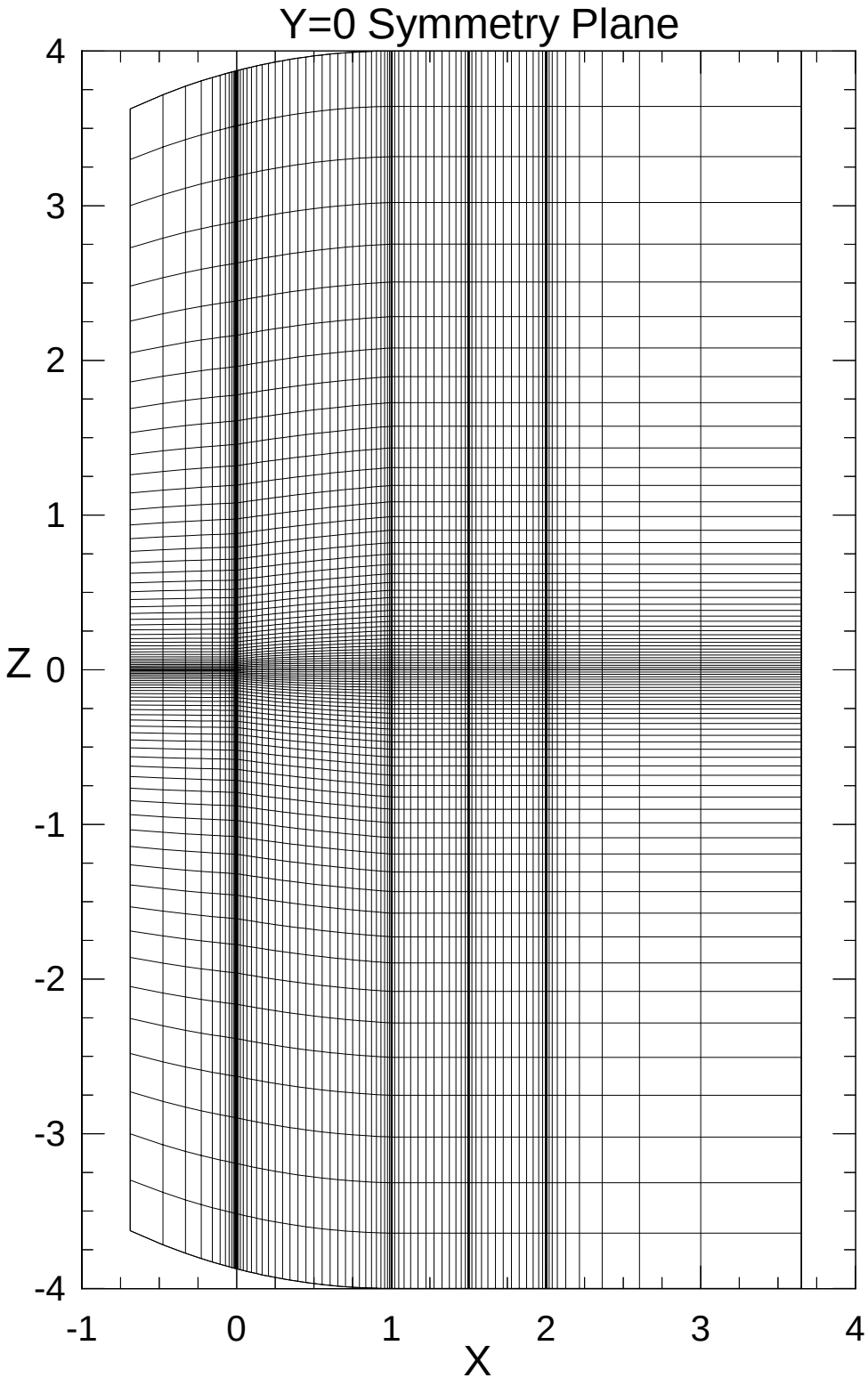

Figure 5.8: Coarse grid: $83 \times 64 \times 42$ cells. Full symmetry *j-plane*.

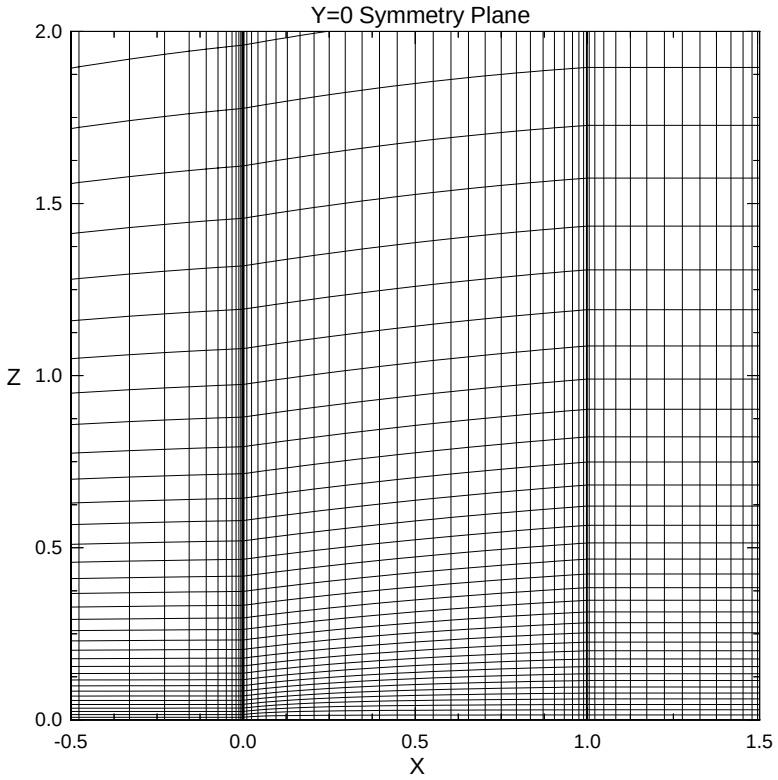

Figure 5.9: Coarse grid: View of symmetry *j-plane* from wing apex to trailing edge of tail.

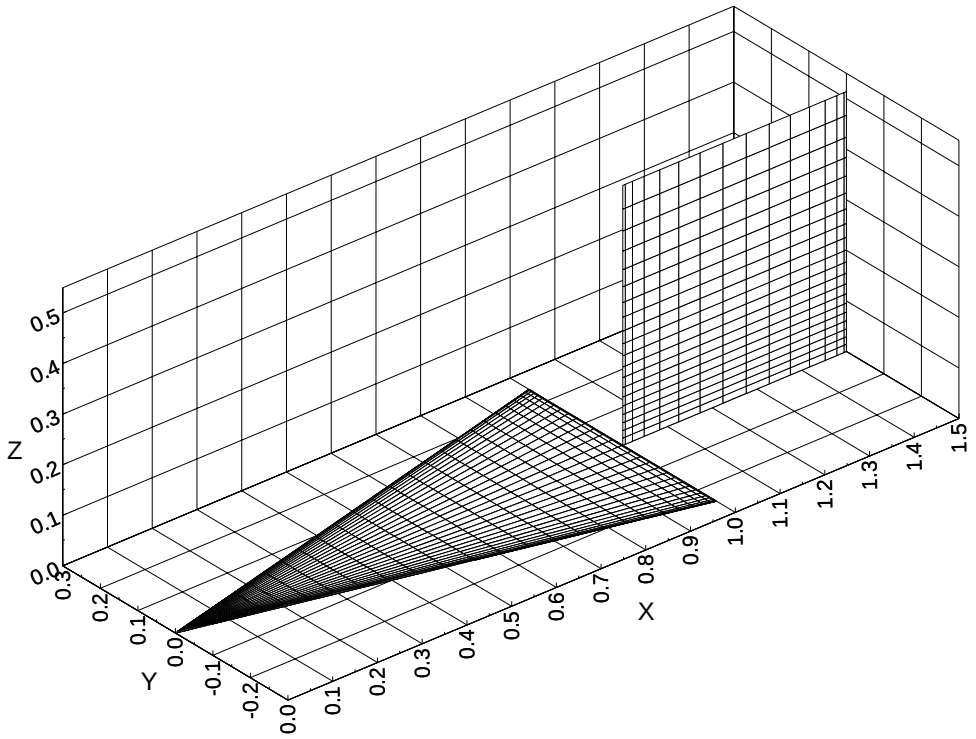

Figure 5.10: Coarse grid: $83 \times 64 \times 42$ cells. Upper wing surface; 30×32 cells. Tail surface 15×20 cells.

5.3 Low Reynolds Number Cases: $Re = 10^4$

5.3.1 Initial Condition Flow Field

At the start of the flow computations, the flow field is solved by impulsively inserting the wing-tail configuration into the freestream. Thus, before the structural dynamics computations can begin, the flow must be allowed to mature to the point where the large transients caused by the impulsive insertion have subsided. Once this developed flow solution is obtained, the tail, which up to this point has been rigid, may now be released to interact with the flow. For both of the low Reynolds number cases considered in this chapter, the flow field buffeting initial condition is taken from the end of a previously run rigid tail case in which the angle-of-attack was impulsively changed from a converged solution at $\alpha = 35^o$ to $\alpha = 38^o$. The solution is obtained by solving the Navier-Stokes equations time-accurately using an implicit, flux-vector splitting scheme. The transition case is integrated for 6000 time steps to a nondimensional time of 10.8. This amount of time is more than enough to insure a converged solution. In the absence of previous solutions, pseudo-time stepping provides a converged solution much more efficiently than time-accurate stepping.

Three-dimensional and top views of nondimensional surface pressure and vortex core streamlines are shown in Figure 5.11. Since this flow is viscous the total pressure on the surfaces is equivalent to the static pressure. The total pressure contours show the gradual decrease of suction power as the vortex moves over the wing. This is due to the diffusion of the vortex after bursting and the adverse pressure gradient from the wake. Close inspection of the wing surface reveals a total pressure spike at the symmetry plane. This spike is a plotting artifact and exist only at the $k = 1$ wing surface plane and is due to an improper interpolation from the cell-centered finite volume coordinates

to the PLOT3D format of vertex coordinates. Thus, it has no effect on the solution. This plotting error exists only in the single tail cases.

The streamlines shown in Figure 5.11 are traced from a position at just above the wing apex such that they are entraned into the vortex cores. By tracing the vortex cores the breakdown region becomes clearly defined where the streamlines 'bell out.' From topological analysis, a spiral saddle point will be located just downstream of the initial core expansion. In this case, the initial expansion starts at $x = 0.23$ and from inspection of the velocity vectors the critical point is located at $x = 0.3$. This difference in location leads to a source of ambiguity in the definition of the location of breakdown. Since a critical point can generally be located more precisely than the start of core expansion, the location of the breakdown will be recorded in reference to the spiral saddle critical point locations.

Another sign of breakdown is the sudden increase in core pressure and total pressure (despite the decrease in axial velocity). In Figure 5.12a, finite diameter, core streamlines, colored by local total pressure, show a constant core total pressure before breakdown that sharply increases at the start of core expansion. Note that the apparent high pressure readings on the streamlines very close to the apex are a result of the core streamlines being colored by the pressure location corresponding to the outer radius of the streamlines, which extends outside the core near the apex where the vortices are very small. In Figure 5.12b, a *j-plane* slicing the right vortex core is shown with flooded total pressure contours. From the contours, the increase in total pressure due to vortex breakdown can clearly be seen. Although there are many other scalar indicators of vortex strength, for this flow field it is found that total pressure provided the best indication of vortex breakdown. In Figures 5.13a and 5.13b, side views at flow angle-of-attack show

surface pressure and right vortex core streamlines. Figure 5.13b shows a close-up view, $x = [0, 0.4]$, of the total pressure colored vortex core streamlines.

Figures 5.14 and 5.15 provide new insight into the structure of three-dimensional vortex breakdown. To the author's knowledge, 2-D and 3-D streamlines of vortex breakdown plotted together have never been published. The value of this type of plot is that it provides a clear spatial relationship between 2-D and 3-D core streamlines. While 3-D streamlines generally provide the clearest indication of a burst vortex, they are less effective at capturing the internal structure of the post breakdown core. Conversely 2-D streamlines are well suited to the latter, but due to the loss of the out-of-plane velocity component, flow features dependent on this component can only be inferred from their in-plane effects. Figure 5.14 shows the full configuration at side and three-dimensional orientations. In-plane streamlines are plotted on an opaque vertical plane ($\Lambda_p = 82^o$) which slices through the three-dimensional vortex core streamlines. Close-up views of the breakdown region with opaque and clear cutting planes are shown in Figure 5.15. Comparison of the 2-D streamlines with the 3-D streamlines shows that the breakdown point is clearly captured by the 3-D streamlines but is not clearly visible at this flow instant in the 2-D cutting plane. This is most likely due to a lack of sufficient grid resolution in the axial direction.

The relationship between in-plane streamlines, velocity vectors, normal Mach number and total pressure is shown in Figure 5.16. The cutting plane is again at ($\Lambda_p = 82^o$) as in the previous two figures, however the oblique cutting plane data have now been transformed (not projected) onto a flat 2-D representation that preserves the spatial aspect ratio, hence the plots use the tangential component x_s instead of x. The transformation to a cutting plane of sweep angle Λ_p is as follows:

$$u_s = u\cos\lambda + v\cos(\frac{\pi}{2} - \lambda) \tag{5.1}$$

$$v_n = u\cos(\frac{\pi}{2} + \lambda) + v\cos\lambda \tag{5.2}$$

$$w_s = w \tag{5.3}$$

$$x_s = \frac{x}{\cos\lambda} \tag{5.4}$$

$$z_s = z \tag{5.5}$$

where u_s and w_s are the in-plane velocity components, v_n is the velocity component normal to the cutting plane and $\lambda = \frac{\pi}{2} - \Lambda_p$. Arrowed streamlines plotted on a axial plane in Figure 5.16a reveal an attracting and repelling 2D foci pair near $x_s = 0.55$. With more grid resolution, other streamline 'kinks' would likely become additional foci. In-plane velocity vectors drawn from a uniform rectangular 30×30 mesh are shown in Figure 5.16b. Contours of the nondimensionalized velocity component normal to the axial cutting plane, M_n are plotted in Figure 5.16c. The dashed lines indicate velocities pointing out of the page.

Comparing the in-plane streamlines with in-plane velocity vectors plotted once again reveals the danger of relying solely on 2-D streamline plots in detecting 3-D critical points associated with breakdown. The vector plot clearly shows the strong flow reversal near $x_s = 0.3$, $z = 0.03$. The streamlines also show this feature, but in a much less pronounced way. Combining information from the in-plane velocity vector plot with out-of-plane Mach number contours of Figure 5.16c confirms the fact that the 2-D foci clearly seen in the in-plane streamline plots *do not* coincide with 3-D spiral saddles or any other 3-D critical points. If they did, there would have to be regions of zero (within numerical error) normal velocity, and there are no such regions in the vicinity of the

off core 2-D foci. Contours of total pressure coefficient in Figure 5.17 show that the minimum C_{p_0} is -3.0 and is located in the unburst vortex core.

In Figures 5.18-5.22, surface flow features are shown. Recently a new numerical visualization technique has become available for simulating surface oil flow patterns. The algorithm is called Line Integral Convolution (LIC) and was developed by Cabral and Leedom [9]. The approach uses linear and curvilinear filtering techniques to blur textures locally along a vector field. To generate the computational surface oil flows in this study, the Animated Flow Integral Convolution (AFLIC) program is used, see Figure 5.18. The source bitmap is made up of white noise and in order to preserve configuration geometry, the flow state from the second grid plane normal to the viscous surfaces is moved to the surface. The value of LIC is its global nature, only a surface needs to be specified. Once the global structure is outlined streamlines restricted to the surface may be used to further enhance to flow depiction. A comparison of a computational wing surface oil flow with streamlines restricted to the $k = 2$ plane is shown in Figure 5.19. The two methods are also compared on the tail surfaces in Figure 5.20. From these plots, it can be seen that LIC produces results very similar to surface streamlines. The physical interpretation of the wing surface flow is that the flow above the surface of the wing is dominated by the primary vortices, which is to be expected at the low Reynolds number of 10^4. Also evident from the wing surface flow is an unsymmetric region of recirculation near the outer trailing edge. Inspection of the tail surface plots of Figure 5.20 reveals a strong separation line on both sides of the tail running diagonally up from the bottom of the tail at the leading edge to half way up the tail at the trailing edge. The separation lines are a result of the flow on the underside of the primary vortices moving away from the tail and merging with the freestream flow.

The relationship between near-surface total Mach number and surface pressure is shown in Figure 5.21. In the Mach number plot, the growth of the boundary layer is evidenced by the progressive decrease of Mach number (even before the breakdown). Close inspection of the pressure contours reveals a slight pressure drop very close to the leading edge. This is indicative of a very small secondary separation. Also evident in the wing surface plots is the flow asymmetry. At this relatively high angle-of-attack, the flow is known to be slightly asymmetric and becomes more so as it increases.

The tail loading distribution is shown in Figure 5.22. Coefficient of pressure contours are plotted on each side along with the differential pressure coefficient. For each plot, pressure contours are drawn in increments of $\Delta C_p = 0.05$ and labeled at $\Delta C_p = 0.1$ intervals. From the plots it can be seen that the greatest gradients in pressure occur at the leading edge of the tail and the gradients in pressure difference occur over the same locations, but are approximately half as steep. The magnitude of the differential pressure is also observed to be about one third of the pressure range on either side.

In Figures 5.23 and 5.24, total pressure coefficient contours and streamlines are plotted on vertical crossflow planes. Total pressure plots at chord stations on the wing, Figure 5.23, reveal a slight vortical asymmetry and confirm the enlargement and weakening of the vortices as the move downstream. The in-plane streamline plots at the same locations confirm that the total pressure minimums are occurring at the vortex cores and that any secondary separation is extremely small. Total pressure contours and streamlines in the crossflow planes surrounding the tail show a significant total pressure gradient near the tail and the main vortices rapidly diffusing and moving upwards. Note that since this data set are not 'i-blanked' the streamline routine tries to plot through the no-slip region of the tail.

In Figure 5.25, the normalized spanwise variation of the coefficient of pressure is plotted at the same chord stations as the previous crossflow plots. Plotting C_p in this fashion provides the clearest indication of flow separation beyond the primary vortices, because an additional suction peak will occur for each additional vortex. In this case, no evidence of a secondary vortex can be seen. Also of note is the increasing asymmetry shown at chord stations 0.7 and 0.9.

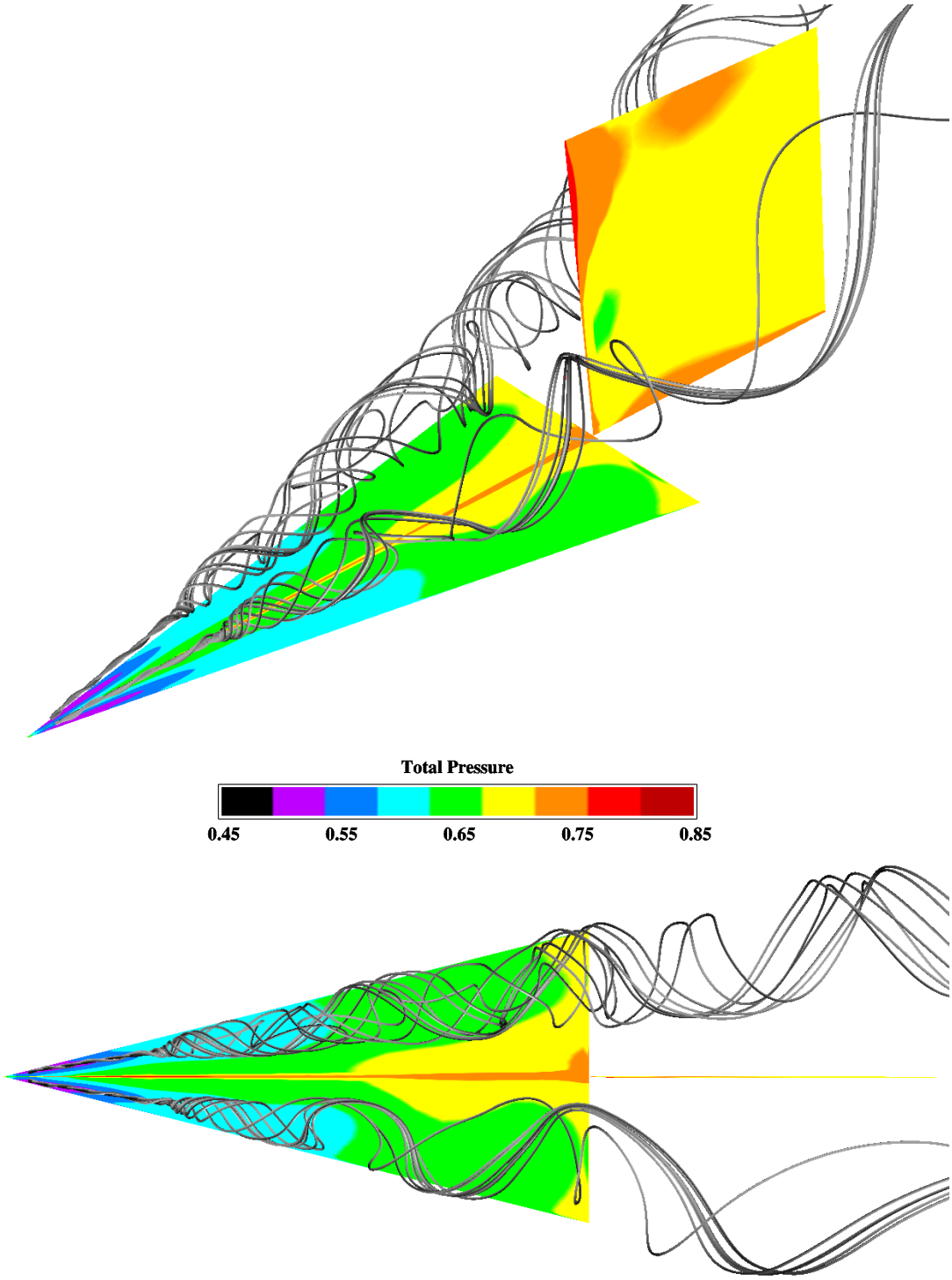

Figure 5.11: Three-dimensional and top views of surface pressure and vortex core streamlines. Initial Condition Flow Field: $Re = 10^4$, $M = 0.4$, $\alpha = 38^o$.

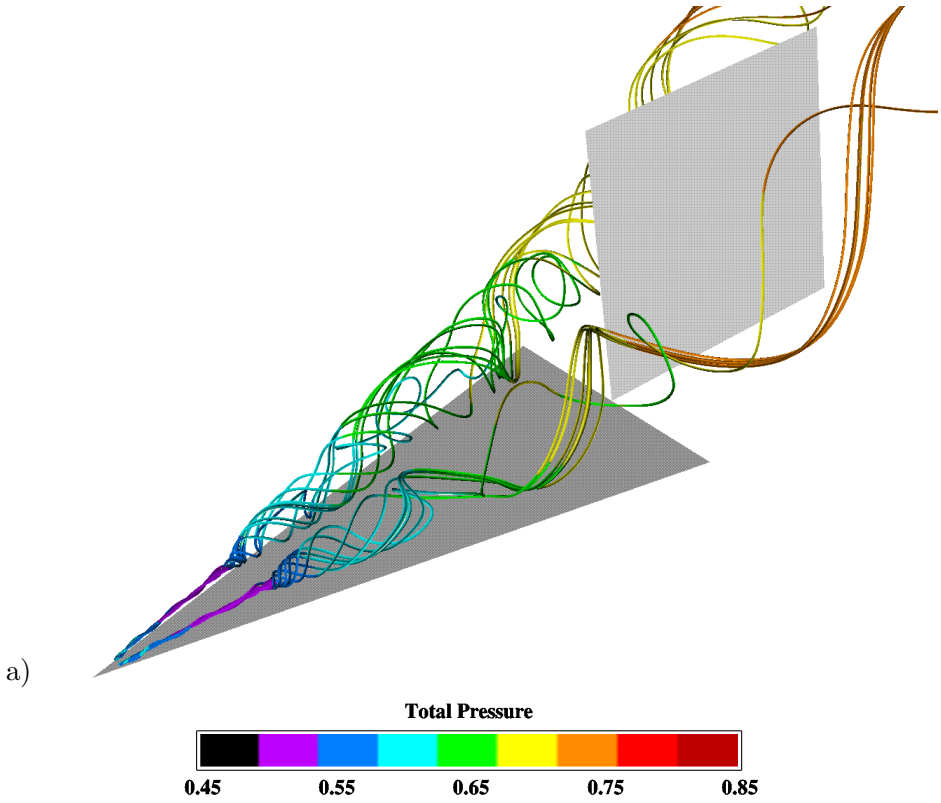

Figure 5.12: a) Three-dimensional view of total pressure colored vortex core streamlines. b) Three-dimensional view of $j = 13$ plane colored with total pressure slicing through vortex core streamlines. Initial Condition Flow Field: $Re = 10^4$, $M = 0.4$, $\alpha = 38^o$.

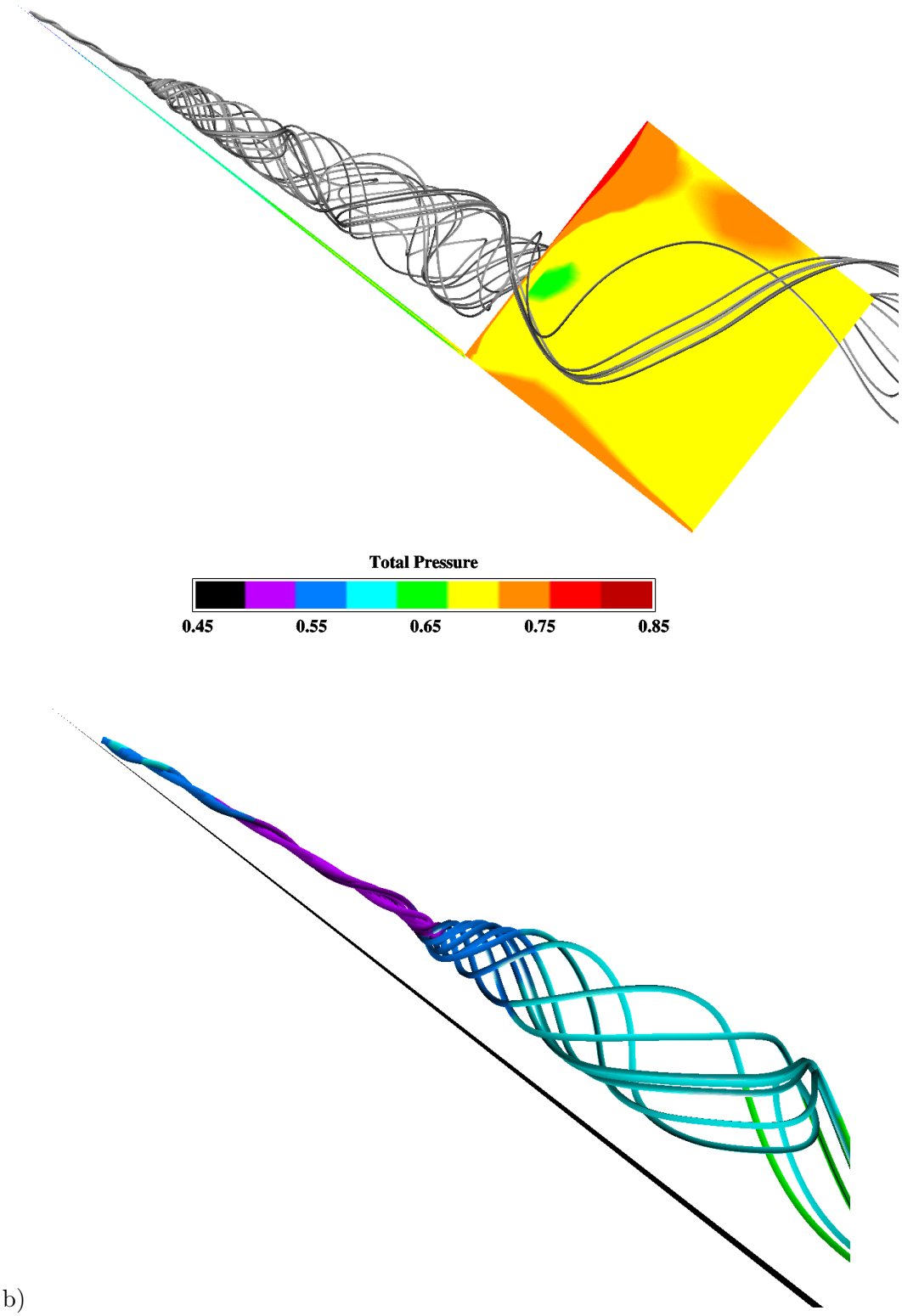

a)

b)

Figure 5.13: a) Side view at incidence showing surface pressure and vortex core streamlines. b) close-up side view, $x = [0, 0.4]$, showing total pressure colored vortex core streamlines. Initial Condition Flow Field: $Re = 10^4$, $M = 0.4$, $\alpha = 38^o$.

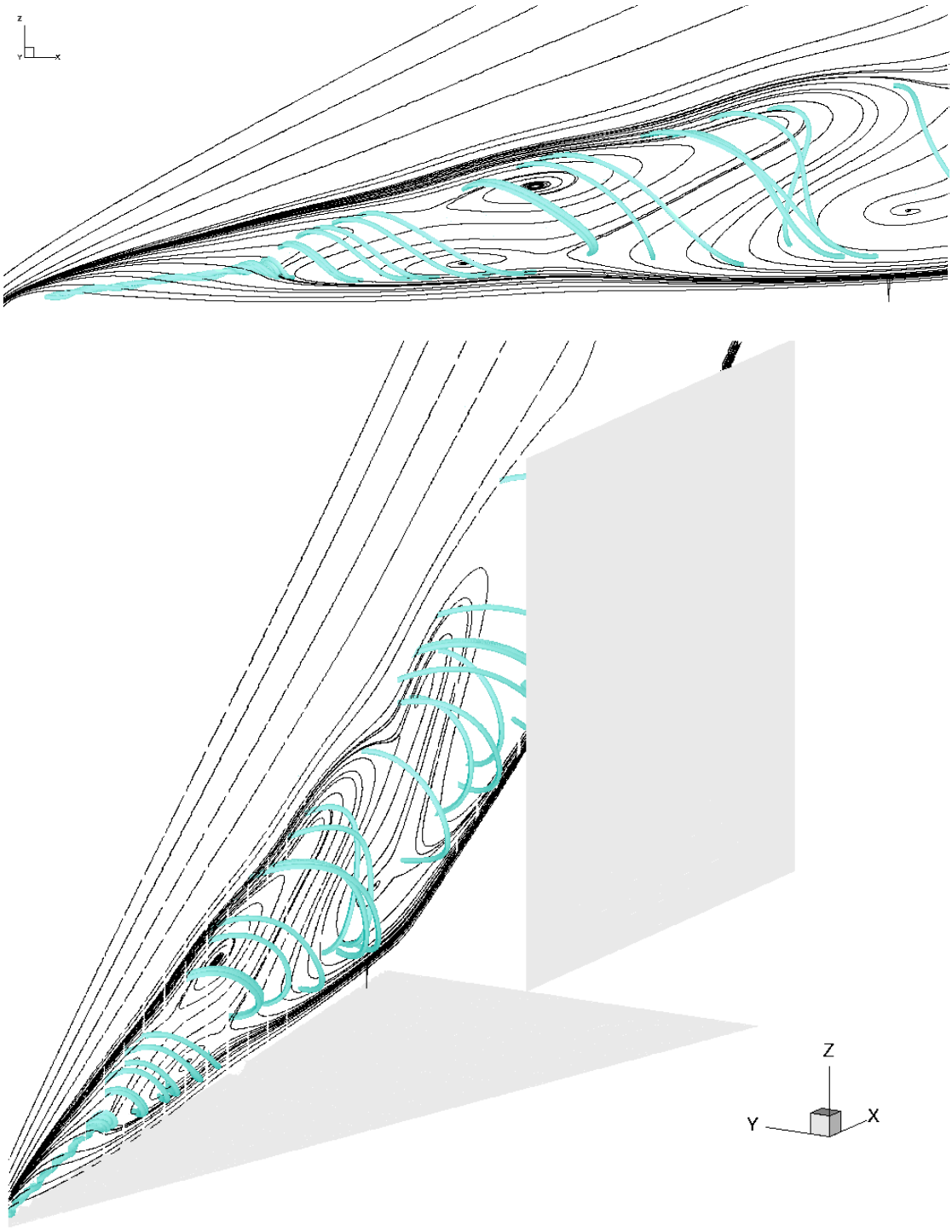

Figure 5.14: Side and three-dimensional views of in-plane streamlines plotted on an opaque vertical plane ($\Lambda_p = 82^o$) slicing through three-dimensional vortex core streamlines. Initial Condition Flow Field: $Re = 10^4$, $M = 0.4$, $\alpha = 38^o$.

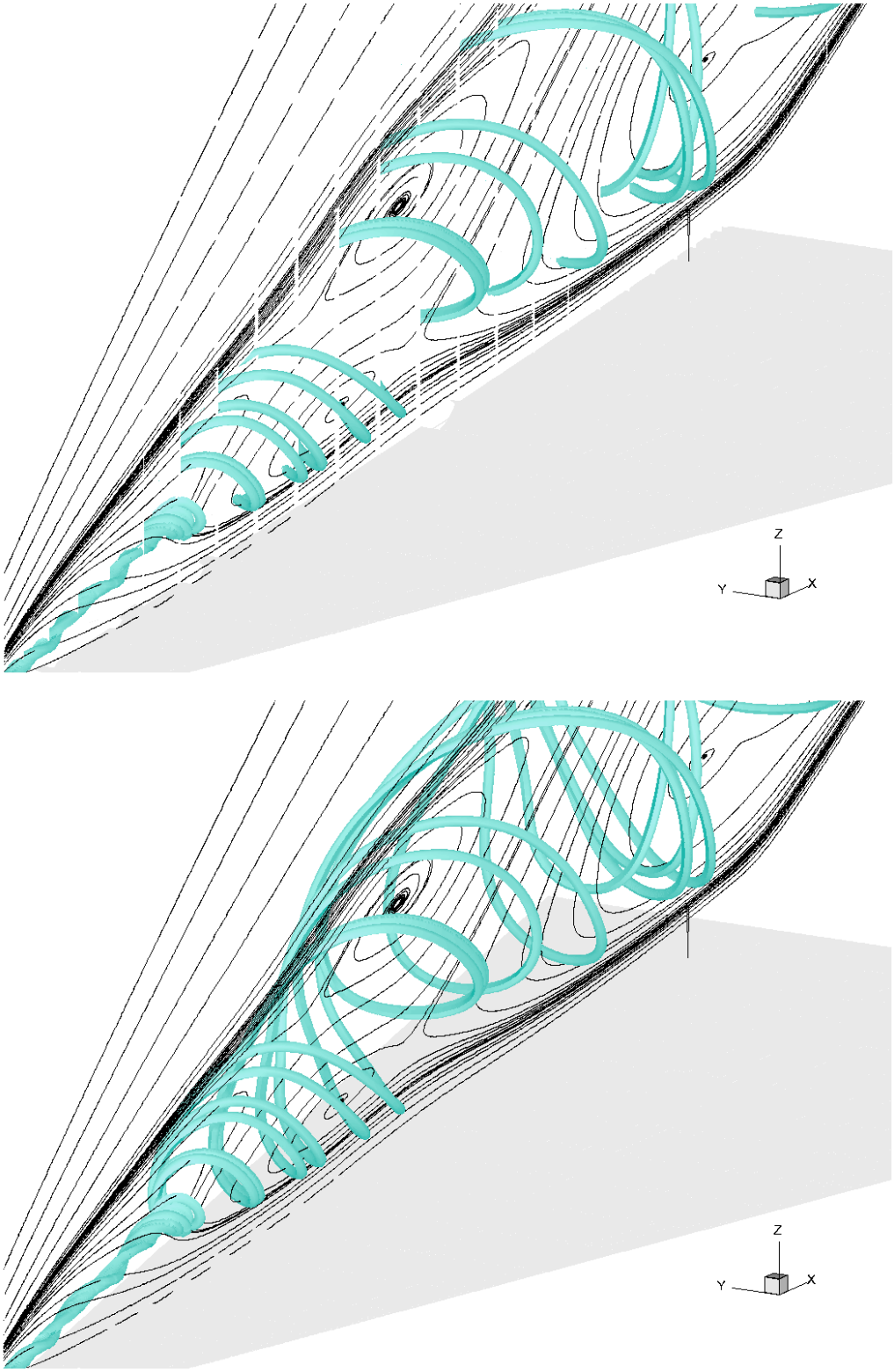

Figure 5.15: Close-up views of in-plane streamlines plotted on opaque and transparent vertical planes ($\Lambda_p = 82^o$) slicing through the three-dimensional vortex core streamlines. Initial Condition Flow Field: $Re = 10^4$, $M = 0.4$, $\alpha = 38^o$.

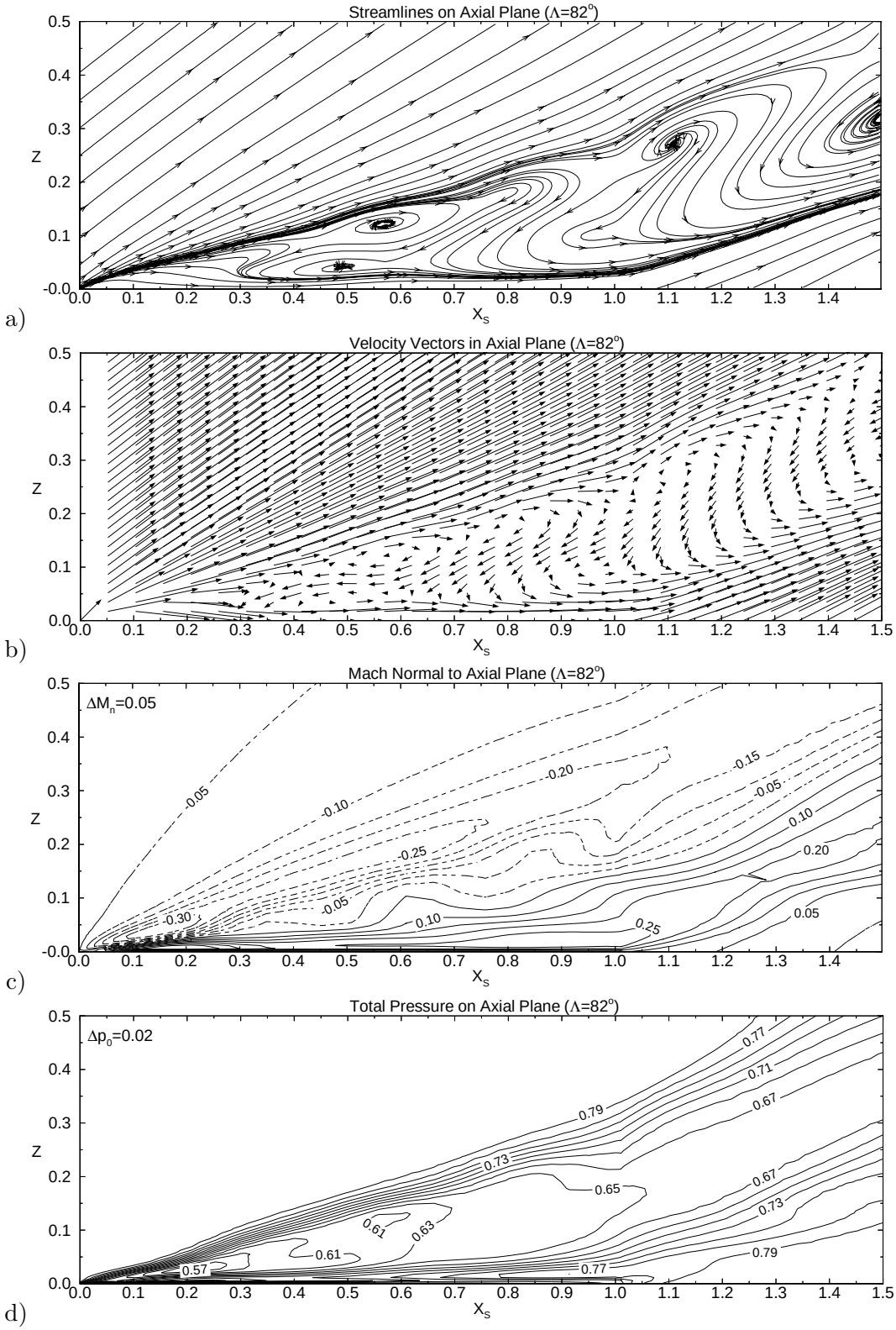

Figure 5.16: a) Streamlines, b) velocity vectors, c) normal Mach contours and d) total pressure contours plotted on a vertical plane which bisects the vortex core. Initial Condition Flow Field: $Re = 10^4$, $M = 0.4$, $\alpha = 38^o$.

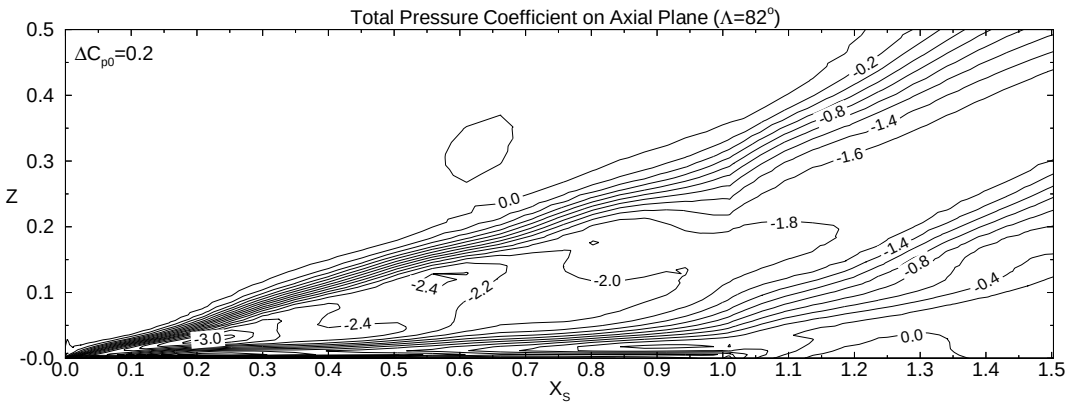

Figure 5.17: Contours of total pressure coefficient plotted on a vertical plane which bisects the vortex core. Initial Condition Flow Field: $Re = 10^4$, $M = 0.4$, $\alpha = 38^o$.

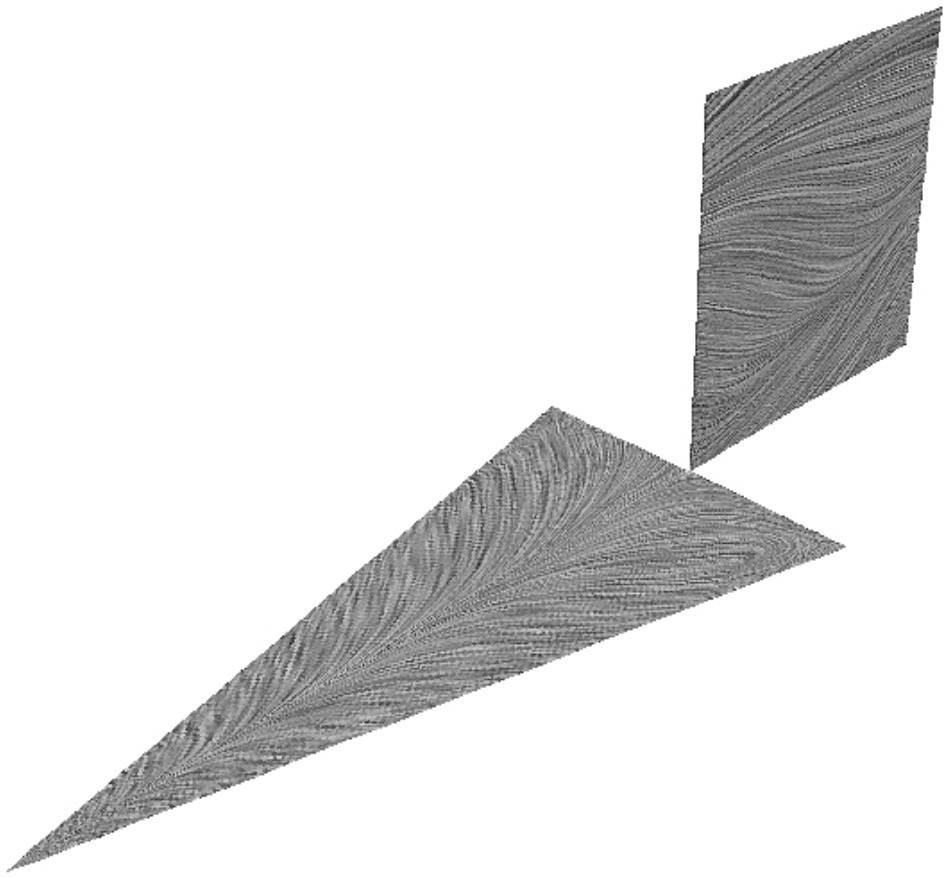

Figure 5.18: Computational surface oil flow plotted using the Line Integral Convolution algorithm of Cabral and Leedom [9]. Initial Condition Flow Field: $Re = 10^4$, $M = 0.4$, $\alpha = 38^o$.

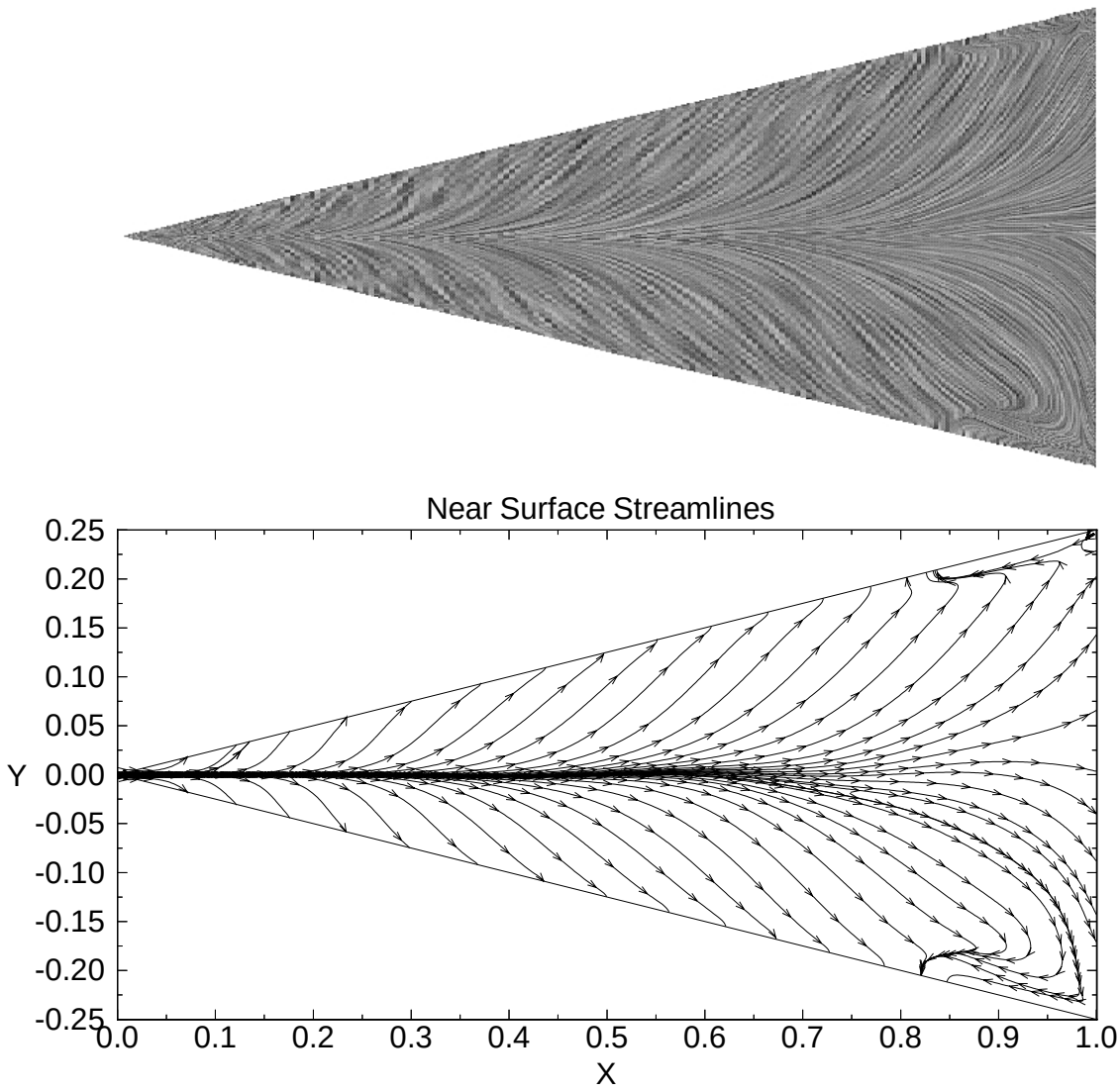

Figure 5.19: Comparison of computational wing surface oil flow with streamlines restricted to the $k = 2$ plane. Initial Condition Flow Field: $Re = 10^4$, $M = 0.4$, $\alpha = 38^o$.

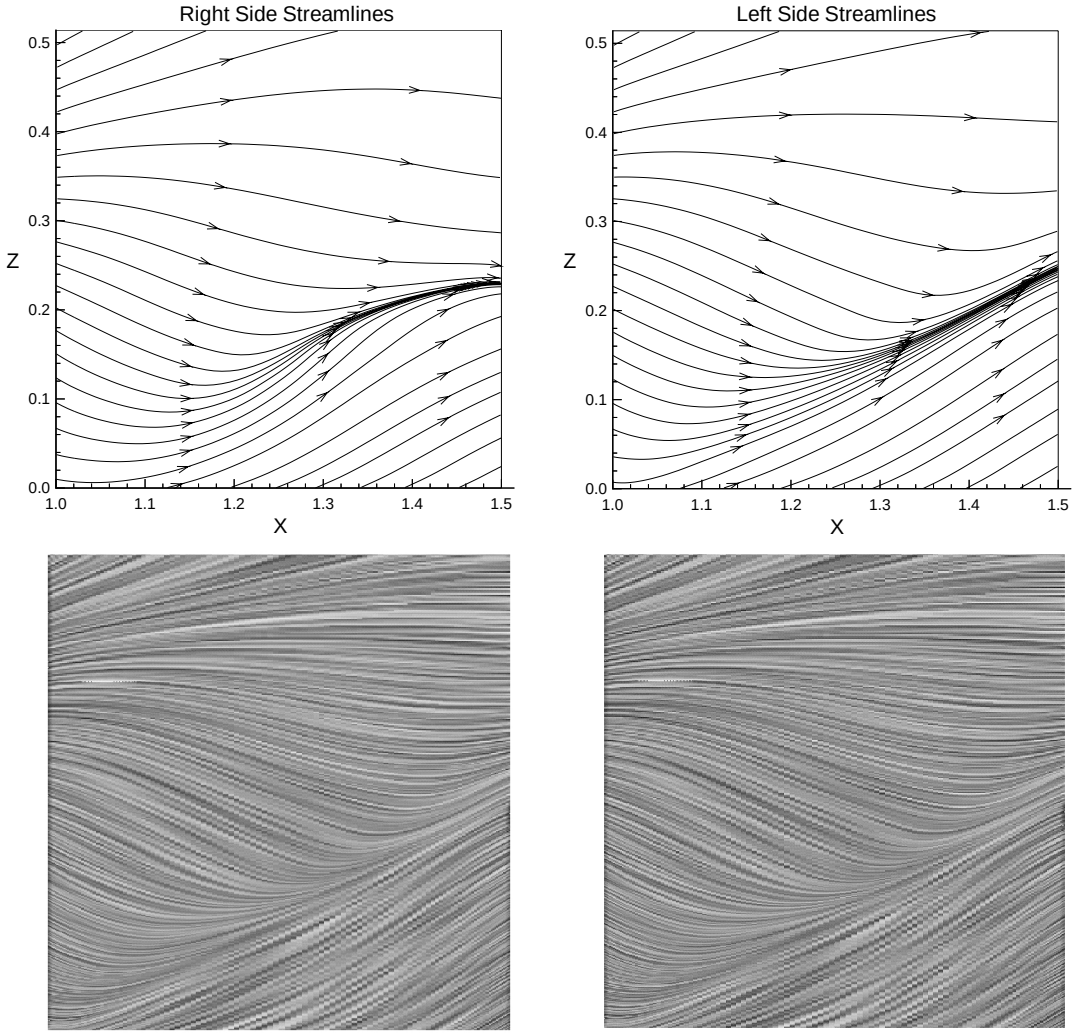

Figure 5.20: Comparison of computational tail surface oil flows with streamlines restricted to the $j = 2$ plane for the right side and $j = jdim - 1$ for the left side. Initial Condition Flow Field: $Re = 10^4$, $M = 0.4$, $\alpha = 38^o$.

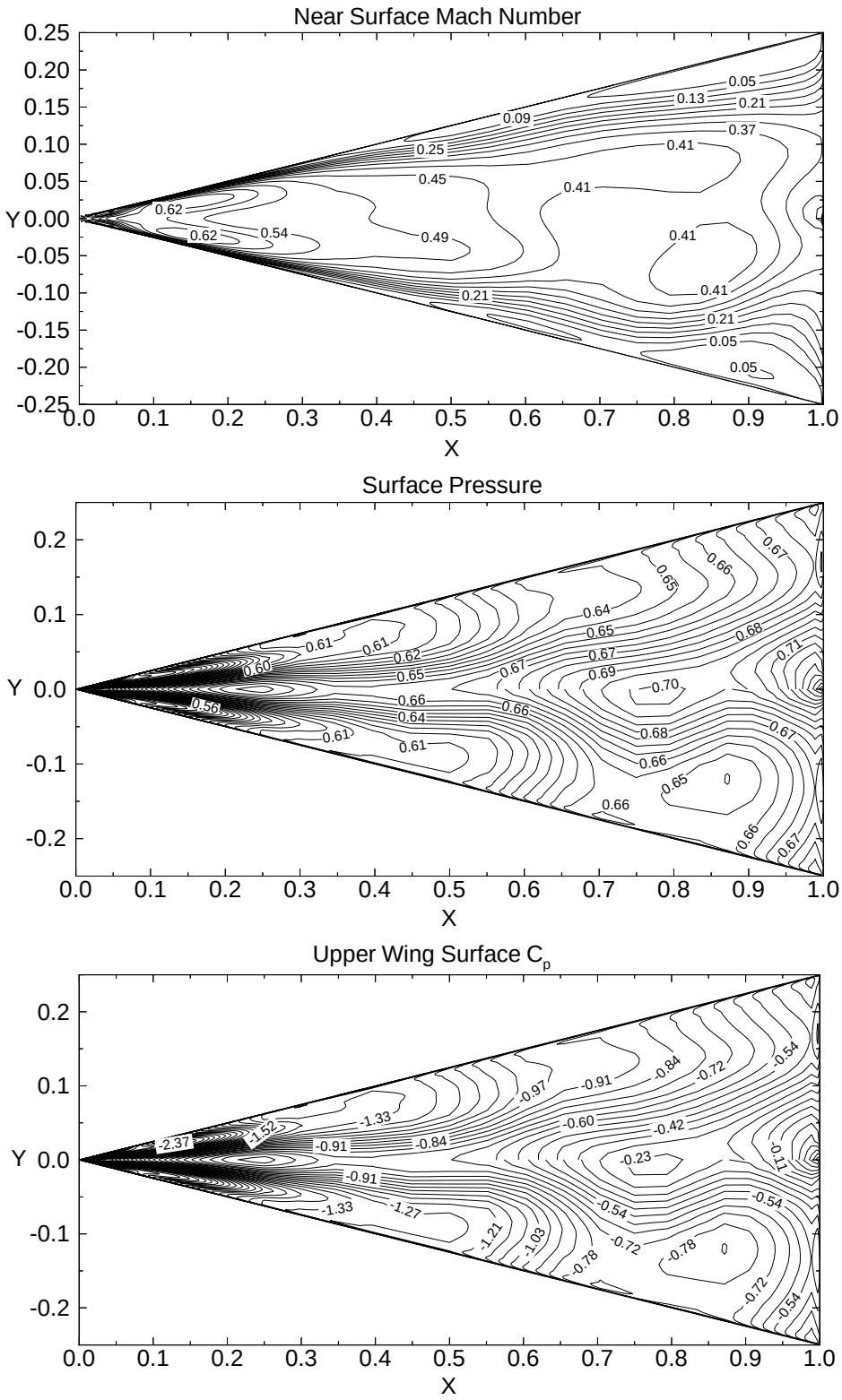

Figure 5.21: Mach number on the $k = 2$ plane above wing, surface pressure and pressure coefficient on wing surface. Initial Condition Flow Field: $Re = 10^4$, $M = 0.4$, $\alpha = 38^o$.

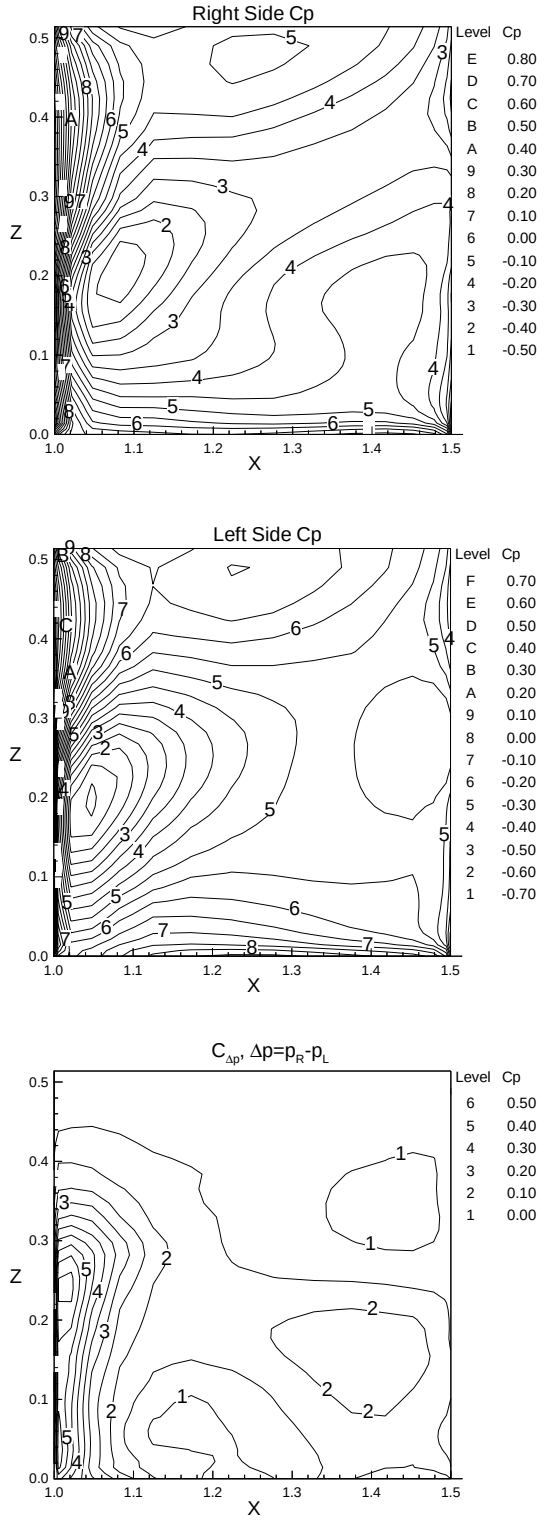

Figure 5.22: Coefficient of pressure on right and left sides of tail, and differential pressure coefficient. Initial Condition Flow Field: $Re = 10^4$, $M = 0.4$, $\alpha = 38^o$.

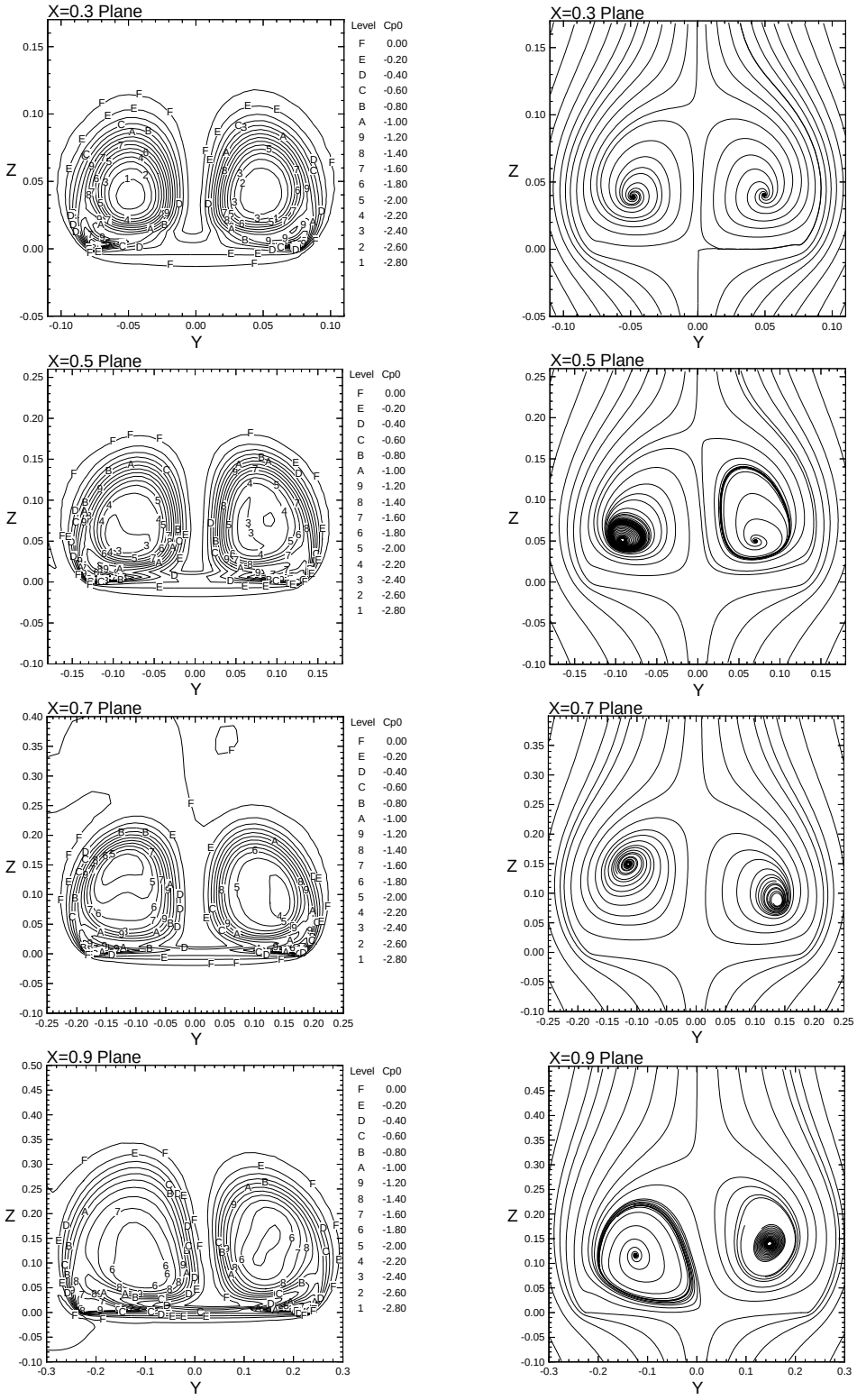

Figure 5.23: Total pressure coefficient and streamlines plotted on vertical crossflow planes above wing. Initial Condition Flow Field: $Re = 10^4$, $M = 0.4$, $\alpha = 38^o$.

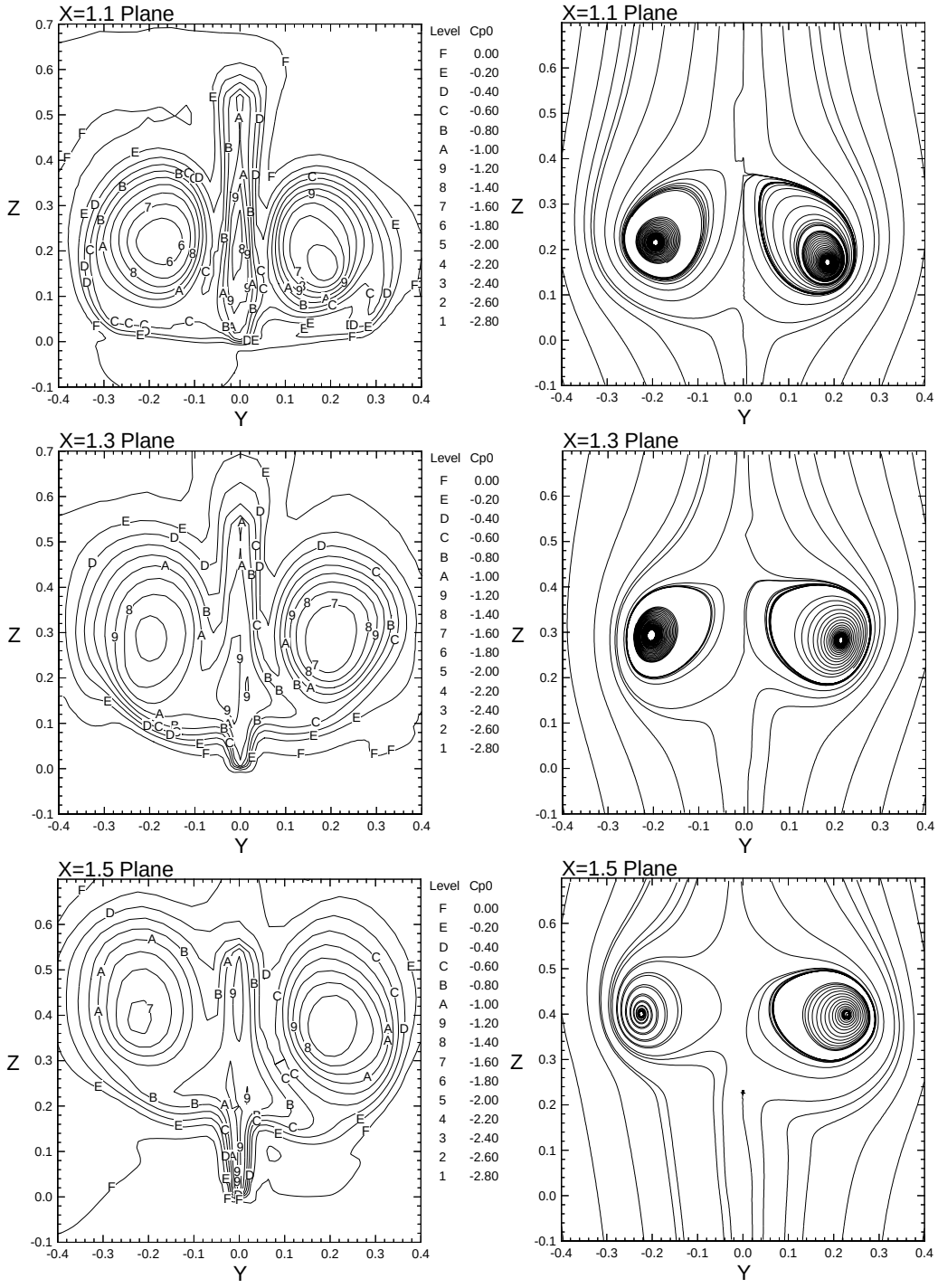

Figure 5.24: Total pressure coefficient and streamlines plotted on vertical crossflow planes near the tail. Initial Condition Flow Field: $Re = 10^4$, $M = 0.4$, $\alpha = 38^o$.

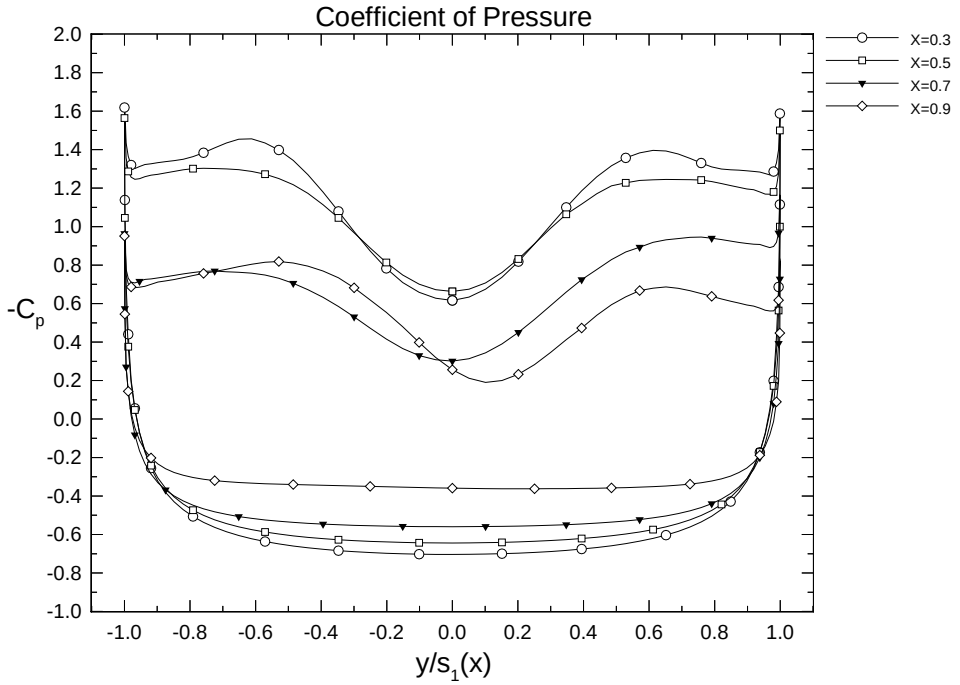

Figure 5.25: Coefficient of pressure on upper and lower wing surfaces at chord stations corresponding to plotted crossflow planes. Initial Condition Flow Field: $Re = 10^4$, $M = 0.4$, $\alpha = 38^o$.

5.3.2 Uncoupled Bending and Torsion Response

In this section, the buffeting response due to uncoupled ($x_\theta = 0$) bending and torsional vibrations is considered. This case is the most basic of this study due to the simple tail geometry, low Reynolds number and the uncoupling of the bending and torsional vibration modes. The purpose of this case is to provide a baseline for studies of the effects of increased Reynolds number and inertial coupling on single tail buffet. This and the other single tail buffeting cases in this chapter will also be compared the twin tail buffeting cases in the following chapters.

As previously discussed in Section 5.2.1, to improve the efficiency of the computations the fine grid used to develop the initial flow state was coarsened by deleting every other *j-plane* and *k-plane*. This reduced the total number of cells by 74%. The coarsened grid is shown in Figures 5.6-5.10. Comparison of C_p plots for the initial flow state generated from the fine grid, see Figure 5.25, with the solution obtained from the coarse grid, Figure 5.26, shows that generally, the coarse grid produces vortices of similar size and strength to the fine grid. Note that the latter C_p plot is also influenced by the response of the tail so only a general comparison can be made.

Three-dimensional and top views of nondimensional surface pressure and vortex core streamlines at $\tau = \frac{tU_\infty}{\bar{\bar{c}}} = 5.28$ are shown in Figure 5.27. The time of $\tau = 5.28$ corresponds to the end of the coupled case in the next section. This buffeting case runs to $\tau = 13.2$. Note that throughout this study nondimensional time is expressed in the more physically meaningful form of $\frac{tU_\infty}{\bar{\bar{c}}}$ rather than the standard CFD form of $\frac{ta_\infty}{c}$. Flooded contours of total pressure show the gradual decrease of suction as the vortex moves over the wing. As previously discussed in Section 5.3.1, the pressure spike on the wing surface at the symmetry plane is only a plotting artifact. Inspection of the core streamlines show

that the coarser grid produces a more gradual vortex breakdown than the fine grid, this makes finding the precise location of the spiral saddle critical point more difficult. Thus, the Topology module of the Flow Analysis Software Toolkit (FAST) was used to solve for the precise locations of all spiral saddle critical points and are marked with 3-D crosses. Only the first critical point in each vortex is significant since it denotes the location of breakdown. From the top view of Figure 5.27 a significant asymmetry can be seen, with the right and left breakdowns occurring at 36%c and 26%c, respectively. Recall that the initial condition was much more symmetric with both breakdowns occurring very near 30%c. Also from the top view, the deflection of the tail surface can clearly be seen. This is the most significant source of flow asymmetry. On the left side of the tail, streamlines can be seen to be stopping at the surface of the tail. This is due to two reasons: The first is the fact that the tail is moving so the no-slip condition of zero surface velocity has become a relative velocity of zero, hence the absolute velocity the stream tracer sees is nonzero at the tail surface. The second reason the streamlines do not pass through the tail in this figure is that FAST does not trace through grid boundaries on non-i-blanked grids. If particle traces were used instead of streamlines, no special treatment of the moving tail would be required. The configuration at angle-of-attack is shown in Figure 5.28. In this side view, the relative position of the critical points can be seen as well as the position of the vortex as it passes by the tail. In Figure 5.29, the computational surface oil flow for the whole configuration is shown. Since for this flow regime (and grid) the LIC oil flow does not provide any greater insight over near-surface streamlines, the latter method will be emphasized in the remaining cases of this chapter. Plots of near-surface streamlines for the tail and wing surfaces are shown in Figure 5.30. The tail streamlines exhibit a separation line at the bottom of the vortex, but unlike the

initial condition flow state, possess a greater asymmetry. The wing surface streamlines are mostly symmetric with no signs of secondary separation. The region of circulation previously observed near the leading edge at $x = 0.9$ is now much weaker than in the fine grid initial condition solution. This is most likely a result of the grid coarsening.

The tail loading distribution for the same instant of time as the previous plots is shown in Figure 5.31. Coefficient of pressure contours are plotted on each side along with the differential pressure coefficient. For each plot, pressure contours are drawn in increments of $\Delta C_p = 0.05$. From the plots, it can be seen that the greatest gradients in pressure no longer occur at the leading edge, but are now more evenly spread out over the forward half of the tail. The range of the net pressure on the deflected tail is also observed to be about three times as large as in the initial condition flow field and is dominated by the low pressure on the left side of the tail. From Figure 5.27, the greater pressure differential is undoubtedly caused by the torsional deflection of the tail into the passing vortex, which is one of the reasons the tail buffeting problem is best solved in a multi-disciplinary fashion.

Wing crossflow planes at the same chord stations as the spanwise C_p plots are shown in Figure 5.32. Contours of total pressure coefficient reveal that the vortex strength captured by the coarse grid is indeed the same as that of the fine grid. Of particular note is the $x = 0.30$ chord station where the right vortex core is unburst and tight, while the left core is burst and weaker.

Crossflow planes near the tail are shown in Figure 5.33. The contours of total pressure, reveal the close proximity of the low pressure left vortex core to the tail surface. The streamlines in the crossflow planes around the tail are seen to pass through the tail, this is due to the motion of the tail as was previously discussed. The only difference

being that unlike FAST, Tecplot will trace through a non-i-blanked grid boundary. A key feature of the crossflow plots of total pressure coefficient and streamlines can be seen in the $x = 1.3$ plane. In this plane the right vortex core, which is defined by the center of rotation and is visible as a focus point in the streamline plot, does not coincide with the local minimum of total pressure. The latter is $0.1c$ below the actual core. This is due to the fact that total pressure is not a purely kinematical quantity, thus the correlation with streamlines is not direct. However, total pressure is a very good indicator of vortical flow and is off in this case only because the vortex core has become very diffuse.

In Figures 5.34-5.40, the buffet loading and response is presented in detail. To get a general idea of the primary vibration modes and loading distributions, the displacements and forces per unit length are plotted against z at regular time intervals in Figures 5.34 and 5.35. These plots indicate that the bending and torsion responses both occur primarily in the first modes. Force and moment distributions at regular time intervals give a qualitative picture of the magnitude and variations of the tail loadings. For a quantitative portrait of the tail loading, mean and RMS distributions are appropriate, see Figure 5.36. Note that the force and moment loadings per unit length are expressed in the standard coefficient form as follows;

$$C_N = \frac{N}{\frac{1}{2}\rho_\infty V_\infty^2 \overline{\overline{c}}} \tag{5.6}$$

$$C_M = \frac{M}{\frac{1}{2}\rho_\infty V_\infty^2 S_t} \tag{5.7}$$

In Figure 5.36, the mean force and moment coefficients show a peak at $z = 0.23$. The RMS moment distribution also peaks at $z = 0.23$. The RMS force distribution shows a constant force variation from the root to $z = 0.2$ above which it declines, the one exception to this rule being the data point at the root. This is due to a small area of separation resulting from flow across the root, recall that the tail is suspended in the

wake. The other peaks in the vicinity of $z = 0.23$ are a result of the primary vortices tailing past the tails. The reason the RMS bending force distribution did not exhibit this same peak is due to the deflections of the tail. Note that because the single tail configuration is symmetric geometrically and with respect to the flow, there should not be any long term directional bias in the buffet loading or response. Hence, for single tail cases, the mean loading represents a type of unsteady residual that should tend to zero as time passes. In this case, the mean loads are an order of magnitude lower than the instantaneous loads.

Recall that the study of tail buffeting was necessitated by the fatigue failure of the vertical tails. This failure takes place at or near the root, thus the buffet loading is best characterized by the root bending and root twisting moments. These moments are nondimensionalized as follows;

$$C_{RBM} = \frac{M_{RB}}{\frac{1}{2}\rho_\infty V_\infty^2 S_t \bar{\bar{c}}} \tag{5.8}$$

$$C_{RTM} = \frac{M_{RT}}{\frac{1}{2}\rho_\infty V_\infty^2 S_t \bar{\bar{c}}} \tag{5.9}$$

Time and frequency domain data are plotted in Figures 5.37 and 5.38 respectively. The time domain data are converted to the frequency domain using Fast Fourier Transform (FFT) techniques. Since CFD stability requirements dictate a very small time step, only every fifth data point is sampled, giving a total of 4000 points. To improve statistical confidence, the sample is subdivided into 7 blocks of 1000 samples each with 50% overlap. To reduce bandwidth leakage, a Hanning window is applied to each block which is then zero padded to a length of 2048 (2^{11}) samples. The time averaged power spectral density (PSD) is obtained by calculating the PSD of each block and averaging them together. The MATLAB signal processing tool box is used to perform the calculations. The mean

and RMS root moment values, maximum amplitudes (A) and dominant frequencies (n_d) are summarized for this case in Table 5.3.

In the same way that the buffet loads are best characterized by integrating along the length of the tail to yield root values, the buffeting response is most clearly shown by looking at the tip displacements and accelerations. Accelerations are important because they are the primary source of structural fatigue as opposed to maximum deflections. Time and frequency domain data are plotted in Figures 5.39 and 5.40, respectively. The time domain data are converted to the frequency domain using the same parameters that were used for the load data. Unlike the loading, the dominate frequencies of the tip bending and rotation accelerations do match each other. The maximum amplitudes of the tip displacements, accelerations and the first two dominant frequencies are summarized in Table 5.4.

Root Loads									
C_{RBM}					C_{RTM}				
Mean	RMS	A	n_{d1}	n_{d2}	Mean	RMS	A	n_{d1}	n_{d2}
0.015	0.026	0.060	0.75	1.75	0.00095	0.029	0.057	0.45	2.0

Table 5.3: Summary of root bending and twisting moment statistics, maximum amplitudes and dominant frequencies. Uncoupled Bending and Torsion Case: $Re = 10^4$, $M = 0.4$, $\alpha = 38^o$.

Tip Response							
Bending				Torsion			
$A(w)$	$A(w_{\tau\tau})$	n_{d1}	n_{d2}	$A(\theta)^o$	$A(\theta_{\tau\tau})^o$	n_{d1}	n_{d2}
0.082	3.5	0.45	1.75	9.8	420	0.45	1.75

Table 5.4: Summary of tip displacement and acceleration statistics, maximum amplitudes and dominant frequencies. Uncoupled Bending and Torsion Case: $Re = 10^4$, $M = 0.4$, $\alpha = 38^o$.

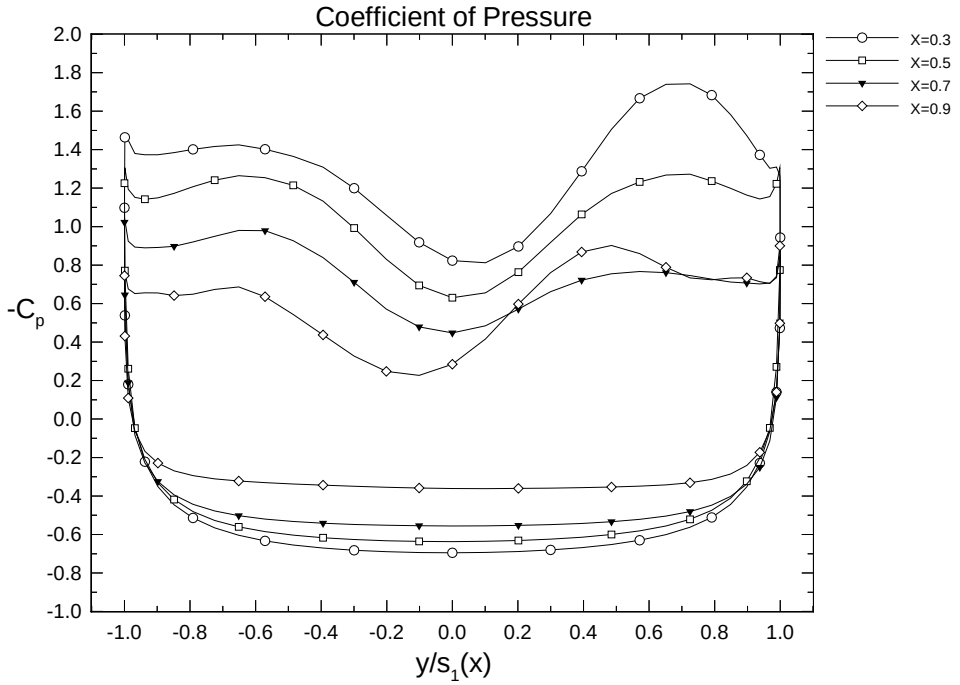

Figure 5.26: Coefficient of pressure on upper and lower wing surfaces at chord stations corresponding to plotted crossflow planes. Uncoupled Bending and Torsion Case: $\tau = 5.28$, $Re = 10^4$, $M = 0.4$, $\alpha = 38^o$.

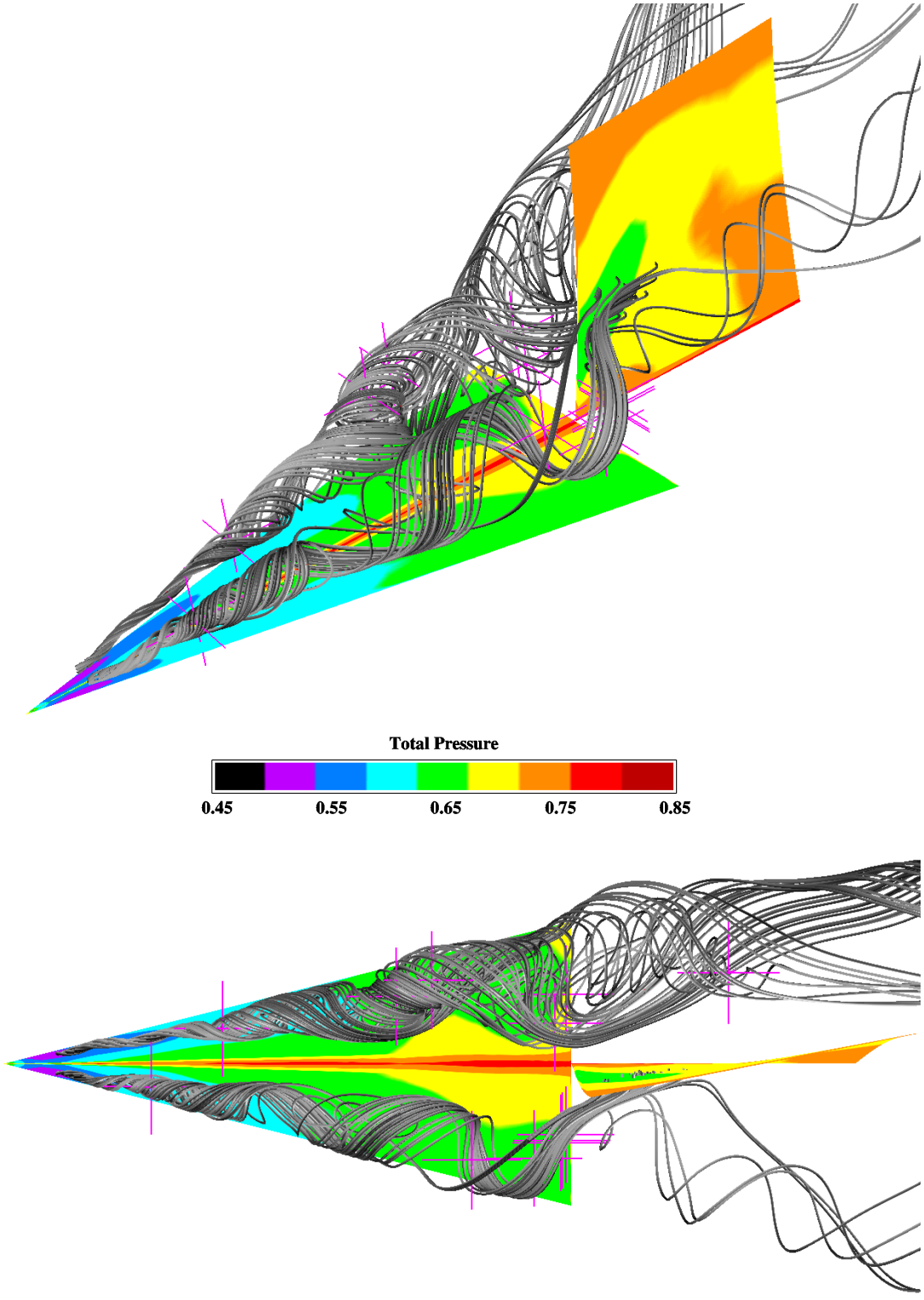

Figure 5.27: Three-dimensional and top views of surface pressure and vortex core streamlines at $\tau = \frac{tU_\infty}{\bar{c}} = 5.28$ and $\Delta\tau = 0.00066$. Purple crosses denote critical points associated with either attracting or repelling spiral saddle points. Uncoupled Bending and Torsion Case: $Re = 10^4$, $M = 0.4$, $\alpha = 38^o$.

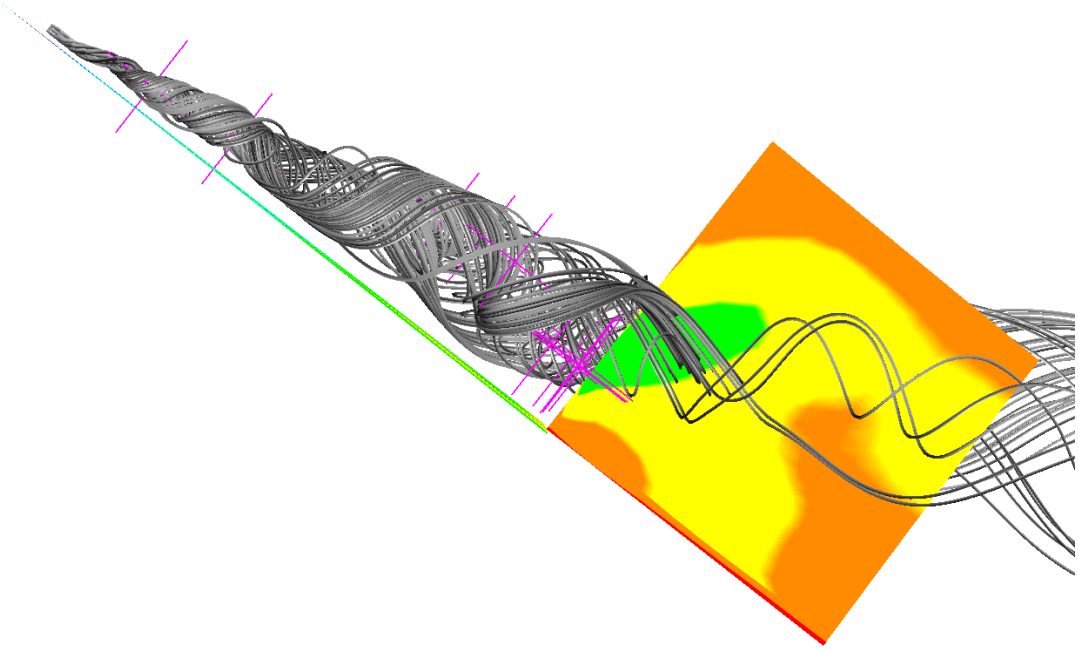

Figure 5.28: Side view at angle-of-attack showing surface pressure, vortex core streamlines, and spiral saddle points at $\tau = 5.28$. Uncoupled Bending and Torsion Case: $Re = 10^4$, $M = 0.4$, $\alpha = 38^o$.

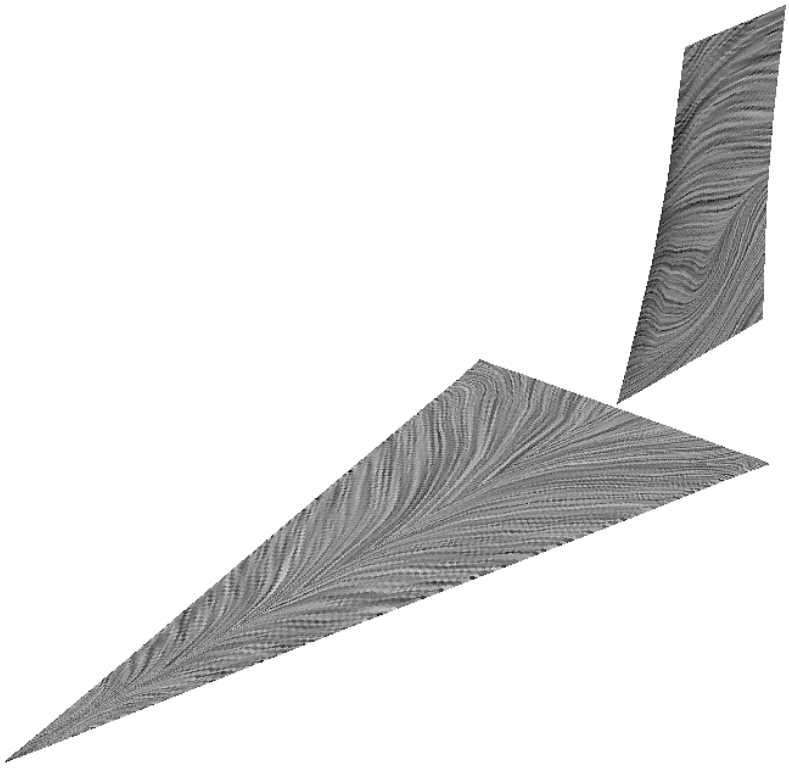

Figure 5.29: Computational surface oil flow at $\tau = 5.28$. Uncoupled Bending and Torsion Case: $Re = 10^4$, $M = 0.4$, $\alpha = 38^o$.

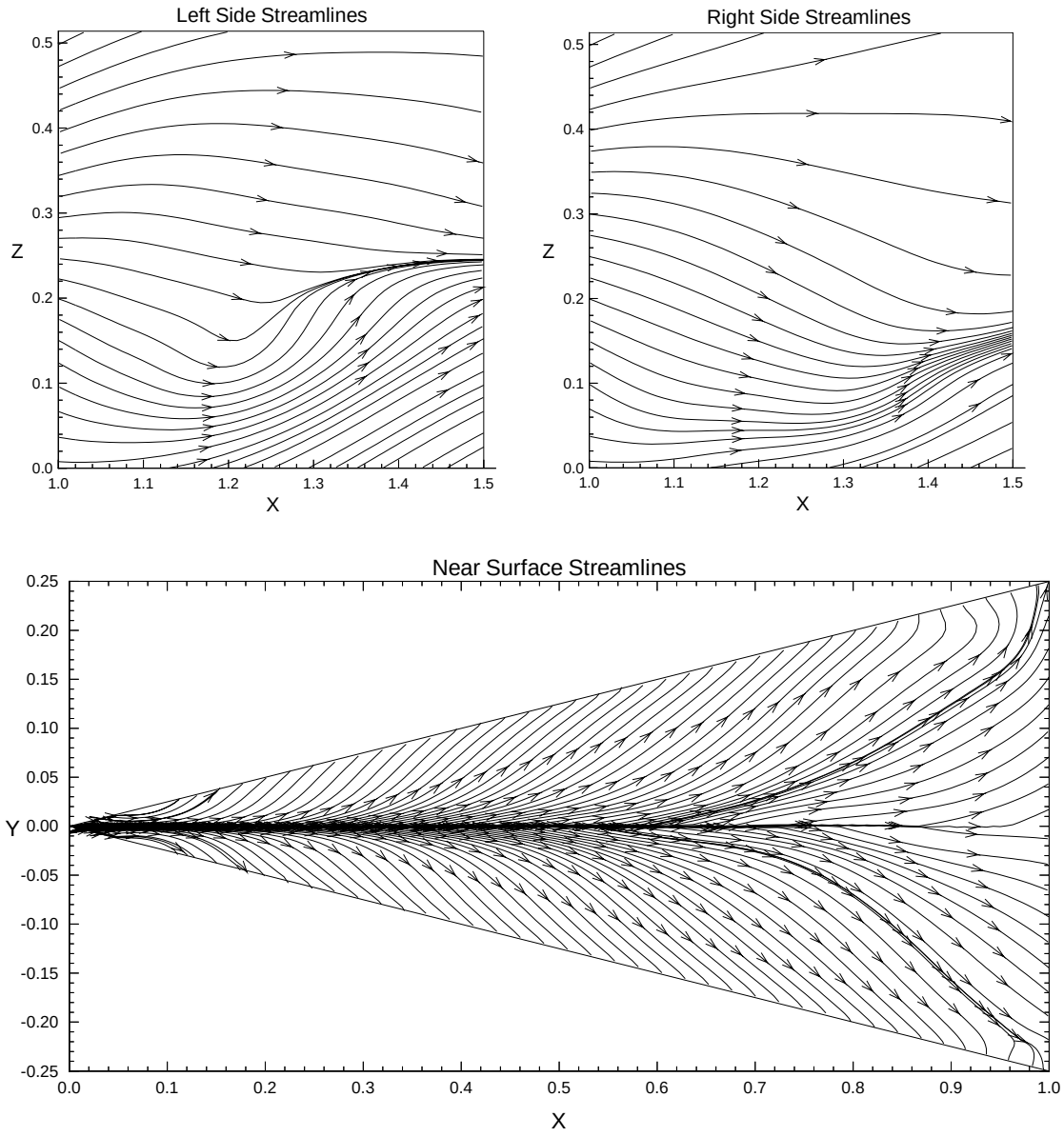

Figure 5.30: Near surface streamlines. Uncoupled Bending and Torsion Case: $\tau = 5.28$, $Re = 10^4$, $M = 0.4$, $\alpha = 38^o$.

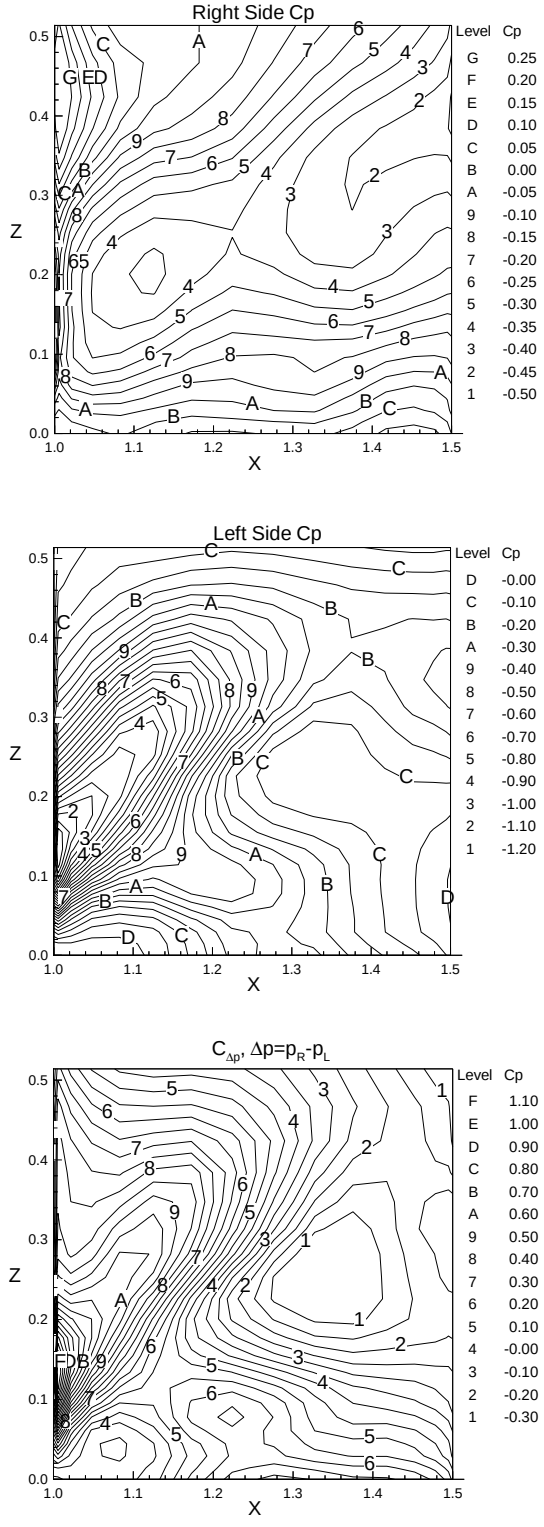

Figure 5.31: Coefficient of pressure on right and left sides of tail, and differential pressure coefficient. Uncoupled Bending and Torsion Case: $\tau = 5.28$, $Re = 10^4$, $M = 0.4$, $\alpha = 38^o$.

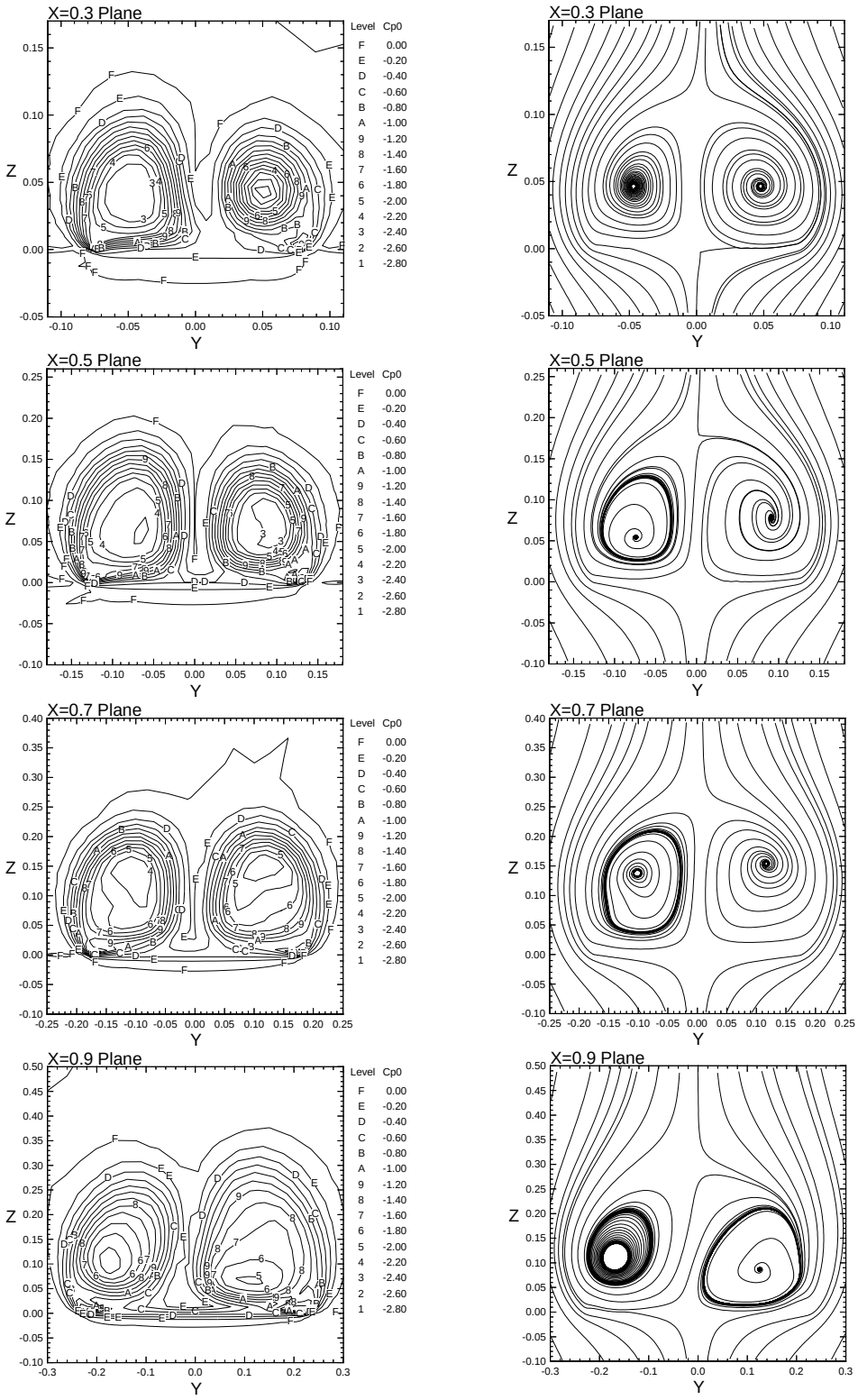

Figure 5.32: Total pressure coefficient and streamlines plotted on vertical crossflow planes above wing. Uncoupled Bending and Torsion Case: $\tau = 5.28$, $Re = 10^4$, $M = 0.4$, $\alpha = 38^o$.

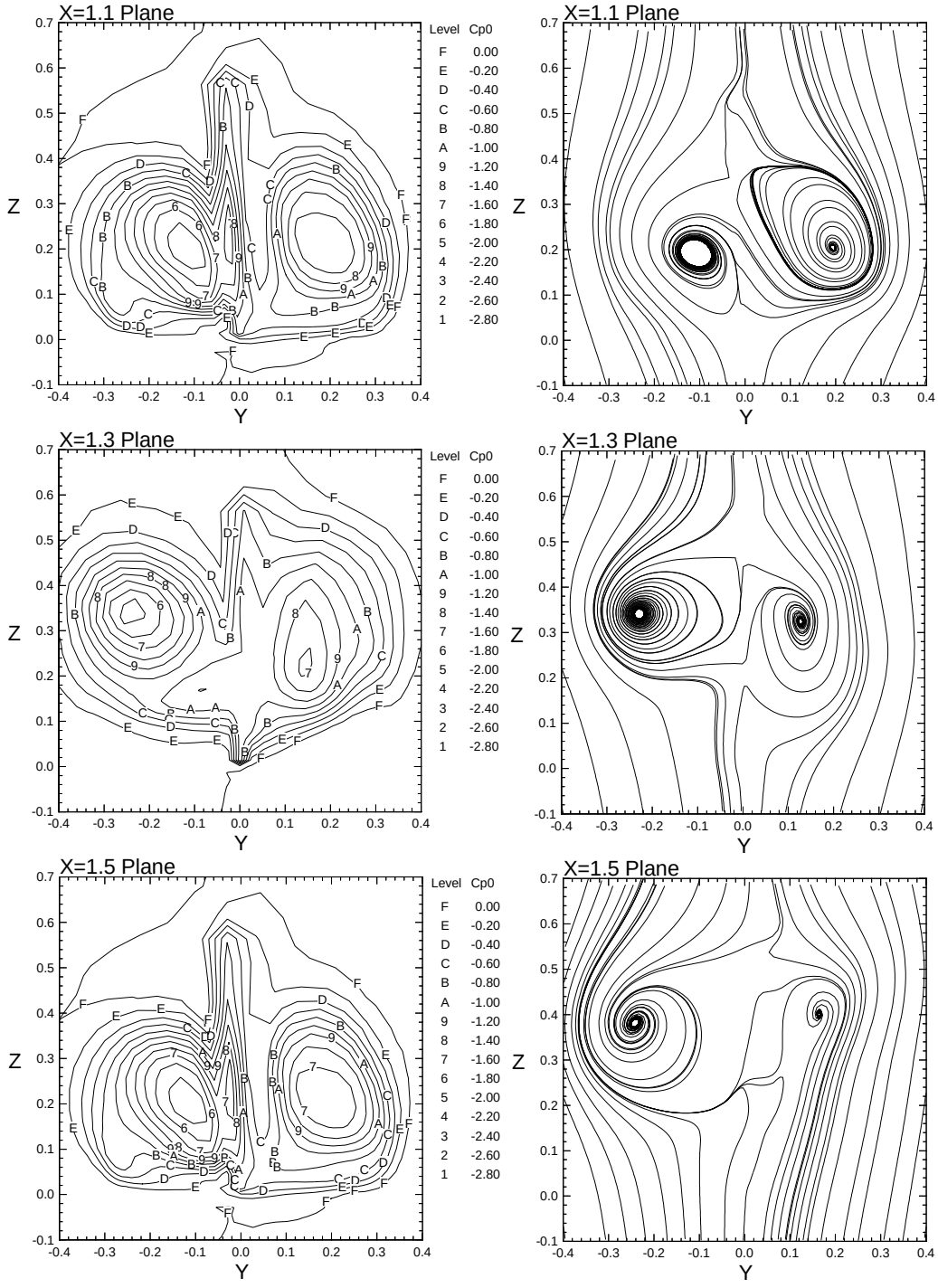

Figure 5.33: Total pressure coefficient and streamlines plotted on vertical crossflow planes near the tail. Uncoupled Bending and Torsion Case: $\tau = 5.28$, $Re = 10^4$, $M = 0.4$, $\alpha = 38^o$.

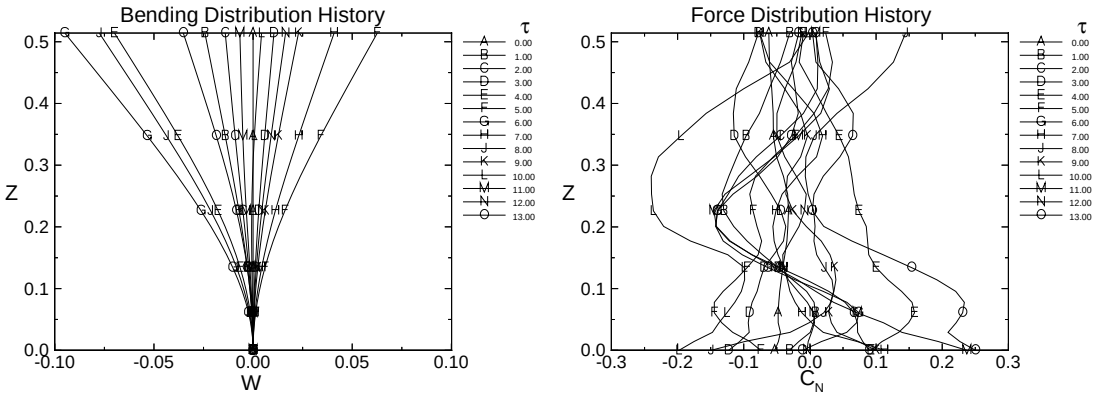

Figure 5.34: Bending deflection and force distributions along the tail span plotted at integer nondimensional time levels. Uncoupled Bending and Torsion Case: $Re = 10^4$, $M = 0.4$, $\alpha = 38^o$.

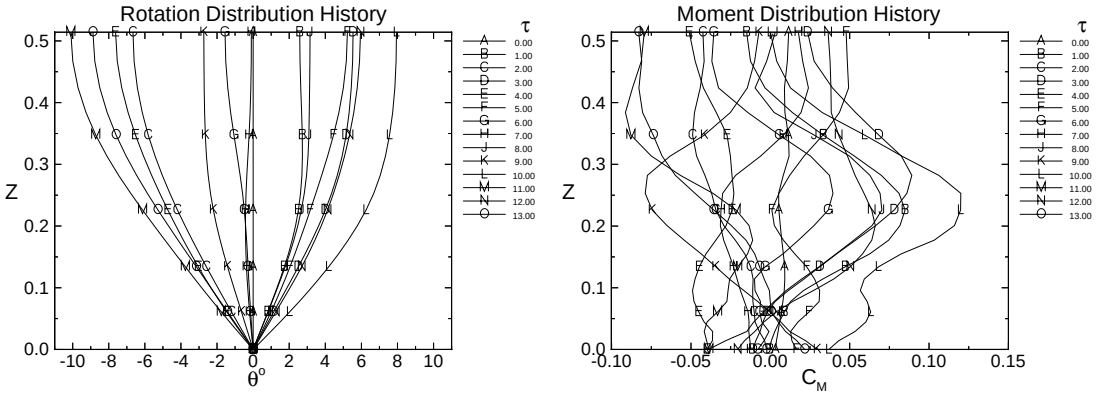

Figure 5.35: Torsion deflection and moment distributions along the tail span plotted at integer nondimensional time levels. Uncoupled Bending and Torsion Case: $Re = 10^4$, $M = 0.4$, $\alpha = 38^o$.

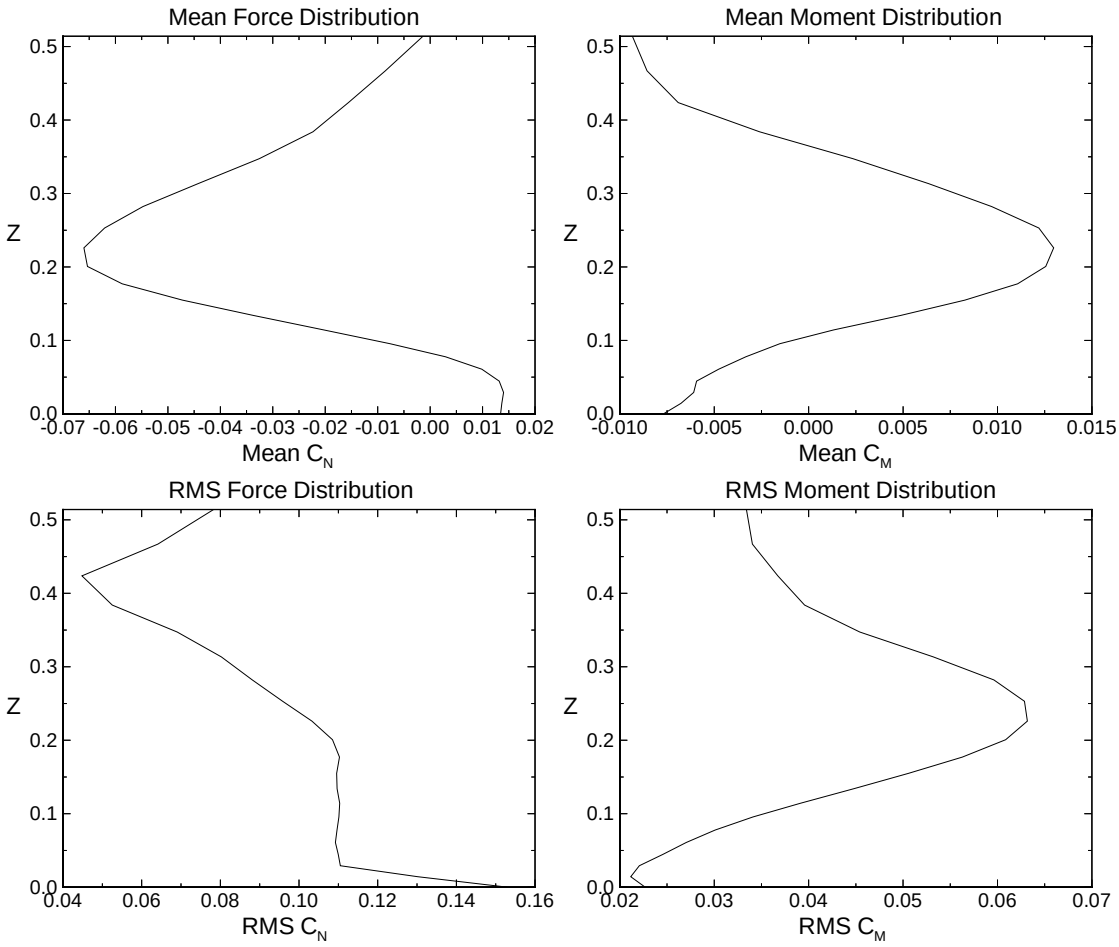

Figure 5.36: Mean and RMS load distributions along the tail span. Uncoupled Bending and Torsion Case: $Re = 10^4$, $M = 0.4$, $\alpha = 38^o$.

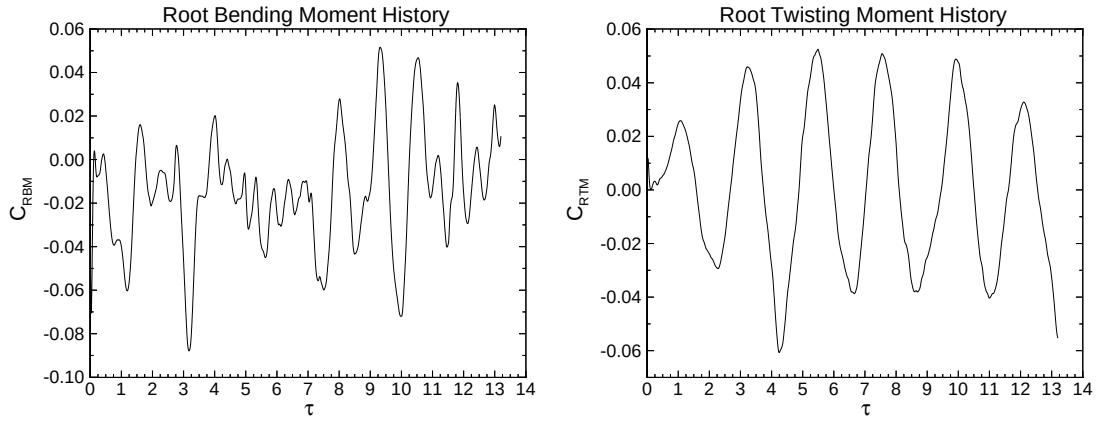

Figure 5.37: History of root bending moment coefficient and root twisting moment coefficient. Uncoupled Bending and Torsion Case: $Re = 10^4$, $M = 0.4$, $\alpha = 38^o$.

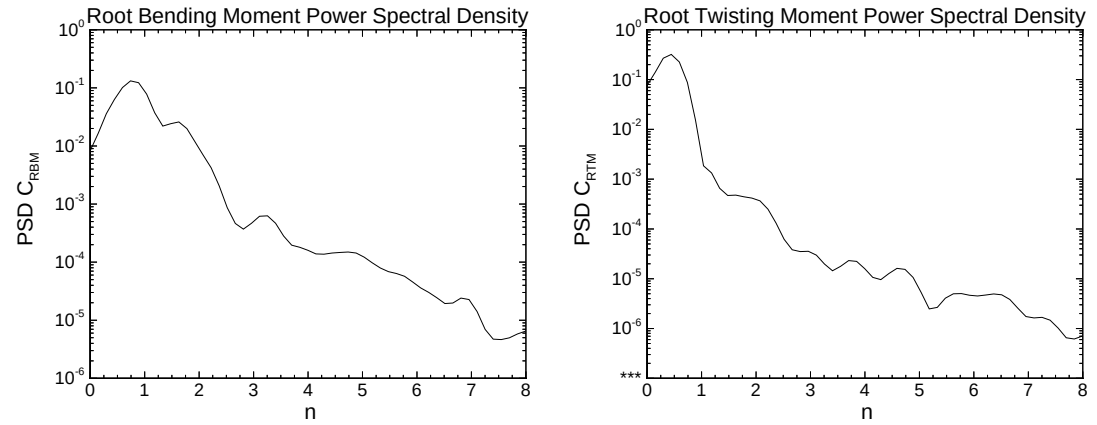

Figure 5.38: Power spectral density of root bending moment coefficient and root twisting moment coefficient versus reduced frequency. Uncoupled Bending and Torsion Case: $Re = 10^4$, $M = 0.4$, $\alpha = 38^o$.

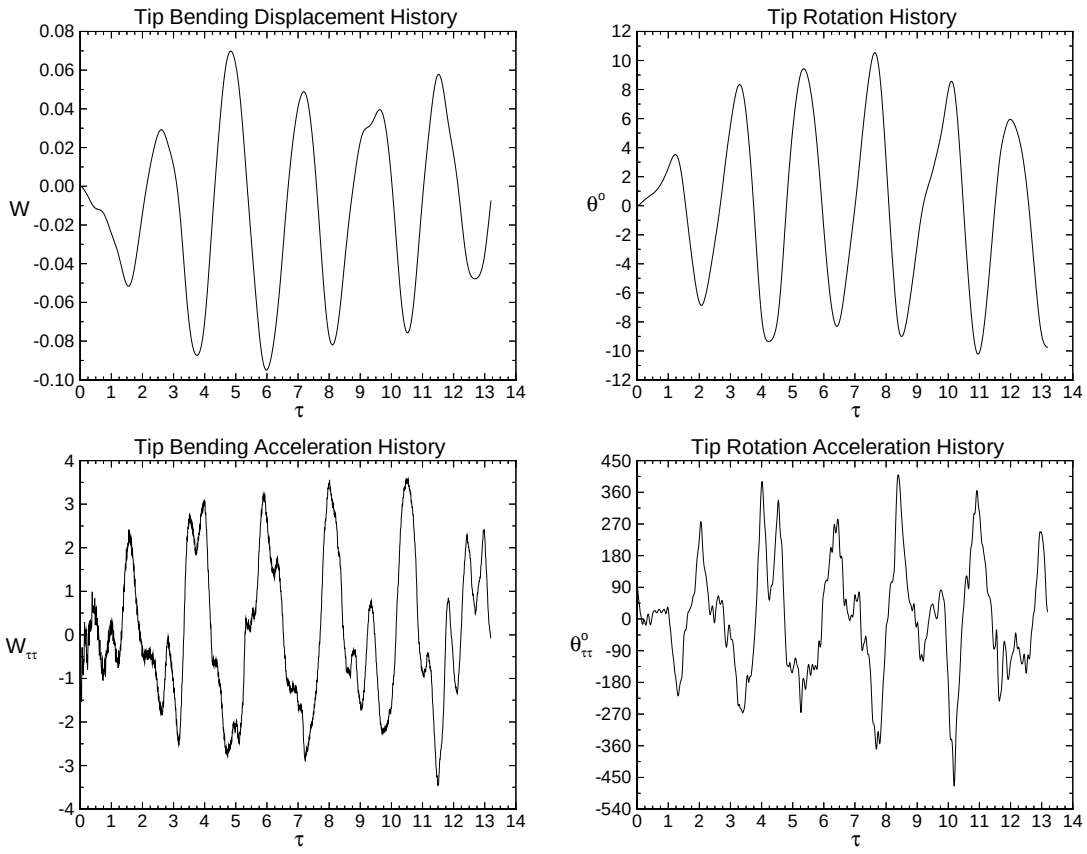

Figure 5.39: History of tip bending and torsion deflections and accelerations. Uncoupled Bending and Torsion Case: $Re = 10^4$, $M = 0.4$, $\alpha = 38^o$.

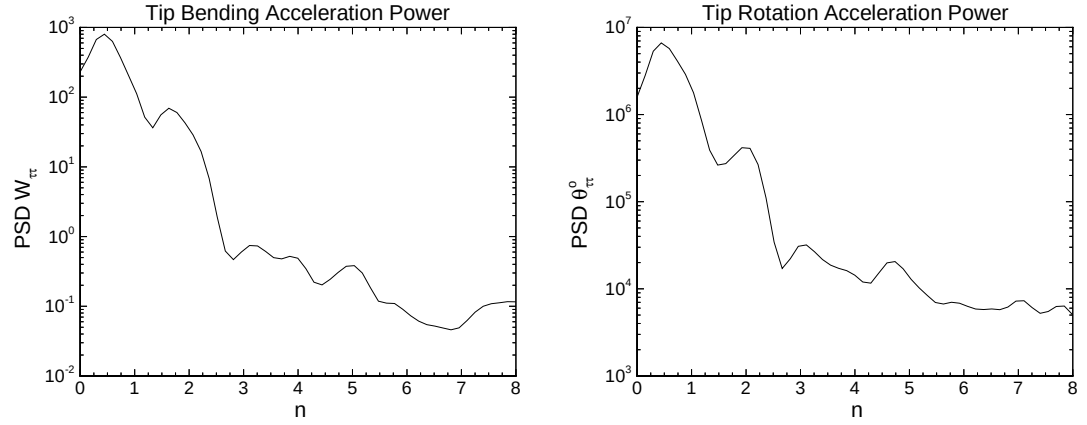

Figure 5.40: Power spectral density of tip bending and torsion accelerations versus reduced frequency. Uncoupled Bending and Torsion Case: $Re = 10^4$, $M = 0.4$, $\alpha = 38^o$.

5.3.3 Coupled Bending and Torsion Response

In this section, the buffeting response due to inertially coupled bending and torsion vibrations is considered. The purpose of this case is to assess the effect of structural coupling on the buffeting response. Note that since the buffeting problem is being solved in a multi-disciplinary fashion, the bending and torsion modes are already coupled by virtue of the aerodynamics. However, the addition of inertial coupling will change the overall coupling between bending and torsional vibrations because of its fundamentally different physical mechanism. For completeness, the full set of figures plotted for the uncoupled case are reproduced in this section for the coupled response. However, since the basic flow field has now been discussed in detail, the buffeting response will now be emphasized.

Figures 5.41- 5.48 depict the flow field at the same time level as in the uncoupled case. The plots of spanwise variation of C_p are the simplest of all the flow field plots presented in this study. However, these plots are packed with information and provide the most succinct and clear depiction of the differences between the present flow field and that of the uncoupled case. Comparing the C_p plots of Figure 5.26 with Figure 5.41 indicates that the two flow fields are very similar to each other but become significantly different by the $x = 0.9$ chord station. This demonstrates the upstream effect that a small difference in tail deflection produces. Examining the 3-D streamline plots in Figure 5.42 shows that the left vortex traces start to differ at the $x = 0.5$ chord location. Note that throughout this study all 3-D streamline plots are created via scripts and therefore have identical seed locations for like grids. From the top view in Figure 5.42, there is no significant difference in the breakdown locations between the two cases.

Contours of the coefficient of differential pressure on the tail surface in Figure 5.46 show 71% greater range of pressure over the tail surface at the instant of

$\tau = 5.28$. Displacement and loading distributions plotted in Figures 5.49 and 5.50 give a more complete picture of the loading. Note that data for the present case only extends to the time level of $\tau = 5.28$ instead of $\tau = 13.2$ as in the uncoupled case. Despite the smaller sample size, the mean and RMS load distributions shown in Figure 5.51 are very similar to the uncoupled case. From the root loading histories in Figure 5.52, the maximum root bending moment coefficient amplitude is 50% higher than that of the uncoupled case. The maximum root twisting moment coefficient amplitude is identical to the value obtained in the uncoupled case. Frequency domain data are obtained using the same method described in the previous section and are plotted in Figure 5.53. From this plot, the dominant reduced frequencies for both bending and twisting moments are $n = 0.5$ with a second peak at $n = 2.0$. Recall that these frequencies are very close to those of the root twisting moment of the uncoupled case. However, in the uncoupled case, the root bending moment peak frequencies did not match those of the root twisting moment. Thus, it appears that coupling the modes together structurally also influences the frequency and magnitude of the aerodynamic loading due to the natural coupling of the deflections with the flow. The mean and RMS root moment values, maximum amplitudes (A) and dominant frequencies (n_d) are summarized in Table 5.5.

Tip displacement and acceleration histories are shown in Figure 5.54. The maximum amplitudes of the bending deflections and accelerations are 50% and 43% higher, respectively, than those of the uncoupled response. Tip torsional displacement and accelerations are 80% and 31% higher, respectively, than the uncoupled response. Power spectral densities of the tip accelerations, shown in Figure 5.55 indicate that the dominant frequencies of the buffeting response match those of the loading, but have greater high-frequency content than the uncoupled case. Thus, it is clear that the initial

coupling of bending and torsional modes, even when small ($x_\theta = 0.05$), has a significant impact on the loading and buffeting response. The maximum amplitudes of the tip displacements, accelerations and the first two dominant frequencies are summarized in Table 5.6.

Root Loads									
C_{RBM}					C_{RTM}				
Mean	RMS	A	n_{d1}	n_{d2}	Mean	RMS	A	n_{d1}	n_{d2}
-0.019	0.042	0.091	0.50	2.00	-0.000042	0.038	0.088	0.50	2.00

Table 5.5: Summary of root bending and twisting moment statistics, maximum amplitudes and dominant frequencies. Coupled Bending and Torsion Case: $Re = 10^4$, $M = 0.4$, $\alpha = 38^o$.

Tip Response							
Bending				Torsion			
$A(w)$	$A(w_{\tau\tau})$	n_{d1}	n_{d2}	$A(\theta)^o$	$A(\theta_{\tau\tau})^o$	n_{d1}	n_{d2}
0.117	5.0	0.50	2.00	17.6	550	0.50	2.00

Table 5.6: Summary of tip displacement and acceleration statistics, maximum amplitudes and dominant frequencies. Coupled Bending and Torsion Case: $Re = 10^4$, $M = 0.4$, $\alpha = 38^o$.

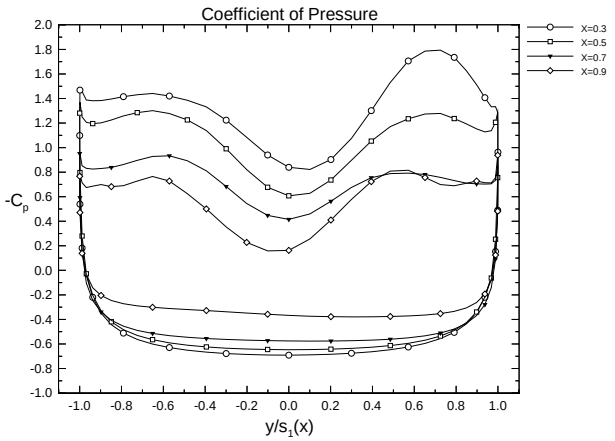

Figure 5.41: Coefficient of pressure on upper and lower wing surfaces at chord stations corresponding to plotted crossflow planes. Coupled Bending and Torsion Case: $\tau = 5.28$, $Re = 10^4$, $M = 0.4$, $\alpha = 38^o$.

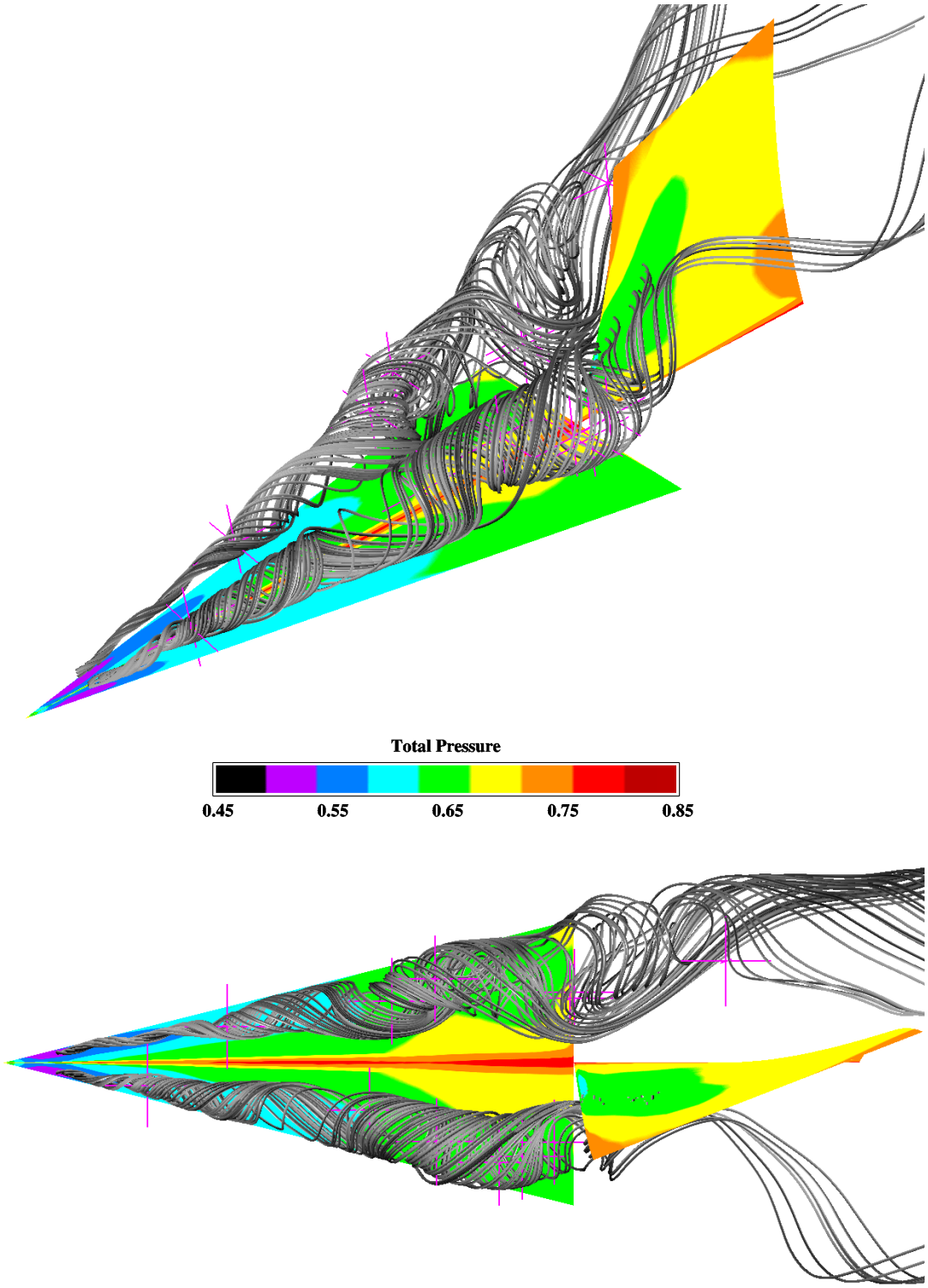

Figure 5.42: Three-dimensional and top views of surface pressure and vortex core streamlines at $\tau = \frac{tU_\infty}{\bar{\bar{c}}} = 5.28$ and $\Delta\tau = 0.00066$. Purple crosses denote critical points associated with either attracting or repelling spiral saddle points. Coupled Bending and Torsion Case: $Re = 10^4$, $M = 0.4$, $\alpha = 38^o$.

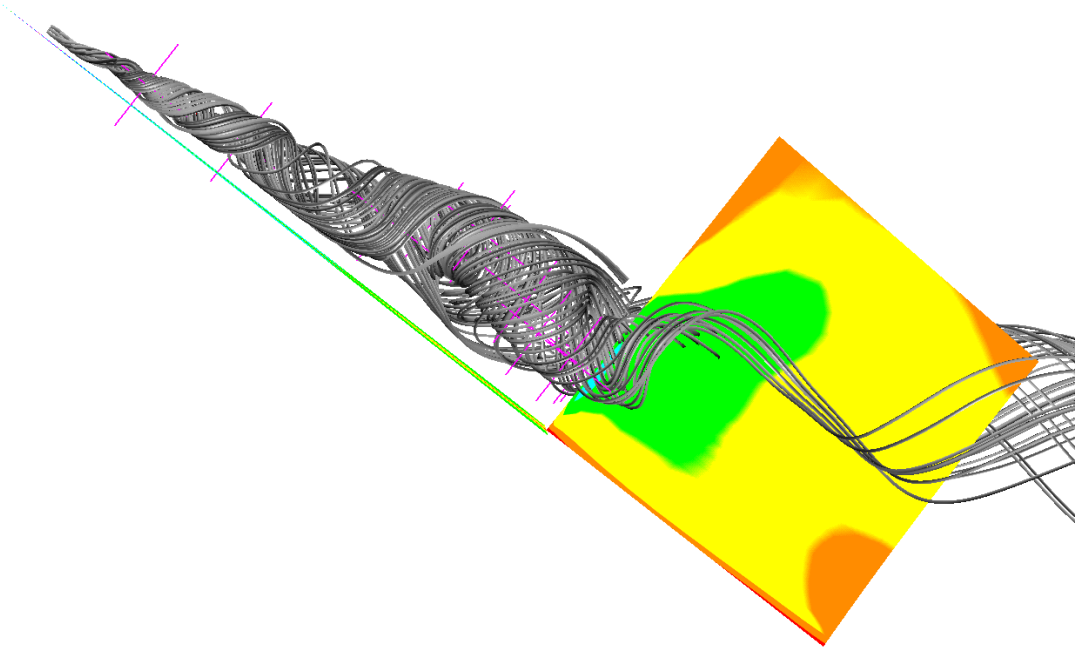

Figure 5.43: Side view at angle-of-attack showing surface pressure, vortex core streamlines, and spiral saddle points at $\tau = 5.28$. Coupled Bending and Torsion Case: $Re = 10^4$, $M = 0.4$, $\alpha = 38^o$.

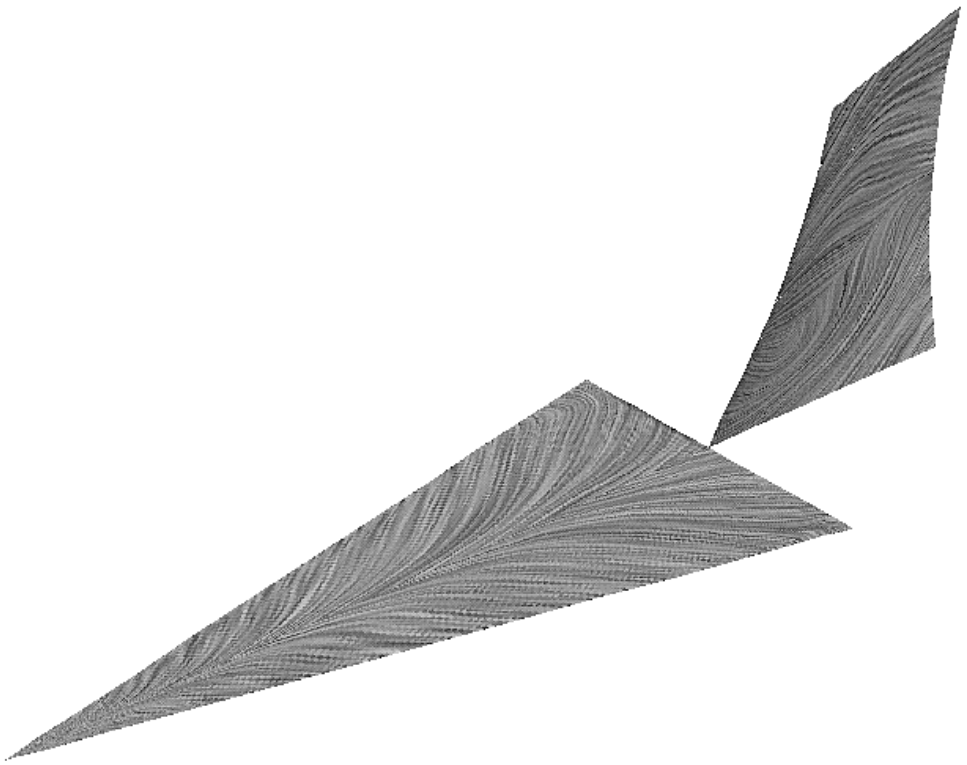

Figure 5.44: Computational surface oil flow at $\tau = 5.28$. Coupled Bending and Torsion Case: $Re = 10^4$, $M = 0.4$, $\alpha = 38^o$.

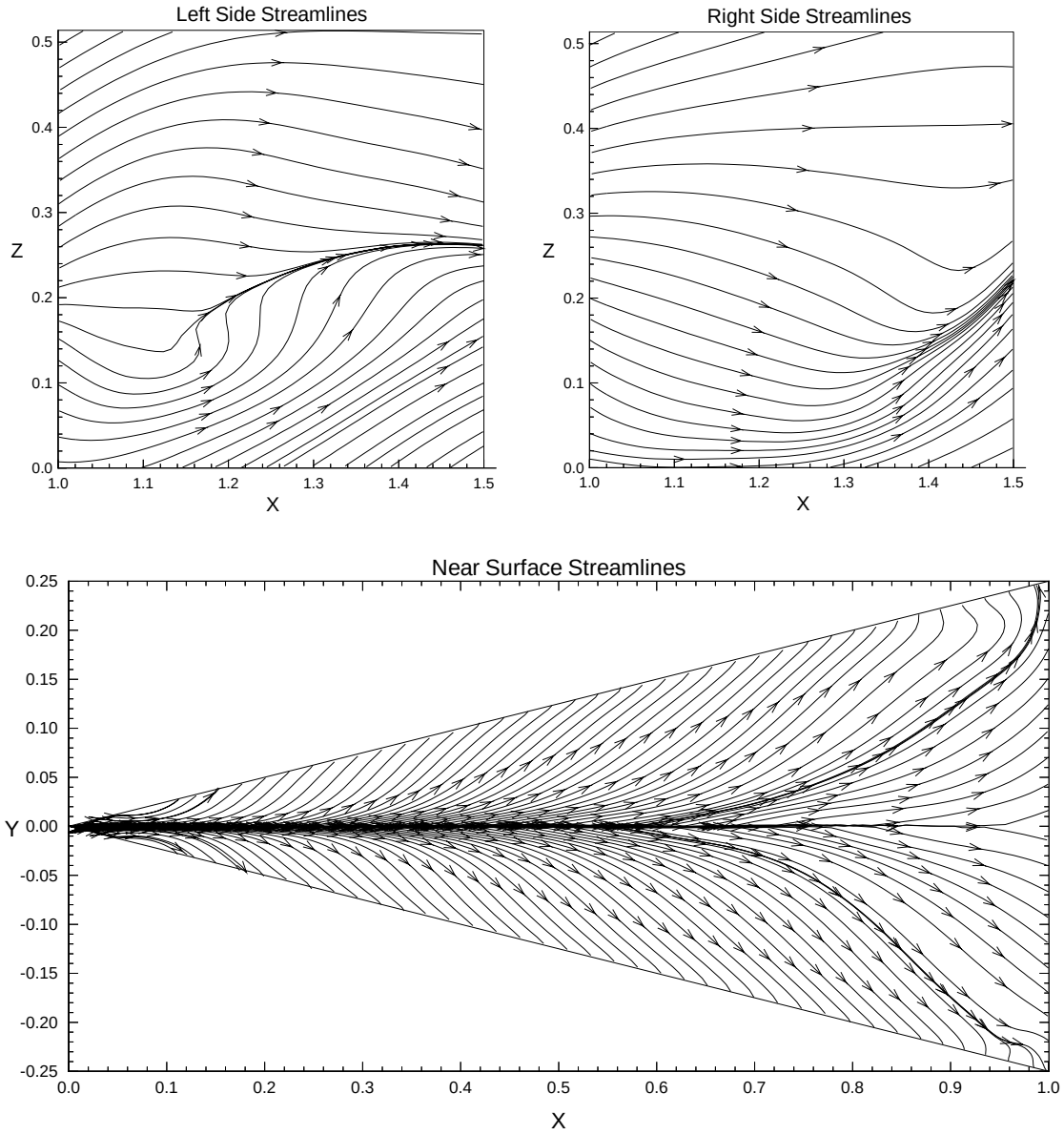

Figure 5.45: Near surface streamlines. Coupled Bending and Torsion Case: $\tau = 5.28$, $Re = 10^4$, $M = 0.4$, $\alpha = 38^o$.

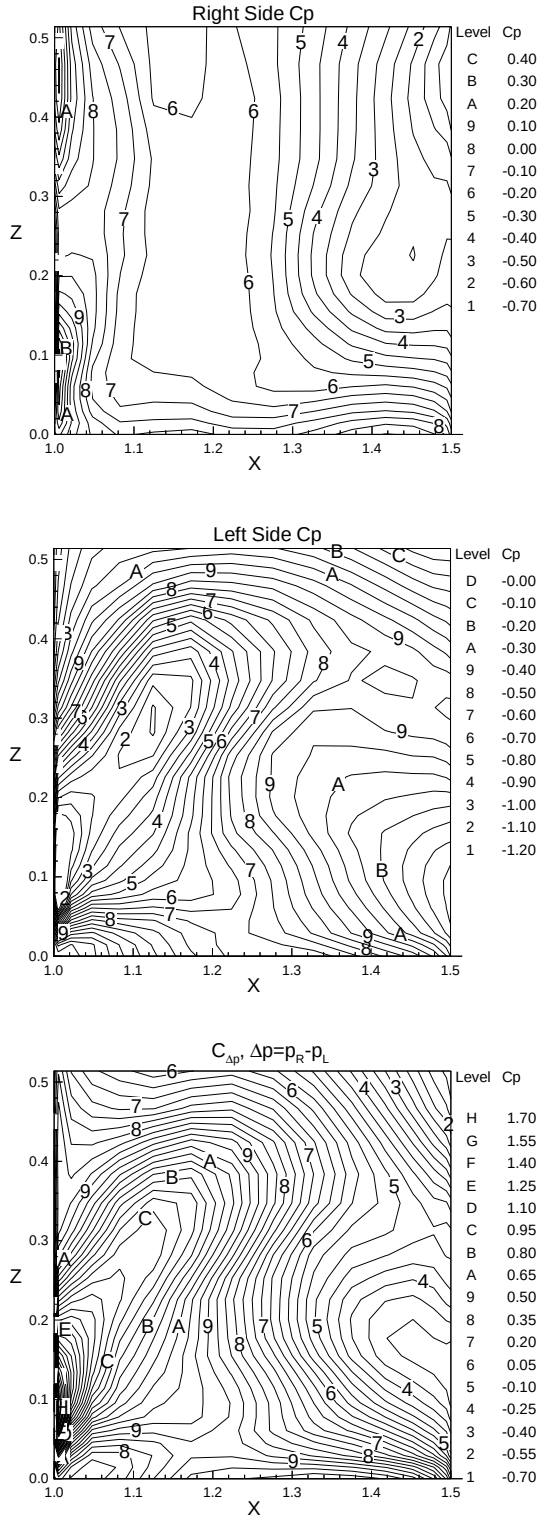

Figure 5.46: Coefficient of pressure on right and left sides of tail, and differential pressure coefficient. Coupled Bending and Torsion Case: $\tau = 5.28$, $Re = 10^4$, $M = 0.4$, $\alpha = 38^o$.

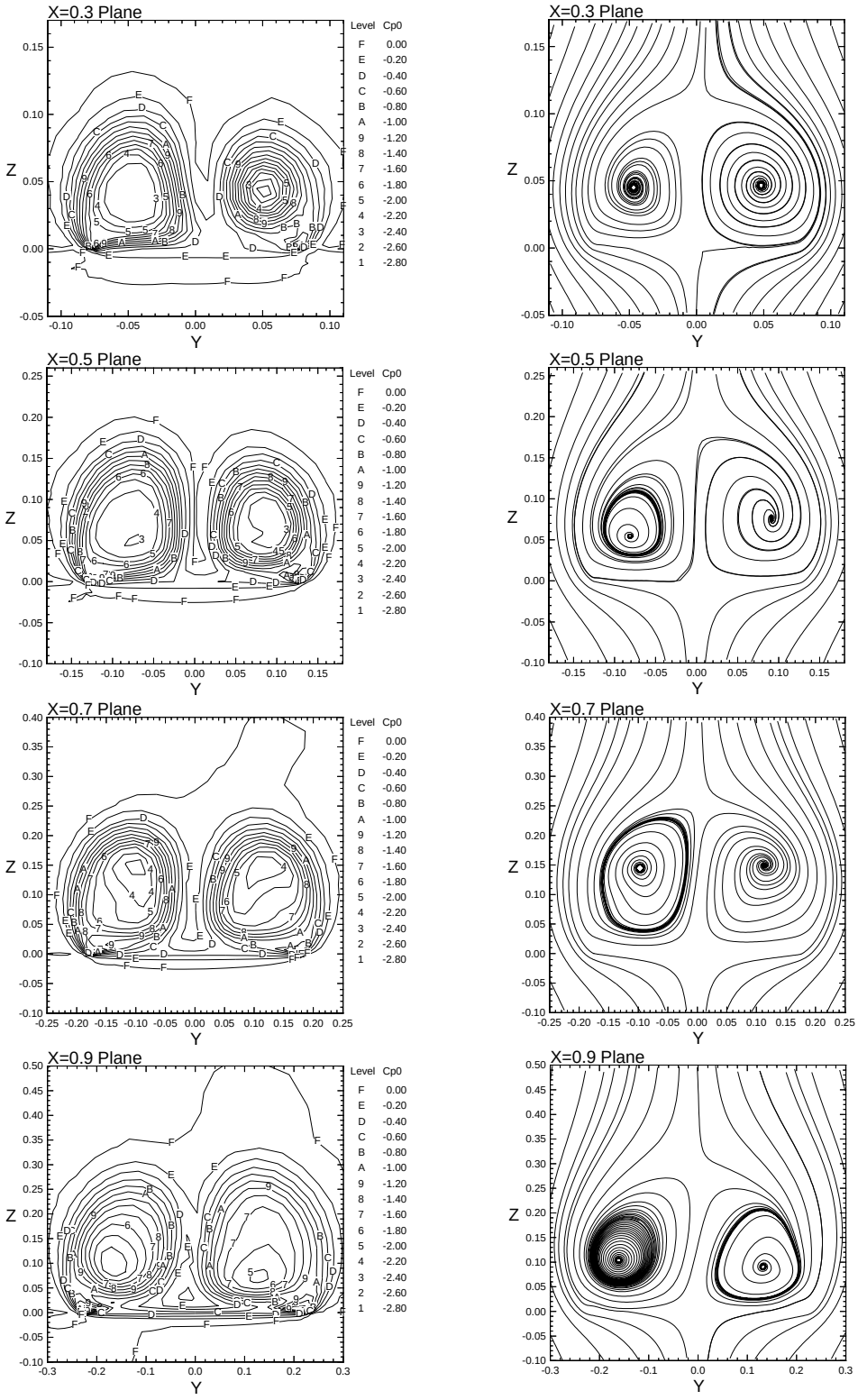

Figure 5.47: Total pressure coefficient and streamlines plotted on vertical crossflow planes above wing. Coupled Bending and Torsion Case: $\tau = 5.28$, $Re = 10^4$, $M = 0.4$, $\alpha = 38^o$.

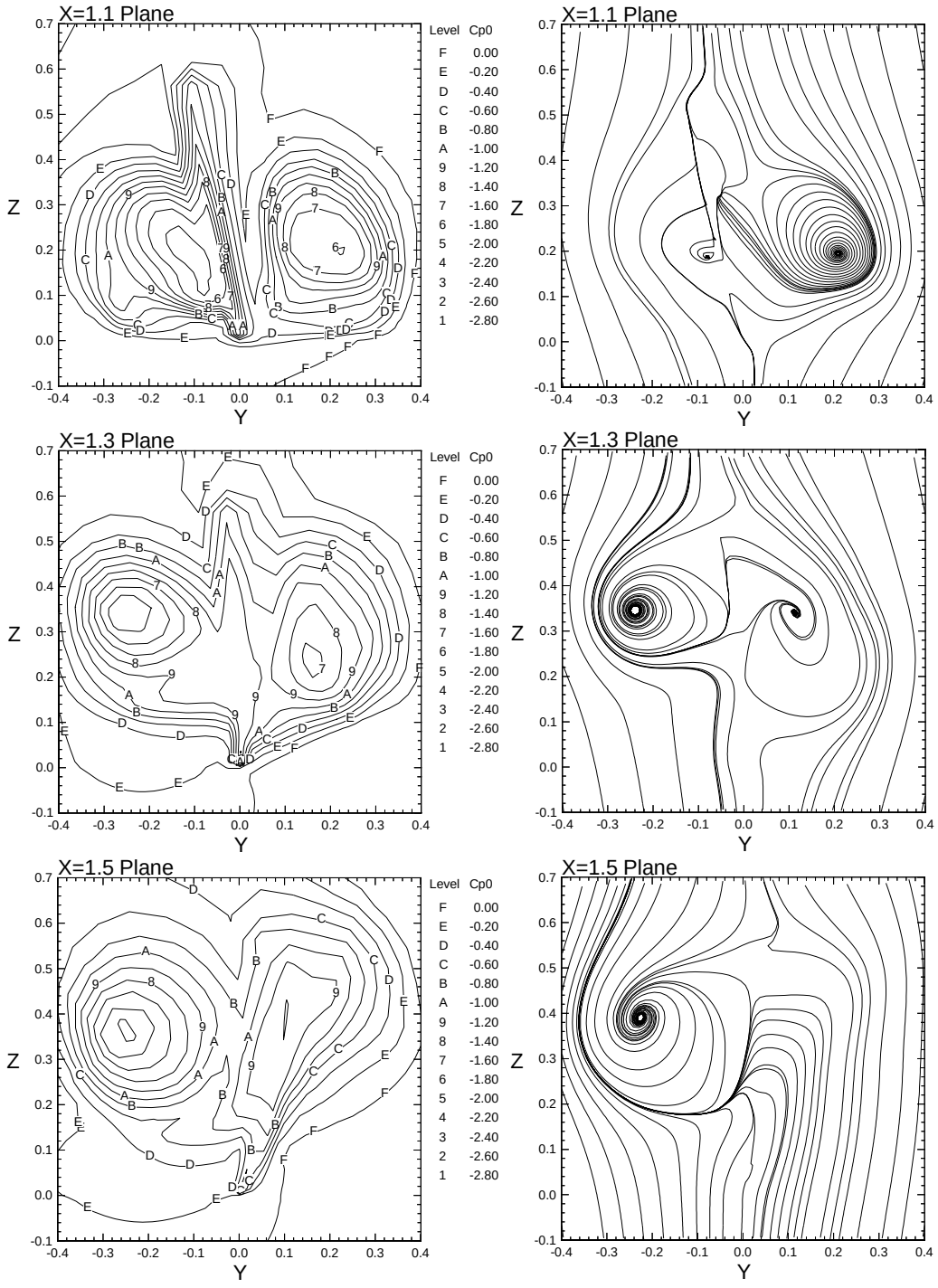

Figure 5.48: Total pressure coefficient and streamlines plotted on vertical crossflow planes near the tail. Coupled Bending and Torsion Case: $\tau = 5.28$, $Re = 10^4$, $M = 0.4$, $\alpha = 38^o$.

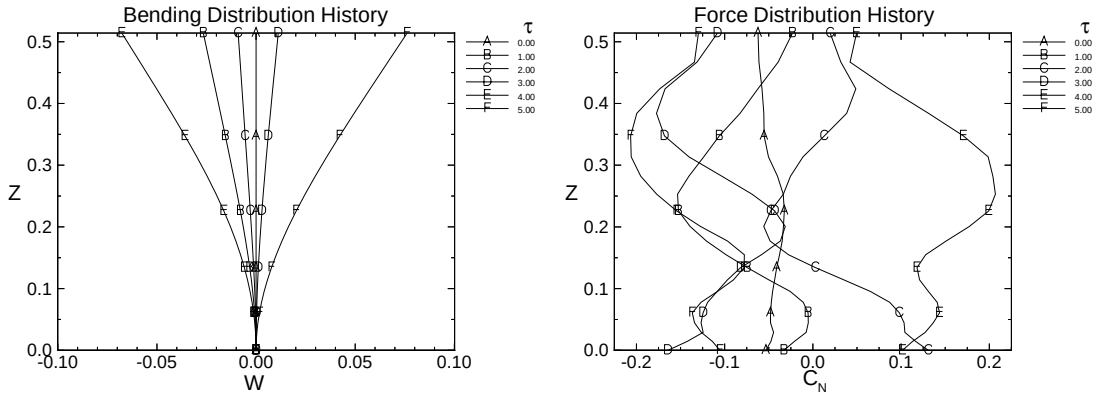

Figure 5.49: Bending deflection and force distributions along the tail span plotted at integer nondimensional time levels. Coupled Bending and Torsion Case: $Re = 10^4$, $M = 0.4$, $\alpha = 38^o$.

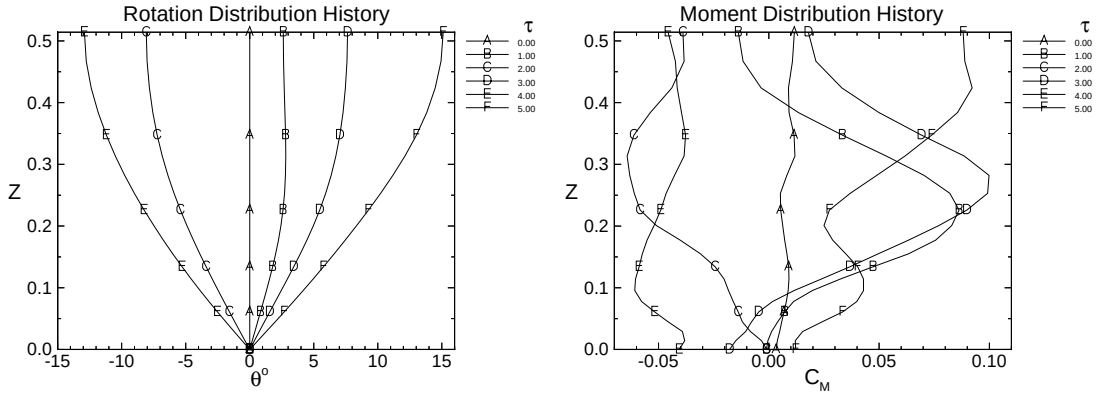

Figure 5.50: Torsion deflection and moment distributions along the tail span plotted at integer nondimensional time levels. Coupled Bending and Torsion Case: $Re = 10^4$, $M = 0.4$, $\alpha = 38^o$.

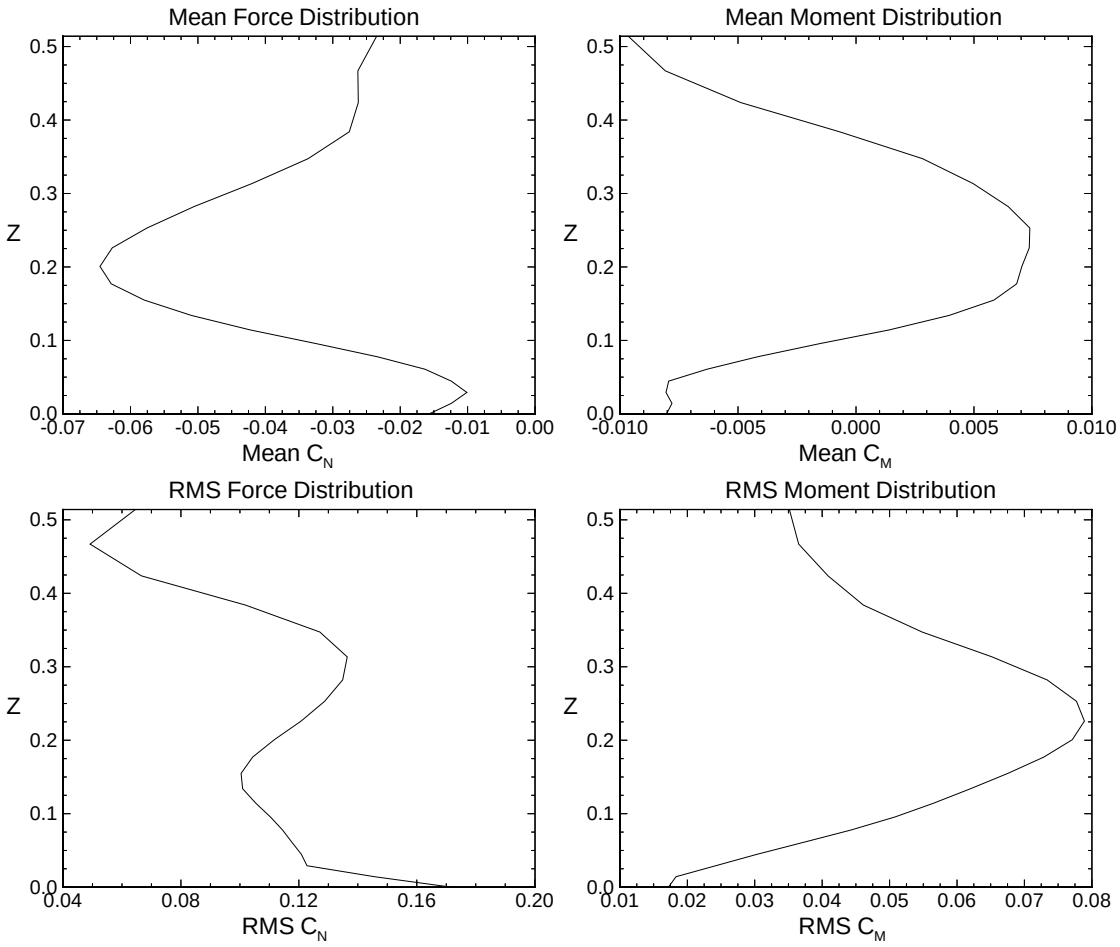

Figure 5.51: Mean and RMS load distributions along the tail span. Coupled Bending and Torsion Case: $Re = 10^4$, $M = 0.4$, $\alpha = 38^o$.

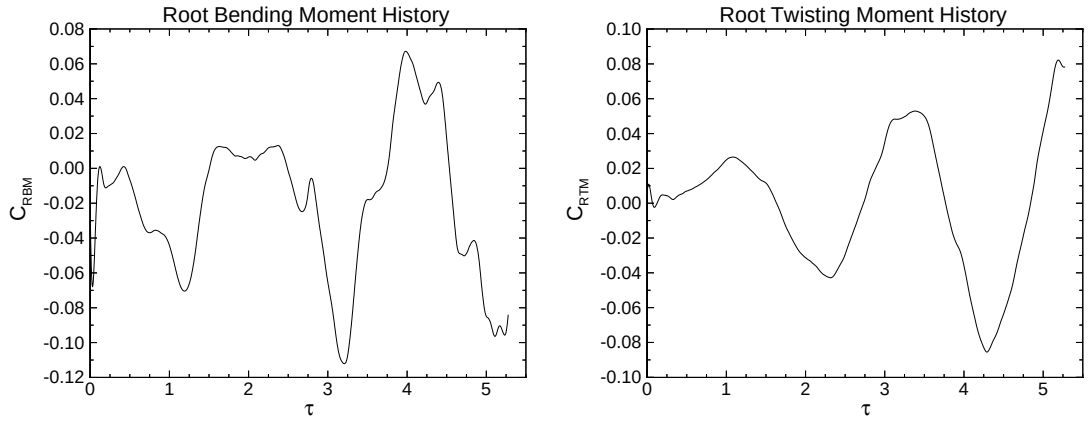

Figure 5.52: History of root bending moment coefficient and root twisting moment coefficient. Coupled Bending and Torsion Case: $Re = 10^4$, $M = 0.4$, $\alpha = 38^o$.

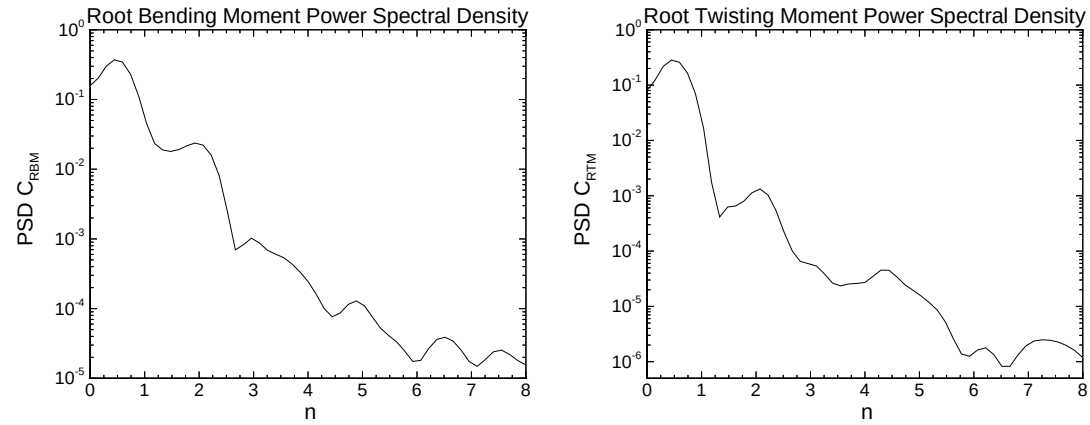

Figure 5.53: Power spectral density of root bending moment coefficient and root twisting moment coefficient versus reduced frequency. Coupled Bending and Torsion Case: $Re = 10^4$, $M = 0.4$, $\alpha = 38^o$.

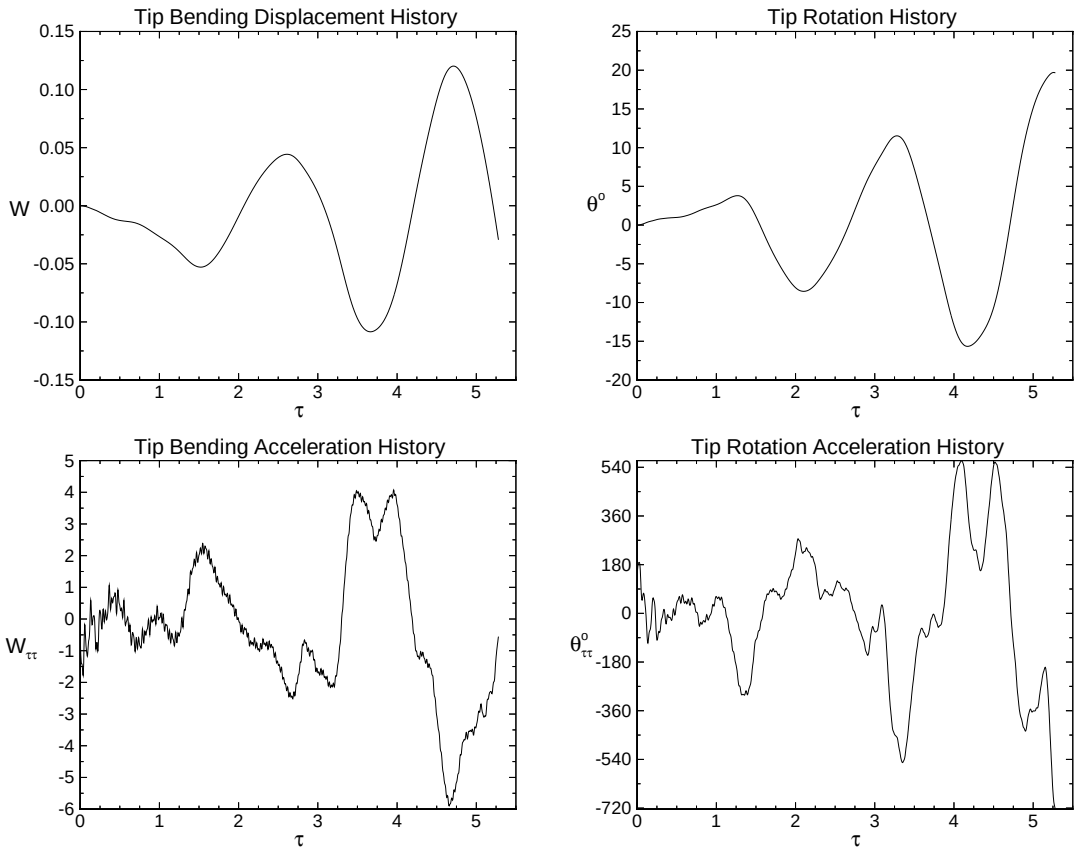

Figure 5.54: History of tip bending and torsion deflections and accelerations. Coupled Bending and Torsion Case: $Re = 10^4$, $M = 0.4$, $\alpha = 38^o$.

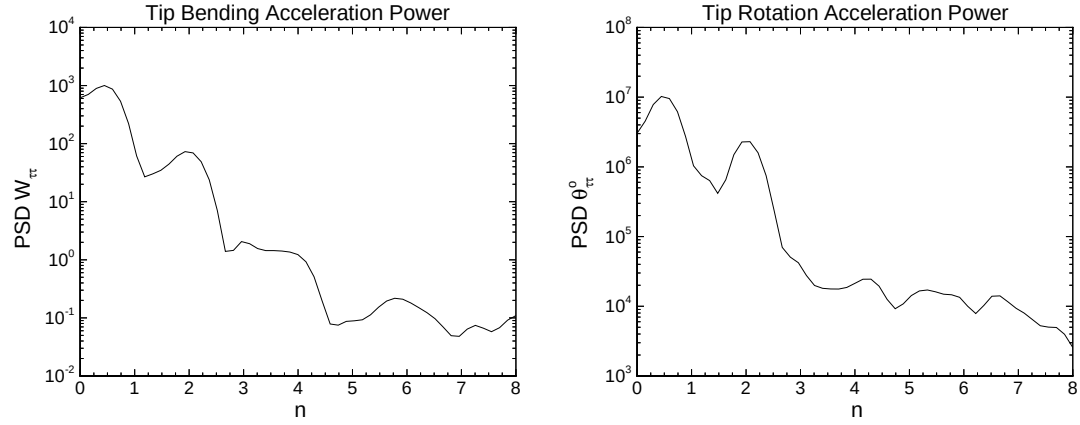

Figure 5.55: Power spectral density of tip bending and torsion accelerations versus reduced frequency. Coupled Bending and Torsion Case: $Re = 10^4$, $M = 0.4$, $\alpha = 38^o$.

5.4 High Reynolds Number Cases: $Re = 10^6$

In the remaining sections of this chapter, the effect of Reynolds number on single tail buffet will be considered. Cases of uncoupled and coupled bending and torsion vibration modes are studied. All other flow and structural parameters will remain unchanged. Also included is a rigid tail case in which the deflections are solved for, but are not imposed in the flow solution. Hence, the flow sees a rigid tail and the structure reacts to the forces generated from the flow past an undeformed tail. The value of the rigid case is that it provides a baseline flow in which the effect of the moving tail on the flow field can be assessed.

5.4.1 Initial Condition Flow Field

The initial flow state for the higher Reynolds number buffeting cases was obtained by taking the initial condition for the low Reynolds number cases and of integrating time-accurately for 2000 more time steps on the coarse grid with $\Delta\tau = 0.00132$. Note that in this case the time step is twice as large as in the low Re cases. Generally the time step must be *decreased* with increasing Re due to stability requirements; however in this case, the time step in the low Re cases was set from a previous large deflection case (not included in this study), in which the strong fluid-structure interactions coupled with a finer grid were the limiting factors. In the present high Re cases, the time step was limited only by CFD stability.

Comparing the 3-D streamline plots of the present coarse $Re = 10^6$ case, given in Figure 5.56, with those of the fine $Re = 10^4$ case, given in Figure 5.11, reveals the effects of both Re and grid resolution. Because the other buffeting cases at low Re were also computed on a coarse grid interpolated from the fine initial condition, the effect of

grid resolution can be separated from the effect of Re. As previously noted, coarsening the grid results in a weaker breakdown and a more diffuse vortex core in general. It is possible that this lack of clarity in the vortex core and breakdown has the effect of driving the natural breakdown instability more unstable with respect to position. This would account for the greater asymmetry seen in all of the coarse grid cases. Recalling that all of the low Re cases had breakdown locations around 30% chord, it can clearly be seen that the effect of increasing the Re from a very low value of 10^4 to a moderate Re of 10^6 pushes back the breakdown by 10%c. This shows that the effect of greatly increased viscosity is to hasten breakdown. However, this trend is well known not to continue with increasing Re. In general, there is very little change in the breakdown flow from moderate (10^6) to high Reynolds numbers (10^7).

Figure 5.57 depicts the side view of the configuration at angle-of-attack and shows that the vortex trajectory remains unchanged with the increased Re. Note that because the grid dimensions changed between this and the low Re initial condition, the number of streamlines are also unequal, all other streamline plots share identical seed locations. The surface flow shown in Figures 5.58 and 5.59 reveals that once again the coarse grid does not capture any secondary flow separation or reattachment. From the wing surface flow, the previous region of recirculation seen near the trailing edge is now completely gone. The tail surface flows however, are still very similar with separation lines occurring in nearly the same locations.

Tail surface C_p plots, Figure 5.60, show pressure levels at nearly the same level as the low Re case. However, the differential pressure range at this time level is 50% lower. Further analysis of the tail loading will be conducted in the following buffeting sections.

In Figures 5.61-5.64, crossflow planes are shown with total pressure coefficient contours, streamlines and velocity vectors drawn from each cell interface. The value of velocity vectors plots is their uniformity and the additional information of velocity magnitude, which streamline plots do not easily show. Note the in all crossflow plots the orientation is such that the viewer is looking upstream. C_{p_0} contours at the same range and levels confirm the vortex size and breakdown position shown by the 3-D streamlines. In the $x = 0.3$ crossflow plane the vortices are much tighter than in the $Re = 10^4$, confirming that the vortices have yet to burst. Another key feature of all the vector plots over the wing is the lack of vortical flow near the leading edges, again confirming the absence of secondary separation.

In Figure 5.65, the normalized spanwise variation of the coefficient of pressure is plotted at the same chord stations as the previous crossflow plots. The main difference between the C_p plots of this case and the low Re case is at the $x = 0.3$ plane. In this case, since breakdown has not yet occurred so the vortices are much stronger and hence exhibit a greater suction force. The asymmetry in C_p also adds credibility to the purely kinematical signs of asymmetric breakdown.

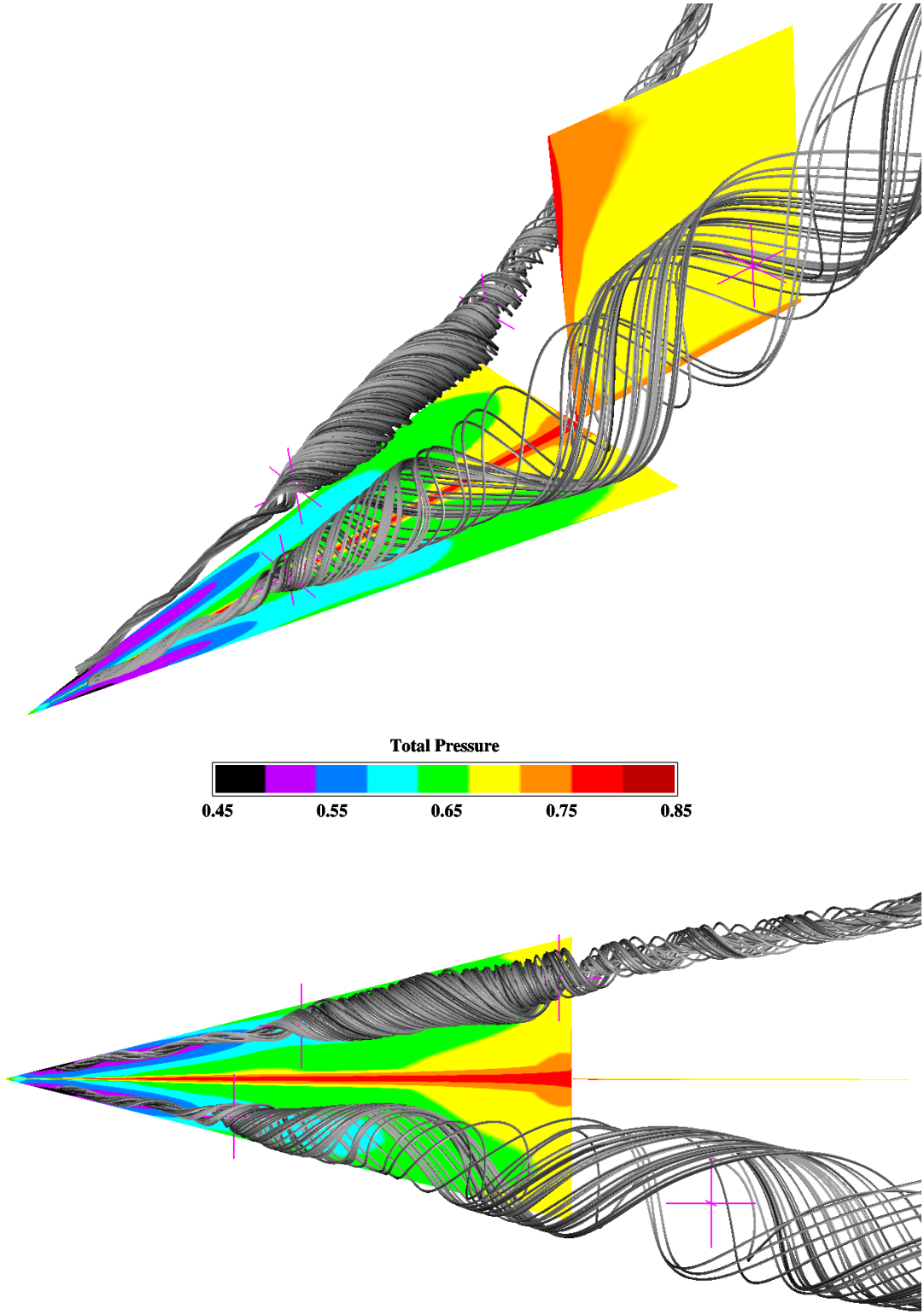

Figure 5.56: Three-dimensional and top views of surface pressure and vortex core streamlines. Purple crosses denote critical points associated with either attracting or repelling spiral saddle points. Initial Condition Flow Field: $Re = 10^6$, $M = 0.4$, $\alpha = 38^o$.

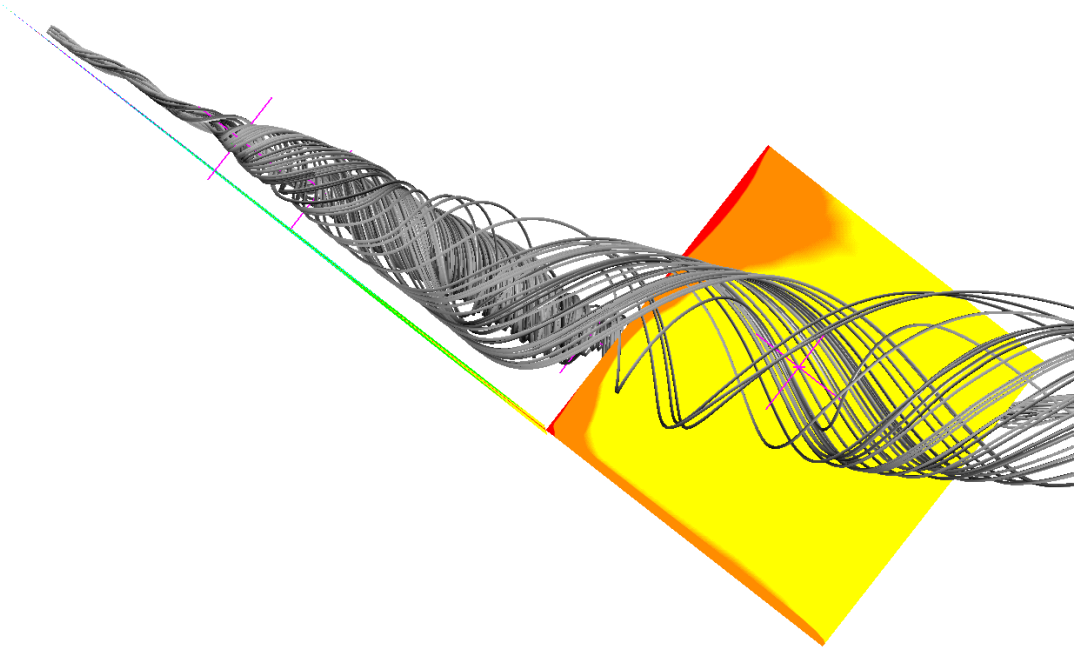

Figure 5.57: Side view at angle-of-attack showing surface pressure, vortex core streamlines, and spiral saddle points. Initial Condition Flow Field: $Re = 10^6$, $M = 0.4$, $\alpha = 38^o$.

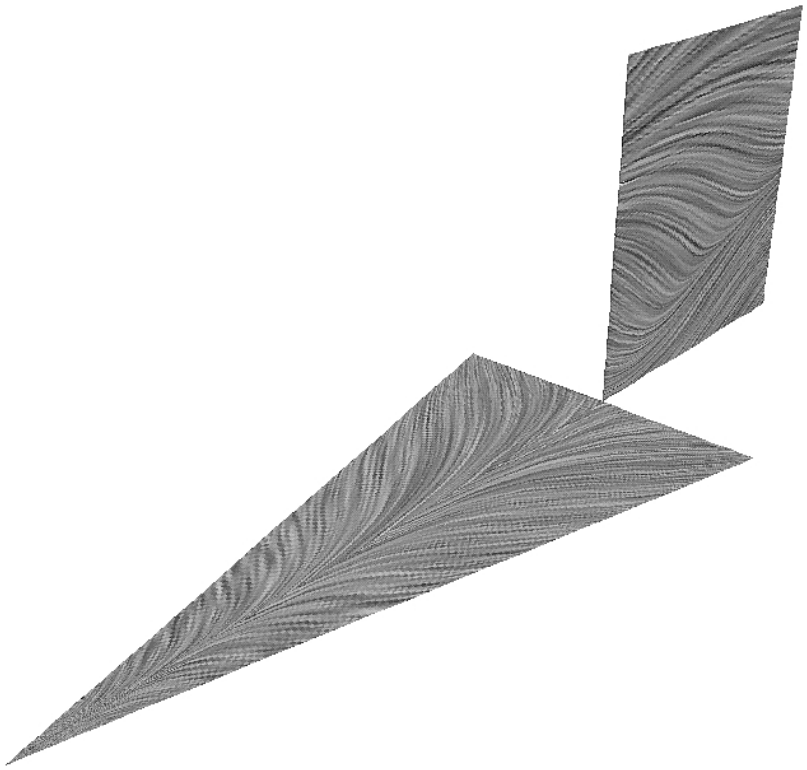

Figure 5.58: Computational surface oil flow. Initial Condition Flow Field: $Re = 10^6$, $M = 0.4$, $\alpha = 38^o$.

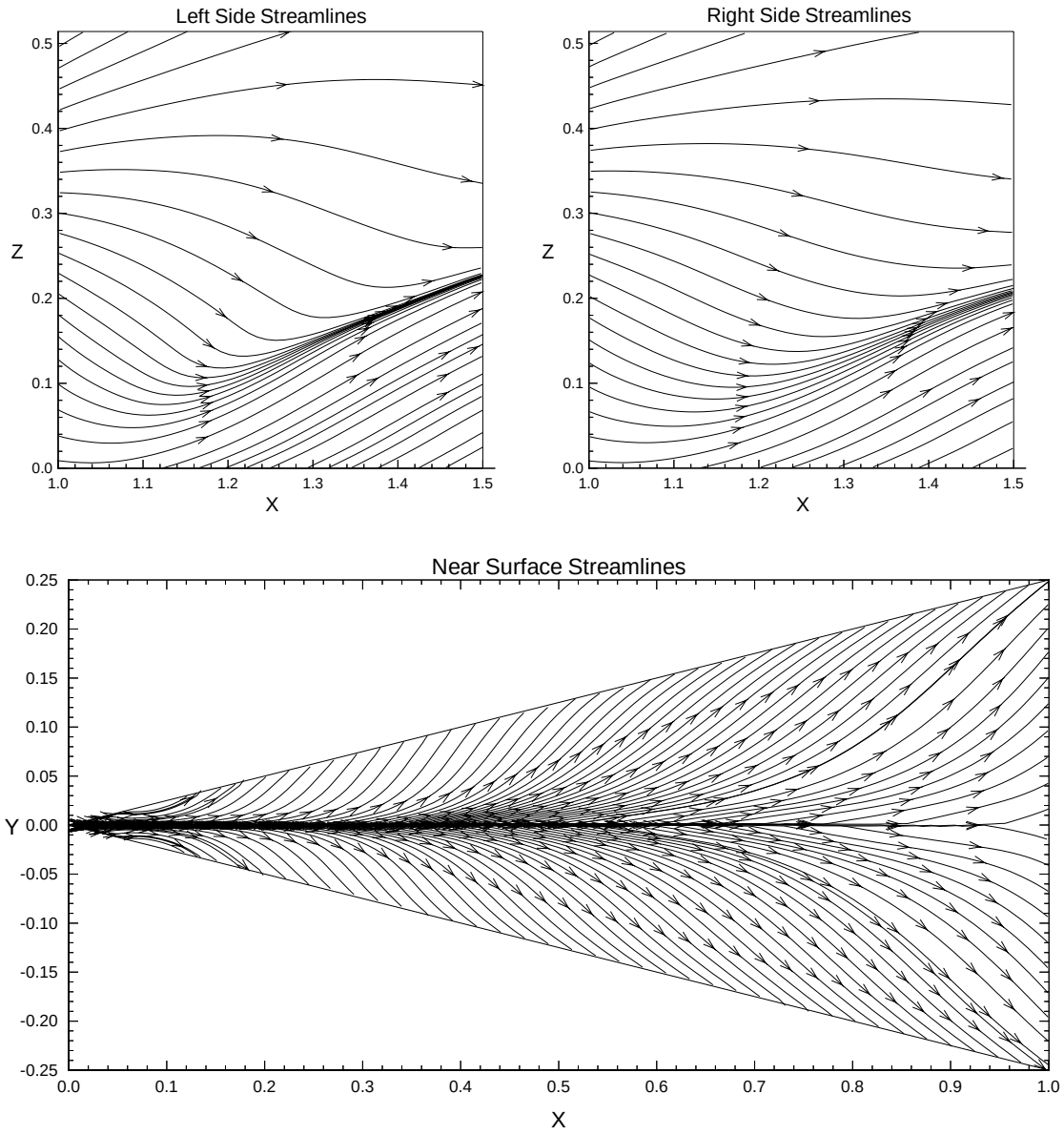

Figure 5.59: Near surface streamlines. Initial Condition Flow Field: $Re = 10^6$, $M = 0.4$, $\alpha = 38^o$.

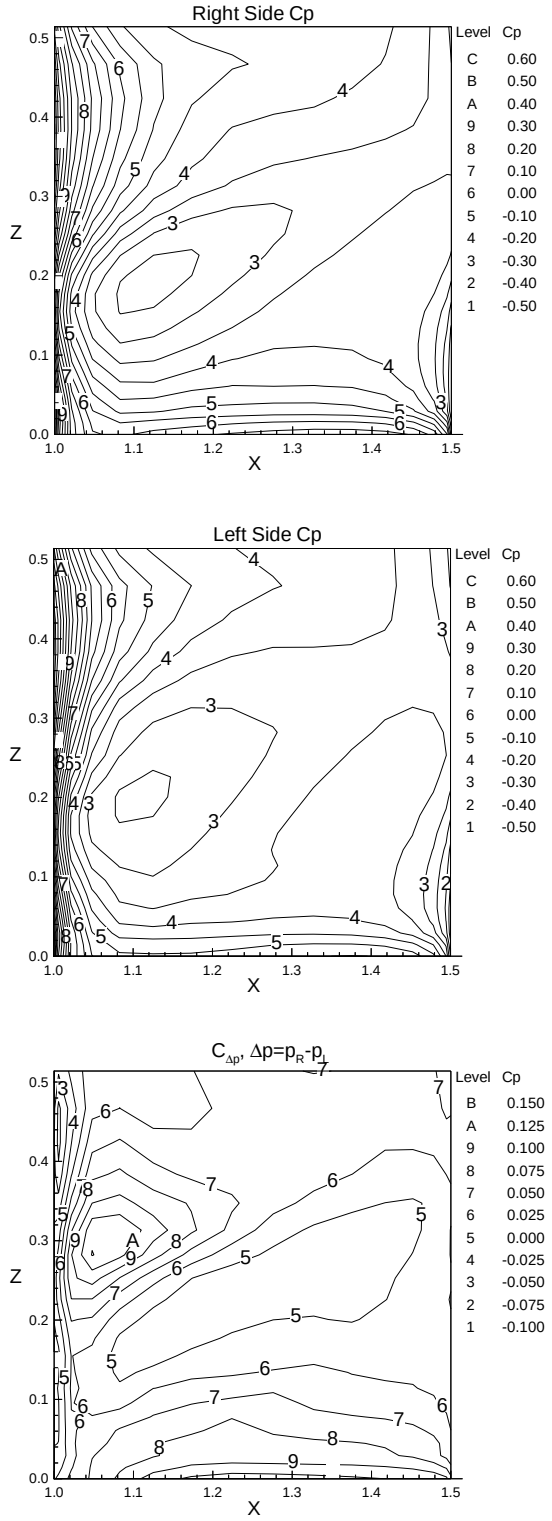

Figure 5.60: Coefficient of pressure on right and left sides of tail, and differential pressure coefficient. Initial Condition Flow Field: $Re = 10^6$, $M = 0.4$, $\alpha = 38^o$.

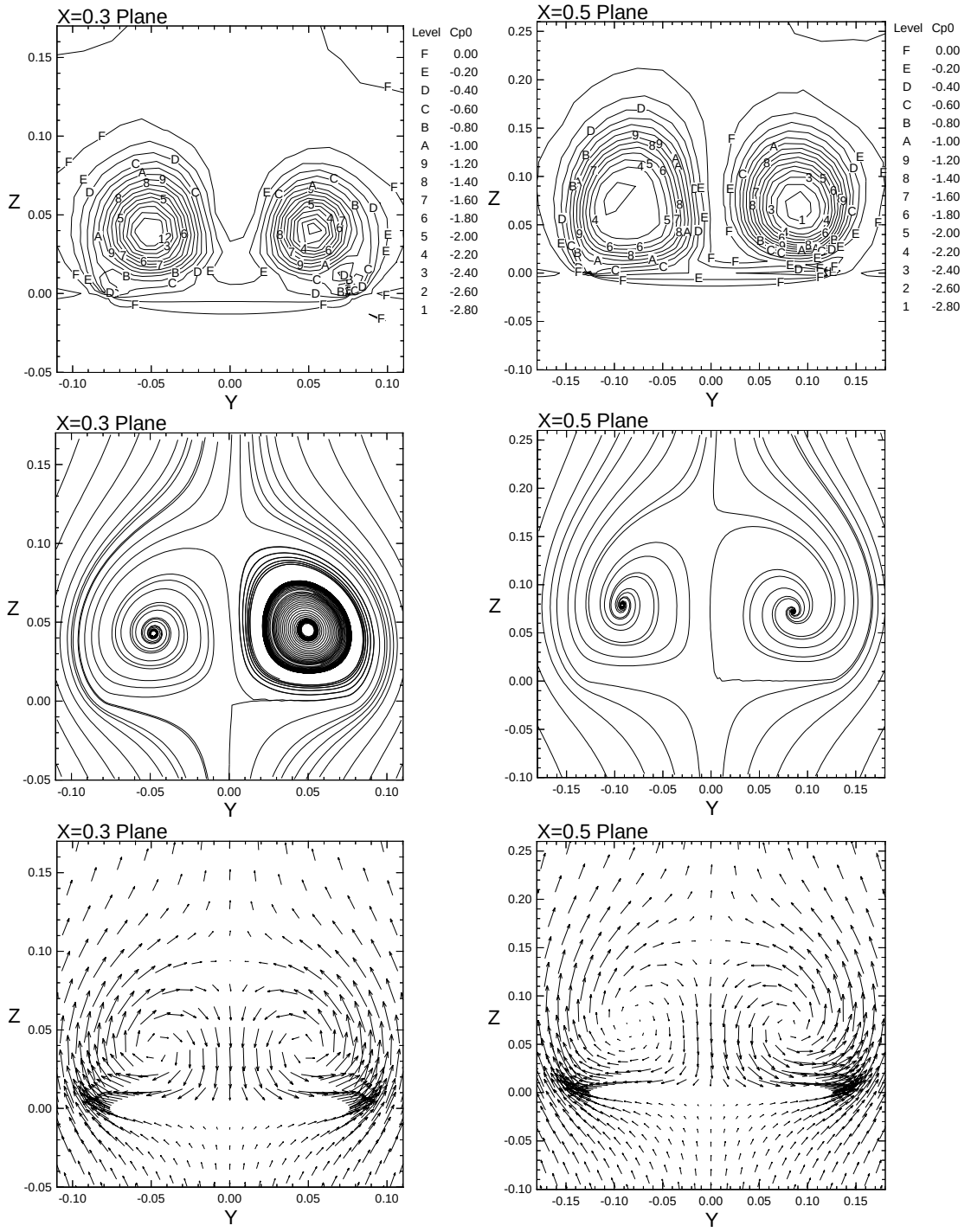

Figure 5.61: Total pressure coefficient, streamlines, and velocity vectors plotted on vertical crossflow planes above wing at chord stations $x = 0.3, 0.5$. Initial Condition Flow Field: $Re = 10^6$, $M = 0.4$, $\alpha = 38^o$.

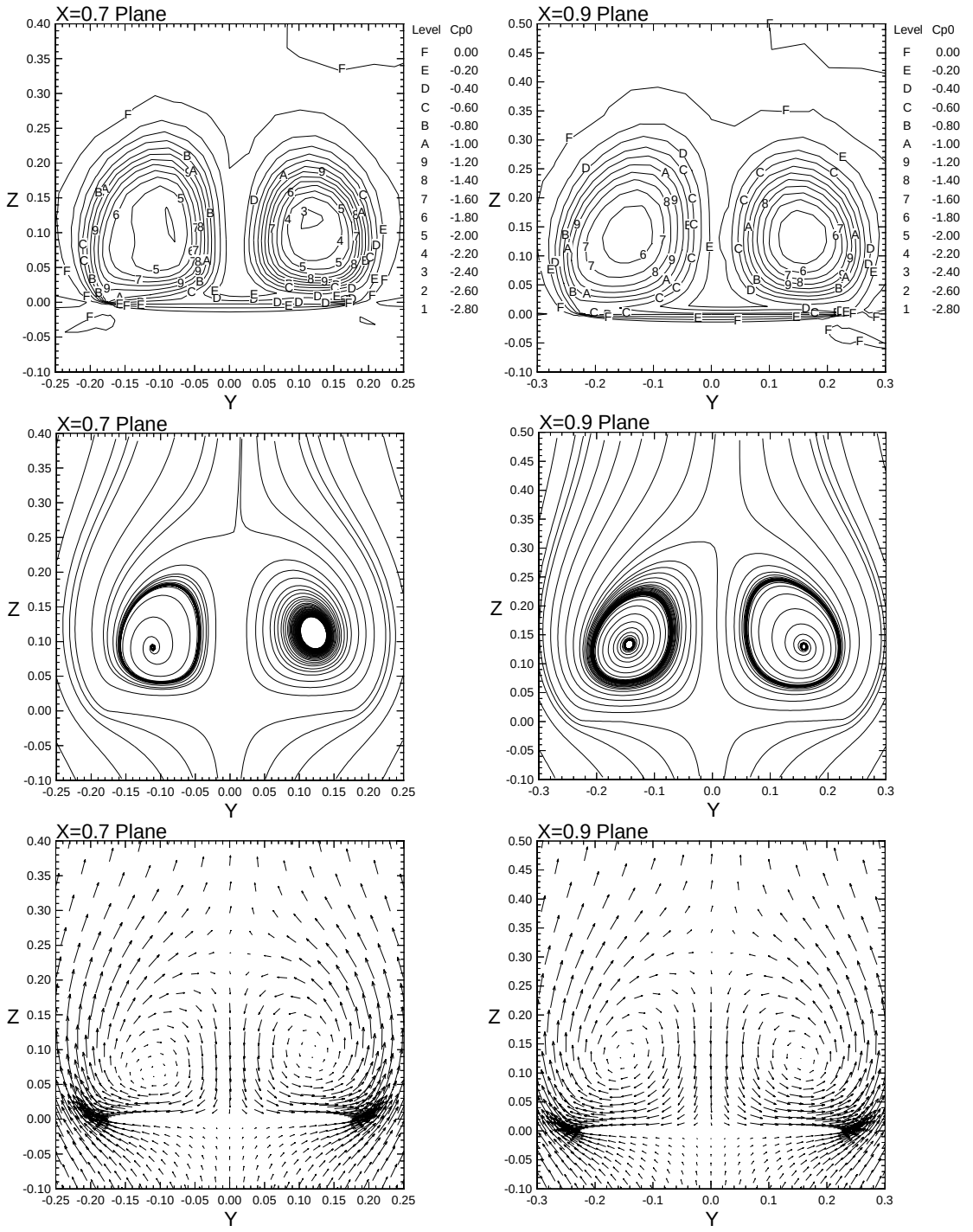

Figure 5.62: Total pressure coefficient, streamlines, and velocity vectors plotted on vertical crossflow planes above wing at chord stations $x = 0.7, 0.9$. Initial Condition Flow Field: $Re = 10^6$, $M = 0.4$, $\alpha = 38^o$.

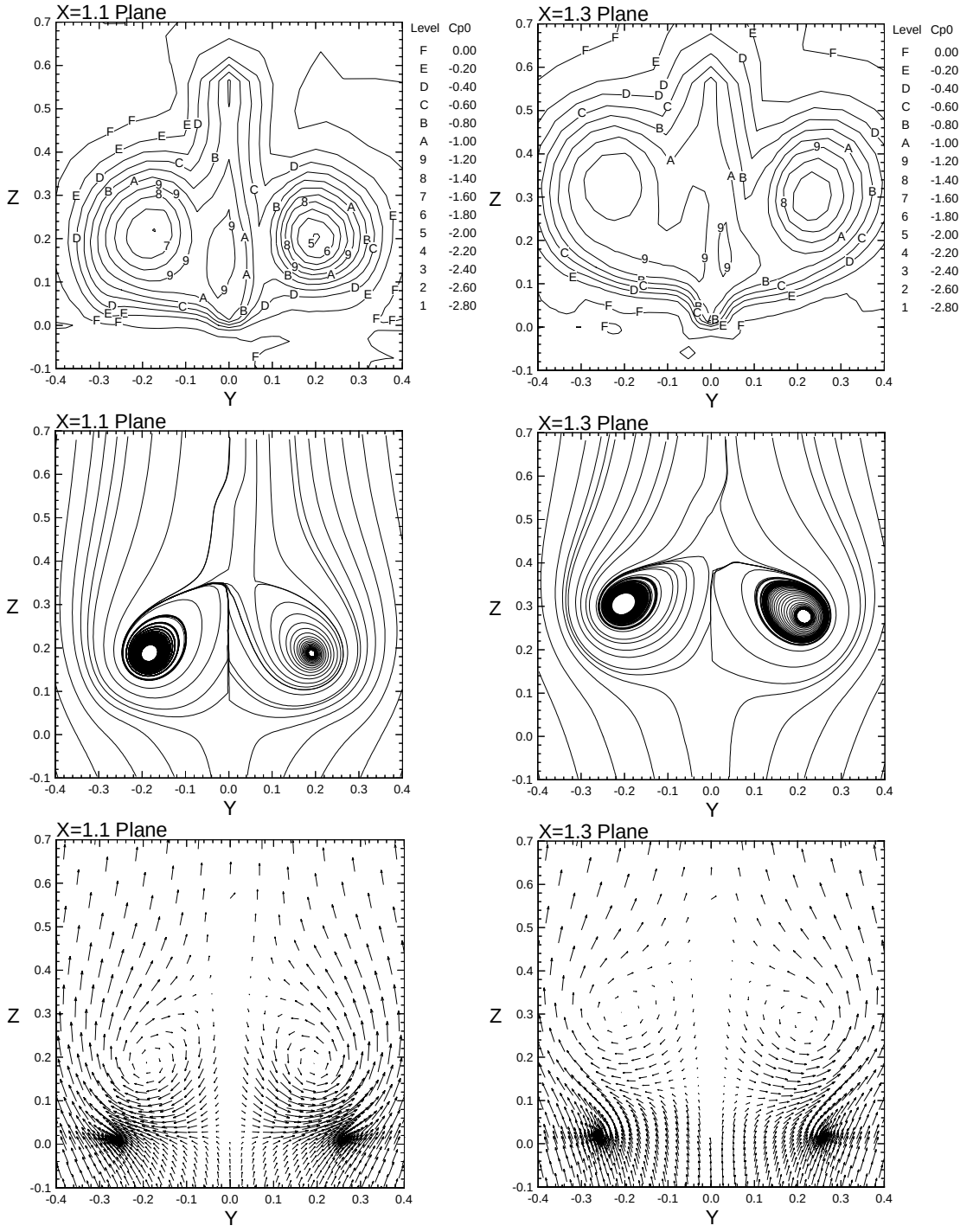

Figure 5.63: Total pressure coefficient, streamlines, and velocity vectors plotted on vertical crossflow planes near the tail at $x = 1.1, 1.3$. Initial Condition Flow Field: $Re = 10^6$, $M = 0.4$, $\alpha = 38^o$.

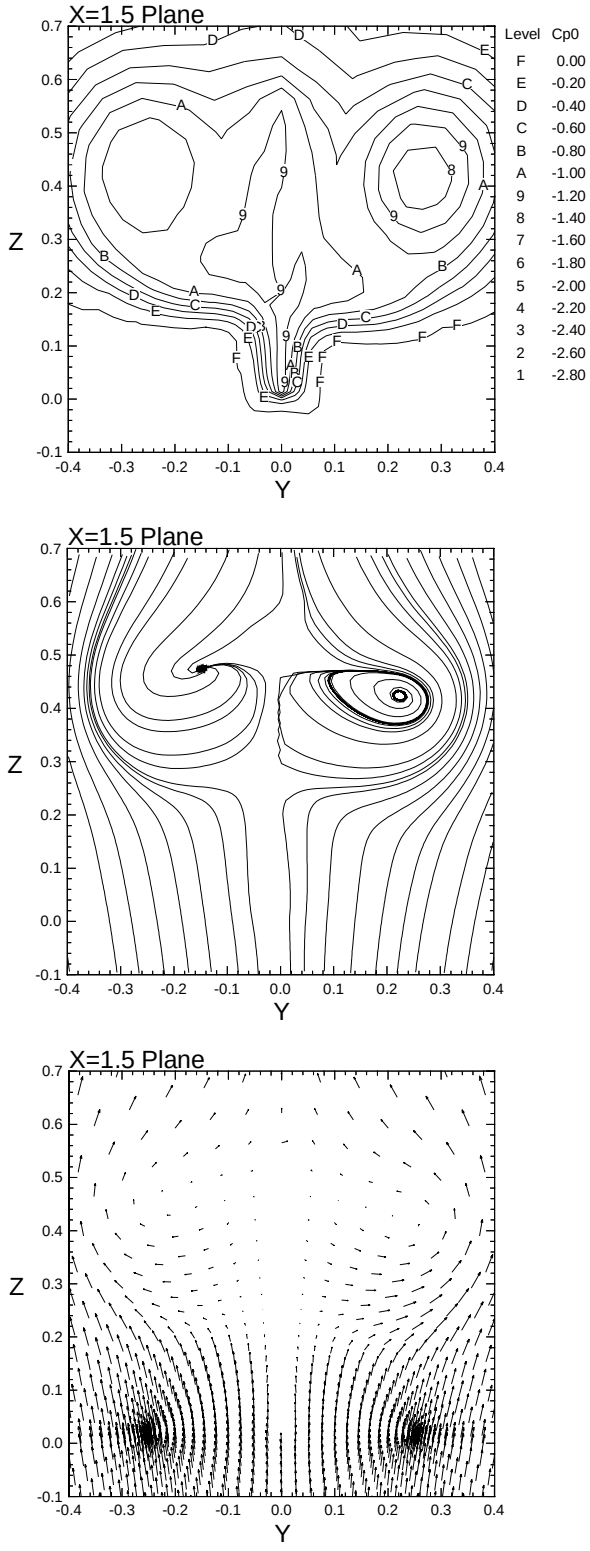

Figure 5.64: Total pressure coefficient, streamlines, and velocity vectors plotted on a vertical crossflow plane at the tail trailing edge, $x = 1.5$. Initial Condition Flow Field: $Re = 10^6$, $M = 0.4$, $\alpha = 38^o$.

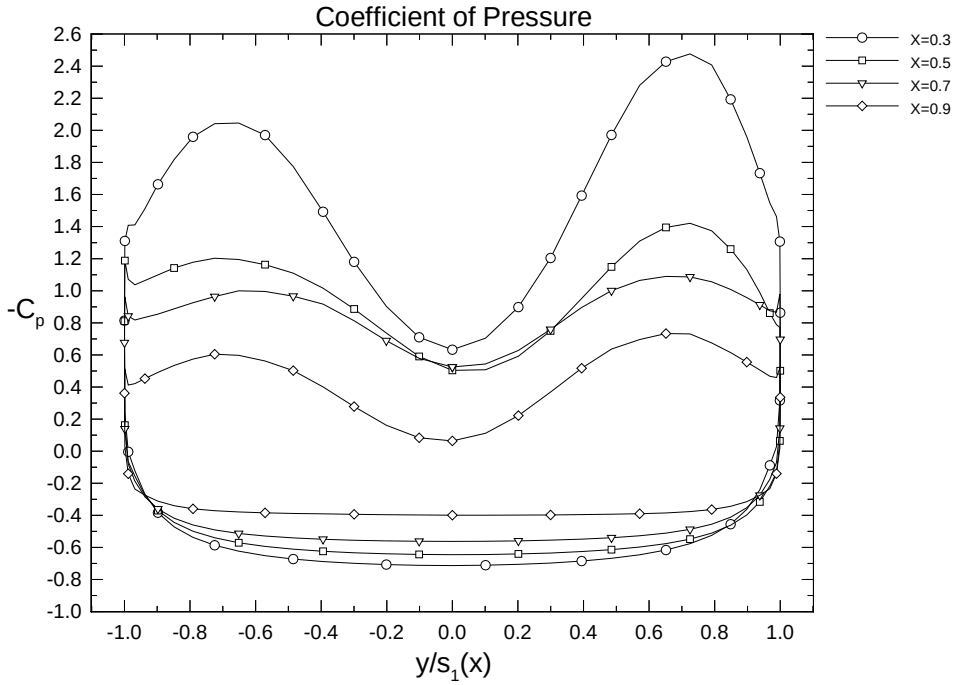

Figure 5.65: Coefficient of pressure on upper and lower wing surfaces at chord stations corresponding to plotted crossflow planes. Initial Condition Flow Field: $Re = 10^6$, $M = 0.4$, $\alpha = 38^o$.

5.4.2 Rigid Tail Load History

The purpose of this case is to provide a baseline from which the effect of structural interaction with the flow can be assessed quantitatively. The two main issues to be resolved are; to what degree does the motion of the tail affect the upstream breakdown location, and secondly, what effect does the exclusion of the fluid-structure interactions have on the predicted buffeting response and loading. To answer these questions, a rigid tail case in which the deflections are solved for, but not imposed back into the flow solution is presented.

The global flow field at the end of the buffeting case is plotted in Figures 5.66-5.71. Comparison of these plots with the initial condition flow field of the previous section reveals the unsteady nature of the global flow. This is most clearly shown by the widely varying position of the breakdown locations.

In Figures 5.72-5.78, the loading and the hypothetical uncoupled bending and torsion buffeting response are plotted. The mean and RMS root moment values, maximum amplitudes and dominant frequencies are summarized in Table 5.7. From the time and frequency domain load data, the loading is largely random with two distinct dominant frequencies. It is also observed that the dominate frequencies for bending and twisting root moments are identical. This proves conclusively that the similarity in dominant frequencies seen in the previous low Re cases is not due to the aerodynamic coupling of the bending and torsional modes.

The maximum amplitudes of the hypothetical tip displacements, accelerations and the first two dominant frequencies are summarized in Table 5.8. Since these displacements are not implemented in the flow solution, there is no aerodynamic damping of the response. The effect is larger displacements and increased high-frequency content.

Both the loading and response of this case will be further discussed in contrast with the following two buffeting cases in the next sections.

Root Loads									
C_{RBM}					C_{RTM}				
Mean	RMS	A	n_{d1}	n_{d2}	Mean	RMS	A	n_{d1}	n_{d2}
-0.021	0.029	0.070	0.75	1.5	0.007	0.014	0.039	0.75	1.5

Table 5.7: Summary of root bending and twisting moment statistics, maximum amplitudes and dominant frequencies. Rigid Tail Case: $Re = 10^6$, $M = 0.4$, $\alpha = 38^o$.

Hypothetical Tip Response							
Bending				Torsion			
$A(w)$	$A(w_{\tau\tau})$	n_{d1}	n_{d2}	$A(\theta)^o$	$A(\theta_{\tau\tau})^o$	n_{d1}	n_{d2}
0.131	6.8	0.50	2.50	42.2	3240	0.88	2.50

Table 5.8: Summary of hypothetical tip displacement and acceleration statistics, maximum amplitudes and dominant frequencies. Rigid Tail Case: $Re = 10^6$, $M = 0.4$, $\alpha = 38^o$.

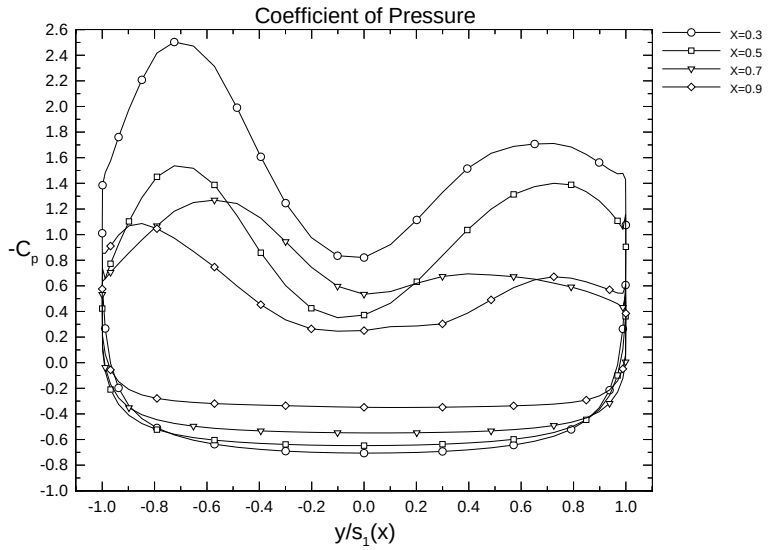

Figure 5.66: Coefficient of pressure on upper and lower wing surfaces at chord stations corresponding to plotted crossflow planes. Rigid Tail Case: $Re = 10^6$, $M = 0.4$, $\alpha = 38^o$.

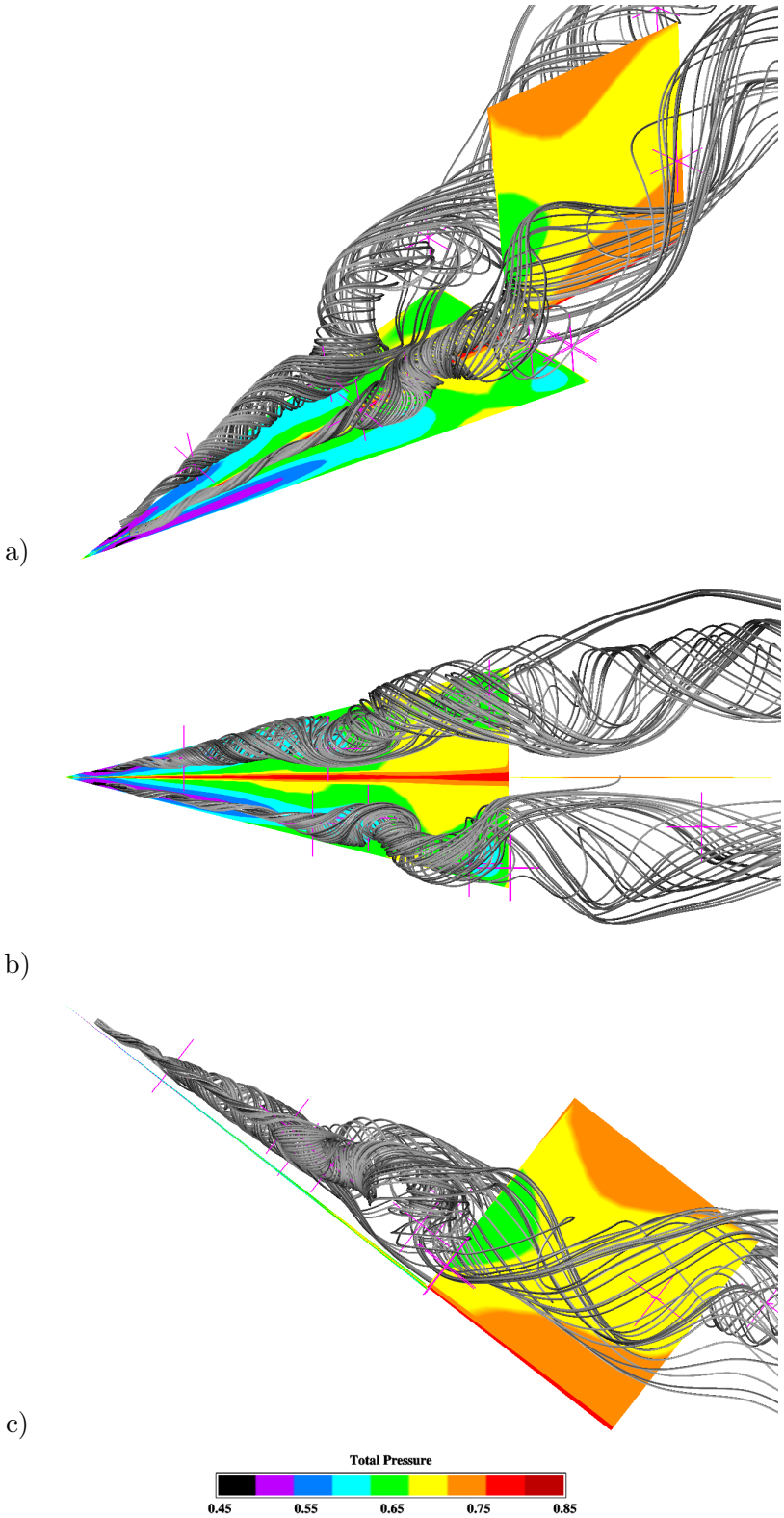

Figure 5.67: a) Three-dimensional, b) top and c) side views of surface pressure and vortex core streamlines at $\tau = \frac{tU_\infty}{\bar{c}} = 13.2$ and $\Delta\tau = 0.00132$. Purple crosses denote critical points associated with either attracting or repelling spiral saddle points. Rigid Tail Case: $Re = 10^6$, $M = 0.4$, $\alpha = 38^o$.

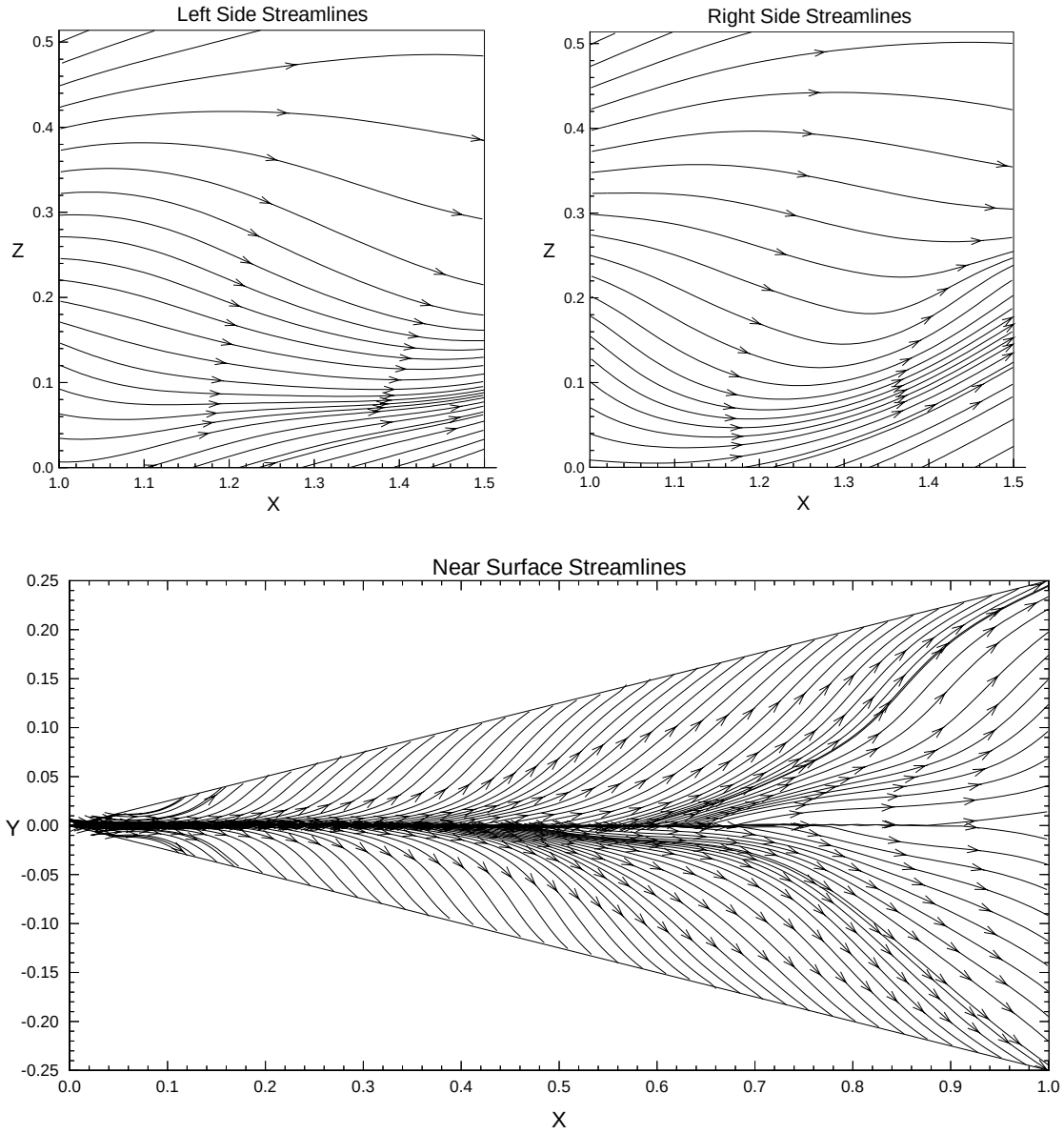

Figure 5.68: Near surface streamlines at $\tau = 13.2$. Rigid Tail Case: $Re = 10^6$, $M = 0.4$, $\alpha = 38^o$.

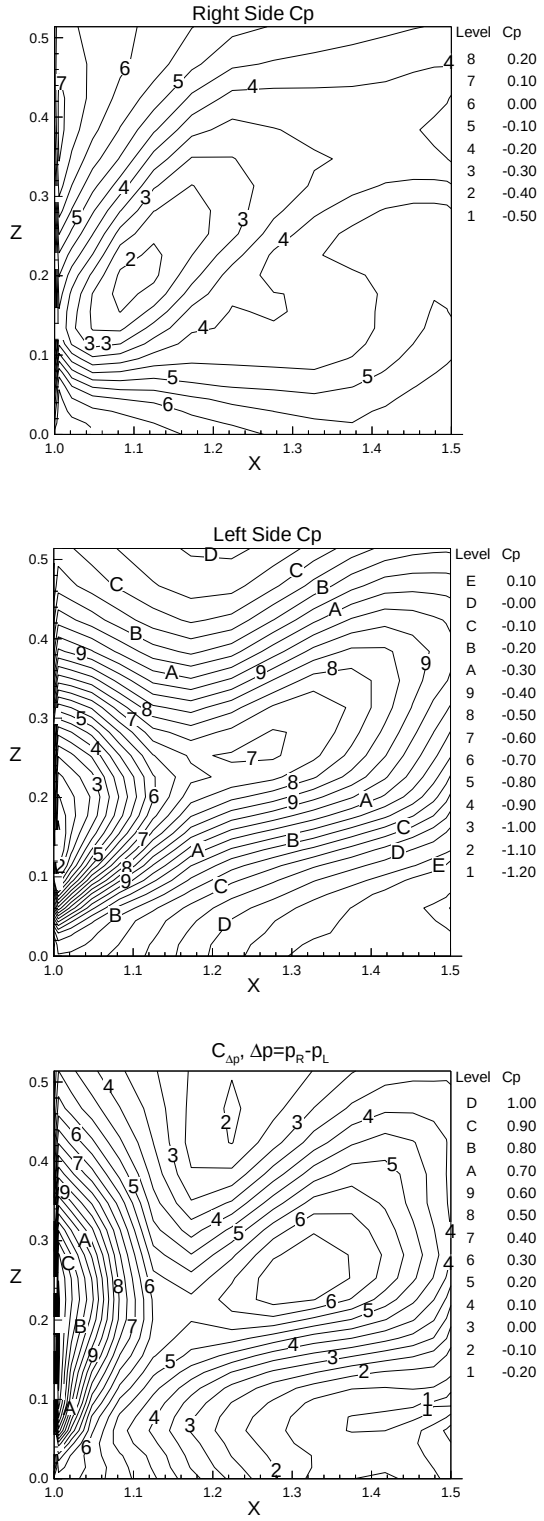

Figure 5.69: Coefficient of pressure on right and left sides of tail, and differential pressure coefficient. Rigid Tail Case: $\tau = 13.2$, $Re = 10^6$, $M = 0.4$, $\alpha = 38^o$.

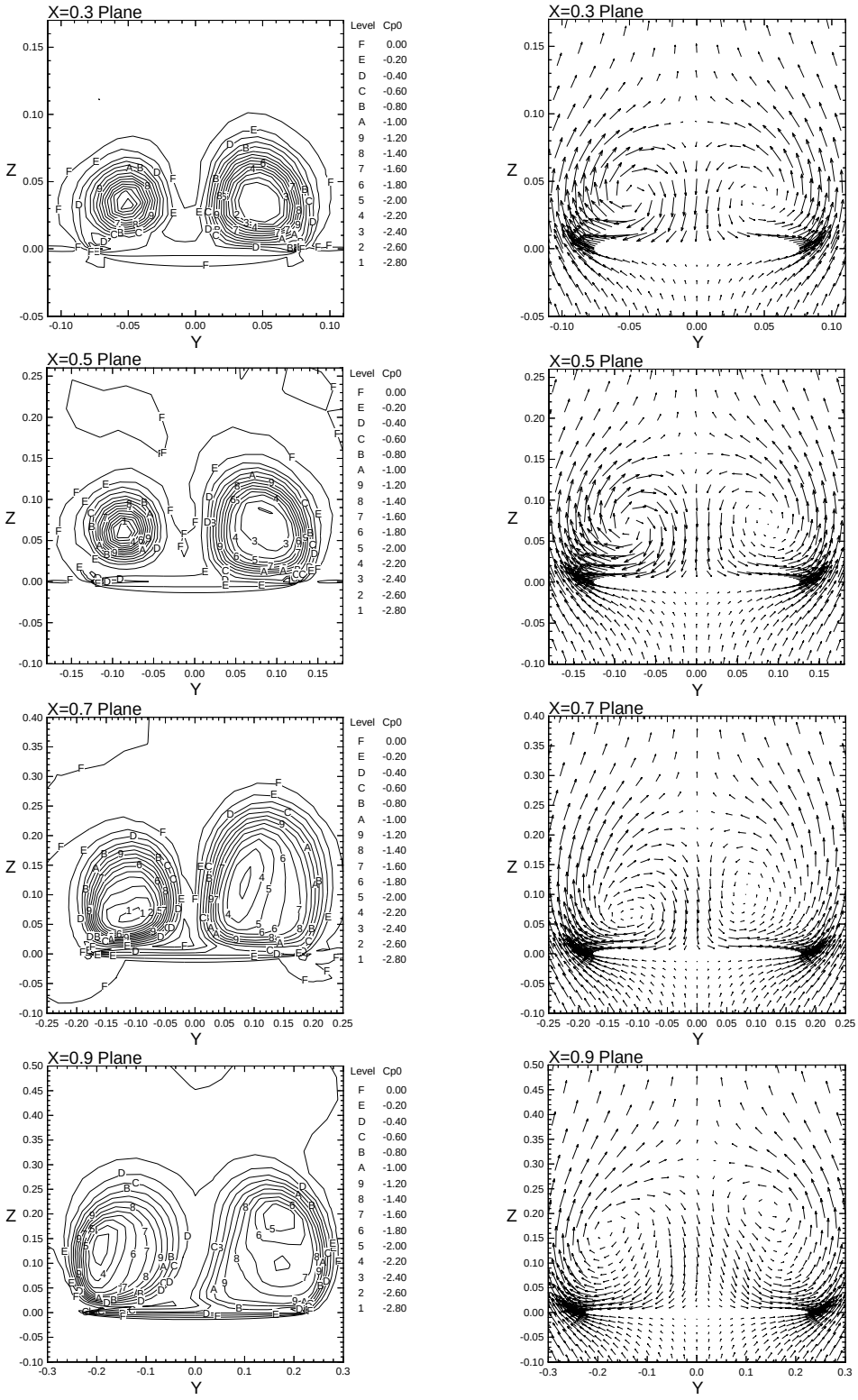

Figure 5.70: Total pressure coefficient and velocity vectors plotted on vertical crossflow planes above wing. Rigid Tail Case: $\tau = 13.2$, $Re = 10^4$, $M = 0.4$, $\alpha = 38^o$.

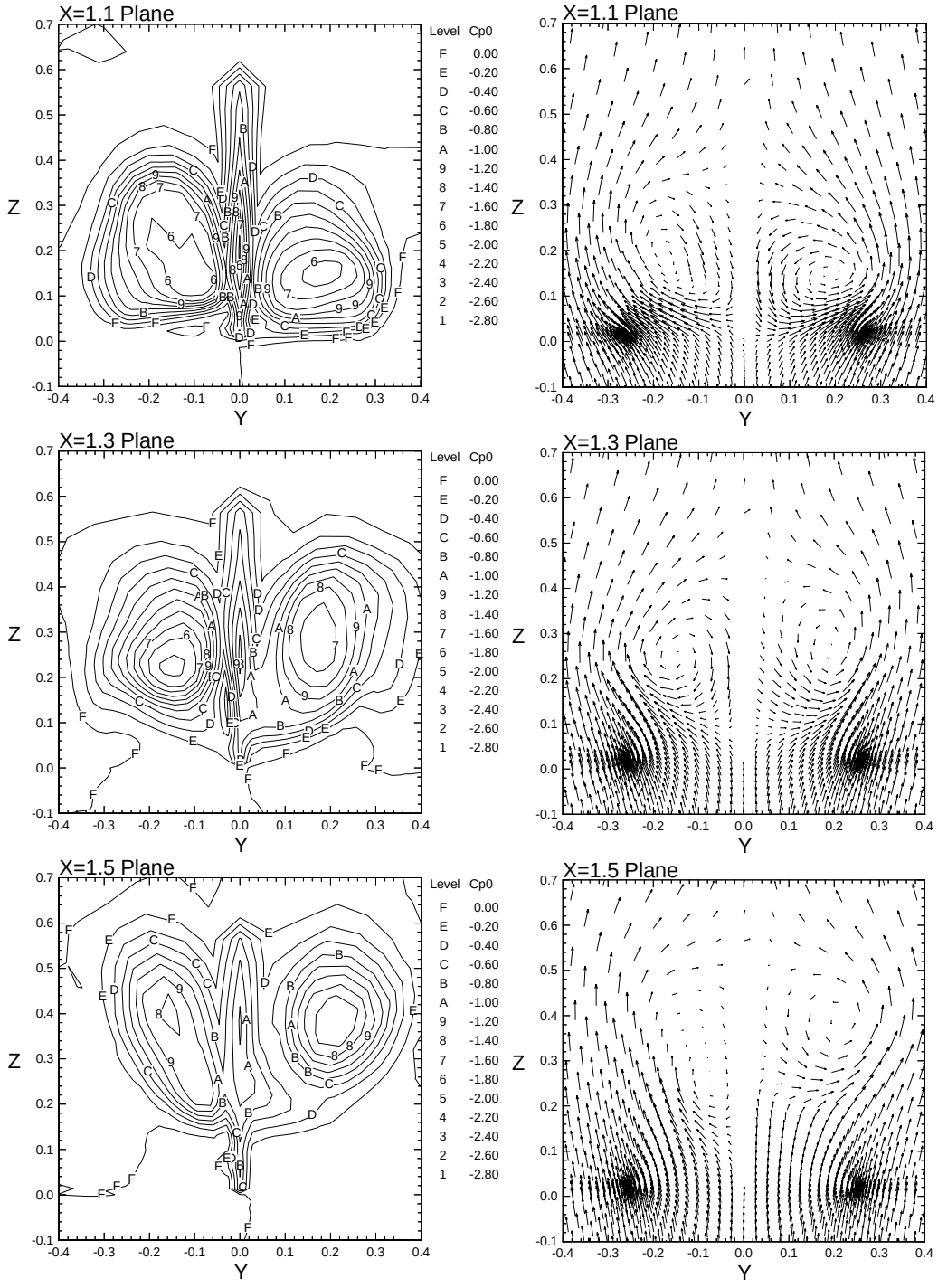

Figure 5.71: Total pressure coefficient and velocity vectors plotted on vertical crossflow planes near the tail. Rigid Tail Case: $\tau = 13.2$, $Re = 10^4$, $M = 0.4$, $\alpha = 38^o$.

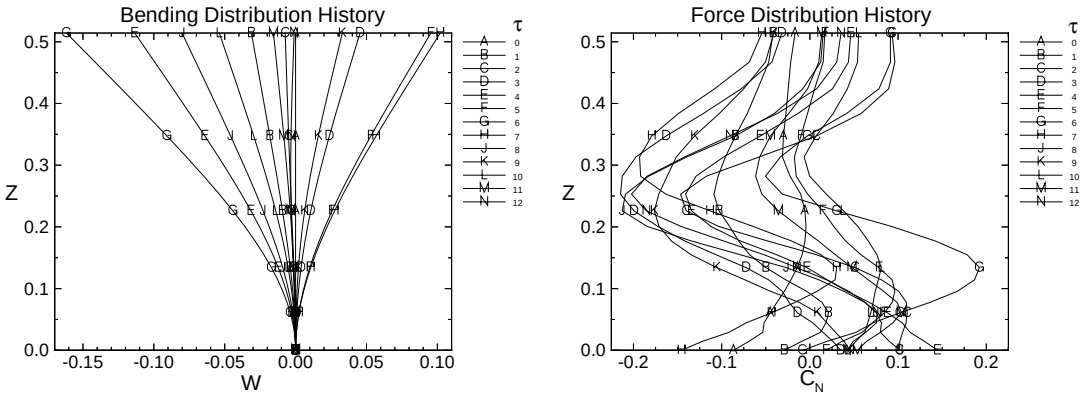

Figure 5.72: Hypothetical Bending deflection and force distributions along the tail span plotted at integer nondimensional time levels. Rigid Tail Case: $Re = 10^6$, $M = 0.4$, $\alpha = 38^o$.

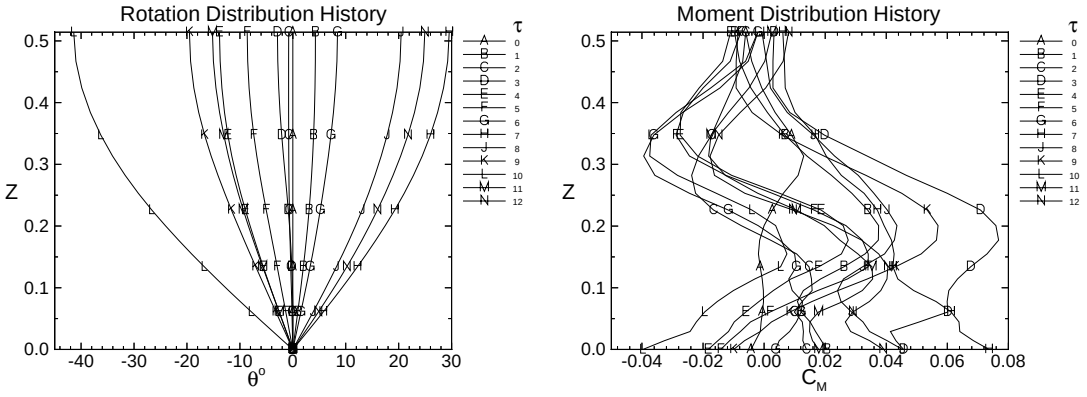

Figure 5.73: Hypothetical torsion deflection and moment distributions along the tail span plotted at integer nondimensional time levels. Rigid Tail Case: $Re = 10^6$, $M = 0.4$, $\alpha = 38^o$.

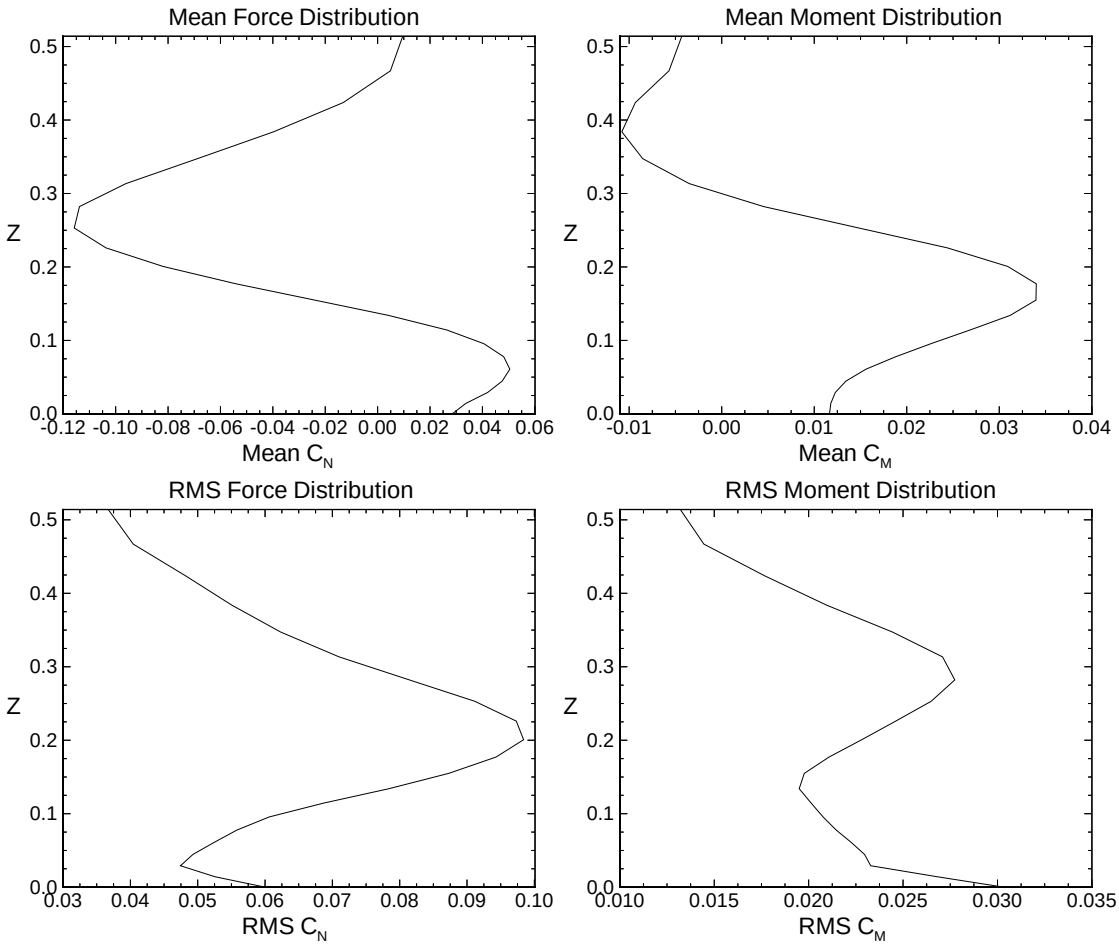

Figure 5.74: Mean and RMS load distributions along the tail span. Rigid Tail Case: $Re = 10^6$, $M = 0.4$, $\alpha = 38^o$.

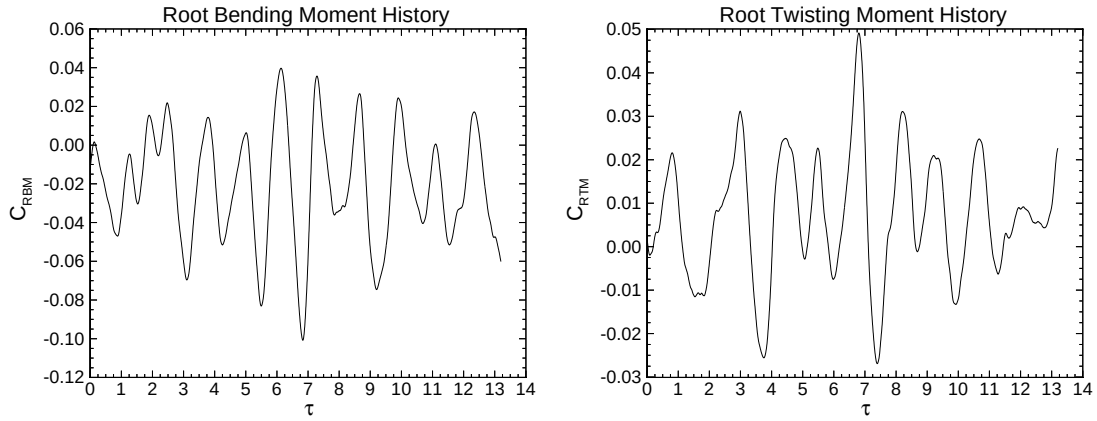

Figure 5.75: History of root bending moment coefficient and root twisting moment coefficient. Rigid Tail Case: $Re = 10^6$, $M = 0.4$, $\alpha = 38^o$.

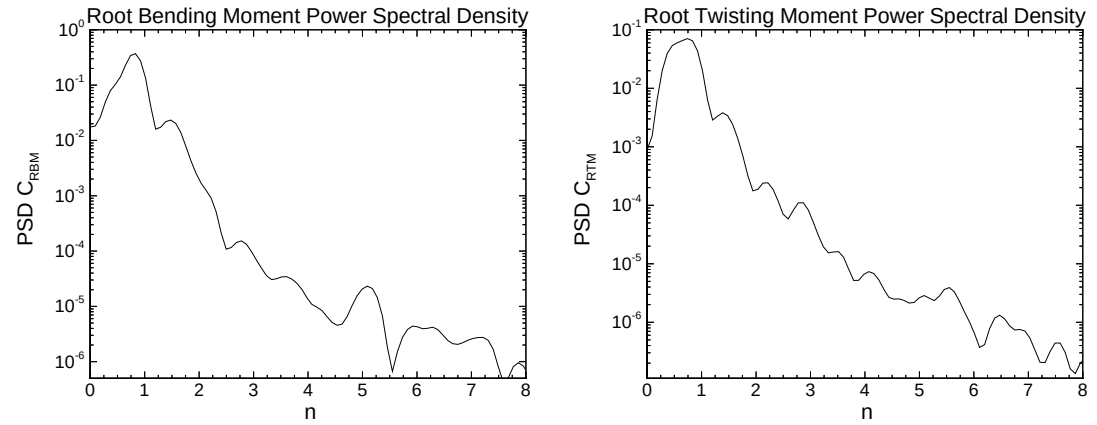

Figure 5.76: Power spectral density of root bending moment coefficient and root twisting moment coefficient versus reduced frequency. Rigid Tail Case: $Re = 10^6$, $M = 0.4$, $\alpha = 38^o$.

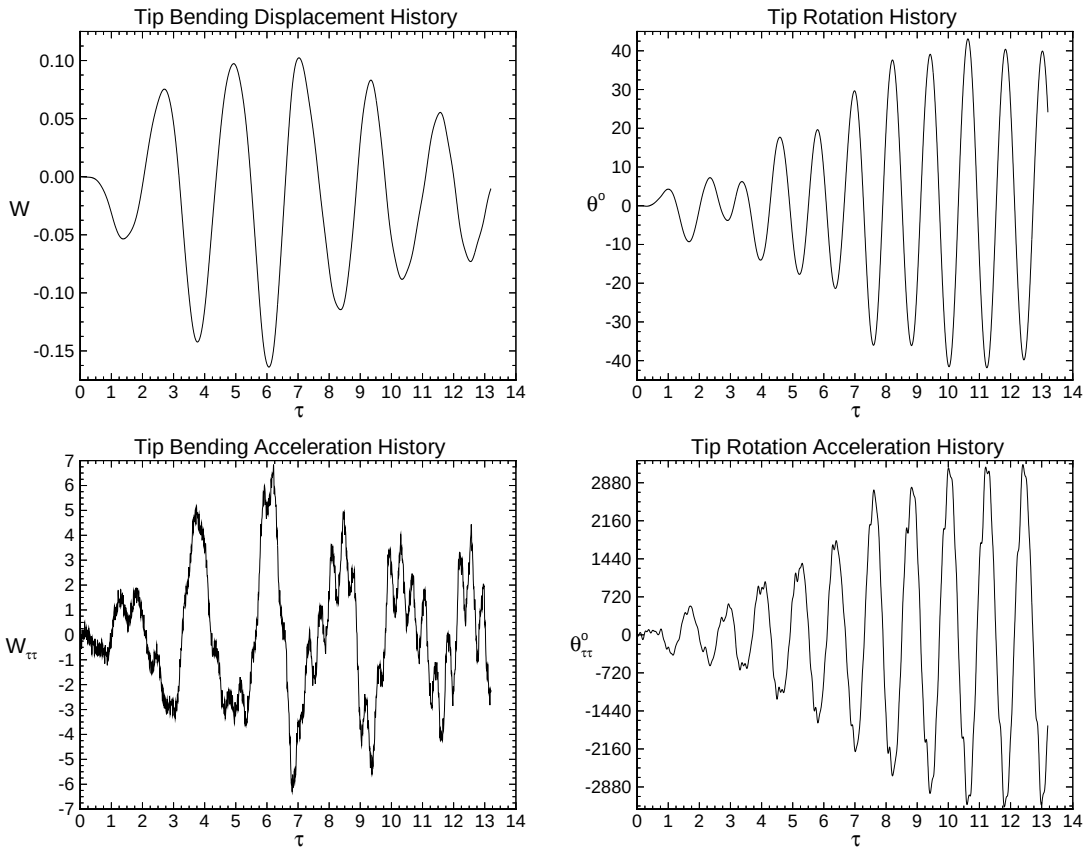

Figure 5.77: History of hypothetical tip bending and torsion deflections and accelerations. Rigid Tail Case: $Re = 10^6$, $M = 0.4$, $\alpha = 38^o$.

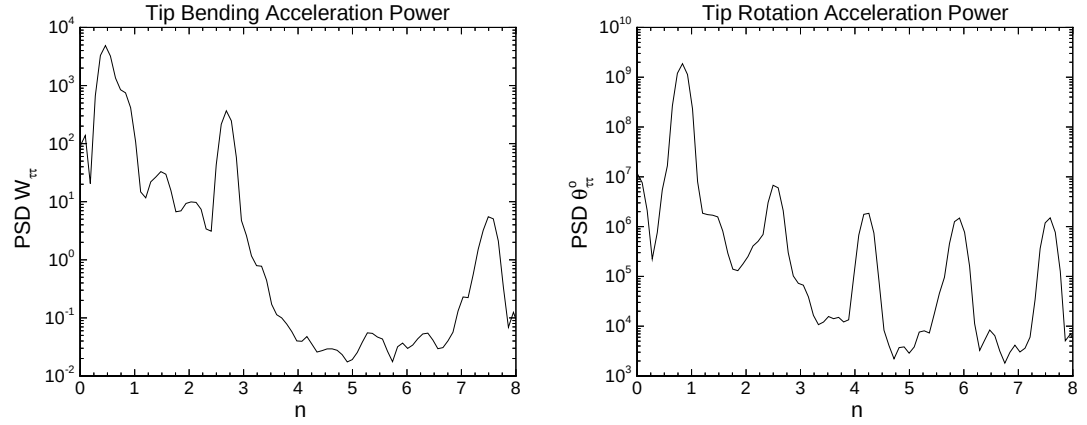

Figure 5.78: Power spectral density of hypothetical tip bending and torsion accelerations versus reduced frequency. Rigid Tail Case: $Re = 10^6$, $M = 0.4$, $\alpha = 38^o$.

5.4.3 Uncoupled Bending and Torsion Response

In this section, the buffeting response due to uncoupled ($x_\theta = 0$) bending and torsion vibrations is considered. Comparison of the results of this case with those of Section 5.3.2 will demonstrate the effect of increased Re on the single tail buffeting response. Comparison with the inertially coupled response in the next section will demonstrate the effect of coupling at high Re.

The global flow field at the end of the buffeting case is plotted in Figures 5.79-5.84. Comparison of these plots with the rigid tail buffeting case of the previous section demonstrates that the motion of the tail has a noticeable effect on the breakdown position, with the right critical point 3%c further aft and the left critical point 7%c farther forward than the locations of the rigid buffeting case at the same time level. Small but noticeable differences also exist in the tail surface flow streamlines, especially at the lower left separation line, Figure 5.81. Inspection of the tail surface C_p plots, Figure 5.82 reveals a more significant difference in the tail flow field. This is particularly noticeable in the differential C_p plots, where the overall range is close, but the distribution of pressure over the tail surface is significantly different. Comparing the crossflow plots, Figures 5.83 and 5.84, with the rigid case, confirms that with increasing distance upstream of the tail the flow is less disturbed. This fact is also shown in the C_p plots, Figure 5.79, where the spanwise variation of C_p at the $x = 0.3$ and $x = 0.5$ chord stations match closely with the rigid case, while the last two at $x = 0.7$ and $x = 0.9$ differ on the right side.

The mean and RMS load distributions in Figure 5.87 show that while the mean loads of the present case are very similar to the rigid case, the RMS loads are very different in both magnitude and distribution. The clearest depiction of the effects of fluid-structure interaction on the buffet loading is shown in the time and frequency domain

data of Figures 5.88 and 5.89. The mean and RMS root moment values, maximum amplitudes and dominant frequencies are summarized in Table 5.9. A key difference between the present case and the rigid loading is that while the bending moment became less periodic the root twisting moment become more periodic. This can also be seen in the PSD plots shown in Figure 5.89 where the bending frequency peak split into two peaks and the twisting frequency peak became narrower. In addition to the changes in frequency, the magnitude of the root twisting moment is 46% higher than the rigid tail case while the root bending moment is 11% lower, see Table 5.10.

The maximum amplitudes of the tip displacements, accelerations and the first two dominant frequencies are summarized in Table 5.11. As expected the present buffeting response is much lower than the hypothetical response calculated from the rigid loading. This is because the rigid case had no source of damping.

With the effects of fluid-structure interactions established, the second issue of this case is the effect of increased Re on the buffet loading and response. Comparison of the loading and response summaries of the present high Re case, shown in Tables 5.9 and 5.11, with the low Re case of Section 5.3.2, see Tables 5.3 and 5.4, indicate that the increase in Re increases the buffet loading and response magnitudes by only a small amount due to a decrease in aerodynamic damping. This loss of damping is also clearly visible in the increased high-frequency content of the loading and especially the response, see Figures 5.89 and 5.91. In Tables 5.12 and 5.13, the effects of Re on the uncoupled bending and torsion buffet loads and response are summarized.

Root Loads									
C_{RBM}					C_{RTM}				
Mean	RMS	A	n_{d1}	n_{d2}	Mean	RMS	A	n_{d1}	n_{d2}
-0.031	0.035	0.062	0.5	1.0	0.0089	0.034	0.057	0.5	2.0

Table 5.9: Summary of root bending and twisting moment statistics, maximum amplitudes and dominant frequencies. Uncoupled Bending and Torsion Case: $Re = 10^6$, $M = 0.4$, $\alpha = 38^o$.

	Root Loads							
	C_{RBM}				C_{RTM}			
Case	RMS	A	n_{d1}	n_{d2}	RMS	A	n_{d1}	n_{d2}
3	0.029	0.070	0.75	1.5	0.014	0.039	0.75	1.5
4	0.035	0.062	0.5	1.0	0.034	0.057	0.5	2.0
% Difference	21%	-11%	-33%	-33%	143%	46%	-33%	33%

Table 5.10: Effect of fluid/structure interaction on root loading.

Tip Response							
Bending				Torsion			
$A(w)$	$A(w_{\tau\tau})$	n_{d1}	n_{d2}	$A(\theta)^o$	$A(\theta_{\tau\tau})^o$	n_{d1}	n_{d2}
0.082	4.8	0.5	2.0	10.8	470	0.5	2.0

Table 5.11: Summary of tip displacement and acceleration statistics, maximum amplitudes and dominant frequencies. Uncoupled Bending and Torsion Case: $Re = 10^6$, $M = 0.4$, $\alpha = 38^o$.

	Root Loads			
	C_{RBM}		C_{RTM}	
	A	n_{d1}	A	n_{d1}
$Re = 10^4$	0.060	0.75	0.057	0.45
$Re = 10^6$	0.062	0.5	0.057	0.5
% Difference	3%	-50%	0%	13%

Table 5.12: Effect of increased Reynolds number on root loading.

	Tip Response					
	Bending			Torsion		
	$A(w)$	$A(w_{\tau\tau})$	n_{d1}	$A(\theta)^o$	$A(\theta_{\tau\tau})^o$	n_{d1}
$Re = 10^4$	0.082	3.5	0.45	9.8	420	0.45
$Re = 10^6$	0.082	4.8	0.5	10.8	470	0.5
% Difference	0%	37%	11%	10%	12%	13%

Table 5.13: Effect of increased Reynolds number tip response.

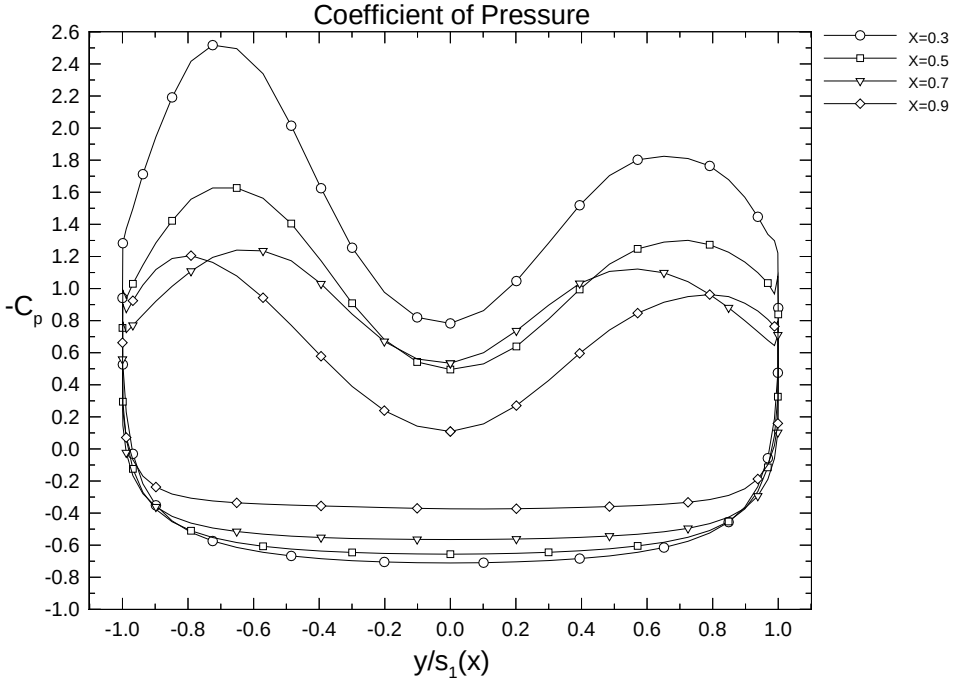

Figure 5.79: Coefficient of pressure on upper and lower wing surfaces at chord stations corresponding to plotted crossflow planes. Uncoupled Bending and Torsion Case: $\tau = 13.2$, $Re = 10^6$, $M = 0.4$, $\alpha = 38^o$.

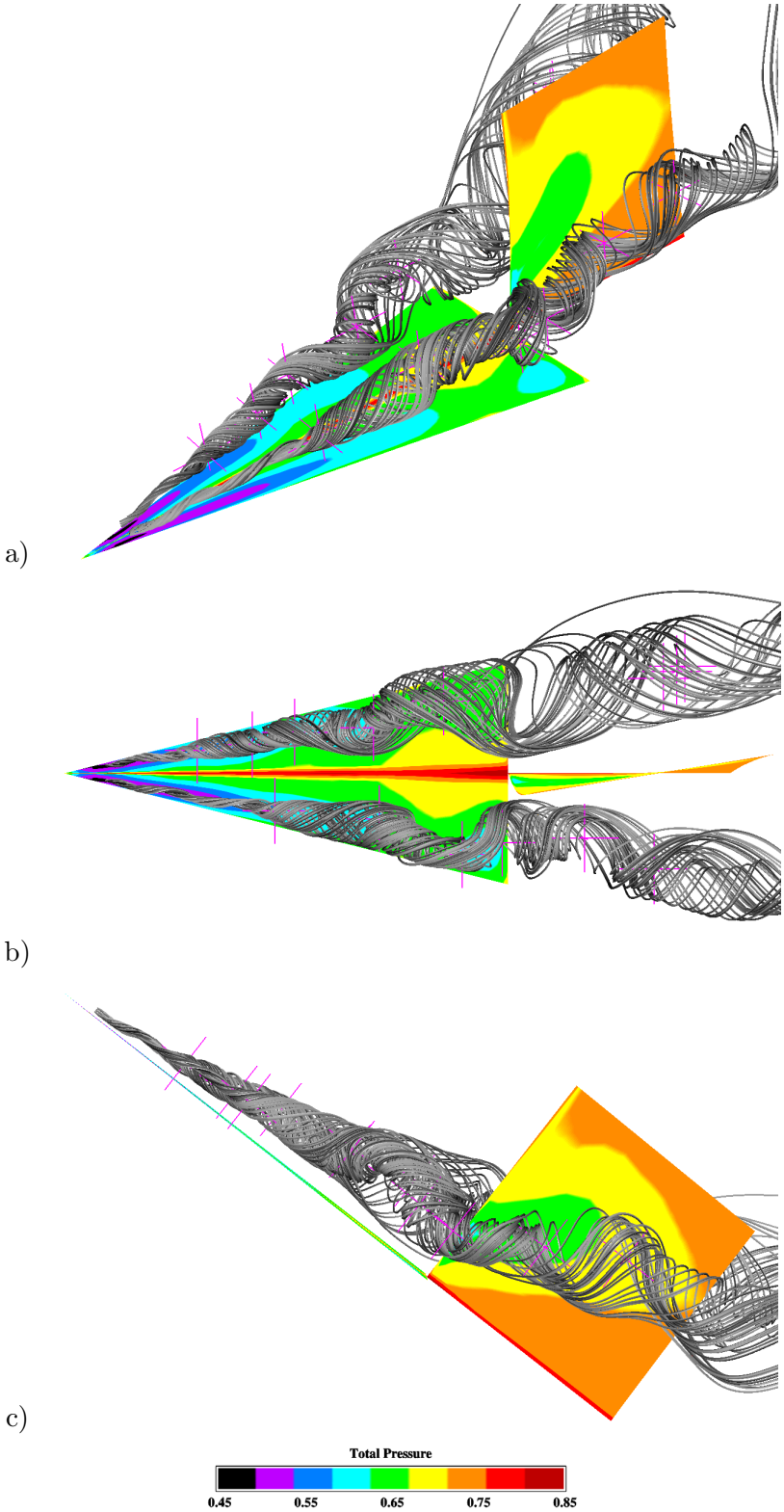

Figure 5.80: a) Three-dimensional, b) top and c) side views of surface pressure and vortex core streamlines at $\tau = \frac{tU_\infty}{\bar{c}} = 13.2$ and $\Delta\tau = 0.00132$. Purple crosses denote critical points associated with either attracting or repelling spiral saddle points. Uncoupled Bending and Torsion Case: $Re = 10^6$, $M = 0.4$, $\alpha = 38^o$.

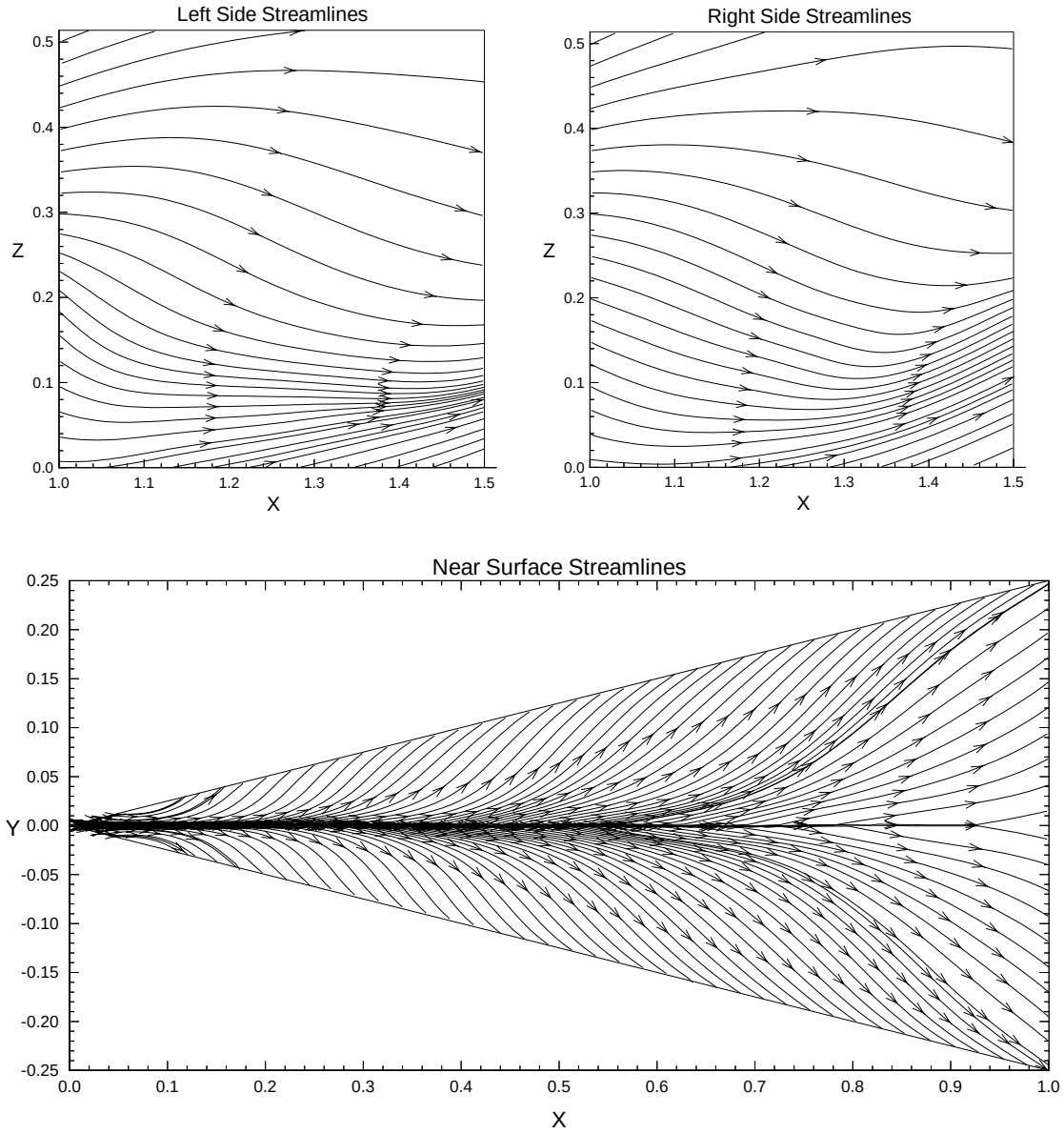

Figure 5.81: Near surface streamlines at $\tau = 13.2$. Uncoupled Bending and Torsion Case: $Re = 10^6$, $M = 0.4$, $\alpha = 38^o$.

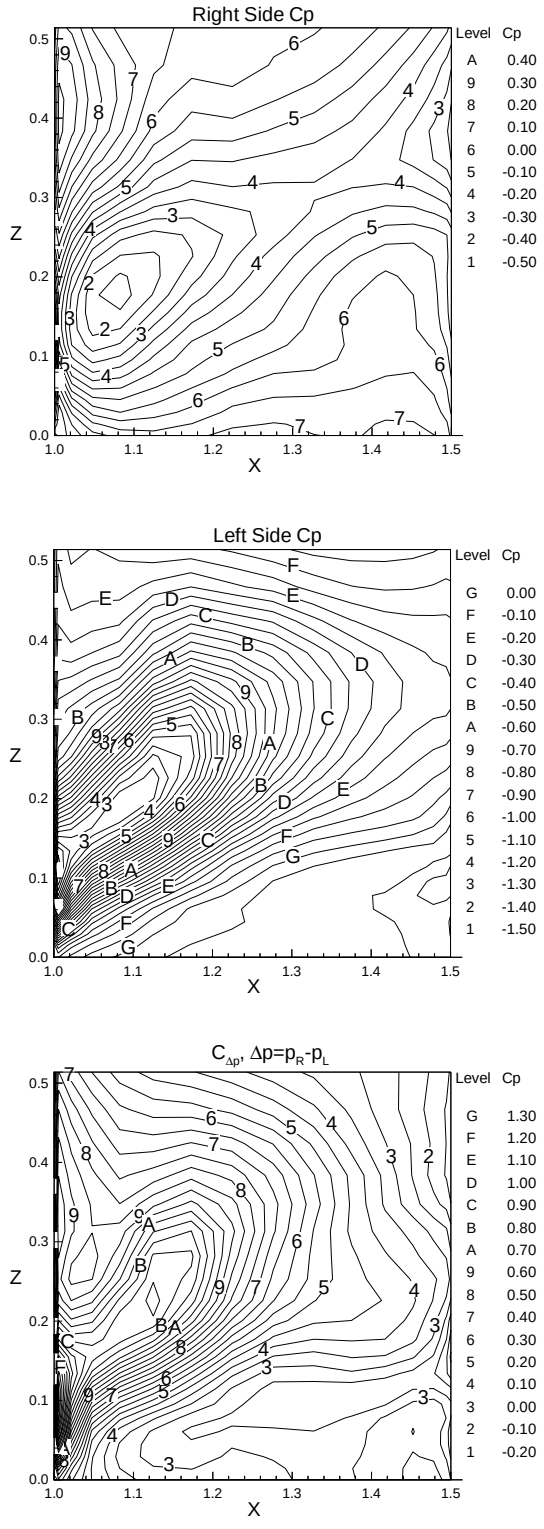

Figure 5.82: Coefficient of pressure on right and left sides of tail, and differential pressure coefficient. Uncoupled Bending and Torsion Case: $\tau = 13.2$, $Re = 10^6$, $M = 0.4$, $\alpha = 38^o$.

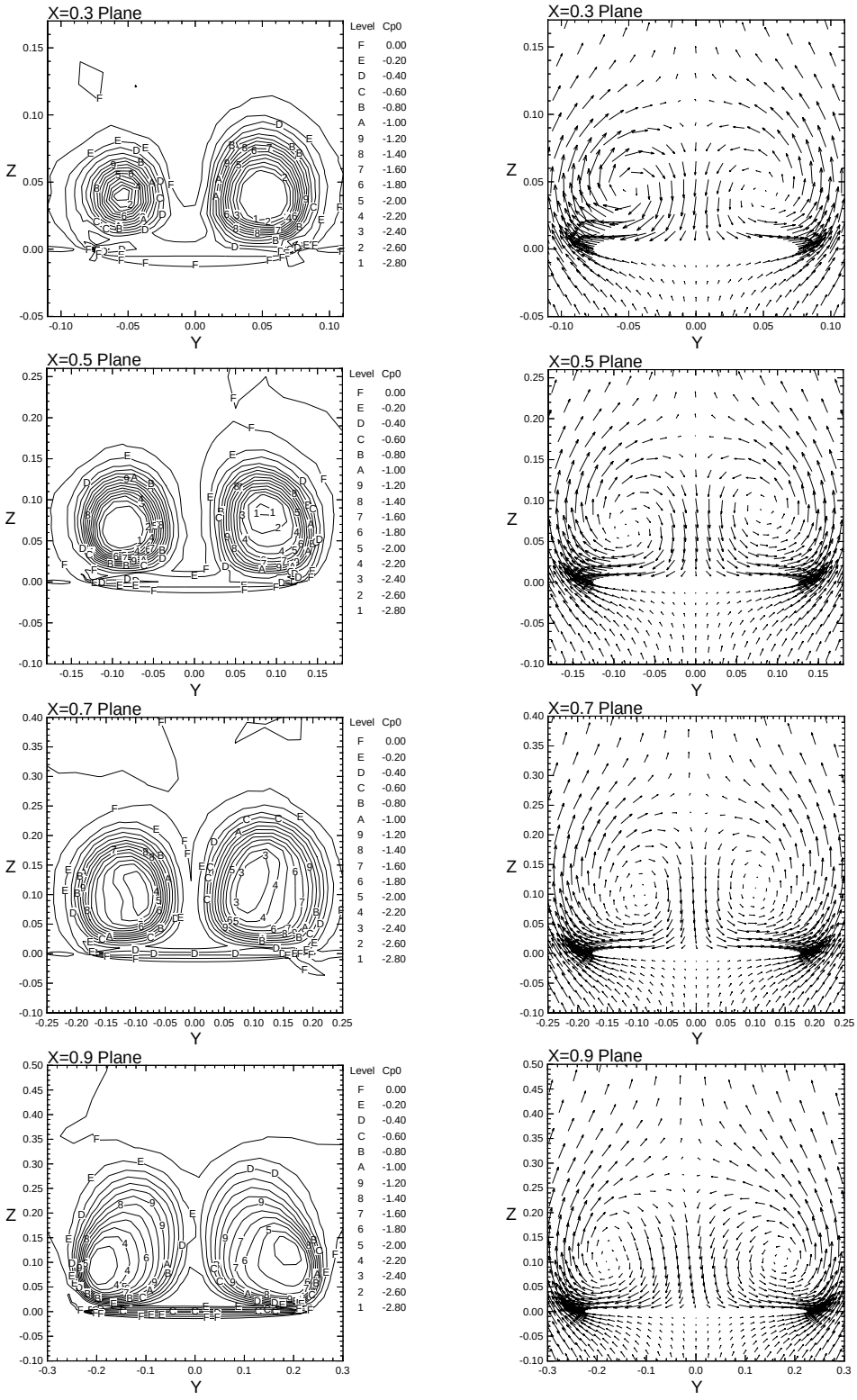

Figure 5.83: Total pressure coefficient and velocity vectors plotted on vertical crossflow planes above wing. Uncoupled Bending and Torsion Case: $\tau = 13.2$, $Re = 10^6$, $M = 0.4$, $\alpha = 38^o$.

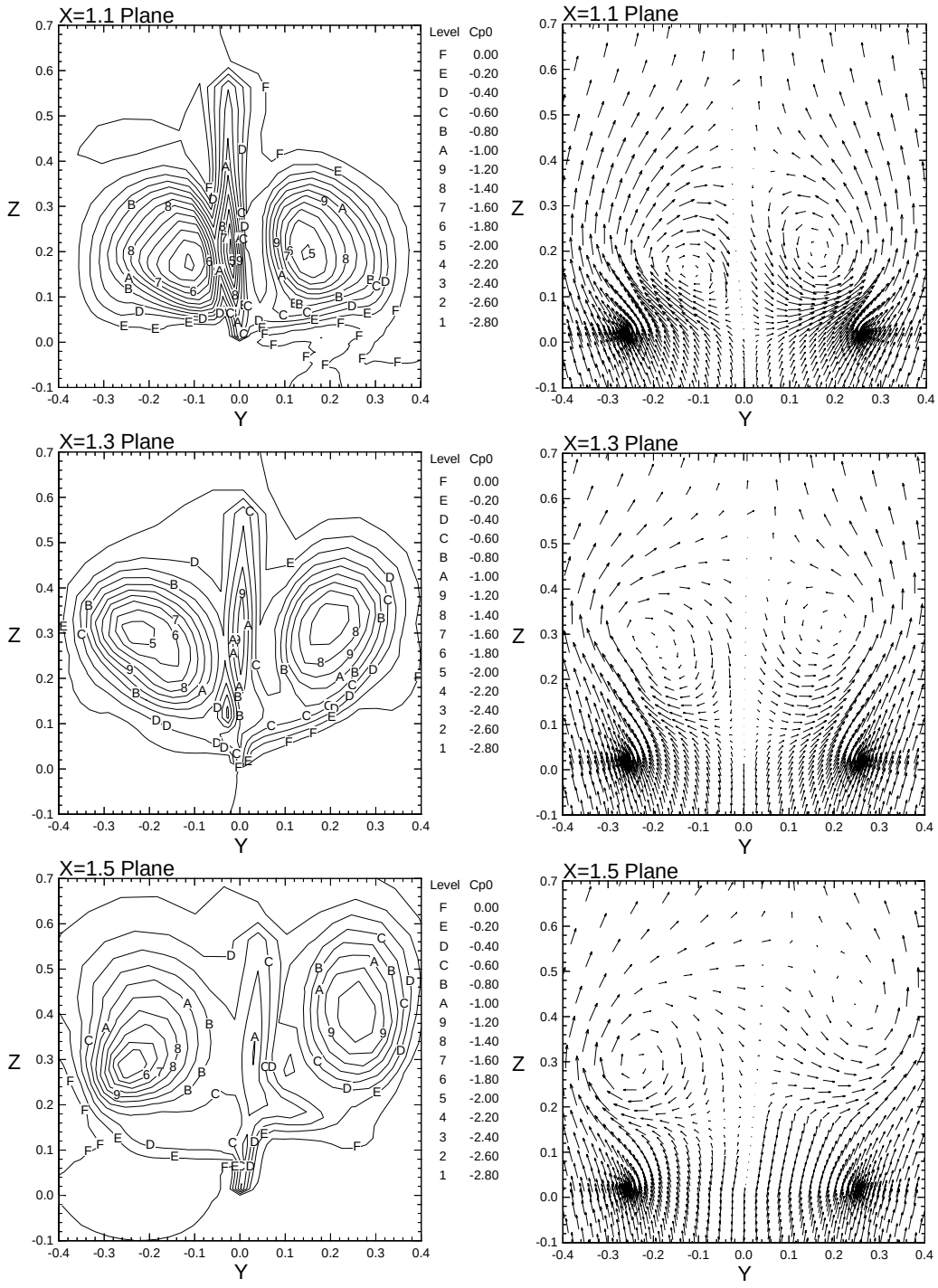

Figure 5.84: Total pressure coefficient and velocity vectors plotted on vertical crossflow planes near the tail. Uncoupled Bending and Torsion Case: $\tau = 13.2$, $Re = 10^6$, $M = 0.4$, $\alpha = 38^o$.

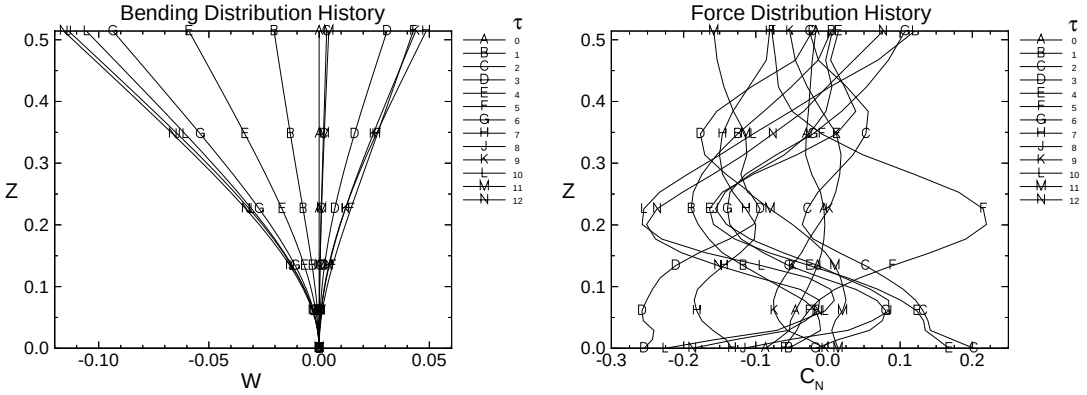

Figure 5.85: Bending deflection and force distributions along the tail span plotted at integer nondimensional time levels. Uncoupled Bending and Torsion Case: $Re = 10^6$, $M = 0.4$, $\alpha = 38^o$.

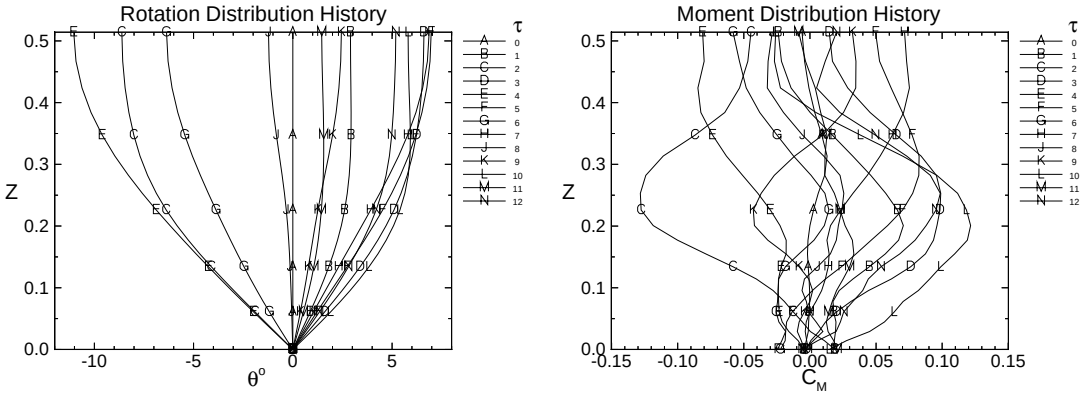

Figure 5.86: Torsion deflection and moment distributions along the tail span plotted at integer nondimensional time levels. Uncoupled Bending and Torsion Case: $Re = 10^6$, $M = 0.4$, $\alpha = 38^o$.

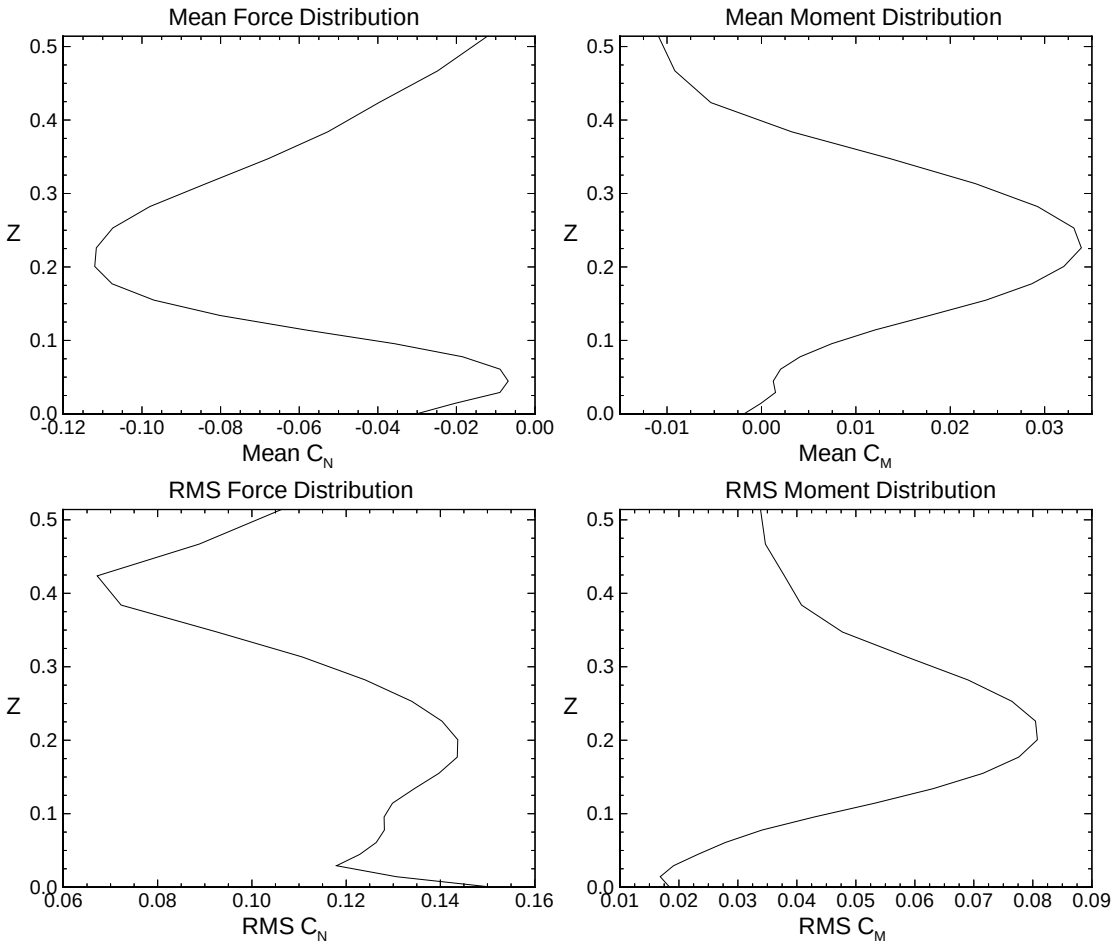

Figure 5.87: Mean and RMS load distributions along the tail span. Uncoupled Bending and Torsion Case: $Re = 10^6$, $M = 0.4$, $\alpha = 38^o$.

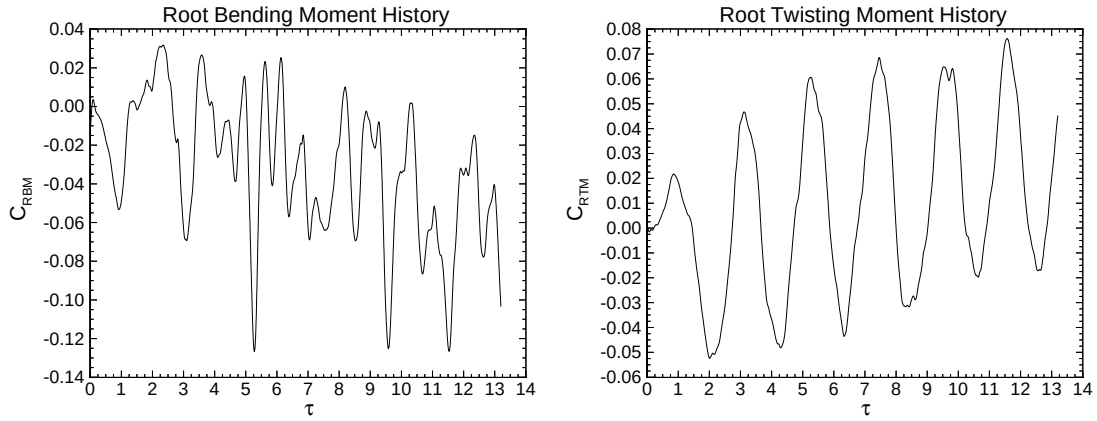

Figure 5.88: History of root bending moment coefficient and root twisting moment coefficient. Uncoupled Bending and Torsion Case: $Re = 10^6$, $M = 0.4$, $\alpha = 38^o$.

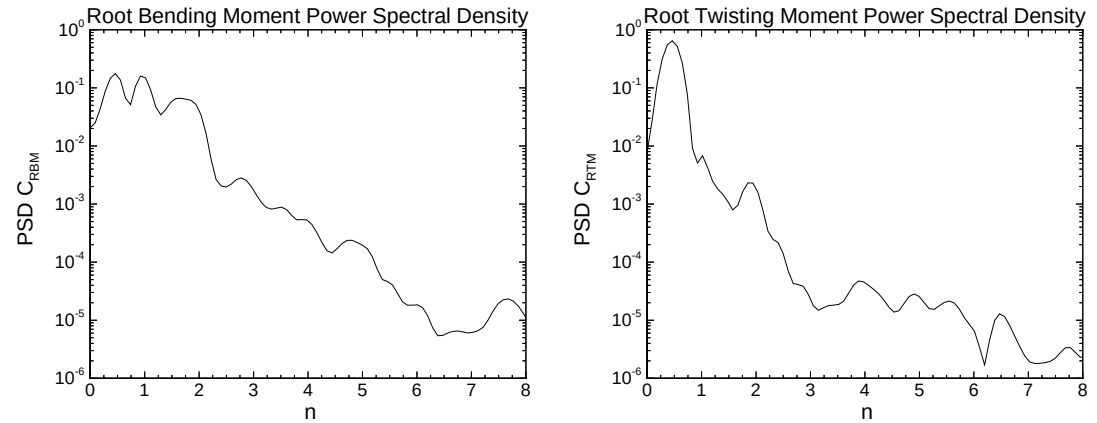

Figure 5.89: Power spectral density of root bending moment coefficient and root twisting moment coefficient versus reduced frequency. Uncoupled Bending and Torsion Case: $Re = 10^6$, $M = 0.4$, $\alpha = 38^o$.

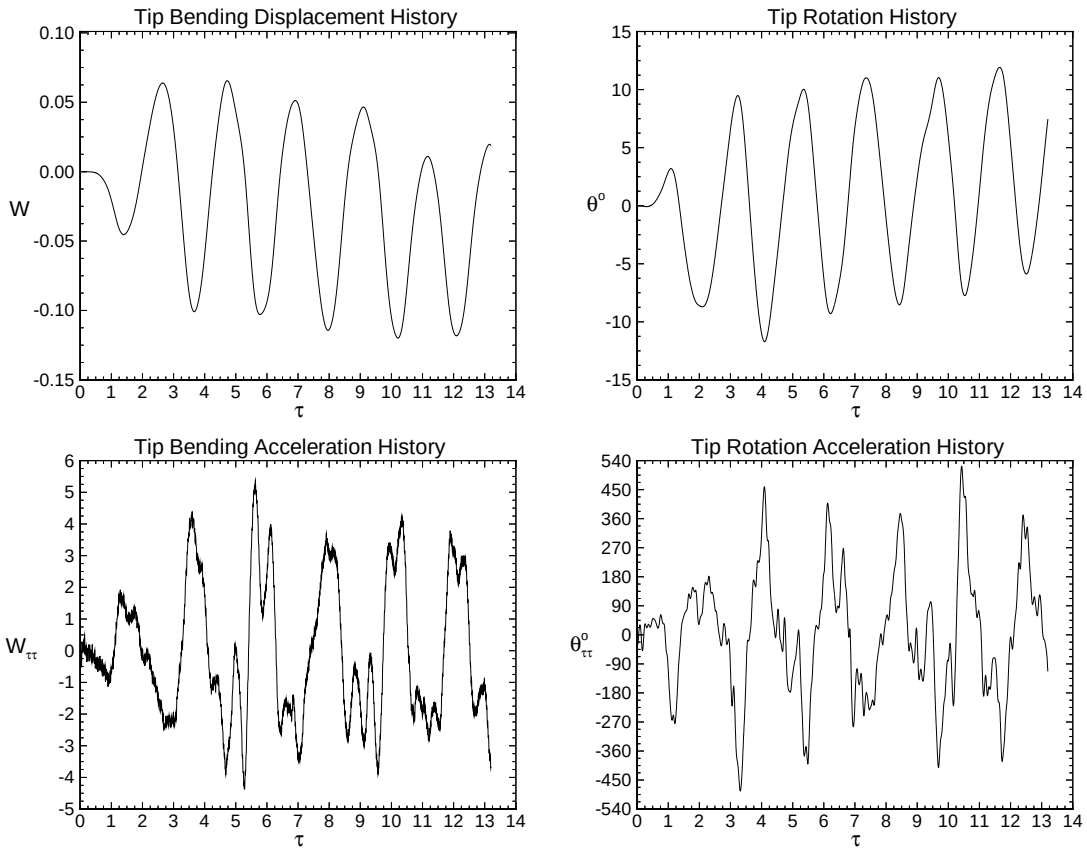

Figure 5.90: History of tip bending and torsion deflections and accelerations. Uncoupled Bending and Torsion Case: $Re = 10^6$, $M = 0.4$, $\alpha = 38^o$.

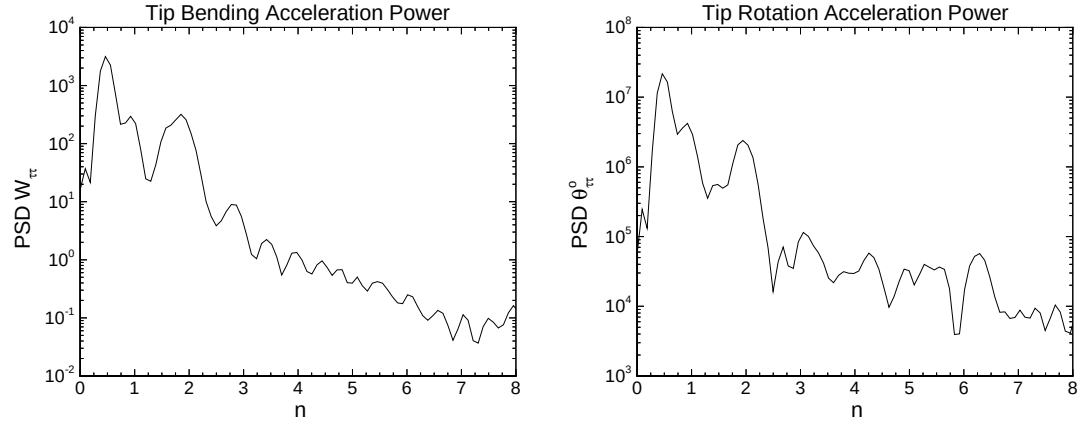

Figure 5.91: Power spectral density of tip bending and torsion accelerations versus reduced frequency. Uncoupled Bending and Torsion Case: $Re = 10^6$, $M = 0.4$, $\alpha = 38^o$.

5.4.4 Coupled Bending and Torsion Response

In this section, the high Reynolds number buffeting response due to inertially coupled bending and torsion vibrations is considered. The purpose of this case is to assess the effect of inertial coupling on the buffeting response in a moderately high Re flow.

Figures 5.92-5.97 show the global flow field at the same time level as the rigid and uncoupled high Re cases of the previous two sections. Examining the spanwise C_p plot at $x = 0.3$, Figure 5.92 confirms the change in position of the right vortex breakdown location as shown in the 3-D streamline plots, given in Figure 5.93. In the previous high Re cases, the right core burst near the 28%c station. In the present case, the right core does not burst until 65%. In all three high Re cases, the left core burst near 53%. Thus, the global flow including the breakdown location is seen to be influenced significantly by the motion of the tail. Note, video animation of the present case has shown that the breakdown locations on both sides are very unsteady. So the breakdown locations are only relevant to a single time level and thus do not indicate any long term bias.

The time and frequency domain load plots, Figures 5.101 and 5.102, indicate that the coupling of the bending and torsional modes has a strong effect on the bending moment history, in frequency and amplitude. This is due to the strong influence the twisted tail exerts on the aerodynamics. The response plots, Figures 5.103 and 5.104, show an increase of over a 100% in all deflections and accelerations. Another sign of the strong aeroelastic coupling, is the attainment of periodicity for this case. Examining the acceleration histories for $\tau > 7$ shows a complex, but repeating pattern for three cycles in both bending and torsion responses. In Tables 5.14 and 5.15, the root moment loads and tip responses are summarized and compared with the uncoupled low Re case.

Case	Root Loads									
	C_{RBM}					C_{RTM}				
	Mean	RMS	A	n_{d1}	n_{d2}	Mean	RMS	A	n_{d1}	n_{d2}
Uncoupled	-0.031	0.035	0.062	0.5	1.0	0.0089	0.034	0.057	0.5	2.0
Coupled	-0.0065	0.067	0.122	0.5	2.0	-0.0024	0.069	0.114	0.5	1.5
% Diff	80%	91%	98%	0%	100%	-127%	103%	100%	0%	-25%

Table 5.14: Effect of inertial coupling on root moment loads at $Re = 10^6$, $M = 0.4$, $\alpha = 38^o$.

Case	Tip Response							
	Bending				Torsion			
	$A(w)$	$A(w_{\tau\tau})$	n_{d1}	n_{d2}	$A(\theta)^o$	$A(\theta_{\tau\tau})^o$	n_{d1}	n_{d2}
Uncoupled	0.082	4.8	0.5	2.0	10.8	470	0.5	2.0
Coupled	0.181	10.0	0.5	2.13	23.4	1220	0.5	2.0
% Diff	120%	1.08%	0%	7%	117%	160%	0%	0%

Table 5.15: Effect of inertial coupling on tip response at $Re = 10^6$, $M = 0.4$, $\alpha = 38^o$.

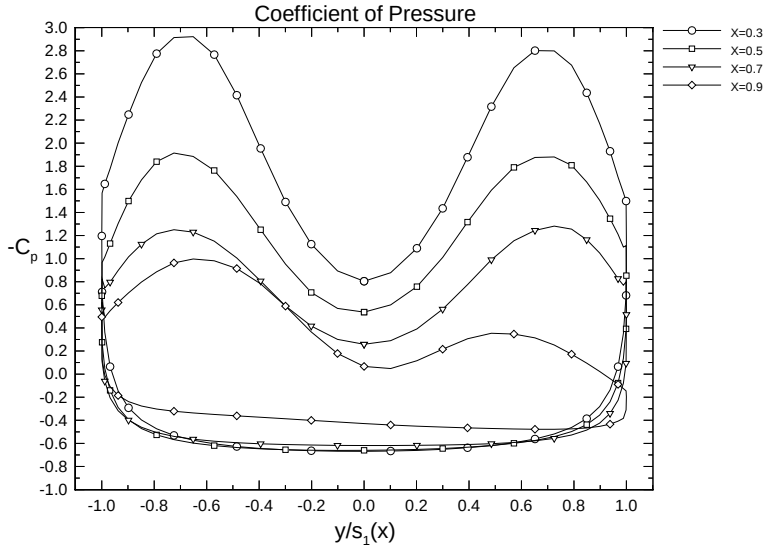

Figure 5.92: Coefficient of pressure on upper and lower wing surfaces at chord stations corresponding to plotted crossflow planes. Coupled Bending and Torsion Case: $\tau = 13.2$, $Re = 10^6$, $M = 0.4$, $\alpha = 38^o$.

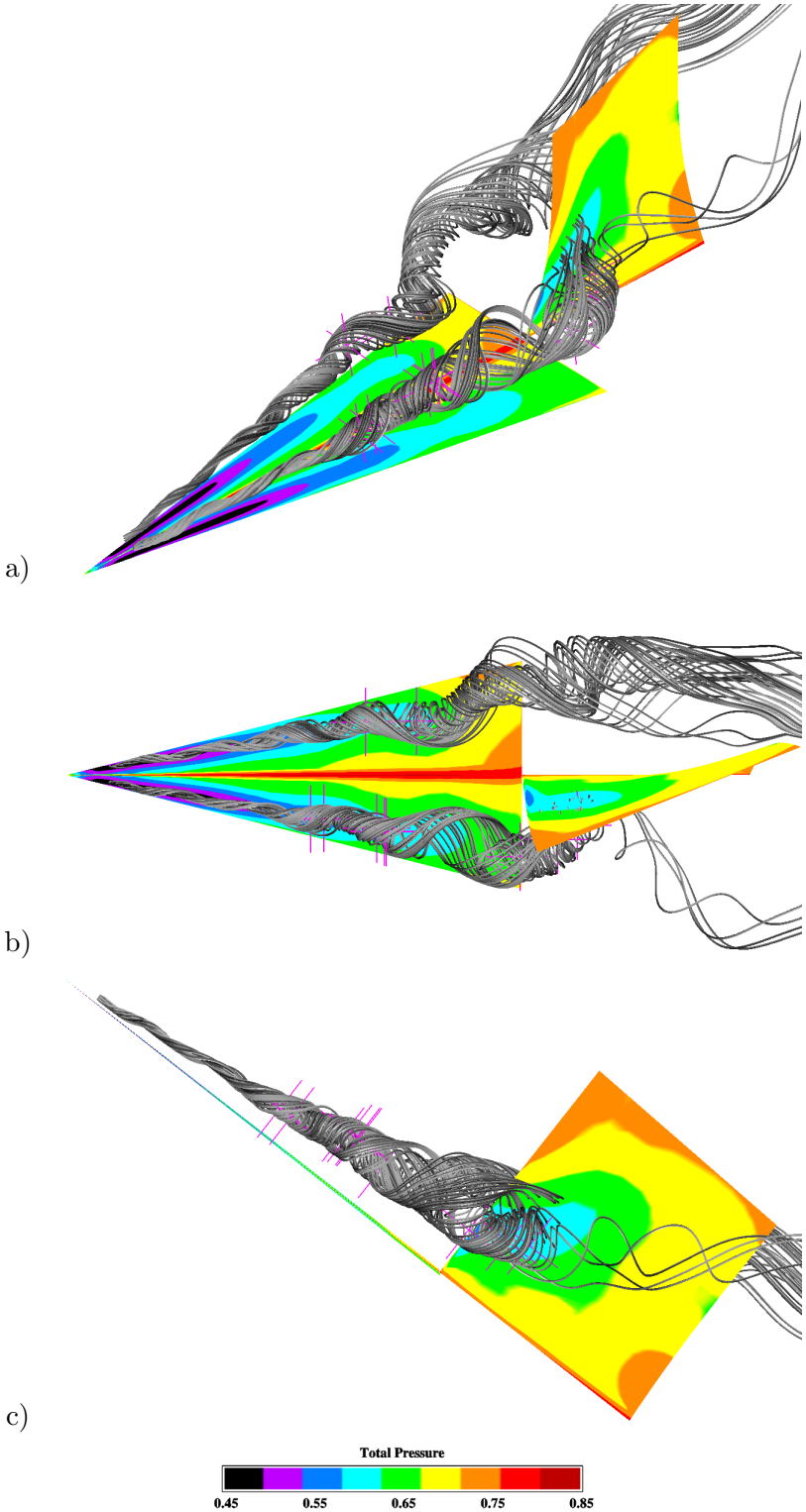

Figure 5.93: a) Three-dimensional, b) top and c) side views of surface pressure and vortex core streamlines at $\tau = \frac{tU_\infty}{c} = 13.2$ and $\Delta\tau = 0.00132$. Purple crosses denote critical points associated with either attracting or repelling spiral saddle points. Coupled Bending and Torsion Case: $Re = 10^6$, $M = 0.4$, $\alpha = 38^o$.

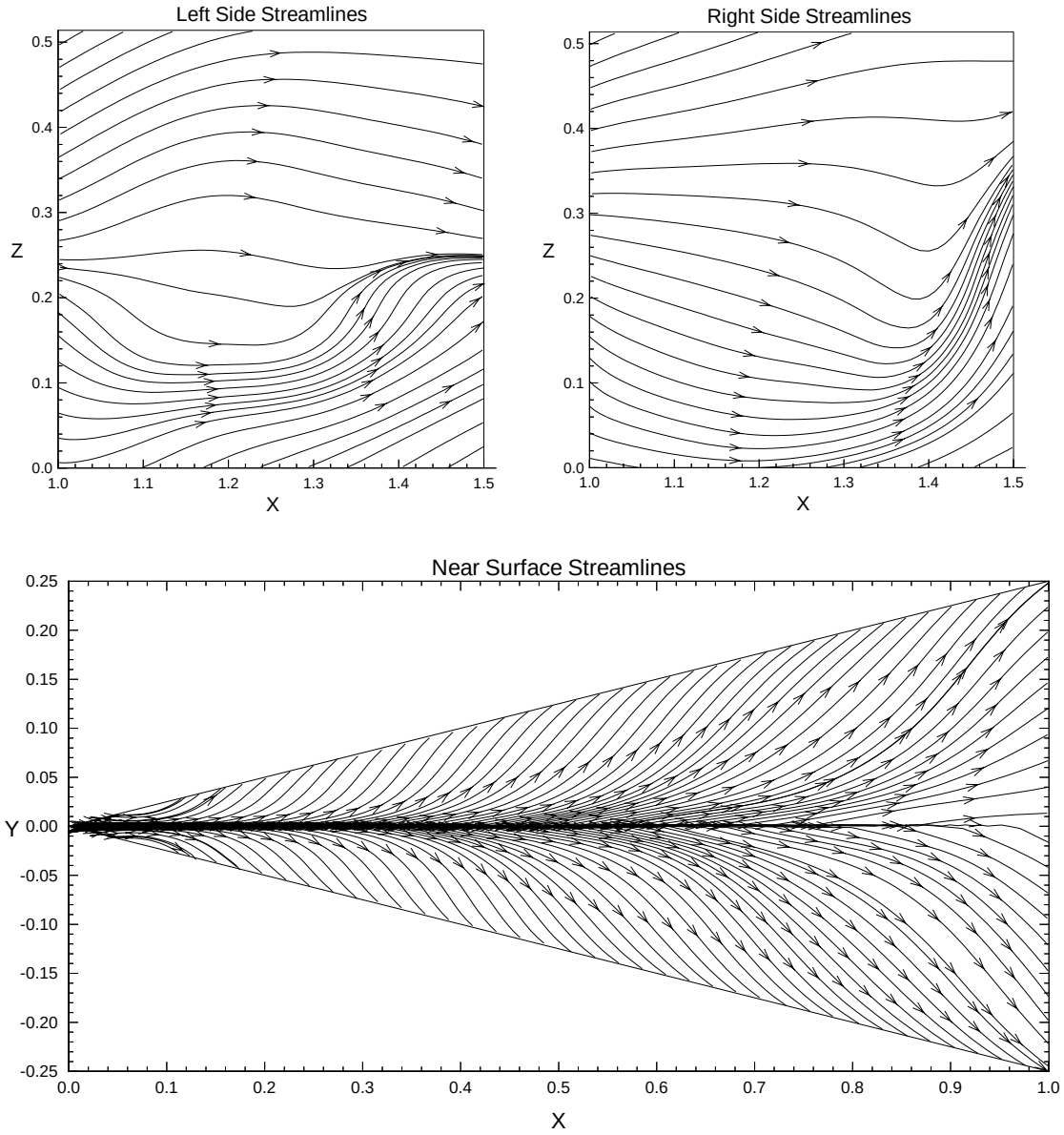

Figure 5.94: Near surface streamlines at $\tau = 13.2$. Coupled Bending and Torsion Case: $Re = 10^6$, $M = 0.4$, $\alpha = 38^o$.

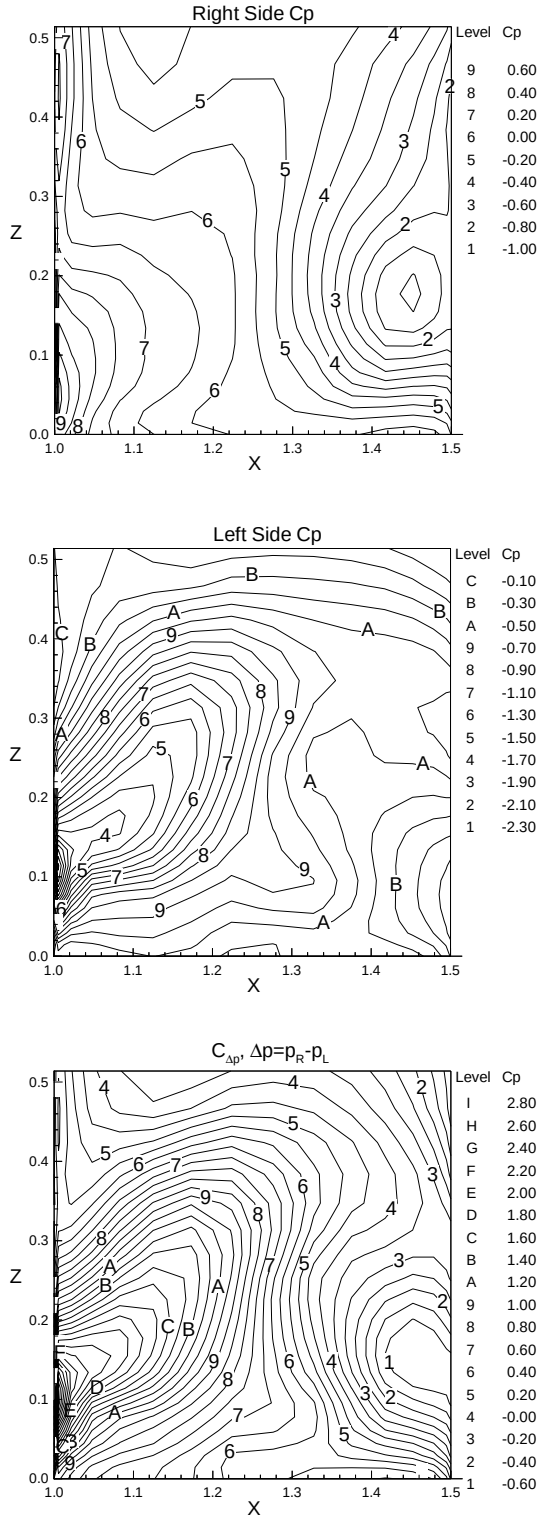

Figure 5.95: Coefficient of pressure on right and left sides of tail, and differential pressure coefficient. Coupled Bending and Torsion Case: $\tau = 13.2$, $Re = 10^6$, $M = 0.4$, $\alpha = 38^o$.

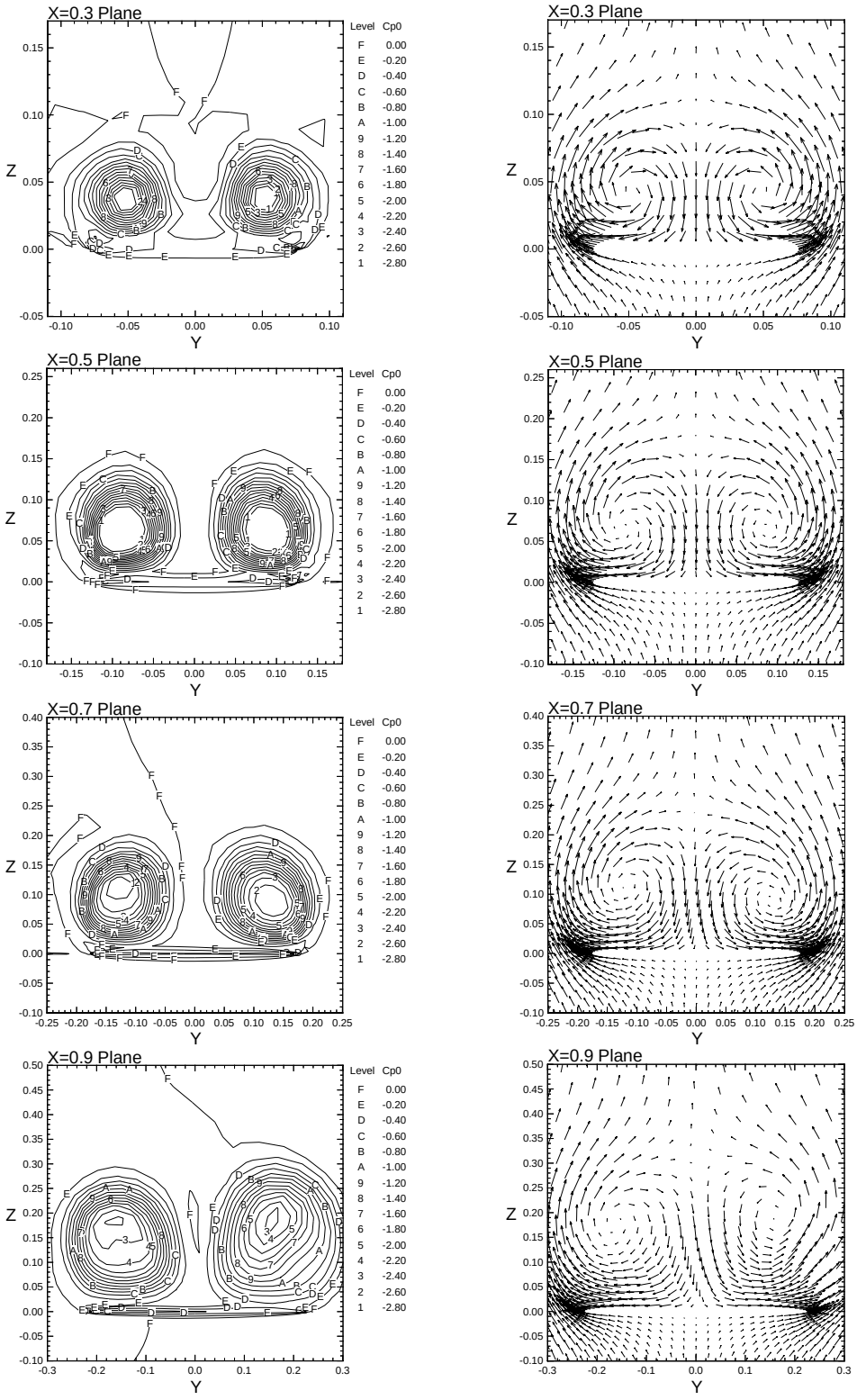

Figure 5.96: Total pressure coefficient and velocity vectors plotted on vertical crossflow planes above wing. Coupled Bending and Torsion Case: $\tau = 13.2$, $Re = 10^6$, $M = 0.4$, $\alpha = 38^o$.

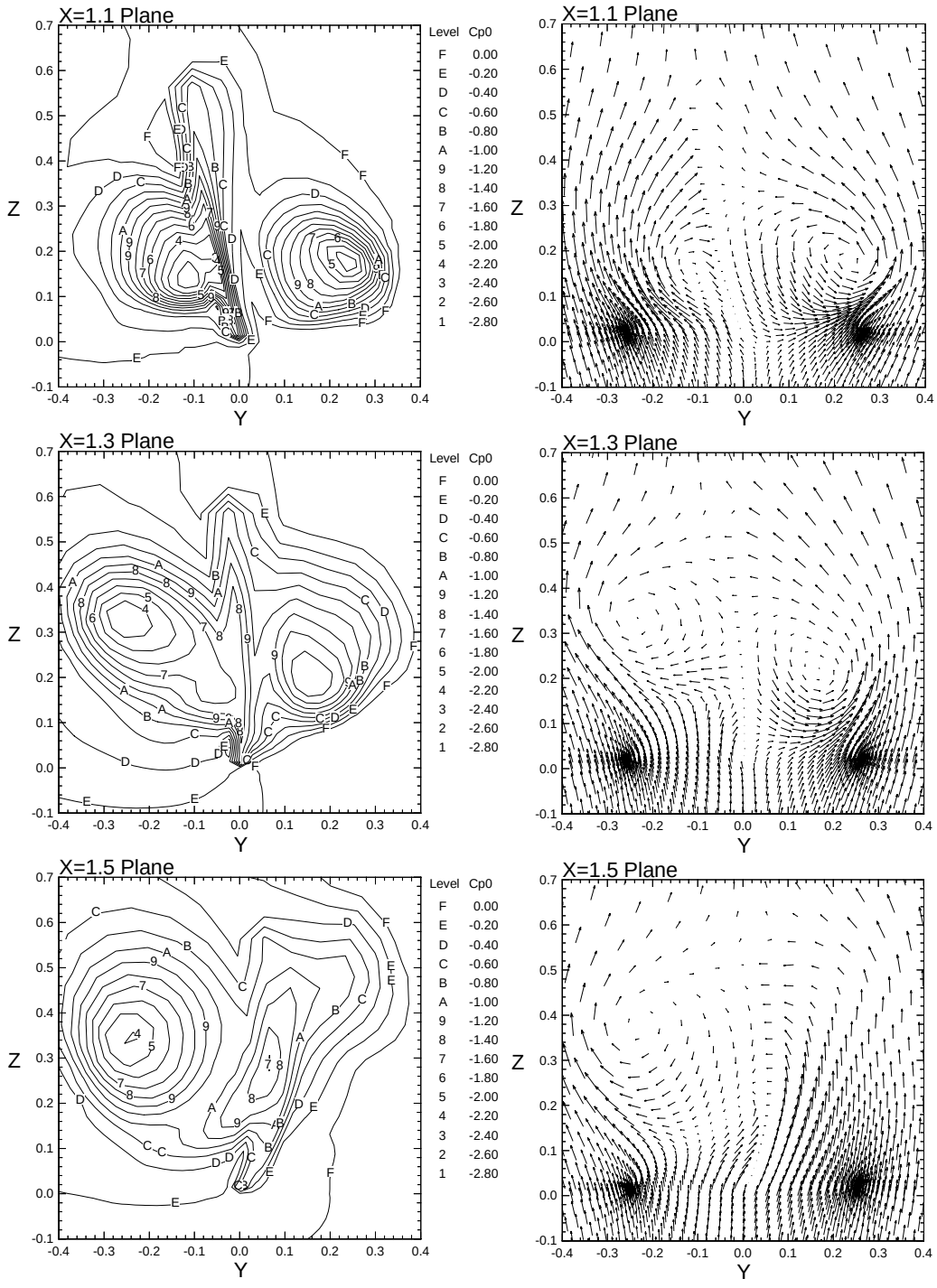

Figure 5.97: Total pressure coefficient and velocity vectors plotted on vertical crossflow planes near the tail. Coupled Bending and Torsion Case: $\tau = 13.2$, $Re = 10^6$, $M = 0.4$, $\alpha = 38^o$.

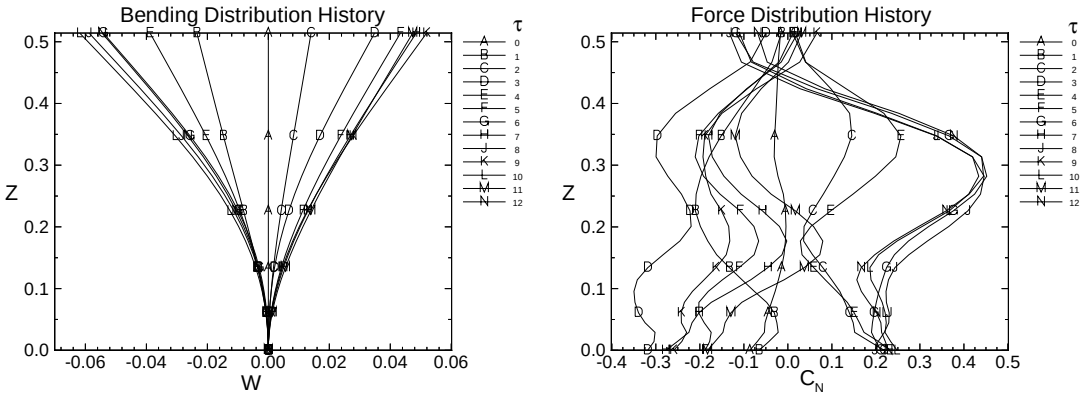

Figure 5.98: Bending deflection and force distributions along the tail span plotted at integer nondimensional time levels. Coupled Bending and Torsion Case: $Re = 10^6$, $M = 0.4$, $\alpha = 38^o$.

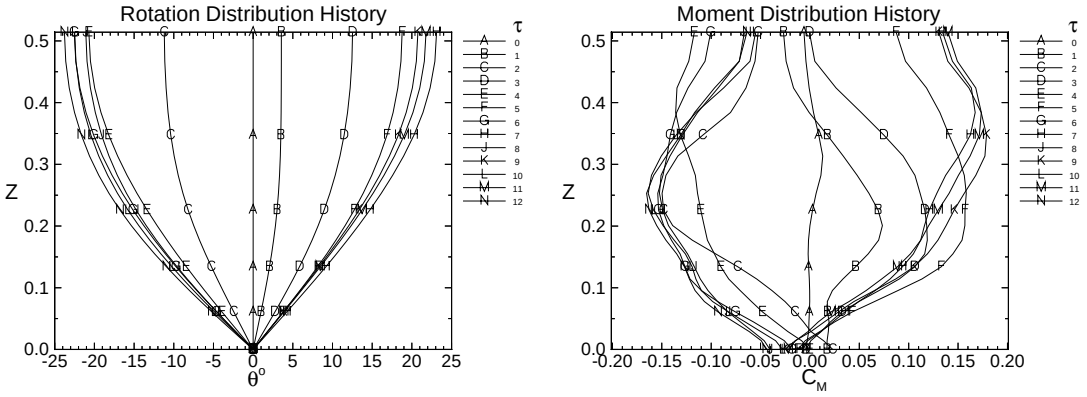

Figure 5.99: Torsion deflection and moment distributions along the tail span plotted at integer nondimensional time levels. Coupled Bending and Torsion Case: $Re = 10^6$, $M = 0.4$, $\alpha = 38^o$.

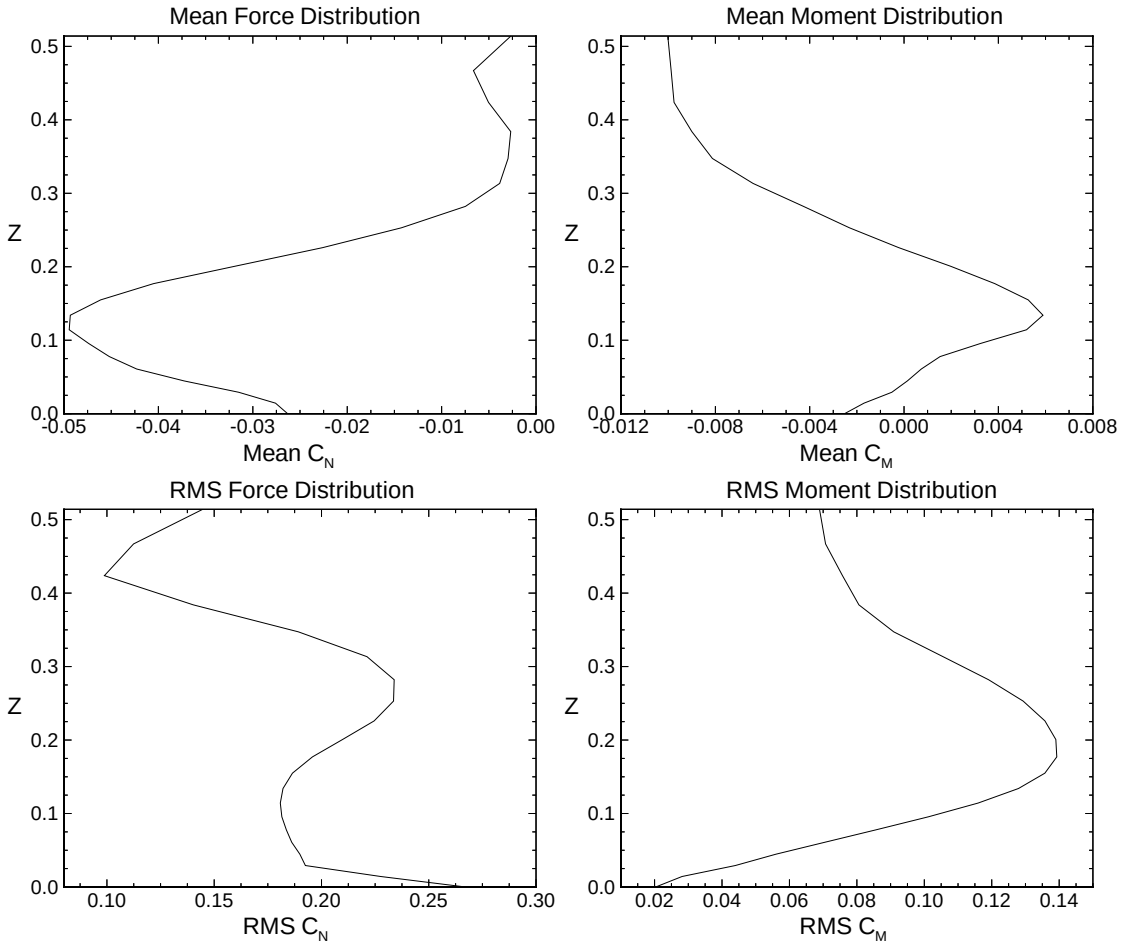

Figure 5.100: Mean and RMS load distributions along the tail span. Coupled Bending and Torsion Case: $Re = 10^6$, $M = 0.4$, $\alpha = 38^o$.

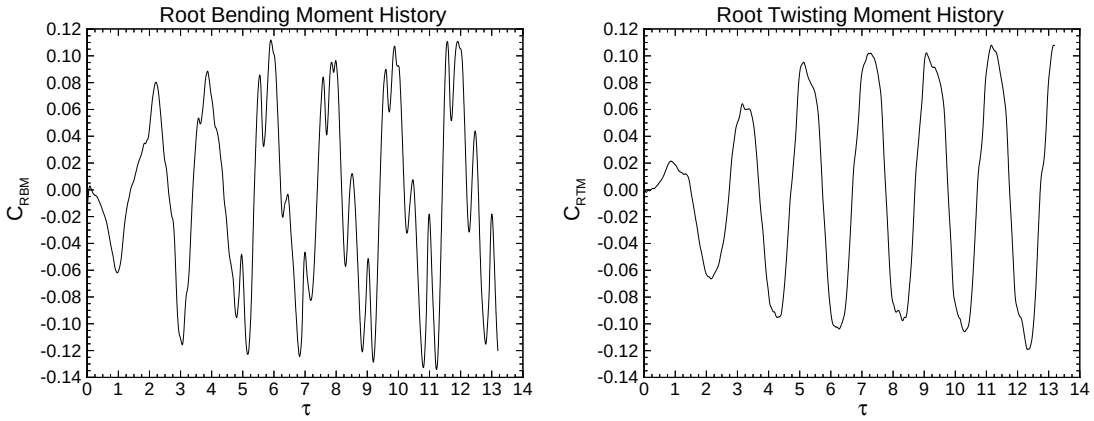

Figure 5.101: History of root bending moment coefficient and root twisting moment coefficient. Coupled Bending and Torsion Case: $Re = 10^6$, $M = 0.4$, $\alpha = 38^o$.

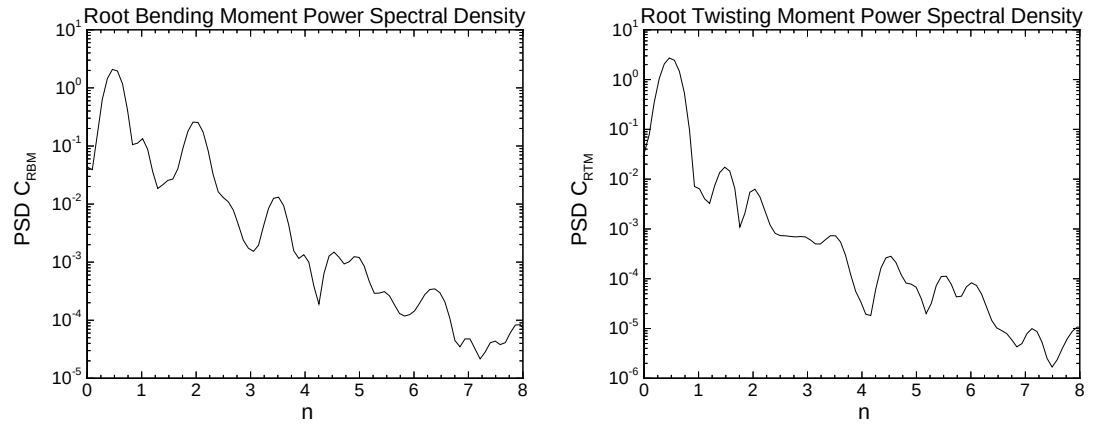

Figure 5.102: Power spectral density of root bending moment coefficient and root twisting moment coefficient versus reduced frequency. Coupled Bending and Torsion Case: $Re = 10^6$, $M = 0.4$, $\alpha = 38^o$.

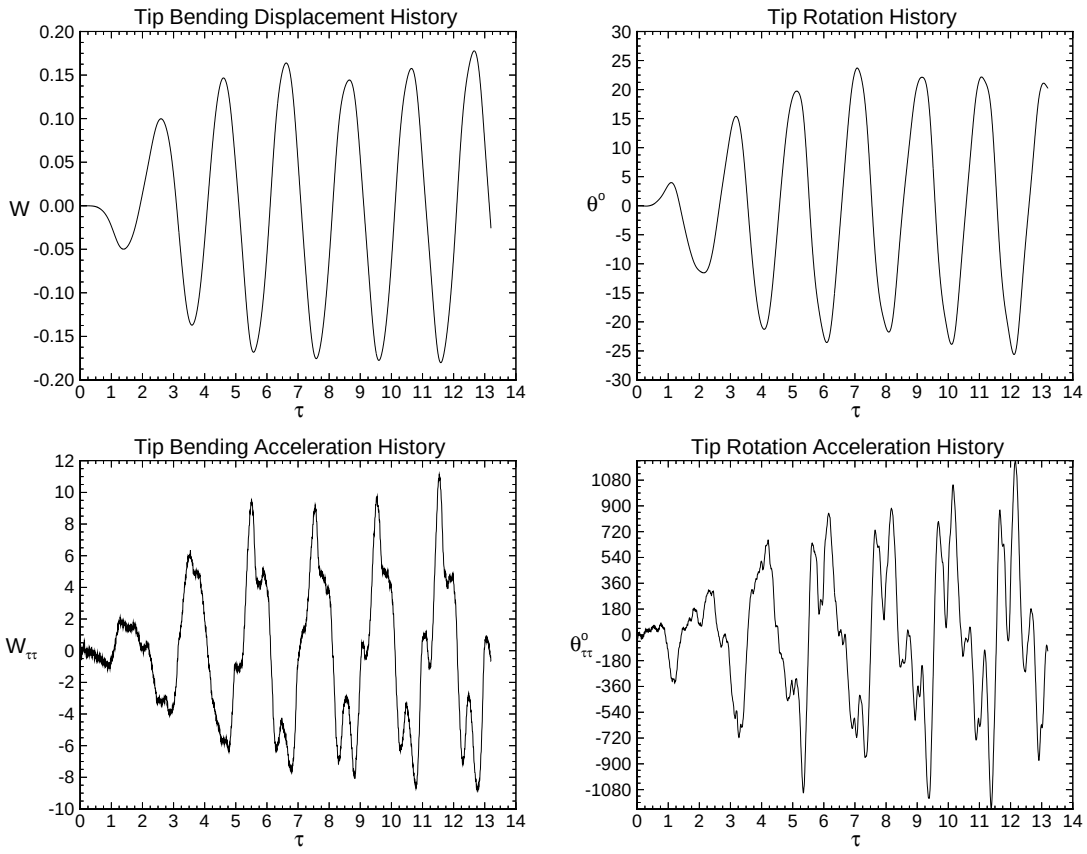

Figure 5.103: History of tip bending and torsion deflections and accelerations. Coupled Bending and Torsion Case: $Re = 10^6$, $M = 0.4$, $\alpha = 38^o$.

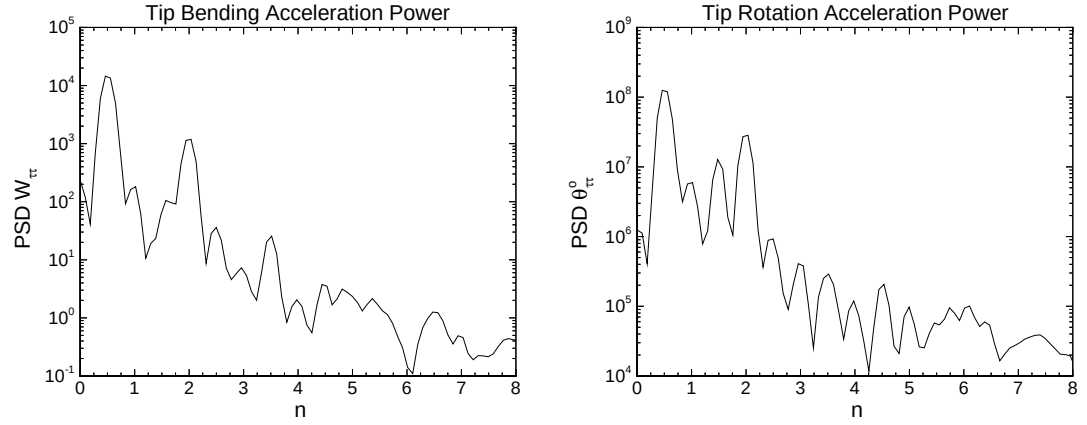

Figure 5.104: Power spectral density of tip bending and torsion accelerations versus reduced frequency. Coupled Bending and Torsion Case: $Re = 10^6$, $M = 0.4$, $\alpha = 38^o$.

5.5 Summary

In this chapter, the simulation of tail buffeting was accomplished using a simple delta wing/single vertical tail configuration. Computational applications have provided fundamental insights into the physical and numerical aspects of vortex breakdown induced tail buffet. The flow conditions, tail dimensions, and material properties were chosen such that the deflections would be large enough to insure interaction with the flow, and the natural frequencies would be high enough to facilitate a practical computational solution. This multi-disciplinary problem was solved sequentially for the fluid flow, the elastic tail deformations and the grid displacements. The flow field was obtained by time-accurately solving the laminar, unsteady, compressible, Navier-Stokes equations using an implicit, upwind, flux-difference splitting finite volume scheme. The elastic vibrations of the tail were modeled by coupled bending and torsion beam equations. These equations were solved accurately in time using the Galerkin method and a five-stage Runge-Kutta-Verner scheme. The grid for the fluid dynamics calculations was continuously deformed using interpolation functions to disperse the displacements smoothly throughout the computational domain. Computations for the single tail cases were performed on a Cray C90 and required one hour per 1678 time steps, or 27 minutes per nondimensional time unit ($\Delta\tau = 0.00132$). The memory required was 20 MW on a 64-bit machine which is equivalent to 80 MB on a 32-bit machine.

In this chapter, the effects of three parameters were assessed; inertial coupling, Reynolds number and fluid/structure interaction. The case definitions are summarized in Table 5.16 and the root loadings and tip responses are listed by case in Tables 5.17 and 5.18, respectively. The effects of inertial coupling were studied at two Reynolds numbers. For $Re = 10^4$, the tip response for the coupled case (2) was 42% and 80%

higher, for bending and torsion deflections, respectively, than that of the uncoupled case (1). Accelerations also rose by 43% and 31% for bending and torsion, respectively. At $Re = 10^6$, the bending and torsion deflections were 121% and 117% higher, respectively and the respective accelerations were 108% and 160% higher. Thus, it is clear that for the single tail configuration inertial coupling increases the tail buffeting response. The mechanism for this is the increase in bending due to torsional deflections, which moves the tail further off center, thus increasing the aerodynamic loading due to asymmetry. This effect is amplified in the $Re = 10^6$ due to the decrease in aerodynamic damping.

In Section 5.4.3, the effect of Re was assessed without the added complication of inertial coupling by comparing cases (1) and (4). The principle differences in loading were in the RMS values, which increased by 34% and 17% for root bending and root twisting moments, respectively. The corresponding tip bending and torsion accelerations increased by 37% and 12%, respectively. The increase in RMS loads and accelerations indicates that with rising Re, flow unsteadiness increases while aerodynamic damping decreases. Examination of the frequency domain plots also reveals this trend by the significant increase in high-frequency content.

As part of the moderately high Reynolds number cases ($Re = 10^6$), the buffet loads were recorded for an undeflected rigid tail case. The purpose of this case was to provide a baseline from which the effects of structural interaction with the flow could be assessed. In Section 5.4.3, comparison of the loads calculated from the moving uncoupled bending and torsion case (4) with the rigid case (3) at the same Re demonstrated that the deflections of the tail contribute significantly to the buffet loads. In addition, the disturbances caused by the large deflections were seen to propagate upstream to influence the breakdown locations. Hypothetical displacements were also calculated for

the rigid case using the same structural model with no attempt made to compensate for the absence of aerodynamic damping. As expected, the undamped response was much higher than the actual buffeting cases. However, it did not diverge since the natural frequencies of the tail were sufficiently distant from the forcing frequencies, see Table 5.2 and Figure 5.76, respectively. With the fundamental issues of inertial coupling, Reynolds number dependence and aeroelastic effects addressed, the following chapters will focus on the effects of tail geometry and wing/tail configuration for twin vertical tail buffeting applications.

Case	Section	Elastic Model	Re	α	x_θ
1	5.3.2	Uncoupled Bending and Torsion	10^4	38^o	0.00
2	5.3.3	Coupled Bending and Torsion	10^4	38^o	0.05
3	5.4.2	Rigid Tail	10^6	38^o	0.00
4	5.4.3	Uncoupled Bending and Torsion	10^6	38^o	0.00
5	5.4.4	Coupled Bending and Torsion	10^6	38^o	0.05

Table 5.16: Single square vertical tail buffeting cases.

	Root Loads									
	C_{RBM}					C_{RTM}				
Case	Mean	RMS	A	n_{d1}	n_{d2}	Mean	RMS	A	n_{d1}	n_{d2}
1	0.015	0.026	0.060	0.75	1.75	0.00095	0.029	0.057	0.45	2.0
2	-0.019	0.042	0.091	0.5	2.0	-0.000042	0.038	0.088	0.5	2.0
3	-0.021	0.029	0.070	0.75	1.5	0.007	0.014	0.039	0.75	1.5
4	-0.031	0.035	0.062	0.5	1.0	0.0089	0.034	0.057	0.5	2.0
5	-0.007	0.067	0.122	0.5	2.0	-0.0024	0.069	0.114	0.5	1.5

Table 5.17: Summary of root bending and twisting moment statistics, maximum amplitudes and dominant frequencies for all single tail cases.

	Tip Response							
	Bending				Torsion			
Case	$A(w)$	$A(w_{\tau\tau})$	n_{d1}	n_{d2}	$A(\theta)^o$	$A(\theta_{\tau\tau})^o$	n_{d1}	n_{d2}
1	0.082	3.5	0.45	1.75	9.8	420	0.45	1.75
2	0.117	5.0	0.5	2.0	17.6	550	0.5	2.0
3	0.131	6.8	0.5	2.5	42.2	3240	0.88	2.5
4	0.082	4.8	0.5	2.0	10.8	470	0.5	2.0
5	0.181	10.0	0.5	2.13	23.4	1220	0.5	2.0

Table 5.18: Summary of tip displacement and acceleration statistics, maximum amplitudes and dominant frequencies all single tail cases.

CHAPTER 6

EFFECT OF AFT FUSELAGE ON TWIN F/A-18 VERTICAL TAIL BUFFETING

6.1 Introduction

The primary focus of this chapter is the determination of the effect of aft fuselage geometry on twin F/A-18 vertical tail buffeting. Three fuselage configurations are considered; wide, narrow and open, see Figure 6.1. The case definitions are summarized in Table 6.1. Secondarily, the effect of the tail response on the loads will be accessed for the wide and narrow configurations by comparing the rigid tail loads with the dynamically interacting cases. Finally, the effect of decreased tail stiffness will be considered for the open fuselage case. Note that because of the high computational cost —greater than 30 C90 hours per case, more than one design parameter was changed in the open case, the most significant of which was the effective tail stiffness. Thus, rigorous comparisons can only be made between the wide and narrow cases.

Since there is no experimental data for the simple delta wing configurations of this chapter, qualitative comparisons will be made with experimental test results for the *full* F/A-18 aircraft. Quantitative comparisons will be made in Chapter 7 for which the chosen configuration has been tested experimentally.

Case	Fuselage	Elasticity	Re	α	$Mach$
1	Wide	Rigid	10^6	30^o	0.4
2	Wide	Flexible Stiff	10^6	30^o	0.4
3	Narrow	Rigid	10^6	30^o	0.4
4	Narrow	Flexible Stiff	10^6	30^o	0.4
5	Open	Flexible Soft	0.75×10^6	30^o	0.3

Table 6.1: Summary of twin F/A-18 vertical tail buffeting cases.

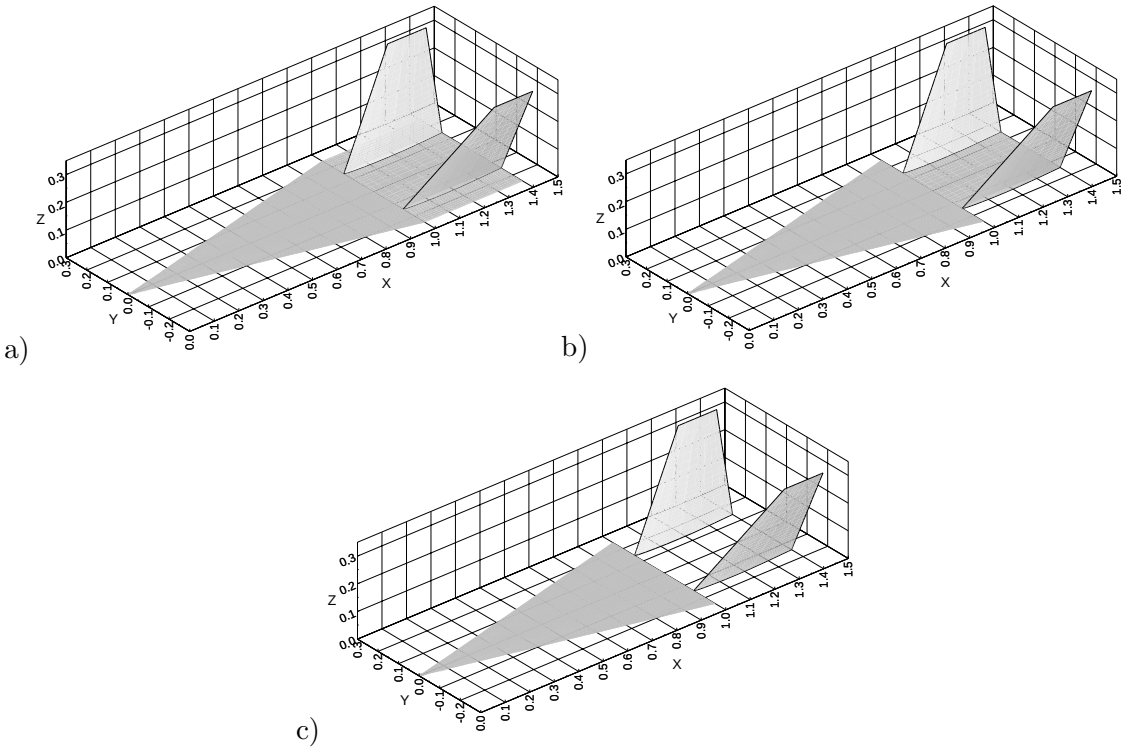

Figure 6.1: a) Wide, b) narrow and c) open fuselage configurations for the delta wing twin F/A-18 vertical tail model.

6.2 Wide Fuselage Model

6.2.1 Model Geometry and Computational Domain

The model consists of a sharp-edged, flat delta wing of aspect ratio 1 (leading edge sweep of $\Lambda = 76^o$) and twin F/A-18 vertical tails placed a distance of ($y = 0.14c$) from the symmetry plane. This placement is chosen to coincide with the vortex core locations. The height of the tails is chosen such that the ratio between the tail separation and height for the model is consistent with the aircraft. This results in a vertical tail height of $0.315c$. Each tail has an aspect ratio of 1.2 and a crop ratio of 0.4. The tails are cantilevered outward at an angle of 20^o, and swept back 35^o at the quarter chord. The tail airfoil section is a NACA 65-A with a base thickness ratio of 5% which decreases linearly to 3% at the tip. See Figure 6.2 for a sketch of the actual F/A-18 and Figure 6.3 for a photo of the left tail.

To accommodate the boundary conditions of the twin tails, a five block, C^0 continuous, O-H type grid with a total of 458,100 cells is used, see Figure 6.4. Block 1 covers the free stream and wing up to the leading edge of the tails, with dimensions of $53 \times 100 \times 49$ in the axial, wrap-around and normal directions, respectively. Block 2 covers the volume between the tails, from the root to the tip and has dimensions of $11 \times 22 \times 29$. Block 3 has the same width and height as block 2 and covers the volume outside of the tails, $11 \times 78 \times 29$. Block 4 covers the downstream region and has dimensions $26 \times 100 \times 49$. Block 5 is an O-grid surrounding blocks 2 and 3 from the tail tip to the outer radial boundary. This grid was constructed to avoid using mixed boundary conditions and has dimensions $11 \times 100 \times 20$. The global grid extends $0.8c$ upstream, $3c$ radially and $3.6c$ downstream. The grid was constructed algebraically as previously discussed in Section 3.5.

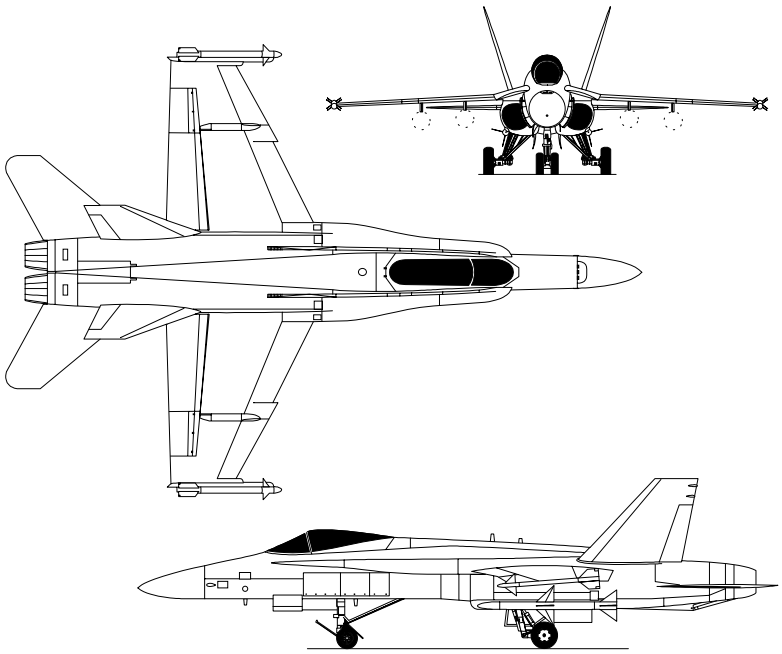

Figure 6.2: Sketch of McDonnell Douglas F/A-18C. *Public domain clip art.*

Figure 6.3: View of F/A-18 tail with retracted wing tips shown. *Photo by author.*

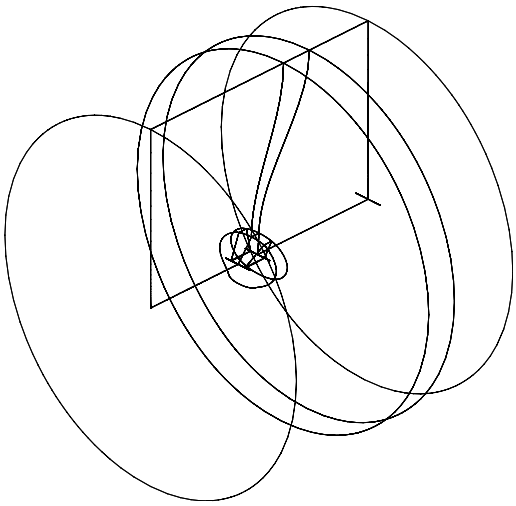

a)

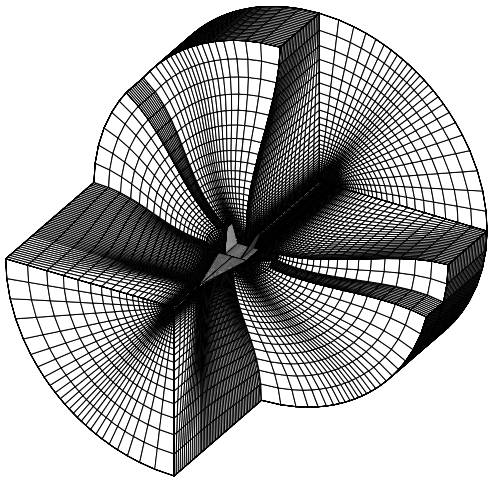

b)

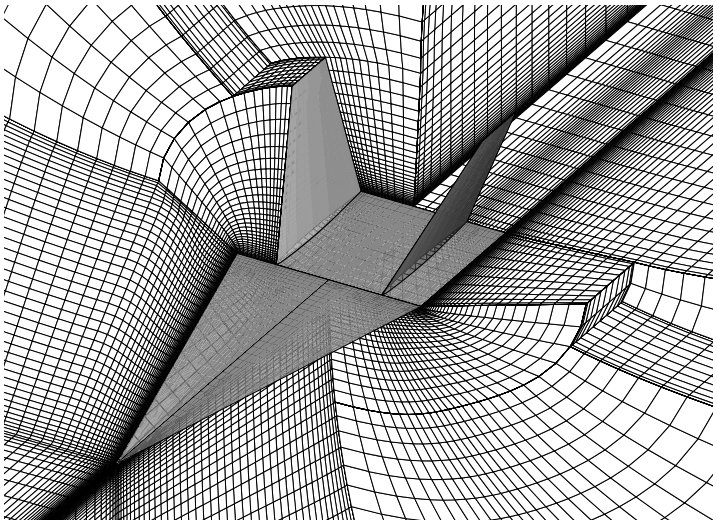

c)

Figure 6.4: a) Block boundaries. b) Cutaway view showing individual blocks. c) Close up view of surface grids. Wide Fuselage Case.

6.2.2 Freestream Flow Conditions

For all of the F/A-18 tail cases under consideration, the configuration angle-of-attack was reduced from the single tail value of 38^o to 30^o and the freestream Mach and Reynolds numbers were held constant at 0.4 and 10^6, respectively, for the wide and narrow cases. The angle-of-attack of 30^o matches the peak α in which maximum tail buffeting occurs on the F/A-18 aircraft. The Mach number was chosen to coincide with the severe tail buffet conditions and to match previous computations. The moderate Reynolds number of 10^6 was chosen to bring the simulation closer to flight Reynolds numbers of order 10^7 and to match previous computations.

6.2.3 Tail Material Properties

In the previous single tail cases, the bending and torsional rigidity was relaxed to allow for maximum structural interaction with the flow. In the remaining cases of this study, the stiffness is increased to more accurately model the real tail, and to explore the effects of higher frequency aeroelastic coupling. The wide and narrow cases represent an extreme in stiffness because the non-dimensional properties used for the arbitrarily thin (0.005c) single tail were kept for the solid F/A-18 tail, which has a root average thickness of $0.0134c$ which tapers to $0.0039c$ at the tip. The root chord of the tail is $0.4c$ with a taper ratio of 0.4. For the wide and narrow fuselage cases, a stiff tail was used, with material dimensionless moduli of elasticity and rigidity, E and G, of 1.8×10^5 and 0.7×10^5, respectively. The nondimensional density, ρ, was 26.1. These material properties correspond to very stiff and very light beam.

For the open fuselage case, much more flexible properties were chosen. The dimensionless moduli of elasticity and rigidity, were reduced by a factor of 40 to 4.6×10^3 and 1.8×10^3. The nondimensional density was increased to 145, which is over 5 times

larger than the stiff case. These properties correspond to balsa wood if the wing root chord is taken to be 18 inches. This material was chosen to match an experimental case of Washburn et al. [12]. Additional flexibility is obtained by reducing the tail thickness used in the structural calculations by 50%. Since this case and all the remaining cases in the study are inertially uncoupled, the distance between the inertial and elastic axes, x_θ is 0.

6.2.4 Initial Conditions, $Re = 10^6$, $M = 0.4$, $\alpha = 30^o$

The initial flow state is obtained by first solving the flow field using local time stepping for 2000 iterations and then solving time accurately for another five nondimensional time with a $\Delta\tau = 0.00036$. The reason for the time accurate integration is to allow for the presence of any large unsteady flow features in the initial condition. The time step is limited by stability and is very low due to the motion of the tail and the small grid spacing near the wing leading edge, the latter being most significant. The number of iterations and time steps used to obtain the initial condition are also relatively high, since no attempt is made to use aggressive convergence acceleration techniques such as coarse to fine mesh sequencing.

Comparing the 3-D streamline plots of the present refined grid case, shown in Figure 6.5, with those of the initial condition for the coarse single tail case at the same Reynolds and Mach numbers, Figure 5.56, dramatically displays the difference grid refinement makes in the capture of the vortex cores and breakdown. Unlike all of the previous single tail cases (including the fine grid case of Section 5.3.1), the cores in the present case remain very tight until the moment of breakdown, upon which they expand much more rapidly and fully. Note that delay in bursting is a result of the decrease in angle-of-attack and more importantly the addition of the aft fuselage, which

translates the region of adverse pressure gradient downstream. Another feature of the refined grid is a more symmetric solution. However, particle trace animations still show an unsteady asymmetry in the breakdown locations.

The surface flow, shown in Figures 6.7 and 6.8, indicate that unlike the previous cases, the secondary flow features are now prominently captured. Looking to the wing near surface streamlines, reveals a primary attachment line at a normalized semispan location of $\frac{y}{s_1} = 0$, secondary attachment lines at $\pm\frac{y}{s_1} = 0.81$ and secondary separation lines at $\pm\frac{y}{s_1} = 0.94$. These locations are verified by the troughs in C_p visible in Figure 6.10. The general relationship between the off surface flow and the surface pressure distribution is illustrated in Figure 6.9. Also, recall the topological sketches, see Figures 2.7 and 2.9, which depict the relationship between the off surface flow and the skin friction lines or near surface streamlines.

The near surface streamlines for the inner and outer sides of the right tail show that the primary vortical flow is impinging on the inner surface of the tail and separating on the outer surface of the tail. Note that only the right tail was plotted due to the observed flow symmetry. A region of reversed flow can also be seen on the lower outer tail surface. This is due to a vortex which forms from the outer leading edge in the vicinity of the tail. The tail prevents the outer vortex from merging with the primary vortex until they are downstream. This is visible in the crossflow planes of Figures 6.11 and 6.12 of the tail.

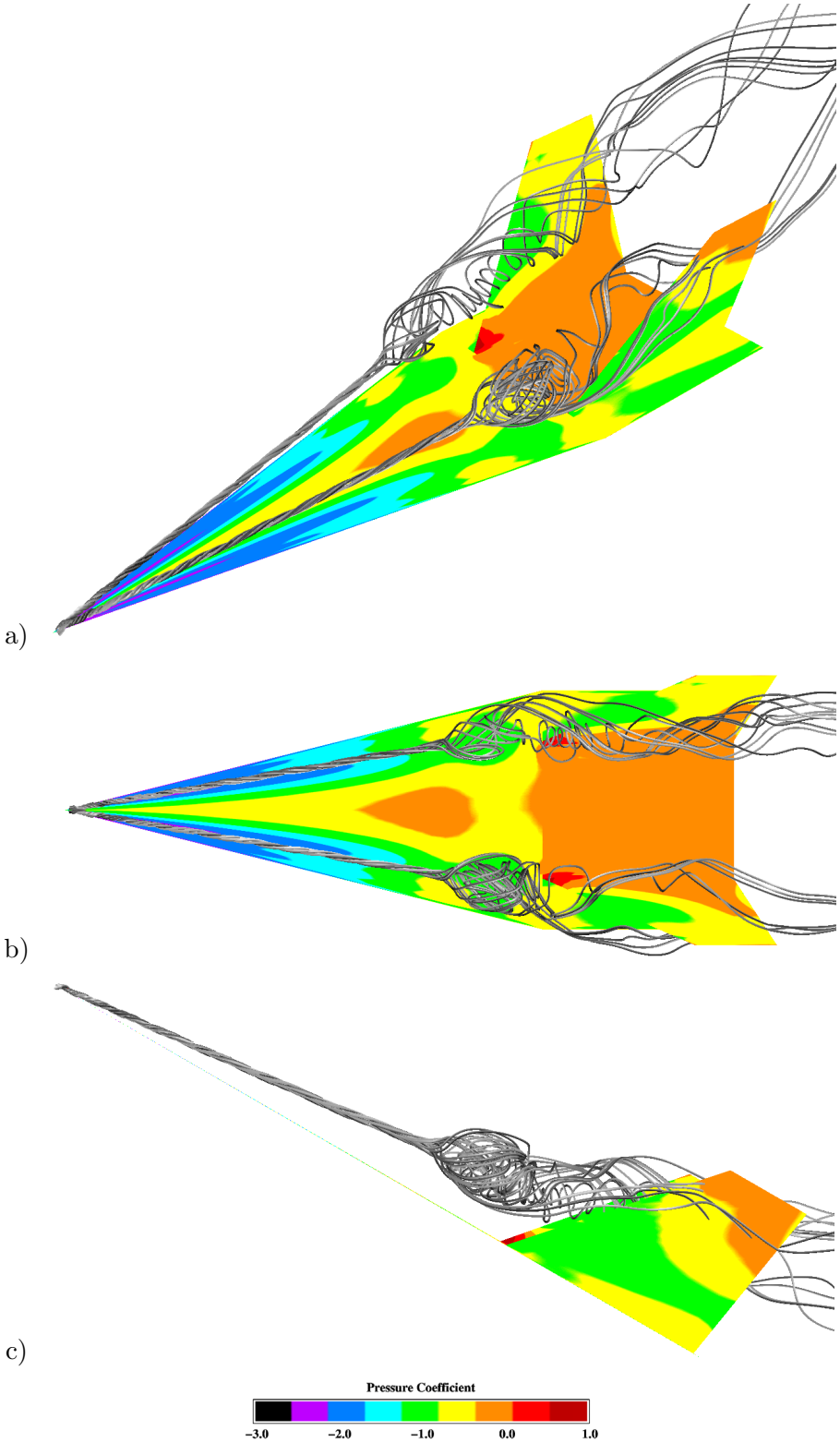

Figure 6.5: a) Three-dimensional, b) top and c) side views of surface pressure and vortex core streamlines. Initial Condition Flow Field: $Re = 10^6$, $M = 0.4$, $\alpha = 30^o$.

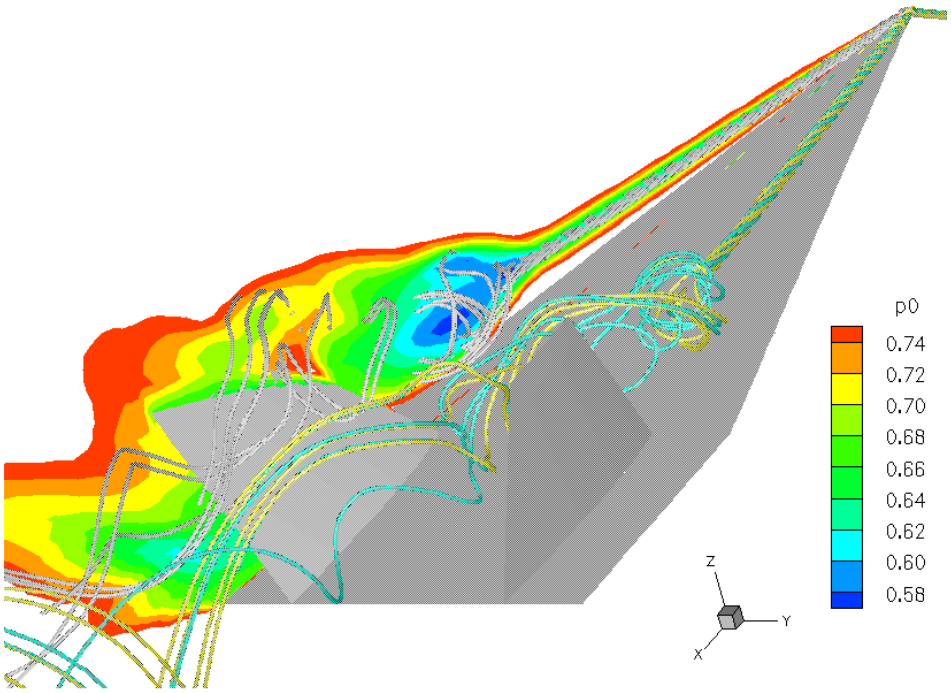

Figure 6.6: Rear view at angle-of-attack showing total pressure contours on a vertical plane bisecting the left vortex core ($\Lambda = 80.4^o$). The right vortex core streamlines are colored yellow and blue as an indicator of swirl ratio. Initial Condition Flow Field: $Re = 10^6$, $M = 0.4$, $\alpha = 30^o$.

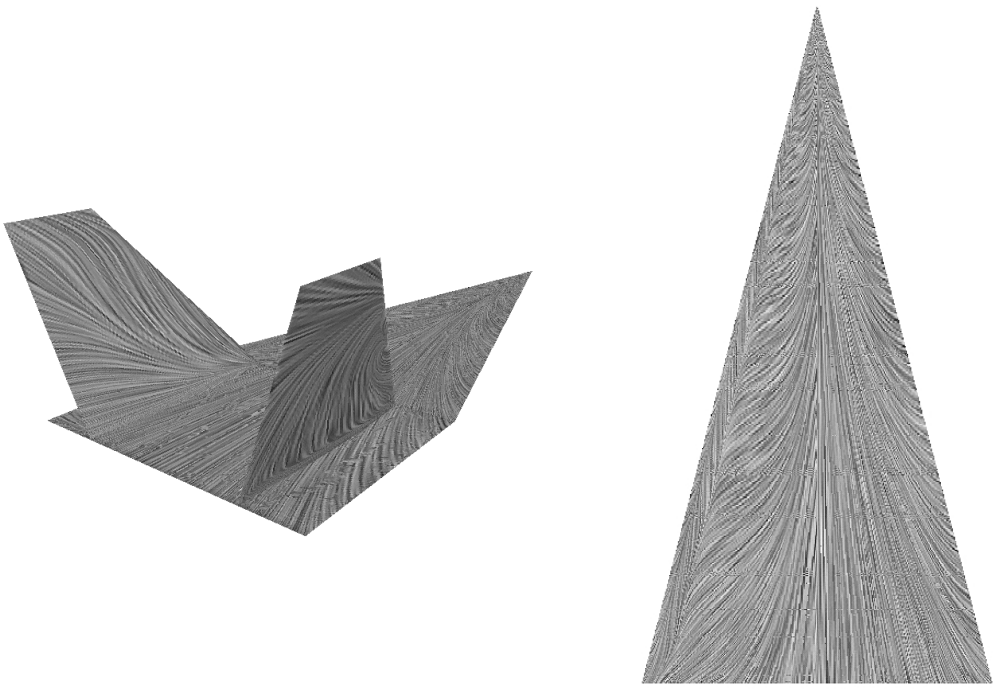

Figure 6.7: Computational surface oil flows. Initial Condition Flow Field: $Re = 10^6$, $M = 0.4$, $\alpha = 30^o$.

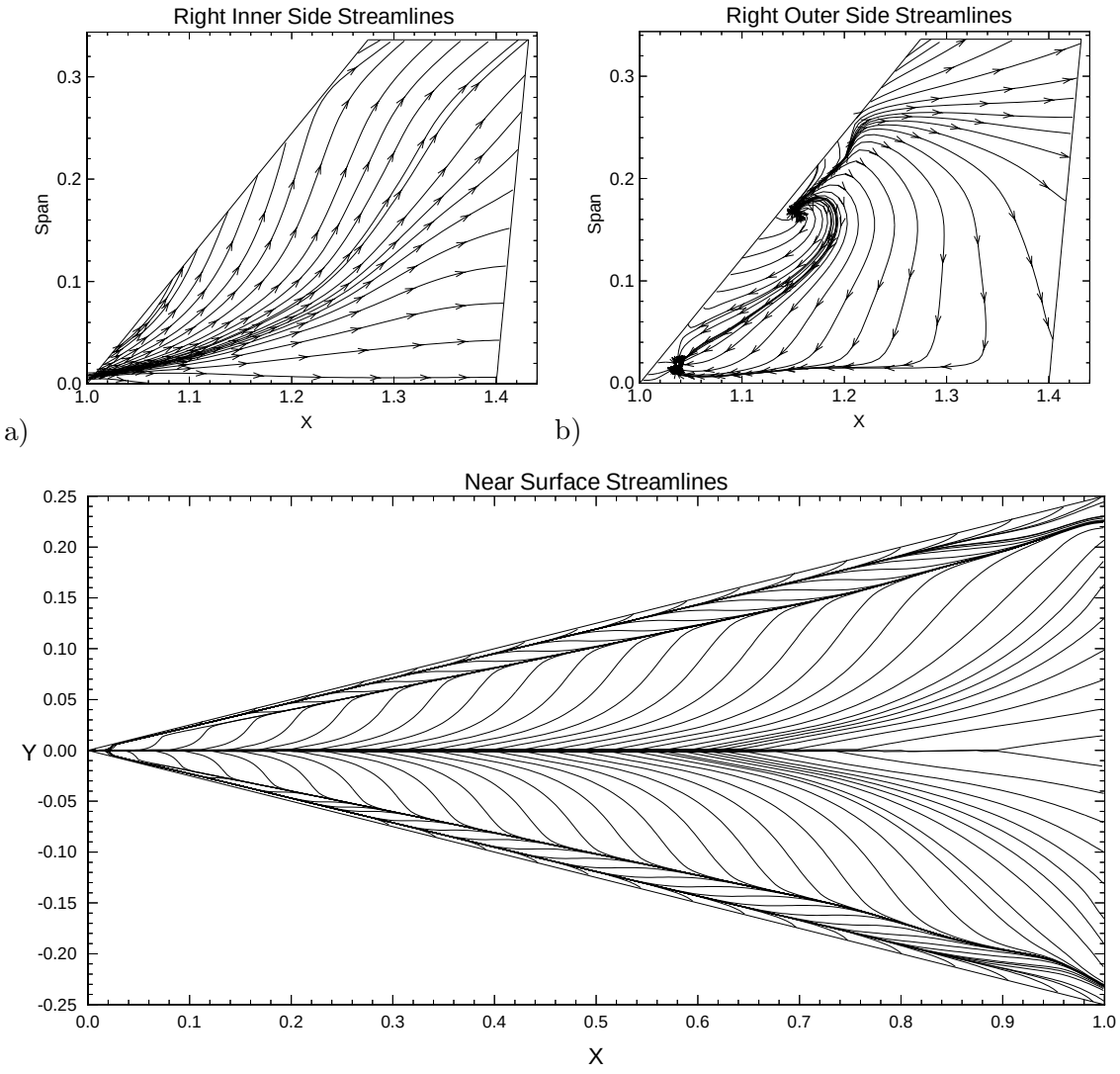

Figure 6.8: Near surface streamlines for the a) inner and b) outer right tail surfaces and the upper wing surface. Initial Condition Flow Field: $Re = 10^6$, $M = 0.4$, $\alpha = 30^o$.

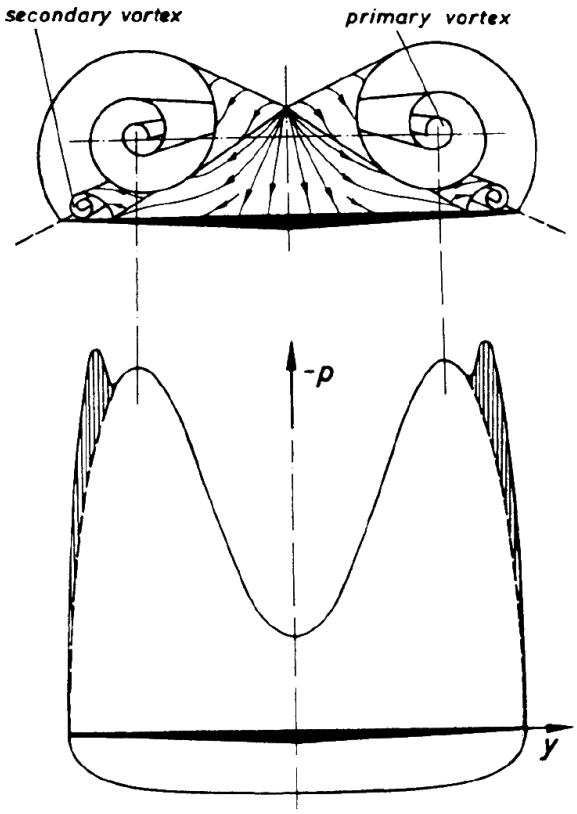

Figure 6.9: Sketch of a primary - secondary vortex system with a corresponding plot of spanwise surface pressure. Hummel [10]

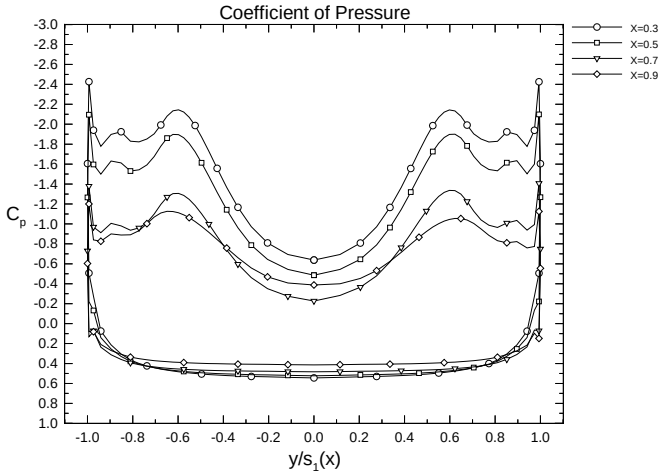

Figure 6.10: Coefficient of pressure on upper and lower wing surfaces at chord stations corresponding to plotted crossflow planes. Initial Condition Flow Field: $Re = 10^6$, $M = 0.4$, $\alpha = 30^o$.

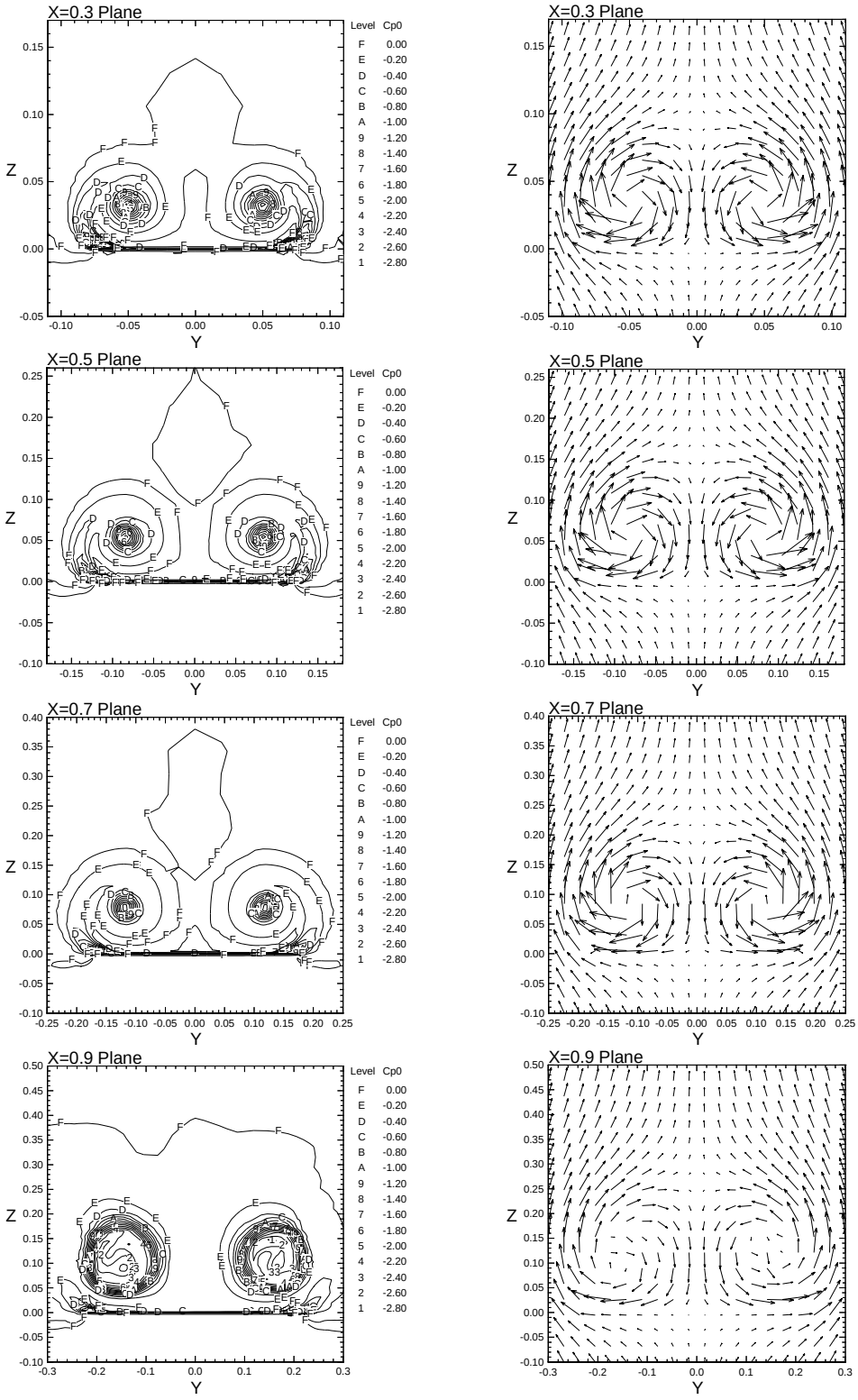

Figure 6.11: Total pressure coefficient and uniformly plotted velocity vectors on vertical crossflow planes above wing. Initial Condition Flow Field: $Re = 10^6$, $M = 0.4$, $\alpha = 30^o$.

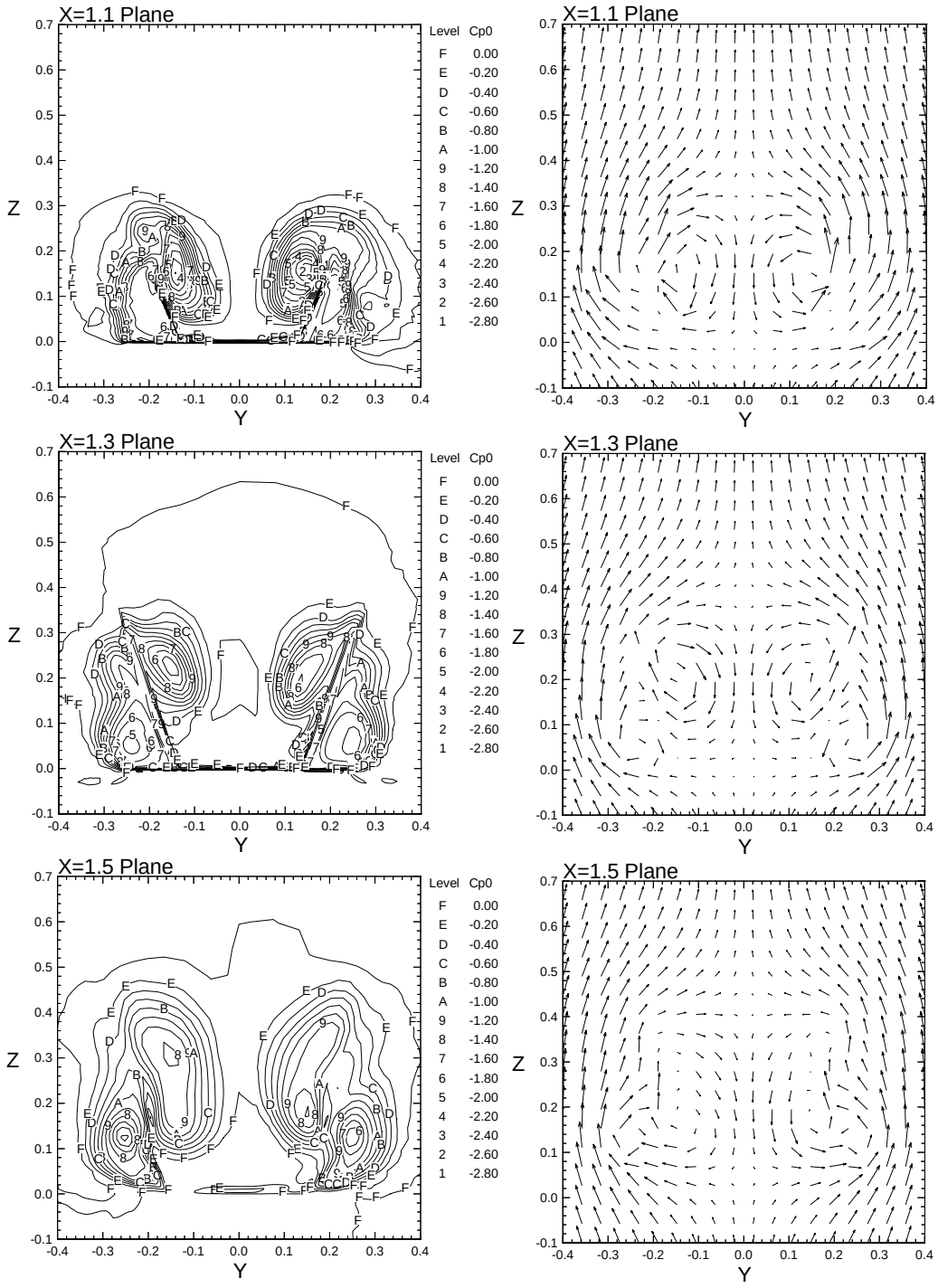

Figure 6.12: Total pressure coefficient and uniformly plotted velocity vectors on vertical crossflow planes near the tails. Initial Condition Flow Field: $Re = 10^6$, $M = 0.4$, $\alpha = 30^o$.

6.2.5 Load Histories for Rigid Tails

The purpose of this case is to provide a baseline from which the effect of decreased aft fuselage size can be studied. Furthermore, since this case is rigid, comparisons with the flexible case in the next section will provide insight into the effect that the dynamic tail response has on the buffet loading.

In Figure 6.13, the force and moment distributions are plotted at several time levels to give a qualitative view of the mean and unsteady flow components. Quantitative plots are shown in Figure 6.14, where the dashed lines represent values for the left tail. Note that because of the global sign convention for forces and moments, a symmetric loading produces loads of opposite signs between each tail. Inspection of the mean and RMS loads for the left and right tails indicate that the steady loads are nearly identical, while the peak unsteady loadings differ by 9% and 18% for the forces and moments, respectively. The plots show that from the tail tip to the mid span there is a symmetric load pushing inward. The low moments in this range indicate that these loads are largely constant or balanced across the tail chord. On the lower half span there is a symmetric load twice as large as outer span and pushing outward. The moments in this range are twice as high as the tip levels and are symmetrically trying to twist the lower leading edge of each tail outward. These observations are confirmed by the plots of mean and RMS differential pressure over each tail surface, see Figure 6.15. The high outward loading is due mainly to the suction created by the small secondary vortex emanating from the outer edge of the aft fuselage. The increased outward moment is due to the primary vortex impinging on the inside lower leading edge of each tail creating a high pressure zone.

In Figure 6.16, differential pressure ($\frac{\Delta p}{q_\infty}$) histories at the 45% chord and 60% span location for both tails are plotted. These positions were chosen to coincide with published experimental results. The time histories show that the loads are non-periodic and unsymmetric with respect to each tail, despite their steady symmetry. Also shown are the buffet excitation spectra, presented in nondimensional RMS form as $\sqrt{nF(n)}$ versus nondimensional frequency n. This form was first suggested by Owen [91] and is recommended for standard use by Mabey [92]. The buffet excitation is defined in terms of freestream dynamic pressure as follows;

$$\frac{\mathrm{PSD}(p)}{q_\infty^2} = \int_{n=0}^{n=\infty} F(n)dn = \int_{\ln n=-\infty}^{\ln n=\infty} nF(n)d(\ln n) \tag{6.1}$$

where

$$\mathrm{PSD}(p) = \text{power spectral density of pressure} \tag{6.2}$$

$$n = \text{nondimensional frequency, } \frac{f\overline{\overline{c}}}{U_\infty} \tag{6.3}$$

$$F(n) = \text{contribution to } \frac{\mathrm{PSD}(p)}{q_\infty^2} \text{ in a frequency band} \Delta n \tag{6.4}$$

The power spectral densities are computed from averaged blocks of data which are zero padded and windowed using a Hanning function as described in the previous chapter. Because of the relatively short sample size, the multiple discrete peaks seen in the inside pressure spectra cannot be trusted to represent the actual flow. It is expected that with additional time the multiple peaks would merge and average out to one peak of roughly the same magnitude and location of the highest of the discrete peaks. The statistics for the point pressure data are summarized in Table 6.2

Root bending and twisting moment histories for each tail, see Figure 6.17, indicate that as in the case of the pressure measurements, neither tail loading is periodic or symmetric with respect to each other. The root moment spectra, see Figure 6.18, show

a more clearly defined single peak than the pressure data, since there is an additional source of averaging inherent in the integration of the loads along the span. The statistics for the root moment data are summarized in Table 6.3. The relatively large variance between the tails in the peak power of C_{RBM} and C_{RTM} is once again due to the brief sample time. However, the peak frequencies for each tail are within 20% of each other.

	Point Pressure Data					
	Right Tail			Left Tail		
	p_{in}	p_{out}	p_{in-out}	p_{in}	p_{out}	p_{in-out}
Mean	8.14	8.49	-0.35	8.14	8.48	-0.34
RMS	0.16	0.04	0.17	0.17	0.05	0.18
n_d	1.9	1.5		2.3	1.2	
Peak Power	1.8	0.5		1.6	0.4	

Table 6.2: Summary of nondimensional pressure ($\frac{p}{q_\infty}$) data at 45% chord and 60% span. Wide Rigid Case: $Re = 10^6$, $M = 0.4$, $\alpha = 30^o$.

	Root Loads							
	C_{RBM}				C_{RTM}			
Tail	Mean	RMS	Peak	n_d	Mean	RMS	Peak	n_d
Right	-0.0088	0.0084	0.0046	1.1	-0.0100	0.0051	0.0034	1.0
Left	0.0068	0.0095	0.0082	1.4	0.0095	0.0041	0.0014	1.2

Table 6.3: Summary of root bending and twisting moment statistics, peak power and dominant frequency. Wide Rigid Case: $Re = 10^6$, $M = 0.4$, $\alpha = 30^o$.

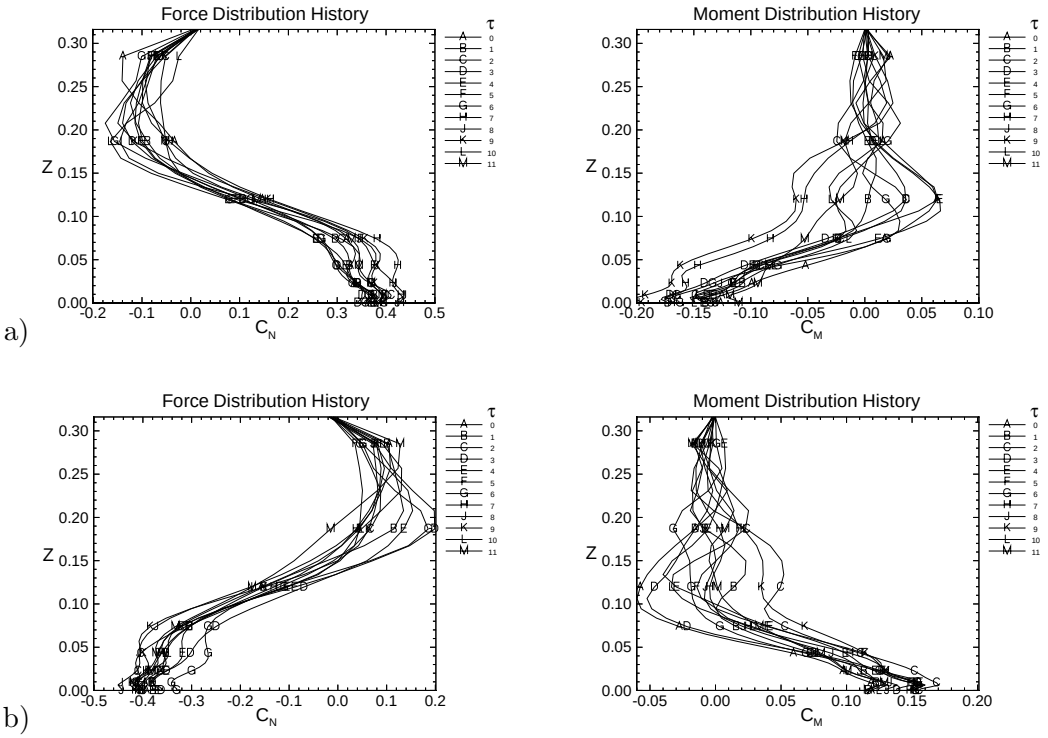

Figure 6.13: Bending force and twisting moment distributions along the tail span plotted at integer nondimensional time levels for a) right and b) left tails. Wide Rigid Case: $Re = 10^6$, $M = 0.4$, $\alpha = 30^o$.

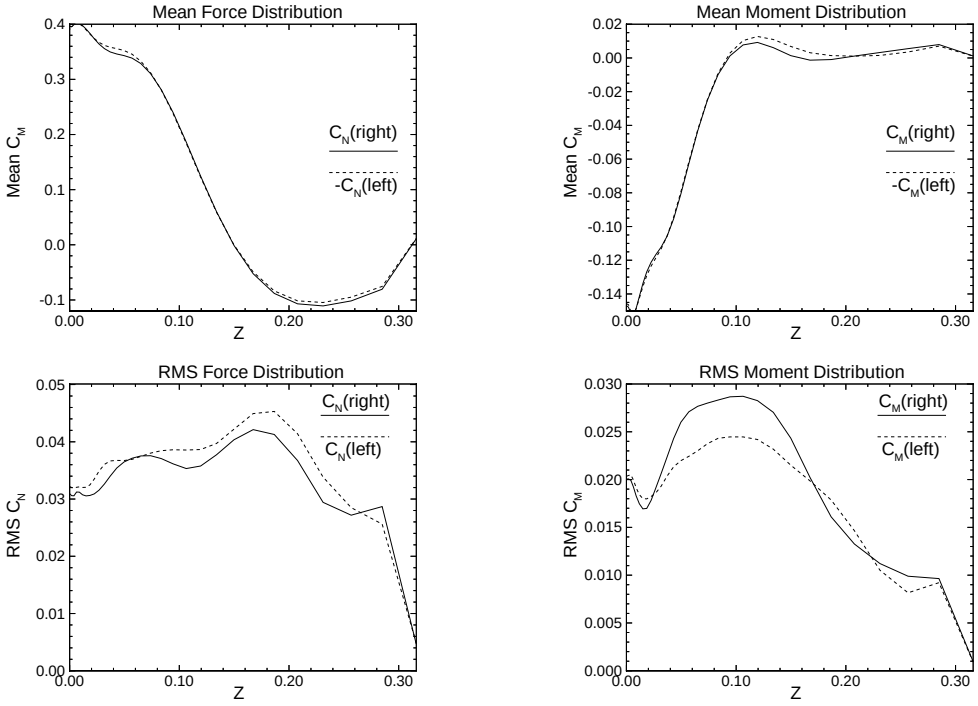

Figure 6.14: Mean and RMS load distributions along the right and left tail spans. Wide Rigid Case: $Re = 10^6$, $M = 0.4$, $\alpha = 30^o$.

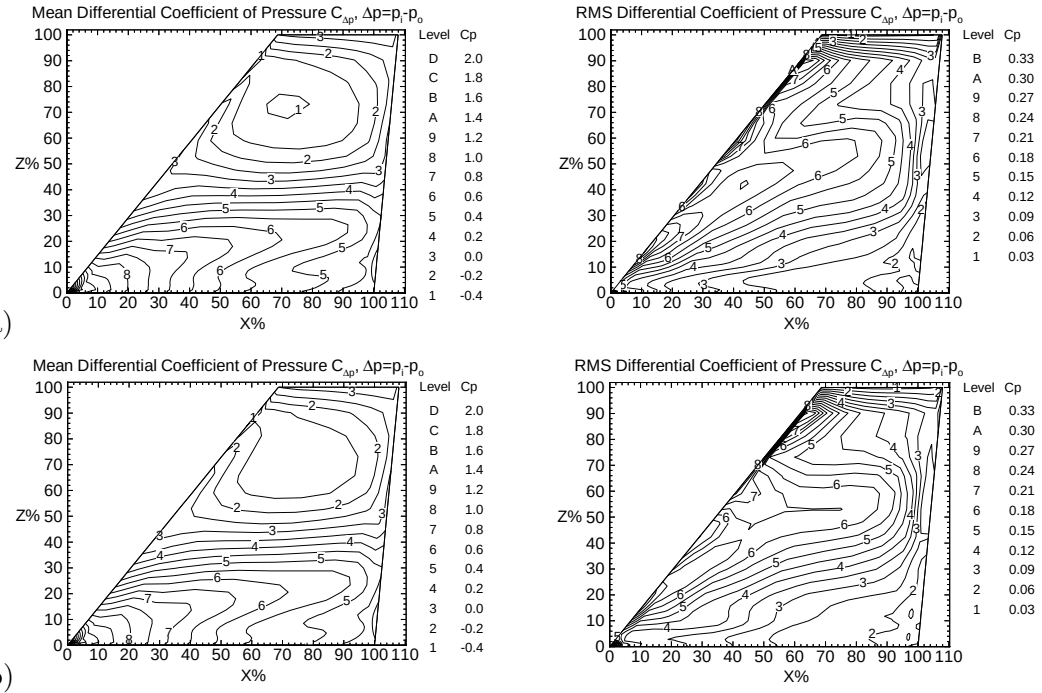

Figure 6.15: Mean and RMS differential coefficient of pressure contours on a) right and b) left tails. Wide Rigid Case: $Re = 10^6$, $M = 0.4$, $\alpha = 30^o$.

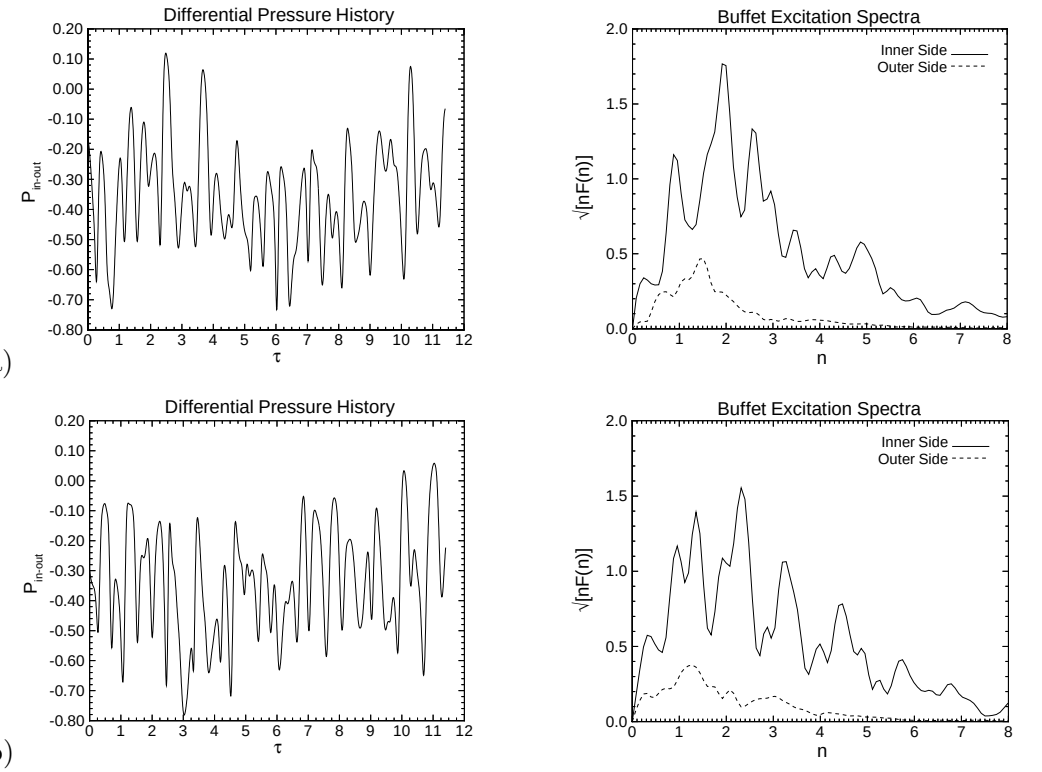

Figure 6.16: Differential pressure ($\frac{\Delta p}{q_\infty}$) histories and buffet excitation spectra ($\sqrt{nF(n)}$) at the 45% chord and 60% span location for a) right and b) left tails. Wide Rigid Case: $Re = 10^6$, $M = 0.4$, $\alpha = 30^o$.

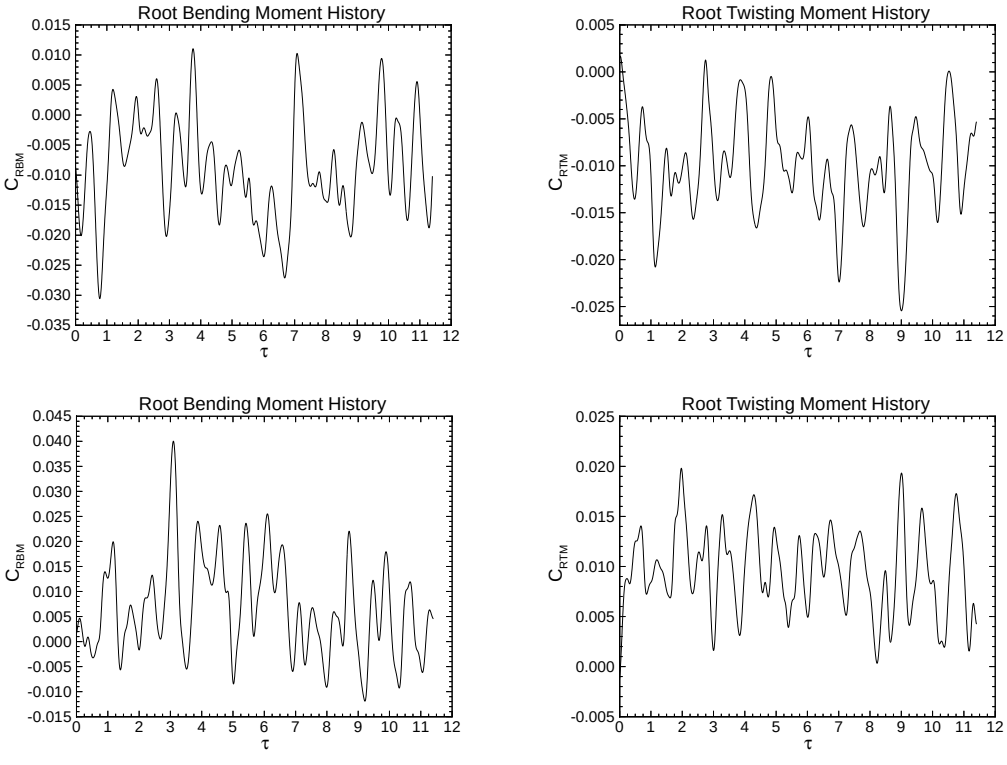

Figure 6.17: History of root bending moment coefficient and root twisting moment coefficient for a) right and b) left tails. Wide Rigid Case: $Re = 10^6$, $M = 0.4$, $\alpha = 30^o$.

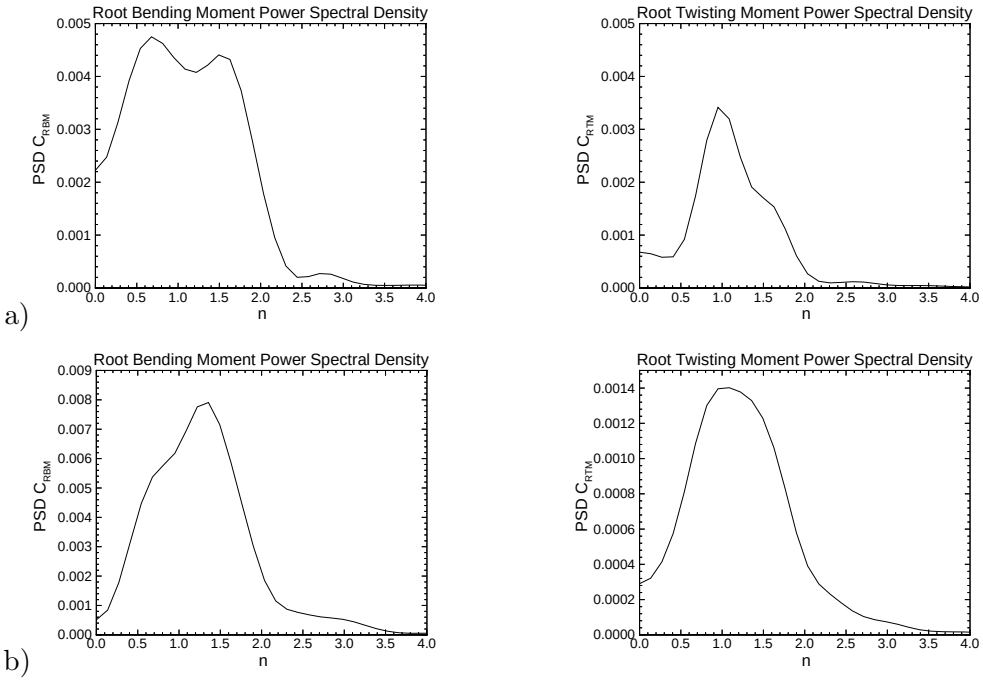

Figure 6.18: Power spectral density of root bending moment coefficient and root twisting moment coefficient versus reduced frequency for a) right and b) left tails. Wide Rigid Case: $Re = 10^6$, $M = 0.4$, $\alpha = 30^o$.

6.2.6 Uncoupled Bending and Torsion Response

In this section, the buffeting response due to inertially uncoupled bending and torsion vibrations of flexible but stiff twin F/A-18 tails is considered. The purpose of this case is to provide a baseline from which the effect of decreased aft fuselage size can be studied. In addition, the effect of the dynamic tail response on the buffet loading will be assessed, by contrasting this case with the rigid case of the previous section.

The qualitative view of the mean and unsteady flow components shown in Figure 6.19, is very similar to the rigid case as are the mean and RMS plots, shown in Figure 6.20. While the mean values between the two cases are almost identical, the RMS values do differ slightly. The most notable difference being the enlargement of the peak in C_N at $z = 0.05$. These observations are confirmed by the plots of mean and RMS differential pressure over each tail surface, see Figure 6.22.

The differential pressure histories at the 45% chord and 60% span location, shown in Figure 6.22, match the rigid case up to about $\tau = 5.5$, after which the accumulation of small differences produces unique solutions. The peaks in the buffet excitation spectra, $\sqrt{nF(n)}$, also match closely with the only difference being the diminished magnitude of the central peak around $n = 2$, which is most likely due to the uncertainty caused by the short sample time.

A comparison of the statistics for the point pressure data is presented in Table 6.4. Since the loads between the tails are largely alike, to improve statistical confidence, their averaged values are compared between cases. For both cases, the mean and RMS point pressure data are identical. The dominant frequencies for the flexible tail are 10% and 7% lower for the inner and outer tail locations, respectively. The peak powers are 18% and 20% lower.

Root bending and twisting moment histories for each tail, see Figure 6.23, match the rigid case up to about $\tau = 6.5$, with the left tail matching more closely than the right. The root moment spectra, see Figure 6.24, also match closely, the main difference being a slightly increased sharpness in the peaks. The statistics for the root moment data for rigid and flexible stiff tail cases are compared in Table 6.5.

The reason for the close similarity between the loads for the rigid and flexible stiff tail cases is due to the very small deflections shown in Figures 6.25-6.28. The bending and torsion distributions for each tail indicate that the tails tend to bend inwards and twist outwards on the lower half span. The distribution plots also indicate that the bending vibration is dominated by the first mode and the torsional vibrations occur mainly in the first and second modes. Tip bending and twisting histories show that the deflections and accelerations are non-periodic and unsymmetric with respect to each tail at a particular instant, but do share the same maximum range. The power spectral densities of acceleration show that the dominant response frequency for bending and torsion occurs around $n = 4$, which is much higher than the loading, but is not surprising given the high stiffness. In the following sections, results from rigid and flexible stiff tail cases of the same structural properties as this case but mounted on a narrow fuselage will be compared to the results in this and the previous wide fuselage case.

	Point Pressure Data					
	Rigid Tail			Flexible Tail		
	p_{in}	p_{out}	p_{in-out}	p_{in}	p_{out}	p_{in-out}
Mean	8.14	8.49	-0.35	8.14	8.49	-0.35
RMS	0.17	0.05	0.18	0.17	0.05	0.18
n_d	2.1	1.4		1.9	1.3	
Peak Power	1.7	0.5		1.4	0.4	

Table 6.4: Comparison of averaged nondimensional pressure ($\frac{p}{q_\infty}$) data at 45% chord and 60% span for rigid and flexible tail, wide fuselage cases: $Re = 10^6$, $M = 0.4$, $\alpha = 30^o$.

	Root Loads							
	C_{RBM}				C_{RTM}			
Tail	Mean +tip inward	RMS	Peak	n_d	Mean +LE inward	RMS	Peak	n_d
Rigid	-0.0078	0.0090	0.0064	1.3	-0.0098	0.0033	0.0024	1.1
Flexible	-0.0073	0.0092	0.0082	1.5	-0.0098	0.0043	0.0022	1.2
% Diff	-6%	2%	28%	13%	0%	30%	-8%	9%

Table 6.5: Comparison of averaged root bending and twisting moment statistics, peak power and dominant frequency for rigid and flexible stiff tail, wide fuselage cases: $Re = 10^6$, $M = 0.4$, $\alpha = 30^o$.

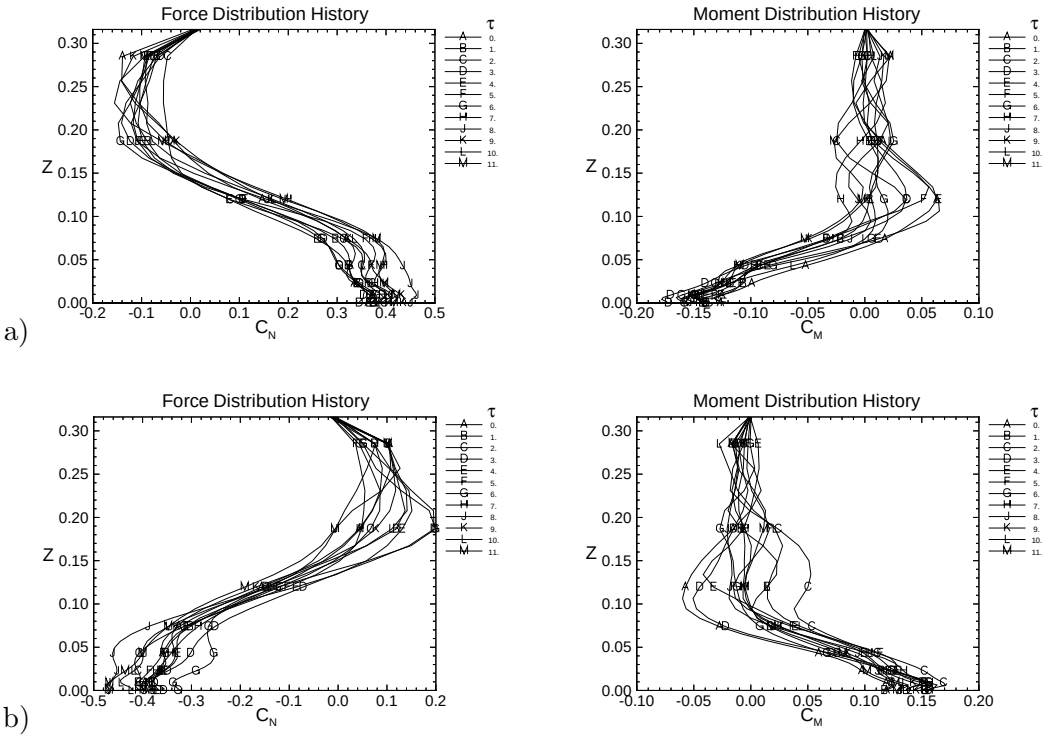

Figure 6.19: Bending force and twisting moment distributions along the tail span plotted at integer nondimensional time levels for a) right and b) left tails. Wide Flexible Case: $Re = 10^6$, $M = 0.4$, $\alpha = 30^o$.

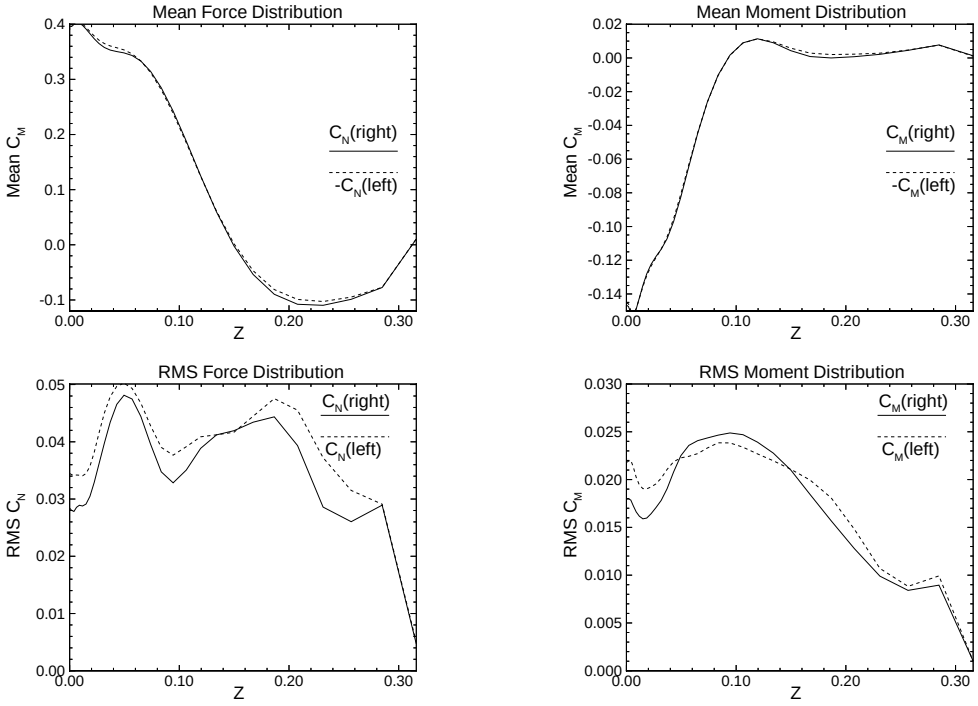

Figure 6.20: Mean and RMS load distributions along the right and left tail spans. Wide Flexible Case: $Re = 10^6$, $M = 0.4$, $\alpha = 30^o$.

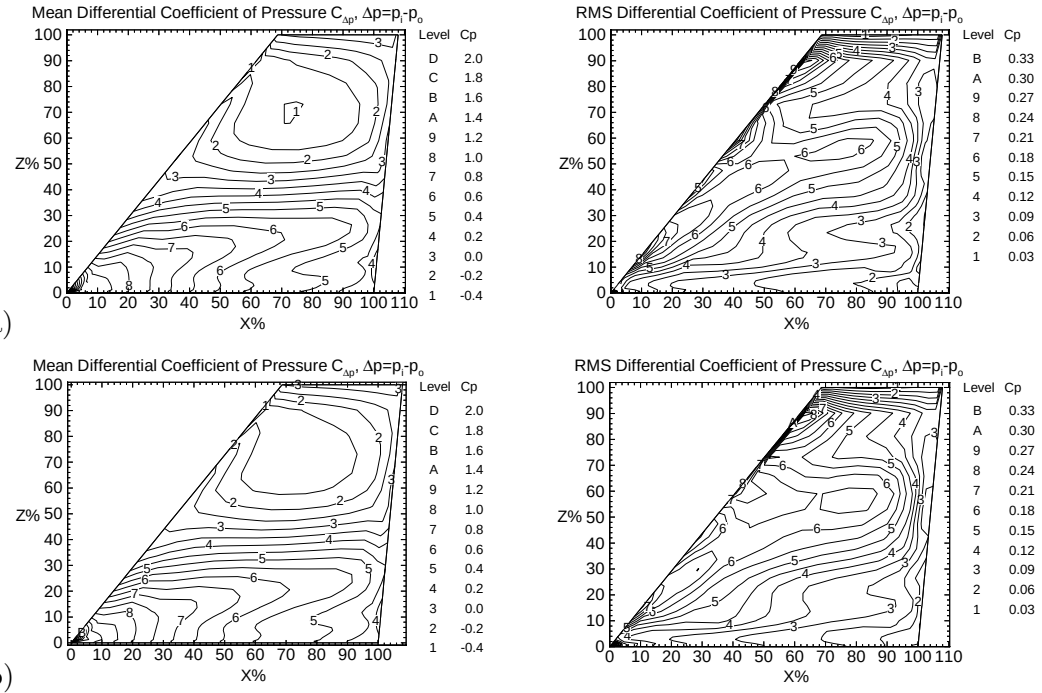

Figure 6.21: Mean and RMS differential coefficient of pressure contours on a) right and b) left tails. Wide Flexible Case: $Re = 10^6$, $M = 0.4$, $\alpha = 30^o$.

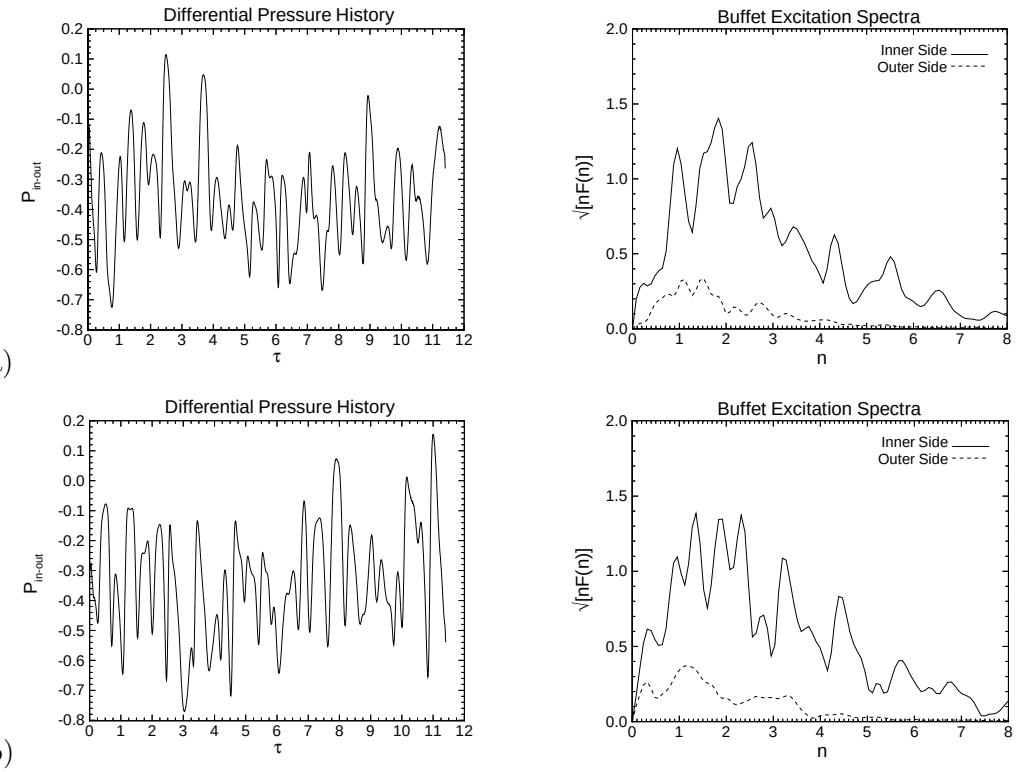

Figure 6.22: Differential pressure ($\frac{\Delta p}{q_\infty}$) histories at the 45% chord and 60% span location for a) right and b) left tails. Wide Flexible Case: $Re = 10^6$, $M = 0.4$, $\alpha = 30^o$.

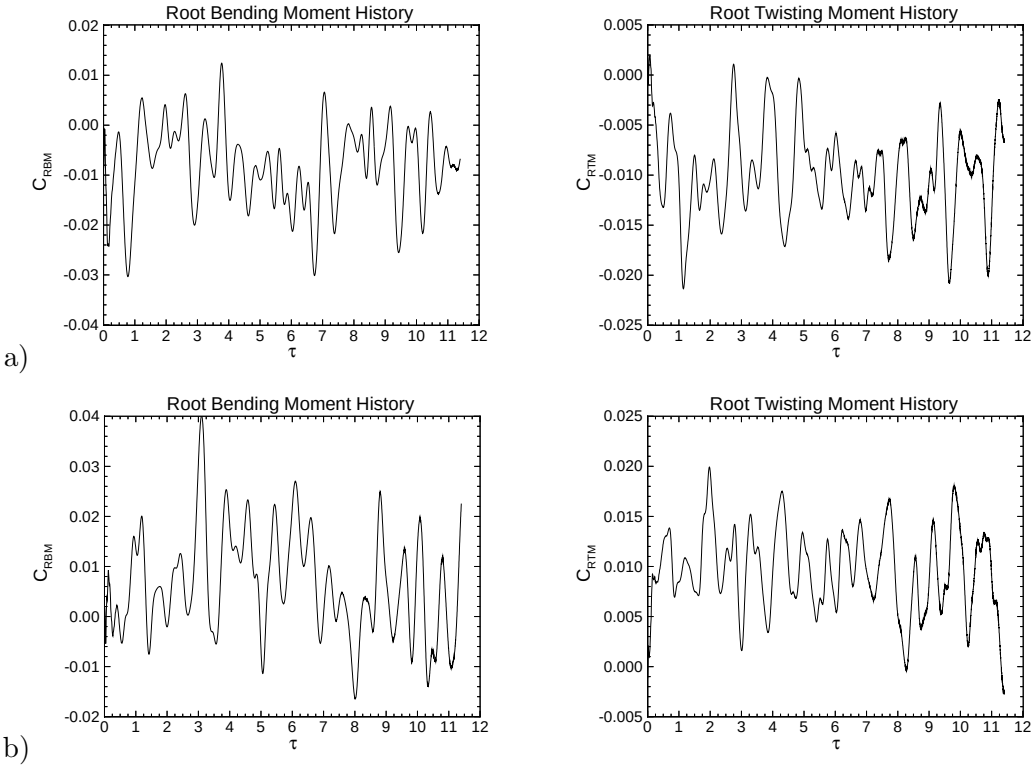

Figure 6.23: History of root bending moment coefficient and root twisting moment coefficient for a) right and b) left tails. Wide Flexible Case: $Re = 10^6$, $M = 0.4$, $\alpha = 30^o$.

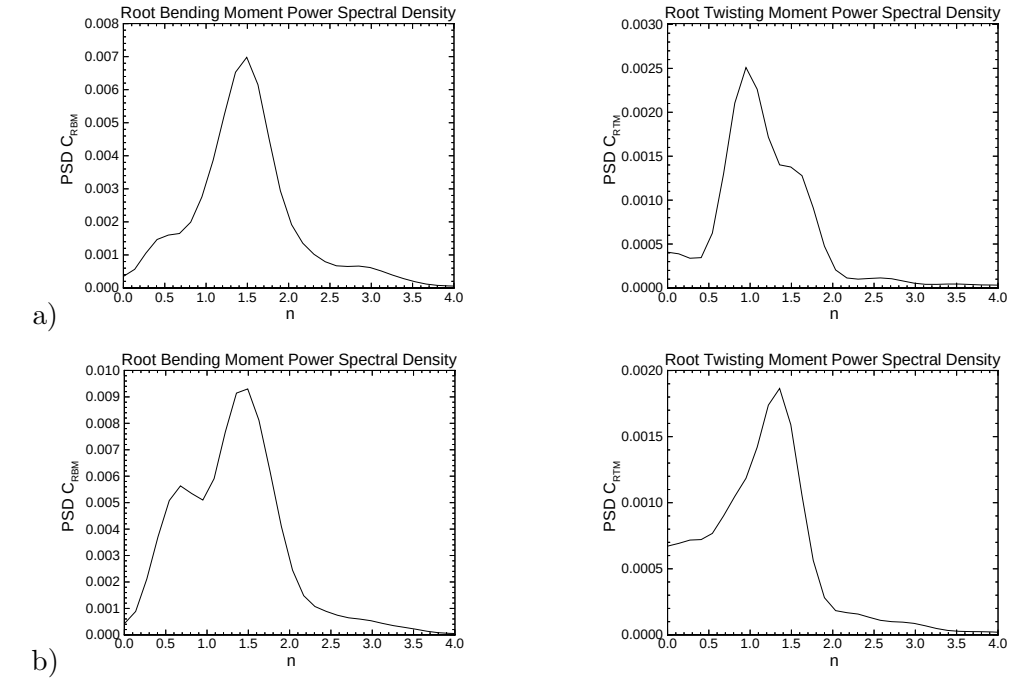

Figure 6.24: Power spectral density of root bending moment coefficient and root twisting moment coefficient versus reduced frequency for a) right and b) left tails. Wide Flexible Case: $Re = 10^6$, $M = 0.4$, $\alpha = 30^o$.

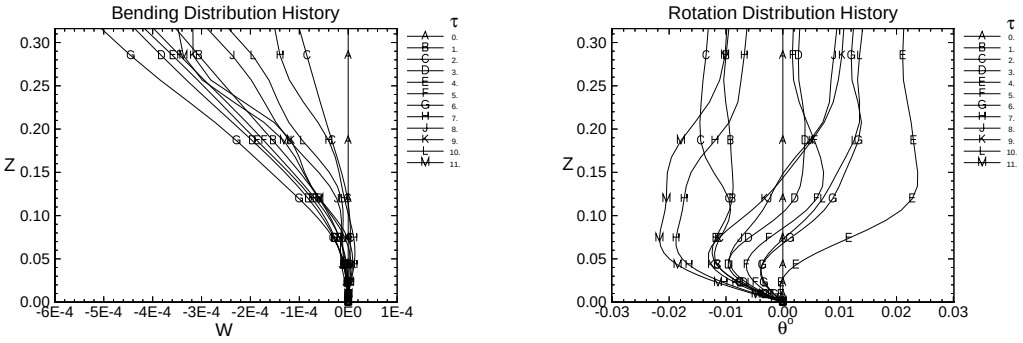

Figure 6.25: Right Tail: Bending and torsion deflection distributions along the tail span plotted at integer nondimensional time levels. Wide Flexible Case: $Re = 10^6$, $M = 0.4$, $\alpha = 30^o$.

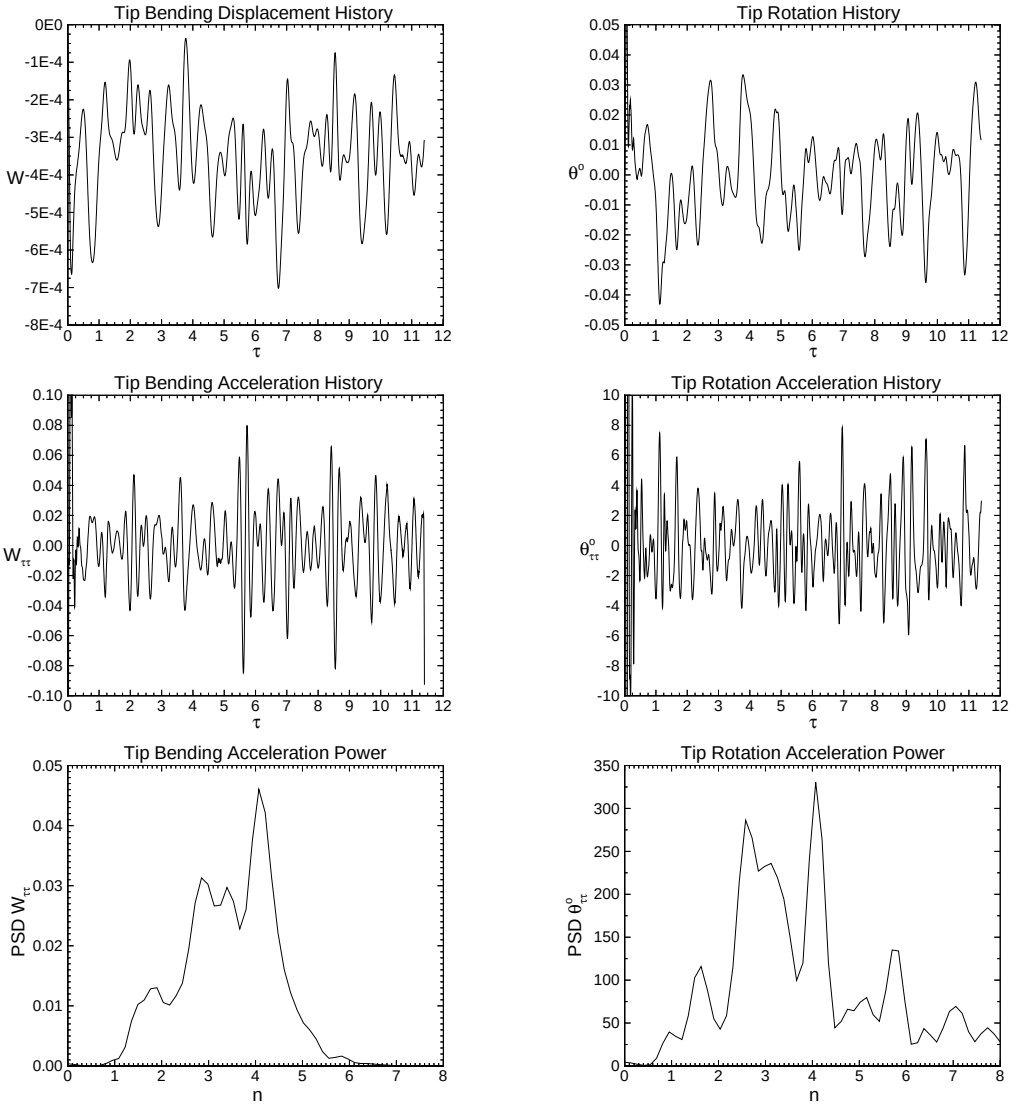

Figure 6.26: Right Tail: Time and frequency domain data for tip bending and torsion deflections and accelerations. Wide Flexible Case: $Re = 10^6$, $M = 0.4$, $\alpha = 30^o$.

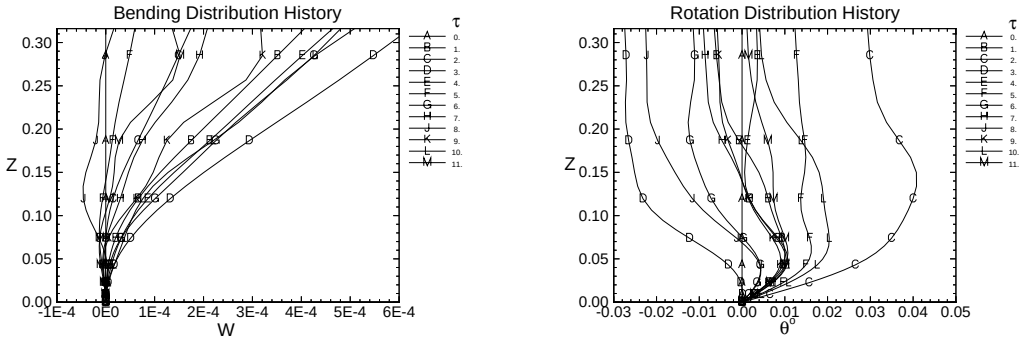

Figure 6.27: Left Tail: Bending and torsion deflection distributions along the tail span plotted at integer nondimensional time levels. Wide Flexible Case: $Re = 10^6$, $M = 0.4$, $\alpha = 30^o$.

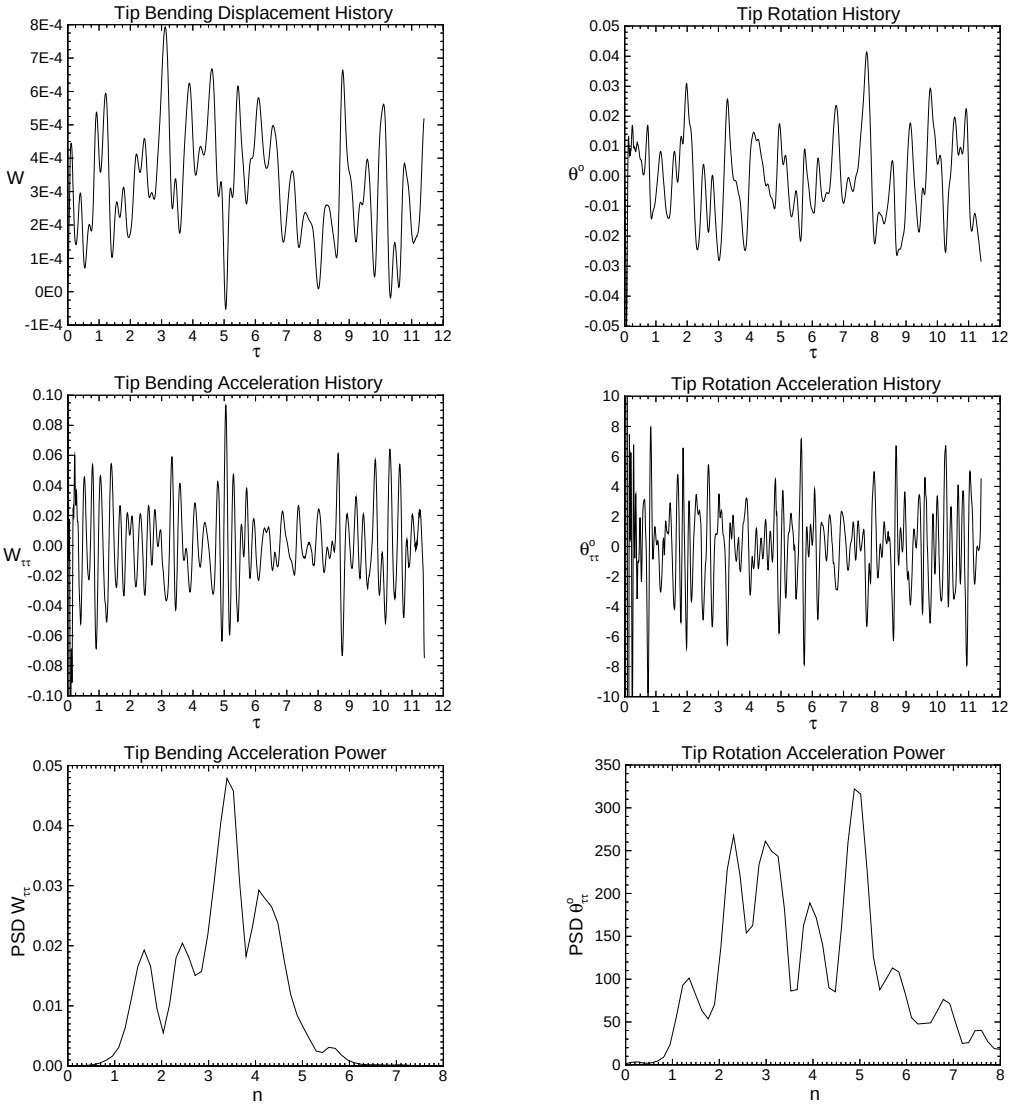

Figure 6.28: Left Tail: Time and frequency domain data for tip bending and torsion deflections and accelerations. Wide Flexible Case: $Re = 10^6$, $M = 0.4$, $\alpha = 30^o$.

6.3 Narrow Fuselage Model

6.3.1 Model Geometry and Computational Domain

For this case, the trailing edge extensions on the outside of each tail have been removed. This narrow fuselage configuration is the closest representation of all the cases in this study to the wing/tail/fuselage arrangement of the F/A-18. The only other change from the previous case is to the bottom surface of the wing. Instead of a completely flat wing with zero thickness, a more realistic Hummel [11] type wing consisting of a lower diamond shaped surface with an apex thickness of $0.021c$ at $x = 0.9c$, see Figure 6.29.The blocking arrangements and number of grid points used in this case is identical to the previous wide case, Figure 6.30. To accommodate the narrow fuselage, a mixed solid/wake boundary condition was written for the $k = 1$ plane of block 3, which covers the volume between the outer sides of the tails.

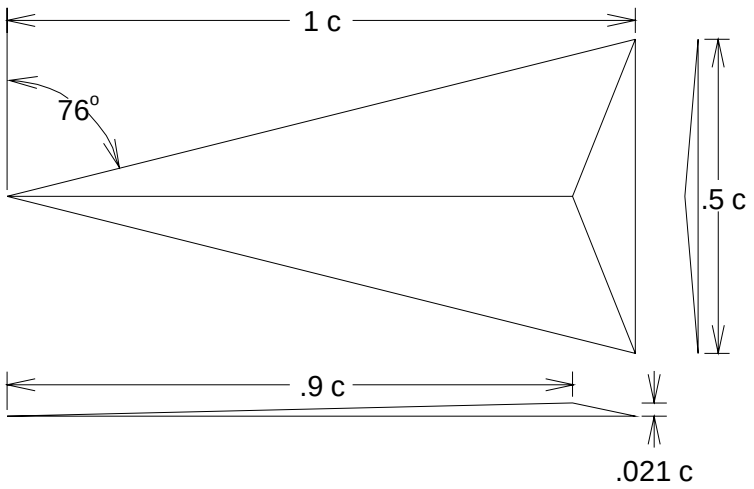

Figure 6.29: Diagram of Hummel [11] type delta wing.

a)

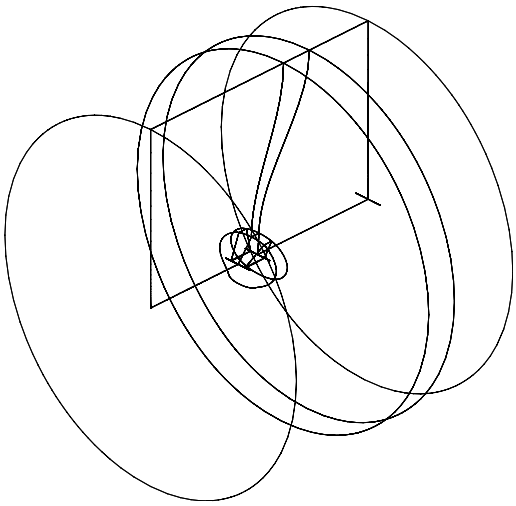

b)

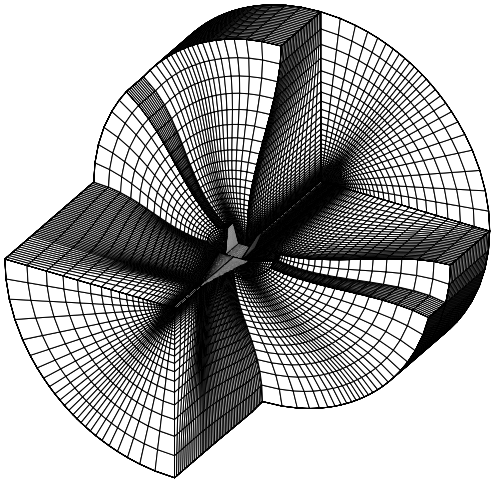

c)

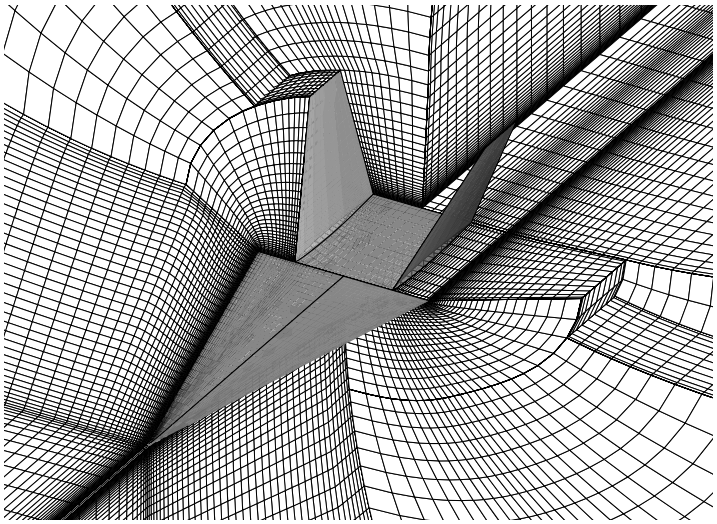

Figure 6.30: a) Block boundaries. b) Cutaway view showing individual blocks. c) Close up view of surface grids. Narrow Fuselage Case.

6.3.2 Freestream Flow Conditions and Tail Material Properties

The flow conditions and tail structural properties for the narrow fuselage case are the same as for the wide fuselage case. The angle-of-attack is 30^o. The freestream Mach and Reynolds numbers are 0.4 and 10^6, respectively. The tail material dimensionless moduli of elasticity and rigidity, E and G, are 1.8×10^5 and 0.678×10^5, respectively. The nondimensional density, ρ, is 26.1.

6.3.3 Initial Conditions, $Re = 10^6$, $M = 0.4$, $\alpha = 30^o$

The initial flow state is obtained by the same method as the wide fuselage case. The flow is first solved using local time stepping for 2000 iterations, time accurate stepping for another five nondimensional time with $\Delta\tau = 0.00036$.

Comparing the 3-D streamline plots of Figure 6.31 with those of the wide fuselage case shows that one effect of a narrower fuselage is a slightly smaller breakdown bubble and a tighter post breakdown core which flows mainly on the inside of the tails. The breakdown location is unaffected and occurs at 78% root chord. The pressure coefficient contours in the same figures also reveal that the principle difference between the wide and narrow fuselage C_p distributions occur on the outer sides of the tails. This is due to the formation of a vortex by the flow rolling up around the edge of the aft fuselage. The imprint of this vortex can be clearly seen on the lower 25% of the tail span.

Near surface streamline plots of the right tail, shown in Figure 6.32, confirm that the flow on the outer side is now dominated by the freestream flow and the small vortex emanating from the bottom of the tail. The influence of this vortex can be seen in the prominent region of separation at the 17% span location of the tail. The wing surface

flow is much the same as it was for the wide fuselage, as is the pressure distribution shown in Figure 6.33.

The wing crossflow planes of total pressure coefficient and velocity vectors shown in Figure 6.34 confirm that there is little difference in the flow over the wing between the two cases. Note that in the crossflow planes of the narrow fuselage the cross section of the wing can now be clearly seen in the pressure contours and in the absence of velocity vectors. The tail crossflow planes confirm that the vortex emanating from the side of the aft fuselage section is much smaller and closer to the tail than in the wide fuselage case.

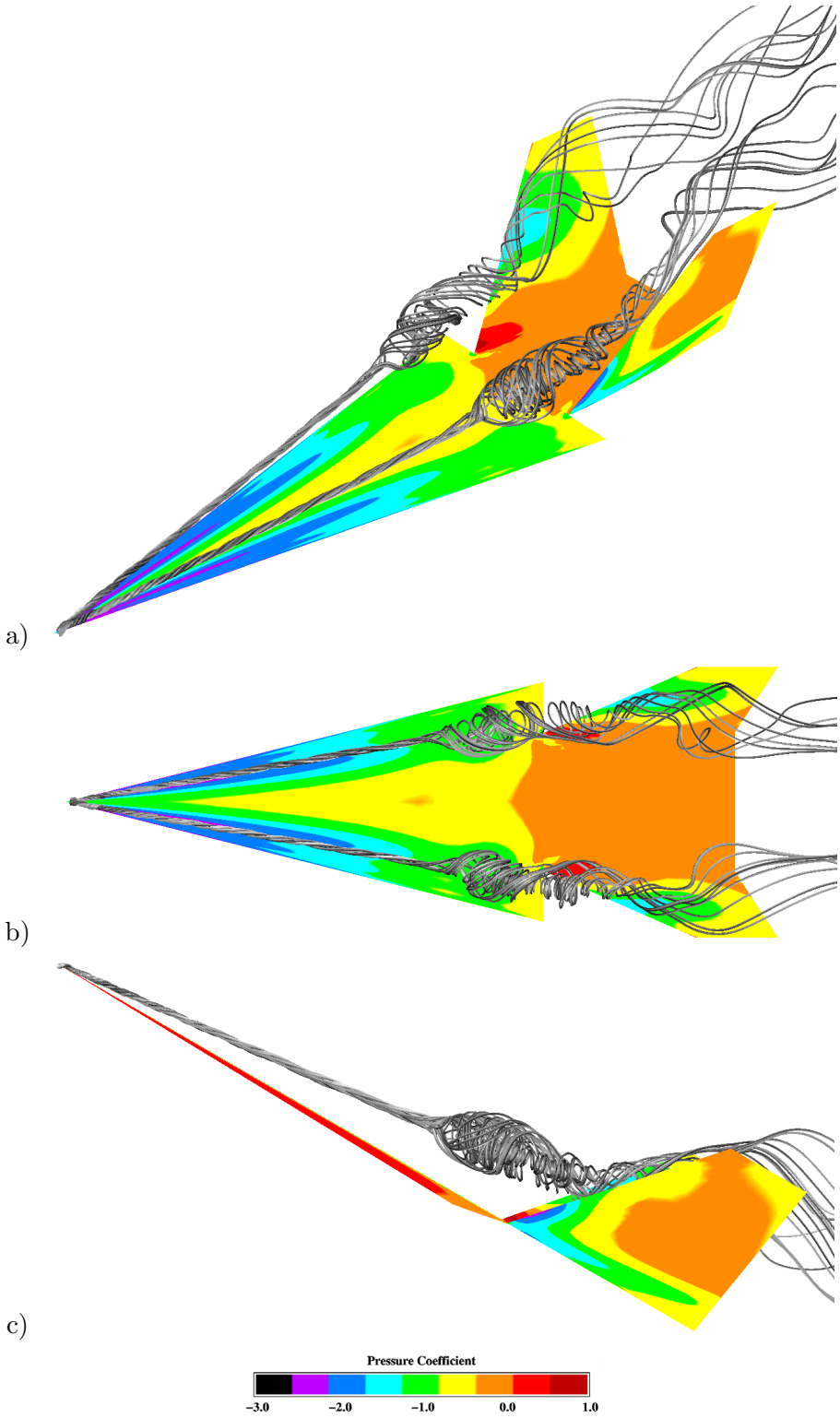

Figure 6.31: a) Three-dimensional, b) top and c) side views of surface pressure and vortex core streamlines. Initial Condition Flow Field: $Re = 10^6$, $M = 0.4$, $\alpha = 30^o$.

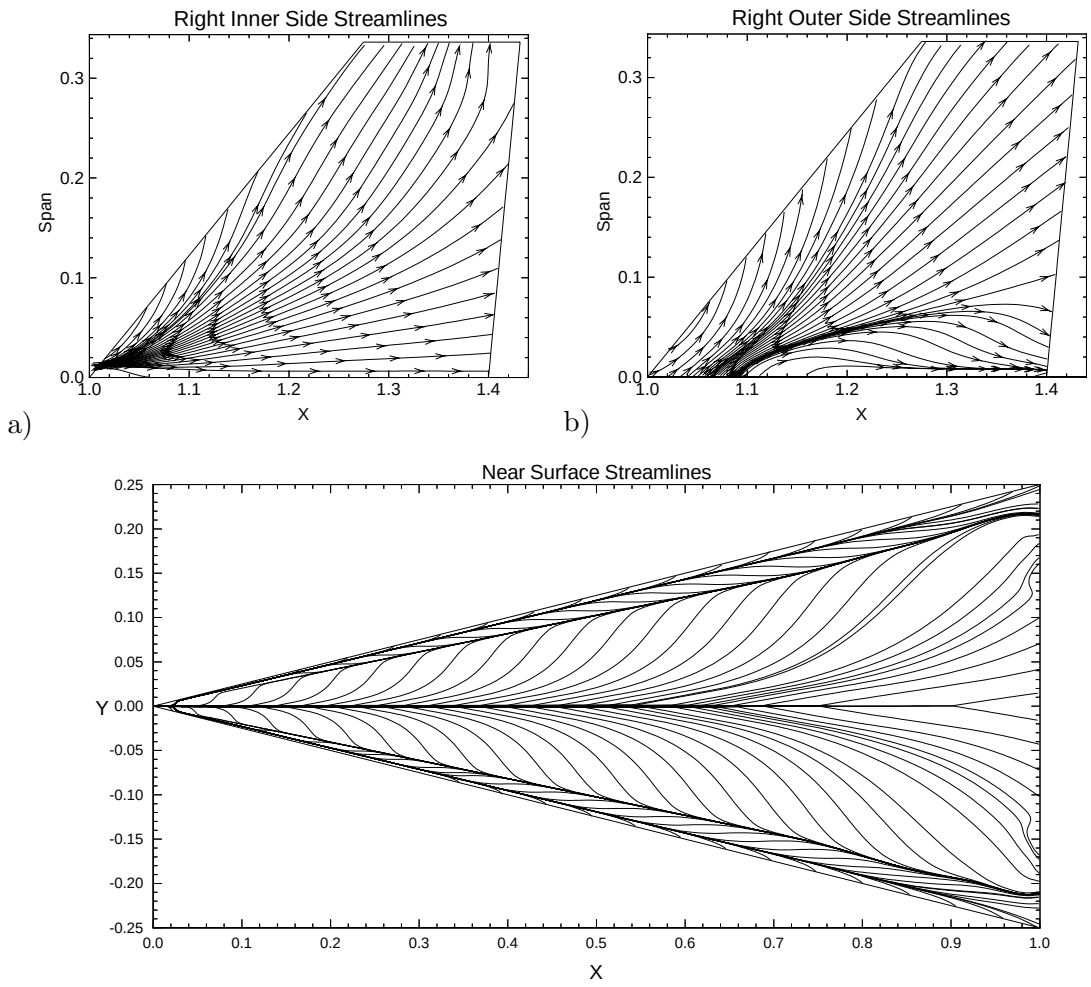

Figure 6.32: Near surface streamlines for the a) inner and b) outer right tail surfaces and the upper wing surface. Initial Condition Flow Field: $Re = 10^6$, $M = 0.4$, $\alpha = 30^o$.

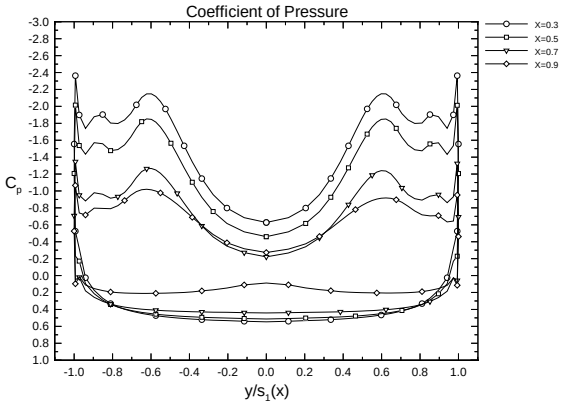

Figure 6.33: Coefficient of pressure on upper and lower wing surfaces at chord stations corresponding to plotted crossflow planes. Initial Condition Flow Field: $Re = 10^6$, $M = 0.4$, $\alpha = 30^o$.

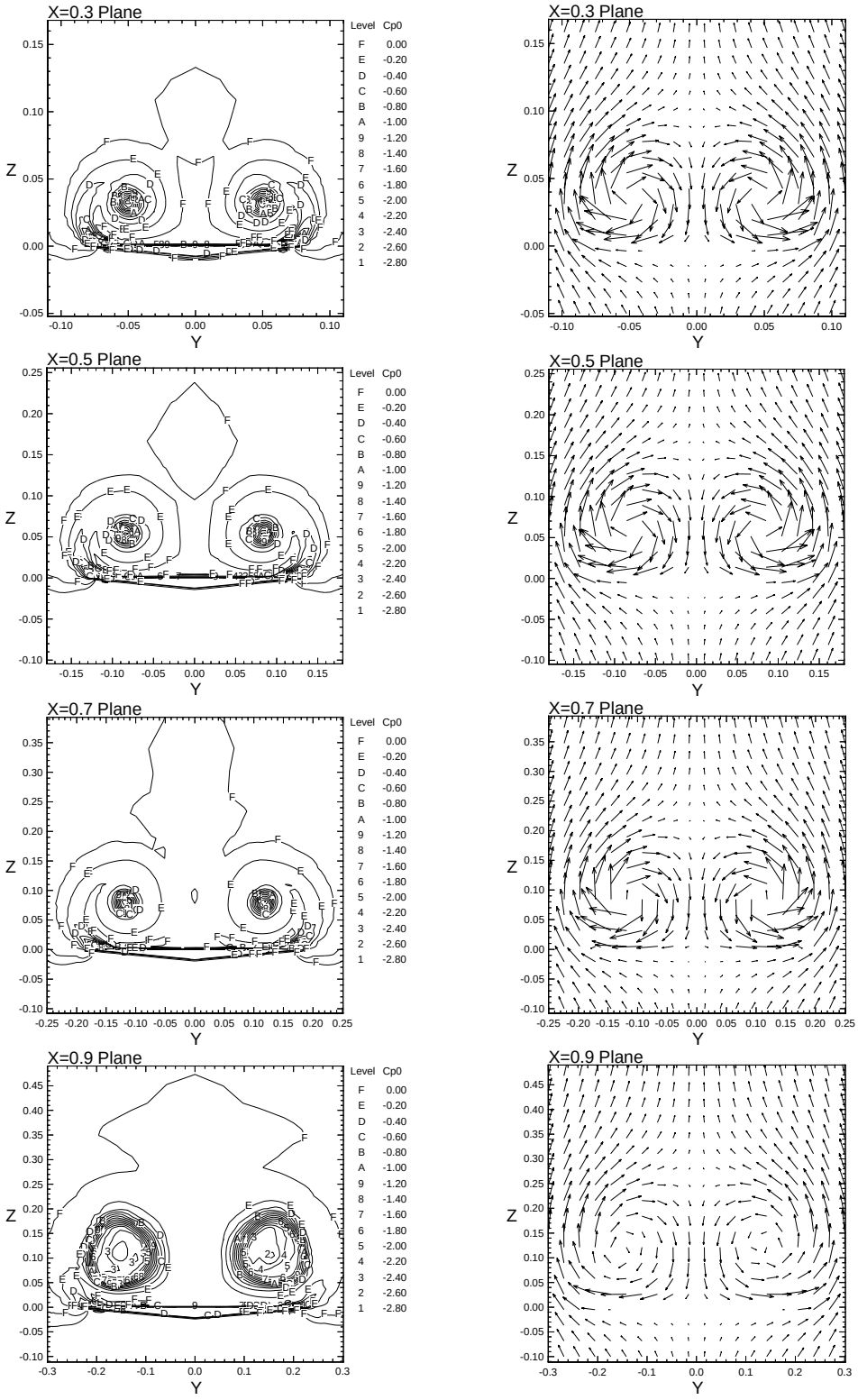

Figure 6.34: Total pressure coefficient and uniformly plotted velocity vectors on vertical crossflow planes above wing. Initial Condition Flow Field: $Re = 10^6$, $M = 0.4$, $\alpha = 30^o$.

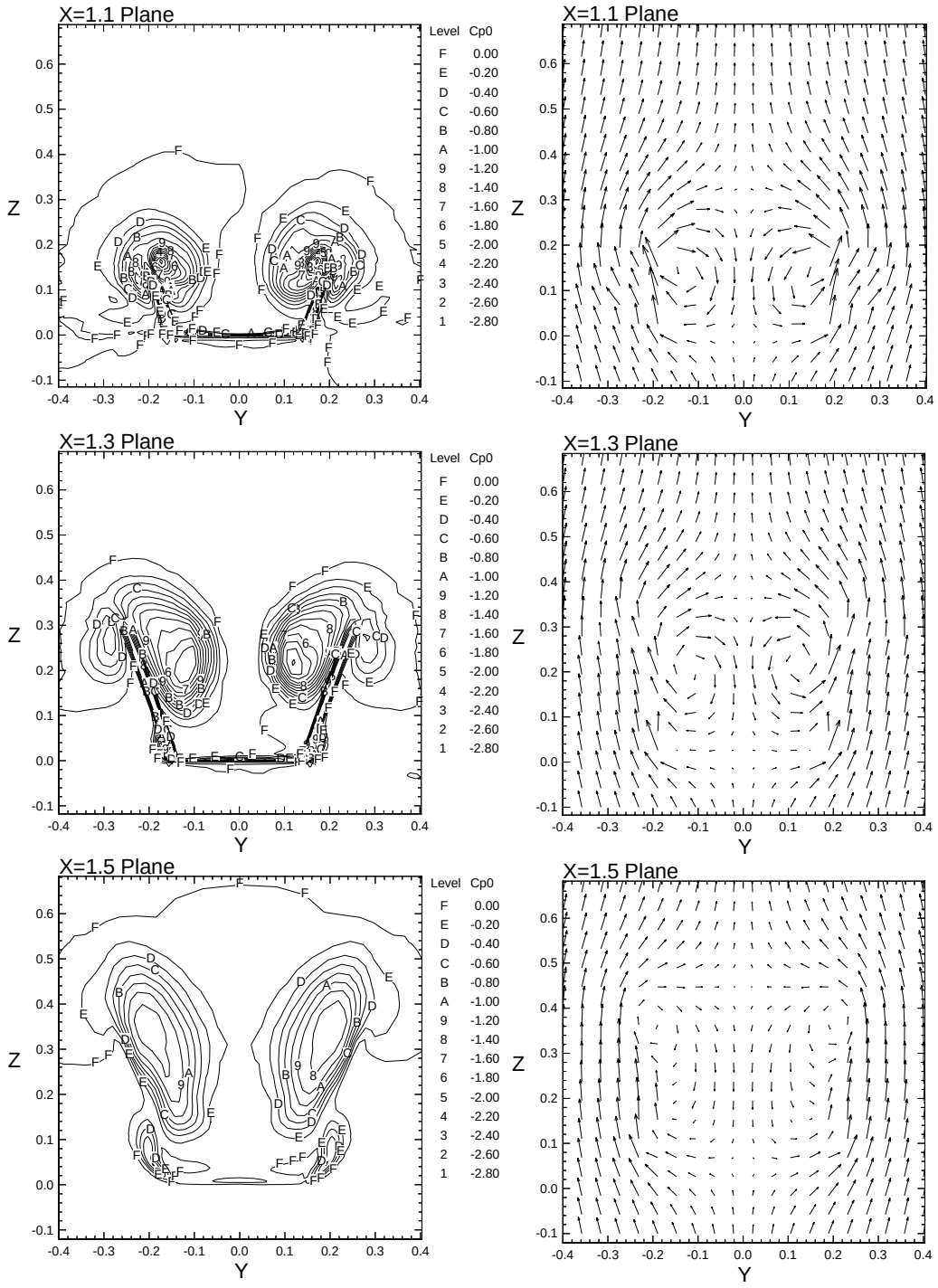

Figure 6.35: Total pressure coefficient and uniformly plotted velocity vectors on vertical crossflow planes near the tails. Initial Condition Flow Field: $Re = 10^6$, $M = 0.4$, $\alpha = 30^o$.

6.3.4 Load Histories for Rigid Tails

The purpose of this case is to determine the effect of a decrease in aft fuselage size without the complicating effects of dynamically deforming tails. Furthermore, comparisons with the flexible case in the next section will provide additional data on the effect that the dynamic tail response has on the buffet loading.

Inspection of the load distribution histories, shown in Figure 6.36 and the mean and RMS load distributions, see Figure 6.37, indicate that the steady loads are again virtually identical between the left and right tails, while the peak unsteady loadings differ by a maximum of $\pm 9\%$ and $\pm 13\%$ for the forces and moments, respectively. Essentially, the effect of the removal of the outer fuselage on the tail loading is to exaggerate or amplify the force and moment distribution of the wide case. This is due primarily to the increased proximity of the aft fuselage vortex to the outer tail surface. In addition, the primary wing vortex now passes mostly by the inside of the tail, due to the increased adverse pressure gradient created by the exposed wake.

The differential point pressure history, shown in Figure 6.39, clearly indicates a lower dominant frequency than in the wide fuselage case. The outer point pressure spectra confirms that the dominant frequency for the narrow case is 50% lower than the wide case. The outer pressure frequency does not change appreciably between the wide and narrow cases. A comparison of the statistics of the right-left averaged point pressure data for the wide and narrow fuselage rigid tail cases is presented in Table 6.6.

Root bending and twisting moment histories and spectra for each tail, shown in Figures 6.40 and 6.41, do not indicate a decrease in frequency with respect to the wide case, as in the point pressure data. This indicates that the effect was local. A comparison of the statistics of the right-left averaged root moment data for the wide and

narrow fuselage rigid tail cases is presented in Table 6.7. From the table it is clear that the main effect of the removal of the outer fuselage panels is to increase the unsteady loads, and hence the buffeting, by 18% and 27% for the RMS root bending and root twisting moment coefficients, respectively. This increase mirrors that observed in the buffet excitation parameter, which increased by 23% for the dominating inner side. Also observed is an very large increase in the mean root bending moment. However, mean loads are less relevant to buffeting.

	Rigid Tail Point Pressure Data					
	Wide Fuselage			Narrow Fuselage		
	p_{in}	p_{out}	p_{in-out}	p_{in}	p_{out}	p_{in-out}
Mean	8.14	8.49	-0.35	8.13	8.79	-0.66
RMS	0.17	0.05	0.18	0.19	0.03	0.20
n_d	2.1	1.4		1.0	1.8	
Peak Power	1.7	0.5		2.1	0.3	

Table 6.6: Comparison of averaged nondimensional pressure ($\frac{p}{q_\infty}$) data at 45% chord and 60% span on rigid tails for the wide and narrow fuselage cases: $Re = 10^6$, $M = 0.4$, $\alpha = 30^o$.

	Rigid Tail Root Loads							
	C_{RBM}				C_{RTM}			
Fuselage	Mean +tip outward	RMS	Peak	n_d	Mean +LE inward	RMS	Peak	n_d
Wide	-0.0078	0.0090	0.0064	1.3	-0.0098	0.0033	0.0024	1.1
Narrow	-0.0716	0.0106	0.0160	1.0	-0.0135	0.0042	0.0016	1.0
% Diff	818%	18%	150%	-23%	38%	27%	-33%	-9%

Table 6.7: Comparison of averaged root bending and twisting moment statistics, peak power and dominant frequency for rigid and stiff tail, wide fuselage cases: $Re = 10^6$, $M = 0.4$, $\alpha = 30^o$.

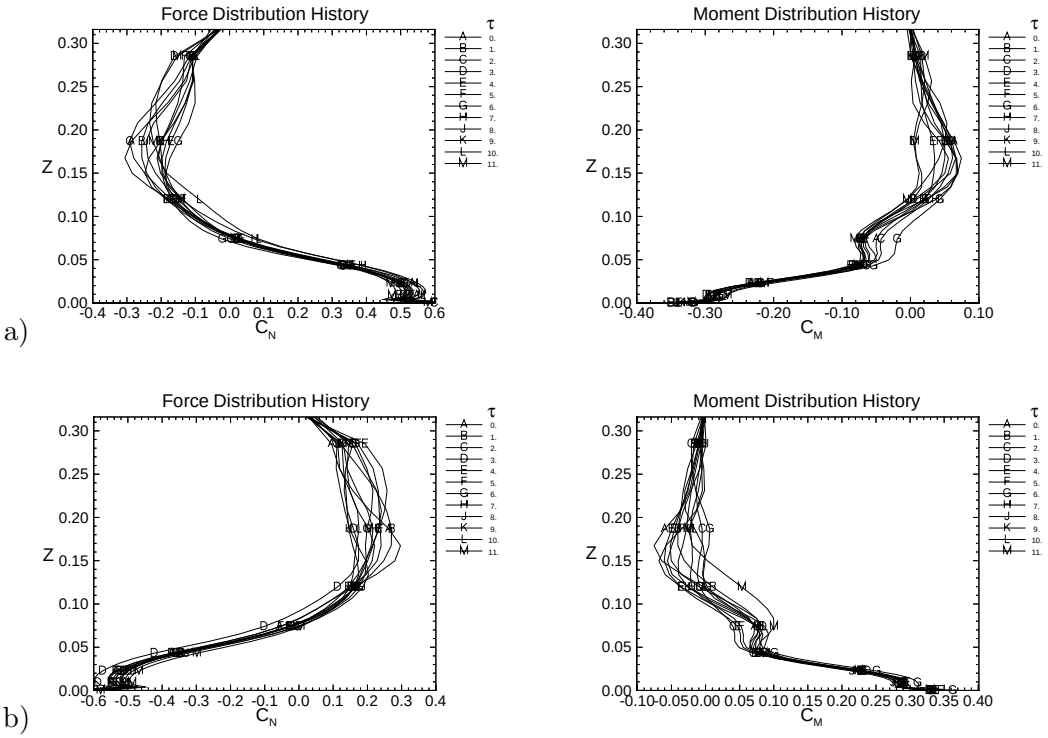

Figure 6.36: Bending force and twisting moment distributions along the tail span plotted at integer nondimensional time levels for a) right and b) left tails. Narrow Rigid Case: $Re = 10^6$, $M = 0.4$, $\alpha = 30^o$.

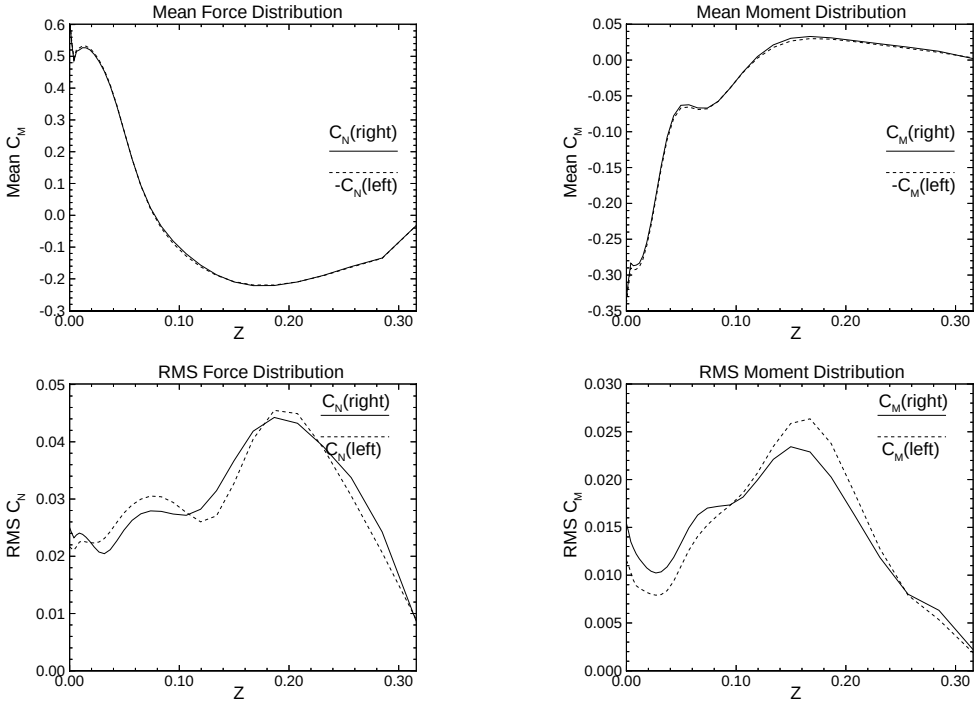

Figure 6.37: Mean and RMS load distributions along the right and left tail spans. Narrow Rigid Case: $Re = 10^6$, $M = 0.4$, $\alpha = 30^o$.

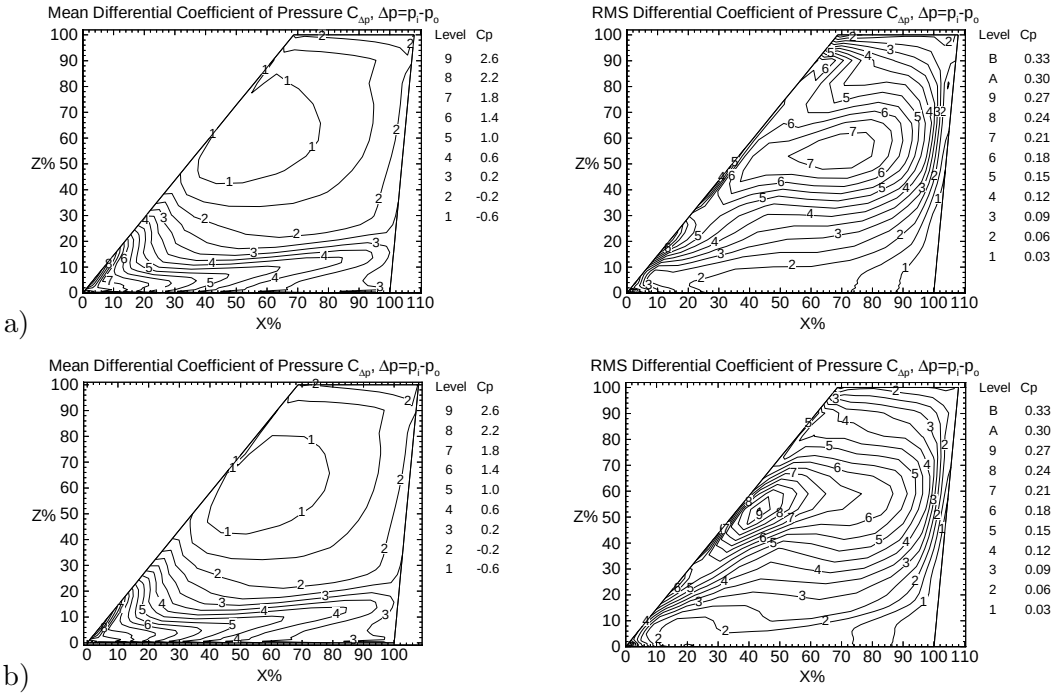

Figure 6.38: Mean and RMS differential coefficient of pressure contours on a) right and b) left tails. Narrow Rigid Case: $Re = 10^6$, $M = 0.4$, $\alpha = 30^o$.

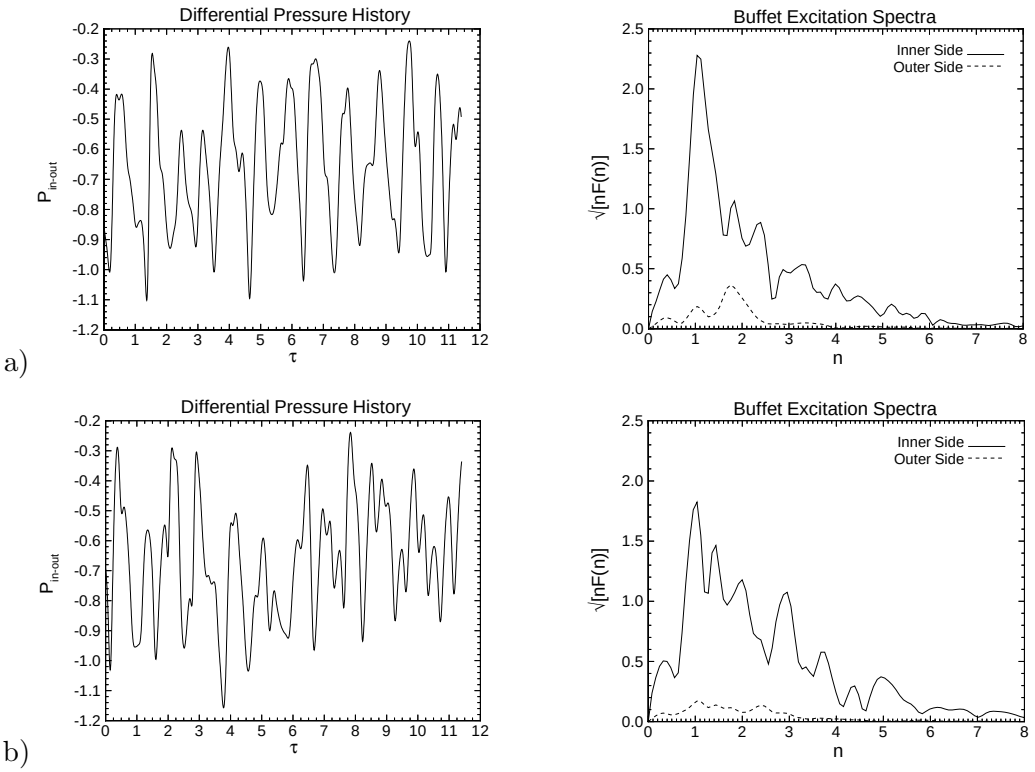

Figure 6.39: Differential pressure ($\frac{\Delta p}{q_\infty}$) histories at the 45% chord and 60% span location for a) right and b) left tails. Narrow Rigid Case: $Re = 10^6$, $M = 0.4$, $\alpha = 30^o$.

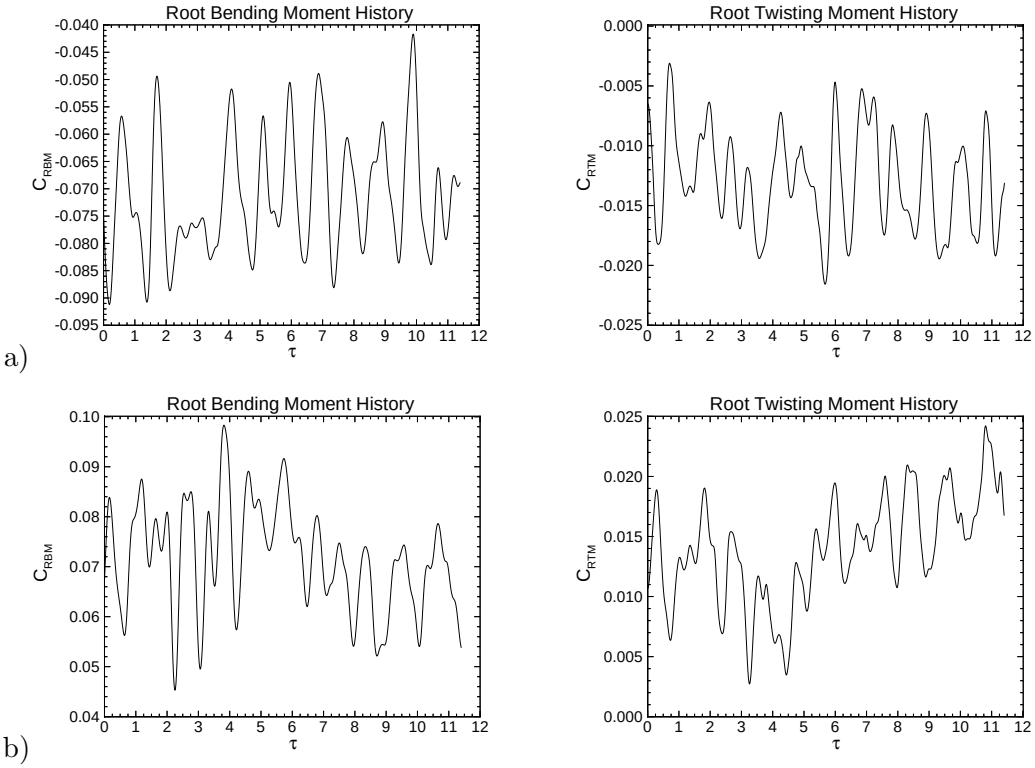

Figure 6.40: History of root bending moment coefficient and root twisting moment coefficient for a) right and b) left tails. Narrow Rigid Case: $Re = 10^6$, $M = 0.4$, $\alpha = 30^o$.

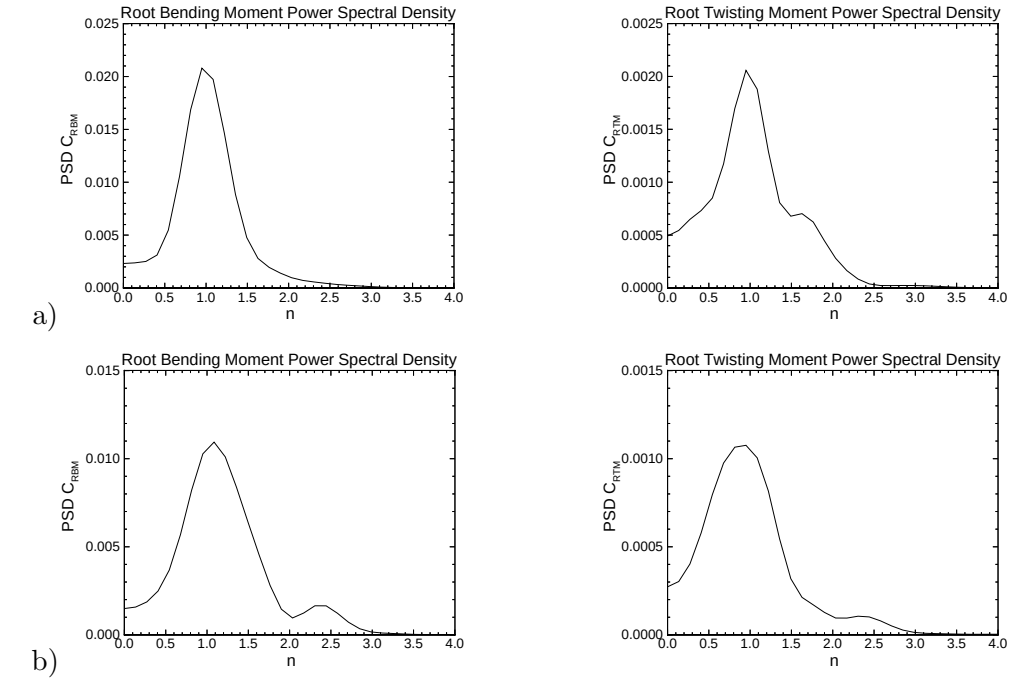

Figure 6.41: Power spectral density of root bending moment coefficient and root twisting moment coefficient versus reduced frequency for a) right and b) left tails. Narrow Rigid Case: $Re = 10^6$, $M = 0.4$, $\alpha = 30^o$.

6.3.5 Uncoupled Bending and Torsion Response

In this section, the buffet response due to inertially uncoupled bending and torsion vibrations of flexible but stiff twin F/A-18 tails is considered for the narrow fuselage case. The results from this case will be compared to the wide flexible case to assess the effect of decreased aft fuselage size on buffet loads and deflections. In addition, generalizations about the effect of the dynamic tail response on the buffet loading will be made, by contrasting this case with the rigid case of the previous section, as well as, considering the wide fuselage results.

As in the rigid tail case of the last section, the principle differences of the narrow fuselage loading, Figures 6.42-6.47, from the loading of the wide fuselage case, Figures 6.19-6.24, are a large increase in magnitude of the steady forces and a decrease in load frequencies, Table 6.8. This is due to the closeness of the aft fuselage vortex to the outer tail surface and the inside passage of the primary wing vortex. A similarity with the wide flexible case is the increase in the unsteady RMS bending loads over the rigid case from 10% to 78%. Thus, one effect of a stiff but flexible tail is to increase the unsteady loading.

Unlike the narrow rigid case, root bending and twisting moment histories and spectra for each tail, Figures 6.46 and 6.41, do indicate a decrease in frequency with respect to the wide flexible case, as in the point pressure data. A comparison of the statistics of the right-left averaged root moment data for the wide and narrow fuselage, flexible tail cases is presented in Table 6.9. From the table it is clear that as with the narrow rigid case, the removal of the outer fuselage panels increase the steady loads substantially. Despite the large increase in steady loads over the wide case, the unsteady RMS loads varied little, increasing for bending and decreasing for torsion.

Comparison of the narrow fuselage buffeting response plots, shown in Figures 6.25-6.28, with the wide case, see Figures 6.25-6.28, indicates that the principle effect of narrowing the fuselage is to increase the mean deflections. The right-left averaged responses are summarized in Table 6.10. Despite the large increase in mean deflections over the wide case, the amplitudes of the deflections and accelerations decreased overall as did the frequency of the accelerations. Hence, the overall buffet loads and response for the narrow case is approximately 30% less than the wide case. This can be attributed to the aerodynamic damping effect of having the outer side of the tail more exposed to the freestream.

	Flexible Tail Point Pressure Data					
	Wide Fuselage			Narrow Fuselage		
	p_{in}	p_{out}	p_{in-out}	p_{in}	p_{out}	p_{in-out}
Mean	8.14	8.49	-0.35	8.13	8.79	-0.66
RMS	0.17	0.05	0.18	0.20	0.03	0.21
n_d	1.9	1.3		1.1	1.9	
Peak Power	1.4	0.4		2.3	0.3	

Table 6.8: Comparison of averaged nondimensional pressure ($\frac{p}{q_\infty}$) data at 45% chord and 60% span on flexible stiff tails for the wide and narrow fuselage cases: $Re = 10^6$, $M = 0.4$, $\alpha = 30^o$.

	Flexible Tail Root Loads							
	C_{RBM}				C_{RTM}			
Fuselage	Mean +tip outward	RMS	Peak	n_d	Mean +LE inward	RMS	Peak	n_d
Wide	-0.0073	0.0092	0.0082	1.5	-0.0098	0.0043	0.0022	1.2
Narrow	-0.0711	0.0112	0.0180	1.0	-0.0123	0.0040	0.0019	1.0
% Diff	873%	22%	120%	-33%	26%	-7%	-14%	-17%

Table 6.9: Comparison of averaged root bending and twisting moment statistics, peak power and dominant frequency for wide and narrow fuselage, flexible tail cases: $Re = 10^6$, $M = 0.4$, $\alpha = 30^o$.

	Averaged Tip Response				
	Bending				
Fuselage	$A(w)$	Mean w +outward	$A(w_{\tau\tau})$	Peak Power	n_d
Wide	0.00032	-0.0004	0.078	0.047	3.8
Narrow	0.00033	-0.0011	0.048	0.032	2.6
% Diff	3%	175%	-38%	-32%	-19%
	Torsion				
Fuselage	$A(\theta)^o$	Mean θ^o +LE inward	$A(\theta_{\tau\tau})^o$	Peak Power	n_d
Wide	0.031	-0.0013	7.0	325.	4.5
Narrow	0.026	0.0190	5.0	108.	2.9
% Diff	-16%	136%	-29%	-67%	-36%

Table 6.10: Effect of fuselage width reduction on buffeting response. $Re = 10^6$, $M = 0.4$, $\alpha = 30^o$.

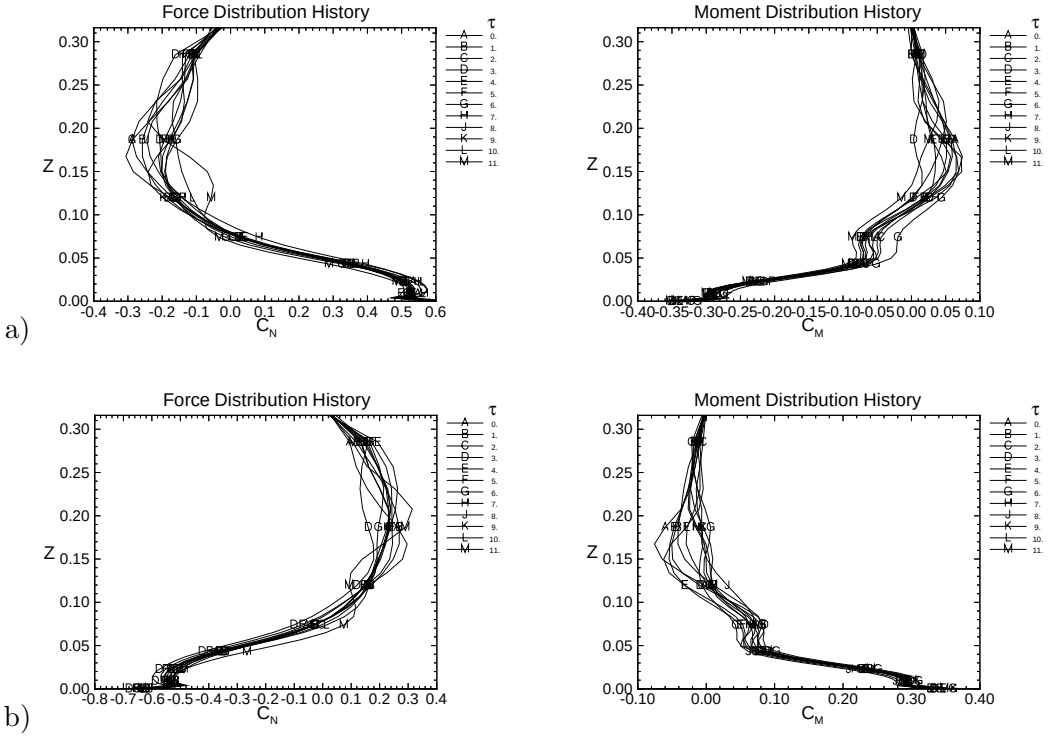

Figure 6.42: Bending force and twisting moment distributions along the tail span plotted at integer nondimensional time levels for a) right and b) left tails. Narrow Flexible Case: $Re = 10^6$, $M = 0.4$, $\alpha = 30^o$.

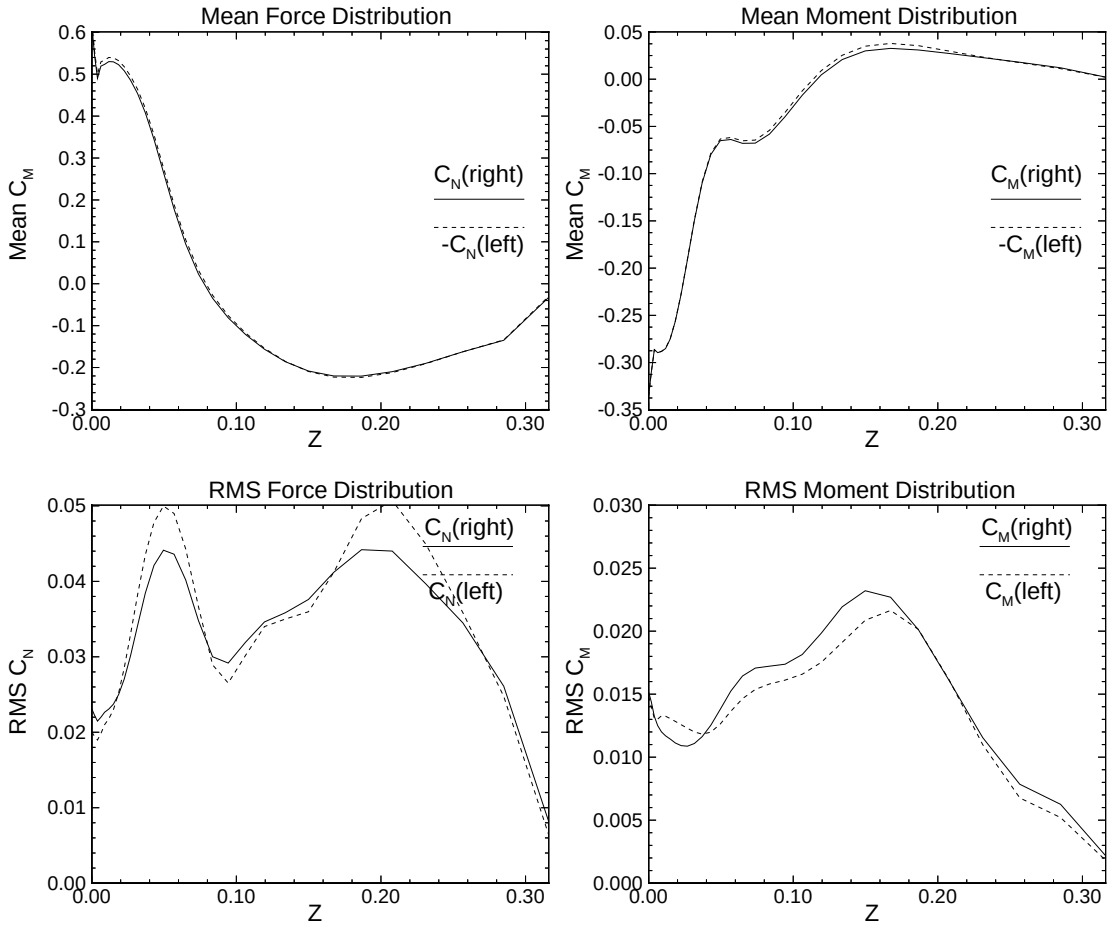

Figure 6.43: Mean and RMS load distributions along the right and left tail spans. Narrow Flexible Case: $Re = 10^6$, $M = 0.4$, $\alpha = 30^o$.

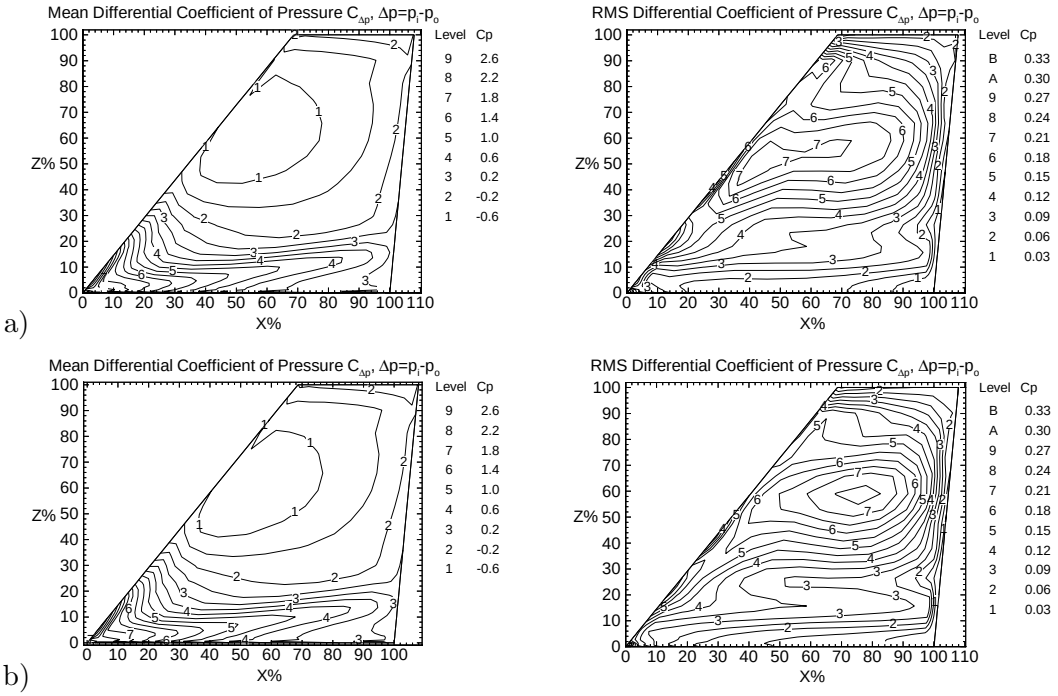

Figure 6.44: Mean and RMS differential coefficient of pressure contours on a) right and b) left tails. Narrow Flexible Case: $Re = 10^6$, $M = 0.4$, $\alpha = 30^o$.

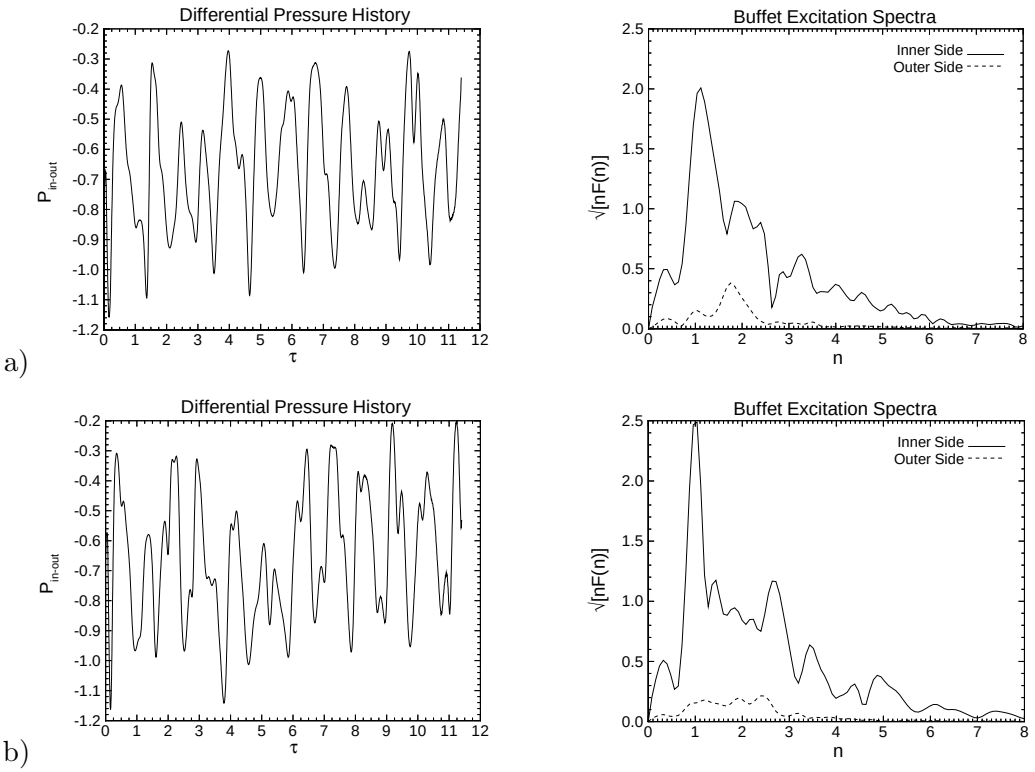

Figure 6.45: Differential pressure ($\frac{\Delta p}{q_\infty}$) histories at the 45% chord and 60% span location for a) right and b) left tails. Narrow Flexible Case: $Re = 10^6$, $M = 0.4$, $\alpha = 30^o$.

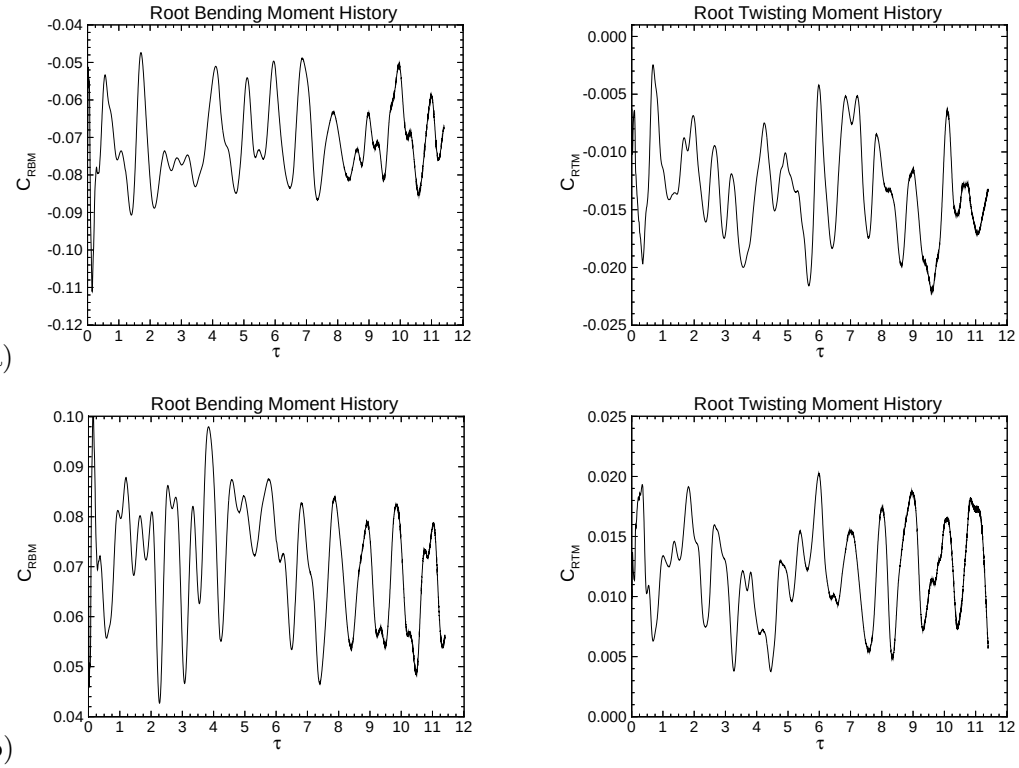

Figure 6.46: History of root bending moment coefficient and root twisting moment coefficient for a) right and b) left tails. Narrow Flexible Case: $Re = 10^6$, $M = 0.4$, $\alpha = 30^o$.

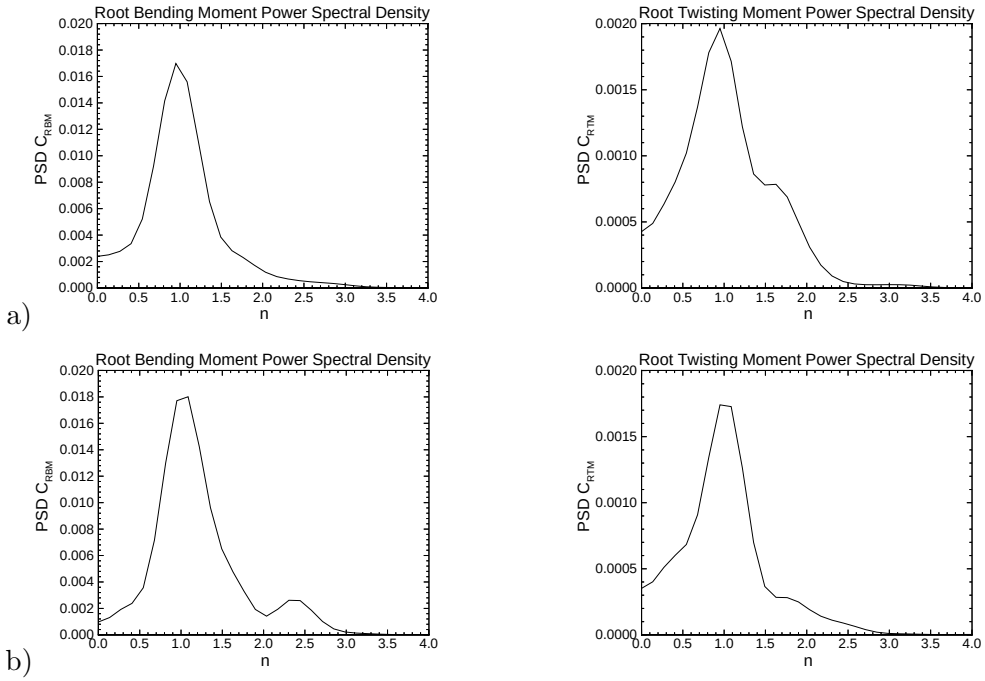

Figure 6.47: Power spectral density of root bending moment coefficient and root twisting moment coefficient versus reduced frequency for a) right and b) left tails. Narrow Flexible Case: $Re = 10^6$, $M = 0.4$, $\alpha = 30^o$.

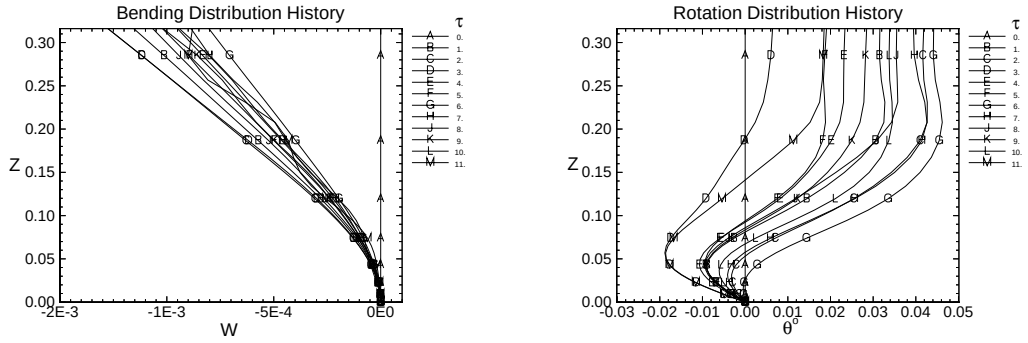

Figure 6.48: Right Tail: Bending and torsion deflection distributions along the tail span plotted at integer nondimensional time levels. Narrow Flexible Case: $Re = 10^6$, $M = 0.4$, $\alpha = 30^o$.

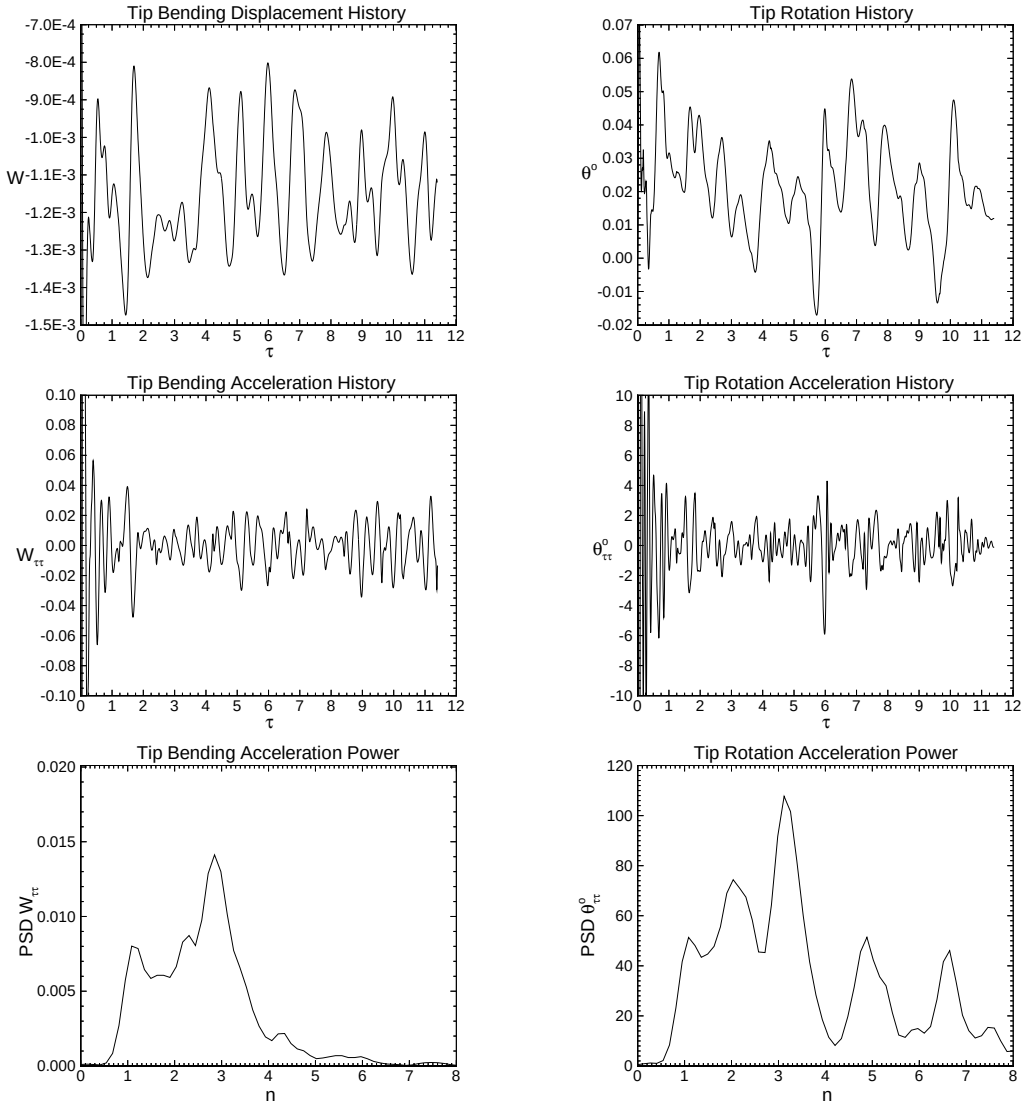

Figure 6.49: Right Tail: Time and frequency domain data for tip bending and torsion deflections and accelerations. Narrow Flexible Case: $Re = 10^6$, $M = 0.4$, $\alpha = 30^o$.

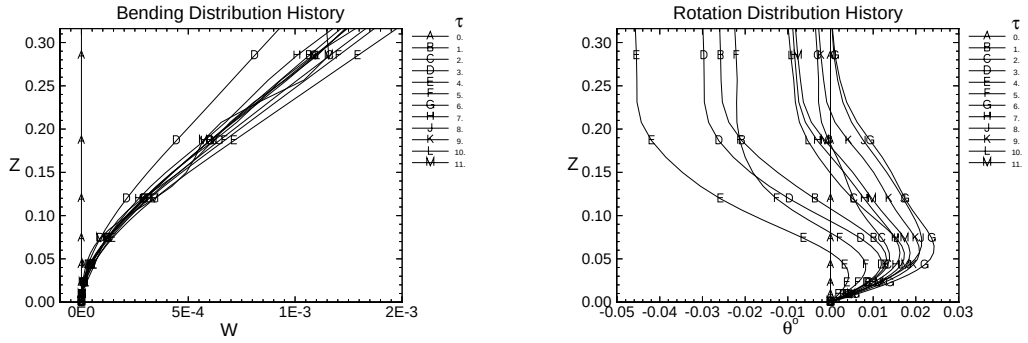

Figure 6.50: Left Tail: Bending and torsion deflection distributions along the tail span plotted at integer nondimensional time levels. Narrow Flexible Case: $Re = 10^6$, $M = 0.4$, $\alpha = 30^o$.

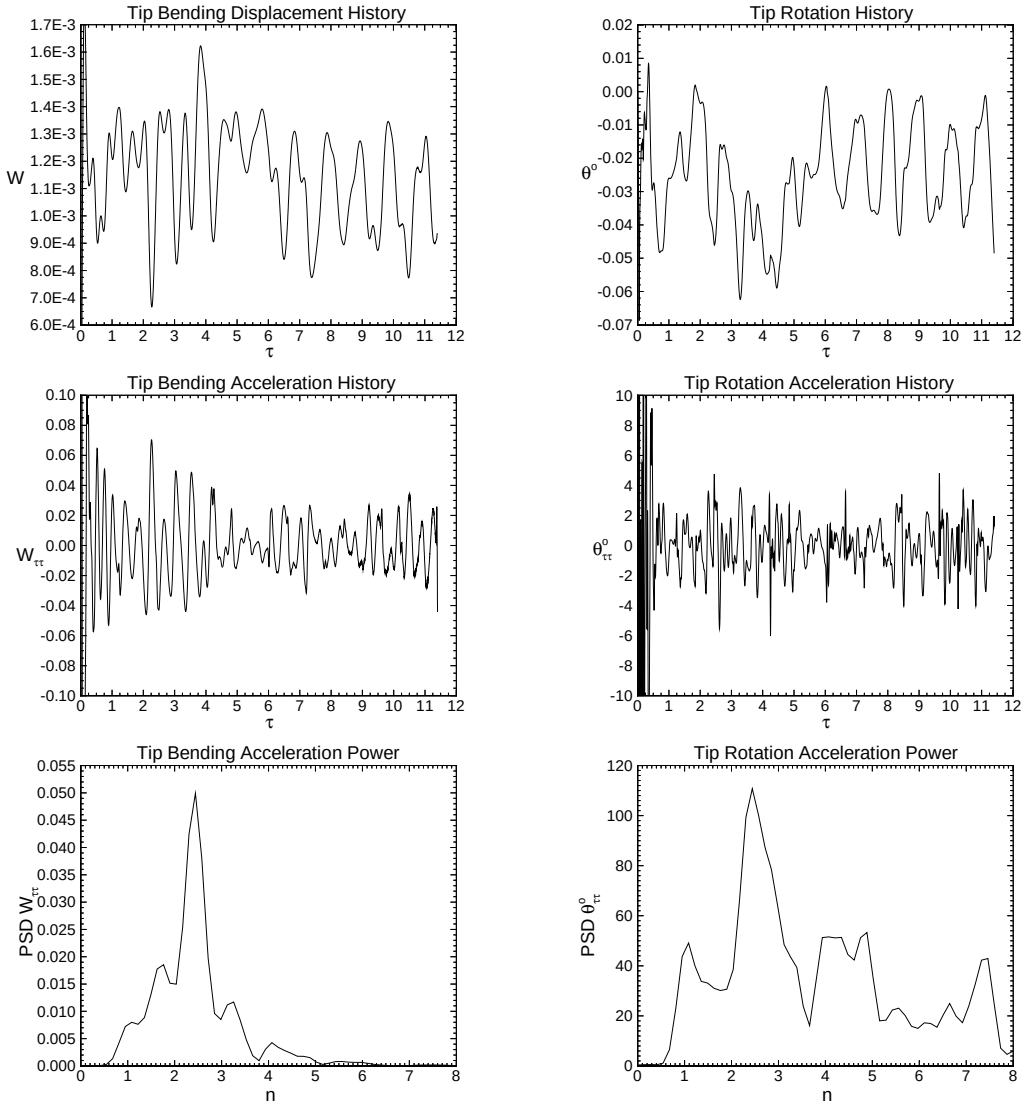

Figure 6.51: Left Tail: Time and frequency domain data for tip bending and torsion deflections and accelerations. Narrow Flexible Case: $Re = 10^6$, $M = 0.4$, $\alpha = 30^o$.

6.3.5.1 Comparison with Experimental Data

The narrow fuselage model, although simple, offers the closest approximation of all the models in this study to the characteristics of the full F/A-18 aircraft vortex/vertical tail configuration. Therefore, before continuing with the remaining F/A-18 case results from the narrow fuselage, the flexible tail case will be compared to published experimental data.

Recall that the standard non-dimensionalization scheme uses the wing mean aerodynamic chord for length, but in this study only the F/A-18 vertical tail is modeled. The delta wing is only a device to create the vortical flow and is not similar to the F/A-18 wing. Hence, in order to compare with F/A-18 data, the length scales must first be referenced to the tail instead of the wing. This is done by replacing all occurences of $\overline{\overline{c}}_{wing}$ with $\overline{\overline{c}}_{tail}$. The converted equations for nondimensional time, frequency, root bending moment and root twisting moment are as follows;

$$\tau = \frac{tV_\infty}{\overline{\overline{c}}_w} \times \frac{\overline{\overline{c}}_w}{\overline{\overline{c}}_t} \tag{6.5}$$

$$n = \frac{f\overline{\overline{c}}_w}{V_\infty} \times \frac{\overline{\overline{c}}_t}{\overline{\overline{c}}_w} \tag{6.6}$$

$$\left(\sqrt{nF(n)}\right)_t = \left(\sqrt{nF(n)}\right)_w \times \sqrt{\frac{\overline{\overline{c}}_t}{\overline{\overline{c}}_w}} \tag{6.7}$$

$$C_{RBM} = \frac{M_{RB}}{\frac{1}{2}\rho_\infty V_\infty^2 S_t \overline{\overline{c}}_w} \times \frac{\overline{\overline{c}}_w}{\overline{\overline{c}}_t} \tag{6.8}$$

$$\text{Peak Power } (C_{RBM})_t = \text{Peak Power } (C_{RBM})_w \times \left(\frac{\overline{\overline{c}}_w}{\overline{\overline{c}}_t}\right)^3 \tag{6.9}$$

The length ratios for the F/A-18 and the CFD model are as follows;

$$\left(\frac{\overline{\overline{c}}_w}{\overline{\overline{c}}_t}\right)_{F/A-18} = \frac{11.52ft}{6.99ft} = 1.648 \tag{6.10}$$

$$\left(\frac{\overline{\overline{c}}_w}{\overline{\overline{c}}_t}\right)_{CFD} = \frac{2/3}{0.297} = 2.245 \tag{6.11}$$

In Tables 6.11 and 6.12, comparisons of point pressure data at 45% chord and 60% span and root bending moment, respectively, are summarized. The purpose of a comparison with full aircraft data is to establish the relevance of the present simplified model in its capability of providing insight into the full aircraft tail buffeting problem. Although nondimensional quantities are compared, the lack of geometric similarity precludes quantitative agreement. However, internal comparisons can be made such as the ratio between buffet excitation frequency and root bending moment, which was 1.08 and 1.1 for the present CFD case and the average experimental data, respectively. The ratio of inner to outer pressure coefficient did not compare as favorably though, with a ratio of over 5 for the CFD and 2 for the experimental values. This is indicative of the differences between the aircraft flow field and the delta wing model. Despite these differences, the inner RMS pressure and the dominant frequencies did match fairly well with differences of 15% and 50%, respectively.

Case	RMS $C_{p_{in}}$	RMS $C_{p_{out}}$	RMS $C_{p_{in}} - C_{p_{out}}$	Buffet n_d	Buffet Peak Power
Present CFD $M = 0.40$ $\alpha = 30^o$	0.21	0.04	0.22	0.49	1.53
Full Scale [81] $M = 0.15$ $\alpha = 32^o$	-	-	0.37	0.33	0.34
Flight [93] $M = 0.24$ $\alpha = 30.3^o$	0.24	0.12	0.30	0.33	-
Full Scale [60] $M = 0.15$ $\alpha = 32^o$	-	-	-	0.35	0.33
Full Scale [93] $M = 0.15$ $\alpha = 30^o$	0.28	0.15	0.36	0.33	-
6% Scale [93] $M = 0.15$ $\alpha = 30^o$	0.22	0.10	-	0.33	-

Table 6.11: Comparison with experimental data for averaged nondimensional pressure ($\frac{p}{q_\infty}$), pressure coefficient (C_p), buffet excitation ($\sqrt{nF(n)}$) dominant frequency (n_d), and buffet excitation peak power at 45% chord and 60% span on the flexible stiff tail for the narrow fuselage case. The length scale is nondimensionalized by $\overline{\overline{c}}_t$.

Case	RMS C_{RBM}	n_d	Peak Power
Present CFD $M = 0.40$ $\alpha = 30^o$	0.025	0.45	0.20
Full Scale [81] $M = 0.15$ $\alpha = 30^o$	0.096	0.30	0.04
Full Scale [94] $M = 0.15$ $\alpha = 30^o$	0.076	-	-
Full Scale [60] $M = 0.15$ $\alpha = 32^o$	0.096	0.30	0.04

Table 6.12: Experimental data comparison of averaged unsteady root bending moment, peak power and dominant frequency for the flexible stiff tail on the narrow fuselage. The length scale is nondimensionalized by $\overline{\overline{c}}_t$.

6.4 Open Fuselage Model

6.4.1 Model Geometry and Computational Domain

In this section, the effects of removing the aft fuselage panels and decreasing the tail stiffness on the buffet loading and response will be assessed. Geometrically the open fuselage configuration differs from the previous case only by the removal of the center fuselage panel. To accommodate the wake boundary condition between the tails, a new blocking strategy was used. Namely, the blocks surrounding the tails were recut to be symmetric with respect to the wake plane. The outer blocks were also consolidated by using mixed boundary conditions for the tail surfaces, see Figure 6.52. The total number of grid cells and clustering remains unchanged from the previous F/A-18 cases. For the remainder of this study the open fuselage configuration will be used, but with highly swept tails. Thus, this case will also serve as a transition case from the F/A-18 tail to the swept tails considered in the following chapter which are modeled after the experimental wind tunnel model of Washburn et al. [12].

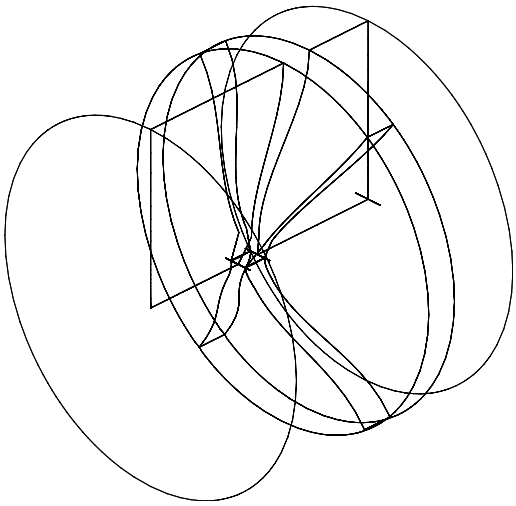

a)

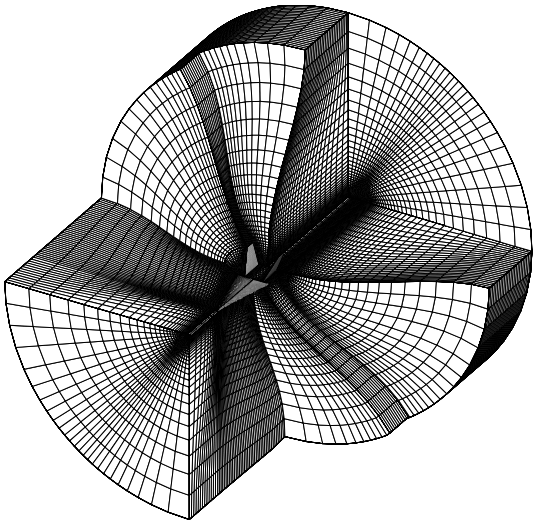

b)

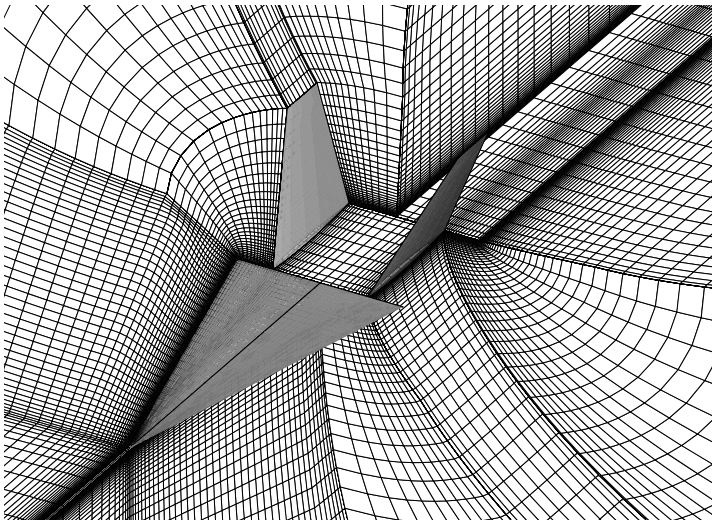

c)

Figure 6.52: a) Block boundaries. b) Cutaway view showing individual blocks. c) Close up view of surface grids. Open Fuselage Case.

6.4.2 Freestream Flow Conditions and Tail Material Properties

Since most flight test data is obtained at $M = 0.3$ or less, the Mach number for this case was reduced from $M = 0.4$ to $M = 0.3$. Although much of the wind tunnel data was obtained at $M = 0.15$, CFD computations had to be restricted to $M = 0.3$ for numerical convergence considerations since CFL3D is a compressible code. The Re was also reduced by 25%. However, flow comparisons with the wide and narrow cases are still valid since it has been shown experimentally that vortex breakdown is fairly insensitive to Re and changes in low subsonic Mach number.

In the single tail model of Chapter 5, the choice of tail structural properties resulted in very large deflections and in the wide and narrow cases of this chapter, the tail stiffness was greatly increased resulting in very small deflections. For the present open fuselage case, the tail material properties were chosen based on the dynamically scaled wind tunnel model of Washburn et al. [12], who used a solid tail made of balsa wood with a thin aluminum core. The Washburn scaling was based on a delta wing root chord of 18 inches. For the present case, the resulting nondimensional material moduli of elasticity and rigidity, E and G, are 4.6×10^3 and 1.8×10^3, respectively. This represents a reduction in stiffness by a factor of 40 over the previous F/A-18 tail cases. The nondimensional density, ρ, is now 147, which is nearly 6 times greater than the previous case. A further decrease in the effective stiffness was achieved by using a tail thickness of 1/2 of the geometric thickness that the CFD computations see.

6.4.3 Initial Conditions, $Re = 0.75 \times 10^6$, $M = 0.3$, $\alpha = 30^o$

The initial flow state is obtained by the same method as in the previous twin tail cases. The flow is first solved using local time stepping for 2000 iterations, time accurate stepping for another five nondimensional time with $\Delta\tau = 0.00036$.

Comparing the 3-D streamline plots of Figure 6.53 with those of the wide and narrow fuselage cases, see Figures 6.5 and 6.31, shows a continuation of the trend of decreasing breakdown bubble diameter with reduced aft fuselage size. The diameter of the open case bubble is 50% smaller than the narrow case. The breakdown location now occurs at 67% root chord, compared to 78% for both the wide and narrow cases. This is due to a large increase in the adverse pressure gradient from the now fully exposed wake.

Near surface streamline plots of the right tail, see Figure 6.54, show that the flow on the outer side is no longer dominated by the the small vortex emanating from the bottom of the tail. The wing surface flow is much the same as it was for the previous cases. The pressure distribution shown in Figure 6.55 now indicates decreases in peak suction for the $x = 0.7, 0.9$ crossflow planes over the narrow case of 20% and 40%, respectively. This is due to the forward movement of the burst location.

Comparison of the wing crossflow planes of total pressure coefficient and velocity vectors, shown in Figure 6.56, with the wide and narrow cases confirm the observations from the C_p plots. Namely, that before breakdown the vortices are essentially of the same strength, and after breakdown the vortices of the open case do not expand as much as with the other cases. Thus, because of the weaker adverse pressure gradient the breakdown is diminished leaving the vortices more intact downstream, as can be seen in the $x = 0.9c$ cross section.

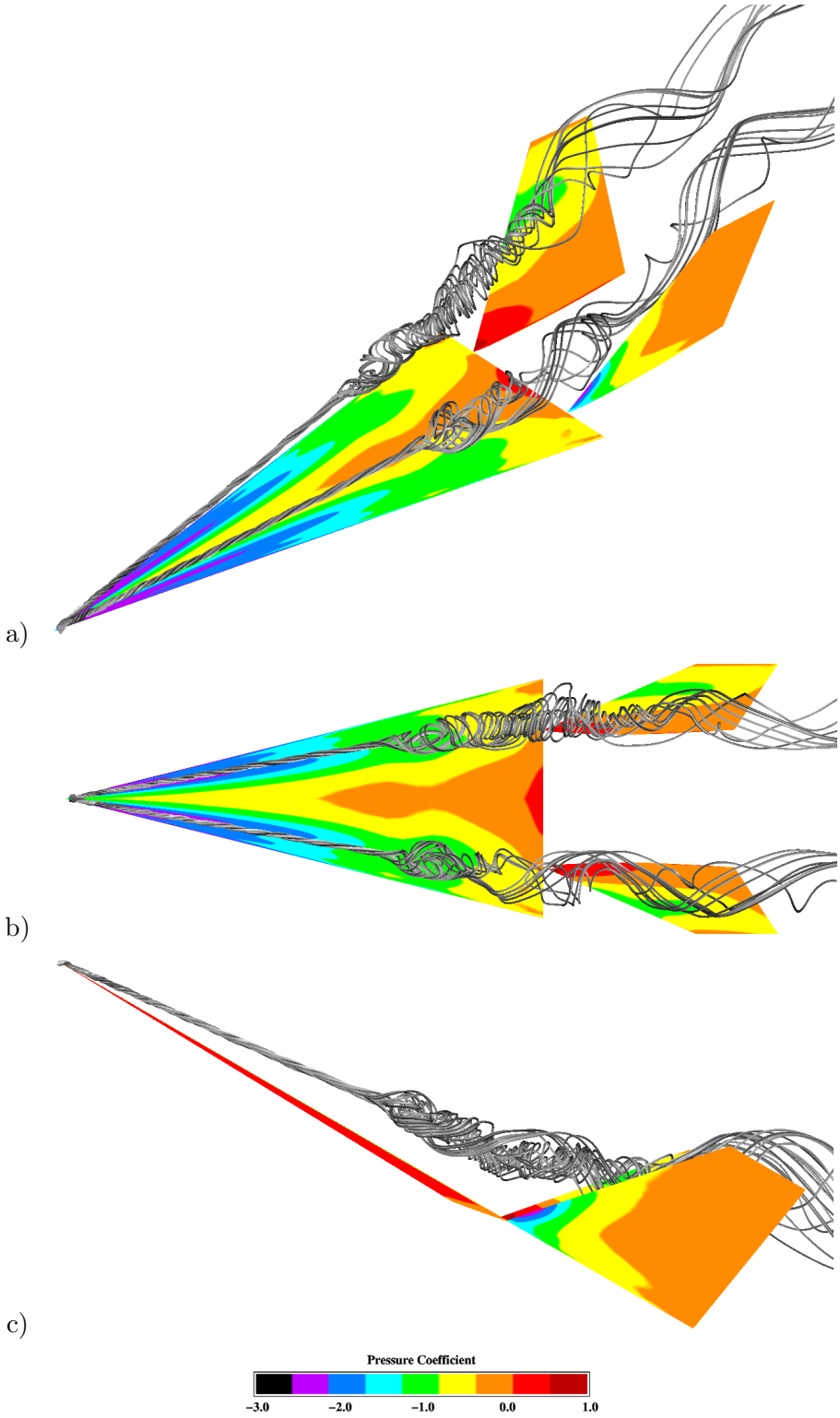

Figure 6.53: a) Three-dimensional, b) top and c) side views of surface pressure and vortex core streamlines. Initial Condition Flow Field: $Re = 0.75 \times 10^6$, $M = 0.3$, $\alpha = 30^o$.

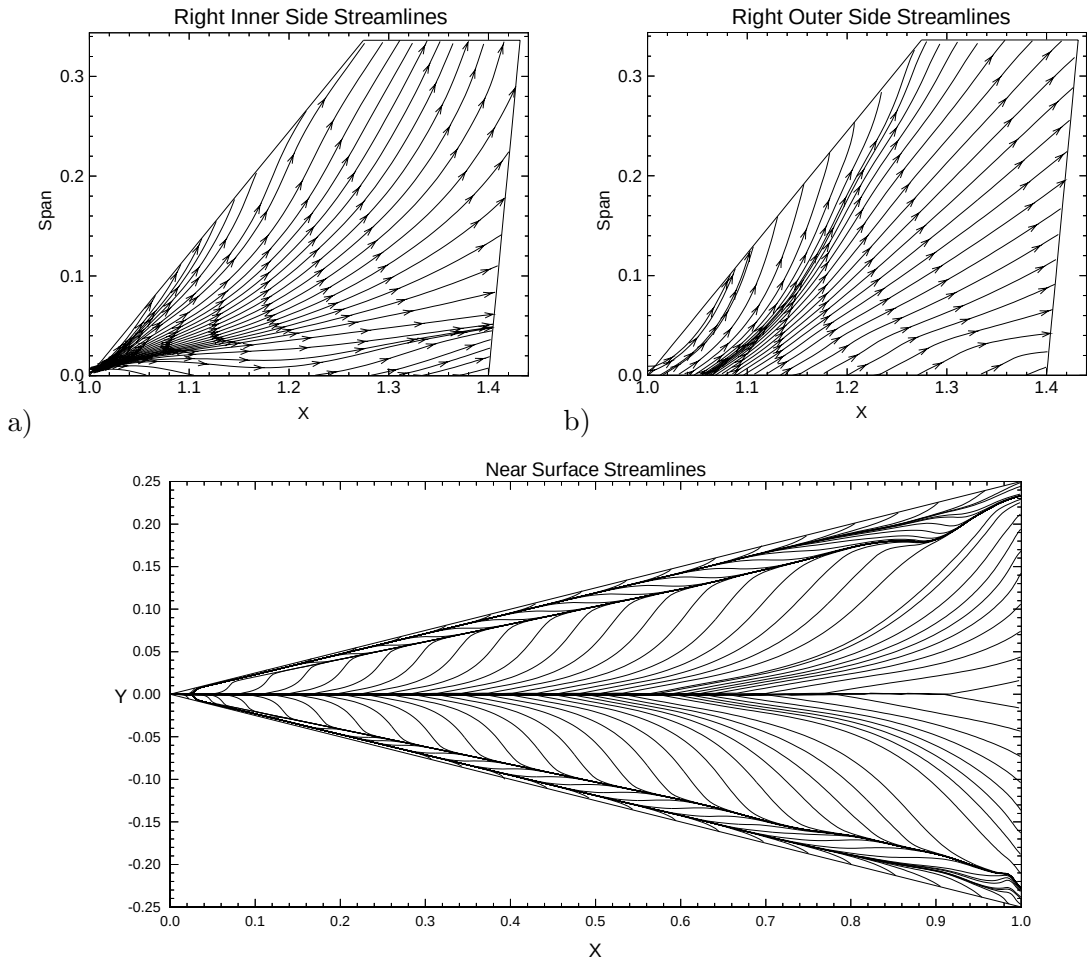

Figure 6.54: Near surface streamlines for the a) inner and b) outer right tail surfaces and the upper wing surface. Initial Condition Flow Field: $Re = 0.75 \times 10^6$, $M = 0.3$, $\alpha = 30^o$.

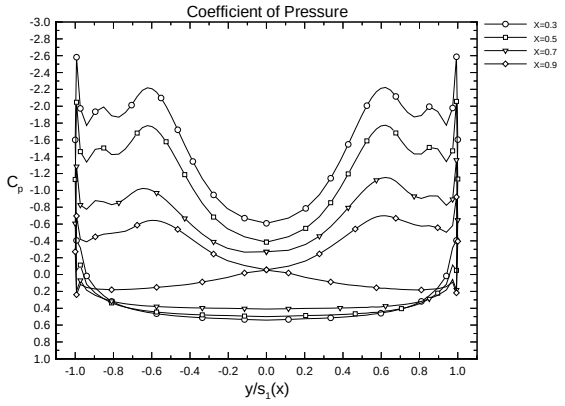

Figure 6.55: Coefficient of pressure on upper and lower wing surfaces at chord stations corresponding to plotted crossflow planes. Initial Condition Flow Field: $Re = 0.75 \times 10^6$, $M = 0.3$, $\alpha = 30^o$.

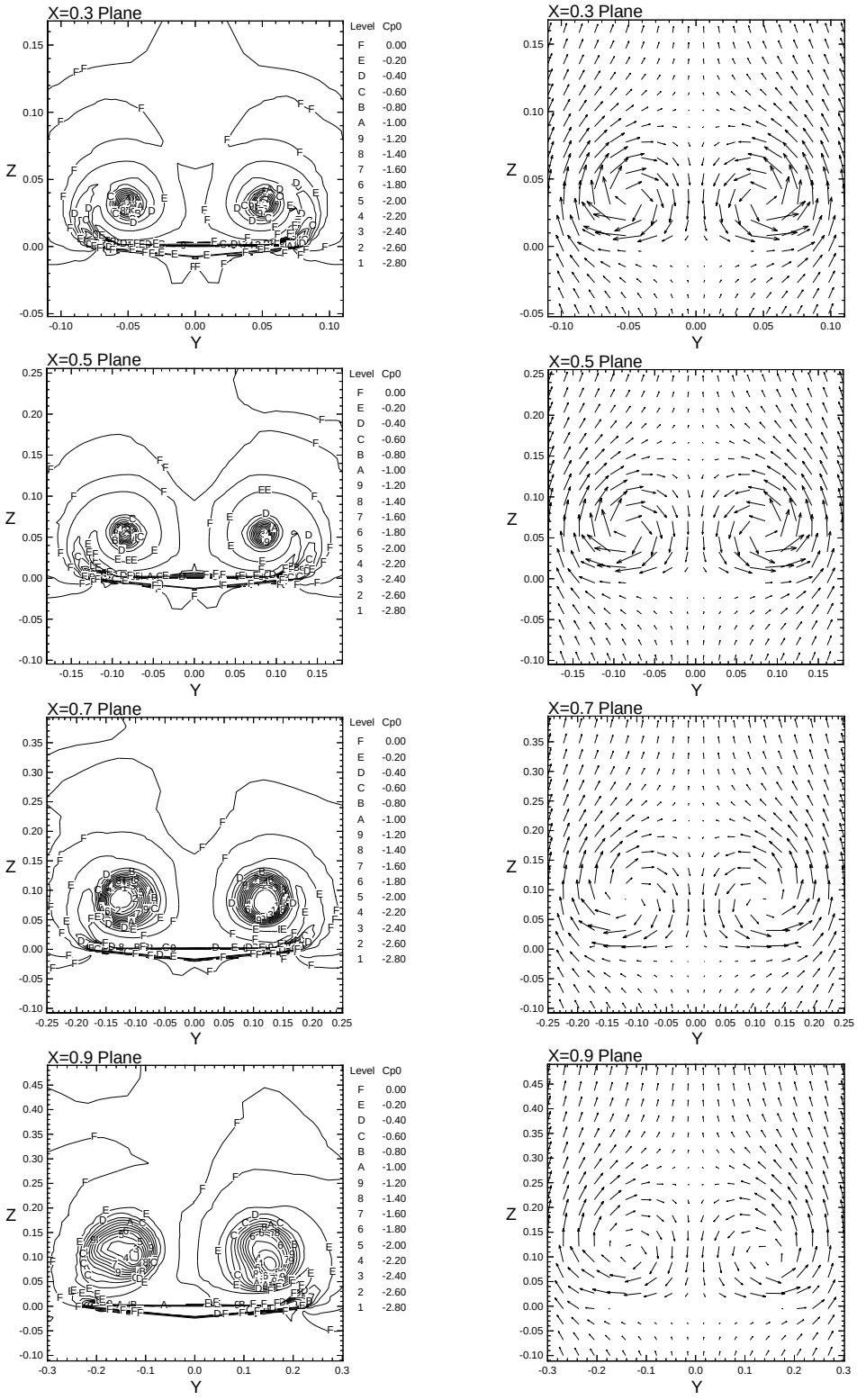

Figure 6.56: Total pressure coefficient and uniformly plotted velocity vectors on vertical crossflow planes above wing. Initial Condition Flow Field: $Re = 0.75 \times 10^6$, $M = 0.3$, $\alpha = 30^o$.

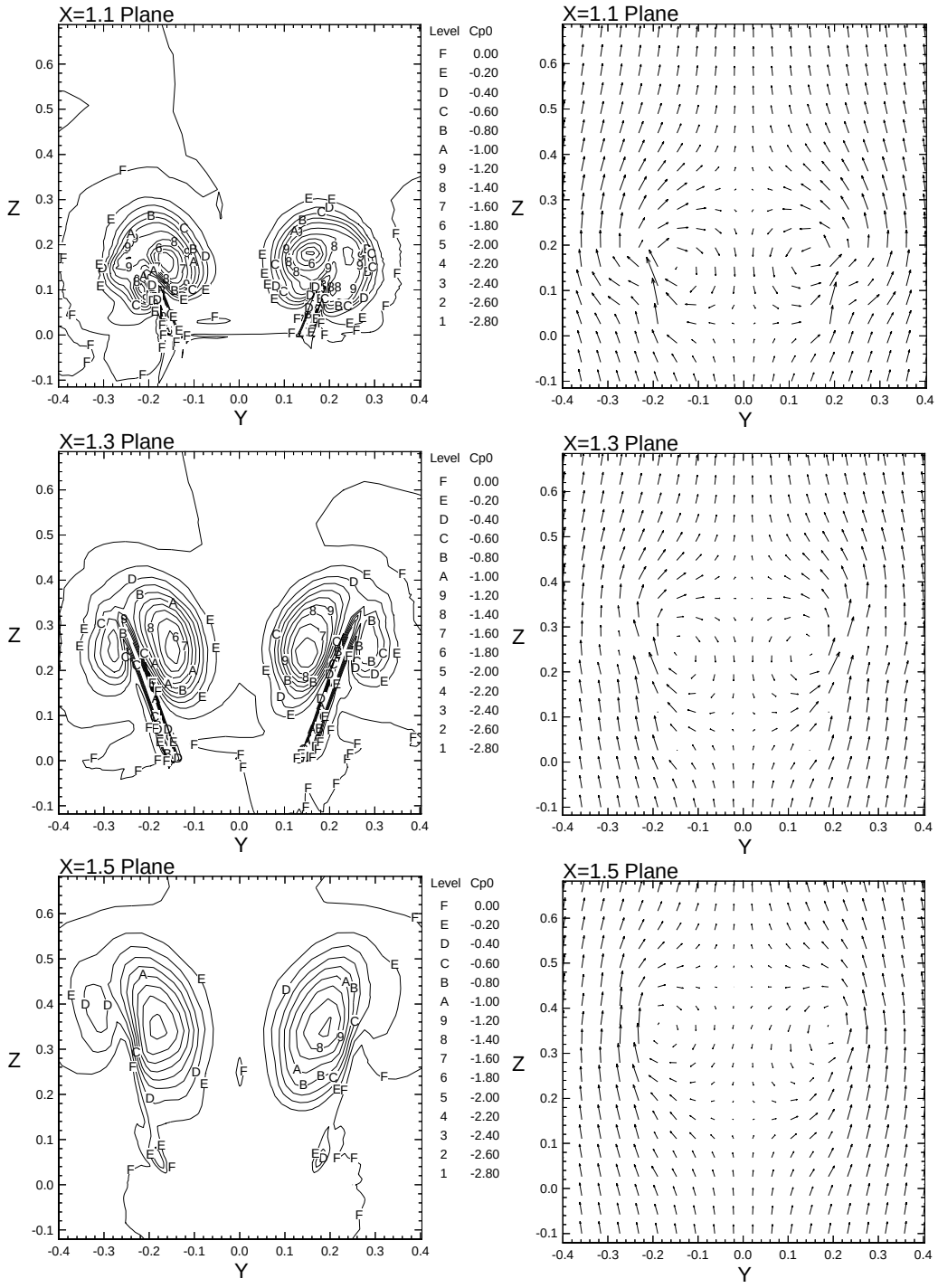

Figure 6.57: Total pressure coefficient and uniformly plotted velocity vectors on vertical crossflow planes near the tails. Initial Condition Flow Field: $Re = 0.75 \times 10^6$, $M = 0.3$, $\alpha = 30^o$.

6.4.4 Uncoupled Bending and Torsion Response

In this section, the buffeting response due to inertially uncoupled bending and torsion vibrations of dynamically scaled flexible twin F/A-18 tails is considered for the open fuselage case. The loads from this case will be compared to the wide and narrow flexible cases to assess the effect of decreased aft fuselage size. Because of the decreased tail stiffness used in the present open fuselage case, rigorous comparisons of the buffeting responses are not possible, however changes in the buffeting response due to relaxed stiffness will be discussed.

In terms of integrated loads, see Figures 6.58 and 6.59, the open fuselage loads closely resemble those of the narrow case, with the main difference being the lessening of the effect of the outer vortex emanating from the root of the tail. The diminished loads near the root can also be seen in the mean and RMS differential pressure distributions, see Figure 6.60. The differential pressure history and spectra, shown in Figure 6.8, indicate that the open case has a smaller amplitude and a peak frequency nearly the same as the narrow case. One significant difference is a strong second peak around $n = 2$ in buffet excitation for the open case. The point pressure data is summarized in Table 6.13, however when comparing the open case with the wide and narrow cases, one must account for the fact that the open case was non-dimensionalized with q_∞ based on $M = 0.3$ instead of $M = 0.4$ thus for all other quantities being equal the non-dimensional pressure for the open case would be $\left(\frac{4}{3}\right)^2$ times larger. Reduced frequency, n, is also affected, but by a factor of just $\frac{4}{3}$. Accounting for this fact, the differential point pressure for the open case is by far the lowest of the three F/A-18 tail cases.

Root bending and twisting moment histories and spectra are plotted in Figures 6.62 and 6.63 and summarized for all F/A-18 tail cases in Table 6.14. Again, the

	Flexible Tail Point Pressure Data								
	Wide Fuselage			Narrow Fuselage			Open Fuselage		
	p_{in}	p_{out}	p_{in-out}	p_{in}	p_{out}	p_{in-out}	p_{in}	p_{out}	p_{in-out}
Mean	8.14	8.49	-0.35	8.13	8.79	-0.66	15.3	15.7	-0.46
RMS	0.17	0.05	0.18	0.20	0.03	0.21	0.14	0.04	0.15
n_d	1.9	1.3		1.1	1.9		1.0	1.6	
Peak Power	1.4	0.4		2.3	0.3		1.9	0.7	

Table 6.13: Comparison of averaged nondimensional pressure ($\frac{p}{q_\infty}$) data at 45% chord and 60% span on flexible stiff tails for the F/A-18 tail cases. Note, for the wide and narrow cases $M = 0.4$, and for the open case $M = 0.3$.

difference in Mach number increases the open case coefficients by $\left(\frac{4}{3}\right)^2$. Thus it is evident that the mean root loads for the open case are closer to the wide case than the narrow case, and the RMS root loads are much smaller in real terms than either of the other F/A-18 cases.

With the reduced stiffness on the open case tails, the buffeting response is now much larger — up to two orders of magnitude, while not being unrealistically large as in the single tail cases. In fact, the maximum deflections are still quite small with a maximum bending deflection of only 5% of the tail span and a maximum twist of only 2^o. The right-left averaged open fuselage response, shown in Figures 6.65 – 6.67, is summarized with the other cases in Table 6.15. To characterize the accelerations, it is useful to evaluate them in dimensional form. The length scale is determined by comparing the tail root chord lengths as follows,

$$\begin{aligned} c_{t_{\mathrm{CFD}}} &= c_{t_{\mathrm{F/A-18}}} \\ 0.4[\mathrm{L_{CFD}}] &= 2.87[\mathrm{m}] \\ 1.0[\mathrm{L_{CFD}}] &= 7.18[\mathrm{m}] \end{aligned} \tag{6.12}$$

which gives a time conversion of

$$\begin{aligned} \tau &= \frac{tU_\infty}{\bar{\bar{c}}} \\ \tau &= \frac{t \times 0.3 \times 340.3\left[\frac{\mathrm{m}}{\mathrm{s}}\right]}{\frac{2}{3} \times 7.18[\mathrm{m}]} \\ \tau &= 21.3t\left[\frac{1}{s}\right] \\ 1.0[\mathrm{T_{CFD}}] &= 0.0469[\mathrm{s}] \end{aligned} \tag{6.13}$$

where $\mathrm{L_{CFD}}$ and $\mathrm{T_{CFD}}$ are units of CFD length and time. One unit of linear CFD acceleration is then given as follows

$$\begin{aligned} 1.0\frac{[\mathrm{L_{CFD}}]}{[\mathrm{T_{CFD}}]^2} &= \frac{7.18[\mathrm{m}]}{(0.0469[\mathrm{s}])^2} \times \frac{[\mathrm{g}]}{9.81\frac{[\mathrm{m}]}{[\mathrm{s}]^2}} \\ 1.0\frac{[\mathrm{L_{CFD}}]}{[\mathrm{T_{CFD}}]^2} &= 332.7[\mathrm{g}] \end{aligned} \tag{6.14}$$

and similarly, angular acceleration is given by

$$1.0\frac{[\mathrm{deg}]}{[\mathrm{T_{CFD}}]^2} = 454.6\frac{[\mathrm{deg}]}{[\mathrm{s}]^2} \tag{6.15}$$

Reduced frequency is converted as,

$$1.0\frac{[\mathrm{cycle}]}{[\mathrm{T_{CFD}}]} = 21.3[\mathrm{Hz}] \tag{6.16}$$

Thus, in dimensional form the peak linear acceleration is over 1000 g. This value is very high, but is not ridiculously high in light of measurements taken by Lee et al. [79] who recorded peak accelerations of 450 g in flight test. The error introduced by numerical differentiation is a major cause of the large values, since the differentiation of velocity will surely exaggerate any errors introduced in the first differentiation of displacement. Also recall that the present tail model was designed to simulate a generic buffeting response with the added constraint of being numerically practical, thus quantitative matching with the full F/A-18 is not expected.

	Flexible Tail Root Loads							
	C_{RBM}				C_{RTM}			
Fuselage	Mean +tip outward	RMS	Peak Power	n_d	Mean +LE inward	RMS	Peak Power	n_d
Wide	-0.0073	0.0092	0.0082	1.5	-0.0098	0.0043	0.0022	1.2
Narrow	-0.0711	0.0112	0.0180	1.0	-0.0123	0.0040	0.0019	1.0
Open	-0.0404	0.0075	0.0100	0.9	-0.0166	0.0024	0.0007	1.4

Table 6.14: Comparison of averaged root bending and twisting moment statistics, peak power and dominant frequency for flexible F/A-18 tail cases.

	Averaged Tip Response				
	Bending				
Fuselage	$A(w)$	Mean w +outward	$A(w_{\tau\tau})$	Peak Power	n_d
Wide	0.00032	-0.0004	0.078	0.047	3.8
Narrow	0.00033	-0.0011	0.048	0.032	2.6
Open	0.00450	-0.0150	1.950	49.0	5.5
	Torsion				
Fuselage	$A(\theta)^o$	Mean θ^o +LE inward	$A(\theta_{\tau\tau})^o$	Peak Power	n_d
Wide	0.031	-0.0013	7.0	325.	4.5
Narrow	0.026	0.0190	5.0	108.	2.9
Open	1.700	-0.0500	970	6.1E6	1.5

Table 6.15: Comparison of stiff(wide, narrow) and soft (open) tail responses.

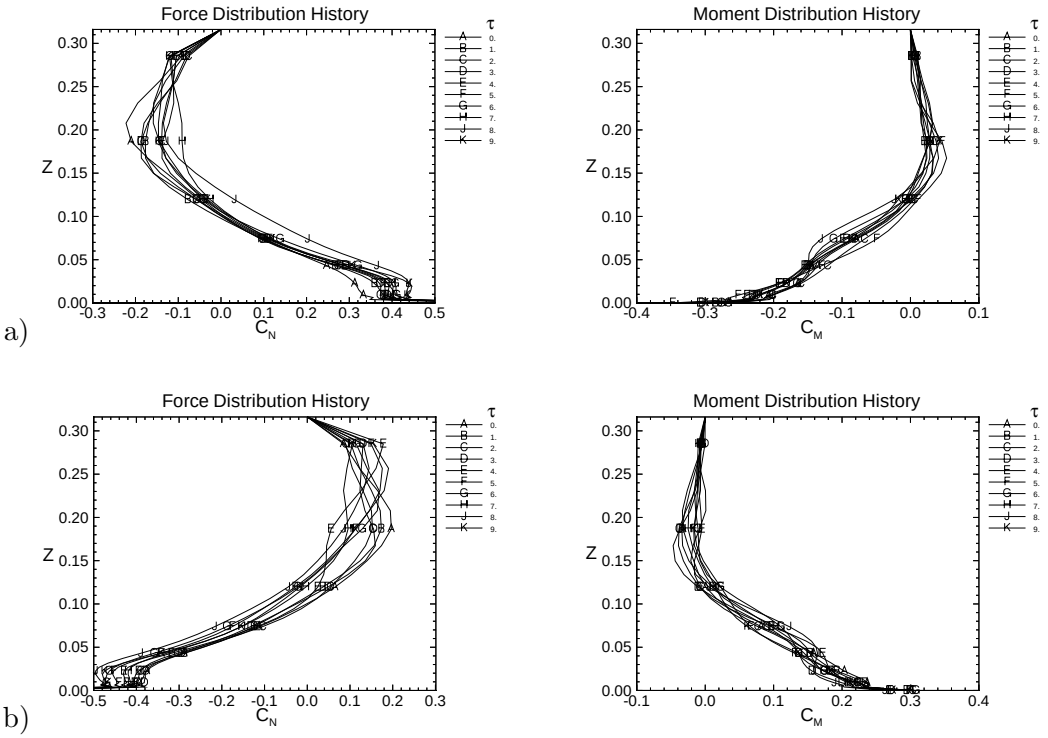

Figure 6.58: Bending force and twisting moment distributions along the tail span plotted at integer nondimensional time levels for a) right and b) left tails. Open Flexible Case: $Re = 0.75 \times 10^6$, $M = 0.3$, $\alpha = 30^o$.

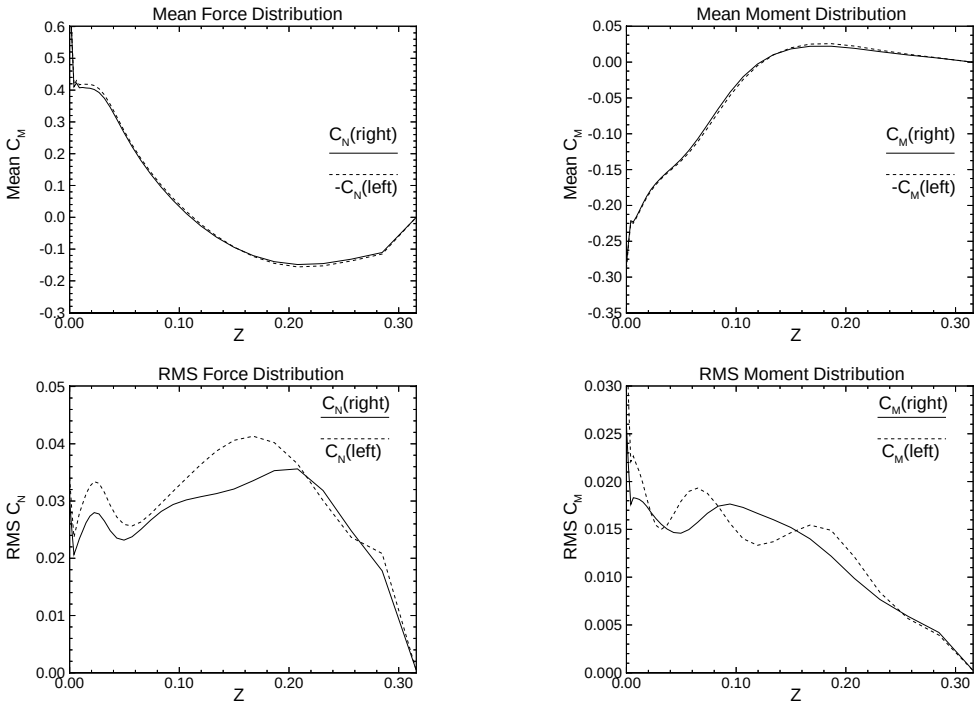

Figure 6.59: Mean and RMS load distributions along the right and left tail spans. Open Flexible Case: $Re = 0.75 \times 10^6$, $M = 0.3$, $\alpha = 30^o$.

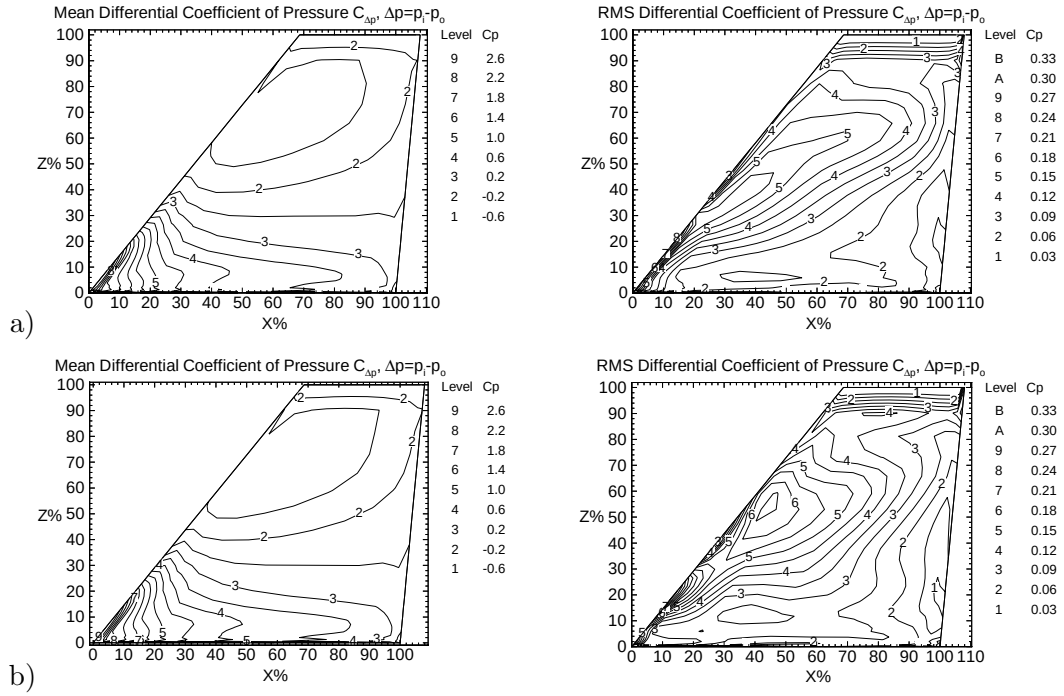

Figure 6.60: Mean and RMS differential coefficient of pressure contours on a) right and b) left tails. Open Flexible Case: $Re = 0.75 \times 10^6$, $M = 0.3$, $\alpha = 30^o$.

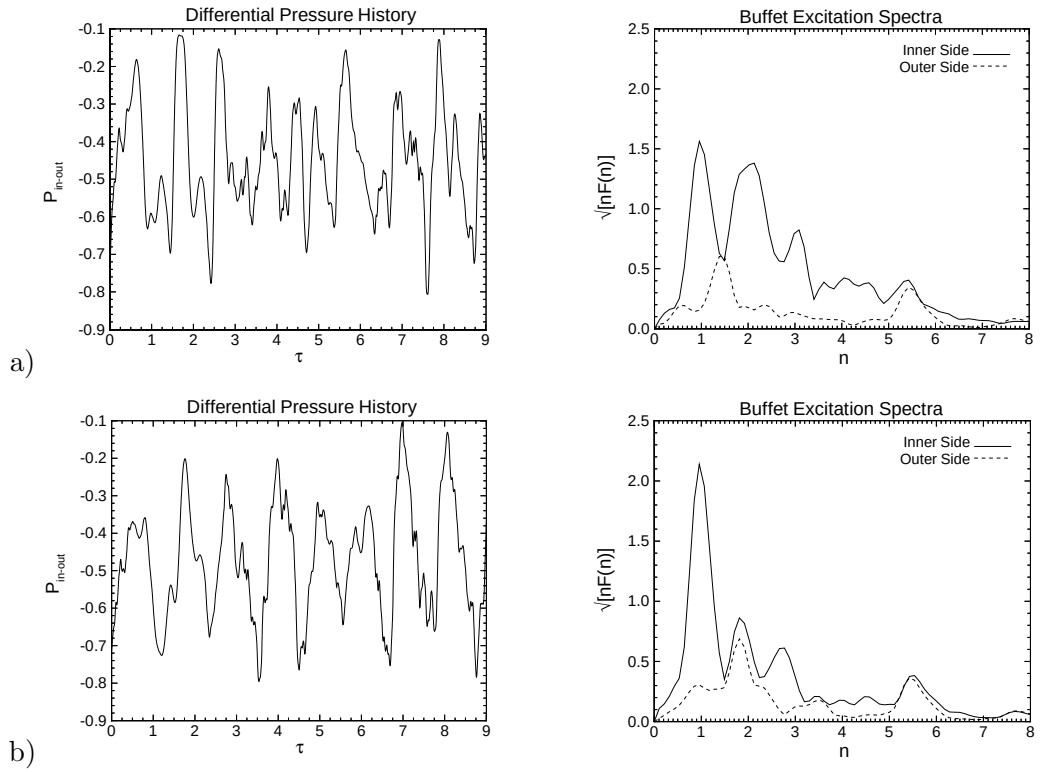

Figure 6.61: Differential pressure ($\frac{\Delta p}{q_\infty}$) histories at the 45% chord and 60% span location for a) right and b) left tails. Open Flexible Case: $Re = 0.75 \times 10^6$, $M = 0.3$, $\alpha = 30^o$.

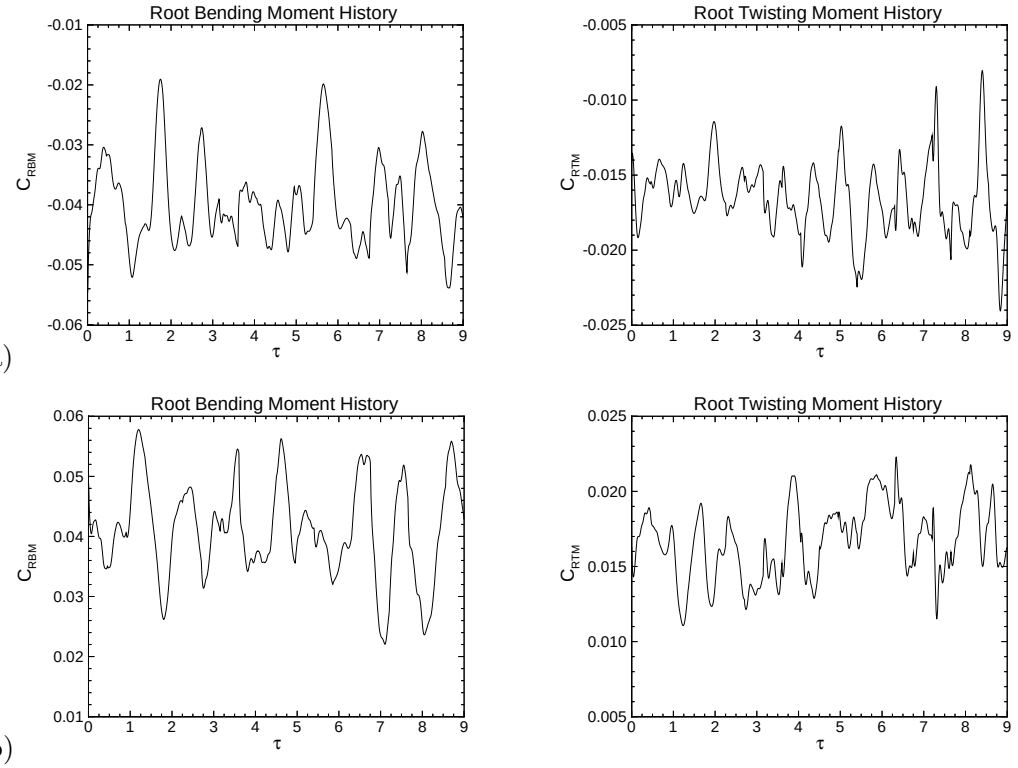

Figure 6.62: History of root bending moment coefficient and root twisting moment coefficient for a) right and b) left tails. Open Flexible Case: $Re = 0.75 \times 10^6$, $M = 0.3$, $\alpha = 30^o$.

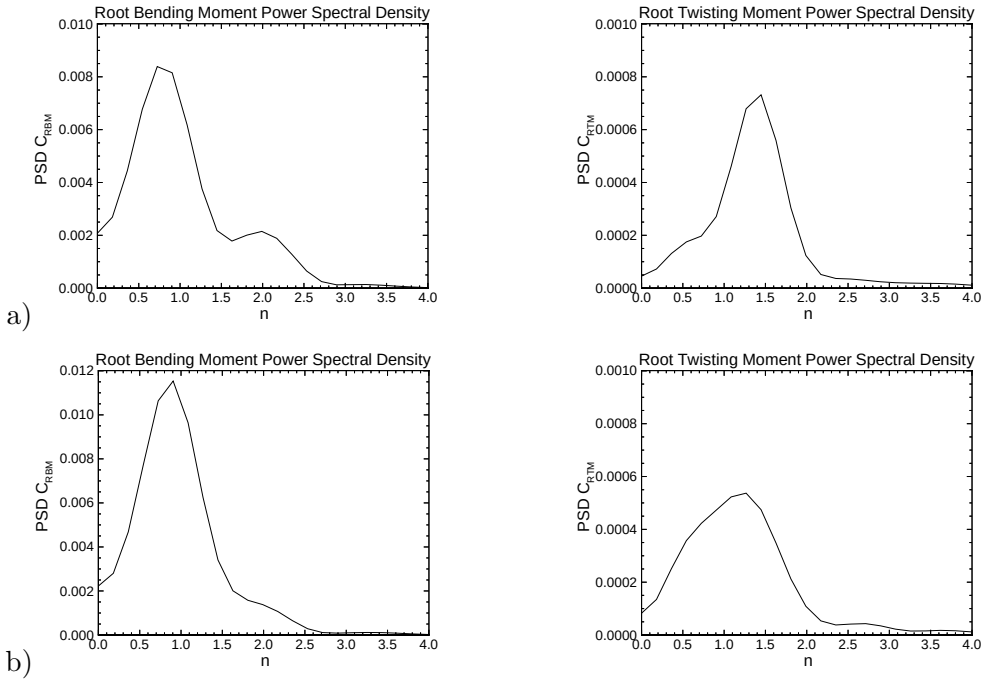

Figure 6.63: Power spectral density of root bending moment coefficient and root twisting moment coefficient versus reduced frequency for a) right and b) left tails. Open Flexible Case: $Re = 0.75 \times 10^6$, $M = 0.3$, $\alpha = 30^o$.

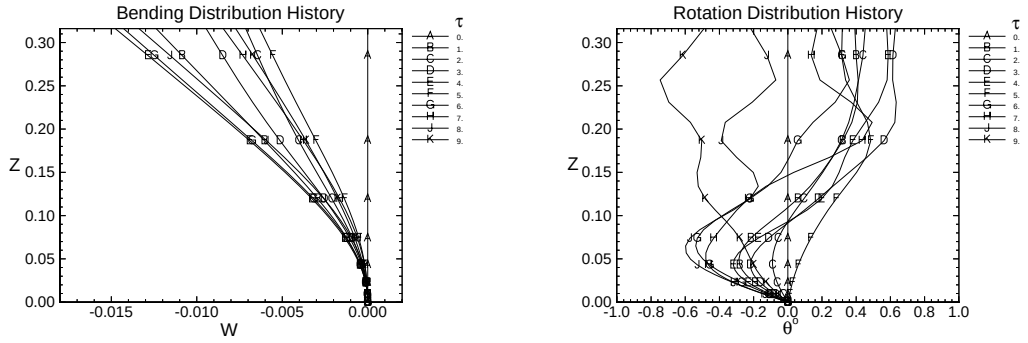

Figure 6.64: Right Tail: Bending and torsion deflection distributions along the tail span plotted at integer nondimensional time levels. Open Flexible Case: $Re = 0.75 \times 10^6$, $M = 0.3$, $\alpha = 30^o$.

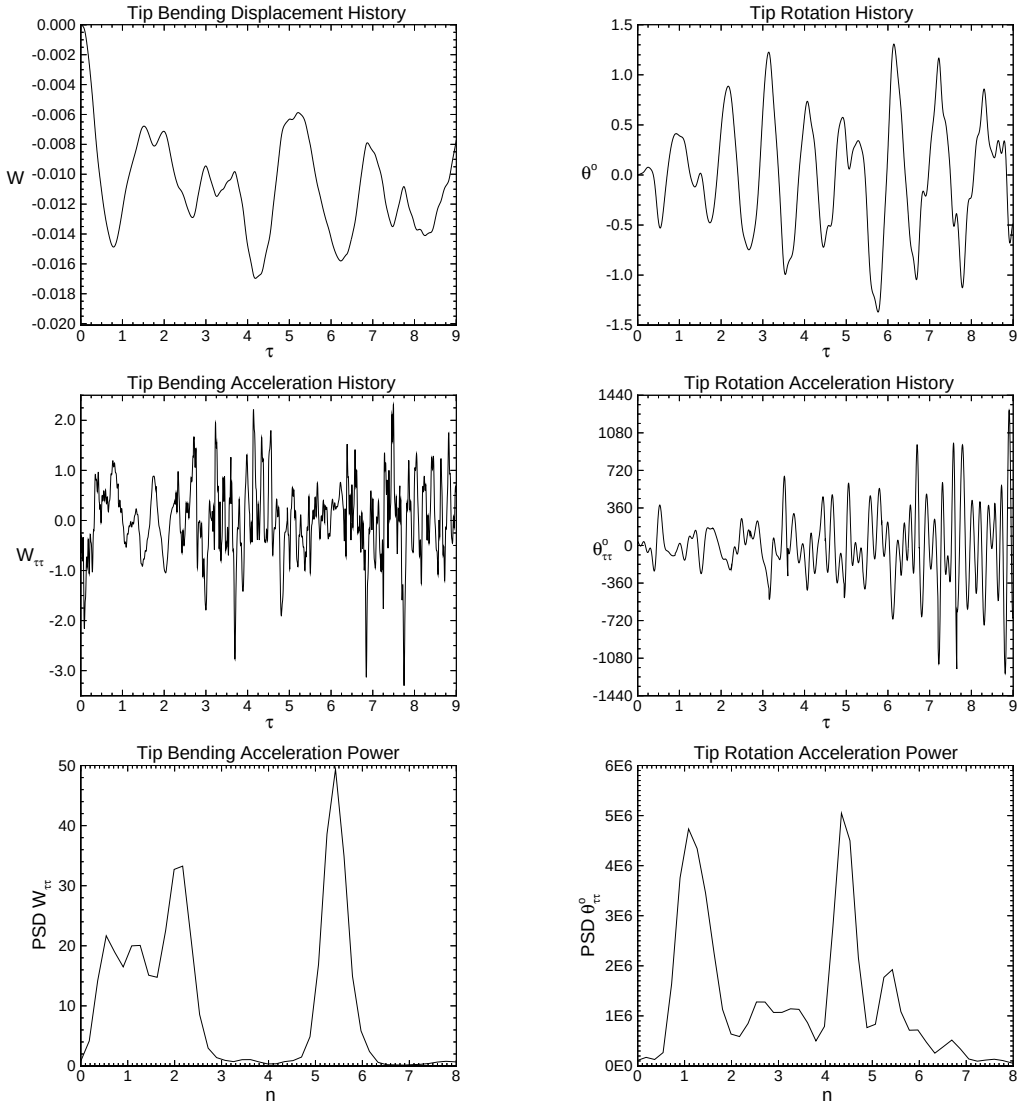

Figure 6.65: Right Tail: Time and frequency domain data for tip bending and torsion deflections and accelerations. Open Flexible Case: $Re = 0.75 \times 10^6$, $M = 0.3$, $\alpha = 30^o$.

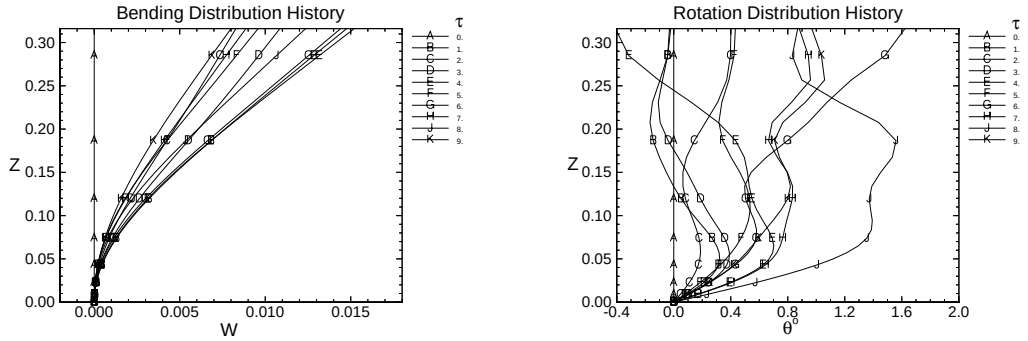

Figure 6.66: Left Tail: Bending and torsion deflection distributions along the tail span plotted at integer nondimensional time levels. Open Flexible Case: $Re = 0.75 \times 10^6$, $M = 0.3$, $\alpha = 30^o$.

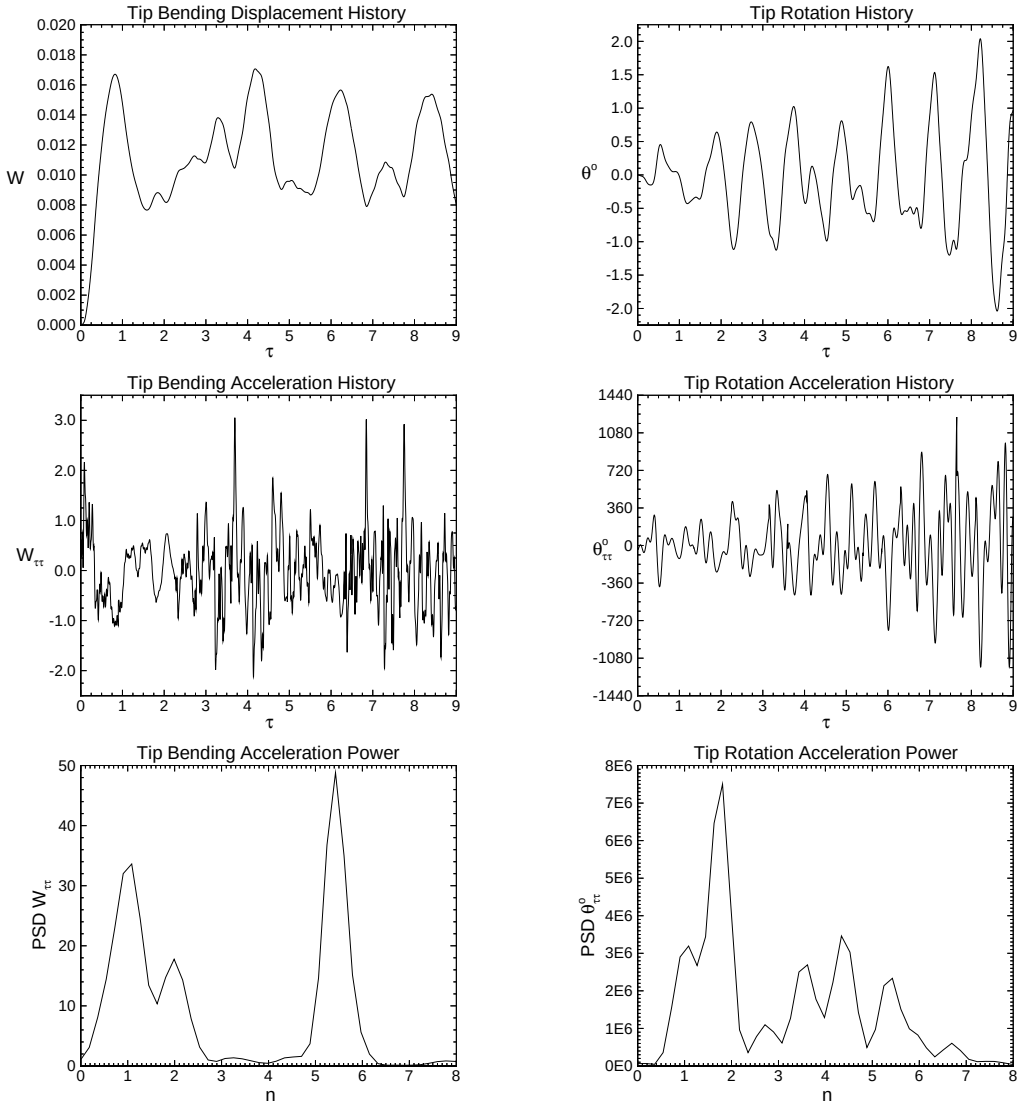

Figure 6.67: Left Tail: Time and frequency domain data for tip bending and torsion deflections and accelerations. Open Flexible Case: $Re = 0.75 \times 10^6$, $M = 0.3$, $\alpha = 30^o$.

6.4.5 Summary

In this chapter, the simulation of twin vertical tail buffeting was accomplished using a delta wing/twin F/A-18 vertical tail configuration. Computational applications provided insight into the effects of aft fuselage geometry on the buffet loading and response. In addition, a lower limit on the magnitude of the amplitude of the dynamic tail response required to affect the buffet loading was established. Finally, a dynamically scaled tail model was tested and validated.

As in the single tail computations, the multi-disciplinary buffeting problem was solved sequentially for the fluid flow, the elastic tail deformations and the grid displacements. The flow field was obtained by time accurately solving the laminar, unsteady, compressible, Navier-Stokes equations using an implicit, upwind, flux-difference splitting finite volume scheme. The elastic vibrations of the tail were modeled by coupled bending and torsion beam equations. These equations were solved accurately in time using the Galerkin method and a five-stage Runge-Kutta-Verner scheme. The grid for the fluid dynamics calculations was continuously deformed using interpolation functions to smoothly disperse the displacements throughout the computational domain. Computations were performed on a Cray C90 and required one hour per 935 time steps including movie output, or nearly 3 hours per nondimensional time ($\Delta\tau = 0.00036$). The memory required was 21 MW on a 64-bit machine which is equivalent to 84 MB on a 32-bit machine.

To determine the effect of aft fuselage geometry on twin F/A-18 vertical tail buffeting, three fuselage configurations were considered; wide, narrow and open. It was found that overall, the narrow fuselage case produced the largest buffet loads. Results for the wide and open cases were mixed with the wide case having lower steady loads

and higher unsteady loads. Comparison of dynamic tail cases with their corresponding rigid cases for the wide and narrow cases showed that even for very small deflections, the loading can be affected by up to 30% for RMS values. However, the very stiff tails of the wide and narrow cases produced deflections that were an order of magnitude lower than the normal grid spacing, which even with moving grids is too small to produce accurate results. Thus, for the open case, dynamically scaled tails were used which produced more realistic deflections of up to 5% tail span and of the same order as the normal grid spacing.

To establish the ability of the present simplified configuration to aid in the full aircraft tail buffeting design problem, results from the narrow fuselage case were compared to experimental full F/A-18 aircraft results. The ratio between buffet excitation frequency and root bending moment, was found to be in good agreement with experimental data. The inside tail loads also match fairly well. However, overall the results were mixed owing to the fact that the aircraft flow field and the delta wing flow field have many differences. But for the purpose of evaluating tail buffeting design modifications, the simple delta wing model does share enough of the physics with the full aircraft to be very useful.

CHAPTER 7

EFFECT OF SPANWISE TAIL LOCATION ON TWIN WASHBURN VERTICAL TAIL BUFFETING

7.1 Introduction

The focus of this chapter is the determination of the effect of spanwise tail location on the tail buffet loading and response. Three spanwise tail positions are considered; corresponding to 33%, 56% and 78% of the wing semispan, see Figure 7.1. The case definitions are summarized in Table 7.1. Quantitative comparisons will also be made with the experimental data of Washburn et al. [12] for the same configuration.

The method of solution and the total number of grid cells used is the same as in the previous F/A-18 cases. For each of the cases considered in this chapter the material properties of the tails are the same as those used in the open F/A-18 case, which consisted of a dynamically scaled tail corresponding to the properties of solid balsa wood for a wing root chord of 18 inches, as in the wind tunnel model of Washburn et al. [12].

7.2 Model Geometry and Computational Domain

Each of the models consist of a sharp-edged, flat delta wing of aspect ratio 1 (leading edge sweep of $\Lambda = 76^o$) and twin swept vertical tails placed at distance of either ($y = 0.082c$, $0.14c$ or $0.195c$) from the symmetry plane. The midspan location is identical to the previous F/A-18 cases, which was chosen to coincide with the vortex core locations. The vertical height of the Washburn tails are $0.22c$ which is 30% lower than the previous F/A-18 tails. The vertical tails are oriented normal to the upper surface

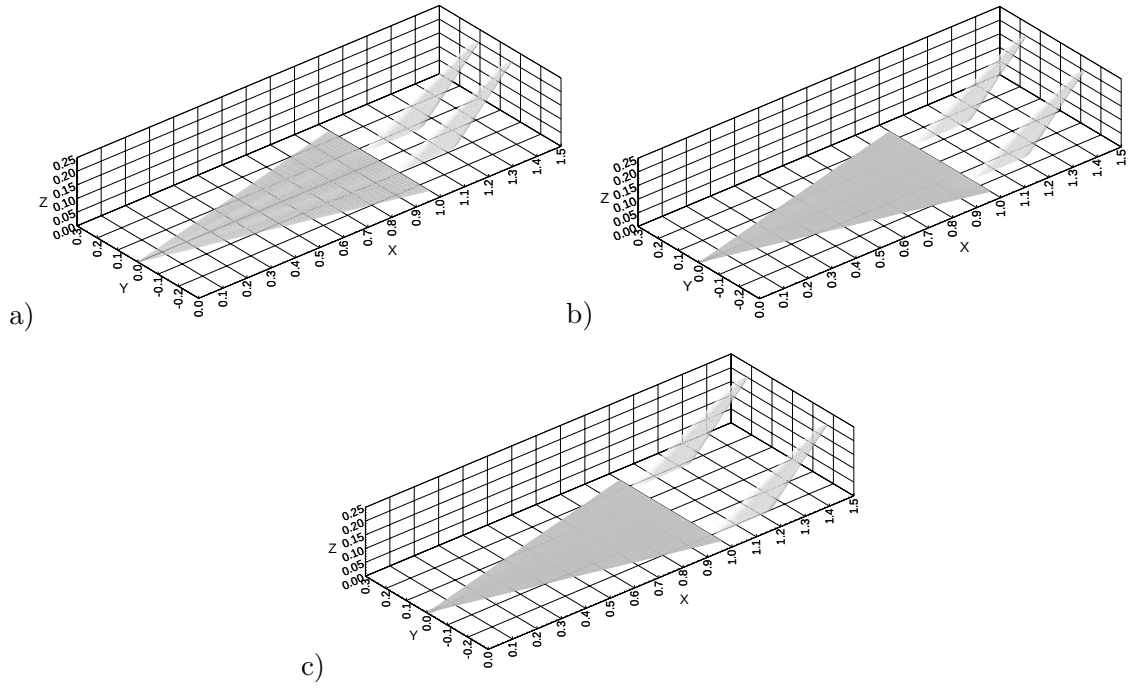

Figure 7.1: a) Inboard, b) midspan and c) outboard tail configurations.

of the wing and have a centerline sweep of 53.5^o. The root chord is 0.35c with a taper ratio of 0.23. See Figure 7.2 for a sketch of the tail with pressure tap locations.

To accommodate the boundary conditions of the twin tails, the same type of five block, C^0 continuous, O-H grid used in the open F/A-18 case, is used for all of the cases in this chapter. The total number of cells for each case is 458,100, with only the distribution in the blocks surrounding the tails changing for each case. The block structure is shown in Figure 7.3 and each of the surface grids are shown in Figure 7.4. The global grid extends $0.8c$ upstream, $3c$ radially and $3.6c$ downstream. These limits were obtained from earlier numerical experiments which showed that primary flow was insensitive to the far-field boundary conditions at the current distance. The grid is constructed algebraically as previously discussed in Section 3.5.

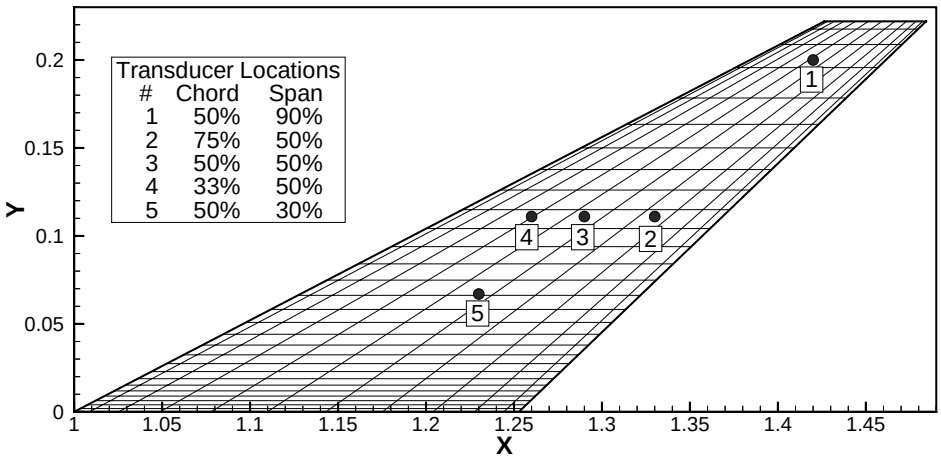

Figure 7.2: Location of Washburn pressure transducers.

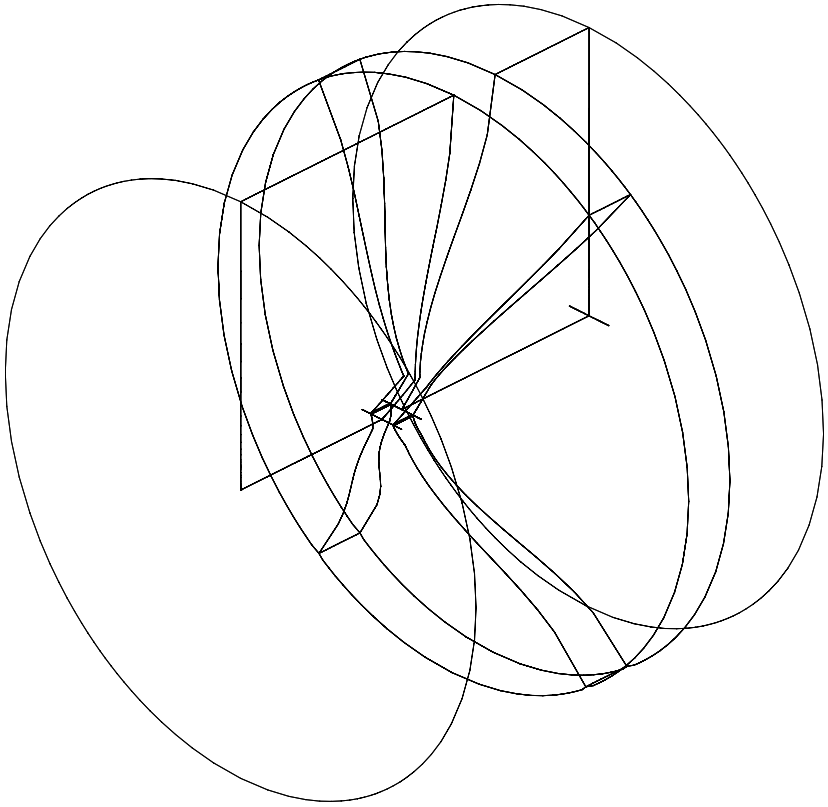

Figure 7.3: Block boundaries for Washburn-type cases.

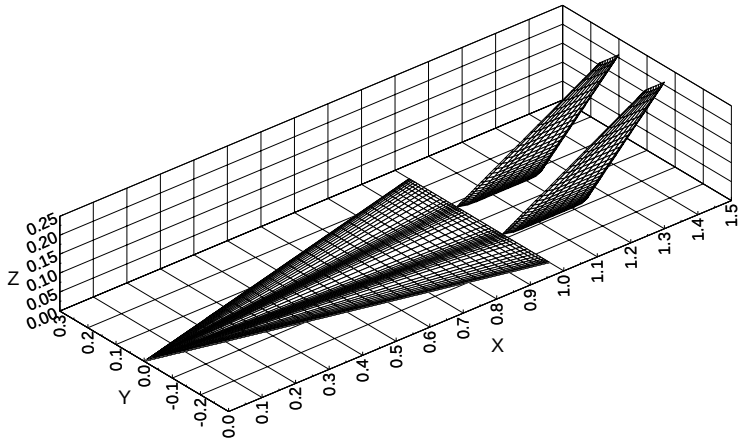

a)

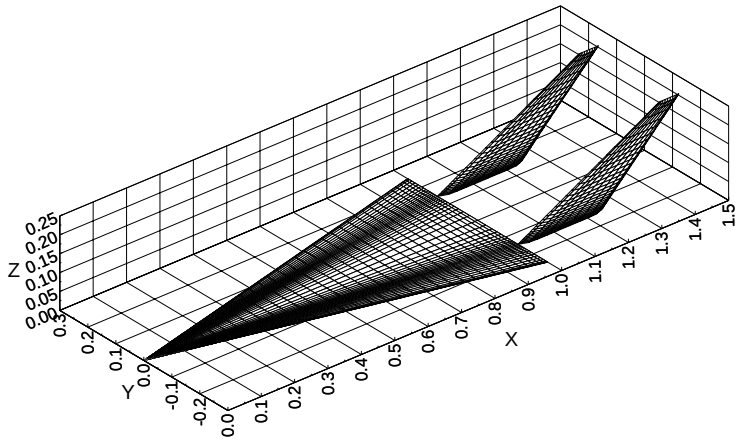

b)

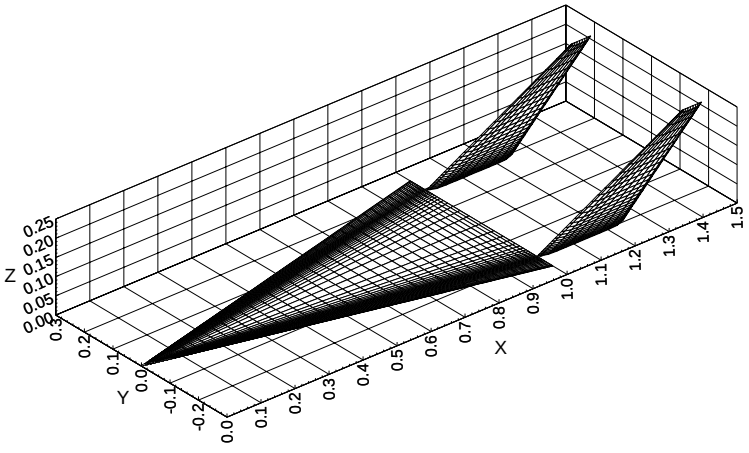

c)

Figure 7.4: Surface grids for a) Inboard, b) midspan and c) outboard tail configurations.

7.3 Freestream Flow Conditions

For all of the Washburn-type tail cases under consideration, the configuration angle-of-attack is increased from the F/A-18 case value of 30^o to 35^o, in order to increase the unsteady loads on the tails. The freestream Mach and Reynolds numbers are changed slightly to 0.3 and 1.25×10^6, respectively, to more closely model the experimental conditions while not posing too stiff of a problem for the compressible solver. The Mach number is chosen to coincide with the severe tail buffet conditions and to match previous computations.

7.4 Tail Material Properties

The nondimensional material properties used for each of the cases considered in this chapter are the same as in the F/A-18 open fuselage case of the previous chapter, and are $E = 4.6 \times 10^3$, $G = 1.8 \times 10^3$ and $\rho = 145$. This corresponds to balsa wood based on the wing root of 18 inches and matches the experimental case of Washburn et al. [12]. Additional flexibility is obtained by reducing the tail thickness used in the structural calculations by 50%. Since this case and all the remaining cases in the study are inertially uncoupled, the distance between the inertial and elastic axes, x_θ is 0.

Case	Tail Location	Re	α	$Mach$
1	Inboard	1.25×10^6	35^o	0.3
2	Midspan	1.25×10^6	35^o	0.3
3	Outboard	1.25×10^6	35^o	0.3
4	Experimental	0.5—1.25 $\times 10^6$	34^o	0.05—0.12

Table 7.1: Summary of twin Washburn-type vertical tail buffeting cases, and experimental range in which nondimensional buffeting data were constant.

7.5 Inboard Twin Tail Model

7.5.1 Initial Conditions, $Re = 1.25 \times 10^6$, $M = 0.3$, $\alpha = 35^o$

The initial flow state is obtained by the same method as in the previous twin tail cases. The flow is solved using local time stepping for 2000 iterations and then time accurate stepping for another five nondimensional time with $\Delta\tau = 0.00036$. Detailed initial condition flow field plots for the inboard case are shown in Figures 7.5-7.10.

Comparing the 3-D streamline plots of Figure 7.5 with the F/A-18 tail, open fuselage case of the previous chapter, see Figure 6.53, demonstrates that one effect of increasing the angle-of-attack from 30^o to 35^o is to move the burst location forward from 67% root chord to 50%. The lower profile of the swept tails also allows the vortices to interact more strongly with the wake, which is indicated by the dispersion of aft streamlines. In Figure 7.6, total pressure isosurfaces are plotted over the existing core streamlines. The burst location is indicated by the isosurface inflection point and matches the burst location determined from the streamlines in Figure 7.5. The decrease in diameter and abrupt end of the total pressure isosurfaces in the region aft of the wing is a result of the increasing overall pressure in the wake.

Near surface streamline plots of the right tail, see Figure 7.7, indicate that the flow on the outer surface is separating due to the nearby vortex. This has been observed in the previous F/A-18 cases, however, unlike those cases, the surface flow on the opposite side of the core is very clean with no evidence of separation due to core spill-over. This is due to the high sweep angle of the Washburn tails and the inboard location of the tails. The curvature of the wing secondary separation line, see Figure 7.7, indicates that the region of recirculation associated with breakdown is much larger than in the F/A-18 cases. Comparison of spanwise pressure distributions, see Figure 7.8, with

those of the open F/A-18 case in Figure 6.55 show an 18% increase in peak suction for the $x = 0.3$ crossflow plane and decreases of up to 18% for the aft planes. The forward suction benefit is due to the increased vortex strength and the aft suction loss is due to the forward movement of the burst point as evidenced by the near wing surface streamlines, all of which are a result of the 5^o increase in angle-of-attack.

In Figures 7.9 and 7.10, total pressure contours and in-plane streamlines are plotted on vertical crossflow planes at 0.1c intervals from $x = 1.0c - 1.5c$. The solid cross sections of the tails are shown in black. The pressure contours indicate both an increase in core size and pressure in the streamwise directions. Secondary vortices emanating from the sharp bottom edges of the tails are clearly evident in the $x = 1.4$ and $x = 1.5$ planes, in both the pressure and the streamline plots.

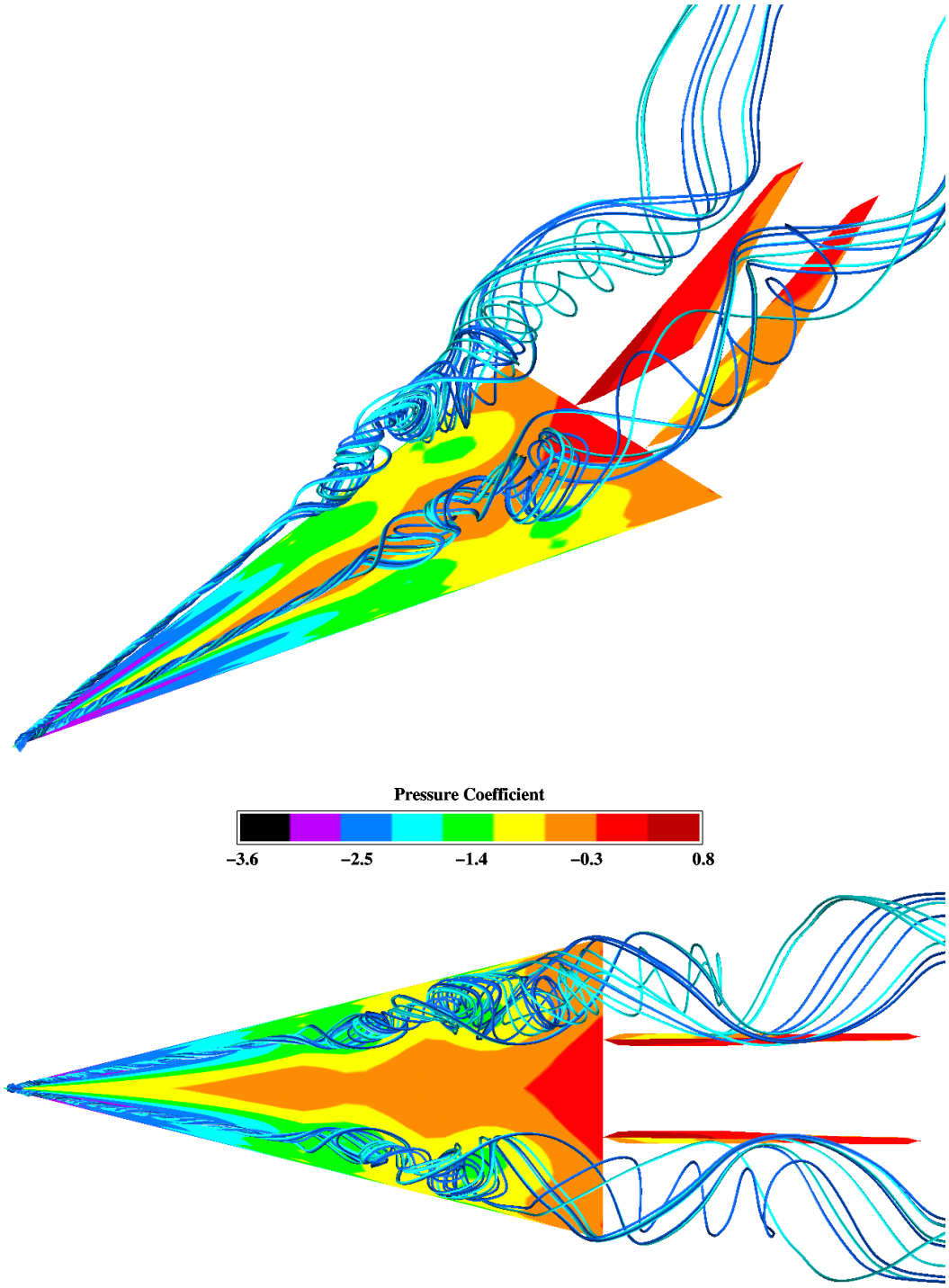

Figure 7.5: Three-dimensional and top views of surface pressure and vortex core streamlines. Inboard Initial Condition: $Re = 1.25 \times 10^6$, $M = 0.3$, $\alpha = 35^o$.

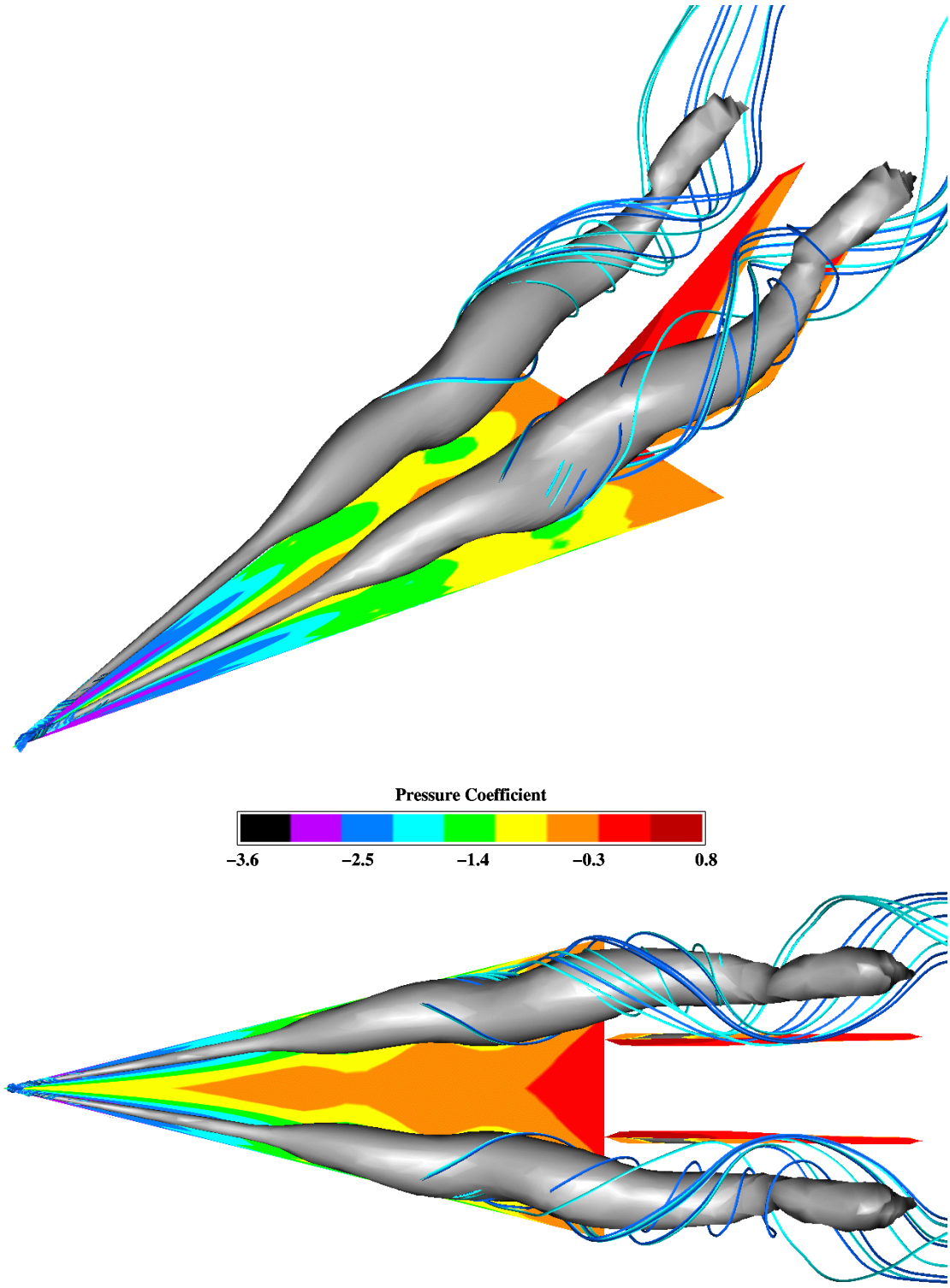

Figure 7.6: Three-dimensional and top views of surface pressure, vortex core streamlines and solid total pressure isosurfaces, $\left(\frac{p_0}{\rho_\infty a_\infty^2} = 0.68\right)$ Inboard Initial Condition: $Re = 1.25 \times 10^6$, $M = 0.3$, $\alpha = 35^o$.

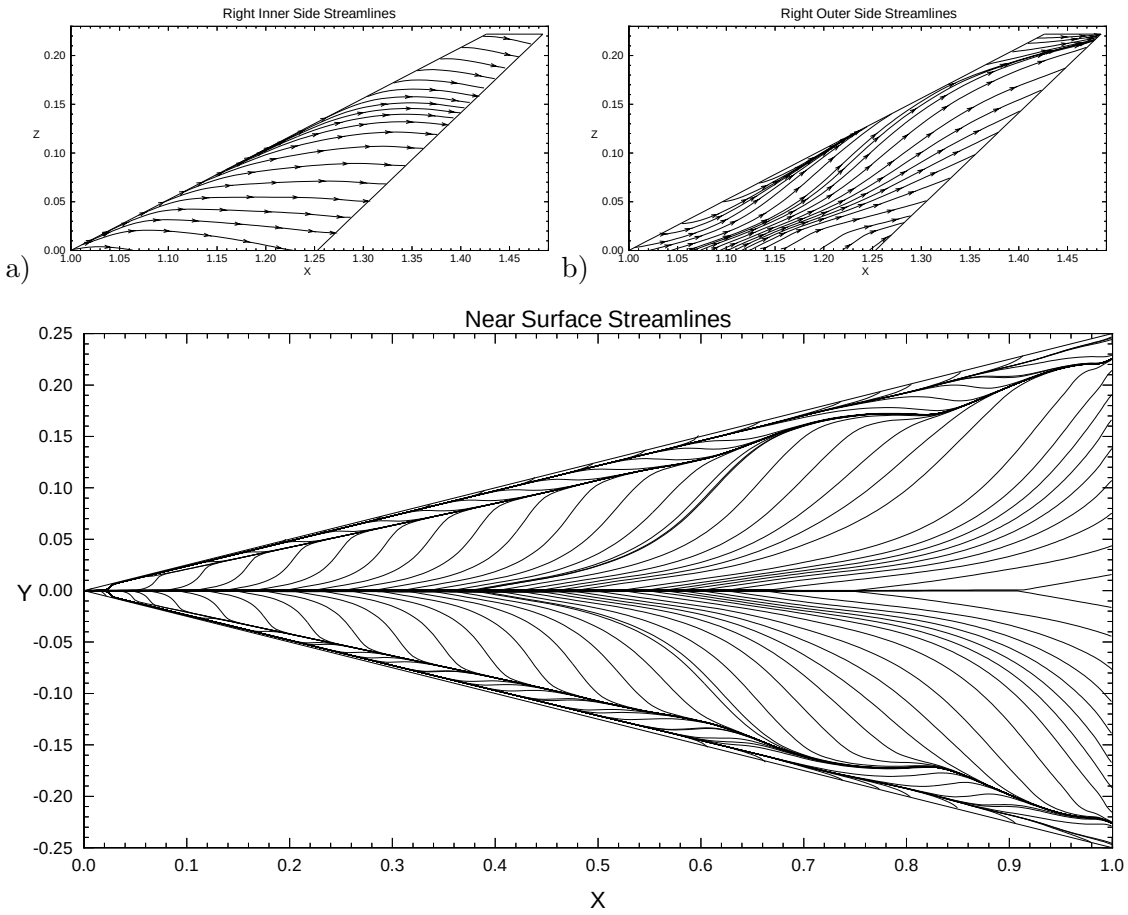

Figure 7.7: Near surface streamlines for the a) inner and b) outer right tail surfaces and the upper wing surface. Inboard Initial Condition: $Re = 1.25 \times 10^6$, $M = 0.3$, $\alpha = 35^o$.

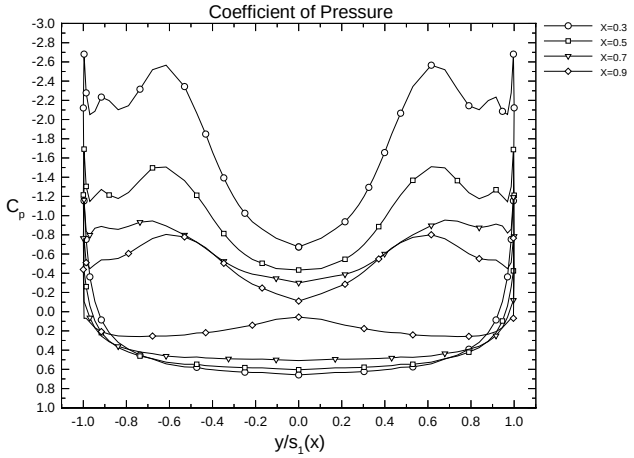

Figure 7.8: Coefficient of pressure on upper and lower wing surfaces at chord stations corresponding to plotted crossflow planes. Inboard Initial Condition: $Re = 1.25 \times 10^6$, $M = 0.3$, $\alpha = 35^o$.

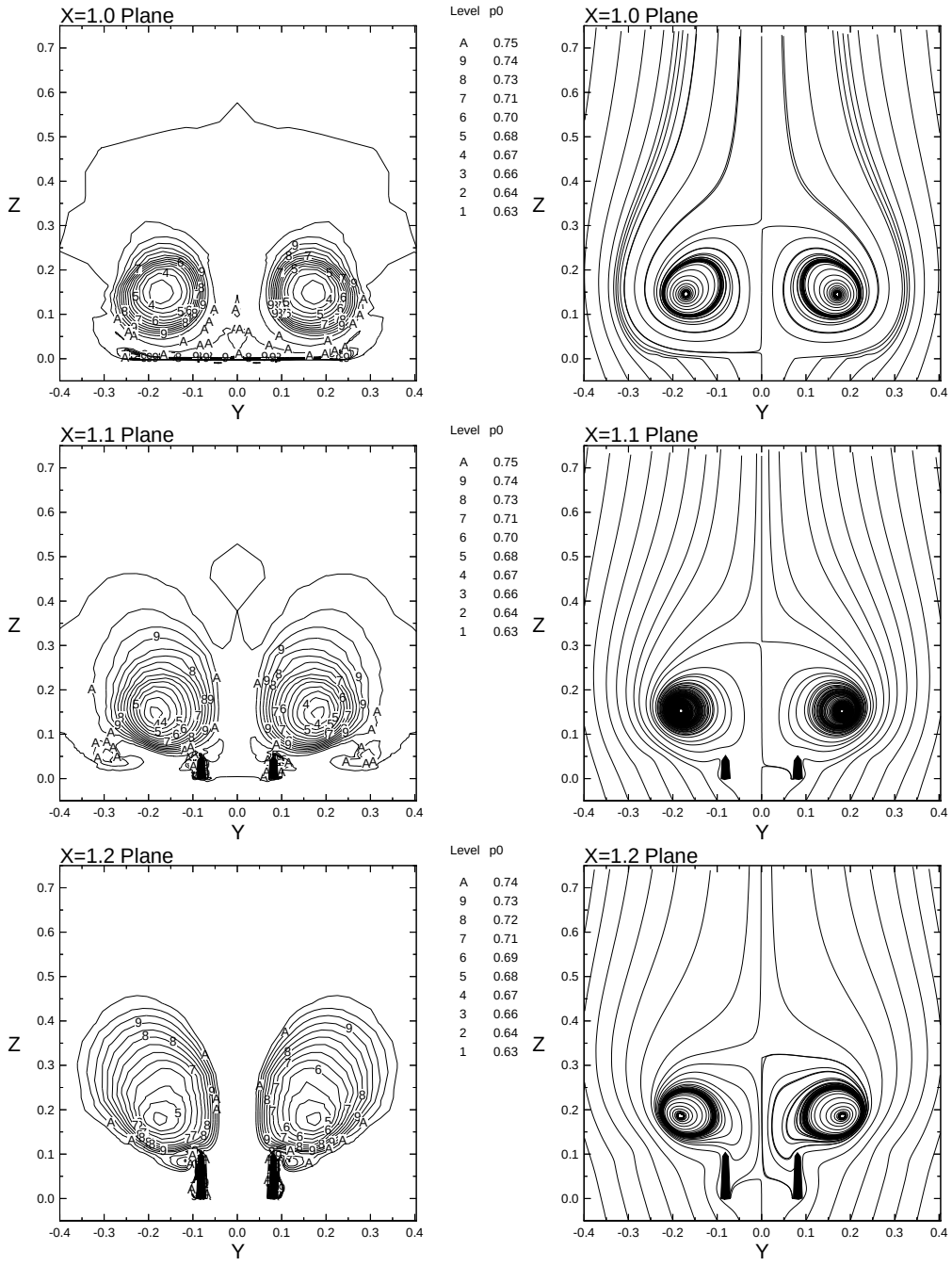

Figure 7.9: Nondimensional total pressure contours and in-plane streamlines plotted on vertical crossflow planes, $x = 1.0, 1.1, 1.2$. Inboard Initial Condition: $Re = 1.25 \times 10^6$, $M = 0.3$, $\alpha = 35^o$.

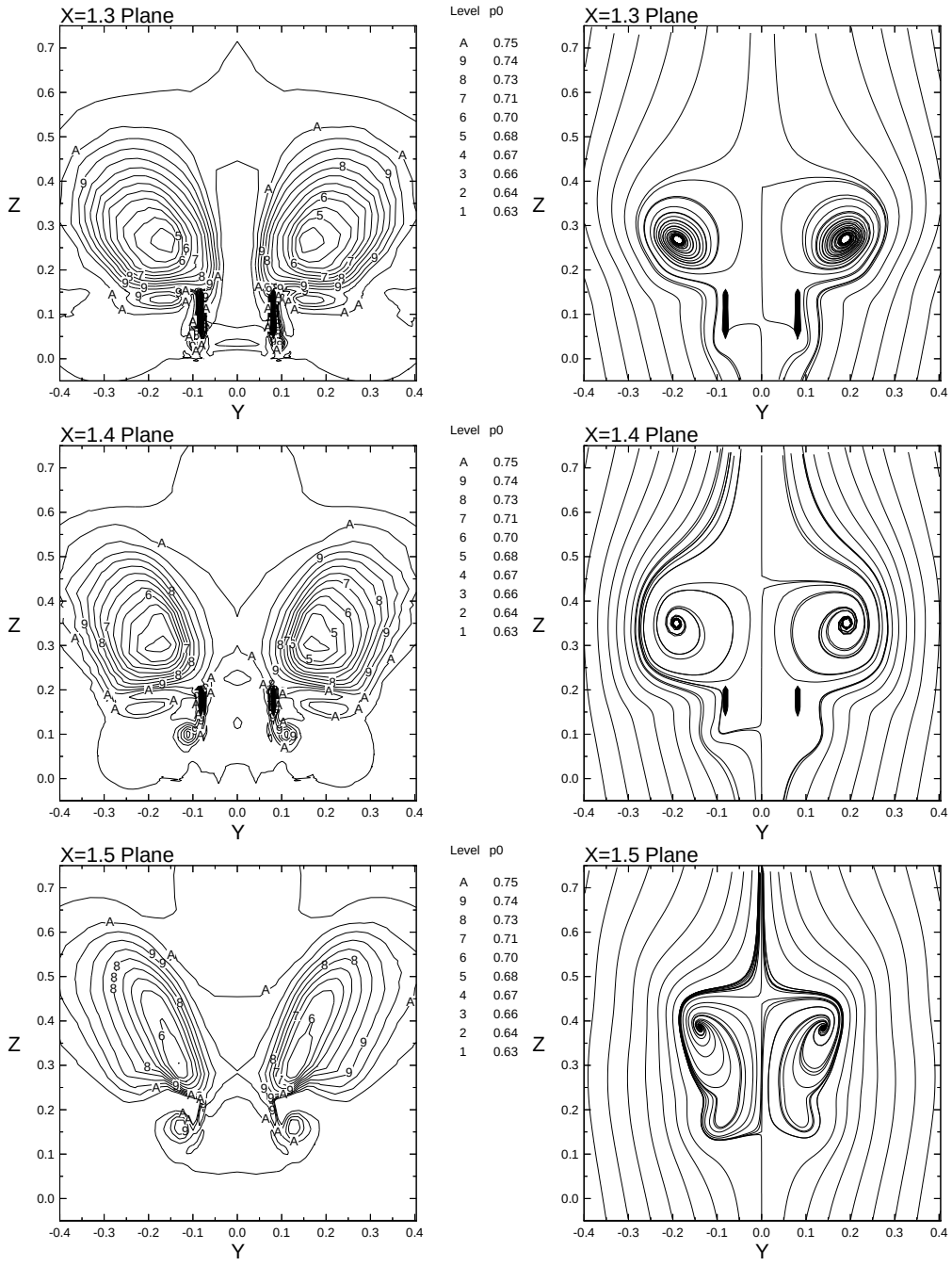

Figure 7.10: Nondimensional total pressure contours and in-plane streamlines plotted on vertical crossflow planes, $x = 1.3, 1.4, 1.5$. Inboard Initial Condition: $Re = 1.25 \times 10^6$, $M = 0.3$, $\alpha = 35^o$.

7.5.2 Uncoupled Bending and Torsion Response

In this section, the buffeting response due to inertially uncoupled bending and torsion vibrations of dynamically scaled, flexible, twin Washburn tails is considered for the inboard tail position. Results from this case will be compared to the midspan and outboard cases in the next two sections to assess the effect of spanwise tail location on tail buffeting. The buffet loads are plotted in Figures 7.11-7.16, and the response is shown in Figures 7.17-7.20.

Lumped load distributions along the tail span, see Figures 7.11 and 7.12, indicate that as with the F/A-18 cases, the mean flow is highly symmetric. The bending loads peak near the root of the tail and decrease monotonically along the span. The twisting moment peaks around 25% span and decreases rapidly on either side of the peak.

Mean and RMS differential pressure distributions for both tails, see Figure 1.13, confirm the similarity in loading between the left and right tails seen in the integrated or lumped loads. Note, at the current high angle-of-attack of $\alpha = 35^o$, flow symmetry is not necessarily guarantied. Single sharp peaks in the frequency response of the buffet excitation parameter are observed on the inner and outer surfaces for both tails, see Figure 7.14. The higher magnitude and greater variation between the tails of the outer side excitation is indicative of the higher unsteadiness of the outer side loads. The differential pressure history and buffet excitation pressure are recorded at pressure tap location 5, shown in Figure 7.2.

Root bending and twisting moment histories and spectra, shown in Figures 7.15 and 7.16, display no evidence of periodicity, but do exhibit strong single dominant frequencies. For both tails, the dominant root bending moment frequency is approximately

30% higher than the root twisting moment. The response of the right and left tails is essentially equivalent. Spanwise deflection plots, see Figure 7.17 and Figure 7.19, indicate that bending is dominated by the first mode, while torsion exhibits higher mode influences. This observation is confirmed in the PSD's of bending and twisting accelerations, see Figures 7.18 and 7.20, which show a sharp peak for bending and a broader plateau of low frequencies for torsion. Tip deflections are centered around an outward bending displacement of $0.045c$ and an outward leading edge rotation of 9^o.

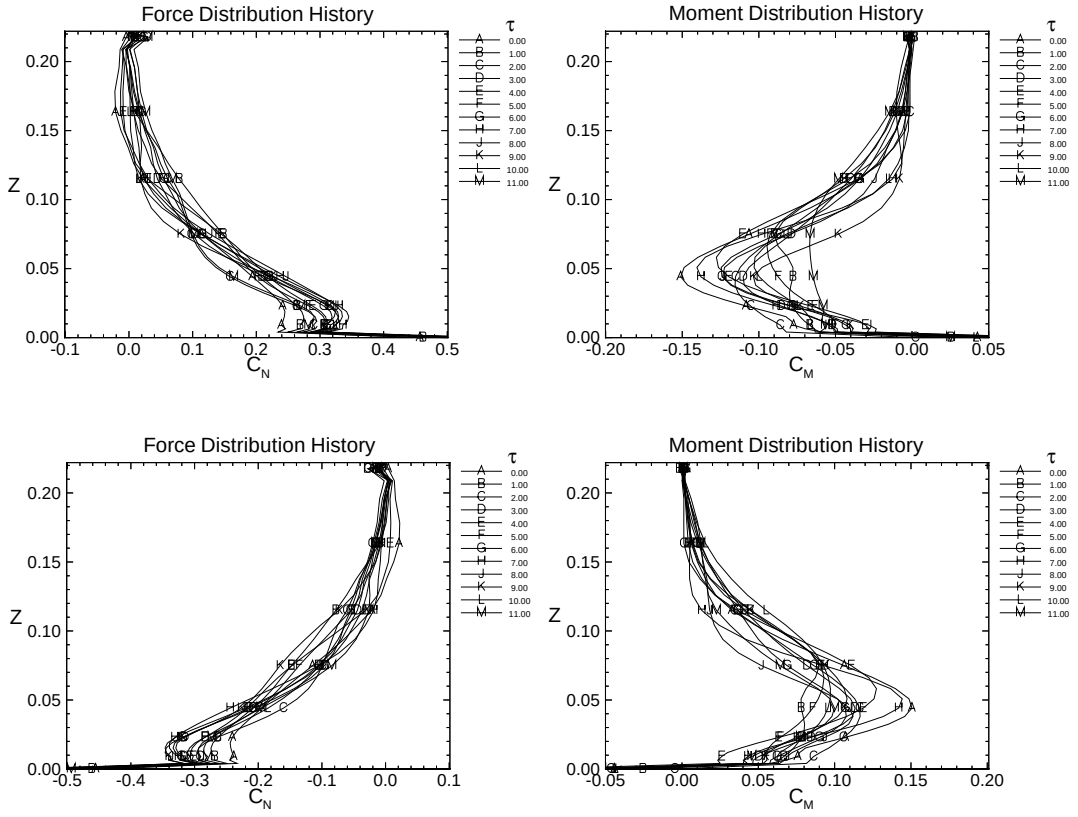

Figure 7.11: Bending force and twisting moment distributions along the tail span plotted at integer nondimensional time levels for a) right and b) left tails. Inboard Case: $Re = 1.25 \times 10^6$, $M = 0.3$, $\alpha = 35^o$.

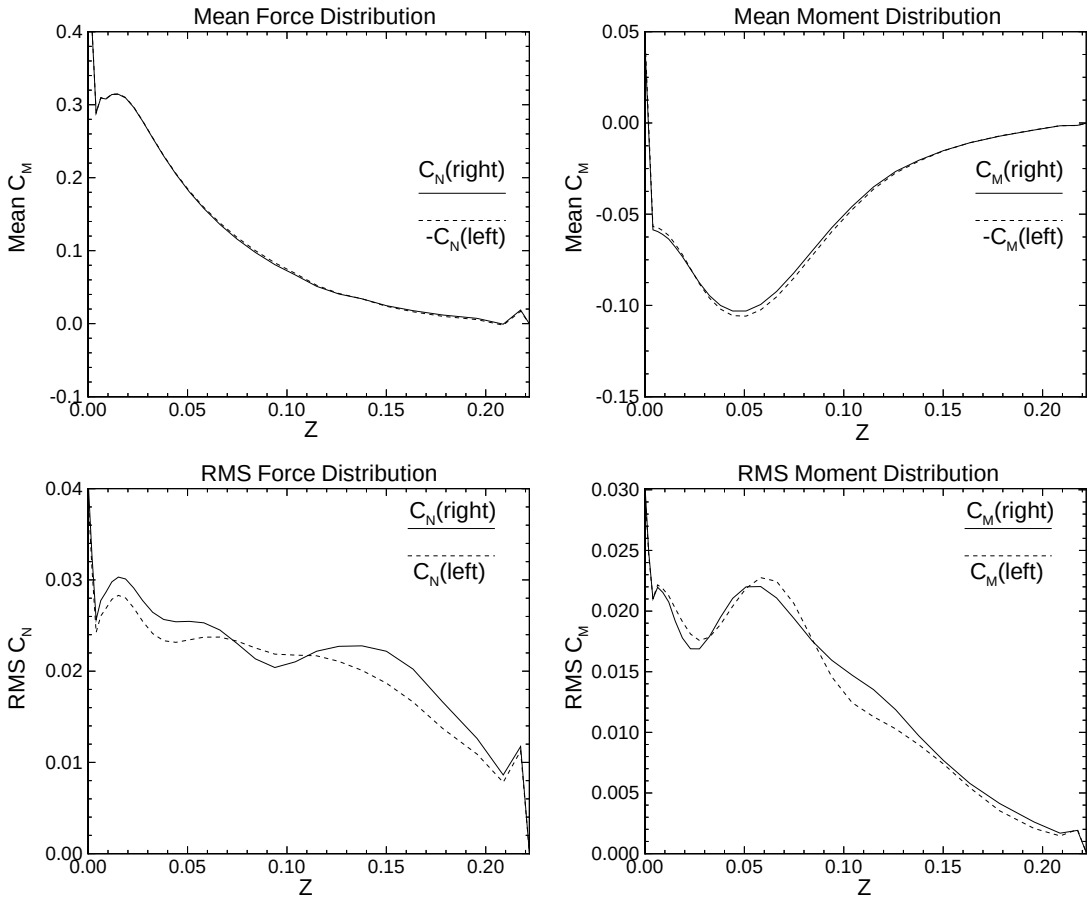

Figure 7.12: Mean and RMS load distributions along the right and left tail spans. Inboard Case: $Re = 1.25 \times 10^6$, $M = 0.3$, $\alpha = 35^o$.

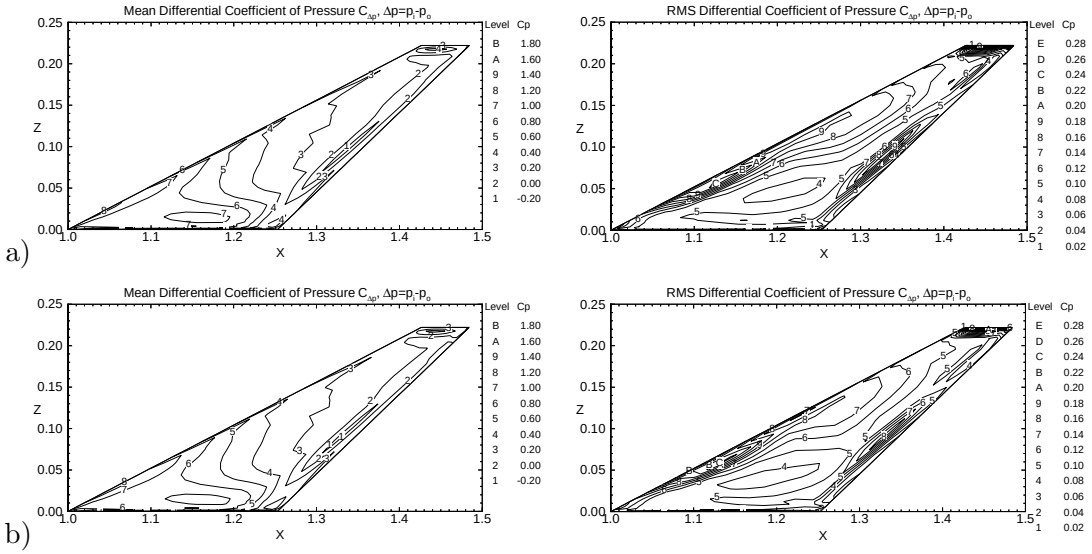

Figure 7.13: Mean and RMS differential coefficient of pressure contours on a) right and b) left tails. Inboard Case: $Re = 1.25 \times 10^6$, $M = 0.3$, $\alpha = 35^o$.

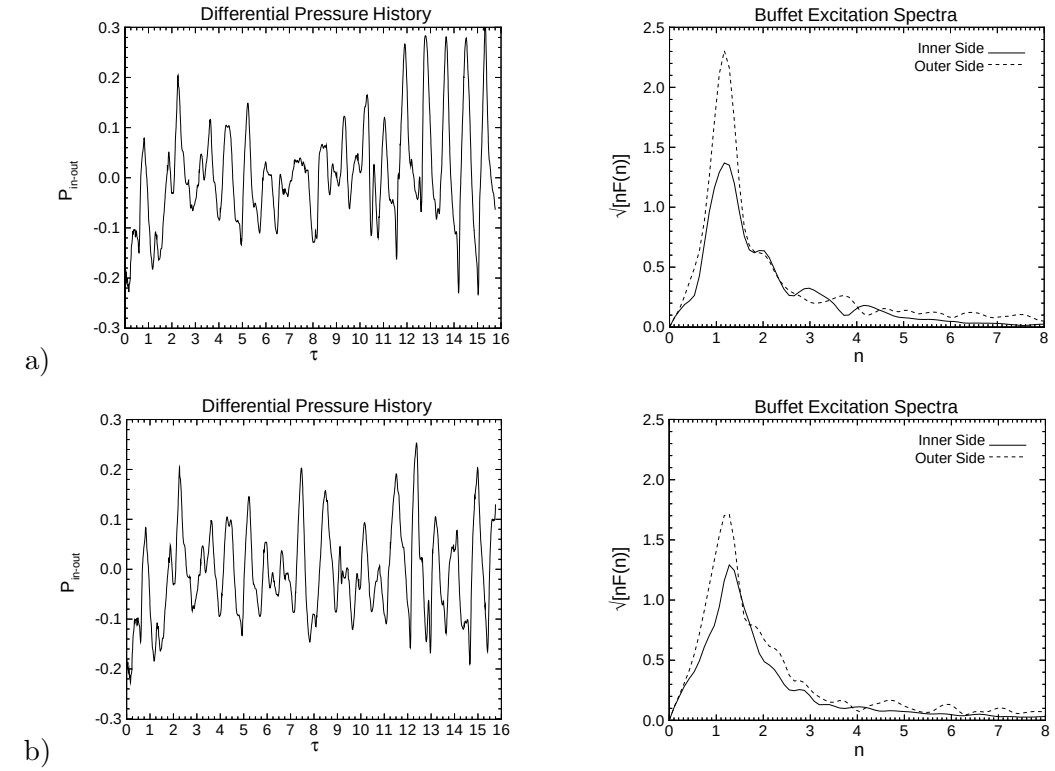

Figure 7.14: Differential pressure ($\frac{\Delta p}{q_\infty}$) histories at the 50% chord and 90% span location for a) right and b) left tails. Inboard Case: $Re = 1.25 \times 10^6$, $M = 0.3$, $\alpha = 35^o$.

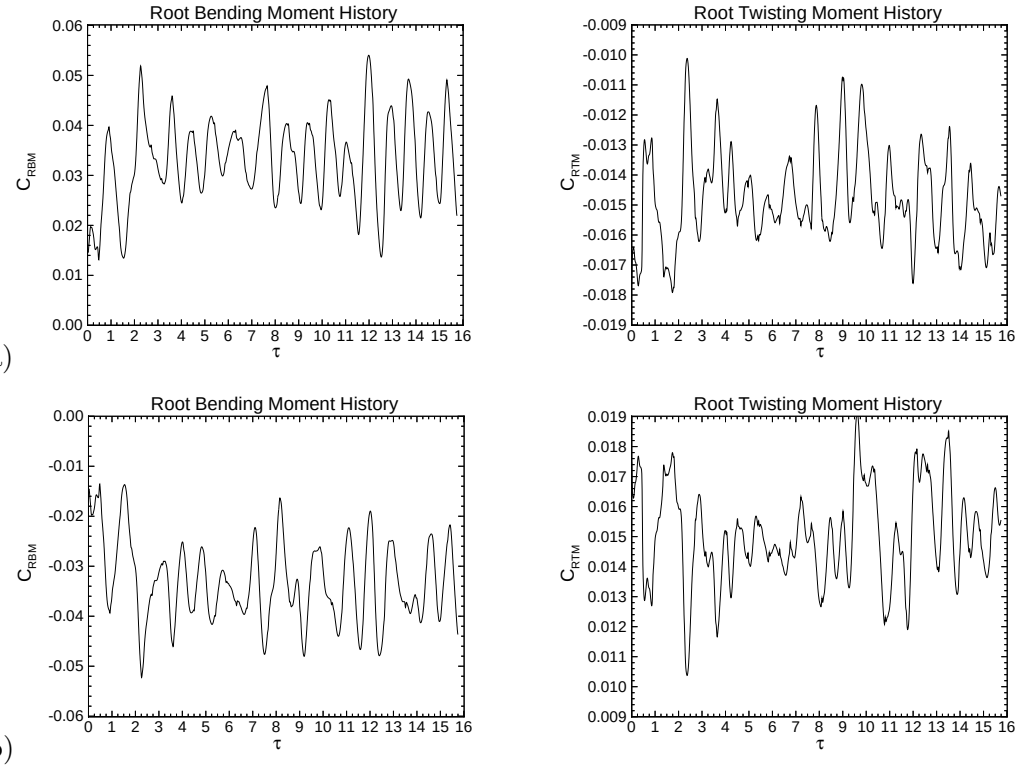

Figure 7.15: History of root bending moment coefficient and root twisting moment coefficient for a) right and b) left tails. Inboard Case: $Re = 1.25 \times 10^6$, $M = 0.3$, $\alpha = 35^o$.

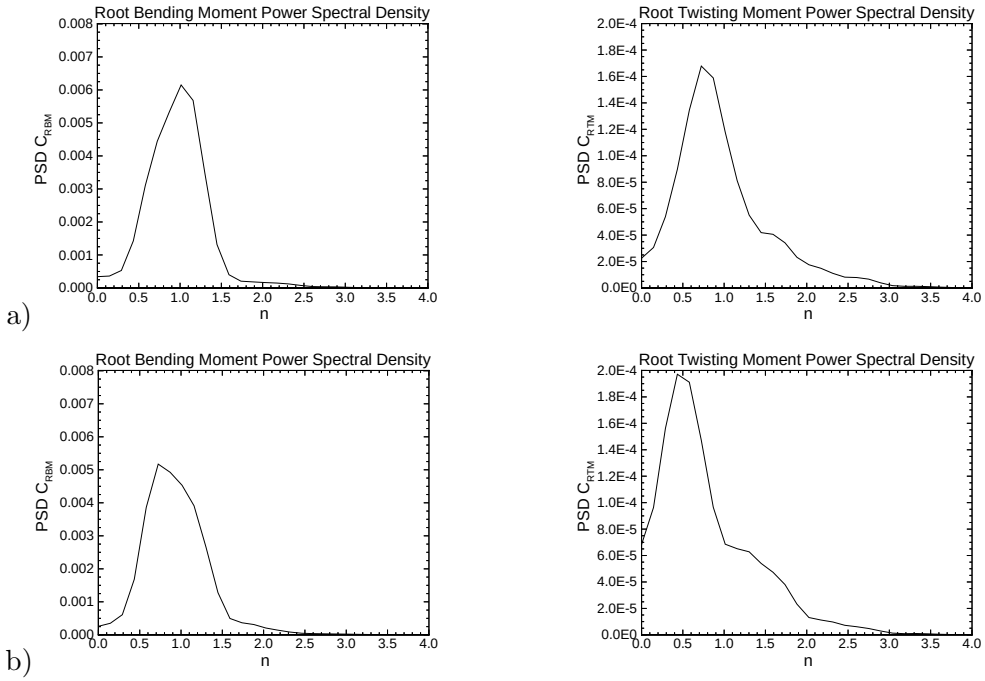

Figure 7.16: Power spectral density of root bending moment coefficient and root twisting moment coefficient versus reduced frequency for a) right and b) left tails. Inboard Case: $Re = 1.25 \times 10^6$, $M = 0.3$, $\alpha = 35^o$.

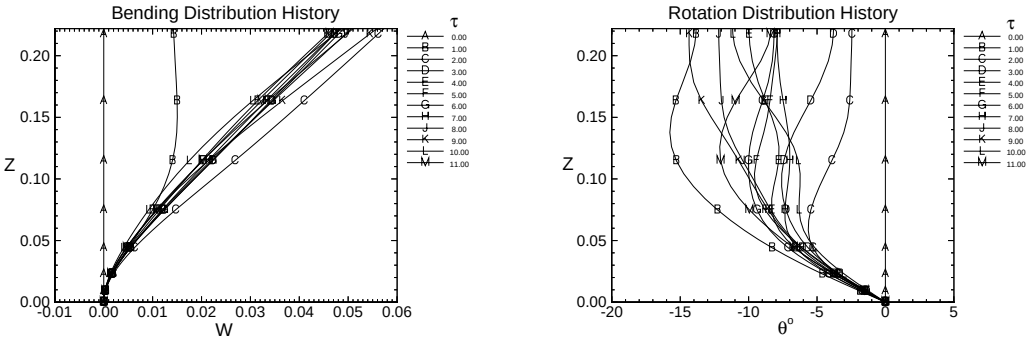

Figure 7.17: Right Tail: Bending and torsion deflection distributions along the tail span plotted at integer nondimensional time levels. Inboard Case: $Re = 1.25 \times 10^6$, $M = 0.3$, $\alpha = 35^o$.

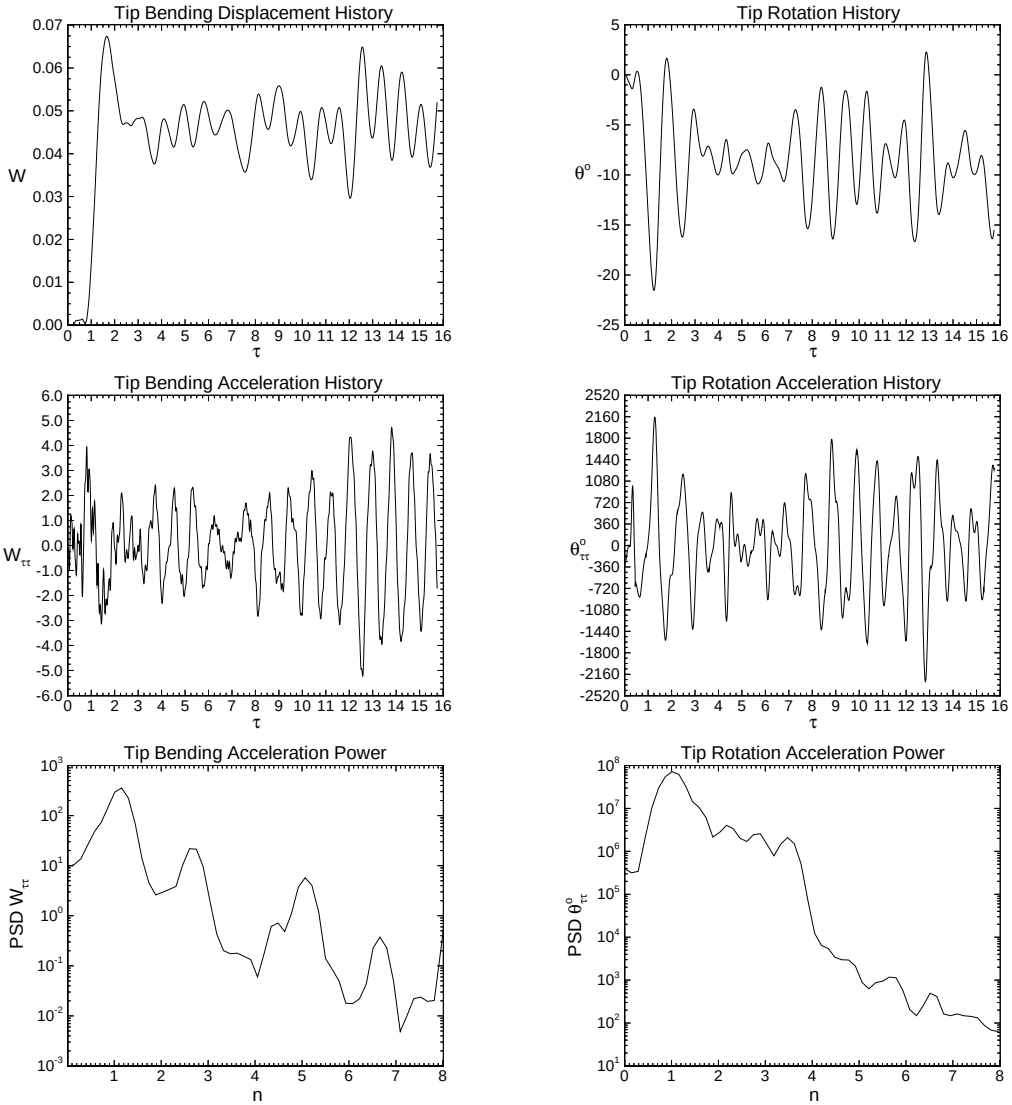

Figure 7.18: Right Tail: Time and frequency domain data for tip bending and torsion deflections and accelerations. Inboard Case: $Re = 1.25 \times 10^6$, $M = 0.3$, $\alpha = 35^o$.

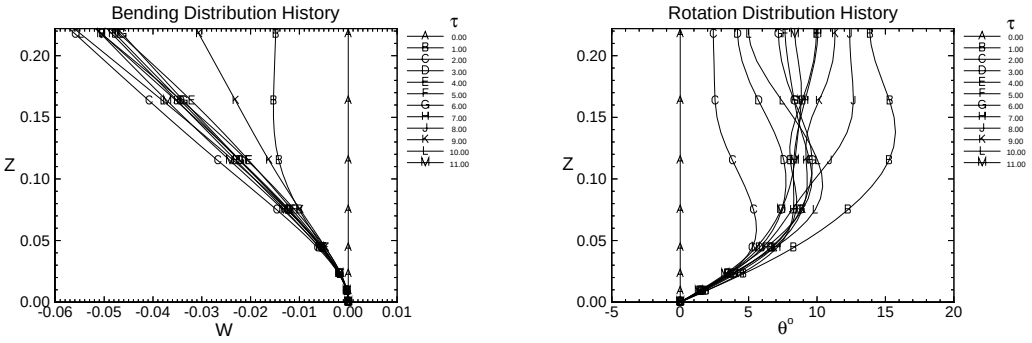

Figure 7.19: Left Tail: Bending and torsion deflection distributions along the tail span plotted at integer nondimensional time levels. Inboard Case: $Re = 1.25 \times 10^6$, $M = 0.3$, $\alpha = 35^o$.

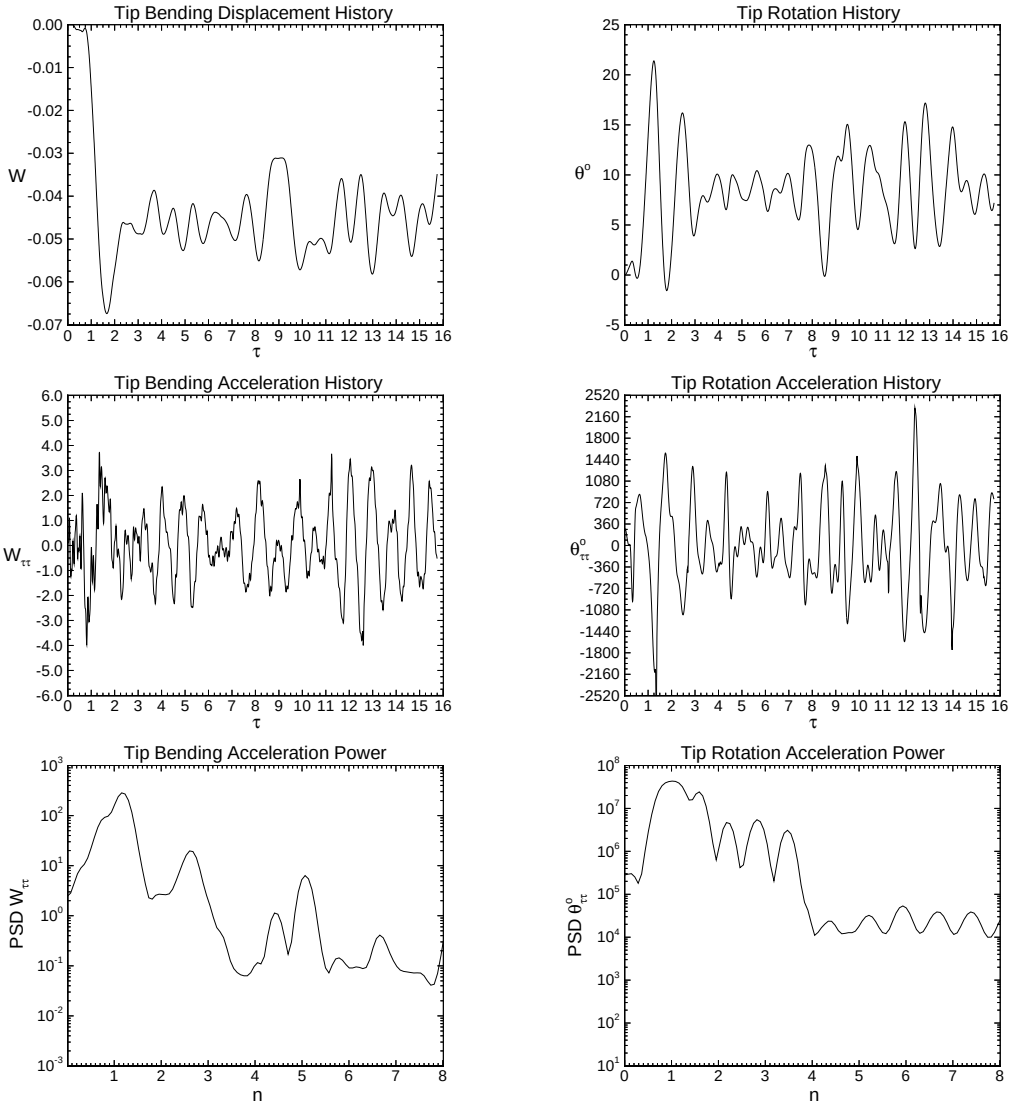

Figure 7.20: Left Tail: Time and frequency domain data for tip bending and torsion deflections and accelerations. Inboard Case: $Re = 1.25 \times 10^6$, $M = 0.3$, $\alpha = 35^o$.

7.6 Midspan Twin Tail Case

7.6.1 Initial Conditions, $Re = 1.25 \times 10^6$, $M = 0.3$, $\alpha = 35^o$

The initial flow state is obtained by the same combination method of local and time accurate stepping previously used with the same time step of $\Delta\tau = 0.00036$. Detailed initial condition flow field plots are shown in Figures 7.21-7.26.

Comparing the 3-D plots of Figures 7.21 and 7.22 with the inboard results, see Figures 7.5 and 7.6, indicate that the midspan case has a smaller burst core diameter than the inboard case. However, the burst location does not change appreciably.

Near surface streamline plots of the right tail, see Figure 7.23, indicate that the flow on the outer surface is separating due to the vortex and like the F/A-18 cases *does* show strong signs of inside separation due to vortex flow spillage over the tail leading edge. Comparisons of the wing secondary separation line, see Figure 7.23, with the inboard case shown in Figure 7.7 indicates that the midspan case does not contain a second strong area of recirculation near $x = 0.9c$ as in the inboard case.

Spanwise peak suction pressure distributions, see Figure 7.24, are higher at $x = 0.5c$ and $x = 0.7c$ than those of the inboard case, see Figure 7.8, and equal at the forward and aft positions. This is indicative of the a stronger core due to the diminished strength of the midspan breakdown.

Comparison of the crossflow total pressure contours and streamlines of Figures 7.25 and 7.26, with the inboard case, shown in Figures 7.9 and 7.10, indicate that the midspan vortex differs only slightly in size and strength from the inboard case for the first three planes. However, in the aft planes from $x = 1.3c - 1.5c$, where the tails are more of an obstruction, the midspan core is much more elongated than in the inboard case. Pressure contours indicate that the secondary vortices emanating from the sharp

bottom edges of the tails are stronger than the inboard case due to the increased crossflow velocity coming from the closer primary vortex. Thus, it is concluded that moving the tail from the inner spanwise position of $y = 0.082c$ to the midspan location of $y = 0.14c$ significantly affects all of the flow downstream of point of breakdown, particularly in the aft region of the tails.

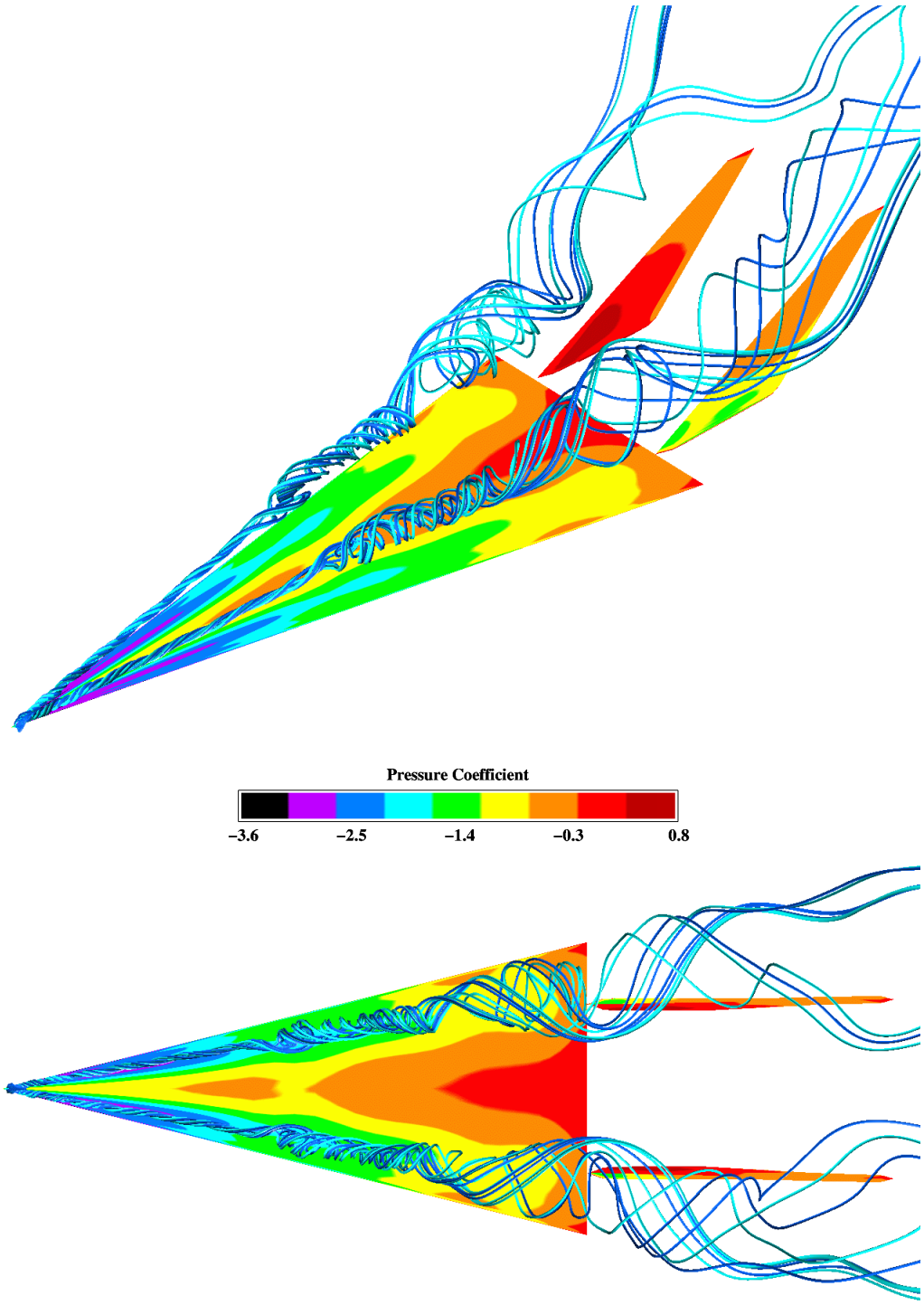

Figure 7.21: Three-dimensional and top views of surface pressure and vortex core streamlines. Midspan Initial Condition: $Re = 1.25 \times 10^6$, $M = 0.3$, $\alpha = 35^o$.

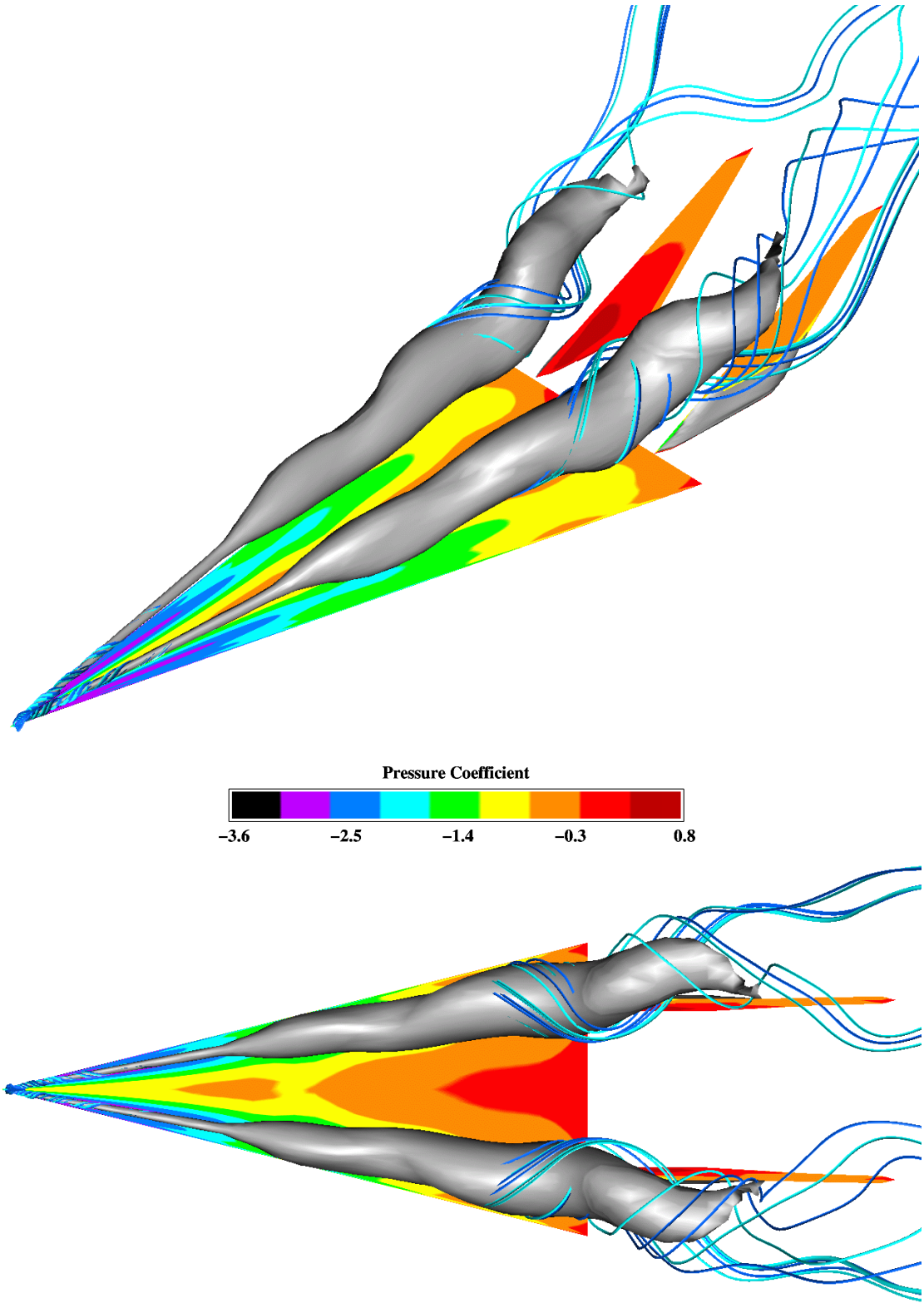

Figure 7.22: Three-dimensional and top views of surface pressure, vortex core streamlines and solid total pressure isosurfaces. Midspan Initial Condition: $Re = 1.25 \times 10^6$, $M = 0.3$, $\alpha = 35^o$.

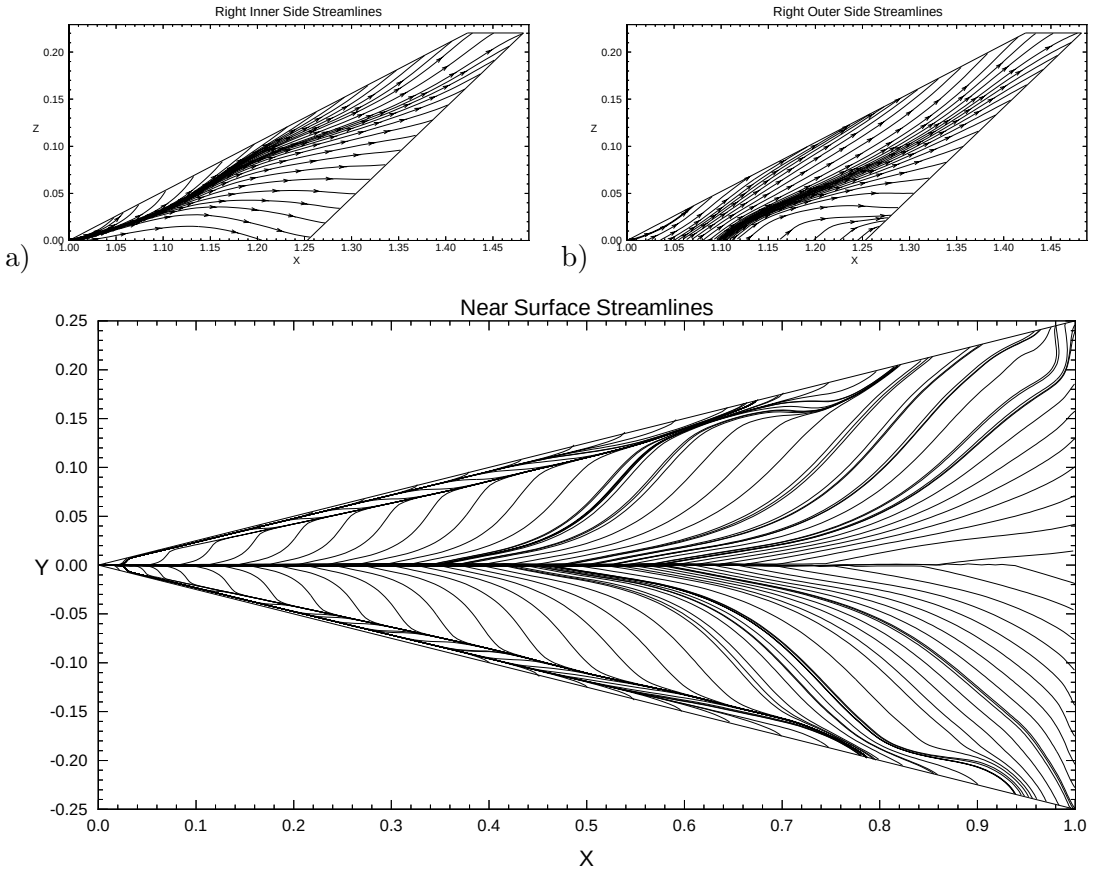

Figure 7.23: Near surface streamlines for the a) inner and b) outer right tail surfaces and the upper wing surface. Midspan Initial Condition: $Re = 1.25 \times 10^6$, $M = 0.3$, $\alpha = 35^o$.

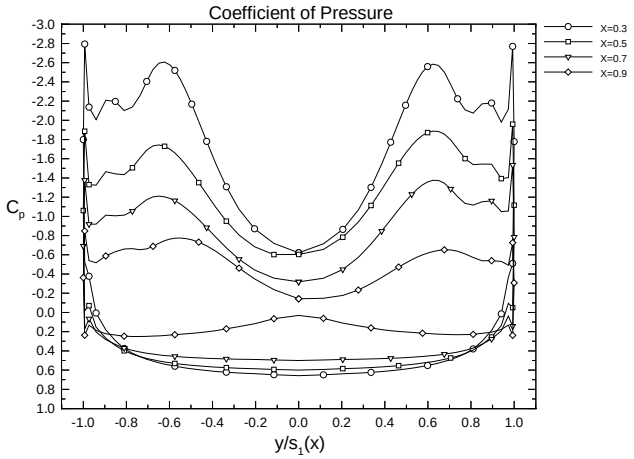

Figure 7.24: Coefficient of pressure on upper and lower wing surfaces at chord stations corresponding to plotted crossflow planes. Midspan Initial Condition: $Re = 1.25 \times 10^6$, $M = 0.3$, $\alpha = 35^o$.

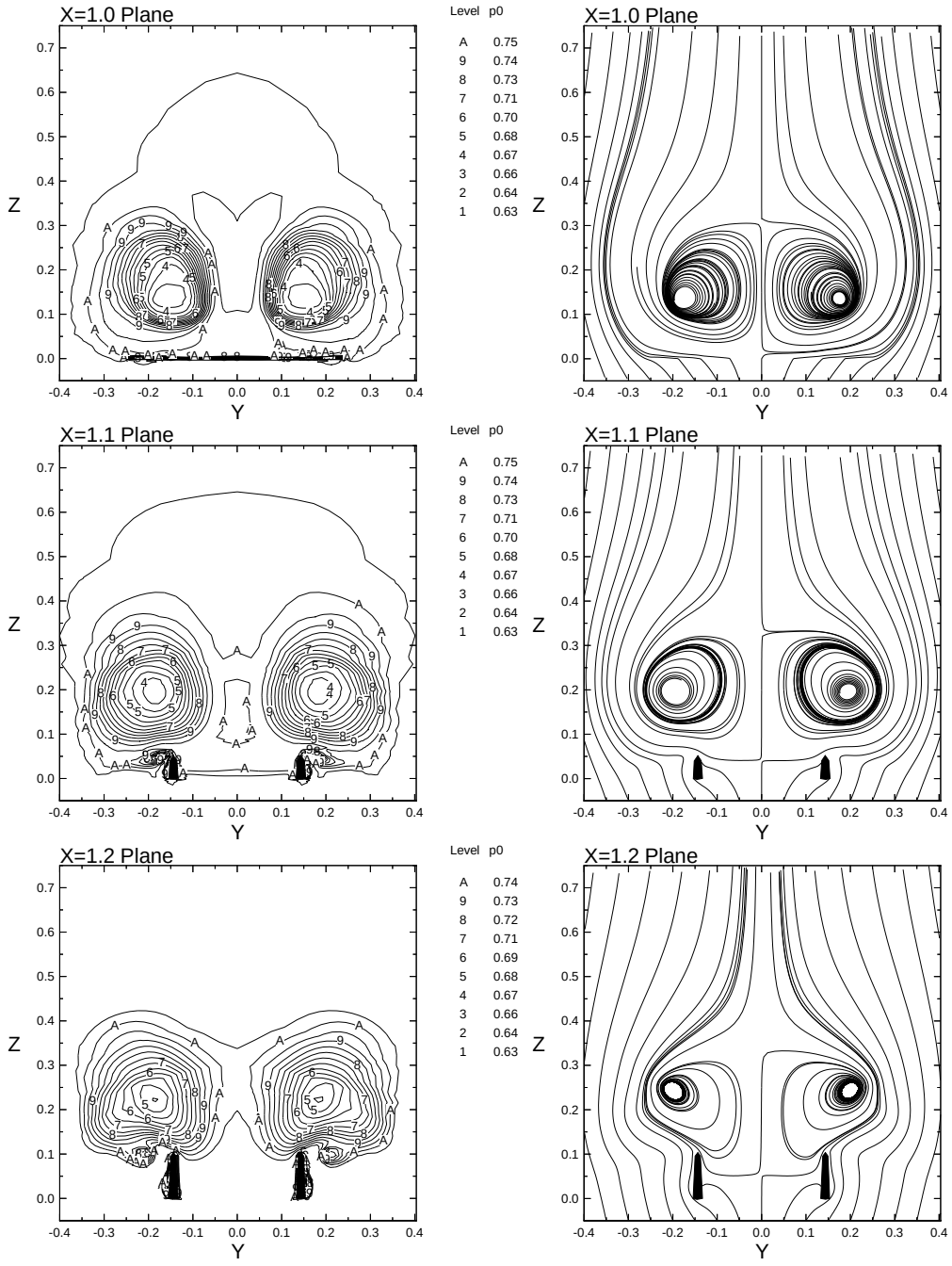

Figure 7.25: Nondimensional total pressure contours and in-plane streamlines plotted on vertical crossflow planes, $x = 1.0, 1.1, 1.2$. Midspan Initial Condition: $Re = 1.25 \times 10^6$, $M = 0.3$, $\alpha = 35^o$.

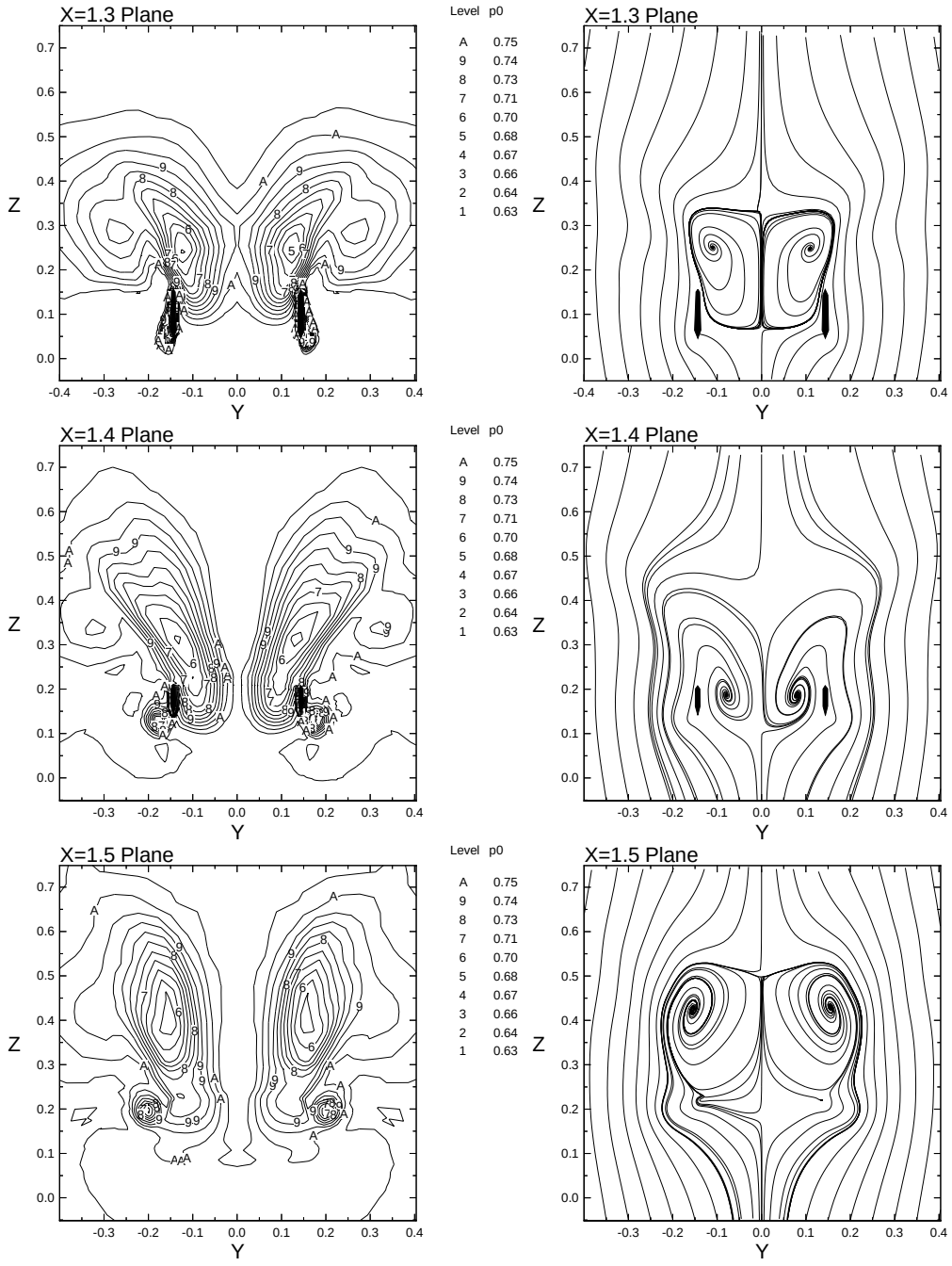

Figure 7.26: Nondimensional total pressure contours and in-plane streamlines plotted on vertical crossflow planes, $x = 1.3, 1.4, 1.5$. Midspan Initial Condition: $Re = 1.25 \times 10^6$, $M = 0.3$, $\alpha = 35^o$.

7.6.2 Uncoupled Bending and Torsion Response

In this section, the buffeting response due to inertially uncoupled bending and torsion vibrations of dynamically scaled, flexible, twin Washburn tails is considered for the midspan tail position. Results will be contrasted with the inboard case to determine the effect of spanwise tail location on tail buffeting. The buffet loads are plotted in Figures 7.27-7.32, and the response is shown in Figures 7.33-7.36.

Lumped load distributions along the tail span, see Figures 7.27 and 7.28, indicate that as with the previous cases, the mean flow is highly symmetric. Bending loads peak near the root of the tail as in the inboard case, but with a 50% increase in the peak mean loading. The more relevant unsteady loads have the same peak magnitude, but drop off more quickly than in the inboard case. The same trends in steady and unsteady loads are also present in the moment data. It is also observed that the vertical location of peak moment magnitude is about half the height of the inboard case.

Mean and RMS differential pressure distributions, shown in Figure 7.29, depict a much lower gradient of RMS loads near the leading and trailing tail edges. Buffet excitation spectra, see Figure 7.30, indicate that the unsteady, differential, midspan loads are much smaller than the inboard results. This is consistent with the midspan tail being more fully immersed in the vortex core, as opposed to the inboard case in which the vortex passes by the outer side the tail. Another difference from the inboard case, is the inclusion of a second peak in the inner side buffet spectra.

Root bending and twisting moment histories and spectra, shown in Figures 7.31 and 7.32, show no evidence of periodicity. Unlike the inboard case, two dominant frequencies are observed for both bending and twisting moments. The double frequencies bracket the single dominant frequencies of the inboard case. The bending moments are

dominated by the lower peak frequency while the twisting moments are equal or stronger in the higher of the two peak frequencies.

The buffeting response, shown in Figures 7.33-7.36, is more close to being periodic than the inboard case and has much smaller steady displacements in bending and torsion. The unsteady displacements for bending are roughly equal, however, the angular deflections are much smaller with an amplitude of 1.5^o, as opposed to the previous 8^o. Detailed comparisons of loading and responses are located at the end of this chapter. Acceleration spectra indicate the presence of three peak bending frequencies with nearly equal magnitudes and up to six rotation peak frequencies, again with nearly the same magnitude. Thus, is it clear that the smaller deflections have allowed the response frequency to sustain very high frequency vibrations.

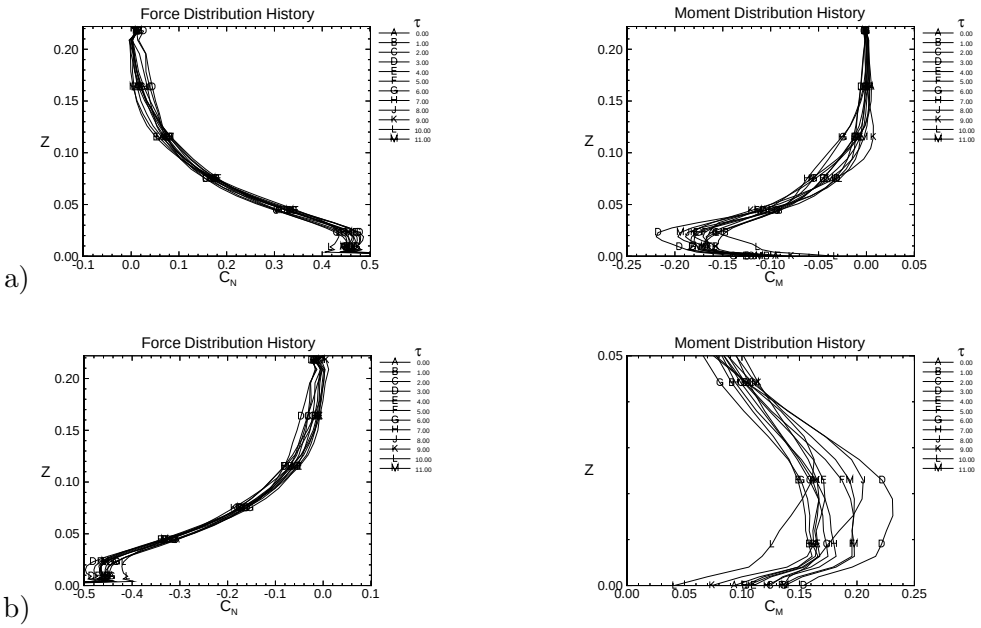

Figure 7.27: Bending force and twisting moment distributions along the tail span plotted at integer nondimensional time levels for a) right and b) left tails. Midspan Case: $Re = 1.25 \times 10^6$, $M = 0.3$, $\alpha = 35^o$.

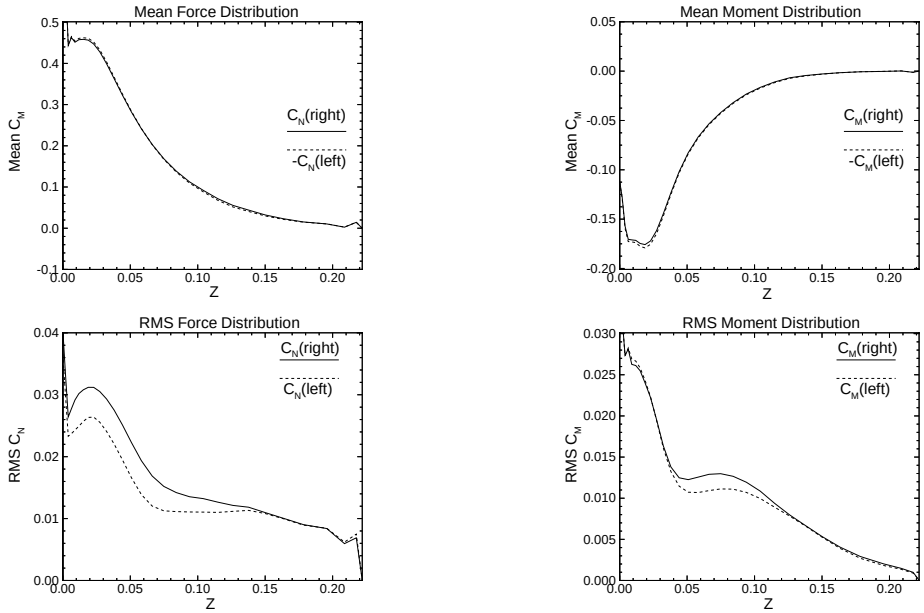

Figure 7.28: Mean and RMS load distributions along the right and left tail spans. Midspan Case: $Re = 1.25 \times 10^6$, $M = 0.3$, $\alpha = 35^o$.

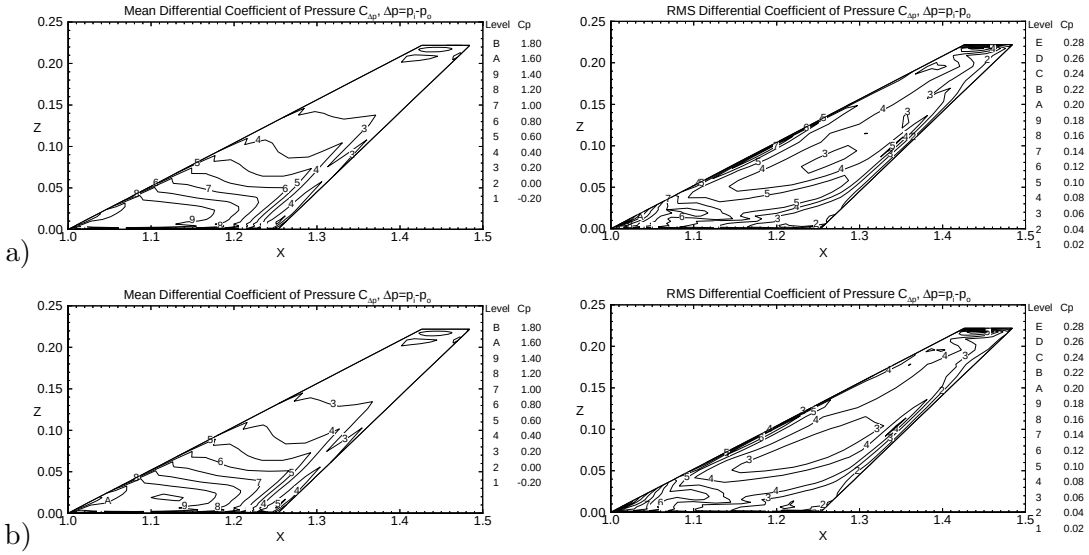

Figure 7.29: Mean and RMS differential coefficient of pressure contours on a) right and b) left tails. Midspan Case: $Re = 1.25 \times 10^6$, $M = 0.3$, $\alpha = 35^o$.

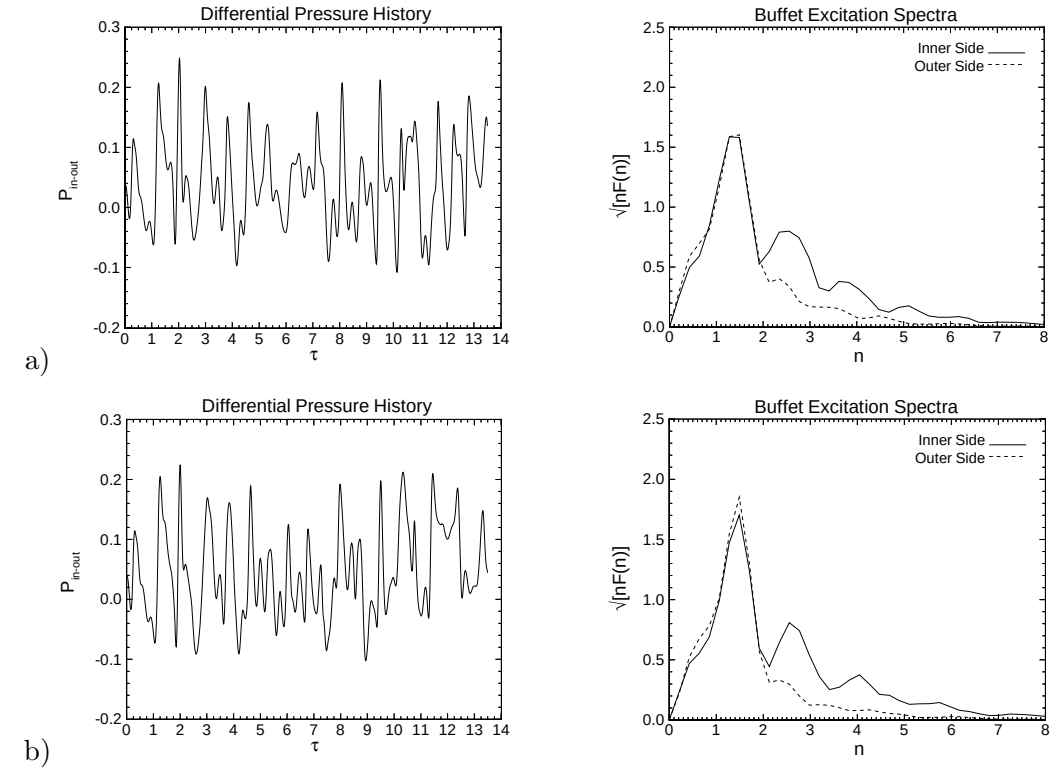

Figure 7.30: Differential pressure ($\frac{\Delta p}{q_\infty}$) histories at the 50% chord and 90% span location for a) right and b) left tails. Midspan Case: $Re = 1.25 \times 10^6$, $M = 0.3$, $\alpha = 35^o$.

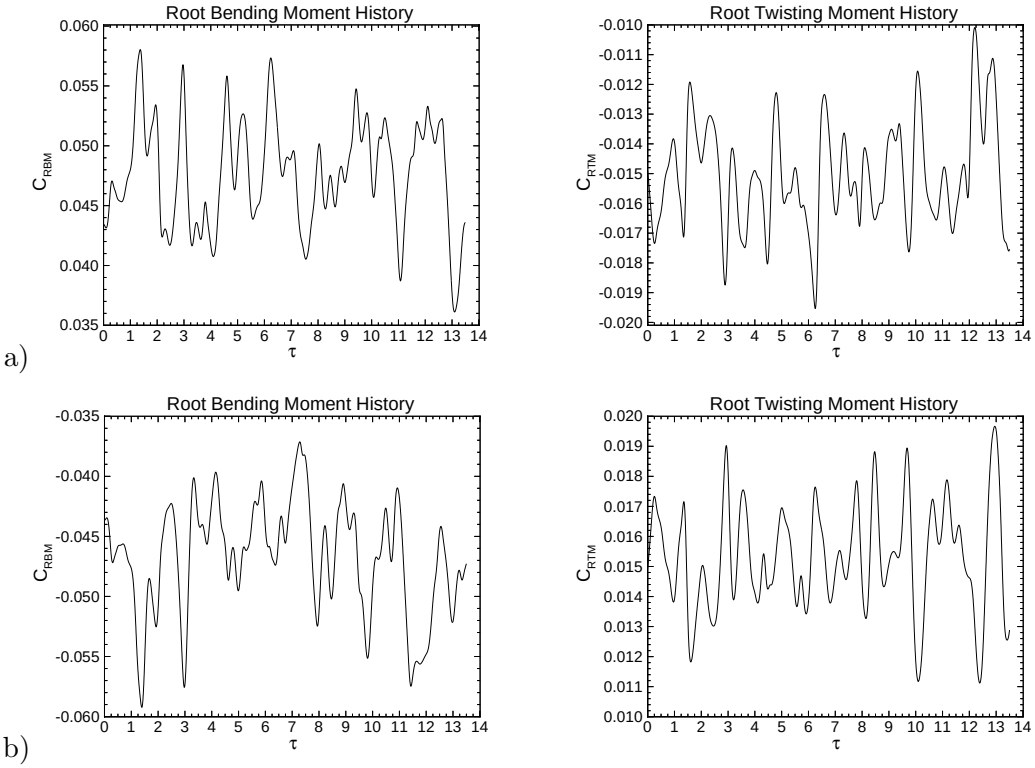

Figure 7.31: History of root bending moment coefficient and root twisting moment coefficient for a) right and b) left tails. Midspan Case: $Re = 1.25 \times 10^6$, $M = 0.3$, $\alpha = 35^o$.

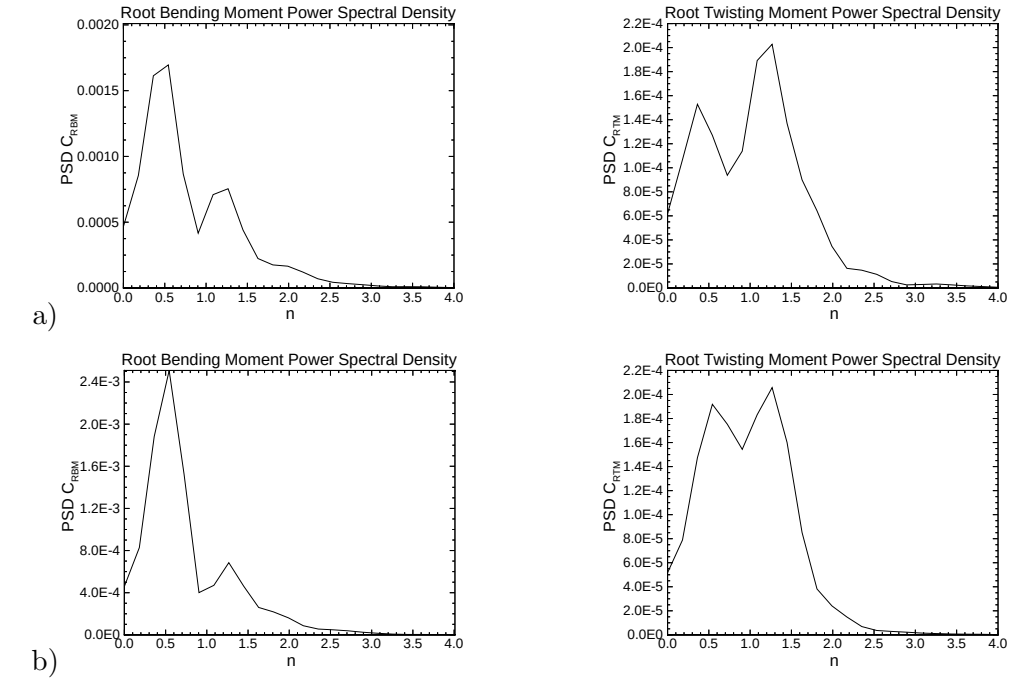

Figure 7.32: Power spectral density of root bending moment coefficient and root twisting moment coefficient versus reduced frequency for a) right and b) left tails. Midspan Case: $Re = 1.25 \times 10^6$, $M = 0.3$, $\alpha = 35^o$.

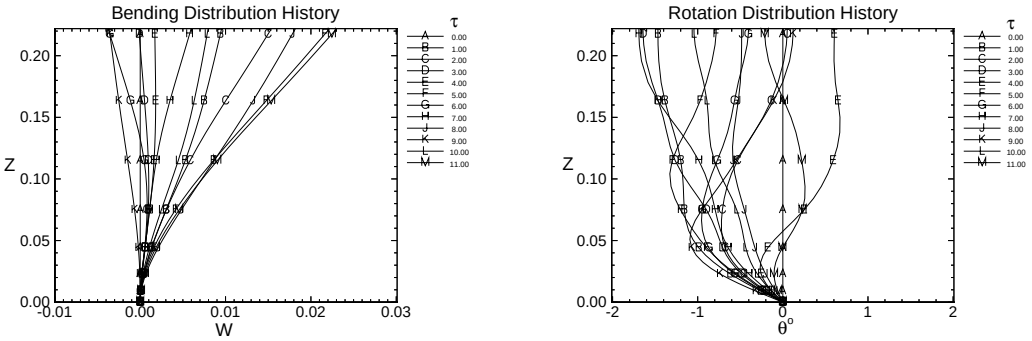

Figure 7.33: Right Tail: Bending and torsion deflection distributions along the tail span plotted at integer nondimensional time levels. Midspan Case: $Re = 1.25 \times 10^6$, $M = 0.3$, $\alpha = 35^o$.

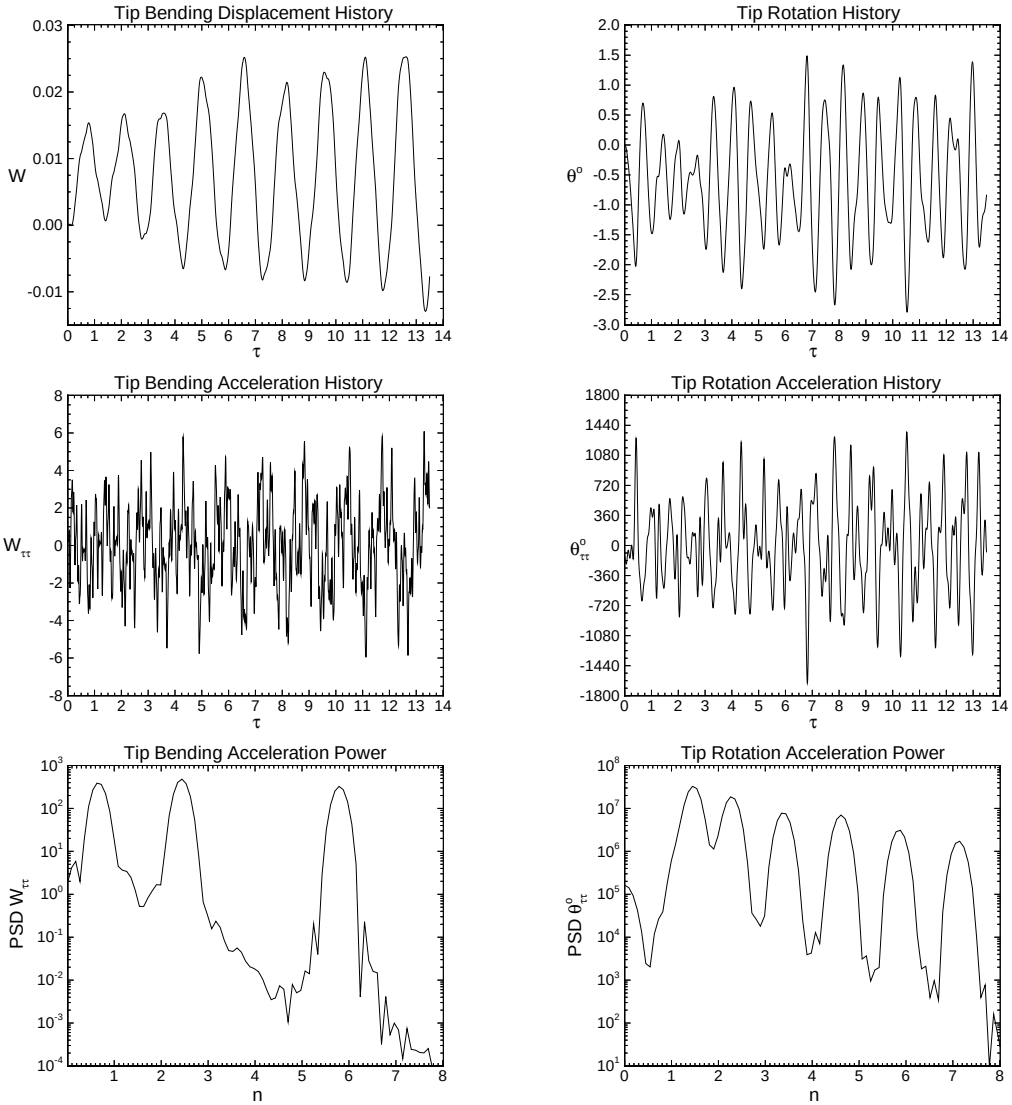

Figure 7.34: Right Tail: Time and frequency domain data for tip bending and torsion deflections and accelerations. Midspan Case: $Re = 1.25 \times 10^6$, $M = 0.3$, $\alpha = 35^o$.

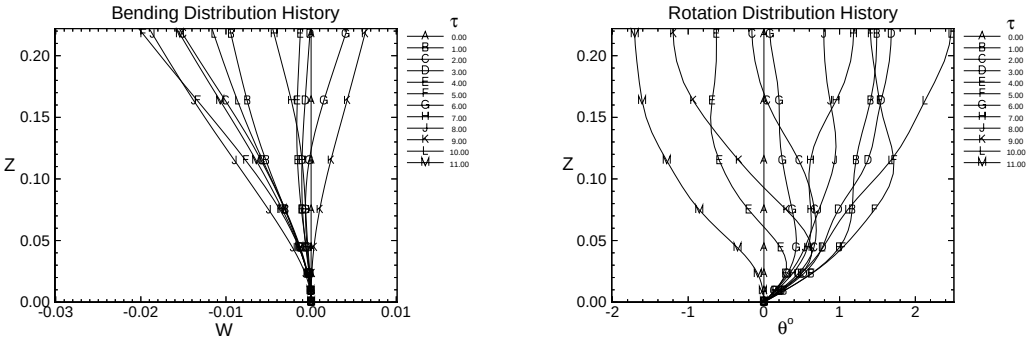

Figure 7.35: Left Tail: Bending and torsion deflection distributions along the tail span plotted at integer nondimensional time levels. Midspan Case: $Re = 1.25 \times 10^6$, $M = 0.3$, $\alpha = 35^o$.

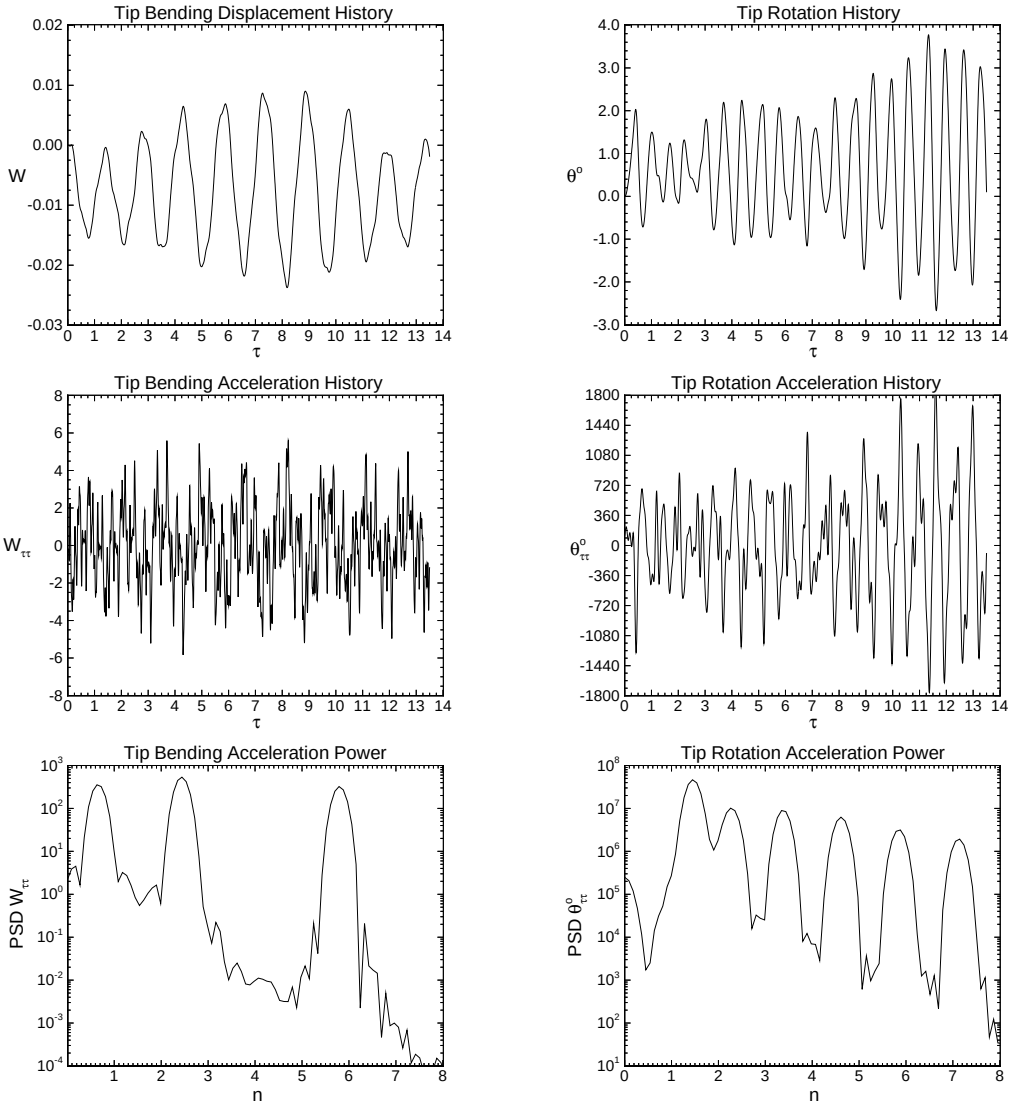

Figure 7.36: Left Tail: Time and frequency domain data for tip bending and torsion deflections and accelerations. Midspan Case: $Re = 1.25 \times 10^6$, $M = 0.3$, $\alpha = 35^o$.

7.7 Outboard Twin Tail Model

7.7.1 Initial Conditions, $Re = 1.25 \times 10^6$, $M = 0.3$, $\alpha = 35^o$

The initial flow state is obtained by the same combination method of local and time accurate stepping previously used in the inboard and midspan cases. Detailed initial condition flow field plots are shown in Figures 7.37-7.42.

Plots of 3-D streamlines and total pressure isosurfaces, see Figures 7.37 and 7.38, indicate that the breakdown flow more closely resembles the inboard case than the midspan case, both in terms of burst core diameter and overall wing surface pressure distribution. However, the magnitude of the peaks in the spanwise C_p plots, see Figure 7.40, more closely match those of the midspan case.

Near surface streamline plots of the right tail, see Figure 7.39, indicate that as in the midspan case, flow on both the outer and inner surfaces indicate strong lines of flow separation. The secondary separation line on the wing, see Figure 7.39, shows an aft recirculation pattern similar to the inboard case.

Comparison of the crossflow total pressure contours and streamlines of Figures 7.41 and 7.42 with the inboard and midspan cases, shows a wide variation of core location with respect to the spanwise tail location. The plots also indicate that the outboard span vortices do not completely clear the tails as they pass by, as in the inboard case, which explains the surface streamline similarities with the midspan case. The secondary vortices emanating from the sharp bottom edges of the tails are the strongest for the outboard case and visible aft of the $x = 1.3$ plane.

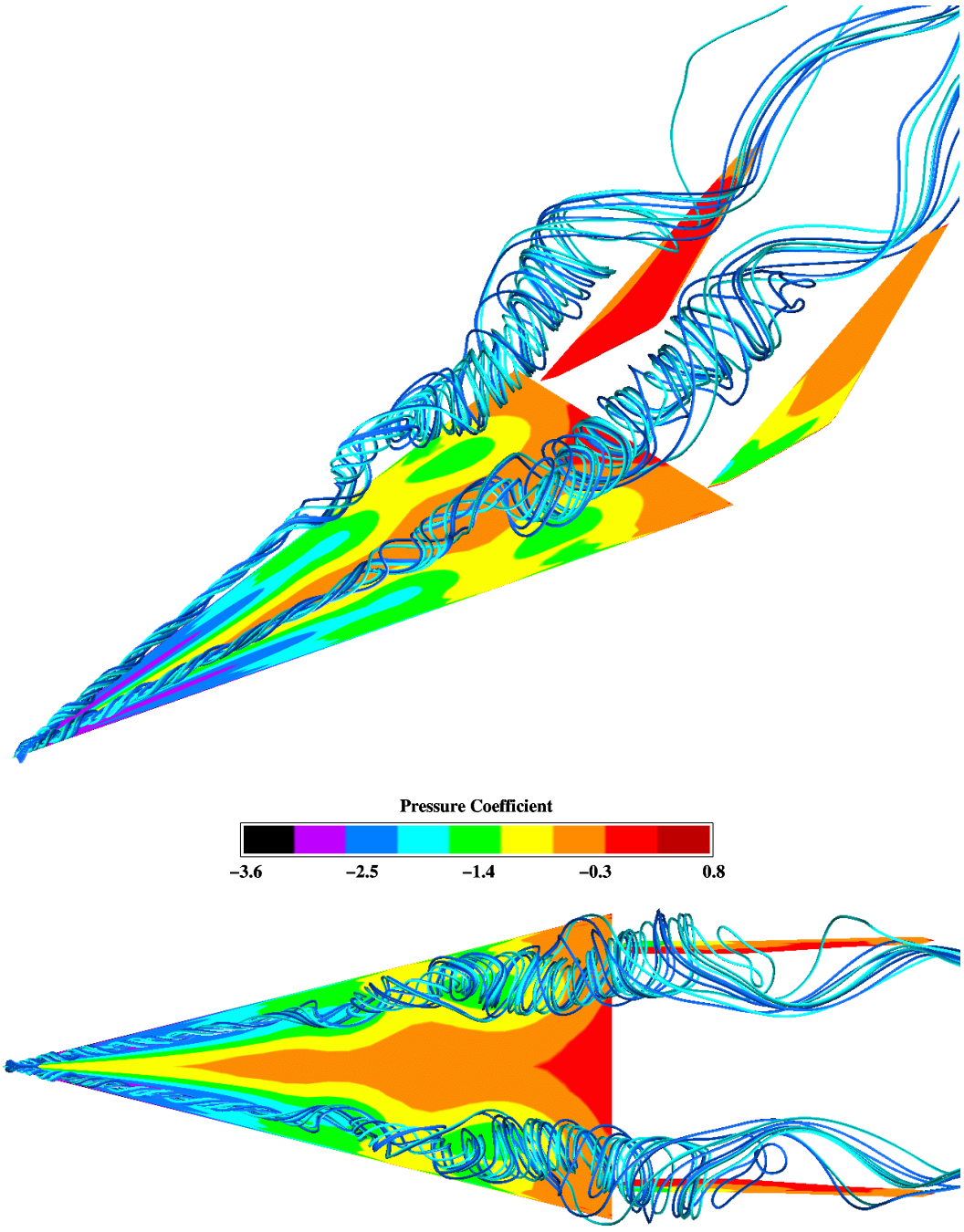

Figure 7.37: Three-dimensional and top views of surface pressure and vortex core streamlines. Outboard Initial Condition: $Re = 1.25 \times 10^6$, $M = 0.3$, $\alpha = 35^o$.

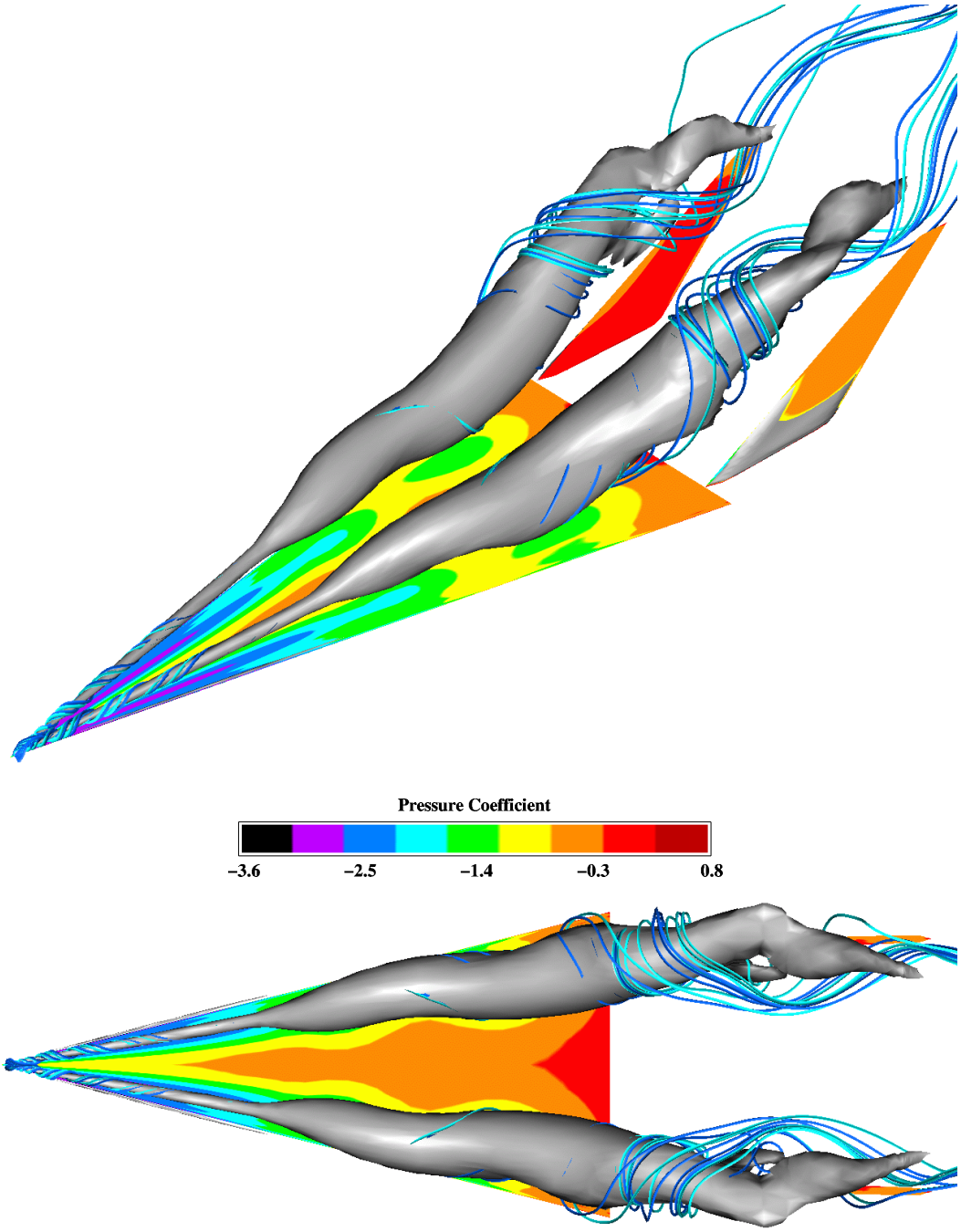

Figure 7.38: Three-dimensional and top views of surface pressure, vortex core streamlines and solid total pressure isosurfaces. Outboard Initial Condition: $Re = 1.25 \times 10^6$, $M = 0.3$, $\alpha = 35^o$.

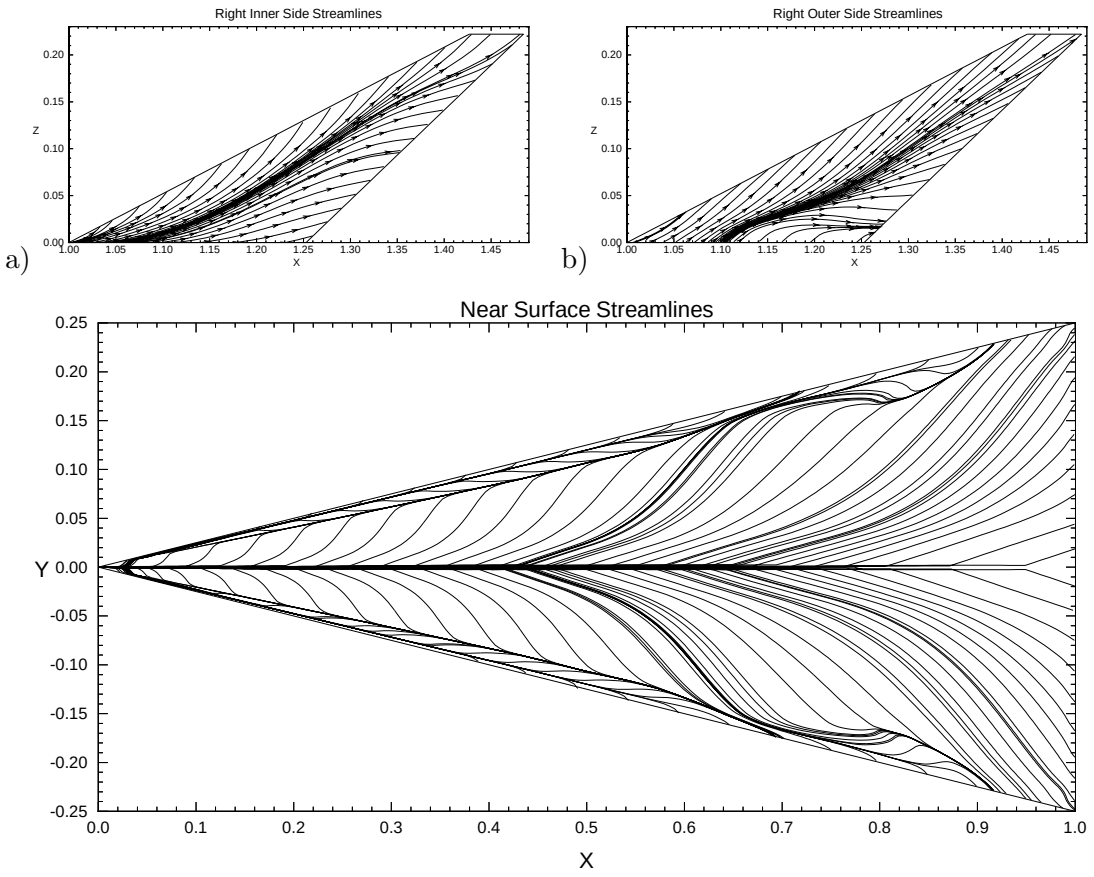

Figure 7.39: Near surface streamlines for the a) inner and b) outer right tail surfaces and the upper wing surface. Outboard Initial Condition: $Re = 1.25 \times 10^6$, $M = 0.3$, $\alpha = 35^o$.

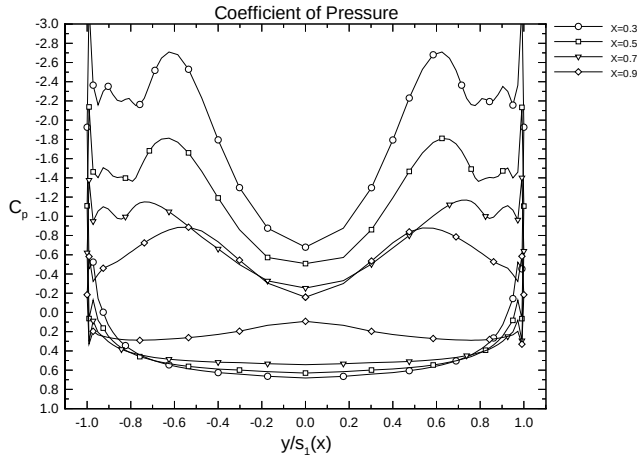

Figure 7.40: Coefficient of pressure on upper and lower wing surfaces at chord stations corresponding to plotted crossflow planes. Outboard Initial Condition: $Re = 1.25 \times 10^6$, $M = 0.3$, $\alpha = 35^o$.

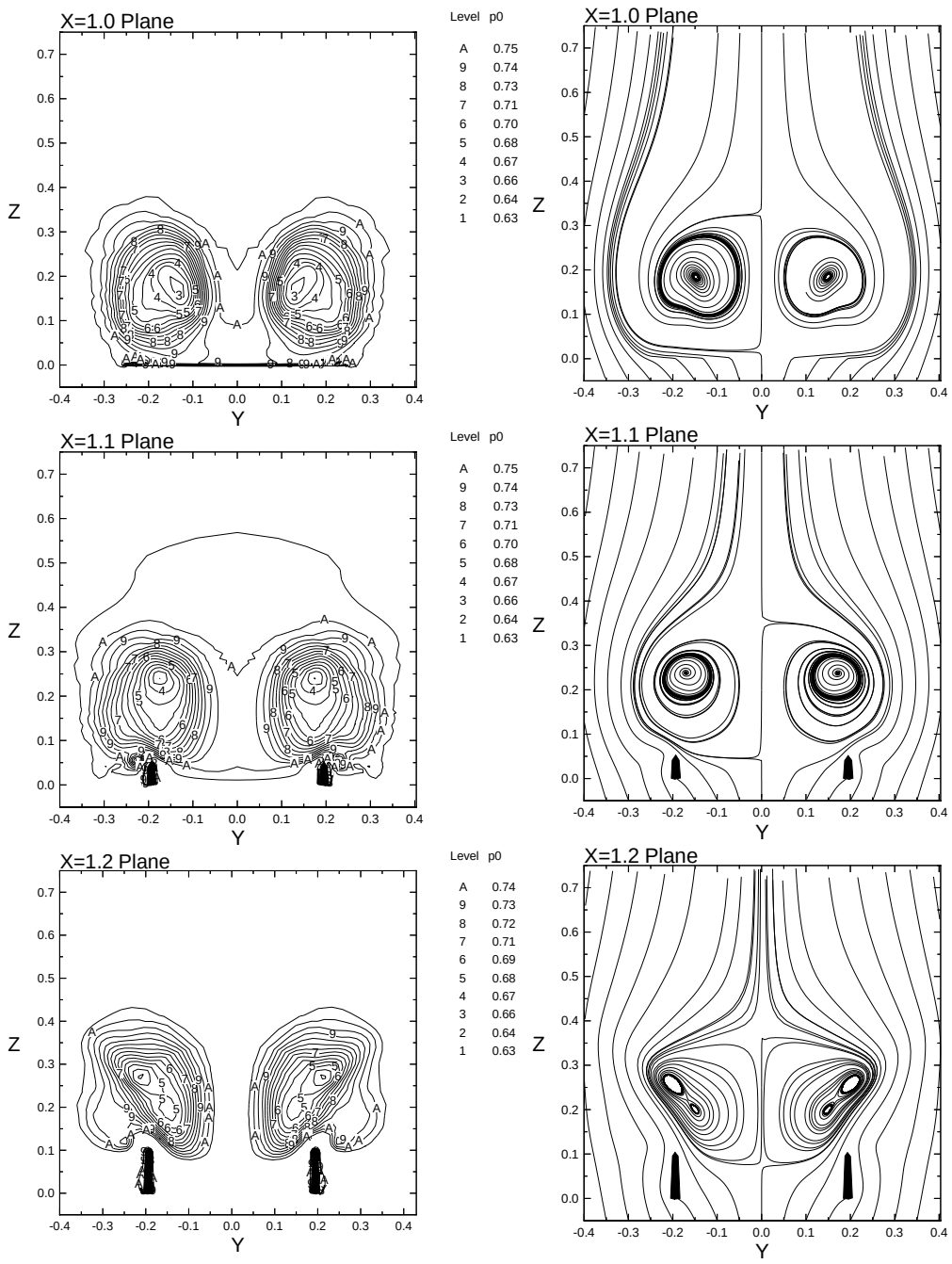

Figure 7.41: Nondimensional total pressure contours and in-plane streamlines plotted on vertical crossflow planes, $x = 1.0, 1.1, 1.2$. Outboard Initial Condition: $Re = 1.25 \times 10^6$, $M = 0.3$, $\alpha = 35^o$.

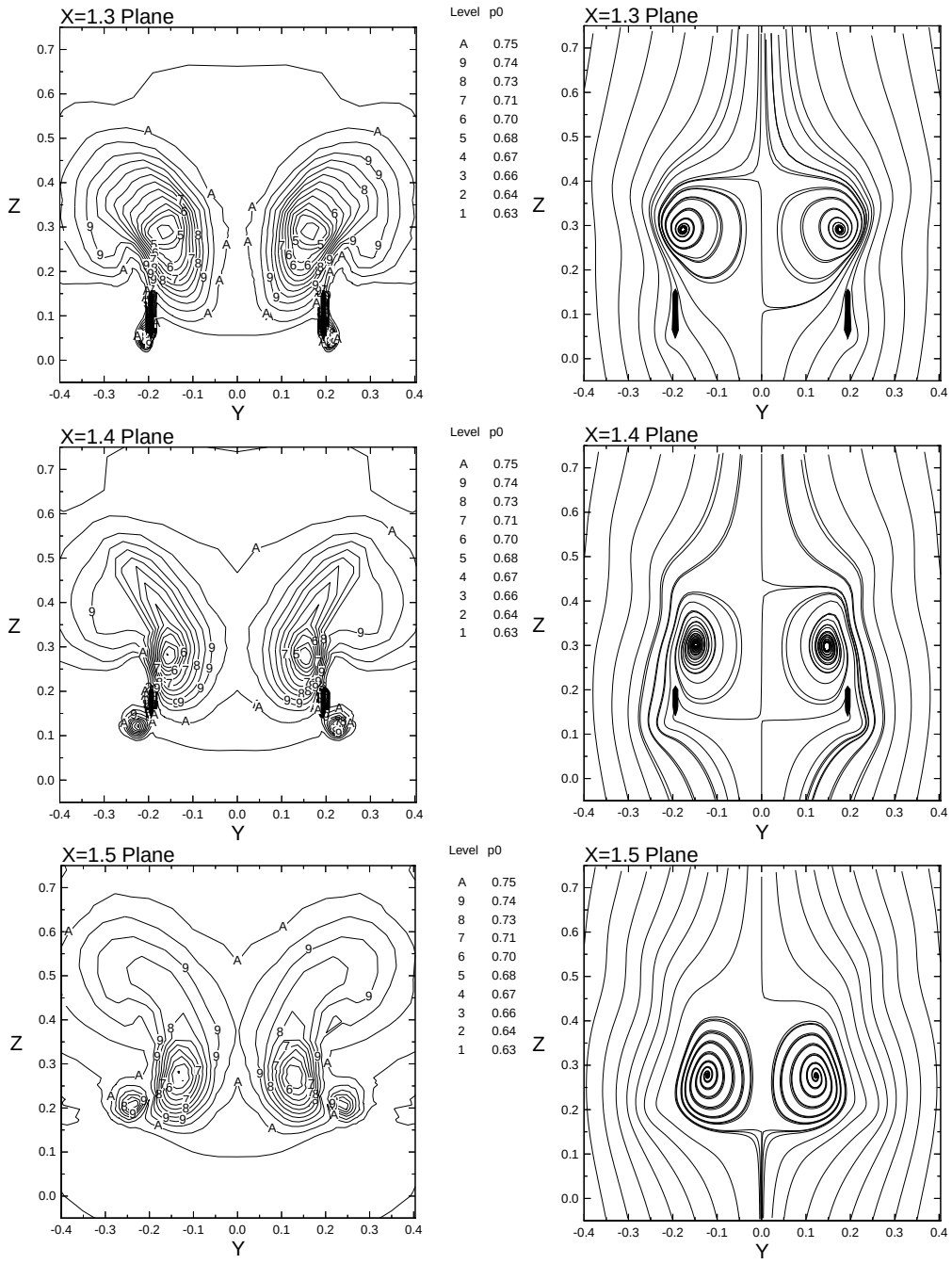

Figure 7.42: Nondimensional total pressure contours and in-plane streamlines plotted on vertical crossflow planes, $x = 1.3, 1.4, 1.5$. Outboard Initial Condition: $Re = 1.25 \times 10^6$, $M = 0.3$, $\alpha = 35^o$.

7.7.2 Uncoupled Bending and Torsion Response

In this section, the buffeting response due to inertially uncoupled bending and torsion vibrations of dynamically scaled, flexible, twin Washburn tails is considered for the outboard tail position. Results will be contrasted with the previous inboard and midspan cases to determine the effect of spanwise tail location on buffeting. The buffet loads are plotted in Figures 7.43-7.48, and the response is shown in Figures 7.49-7.52.

Lumped load distributions along the tail span, shown in Figures 7.43 and 7.44, closely resemble those of the midspan case in bending and are up 30% lower in torsion. Mean and RMS differential pressure distributions, see Figure 7.45, indicate the absence of edge RMS gradients which were present in the inboard case and to a lesser extent in the midspan case. Buffet excitation spectra, see Figure 7.46, indicate that the unsteady point loads at tap 5 are as much as 70% lower than the midspan and inboard cases, with the outer side loads being half of the inner side loads. As with the inboard case, the loads are dominated by a single frequency of approximately the same value as in the inboard case, which matches and the lower of the two midspan dominant frequencies.

Root bending and twisting moment histories and spectra, see Figures 7.47 and 7.48, also indicate a decrease in loading by up to 50% from the midspan and inboard cases, with no evidence of periodicity. Twin dominant frequencies are observed in torsion but not in bending. Thus, the frequency response for bending resembles the inboard case, while the torsional response more closely matches that of the midspan case.

The buffeting response, shown in Figures 7.49-7.52, resembles the inboard case in terms of its lack of periodicity. Deflections are half of those of the midspan case, and fully an order of magnitude lower than the inboard case. Accelerations are less than half of the midspan and inboard case values. The bending response occurs in three

diminishingly powerful frequencies and while the torsional response occurs in at least five equally powerful frequency bands, similar to the midspan case, but with much lower peaks.

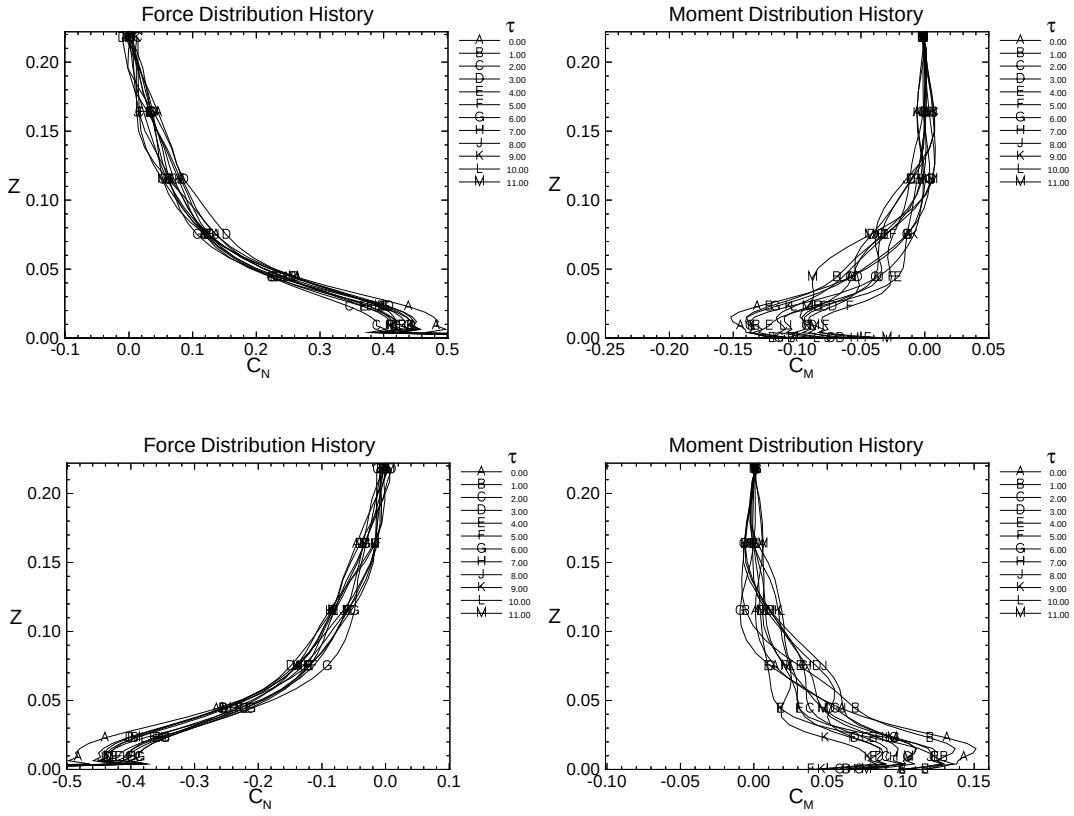

Figure 7.43: Bending force and twisting moment distributions along the tail span plotted at integer nondimensional time levels for a) right and b) left tails. Outboard Case: $Re = 1.25 \times 10^6$, $M = 0.3$, $\alpha = 35^o$.

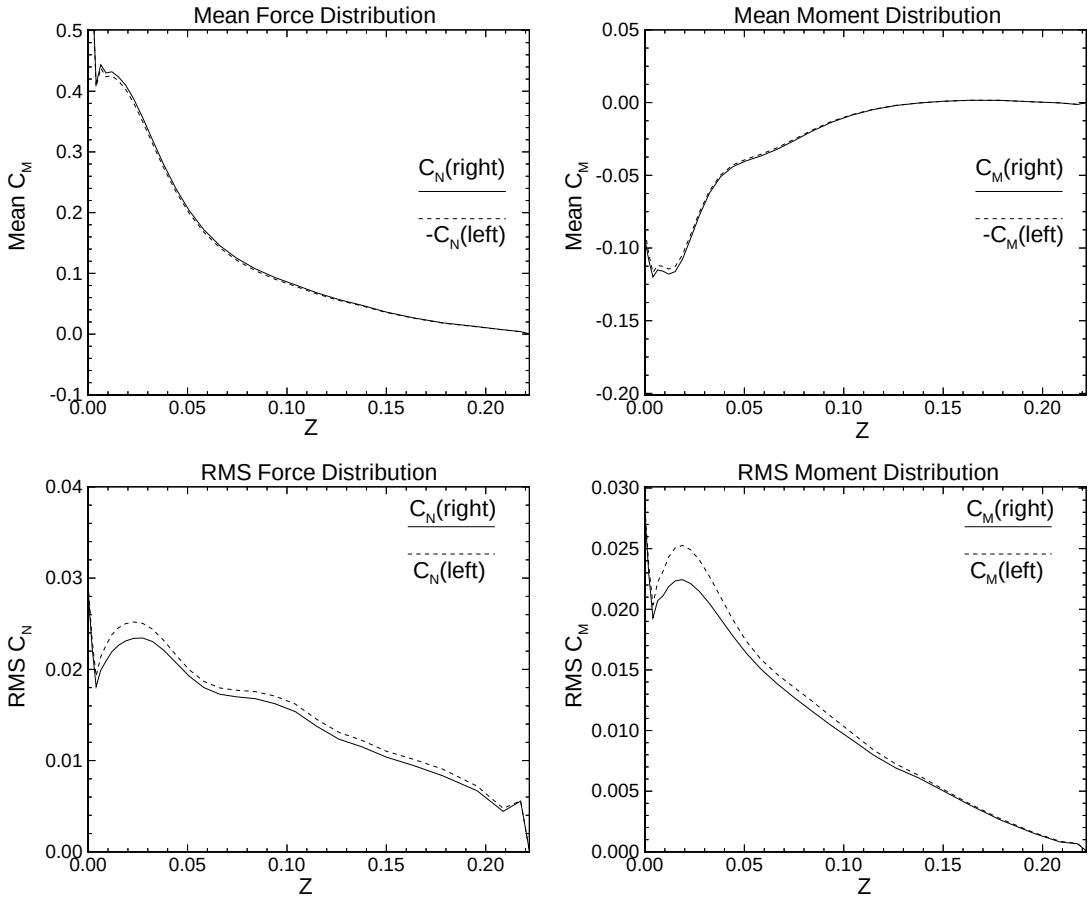

Figure 7.44: Mean and RMS load distributions along the right and left tail spans. Outboard Case: $Re = 1.25 \times 10^6$, $M = 0.3$, $\alpha = 35^o$.

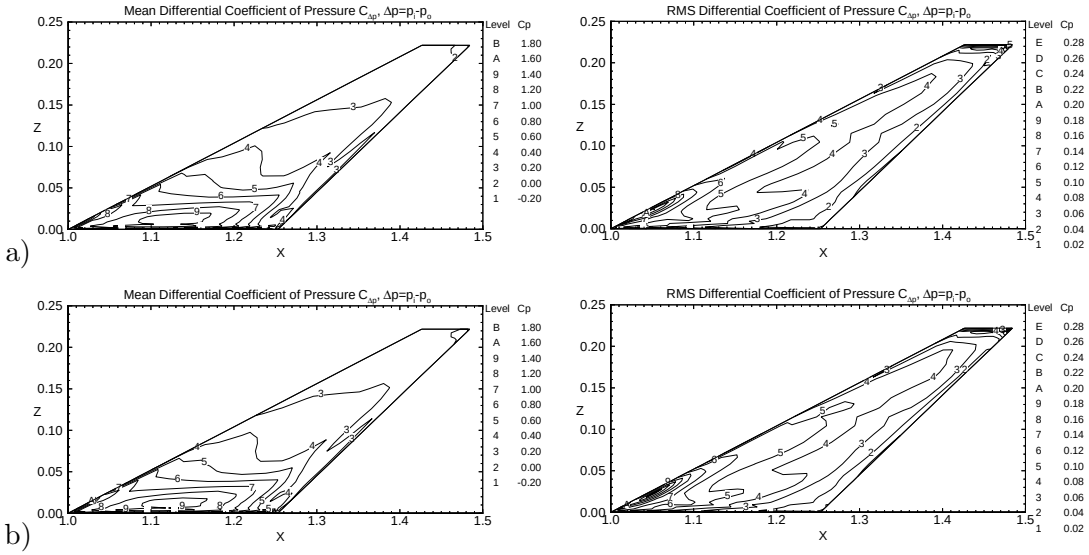

Figure 7.45: Mean and RMS differential coefficient of pressure contours on a) right and b) left tails. Outboard Case: $Re = 1.25 \times 10^6$, $M = 0.3$, $\alpha = 35^o$.

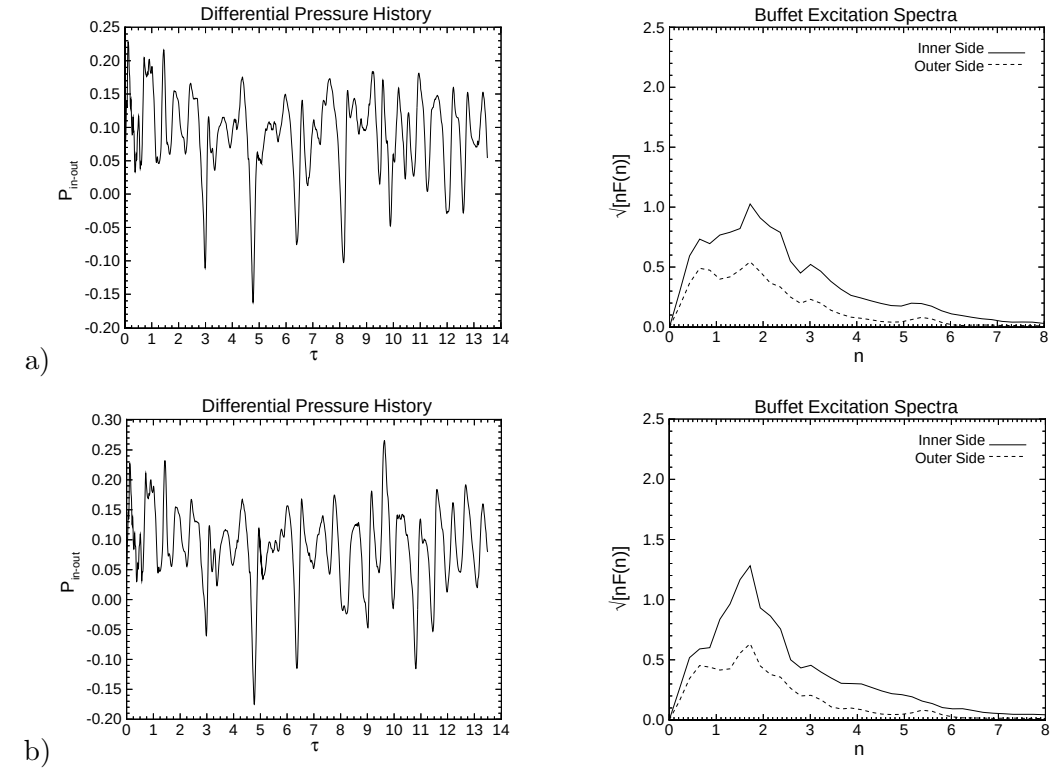

Figure 7.46: Differential pressure ($\frac{\Delta p}{q_\infty}$) histories at the 50% chord and 90% span location for a) right and b) left tails. Outboard Case: $Re = 1.25 \times 10^6$, $M = 0.3$, $\alpha = 35^o$.

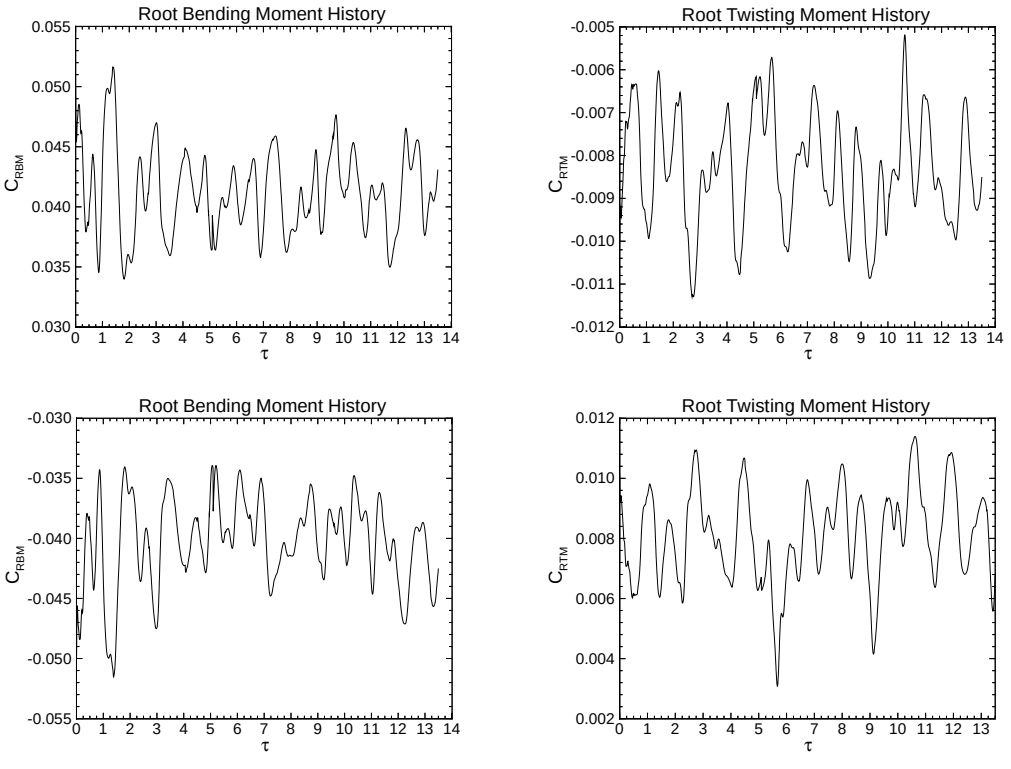

Figure 7.47: History of root bending moment coefficient and root twisting moment coefficient for a) right and b) left tails. Outboard Case: $Re = 1.25 \times 10^6$, $M = 0.3$, $\alpha = 35^o$.

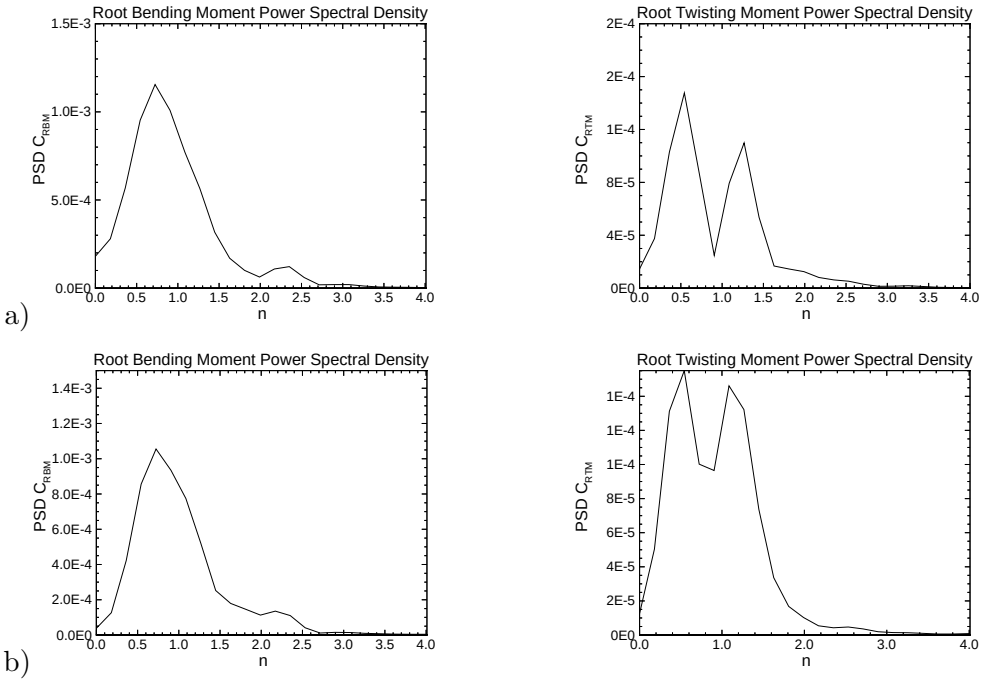

Figure 7.48: Power spectral density of root bending moment coefficient and root twisting moment coefficient versus reduced frequency for a) right and b) left tails. Outboard Case: $Re = 1.25 \times 10^6$, $M = 0.3$, $\alpha = 35^o$.

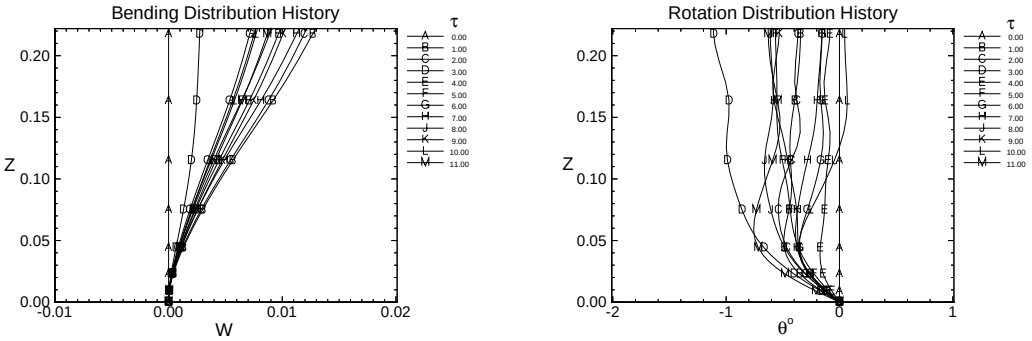

Figure 7.49: Right Tail: Bending and torsion deflection distributions along the tail span plotted at integer nondimensional time levels. Outboard Case: $Re = 1.25\times10^6$, $M = 0.3$, $\alpha = 35^o$.

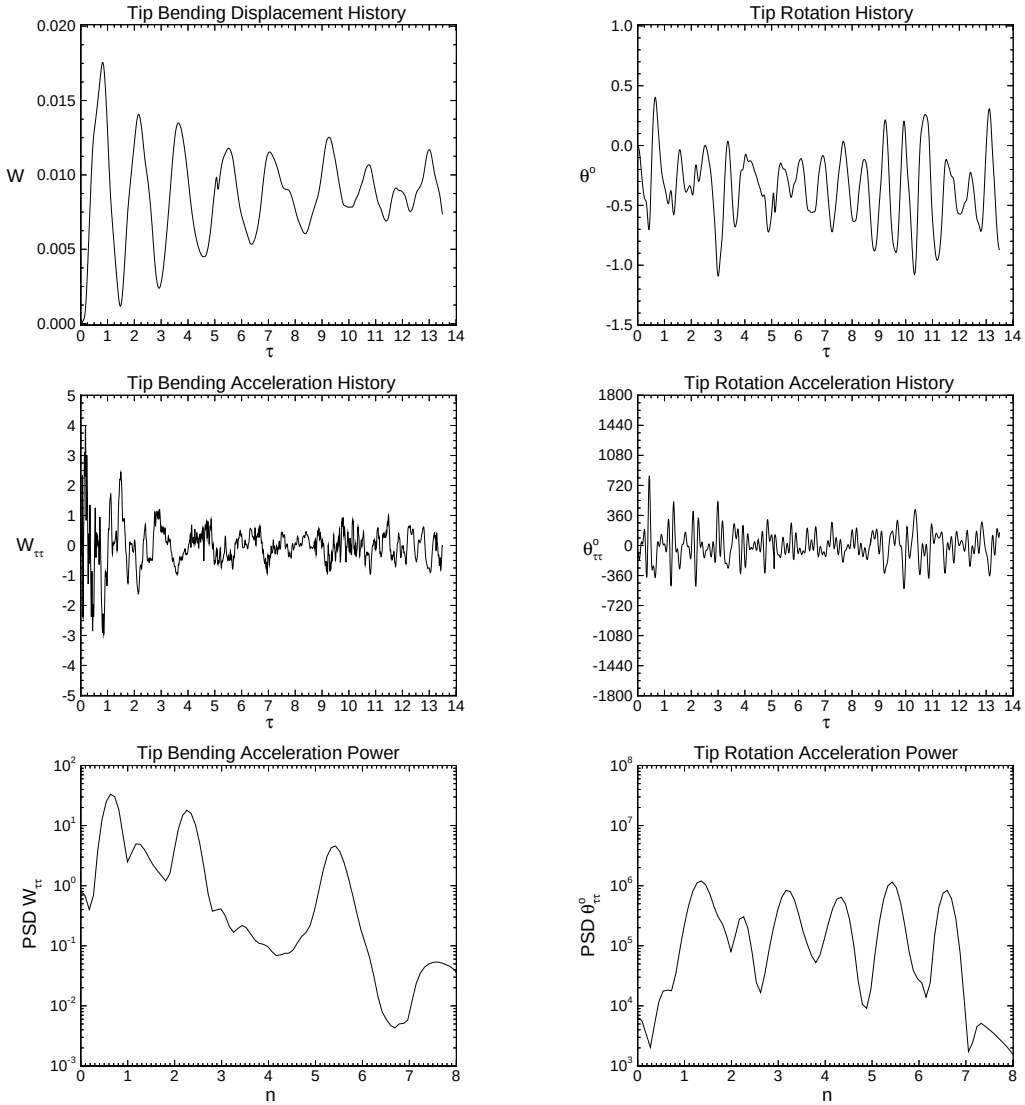

Figure 7.50: Right Tail: Time and frequency domain data for tip bending and torsion deflections and accelerations. Outboard Case: $Re = 1.25 \times 10^6$, $M = 0.3$, $\alpha = 35^o$.

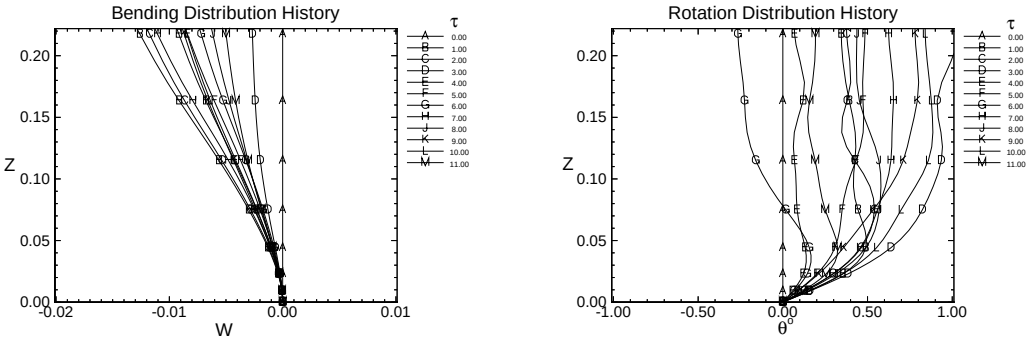

Figure 7.51: Left Tail: Bending and torsion deflection distributions along the tail span plotted at integer nondimensional time levels. Outboard Case: $Re = 1.25\times10^6$, $M = 0.3$, $\alpha = 35^o$.

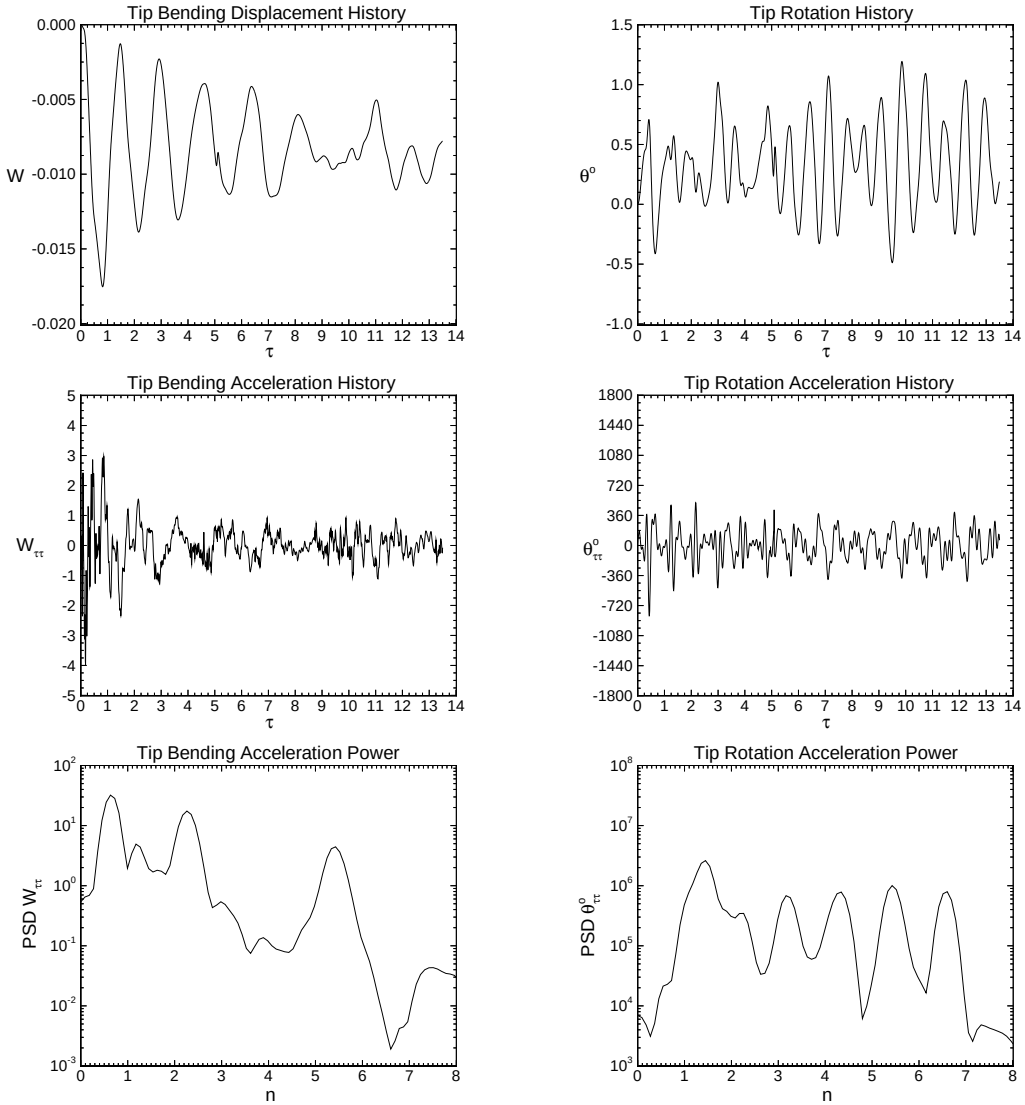

Figure 7.52: Left Tail: Time and frequency domain data for tip bending and torsion deflections and accelerations. Outboard Case: $Re = 1.25 \times 10^6$, $M = 0.3$, $\alpha = 35^o$.

7.8 Experimental Validation

To assess the accuracy of the computations of this study, experimental validation is sought from the data of Washburn, Jenkins and Ferman [12]. They performed low-speed wind tunnel experiments on configurations discussed in this chapter. Comparison of inboard and outboard RMS pressures, at the five stations, see Figure 7.2, show that the computations differ from experiment by up to 71%, with other points much closer at around ±20% as indicated in Tables 7.2 and 7.3. This is most likely due to the short physical time in which the computations were run, which degrade all unsteady measurements. The buffet excitation frequencies are typically more robust and show good agreement considering the imprecision of the data and the massive undertaking that 3-D unsteady CFD is. Finally, root bending coefficients show fair agreement in Table 7.5, with the mean values considerably more close to experiment than the RMS values.

Inboard RMS Pressure Validation					
Tap Location	1	2	3	4	5
EXP p_{in}	0.17	0.07	0.07	0.10	0.07
CFD p_{in}	0.13	0.09	0.12	0.14	0.07
% Difference	-24%	29%	71%	40%	0%
EXP p_{out}	0.21	0.10	0.21	0.24	0.09
CFD p_{out}	0.17	0.08	0.09	0.10	0.07
% Difference	-20%	-20%	-57%	-58%	-22%
CFD p_{in-out}	0.11	0.09	0.14	0.17	0.09

Table 7.2: Comparison of right tail RMS nondimensional pressures ($\frac{p}{q_\infty}$) with experimental data of Washburn et al. [12]. Inboard Case: $\alpha = 35^o$, $M = 0.3$, $Re = 1.25 \times 10^6$.

Outboard RMS Pressure Validation					
Tap Location	1	2	3	4	5
EXP p_{in}	0.18	0.07	0.11	0.14	0.08
CFD p_{in}	0.11	0.05	0.07	0.09	0.06
% Difference	-39%	-28%	-36%	-35%	-25%
EXP p_{out}	0.08	0.06	0.04	0.05	0.04
CFD p_{out}	0.06	0.04	0.04	0.04	0.04
% Difference	-25%	-33%	0%	-20%	0%
CFD p_{in-out}	0.07	0.06	0.08	0.10	0.08

Table 7.3: Comparison of right tail RMS nondimensional pressures ($\frac{p}{q_\infty}$) with experimental data of Washburn et al. [12]. Outboard Case: $\alpha = 35^o$, $M = 0.3$, $Re = 1.25 \times 10^6$.

Buffet Excitation Frequency Validation				
	Inboard		Outboard	
	n_{d1}	n_{d2}	n_{d1}	n_{d2}
EXP	1.3	2.5	1.4	3.0
CFD	1.2	2.0	1.8	3.0
% Difference	-8%	-20%	29%	0%

Table 7.4: Comparison of right tail dominant frequencies for buffet excitation, $\sqrt{nF(n)}$, with experimental data of Washburn et al. [12] using length scale of $\overline{\overline{c}}$. Case: $\alpha = 35^o$, $M = 0.3$, $Re = 1.25 \times 10^6$.

Root Bending Moment Coefficient Validation						
	Inboard		Midspan		Outboard	
	C_{RBM}		C_{RBM}		C_{RBM}	
	Mean	RMS	Mean	RMS	Mean	RMS
EXP	0.046	0.018	0.043	0.012	0.033	0.010
CFD	0.033	0.009	0.048	0.005	0.041	0.004
% Difference	-28%	-50%	12%	-58%	24%	-60%

Table 7.5: Comparison of right tail root bending moment coefficient statistics with experimental data of Washburn et al. [12] using length scale of $\overline{\overline{c}}$. Case: $\alpha = 35^o$, $M = 0.3$, $Re = 1.25 \times 10^6$.

7.9 Summary

In this chapter, the simulation of twin vertical tail buffeting is accomplished using the delta wing/twin vertical tail configuration of Washburn et al. [12]. Computational applications demonstrate the effect of spanwise tail location on the buffet loading and response, and are in good agreement with experimental data. Overall, the inboard tail location produces the largest buffeting response, which is particularly high in torsion.

It was observed from the 3-D streamline and nondimensional total pressure isosurfaces, that the location and size of the breakdown does not vary with the spanwise location of the tails, for the present angle-of-attack of 35^o. This is due to the small tail span and high sweep angle, which minimizes tail contact with the vortex cores.

In Table 7.6, the statistics of right tail point pressure data at 50% chord and 90% span indicate that the inboard span produces the largest unsteady pressure loads. The outboard span has the greatest differential mean loading by a factor of two over the other cases, as well as, higher individual frequencies for inner and outer pressures. However, this is only one point so it does not necessarily characterize the whole buffet loading. Note, because of the high degree of symmetry shown in the plots, only the results fot the right tail are tabulated.

More complete measures of the buffet loading are the root bending and twisting moments, see Table 7.7. The unsteady RMS loads are most critical to assessing the buffet. The short physical sample time degrades the precision of peak power, however, the dominant frequencies are fairly robust. From this table it is evident that the inboard span location has by far the most severe buffeting in bending and is a close second in torsion to the midspan case. The outer span has the smallest overall loading.

In Table 7.8, the statistics of right tail buffeting response show that for bending, the inboard and midspan positions produce a response over five times as large as the

outboard case. In torsion, the midspan and outboard are much closer together and smaller than the inboard case by a factor of up to ten. Thus, from the deflections and accelerations it is concluded that the inner case experiences that largest buffeting with a strong component of torsion, followed by the midspan and then outboard cases.

	Point Pressure Data								
	Inboard Span			Middle Span			Outboard Span		
	p_{in}	p_{out}	p_{in-out}	p_{in}	p_{out}	p_{in-out}	p_{in}	p_{out}	p_{in-out}
Mean	15.67	15.67	0.0046	15.54	15.50	0.041	15.58	15.49	0.0902
RMS	0.118	0.163	0.1010	0.132	0.131	0.071	0.106	0.060	0.061
n_d	1.2	1.2		1.3	1.3		1.8	1.7	
Peak Power	1.4	2.3		1.6	1.6		1.0	0.5	

Table 7.6: Comparison of right tail nondimensional pressure ($\frac{p}{q_\infty}$) data at 50% chord and 90% span at each tail location. Case: $\alpha = 35^o$, $M = 0.3$, $Re = 1.25 \times 10^6$.

	Right Root Loads							
	C_{RBM}				C_{RTM}			
Fuselage	Mean +tip outward	RMS	Peak Power	n_d	Mean +LE inward	RMS	Peak Power	n_d
Inboard	0.033	0.0086	0.0060	1.0	-0.015	0.0015	1.7E-4	0.7
Midspan	0.048	0.0045	0.0017	0.5	-0.015	0.0017	2.0E-4	1.3
Outboard	0.041	0.0035	0.0012	0.7	-0.008	0.0013	1.8E-4	0.5

Table 7.7: Comparison of averaged root bending and twisting moment statistics, peak power and dominant frequency for each tail location. Case: $\alpha = 35^o$, $M = 0.3$, $Re = 1.25 \times 10^6$.

	Right Tip Response						
	Bending						
Tail Location	$A(w)$	Mean w +outward	$A(w_{\tau\tau})$	Power$_1$	n_{d1}	Power$_2$	n_{d2}
Inboard	0.018	0.048	5	300	1.1	20	2.7
Midspan	0.019	0.008	6	400	0.7	400	2.5
Outboard	0.003	0.009	1	30	0.6	20	2.3
	Torsion						
Tail Location	$A(\theta)^o$	Mean θ^o +LE inward	$A(\theta_{\tau\tau})^o$	Power$_1$	n_{d1}	Power$_2$	n_{d2}
Inboard	10	-9	1800	8E7	1.1	2E6	3.5
Midspan	2	0.5	1215	3E7	1.6	2E7	2.3
Outboard	0.7	-0.4	450	1E6	1.4	8E6	3.2

Table 7.8: Comparison of buffet responses for each tail location. Case: $\alpha = 35^o$, $M = 0.3$, $Re = 1.25 \times 10^6$.

CHAPTER 8

CONTROL OF TWIN TAIL BUFFETING

8.1 Introduction

In this chapter, the effectiveness of controlling vertical tail buffeting through the use of an apex flap is investigated computationally. In preliminary numerical experiments, several of the control schemes discussed in Section 2.4 were evaluated, including many slot and jet blowing arrangements on the wing and tails. However, none of the pneumatic methods were nearly as effective at delaying breakdown as the present scheme, and worse, they significantly *increased* the level of buffeting. The success of the apex flap, hinges on its ability to preserve the core by decreasing the adverse pressure gradient over the wing. Attempts to overcome the adverse pressure gradient by injection of axial momentum directly into the vortex core was unsuccessful even at unrealistically high levels of mass flow rates. Thus, the simpler and more robust method of increasing the wing camber by an apex flap was selected.

The chosen configuration for the apex flap case is the inboard Washburn tail case of the previous chapter, which had the highest level of buffeting for all of the cases studied. The method of solution, number grid cells, and the material properties of the tails are the same as in the previous Washburn cases. The apex flap refers to the portion of the delta wing forward of $x = 0.4c$, which is capable of rotating through a deflection angle β, where the positive sense results in a local decrease of angle-of-attack. The method of control in this study is totally passive. However, the apex flap concept could be readily extended to an active control system, where the deflection angle is adjusted

based on angle-of-attack and breakdown location. The breakdown location would be known based on its surface pressure signature. For the present study, only a single optimum deflection angle is evaluated, $\beta = 15^o$. This angle was experimentally [14] found to produce the greatest delay in the onset of breakdown.

Ideally one would like to prevent breakdown completely or at least delay it until after the tails, however the strong adverse pressure gradient at the trailing edge insures that the breakdown location does not occur past the trailing edge. In Figure 1.1, the breakdown position closest to the tail ($\alpha = 20^o$) actually produced the lowest buffeting, while the highest levels resulted from a breakdown position much farther away for $\alpha = 30^o$. Thus, the hope is that by delaying the onset of breakdown, the aircraft will not only benefit from increased vortex lift, but will also experience less tail buffeting, a rare engineering "win - win" situation. The computational validation of this theory is the subject of this chapter.

8.2 Initial Conditions

The initial flow state was obtained by the same method as in the previous twin tail cases. The flow is first solved using local time stepping for 2000 iterations, time-accurate stepping for another five nondimensional time with $\Delta\tau = 0.00036$. Detailed initial condition flow field plots for the inboard tail, deflected apex flap case are shown in Figures 8.1-8.6. The initial conditions for the undeflected baseline case are shown in Figures 7.5-7.10 of the preceding chapter.

The 3D streamline and total pressure isosurface plots, shown in Figures 8.1 and 8.2, clearly demonstrate the effectiveness of apex flap deflection on the delay of breakdown. The original burst location was 50%c and now occurs very late at 94%c. The

sparseness of streamlines is a result of using the same seed points as in the baseline case, which were non-optimal for showing the breakdown in this case. The isopressure surfaces show that the size of the breakdown has actually increased due to the flap deflection. The near surface streamlines of the present case, see Figure 8.3, differ from the baseline case, see Figure 7.7, by the lack of curvature of the line of secondary separation on the wing, due to the aft position of the breakdown. The outside tail surface streamlines show, that for the apex flap case, the separation line along the leading edge of the tail is much more clearly defined, indicating a stronger entrainment of fluid from the tail than in the baseline case.

In Figure 8.4, the spanwise coefficient of pressure is plotted for the deflected and baseline cases at several chord stations. Sections, $x = 0.5c$ and $x = 0.7c$ show the beneficial gain in lift due to the delay in breakdown. The coefficient of lift for the apex flap case is $C_L = 1.11$ which is 6% higher than the baseline C_L of 1.05.

Comparison of the tail crossflow planes, shown in Figures 7.9-7.10 and Figures 8.5-8.6, indicate that the vortices of the baseline case are generally more compact due to the smaller burst size as well as the greater distance upstream. The core total pressures are about the same.

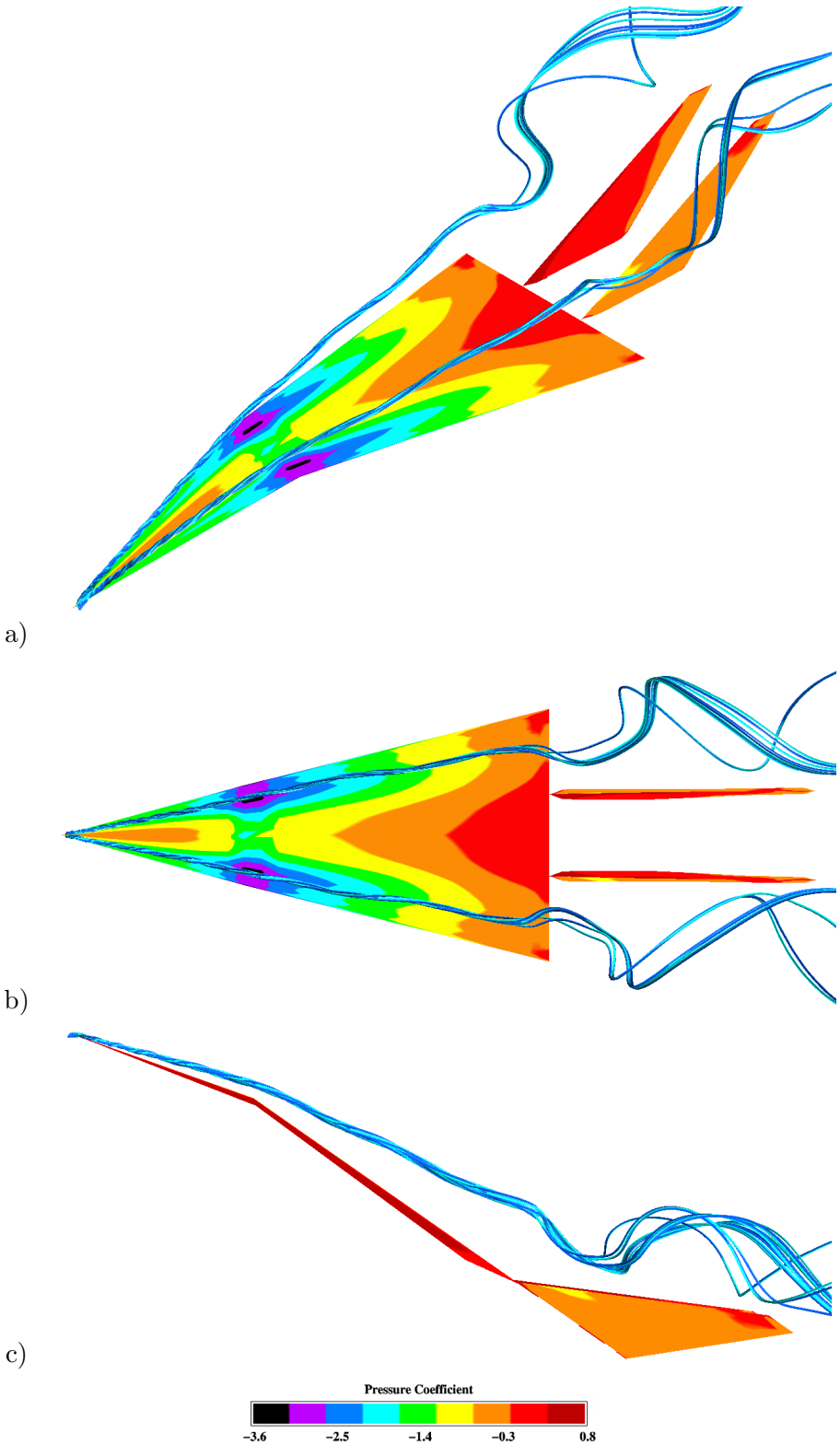

Figure 8.1: a) Three-dimensional, b) top and c) side views of surface pressure and vortex core streamlines. Initial Condition: $\beta_{\text{Flap}} = 15^o$, $Re = 1.25 \times 10^6$, $M = 0.3$, $\alpha = 35^o$.

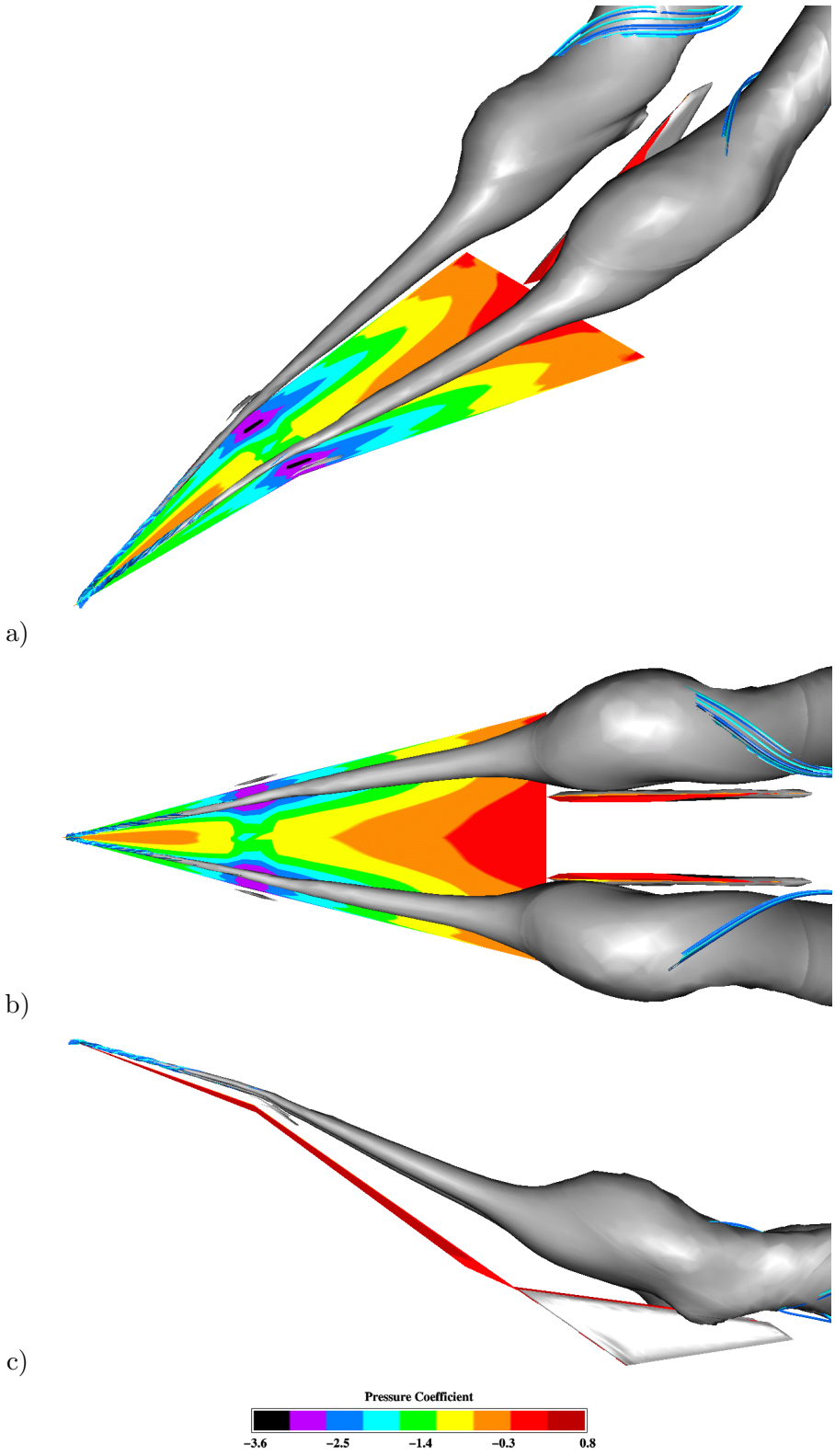

Figure 8.2: a) Three-dimensional, b) top and c) side views of surface pressure and vortex core streamlines and solid total pressure isosurfaces, $\left(\frac{p_0}{\rho_\infty a_\infty^2} = 0.68\right)$ Initial Condition: $\beta_{\text{Flap}} = 15^o$, $Re = 1.25 \times 10^6$, $M = 0.3$, $\alpha = 35^o$.

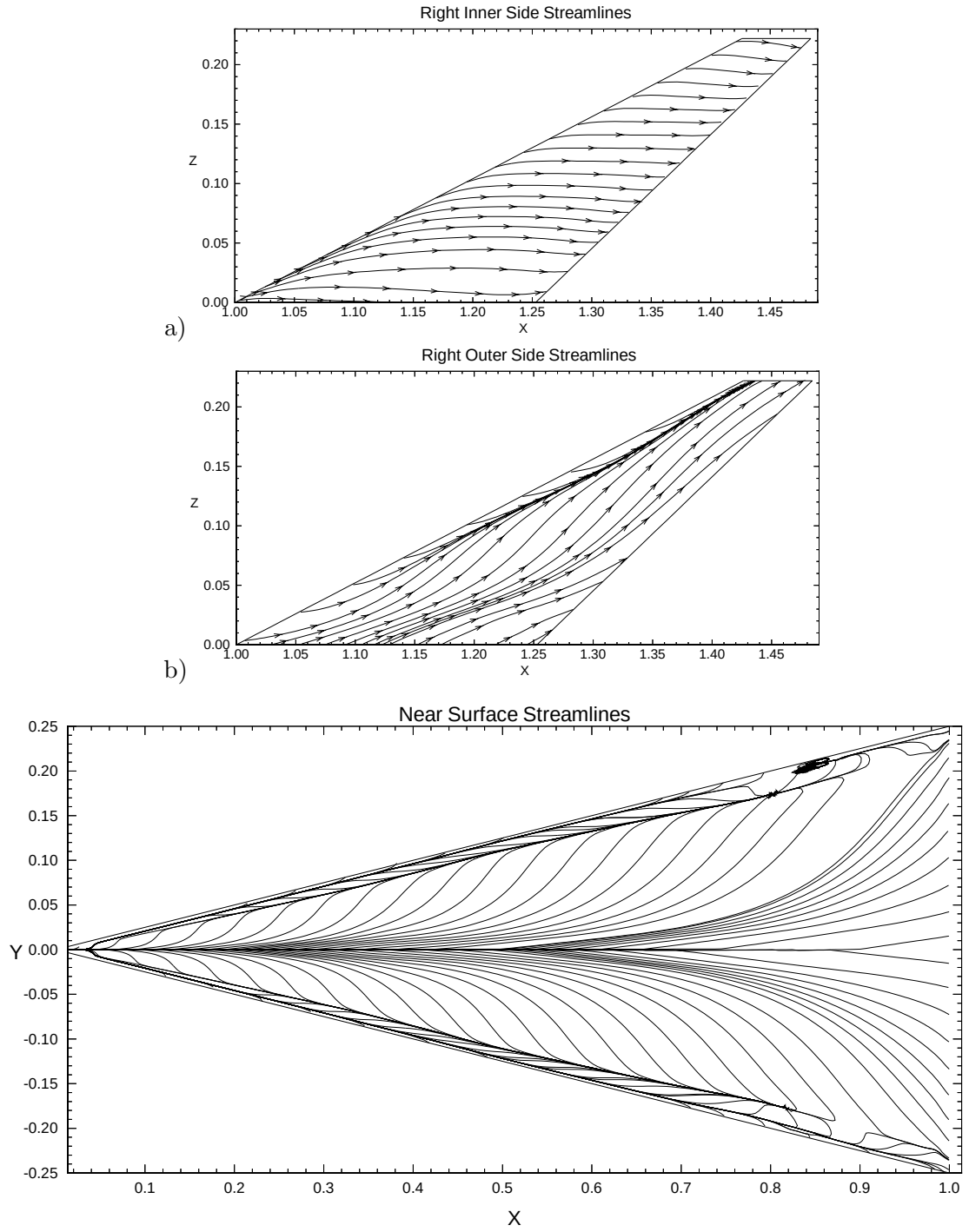

Figure 8.3: Near surface streamlines for the a) inner and b) outer right tail surfaces and the upper wing surface. Initial Condition: $\beta_{\text{Flap}} = 15^o$, $Re = 1.25 \times 10^6$, $M = 0.3$, $\alpha = 35^o$.

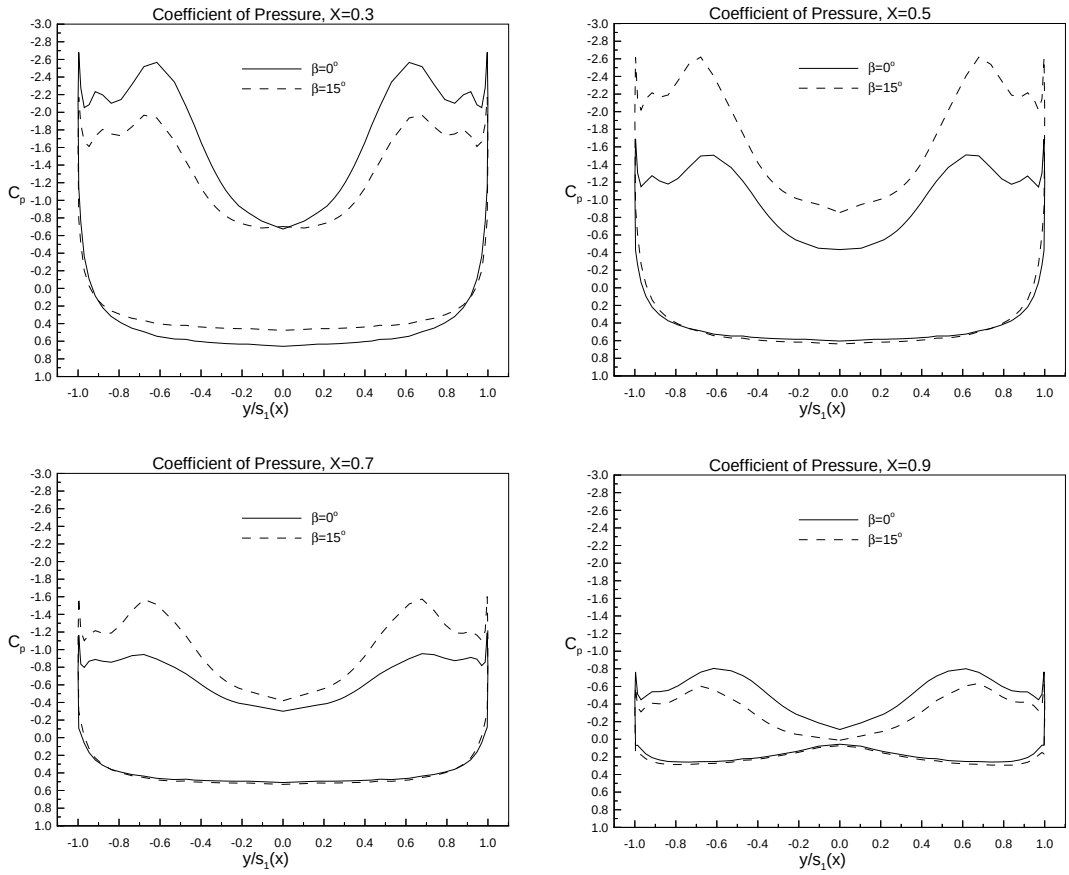

Figure 8.4: Effect of apex flap deflection on wing surface coefficient of pressure at several chord stations. Initial Condition: $\beta_{\text{Flap}} = 15^o$, $Re = 1.25 \times 10^6$, $M = 0.3$, $\alpha = 35^o$.

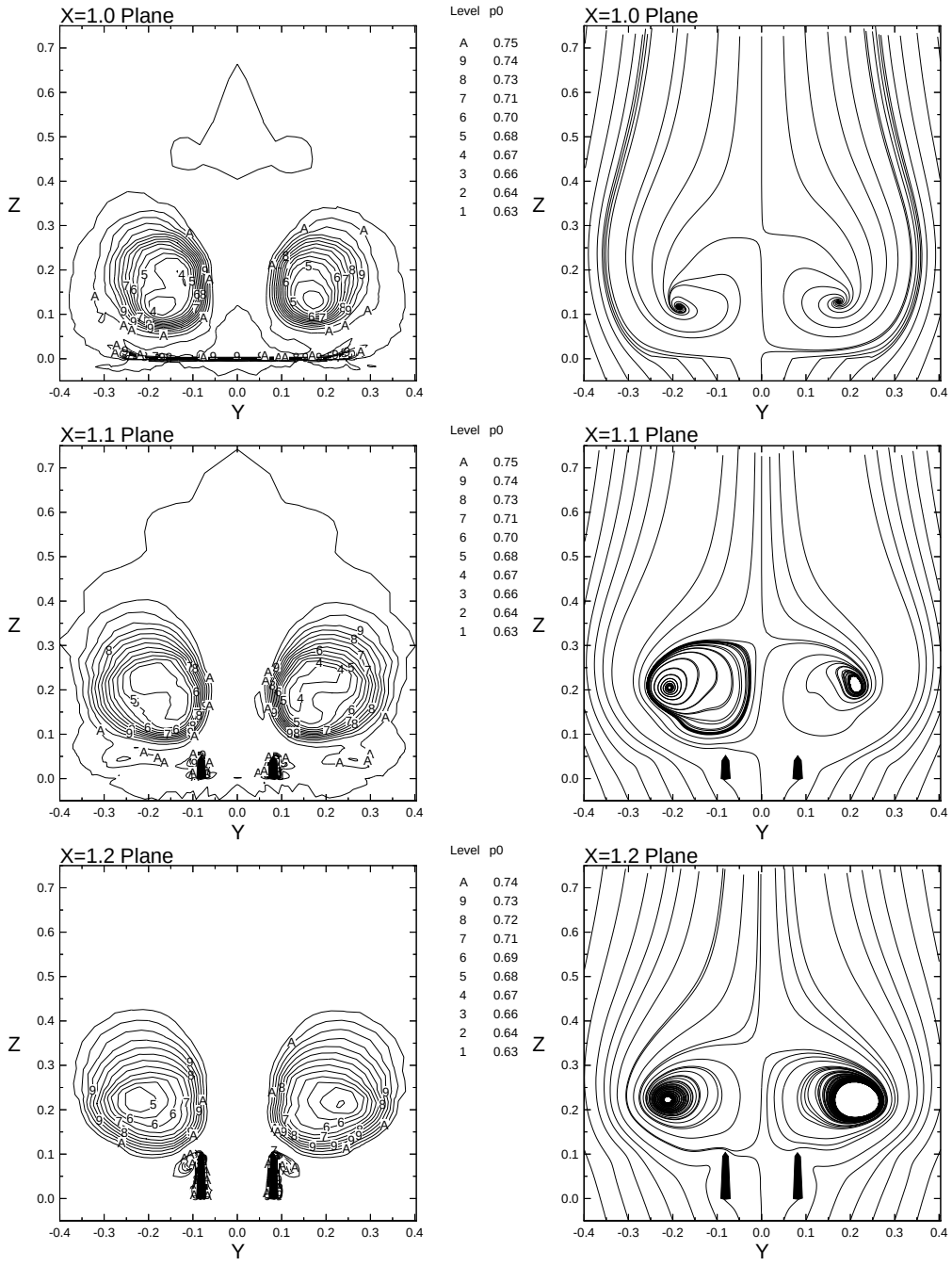

Figure 8.5: Nondimensional total pressure contours and in-plane streamlines plotted on vertical crossflow planes, $x = 1.0, 1.1, 1.2$. Initial Condition: $\beta_{Flap} = 15^o$, $Re = 1.25 \times 10^6$, $M = 0.3$, $\alpha = 35^o$.

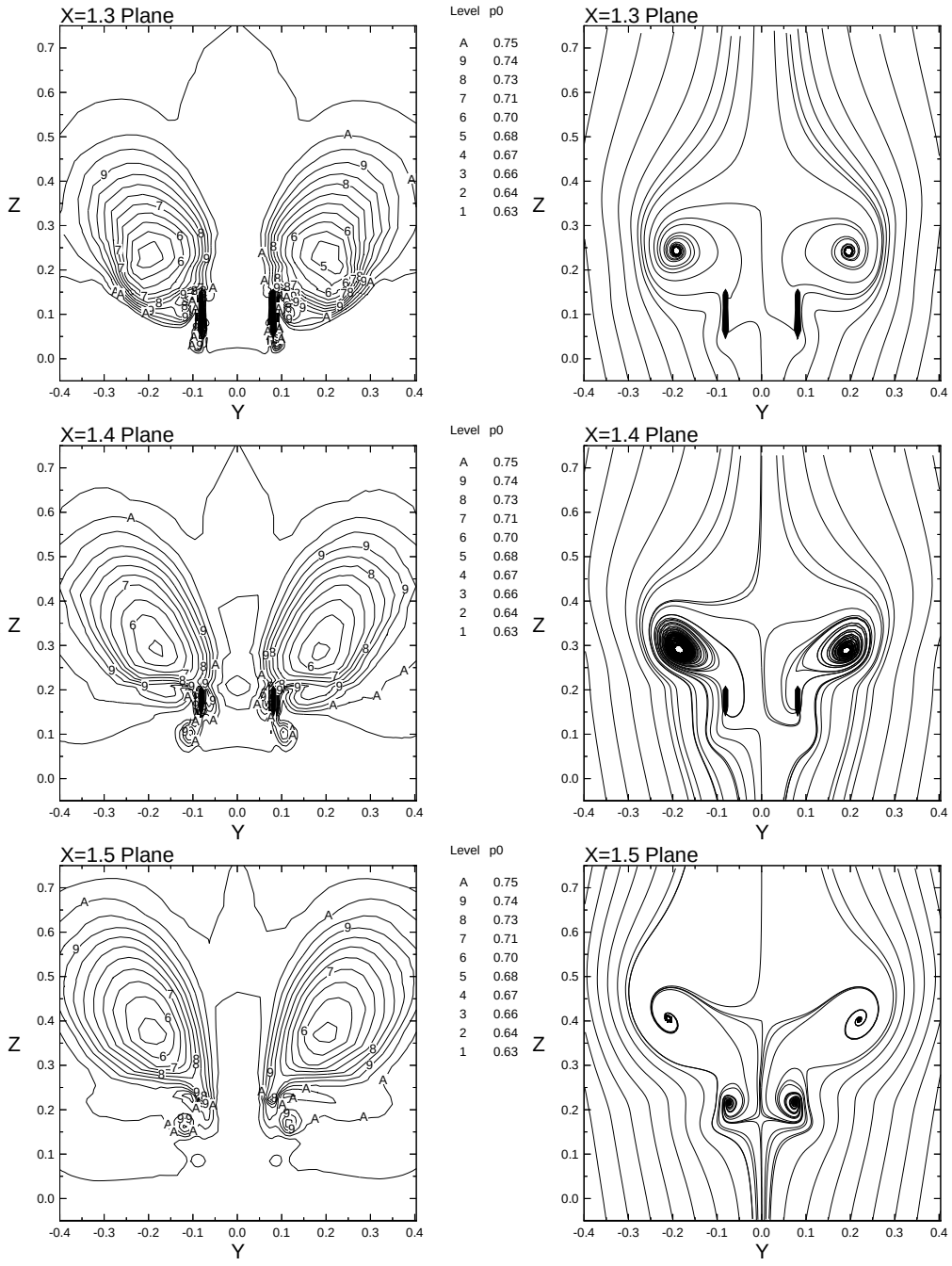

Figure 8.6: Nondimensional total pressure contours and in-plane streamlines plotted on vertical crossflow planes, $x = 1.3, 1.4, 1.5$. Initial Condition: $\beta_{Flap} = 15^o$, $Re = 1.25 \times 10^6$, $M = 0.3$, $\alpha = 35^o$.

8.3 Uncoupled Bending and Torsion Response

The right tail buffet loads of the baseline and deflected apex flap cases are compared in Figures 8.7 - 8.10. The effect of the apex flap is mixed in the lumped mean and RMS loads, with the RMS moment loads showing the clearest trend of being up to 30% lower than the undeflected case. Comparison of the area mean and RMS loads, shown in Figure 7.5.2 and Figure 8.8 indicate that the overall levels are the same with RMS distributions exhibiting the greatest differences in their gradients.

Differential point pressure history and point buffet excitation spectra are compared in Figure 8.9. The buffet excitation show a dramatic decrease in buffeting for the apex flap case, at around 50% of the baseline case. However, this is only at one location so it does not necessarily represent the whole tail. Better measures of the global buffet loads are the root bending and twisting moments, see Figure 8.10. These plots show that the integrated buffet levels are roughly equal between the two cases. Given the favorable change in wing loading from the apex flap, even a unchanged buffet loading is acceptable since additional wing loading may be exchanged for a lower configuration angle-of-attack which would lower the buffeting levels.

The final measure of the degree of buffeting is the response, see Figure 8.11. As in the root moment data, the response also indicates that there is very little change in the response due to the apex flap deflection. Hence, it is concluded that the apex flap is an efficient and harmless means of delaying vortex bursting and increasing aircraft nose authority without increasing the level of tail buffeting.

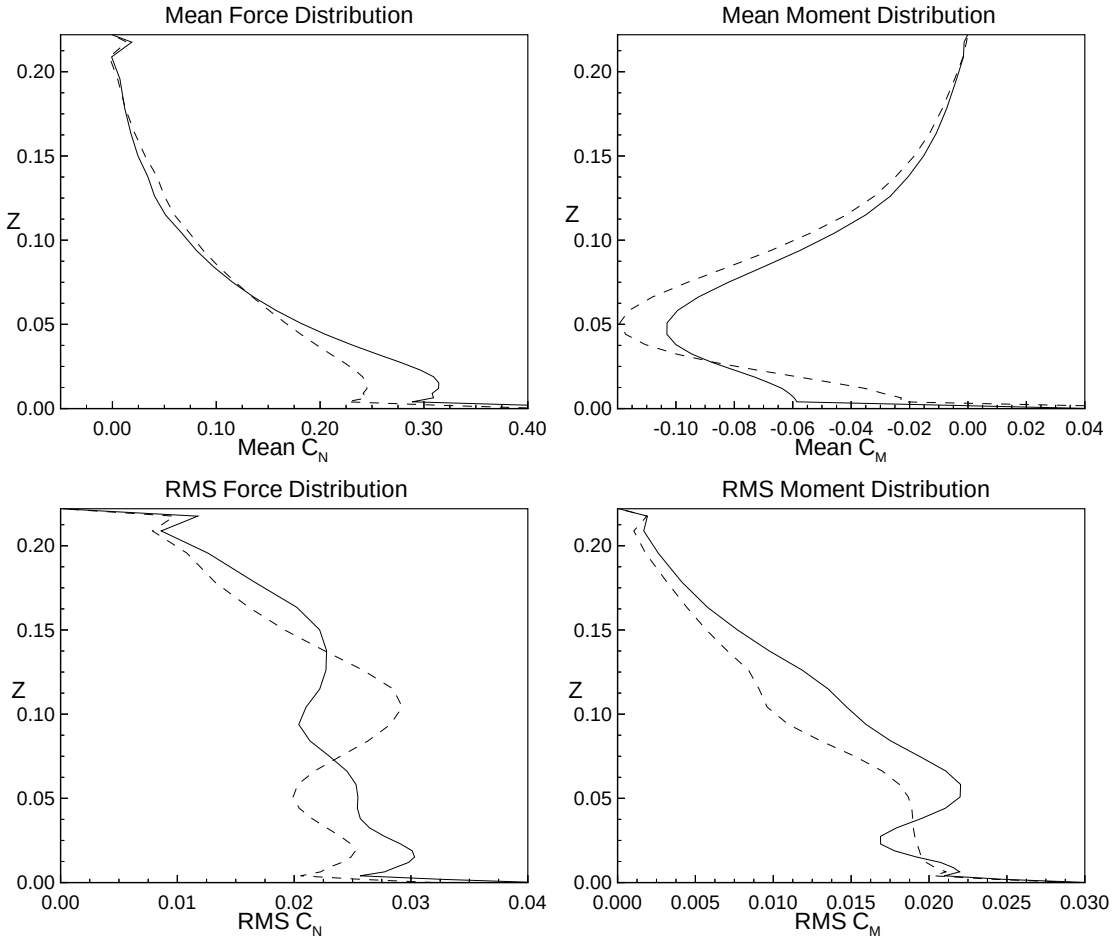

Figure 8.7: Effect of apex flap on mean and RMS load distributions along the right tail span. $\beta_{Flap} = 15^o$, $Re = 1.25 \times 10^6$, $M = 0.3$, $\alpha = 35^o$.

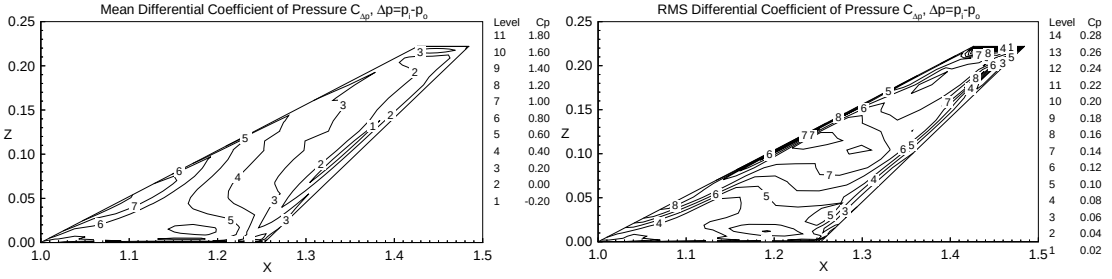

Figure 8.8: Right tail mean and RMS differential coefficient of pressure contours. $\beta_{Flap} = 15^o$, $Re = 1.25 \times 10^6$, $M = 0.3$, $\alpha = 35^o$.

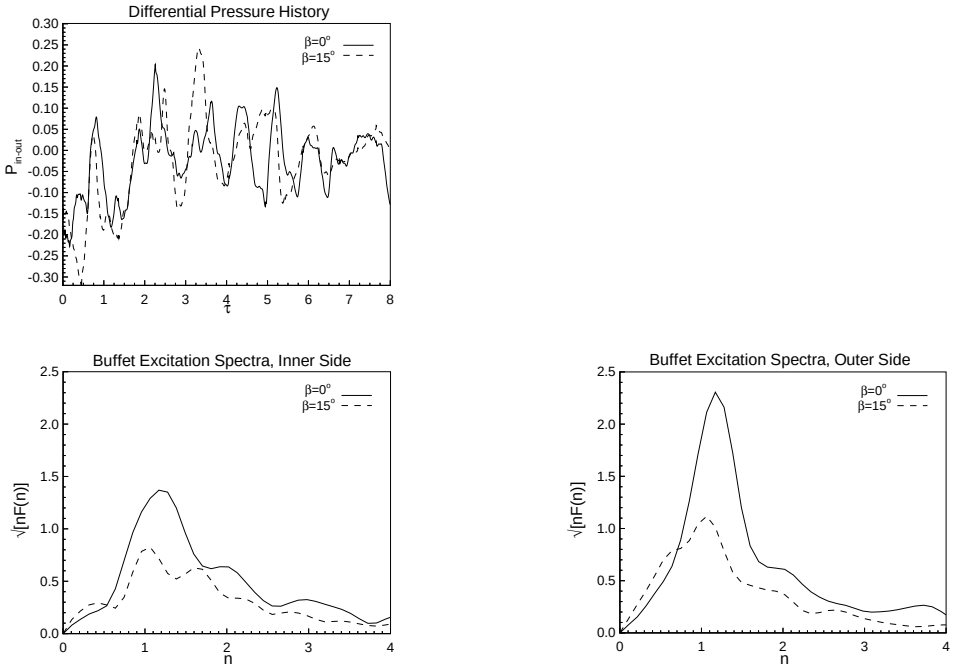

Figure 8.9: Effect of apex flap on differential pressure ($\frac{\Delta p}{q_\infty}$) histories at the 50% chord and 90% span location for the right tail. $\beta_{Flap} = 15^o$, $Re = 1.25 \times 10^6$, $M = 0.3$, $\alpha = 35^o$.

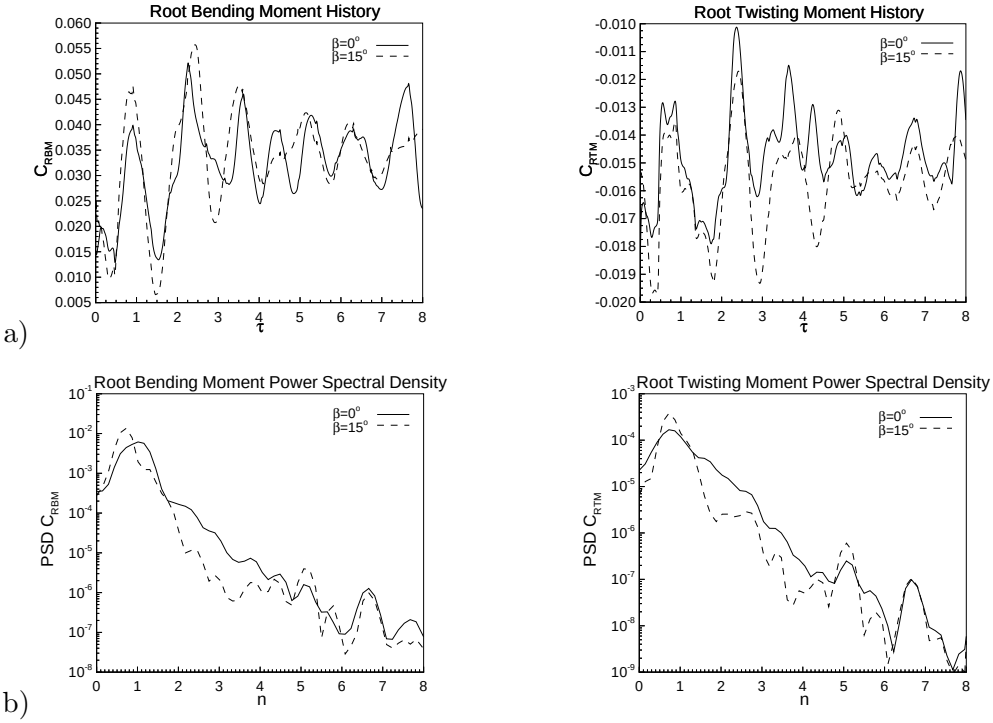

Figure 8.10: Effect of apex flap on a) history and b) power spectral density of root bending moment coefficient and root twisting moment coefficient versus reduced frequency for the right tail. $\beta_{Flap} = 15^o$, $Re = 1.25 \times 10^6$, $M = 0.3$, $\alpha = 35^o$.

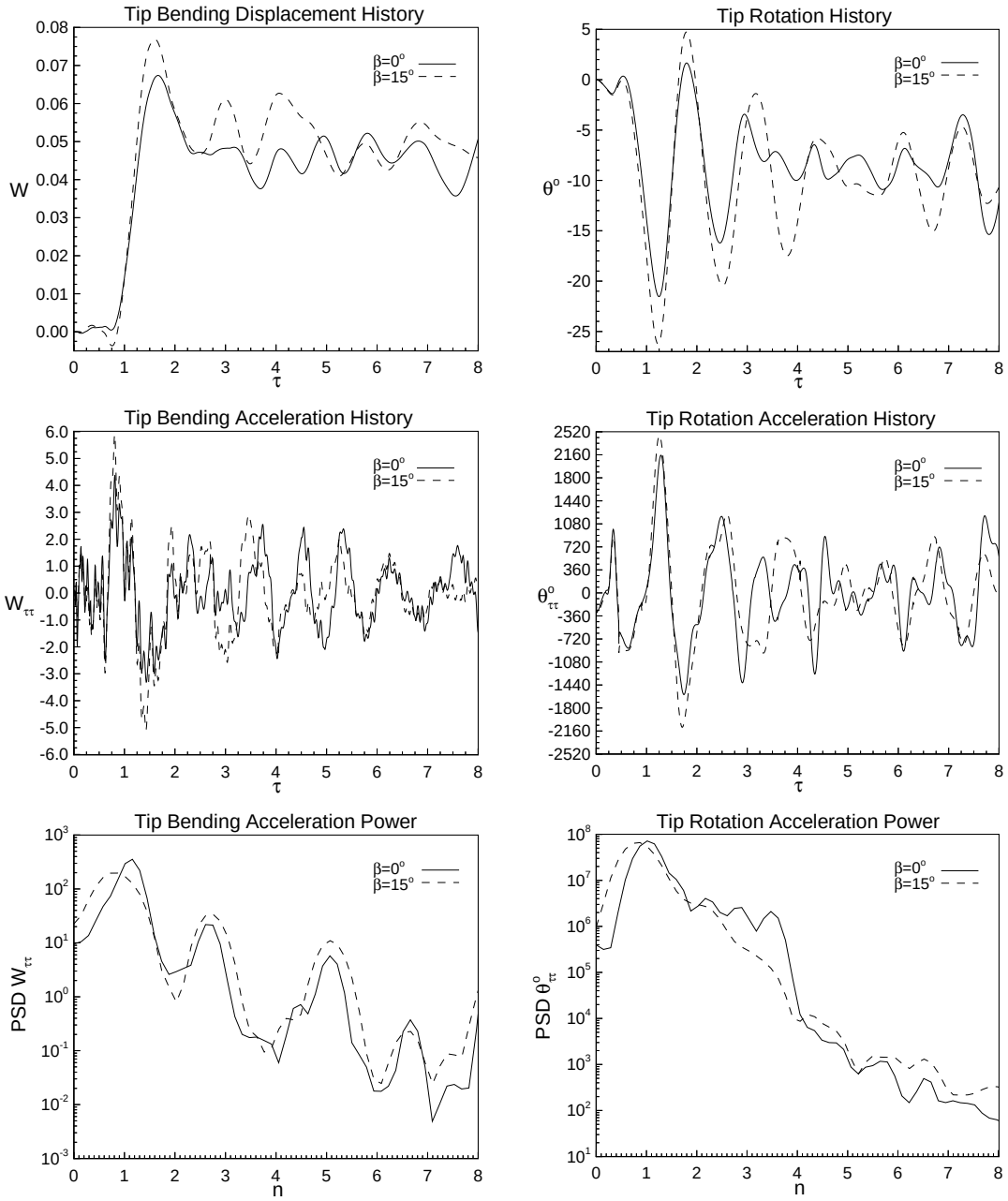

Figure 8.11: Effect of apex flap on time and frequency domain data for right tail tip bending and torsion deflections and accelerations. $\beta_{Flap} = 15^o$, $Re = 1.25 \times 10^6$, $M = 0.3$, $\alpha = 35^o$.

8.4 Summary

In this chapter, the issue of control was addressed. Results were presented for an apex flap deflection scheme which delays the onset of vortex breakdown. The configuration used was the inboard Washburn tail case of the previous chapter, which had the highest level of buffeting for all of the cases studied. The flap was deflected by a single optimum angle which was experimentally [14] found to produce the greatest delay in the onset of breakdown. The flap was found to be very effective in delaying the breakdown, increasing the location from 50%c to 94%c, which resulted in a 6% increase in lift coefficient over the baseline case of $C_L = 1.05$. The effect of the apex flap was mixed in the lumped mean and RMS loads, with the RMS moment loads showing the clearest trend of being up to 30% lower than the undeflected case. Comparison of the area mean and RMS loads, showed that the overall levels are the same with RMS distributions showing the greatest differences in gradients. Differential point pressure histories and point buffet excitation spectra show a dramatic decrease in buffeting for the apex flap case, at around 50% of the baseline case. However, this is only at one location so it does not necessarily represent the whole tail. The integrated buffet load levels are roughly equal between the two cases. Given the favorable change in wing loading from the apex flap, even an unchanged buffet loading is acceptable since additional wing loading may be exchanged for a lower configuration angle-of-attack, which would lower the buffet levels. As with in the root moment data, very little change in the response was observed due to the apex flap deflection. Hence, it is concluded that the apex flap is an efficient and harmless means of delaying vortex bursting and increasing aircraft nose authority without increasing the level of tail buffeting. Furthermore, it is noted that trading the increased lift and pitching moment for a lower angle-of-attack may result in a lower level of vertical tail buffet.

CHAPTER 9

CONCLUSIONS

9.1 Overview

A simulation of tail buffet has been accomplished using several delta wing-vertical tail configurations. Computational applications have provided fundamental insights into the physical and numerical aspects of vortex breakdown induced tail buffet. Favorable comparisons with experimental data indicate that the present aeroelastic method is well suited to providing qualitative insight into tail buffet, as well as, quantitative data for spatially refined, long-duration simulations.

This multi-disciplinary problem was solved sequentially for the flow field, elastic deformations and grid displacements. The flow field was obtained by time accurately solving the laminar, unsteady, compressible, Navier-Stokes equations using an implicit, upwind, flux-difference splitting, finite volume scheme. The elastic vibrations of the tail were modeled by coupled bending and torsion beam equations. These equations were solved accurately in time using the Galerkin method and a five-stage Runge-Kutta-Verner scheme. The grid for the fluid dynamics calculations was continuously deformed using interpolation functions to disperse the displacements smoothly throughout the computational domain. Tail buffet applications included; single tail cases, twin F/A-18 tail cases and twin highly swept generic tail cases. The use of an apex flap for buffet control was also computationally simulated.

In Chapter 1, the motivation and scope of the present research was presented. A survey of the literature on vortex breakdown flows, and the resulting tail buffet problem

was presented in Chapter 2. The review gave a historical perspective of vortical flow research emphasizing early physical observations. The experimental literature was then reviewed focusing on key physical issues of vortical flow. Next, numerical simulations of vortex breakdown and buffet were surveyed. The review concluded with an introduction to vortex breakdown control techniques.

In Chapter 3, the analytical and numerical basis of the fluid dynamics formulation was established. The laminar, unsteady, compressible, Navier-Stokes equations were written in strong conservation form in time-dependent, body-conformed coordinates. The computational scheme was then formulated, as an implicit, upwind, Roe flux-difference splitting, finite volume scheme. Initial and boundary conditions were discussed. Issues regarding single and multiblock CFD gridding were then presented.

In Chapter 4, the analytic and numerical formulation of the structural tail buffet problem was given. The governing equations for coupled bending and torsional vibrations of a beam were obtained using Hamilton's energy principle. The Galerkin method for solving the coupled bending and torsion beam equations was presented. The general solution method employed for sequentially solving coupled sets of fluid, structure and grid equations was then given.

Chapters 5 through 8 contain numerical results for the single and twin tail investigations conducted in this study. In Chapter 5, the fundamental issues of structural inertial coupling, Reynolds number dependence and aeroelastic effects were considered with regard to single vertical tail buffet. For $Re = 10^4$, the tip response for the coupled case was 42% and 80% higher than the uncoupled case, for bending and torsion deflections, respectively. Accelerations also rose by 43% and 31% for bending and torsion, respectively. At $Re = 10^6$, the bending and torsion deflections were 121% and 117%

higher, respectively, and the respective accelerations were 108% and 160% higher. Thus, it is clear that for the single tail configuration inertial coupling increases the tail buffet response. The mechanism for this is the increase in bending due to torsional deflections, which moves the tail further off center, thus increasing the aerodynamics loading due to asymmetry. This effect is amplified in the $Re = 10^6$ due to the decreased aerodynamic damping. The effects of increased Reynolds number on the uncoupled, single tail case loading occurred mainly in the RMS values, which increased by 34% and 17% for root bending and root twisting moments, respectively. The corresponding tip bending and torsion accelerations increased by 37% and 12%, respectively. The increase in RMS loads and accelerations indicates that with rising Re, flow unsteadiness increases while aerodynamic damping decreases. Examination of the frequency domain plots also reveals this trend by the significant increase in high-frequency content. Comparison of the loads calculated from the elastic, uncoupled bending and torsion case with the rigid case at the same Re demonstrated that the large tail deflections contribute significantly to the loading. In addition, the disturbances caused by the large deflections were seen to propagate upstream to influence the breakdown locations.

In Chapter 6, the determination of the effect of aft fuselage geometry on twin F/A-18 vertical tail buffet was addressed. Three fuselage configurations were considered; wide, narrow and open. Secondarily, the effect of the tail response on the loads was accessed for the wide and narrow configurations by comparing the rigid tail loads with the elastic interacting cases. Finally, the effect of decreased tail stiffness was considered for the open fuselage case. It was found that overall, the narrow fuselage case produced the largest buffet loads. Results for the wide and open cases were mixed with the wide case having lower steady loads and higher unsteady loads. Comparison of elastic tail

cases with their corresponding rigid cases for the wide and narrow cases showed that even for very small deflections, the loading can be affected by up to 30% for RMS values. However, the very stiff tails of the wide and narrow cases produced deflections that were an order of magnitude lower than the normal grid spacing, which even with moving grids is too small to produce accurate results. For the open case, dynamically scaled tails were used which produced more realistic deflections of up to 5% tail span and of the same order as the normal grid spacing. To establish the ability of the present simplified configuration to aid in the full aircraft tail buffet design problem, results from the narrow fuselage case were compared to experimental full F/A-18 aircraft results. The ratio between buffet excitation frequency and root bending moment was found to be in good agreement with experimental data. The inside tail loads also matched fairly well. However, overall the results were mixed owing to the fact that the aircraft flow field and the delta wing flow field have many differences. But for the purpose of evaluating tail buffet design modifications, the simple delta wing/tail configuration does share enough of the physics with the full aircraft to be very useful.

In Chapter 7, the effect of spanwise tail location on the tail buffet loading and response was determined using the delta wing/twin vertical tail configuration of Washburn, Jenkins and Ferman [12]. Three spanwise tail positions were considered; corresponding to 33%, 56% and 78% of the wing semi-span. Quantitative results agreed well with the experimental data of Washburn et al. [12]. The inner span location had by far the most severe buffeting in bending and was a close second in torsion to the midspan case. The outer span has the smallest overall loading. It was observed that the spanwise placement of the tails has little effect on the upstream breakdown flow. This is a result of the small span and high sweep of the tails, which minimize contact with the

cores. Comparison of inboard and outboard RMS pressures with the experimental data of Washburn et al. [12] at five stations show that the computations differ from experiment by up to 71%, with other points much closer at around ± 20%. This is likely due to the short physical time in which the computations were run, which degrade all unsteady measurements. The buffet excitation frequencies are typically more robust and show good agreement considering the imprecision of the data and the massive undertaking 3D unsteady CFD is. Finally, root bending coefficients show fair agreement, with the mean values being considerably closer to the experimental data than the RMS values.

In Chapter 8, the issue of control was addressed. Results were presented for an apex flap deflection scheme which delays the onset of vortex breakdown. The configuration used is the inboard Washburn tail case of Chapter 7, which had the highest level of buffeting for all of the cases studied. The flap was deflected by a single optimum angle which was experimentally [14] found to produce the greatest delay in the onset of breakdown. The flap was found to be very effective in delaying the breakdown, increasing the location from 50%c to 94%c, which resulted in a 6% increase in lift coefficient and pitching moment. However, the integrated buffet loads and tip responses were roughly equivalent for the two cases. Given the favorable change in wing loading from the apex flap, even an unchanged buffet loading is acceptable since additional wing loading may be exchanged for a lower configuration angle-of-attack, which would lower the buffet levels. Hence, it is concluded that the apex flap is an efficient and harmless means of delaying vortex bursting and increasing aircraft nose authority without increasing the level of tail buffet. Furthermore, it is noted that trading the increased lift and pitching moment for a lower angle-of-attack may result in a lower level of vertical tail buffet.

9.2 Recommendations for Future Research

The advantage of numerical modeling over wind tunnel experimentation is the ability to easily incorporate a wide variety of active and passive control solutions, such as suction or blowing and/or control surface deflections. Moreover, it is still less expensive to perform these studies computationally than experimentally. With the development of a simple numerical model of vortex breakdown induced tail buffet complete, the time has come to look forward to a more mature structural model. However, the elegance and simplicity of the robust natural vortex-breakdown flow over the delta wing need not be exchanged for a full aircraft yet. At this stage, there are still many basic problems to solve. Thus, the key areas in which future research is recommended are as follows:

- The implementation of more accurate structural models, such as those provided by plate equations or finite element methods.
- The implementation of *active* controls on the wing to delay or diffuse the vortex breakdown flow.
- The addition of *active* control surfaces on the tail to dampen the buffet response.
- The implementation of fully dynamic grids to simulate and control tail buffeting during simulated flight maneuvers.
- Full aircraft simulations to test specific control solutions developed using the simple delta wing model.

REFERENCES

[1] NASA Dryden WWW Page, `http://www.dfrc.nasa.gov`.

[2] Werlé, H., "Sur l' éclatement des tourbillions d'apex d'une aile delta aux faibles vitesses," *La Recherche Aéronautique*, Vol. 74, January/February 1960, pp. 23–30.

[3] Lambourne, N. and Bryer, D., "The Bursting of Leading-Edge Vortices-Some Observations and Discussion of the Phenomenon," R. and M. No. 3282, Aerodynamics Division, National Physical Laboratory, London, England, April 1961.

[4] Sarpkaya, T., "On Stationary and Travelling Vortex Breakdowns," *Journal of Fluid Mechanics*, Vol. 45, No. 3, 1971, pp. 545–559.

[5] Globus, A., Levit, C., and Lasinski, T., "A Tool for Visualizing the Topology of Three-Dimensional Vector Fields," Report RNR-91-017, NASA ARC, 1992.

[6] Délery, J. M., "Physics of Vortical Flows," *Journal of Aircraft*, Vol. 29, No. 5, Sept.-Oct. 1992, pp. 856–876, See also AGARD/NATO "Vortex Flow Aerodynamics," CP 494.

[7] Werlé, H., *Houille Blanche*, Vol. 18, 1963, pp. 587–595.

[8] Lee, B. and Valerio, N., "Vortical Flow Structure near the F/A-18 LEX at High Incidence," *Journal of Aircraft*, Vol. 31, No. 5, 1994, pp. 1221–1223.

[9] Cabral, B. and Leedom, L. C., "Imaging Vector Fields Using Line Integral Convolution," *Computer Graphics (SIGGRAPH '93 Proceedings)*, edited by J. T. Kajiya, Vol. 27, Aug. 1993, pp. 263–272.

[10] Hummel, D., "On the Vortex Formation Over a Slender Wing at Large Angles of Incidence," CP No. 247, AGARD, 1979.

[11] Hummel, D. and Srinivasan, P., "Vortex Breakdown Effects on the Low-Speed Aerodynamic Characteristics of Slender Delta Wings in Symmetrical Flow," *Journal of Royal Aeronautical Society*, Vol. 71, 1966, pp. 319–322.

[12] Washburn, A. E., Jenkins, L. N., and Ferman, M. A., "Experimental Investigation of Vortex-Fin Interaction," AIAA CP 93-0050, Jan. 1993.

[13] Fisher, D. F. and Meyer, Jr., R. R., "Flow Visualization Techniques for Flight Research," NASA TM 100455, 1988.

[14] Klute, S. M., Martin, R. A., Rediniotis, O. K., and Telionis, D. P., "Flow Control Over Delta Wings at High Angles of Attack," AIAA CP 93-3494, 1993.

[15] Newsome, R. and Kandil, O., "Vortical Flow Aerodynamics - Physical Aspects and Numerical Simulation," AIAA CP 87-0205, 1987.

[16] Escudier, M., "Vortex Breakdown: Observations and Explanations," *Progress in Aerospace Sciences*, Vol. 25, No. 2, 1988, pp. 189–229.

[17] Rockwell, D., "Three-Dimensional Flow Structure on Delta Wings at High Angle-of-Attack: Experimental and Computational Issues," AIAA CP 93-0550, 1993.

[18] Polhamus, E., "Vortex Lift Research: Early Contributions and Some Current Challenges," N86-27191, NASA, October 1985.

[19] Ludwieg, H., "Sweptback Wings at High Velocities (Preliminary Results)," Translation Report No. R-30-18, Part 7, Goodyear Aircraft Corp., August 1970.

[20] Busemann, A., "Aerodynamic Forces at Supersonic Speeds," Luftfahrtforschung, Bd 12, Nr 6, October 1935.

[21] Wilson, H. and Lovell, J., "Full-Scale Investigation of the Maximum Lift Flow Characteristics of an Airplane Having Approximately Triangular Planform," RM L6K20, NACA, November 1946.

[22] Peckham, D. and Atkinson, S., "Preliminary Results of Low Speed Wind Tunnel Test on a Gothic Wing of Aspect Ratio 1.0," CP-508, Aeronautical Research Council, August 1957.

[23] Elle, B., "An Investigation at Low Speed of the Flow Near the Apex of Thin Delta Wings with Sharp Leading Edges," 19,780-Perf. 1621-F.M. 2629, Aeronautical Research Council, January 1958.

[24] Elle, B., "On the breakdown at High Incidences of the Leading Edge Vortices on Delta Wings," *Journal of the Royal Aeronautical Society*, Vol. 64, August 1960, pp. 491–493.

[25] Squire, H., "Analysis of the Vortex Breakdown Phenomenon. Part I," Report No. 102, Imperial College of Science and Technology, Aeronautics Department, August 1962.

[26] Harvey, J., "Some Observations of the Vortex Breakdown," *Journal of the Royal Aeronautical Society*, Vol. 68, May 1962, pp. 343–346.

[27] Benjamin, T., "Theory of the Vortex Breakdown Phenomenon," *Journal of Fluid Mechanics*, Vol. 14, No. 4, 1962, pp. 593–629.

[28] Benjamin, T., "Some Developments in the Theory of the Vortex Breakdown," *Journal of Fluid Mechanics*, Vol. 28, No. 1, 1967, pp. 65–84.

[29] Leibovich, S., "Vortex Stability and Breakdown: Survey and Extension," *AIAA Journal*, Vol. 22, No. 9, 1984, pp. 1817–1824.

[30] Sarpkaya, T., "Effect of the Adverse Pressure Gradient on Vortex Breakdown," *AIAA Journal*, Vol. 12, No. 5, May 1974, pp. 602–607.

[31] Sarpkaya, T., "Vortex Breakdown in Swirling Conical Flows," *AIAA Journal*, Vol. 9, No. 9, September 1971, pp. 1791–1799.

[32] Kirkpatrick, D., "Experimental Investigation of the Breakdown of a Vortex in a Tube," Technical Note No. 2963, Royal Aircraft Establishment, 1965.

[33] Faler, J. and Leibovich, S., "Disrupted States of Vortex Flow and Vortex Breakdown," *Physics of Fluids*, Vol. 20, No. 9, 1977, pp. 1385–1400.

[34] Escudier, M. and Zehnder, N., "Vortex Flow Regimes," *Journal of Fluid Mechanics*, Vol. 115, 1982, pp. 105–121.

[35] Escudier, M. and Keller, J., "Vortex Breakdown: A Two State Transition," CP No. 342, AGARD, April 1983, Paper No. 25., Aerodynamics in Three Dimensions.

[36] Tobak, M. and Peake, D., "Topology of Three-Dimensional Flow Separation," *Annual Review of Fluid Mechanics*, Vol. 14, 1982, pp. 61–85.

[37] Levit, C., "Visualizing the Topology of Vector Fields: An Annotated Bibliography," Report RNR-92-032, NASA ARC, Nov. 1992.

[38] Gartshore, I., "Recent Work in Swirling Incompressible Flow," Report LR-343 No. 6968, National Research Council of Canada, 1962.

[39] Spall, R., *A Numerical Study of Three-Dimensional Vortex Breakdown*, Ph.D. Dissertation, Dept. of Mechanical Engineering and Mechanics, Old Dominion University, Norfolk, VA, May 1987.

[40] Kandil, O., Kandil, H., and Liu, C., "Computation of Steady and Unsteady Compressible Quasi-Axisymmetric Vortex Flow and Breakdown," AIAA CP 91-0752, January 1991.

[41] Kandil, O., Kandil, H., and Liu, C., "Supersonic Quasi-Axisymmetric Vortex Breakdown," AIAA CP 91-3311, September 1991.

[42] Kandil, O., Kandil, H., and Liu, C., "Critical Effects of Downstream Boundary Conditions on Vortex Breakdown," AIAA CP 92-2601, June 1992.

[43] Kandil, O., Kandil, H., and Liu, C., "Shock/Vortex Interaction and Vortex Breakdown Modes," *IUTAM Symposium of Fluid Dynamics of High Angle of Attack*, No. T.1.3, Tokyo, Japan, September 1992.

[44] Kandil, H. A., *Navier-Stokes Simulation of Quasi-Axisymmetric and Three-Dimensional Supersonic Vortex Breakdown*, Ph.D. Dissertation, Dept. of Mechanical Engineering and Mechanics, Old Dominion University, Norfolk, VA, May 1993.

[45] Taylor, S., Kjelgaard, S., Weston, J., Thomas, W., and Sellers, W., "Experimental and Computational Study of the Subsonic Flow About a 75^o Swept Delta Wing," AIAA CP 87-2425, 1987.

[46] Gordnier, R. and Visbal, M., "Numerical Simulation of the Unsteady Vortex Structure Over a Delta Wing," AIAA CP 91-1811, 1991.

[47] Webster, W. and Shang, J., "Numerical Simulation of Vortex Breakdown Over a Delta Wing," AIAA CP 91-1814, 1991.

[48] Kandil, O., Kandil, H., and Liu, C., "Shock-Vortex Interaction Over a 65^o Delta Wing in Transonic Flow," AIAA CP 93-2973, 1993.

[49] Rizk, Y., Schiff, L., and Gee, K., "Numerical Simulation of the Viscous Flow Around a Simplified F/A-18 at High Angles of Attack," AIAA CP 90-2999, 1990.

[50] Ekaterinaris, J. and Schiff, L. B., "Numerical Simulation of Incidence and Sweep Effects on Delta Wing Vortex Breakdown," *Journal of Aircraft*, Vol. 31, No. 5, 1994, pp. 1043–1049.

[51] Rizzetta, D., "Numerical Simulation of the Interaction between a Leading-Edge Vortex and a Vertical Tail," AIAA CP 96-2012, June 1996.

[52] Anon., "Technical Report by the Accident Investigation Subcommittee on the Accident to the Aeroplane G-AAZK at Meopham, Kent (England), on 21 July 1930," Reports and Memoranda No. 1360, Aeronautical Research Council, 1931.

[53] White, J. and Hood, M., "Wing-Fuselage Interference, Tail Buffeting and Air Flow About the Tail of a Low-Wing Monoplane," Technical Report No. 482, NACA, 1934.

[54] Abdrashitov, G., "Tail Buffeting," Report No. 395; NACA TM-1041, Central Aero-Hydrodynamical Institute, Moscow, 1935; 1943.

[55] Triplett, W., "Pressure Measurements on Twin Vertical Tails in Buffeting Flow," *Journal of Aircraft*, Vol. 20, No. 1, 1983, pp. 920–925.

[56] Fisher, D., Del Frate, J., and Richwine, D., "In-Flight Visualization Characteristics of the NASA F-18 High Alpha Research Vehicle at High Angles of Attack," SAE 892222, September 1989.

[57] Erickson, G., Hall, R., Banks, D., Frate, D., J.H., Schreiner, J., Hanley, R., and Pulley, C., "Experimental Investigation of the F/A-18 Vortex Flows at Subsonic Through Transonic Speeds," AIAA CP 89-2222, 1989.

[58] Lee, B. and Brown, D., "Wind Tunnel Studies of F/A-18 Tail Buffet," AIAA CP 90-1432, 1990.

[59] Cole, S., Moss, S., and Doggett, Jr., R., "Some Buffet Response Characteristics of a Twin-Vertical-Tail Configuration," NASA TM 102749, 1990.

[60] Moses, R. W. and Pendleton, E., "A Comparison of Pressure Measurments Between a Full-Scale and a 1/6-Scale F/A-18 Twin Tail During Buffet," Technical Memorandum 110282, NASA LaRC, August 1996.

[61] Edwards, J., "Assessment of Computational Prediction of Tail Buffeting," Technical Memorandum 101613, NASA LaRC, January 1990.

[62] Rizk, Y., Guruswamy, G., and Gee, K., "Numerical Investigation of Tail Buffet on F-18 Aircraft," AIAA CP 92-2673, 1992.

[63] Rizk, Y., Guruswamy, G., and Gee, K., "Computational Study of F-18 Vortex Induced Tail Buffet," AIAA CP 92-4699, 1992.

[64] Gee, K., Murman, S., and Schiff, L., "Computational Study of F-18 Vortex Induced Tail Buffet," AIAA CP 95-3440, 1995.

[65] Krist, S., Washburn, A., and Visser, K., "A Computational and Experimental Investigation of a Delta Wing with Vertical Tails," AIAA CP 93-3009, July 1993.

[66] Findlay, D., "Numerical Analysis of Vertical Tail Buffet," AIAA CP 97-0621, January 1997.

[67] Kandil, O., Kandil, H., and Massey, S., "Simulation of Tail Buffet Using Delta Wing-Vertical Tail Configuration," AIAA CP 93-3688, August 1993.

[68] Kandil, O. and Flanagan, M., "Vertical Tail Buffet in Vortex Breakdown Flows," August 1993, In proceedings of the 5th International Symposium on Computational Fluid Dynamics, Sendai, Japan.

[69] Flanagan, M., *Simulation of Vertical Tail Buffet in Internal Vortex Breakdown Flows*, Master's Thesis, Dept. of Aerospace Engineering, Old Dominion University, Norfolk, VA, December 1993.

[70] Kandil, O., Massey, S., and Kandil, H., "Computations of Vortex-Breakdown Induced Tail Buffet Undergoing Bending and Torsional Vibrations," AIAA CP 94-1428, 1994.

[71] Massey, S. J., *Direct Numerical Simulation of Vortex Breakdown Induced Tail Buffet*, Master's Thesis, Dept. of Aerospace Engineering, Old Dominion University, Norfolk, VA, May 1994.

[72] Kandil, O., Massey, S., and Sheta, E., "Structural Dynamic / CFD Interaction for Computation of Vertical Tail Buffet," Royal Aeronautical Society Paper No 16.52, June 1995.

[73] Kandil, O., Sheta, E., and Massey, S., "Buffet Responses of a Vertical Tail in Vortex Breakdown Flows," AIAA CP 95-3464, August 1995.

[74] Kandil, O., Sheta, E., and Massey, S., "Twin Tail / Delta Wing Configuration Buffet Due to Unsteady Vortex Breakdown Flow," AIAA CP 96-2517, June 1996.

[75] Kandil, O., Massey, S., and Sheta, E., "Aerostructural Vortical Flow Interactions with Applications to F/A-18 and F-117 Tail Buffet," September 1996.

[76] Kandil, O., Kandil, H., and Liu, C., "Three-Dimensional Supersonic Vortex Breakdown," AIAA CP 93-0526, January 1993.

[77] El-Din, H. S., *Simulation of Active Control of Asymmetric Flows Around Slender Pointed Forebodies*, Ph.D. Dissertation, Dept. of Aerospace Engineering, Old Dominion University, Norfolk, VA, December 1994.

[78] Malcolm, G. N., "Forebody Vortex Control - A Progress Review," AIAA CP 93-3540, 1993.

[79] Lee, B., Brown, D., Zgela, M., and Poirel, D., "Wind Tunnel Investigation of Tail Buffet on the F-18 Aircraft," *AGARD Conference Proceedings No. 483, Paper 1*, 1990.

[80] Meyn, L. A. and James, K. D., "Full Scale Wind Tunnel Studies of F/A-18 Tail Buffet," AIAA CP 93-3519, 1993.

[81] Pettit, C. L., Brown, D., and Pendleton, E., "Wind Tunnel Test of Full-Scale F/A-18 Twin Tail Buffet: A Summary of Pressure and Response Measurements," AIAA CP 94-3476, 1994.

[82] Shah, G. H., "Wind-Tunnel Investigation of Aerodynamic and Tail Buffet Characteristics of Leading-Edge Extension Modifications to the F/A-18," AIAA CP 91-2889, August 1991.

[83] Hauch, R., Jacobs, J., Ravindra, K., and Dima, C., "Reduction of Vertical Tail Buffet Response Using Active Control," AIAA CP 95-1080, 1995.

[84] Roe, P. L., "Approximate Riemann Solvers, Parameter Vectors, and Difference Schemes," *Journal of Computational Physics*, Vol. 43, October 1981, pp. 357–372.

[85] Krist, S. L., Biedron, R. T., and Rumsey, C. L., *CFL3D User's Manual (Version 5.0)*, Aerodynamics and Acoustic Methods Branch, NASA-Langley Research Center, Hampton, VA, 1st ed., November 1996.

[86] Walters, R. and Thomas, J., "Advances in Upwind Relaxation Methods," *State-of-the-Art Surveys on Computational Mechanics*, edited by A. Noor and J. Oden, ASME, New York, 1989, pp. 145–183.

[87] Beam, R. and Warming, R., "An Implicit Factored Scheme for the Compressible Navier-Stokes Equations," *AIAA Journal*, Vol. 16, No. 4, 1978, pp. 398–402.

[88] Godunov, S., "A Difference Scheme for Numerical Computation of Discontinous Solution of Hydrodynamic Equations," *Math. Sbornik*, Vol. 47, 1959, pp. 271–306, (in Russian).

[89] Hirsch, C., *Numerical Computation of Internal and External Flows*, Vol. 2, Wiley, New York, 1990.

[90] Vatsa, V., Thomas, J., and van Leer, B., "Navier-Stokes Computations of Prolate Spheroids at Angle-of-Attack," AIAA CP 87-2627, August 1987.

[91] Owen, T., "Techniques of Pressure Fluctuation Measurements Employed in RAE Low Speed Wind Tunnels," Report AGARD-R-172, 1958.

[92] Mabey, D., "Some Aspects of Aircraft Dynamic Loads due to Flow Separation," Report AGARD-R-750, October 1987.

[93] Meyn, L., James, K., and Geenen, R., "Correlation of F/A-18 Tail Buffet Results," July 1994, In Proceedings of the 4th High-Alpha Projects and Technology Conference, Dryden Flight Research Center.

[94] James, K. and Meyn, L., "Dependence of Integrated Vertical-Tail Buffet Loads for F/A-18 on Sensor Density," SAE 941140, April 1994.

VITA

Steven James Massey was born in Newport News, Virginia, on May 3, 1967, the son of Marlin and Barbara Massey. His interest in engineering and computers developed at a young age and was cheerfully encouraged by his parents. His programming experience began with a borrowed Radio Shack TRS-80 in 1981. The following year, his parents bought him an Apple II+ and he has been staring at pixels ever since. In May 1990, he graduated from Virginia Polytechnic Institute & State University, with a Bachelor of Science in Aerospace Engineering and a minor in Mathematics. He began full-time graduate study in the Department of Mechanical Engineering and Mechanics at Old Dominion University in January 1992 and received his Master of Science in Engineering Mechanics in May 1994. After graduation, he continued his research with Prof. Kandil in the newly formed Department of Aerospace Engineering. Since July 1997, he has been working for Analytical Services & Materials, Inc. at their NASA Dryden location. He now lives in Palmdale, California, with his wife of seven years, Lisa, and they are expecting their first child in July 1998.